REPAIR AND STRENGTHENING OF PRE-1970 REINFORCED CONCRETE CORNER BEAM-COLUMN JOINTS USING CFRP COMPOSITES

A Dissertation
Presented to
The Academic Faculty

by

Murat Engindeniz

In Partial Fulfillment
Of the Requirements for the Degree
Doctor of Philosophy in the
School of Civil and Environmental Engineering

Georgia Institute of Technology
August 2008

REPAIR AND STRENGTHENING OF PRE-1970 REINFORCED CONCRETE CORNER BEAM-COLUMN JOINTS USING CFRP COMPOSITES

Approved by:

Dr. Abdul-Hamid Zureick, Co-advisor
School of Civil and Environmental Engineering
Georgia Institute of Technology

Dr. Lawrence F. Kahn, Co-advisor
School of Civil and Environmental Engineering
Georgia Institute of Technology

Dr. Roberto T. Leon
School of Civil and Environmental Engineering
Georgia Institute of Technology

Dr. Erian A. Armanios
School of Aerospace Engineering
Georgia Institute of Technology

Dr. Russell T. Gentry
College of Architecture
Georgia Institute of Technology

Date Approved: April 24, 2008

ACKNOWLEDGEMENTS

The author is grateful to his advisors Dr. Abdul-Hamid Zureick and Dr. Lawrence F. Kahn for giving him the opportunity to develop this project and for providing him with the guidance, technical expertise, and financial support that made this project possible.

Thanks are also due to the thesis committee members Dr. Roberto T. Leon, Dr. Erian A. Armanios, and Dr. Russell T. Gentry for their time and suggestions.

This research was funded in part by the School of Civil and Environmental Engineering at Georgia Tech and in part by the private industry. Materials and services donated by Sika, LaFarge, Thomas Concrete, Gerdau Ameristeel, Engineered Restorations, and Precision Concrete are thankfully acknowledged. Special thanks are extended to the President of ICRI Georgia Chapter, Mr. Ron Thomas for mobilizing much of the donations during the retrofit stage. The opinions, conclusions, and recommendations presented herein are those of the author and do not necessarily represent the opinions and recommendations of the cooperating organizations.

All experiments were conducted at Georgia Tech Structures Laboratory. The required physical labor could not have been handled by the author without the help of the facility manager Jeremy Mitchell; former research engineer Marcus Millard; fellow graduate students Victor Garas, Kennan Crane, Jonathan Hurff; former fellow graduate student John Bunyasaranand and now Drs. Mauricio Lopez and Jason McCormick; former undergraduate assistant Cliff Bishop; and numerous other students who gave a hand with various parts of the project. Their time and efforts are sincerely appreciated.

Last but not least, the author cannot overstate his gratefulness to his parents Müjgan and Ali Engindeniz, his sisters Özen Engindeniz and Özlem Çulhan, his brother-in-law Erhan Çulhan, his nephew Bora Çulhan, and his girlfriend Berrin Doğusoy for their loving support, encouragement, and patience. Their love, in which the author did

and will find the strength to get through difficult times, was always felt even from thousands of miles away. This thesis is dedicated to them.

TABLE OF CONTENTS

LIST OF TABLES

LIST OF FIGURES

LIST OF SYMBOLS AND ABBREVIATIONS

A	Cross-sectional area of steel tubes in reaction frame atop column
$[A]$	Extensional stiffness matrix of CFRP laminate
A_{ch}	Area of column core enclosed by outside perimeter of transverse reinforcement
A_{cp}	Total area of beam cross-section including effective flange width
A_{fv}	Area of CFRP shear reinforcement
A_g	Gross area of column cross-section
A_o	Area enclosed by the shear flow path
A_{oh}	Area enclosed by beam stirrups
A_s	Area of tension steel reinforcement
A_{sh}	Total cross-sectional area of steel hoop reinforcement
A_t	Area of steel transverse reinforcement for torsion
A_v	Area of steel transverse reinforcement for shear
C	Calibration constant for Wheatstone bridges
C_{b1}	Resultant compressive force in EW beam at beam-joint interface
C_{b2}	Resultant compressive force in NS beam at beam-joint interface
C_E	Environmental reduction factor
C_{lc}	Resultant compressive force in lower column at column-joint interface
C_{s1}	Total compressive force at EW beam-slab interface
C_{s2}	Total compressive force at NS beam-slab interface
C_{uc}	Resultant compressive force in upper column at column-joint interface

DL	Service dead load
E_c	Elastic modulus of concrete
E_{CFRP}	Elastic modulus of CFRP
E_f	Elastic modulus of carbon fiber
E_m	Elastic modulus of epoxy resin
E_s	Elastic modulus of steel
E_x	Longitudinal elastic modulus of CFRP laminate
E_y	Transverse elastic modulus of CFRP laminate
E_{11}	Longitudinal elastic modulus of unidirectional CFRP lamina
E_{22}	Transverse elastic modulus of unidirectional CFRP lamina
E^i	Hysteretic energy dissipated in i^{th} cycle
E^{tot}	Cumulative dissipated hysteretic energy
$(EI)_{lc}$	Bending rigidity of lower column
$(EI)_{uc}$	Bending rigidity of upper column
G_c	Shear modulus of concrete
G_f	Shear modulus of carbon fiber
G_m	Shear modulus of epoxy resin
G_{xy}	Shear modulus of CFRP laminate
G_{12}	Shear modulus of unidirectional CFRP lamina
K_a	Confinement effectiveness coefficient for CFRP
K_e	Confinement effectiveness coefficient for steel hoop reinforcement
K_p	Peak-to-peak hysteretic stiffness

L	Clear span length of beam in actual frame [$= 2L_b$]
L'	Span length of beam in actual frame measured from column centerlines [$= 2L_b'$]
L_b	Beam length measured from column face to loading point
L_b'	Beam length measured from column centerline to loading point
L_c	Clear height of the column in actual frame
L_{lc}	Clear length of lower column
L_{lc}'	Length of lower column measured from beam centerline considering beam effective flange width
L_{uc}	Clear length of upper column
L_{uc}'	Length of upper column measured from beam centerline considering beam effective flange width
L_i	Gage length of i^{th} LVDT in joint panels
L_u	Length of U-wrapped portion of beams
LL	Service live load
M_{cr}^+	Cracking moment of beams for positive strong-axis bending
M_n^+	Positive moment capacity of beams for strong-axis bending
M_n^-	Negative moment capacity of beams for strong-axis bending
M_{x1}	Torsional moment in EW beam at beam-joint interface
M_{x2}	Torsional moment in NS beam at beam-joint interface
M_{y1}	Weak-axis bending moment in EW beam at beam-joint interface
M_{y2}	Weak-axis bending moment in NS beam at beam-joint interface
M_z	Strong-axis beam bending moment

M_{z1}	Strong-axis bending moment in EW beam at beam-joint interface
M_{z2}	Strong-axis bending moment in NS beam at beam-joint interface
$N_i \quad (i = 1,2,3,4)$	Axial forces on sides of beam in space truss analogy
P	Load applied at end of beam
P_b	Balanced column axial load
P_{col}	Applied column axial load
P_{EW}	Load applied at end of EW beam
$P_{l.col}$	Axial load in lower column [$= P_{col} \pm (P_{EW} + P_{NS})$]
$- P_{max}$	Beam end load at downward peak of a loading cycle
$+ P_{max}$	Beam end load at upward peak of a loading cycle
P_{NS}	Load applied at end of NS beam
P_o	Compressive load capacity of column
P_t	Force in steel tubes in reaction frame atop column
$P_{u.col}$	Axial load in upper column [$= P_{col}$]
P_u^{CFRP}	Load capacity per layer per inch width of CFRP sheets
S_g	Gage factor of strain gages used in Wheatstone bridges
T	Applied torsional moment
T_b	Total normal tensile force applied to joint at beam-joint interface
T_{b1}	Resultant tensile force in EW beam at beam-joint interface
T_{b2}	Resultant tensile force in NS beam at beam-joint interface
T_g	Glass-transition temperature of impregnating resin (epoxy)
T_{lc}	Resultant tensile force in lower column at column-joint interface

T_n	Torsional moment capacity
T_{s1}	Tensile force in NS slab bars
T_{s1}^{top}	Tensile force in NS slab top bars
T_{s1}^{bot}	Tensile force in NS slab bottom bars
T_{s2}	Tensile force in EW slab bars
T_{s2}^{top}	Tensile force in EW slab top bars
T_{s2}^{bot}	Tensile force in EW slab bottom bars
T_{s2}^{*}	Part of tensile force in EW slab bars transferred to joint
T_t^{top}	Total tensile force induced in beam top bars due to torsion
T_t^{bot}	Total tensile force induced in beam bottom bars due to torsion
T_u	Total factored torsional moment
T_{uc}	Resultant tensile force in upper column at column-joint interface
V_{b1}^{h}	Horizontal shear force at EW beam-joint interface
V_{b1}^{v}	Vertical shear force at EW beam-joint interface
V_{b2}^{h}	Horizontal shear force at NS beam-joint interface
V_{b2}^{h*}	Horizontal shear force carried by upper half of NS beam-joint interface
V_{b2}^{v}	Vertical shear force at NS beam-joint interface
V_c	Shear strength provided by concrete
V_{CFRP}	CFRP contribution to joint shear force capacity
V_{col}	Column shear force

V_{col}^{EW} Column shear force in EW direction

V_{col}^{NS} Column shear force in NS direction

$\left(V_{col}^{b}\right)_{max}$ Maximum bidirectional column shear force $\left[=\left(\sqrt{\left(V_{col}^{EW}\right)^2+\left(V_{col}^{NS}\right)^2}\right)_{max}\right]$

$\left(V_{col}^{EW}\right)_{max}$ Maximum column shear force measured in EW direction

$\left(V_{col}^{NS}\right)_{max}$ Maximum column shear force measured in NS direction

V_f Fiber volume ratio of CFRP

$V_i \quad (i = 1,2,3,4)$ Shear forces along sides of beam in space truss analogy

V_{in} Input voltage applied to Wheatstone bridges

V_{jh} Horizontal joint shear force

V_{jh}^{EW} Horizontal joint shear force in EW direction

V_{jh}^{max} Horizontal joint shear force corresponding to yielding of all beam top bars

V_{jh}^{sg} Horizontal joint shear force obtained by using strain gage data

$\left(V_{jh}^{t}\right)_1$ Increase in joint shear force due to torsion on longitudinal beam

$\left(V_{jh}^{t}\right)_2$ Increase in joint shear force due to torsion on transverse beam

V_m Resin volume ratio of CFRP

V_{max} Maximum beam vertical shear force estimated based on negative moment capacity

V_n Shear force capacity

V_{out} Output voltage from Wheatstone bridges

V_s Shear strength provided by steel transverse reinforcement

V_{s1}^{h}	Horizontal shear force at EW beam-slab interface
V_{s1}^{v}	Vertical shear force at EW beam-slab interface
V_{s2}^{h}	Horizontal shear force at NS beam-slab interface
V_{s2}^{v}	Vertical shear force at NS beam-slab interface
V_v	Void volume ratio of CFRP
W_f	Fiber weight ratio of CFRP
W_m	Resin weight ratio of CFRP
a	Vertical distance from beam top and bottom surfaces to potentiometers used for monitoring joint global rotation
$[a]$	Elastic compliance matrix of CFRP laminate
b	Vertical distance from beam top and bottom surfaces to potentiometers used for monitoring beam concentrated rotation
b_c	Column width
b_e	Effective overhanging flange width of beams
b_j	Joint effective width
b_w	Beam width
b_ϕ	Horizontal distance between potentiometers used for monitoring beam twist
d	Beam effective depth for strong-axis bending
d_b	Reinforcing bar diameter
d_b^{long}	Diameter of column longitudinal bars confined with steel hoop reinforcement
d_c	Column effective depth
d_f	Depth of CFRP shear reinforcement

$f_c^{'}$	Compressive strength of concrete
$f_{cc}^{'}$	Compressive strength of confined concrete
f_{fe}^{CFRP}	Maximum effective stress of CFRP
f_l	Confining pressure provided by steel hoop reinforcements or CFRP wraps
f_y	Lower yield (plateau) stress of reinforcing bars
$f_y^{'}$	Upper yield stress of reinforcing bars
f_u	Ultimate stress of reinforcing bars
$f_u^{'}$	Stress in reinforcing bars at break
h_b	Beam depth
h_c	Column width
h_j	Height of joint panel
h_{s1}^{top}	Distance from the NS slab top bars to beam mid-depth
h_{s1}^{bot}	Distance from the NS slab bottom bars to beam mid-depth
h_{s1}^{c}	Distance from compression resultant at EW beam-slab interface to beam mid-depth
h_{s2}^{c}	Distance from compression resultant at NS beam-slab interface to beam mid-depth
h_{s2}^{top}	Distance from EW slab top bars to beam mid-depth
h_{s2}^{bot}	Distance from EW slab bottom bars to beam mid-depth
h_w	Height of CFRP-wrapped portion of columns
h_x	Horizontal spacing of crossties or legs of overlapping hoops

h_1, h_2	Geometrical parameters used in determining beam displacements caused by joint shear deformation (Figure D.1)
jd	Internal moment arm between tension and compression resultants during strong-axis bending of beams
l_d	Development length of reinforcing bar
l_{df}	Development length of CFRP
l_{dh}	Horizontal development length of reinforcing bars with standard hooks
l_{ls}	Lap-splice length of column longitudinal bars
n	Number of CFRP layers for which development is calculated
n_f	Number of layers of CFRP shear reinforcement
n_{jh}	Number of layers of horizontal CFRP sheets used for joint shear strengthening
n_s	Number of layers of CFRP strips used for improving beam positive moment capacity
n_w	Number of layers of CFRP column wraps
p_{cp}	Perimeter of beam cross-section including effective flange width
r	Radius of edges of column section to be wrapped
s	Spacing of column or beam transverse reinforcement
s_f	Spacing of CFRP shear reinforcement
t	Thickness per layer of CFRP
t_l	Total thickness of CFRP laminate
t_s	Slab thickness
w	Factored service gravity load [$= 1.0DL + 0.25LL$]
w_c	Unit weight of concrete
w_e	Width of cracks in beam bottom bar embedment region

w_f	Width of CFRP shear reinforcement
w_j	Width of joint shear cracks
w_s	Width of CFRP strips used for improving beam positive moment capacity
w_{uc}	Width of cracks in upper column lap-splice region
x	Difference between readings of potentiometers used for monitoring joint global rotation
x_o	Width of beam reinforcement cage
x_1, x_2	Geometrical parameters used in determining beam displacements caused by combined joint shear deformation and total column rotation (Figure D.2)
y	Difference between readings of potentiometers used for monitoring beam concentrated rotation
y_o	Height of beam reinforcement cage
y_1, y_2	Geometrical parameters used in determining beam displacements caused by beam concentrated rotation (Figure D.3)
z	Difference between readings of potentiometers used for monitoring beam twist
Δ_b	Displacement applied at beam loaded ends
Δ^{be}	Beam end displacement caused by beam elastic deformations
Δ^{ce}	Beam end displacement caused by column elastic deformations
Δ^{bj}	Beam end displacement caused by beam concentrated rotations
Δ^{cj}	Beam end displacement caused by column concentrated rotations
Δ^{js}	Beam end displacement caused by joint shear deformations
Δ_y	Beam end displacement at first yield
ΔL_i	Measured change in gage length of i^{th} LVDT in joint panels
$\sum M_c / \sum M_b$	Column-to-beam flexural strength ratio
α	Angle of inclination of CFRP shear reinforcement

φ	Angle of an arbitrary direction measured counterclockwise from horizontal axis at which strain is to be determined
γ	Joint shear strength factor
γ_s	Average joint shear strain
$(\gamma_s)_{max}$	Maximum average joint shear strain
γ_{xz}	Joint shear strain
$(\gamma_{xz})_i$	i^{th} estimate of joint shear strain
γ_1	Horizontal component of average joint shear strain
γ_2	Vertical component of average joint shear strain
δ	Bending rigidity ratio of columns [$=(EI)_{lc}/(EI)_{uc}$]
δ_f	Density of carbon fiber
δ_m	Density of epoxy resin
$\varepsilon_{cc}^{'}$	Maximum usable compressive strain of confined concrete
ε_{cu}	Ultimate compressive strain of concrete
ε_{fe}^{CFRP}	Maximum effective strain of CFRP
ε_{fu}^{CFRP}	Design rupture strain of CFRP
ε_i	Strain obtained from i^{th} LVDT in joint panels
ε_{max}	Maximum strain developed by a CFRP retrofit component
ε_{sh}	Strain in reinforcing bar at onset of strain hardening
ε_u	Strain in reinforcing bar at ultimate (break)
ε_u^{CFRP}	Rupture strain of CFRP
ε_x	Strain in horizontal direction of joint panel

ε_y	Strain in reinforcing bar corresponding to lower yield stress (f_y) within proportional limit
ε_z	Strain in vertical direction of joint panel
ε_φ	Strain in joint panel in an arbitrary direction with an angle of φ measured counterclockwise from horizontal axis
θ	Interstory drift ratio
θ_{EW}	Interstory drift ratio in EW direction
θ_{NS}	Interstory drift ratio in NS direction
θ_{bj}	Concentrated rotation of beams with respect to joint
θ_{cj}	Concentrated rotation of column with respect to joint
θ_c^{tot}	Total column rotation (elastic plus concentrated)
θ_j	Total global rotation of joint in space
θ_{ucj}	Rotation of upper column with respect to joint due to loss of anchorage in column lap-splice
θ_1	Rotation at column base under combined joint shear deformation and total column rotation
θ_2	Rotation at top of column under combined joint shear deformation and total column rotation
ν_f	Poisson's ratio of carbon fiber
ν_m	Poisson's ratio of epoxy resin
ν_s	Poisson's ratio of steel
ν_{xy}	Poisson's ratio of CFRP laminate
ν_{12}	Poisson's ratio of unidirectional CFRP lamina
ρ''	Volumetric ratio of joint transverse reinforcement

ρ_{col}	Column longitudinal reinforcement ratio
ρ_f	Transverse reinforcement ratio provided by CFRP wrap
ρ_s	Volumetric ratio of column steel hoop reinforcement
ρ_x	Transverse reinforcement ratio of column in *x*-direction
ρ_y	Transverse reinforcement ratio of column in *y*-direction
τ'_{jh}	Normalized unidirectional joint shear stress
τ'^{b}_{jh}	Normalized bidirectional joint shear stress [$= \sqrt{\left(\tau'^{EW}_{jh}\right)^2 + \left(\tau'^{NS}_{jh}\right)^2}$]
$\left(\tau'^{b}_{jh}\right)_{max}$	Maximum normalized bidirectional joint shear stress
τ'^{EW}_{jh}	Normalized joint shear stress in EW direction
τ'^{NS}_{jh}	Normalized joint shear stress in NS direction
ϕ	Strength reduction factor
ϕ_t	Beam twist angle
CFRP	Carbon fiber-reinforced polymer
CMU	Concrete masonry unit
DSC	Differential scanning calorimetry
FRP	Fiber-reinforced polymer
GFRP	Glass fiber-reinforced polymer
GLD	Gravity-load-design
PGA	Peak ground acceleration

SUMMARY

The results of an experimental investigation are presented which examine the seismic adequacy of pre-1970 reinforced concrete (RC) corner beam-column joints and the efficacy of carbon fiber-reinforced polymer (CFRP) composites for both pre- and post-earthquake retrofit of such joints.

Four full-scale corner beam-column-slab subassemblages built with identical dimensions and pre-1970 reinforcement details were subjected to a reverse-cycle bidirectional displacement history consisting of alternate and simultaneous cycles in the two primary frame directions before and/or after retrofit. Two of the specimens were first subjected to severe and moderate levels of damage, respectively, then repaired by epoxy injection, and strengthened by adding a #7 reinforcing bar within the clear cover at the column inside corner and by externally bonding multiple layers of carbon fabric to form a carbon-epoxy retrofit system. Two other specimens, one of which had a significantly lower concrete compressive strength, were strengthened in their as-built condition. The CFRP scheme was improved in light of the findings as the experimental program progressed.

Pre-1970 RC corner beam-column joints were found to be severely inadequate in meeting seismic demands because of column bar yielding, joint shear failure, loss of anchorage of beam bottom bars, failure of column lap-splices, and the resulting loss of stiffness and strength that dominate their behavior even at relatively low interstory drift levels. Bidirectional loading played a significant role in such response. It was shown, however, that such joints can be strengthened easily both before and after earthquake damage by using CFRP composite schemes. Regardless of the level of existing damage and concrete strength, a "rigid" joint behavior up to interstory drift ratios of at least 2.4% and joint shear strength factors ranging from 1.06 to $1.41\sqrt{MPa}$ were achieved; such

shear strength factors are larger than the value of $1.00\sqrt{MPa}$ recommended for use with seismically designed, code-conforming corner beam-column joints. A ductile beam hinging mechanism was achieved and energy dissipation capacity was improved efficiently for joints with concrete strengths ranging from 26 to 34 MPa. The subassemblage with significantly low-strength concrete (15 MPa) had low overall lateral stiffness and reduced reinforcement anchorages which prevented the formation of beam hinging. In cases of such low-strength concrete, more invasive operations may be required so that the improved joint shear strength can be mobilized. It is recommended that bidirectional loading be always considered in both pre- and post-retrofit evaluation of corner joints.

CHAPTER 1

INTRODUCTION

1.1 PURPOSE AND OBJECTIVES

The purpose of this research was to experimentally determine if carbon fiber-reinforced polymer (CFRP) could be effectively used to repair and strengthen reinforced concrete (RC) corner beam-column joints for improved seismic performance. The research focused on corner beam-column joints which modeled those typically found in RC buildings constructed prior to 1970; such structures lacked reinforcement details that provide strength and ductility. In particular, the research focused on five primary objectives:

1. Establish seismic adequacy of pre-1970 corner joints under bidirectional loading,
2. Investigate the efficacy of CFRP composites to improve joint strength and ductility,
3. Investigate the effect of severe, moderate, or no initial damage on the efficacy of retrofit with CFRPs,
4. Ensure the applicability of the retrofit schemes to actual structures by accounting for the presence of floor members, and ensure the ease of retrofit construction by avoiding massive interventions to building appearance and occupancy,
5. Investigate the effects of bidirectional loading and floor members on force transfer mechanisms pertaining to the behavior of the joint both before and after retrofit.

1.2 SCOPE

All tests were conducted on full-scale specimens representing the corner of a building isolated between two stories at the inflection points of beams and columns under lateral

Table 1.1 — Outline of experimental program.

Test	Specimen	Retrofit Scheme	Maximum Applied Interstory Drift
Test 1	Specimen 1	-	±1.9% (severe damage)
Test 2	Specimen 1	Scheme 1	±3.7%
Test 3	Specimen 2	-	±1.4% (moderate damage)
Test 4	Specimen 2	Scheme 2	±3.7%
Test 5	Specimen 3	Scheme 2	±3.7%
Test 6	Specimen 4	Scheme 3	±3.7%

loading. A total of six tests were conducted on four specimens that were built to mimic pre-1970 design and construction practices according to the experimental program outlined in Table 1.1. All specimens were identical in member sizes and steel reinforcement detailing. Variations between the tests were in concrete strength, CFRP details and lay-up, and in the level of damage (severe, moderate, or none) induced prior to retrofit. Cyclic lateral loads were simulated by quasistatic cyclic loading of the beams in the vertical direction. Gravity load effects present at the time of lateral loading were accounted for by applying a compressive column axial load and negative beam moments at the joint prior to cyclic loading.

1.3 NEED FOR RESEARCH

Reinforced concrete buildings constructed with no or inadequate consideration of seismic effects, which are commonly referred to as gravity-load-designed buildings, constitute a significant portion of the building inventory in many countries and pose a significant risk for high economic and life losses in earthquakes. A major group of deficiencies, which could cause significant damages in such buildings including total loss of vertical load carrying capacity and collapse, are in beam-column joint regions. In the United States, special provisions for seismic design were included in the ACI 318 Building Code first in

1971 [1.1], and the first guideline for the design of RC beam-column joints was published in 1976 [1.2]. Other major developments pertaining to evolution of seismic design provisions took place throughout the 1970s after the 1971 San Fernando earthquake [1.3] including revision of the 1973 Uniform Building Code (UBC), adoption of new seismic requirements and ductile detailing practices in the 1976 UBC [1.4] based on the work of Structural Engineers Association of California (SEAOC), and publication of a report by the Applied Technology Council (ATC) in 1978 [1.5] which was later used by the UBC and SEAOC to revise their recommendations and building code. For brevity, buildings constructed prior to the adoption of these codes and recommendations can be referred to as "pre-1970" buildings.

An example of the severity of damages in recent earthquakes that were attributed to inadequacies in beam-column joints is shown in Figure 1.1. As shown, joints around the perimeter of the building are more vulnerable than the interior joints. This is mainly because (1) unlike interior joints, exterior joints are confined by only two or three framing beams; (2) axial loads in exterior columns are smaller under gravity loads and can reduce significantly due to overturning effects during lateral loading; and (3) exterior joints are subjected to torsional effects created by the presence of the slab only on one side of the beams. The vulnerability is increased even more in the case of corner joints (Figure 1.1a, b, d-f) since corner joints are: (1) the least confined of all exterior joints, (2) subjected to bidirectional demands due to combination of actions from two perpendicular frames, and (3) susceptible to effects caused by the torsional behavior of the entire building because generally they are the farthest away from the center of rigidity.

The ACI-ASCE Committee 352, *Joints and Connections in Monolithic Concrete Structures*, recommended further research to establish the adequacy of older joints and to develop methods of improving their performance [1.6]. A comprehensive review of the technical literature in this area was conducted at the initiation of the present study and published in 2005 [1.7]; it is presented in Chapter 2. This review indicated that fiber-

reinforced polymer (FRP) composites have great potential for achieving desirable ductile beam failure mechanisms in pre-1970 joints and for overcoming the limitations of other joint strengthening techniques such as laborious and massive construction operations. As with most other joint strengthening techniques, however, experimental validation of strengthening with FRPs was limited to testing of planar one-way joints (i.e. joints with no transverse beams or slab) where the presence of floor members and the possibility of bidirectional loading were not considered. Promising results from such planar joint tests have recently led to more realistic testing of FRP-strengthened beam-column joints even as part of complete three-dimensional RC frame structures; such recent research is reviewed in Appendix A.

Although the implementation of joint strengthening technology with FRPs has begun (Figure 1.2), the lack of comprehensive design guidelines prevents wider acceptance and implementation. Guidelines drafted by various international organizations for the design and construction of externally bonded FRP composites for strengthening RC structures currently do not cover strengthening of beam-column joints due to inadequacy of the state-of-the-art [1.8-1.12]. In order for joint retrofit guidelines to be developed, extensive testing of critical joint types strengthened with different design approaches is necessary.

1.4 THESIS FORMAT

The outcomes of the research whose context was introduced in this chapter are presented in the following chapters as follows.

Chapter 2 summarizes the data found in the literature at the initiation of this study on the performance of nonseismically designed beam-column joints and on the techniques studied for their repair and strengthening.

Chapter 3 establishes the seismic adequacy of pre-1970 RC corner beam-column joints under bidirectional loading based on the performances of Specimen 1 and Specimen 2 in their as-built condition.

Chapter 4 investigates if a corner joint that has undergone severe damage can be repaired and strengthened with CFRP composites based on the results from re-testing of Specimen 1 after retrofit.

Based on comparisons of Specimen 1 and Specimen 2, Chapter 5 examines the extent of further improvements that can be obtained if the initial damage is moderate and presents the improvements to the CFRP design used in Specimen 2.

Chapter 6 evaluates the efficacy of the CFRP schemes for pre-earthquake strengthening of corner joints with moderate-strength concrete in one case (Specimen 3) and low-strength concrete in another case (Specimen 4).

Chapter 7 presents the major conclusions and design recommendations drawn from this study and suggests future research in certain areas.

Appendix A reviews the literature pertaining to FRP-strengthening of RC beam-column joints that have become available during the course of this study.

Appendices B, C, and D provide additional details of the experimental program, test results, and some calculations to an extent that was not vital to the presentation in the preceding chapters.

Appendix E presents the approach and calculations for the design of CFRP retrofit schemes.

Appendix F presents the analytically predicted strengths of the as-built beams and columns, and quantifies three-dimensional effects on joint shear stress based on analytical approximations.

(a)

(b)

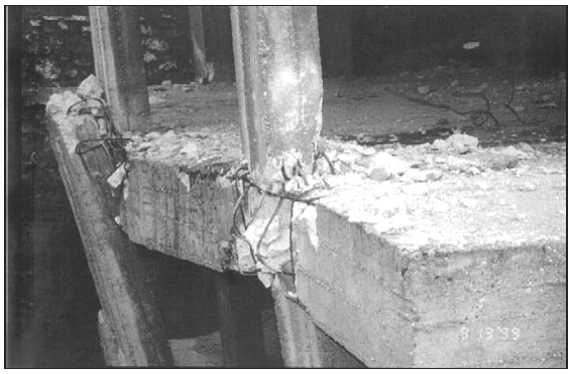

(c)

(d)

(e)

(f)

Figure 1.1 — Damage to beam-column joints in (a-d) 1999 İzmit, Turkey, (e) 1999 Chi-Chi, Taiwan, and (f) 1994 Northridge, CA earthquakes.

Photo credits: (a) Prof. Güney Özcebe, personal communication (1999); (b, c) Said and Nehdi [1.13]; (d) Ghobarah and Said [1.14]; (e) NISEE, UC Berkeley [1.15]; (f) Moehle [1.16].

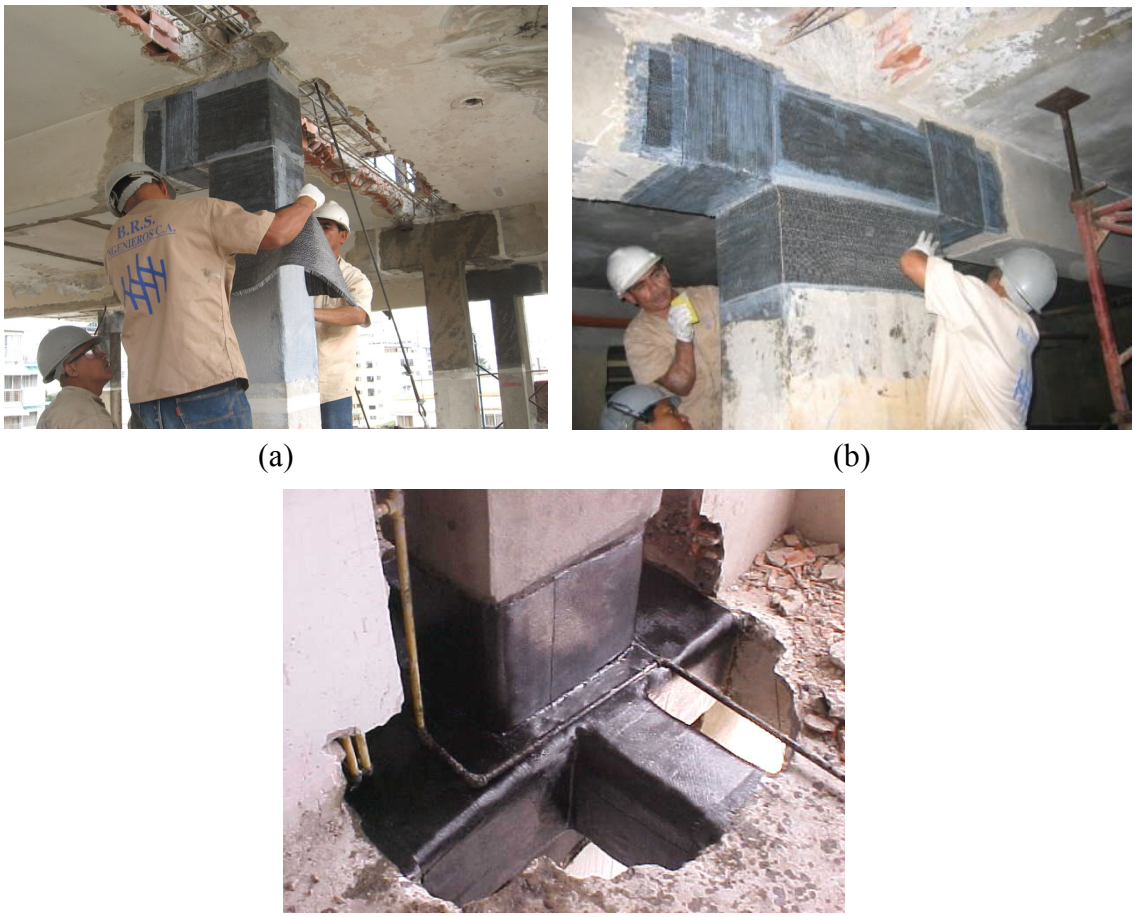

(a) (b)

(c)

Figure 1.2 — Implementation of FRP joint strengthening schemes in construction.

Photo credits: (a) B.R.S. Ingenieros C.A. [1.17], and (b, c) Jose Rendón, personal communication (2007).

1.5 REFERENCES

[1.1] ACI Committee 318 (1971). *Building code requirements for reinforced concrete (ACI 318-71)*, American Concrete Institute, Farmington Hills, MI.

[1.2] ACI-ASCE Committee 352 (1976). "Recommendations for design of beam-column joints in monolithic reinforced concrete structures (ACI 352R-76)." *ACI Journal Proceedings*; 73(7), 375-393.

[1.3] FEMA (1998). *Promoting the adoption and enforcement of seismic building codes: A guidebook for state earthquake and mitigation managers (FEMA 313)*, Federal Emergency Management Agency, Washington, D.C.

[1.4] ICBO (1976). *Uniform Building Code (UBC)*, International Conference of Building Officials, Whittier, CA.

[1.5] ATC (1978). *Tentative provisions for the development of seismic regulations for buildings (ATC-3-06)*, Applied Technology Council, Redwood City, CA.

[1.6] ACI-ASCE Committee 352 (2002). *Recommendations for design of beam-column connections in monolithic reinforced concrete structures (ACI 352R-02)*, American Concrete Institute, Farmington Hills, MI.

[1.7] Engindeniz, M., Kahn, L. F., and Zureick, A. (2005). "Repair and strengthening of reinforced concrete beam-column joints: State of the art." *ACI Structural Journal*; 102(2), 187-197.

[1.8] *fib* (2001). *Externally bonded FRP reinforcement for RC structures, Bulletin 14*, International Federation for Structural Concrete, Lausanne, Switzerland.

[1.9] ACI Committee 440.2 (2002). *Guide for the design and construction of externally bonded FRP systems for strengthening concrete structures (ACI 440.2R-02)*, American Concrete Institute, Farmington Hills, MI.

[1.10] ISIS Canada (2001). *Strengthening reinforced concrete structures with externally-bonded fibre reinforced polymers*, Design Manual No. 4, The Canadian Network of Centres of Excellence on Intelligent Sensing for Innovative Structures, Winnipeg, Manitoba, Canada.

[1.11] AFGC (2003). *Repair and strengthening of concrete structures by means of composite materials – Interim recommendations*, French Association of Civil Engineering, Paris, France. (In French)

[1.12] CNR-DT 200 (2004). *Guide for the design and construction of externally bonded FRP systems for strengthening existing structures*, Italian National Research Council, Rome, Italy.

[1.13] Said, A. M., and Nehdi, M. L. (2004). "Use of FRP for RC frames in seismic zones – Part I: Evaluation of FRP beam-column joint rehabilitation techniques." *Applied Composite Materials*, 11(4), 205-226.

[1.14] Ghobarah, A., and Said, A. (2002). "Shear strengthening of beam-column joints." *Engineering Structures: The Journal of Earthquake, Wind and Ocean Engineering*; 24(7), 881-888.

[1.15] National Information Service for Earthquake Engineering, University of California Berkeley. <http://nisee.berkeley.edu> (May 2003).

[1.16] Moehle, J. P. (2000). "State of research on seismic retrofit of concrete building structures in the US." *US-Japan Symposium and Workshop on Seismic Retrofit of Concrete Structures - State of Research and Practice*.

[1.17] B.R.S. Ingenieros C.A. <http://www.brsingenieros.com.ve> (December 2007).

CHAPTER 2

REPAIR AND STRENGTHENING OF REINFORCED CONCRETE BEAM-COLUMN JOINTS: STATE OF THE ART

2.1 INTRODUCTION

The latest report by Joint ACI-ASCE Committee 352 (ACI 352R-02) states that joints in structures built before the development of current design guidelines need to be studied in detail to establish their adequacy and that methods of connection repair and strengthening need to be developed. Prior to developing new strengthening schemes, it is important that the findings from research previously conducted on other strengthening techniques be known. This chapter presents a comprehensive up-to-date literature search pertaining to the performance of, as well as to the repair and strengthening techniques for, nonseismically designed reinforced concrete beam-column joints, reported between 1975 and 2003. These techniques included: 1) epoxy repair; 2) removal and replacement; 3) concrete jacketing; 4) concrete masonry unit jacketing; 5) steel jacketing and addition of external steel elements; and 6) strengthening with fiber-reinforced polymeric (FRP) composite applications. Each method of repair or strengthening is reviewed with emphasis on its application details, required labor, range of applicability, and performance. Relative advantages and disadvantages of each method are discussed.

2.2 BACKGROUND

The performance of beam-column joints has long been recognized as a significant factor that affects the overall behavior of reinforced concrete (RC) framed structures subjected to large lateral loads.

The first design guidelines for reinforced concrete beam-column joints were published in 1976 in the U.S. [2.1] and in 1982 in New Zealand [2.2]. Buildings

constructed before 1976 may have significant deficiencies in the joint regions. Especially since the 1985 Mexico earthquake, a considerable amount of research has been devoted to identifying the critical details of nonseismically designed buildings as well as to developing methods of strengthening. Through their reviews of detailing manuals and design codes from the past five decades and their consultation with practicing engineers, Beres et al. [2.3] (among others) identified seven details (shown in Figure 2.1) as typical and potentially critical to the safety of gravity load-designed (GLD) structures in an earthquake. Most of the repair and strengthening schemes proposed thus far, however, have a very limited range of applicability either due to lack of consideration of floor members or to architectural restrictions. The current recommendations by Joint ACI-ASCE Committee 352 [2.4] reads: "These joints need to be studied in detail to establish their adequacy and to develop evaluation guidelines for building rehabilitation. Methods for improving performance of older joints need to be studied. Scarce information is available on connection repair and strengthening."

2.3 RESEARCH SIGNIFICANCE

The objective of this chapter is the collection of current information on repair and strengthening of nonseismically designed joints so that engineers and researchers may more efficiently proceed to develop improved seismic retrofits. The performance of nonseismically designed joints is summarized first. Then, each method of repair or strengthening is reviewed with emphasis on its performance and relative advantages and disadvantages with respect to the application details, required labor, and range of applicability. Strengthening methods that may indirectly affect the performance of existing joints (for example, adding steel bracing or shear walls) are outside the scope of this study.

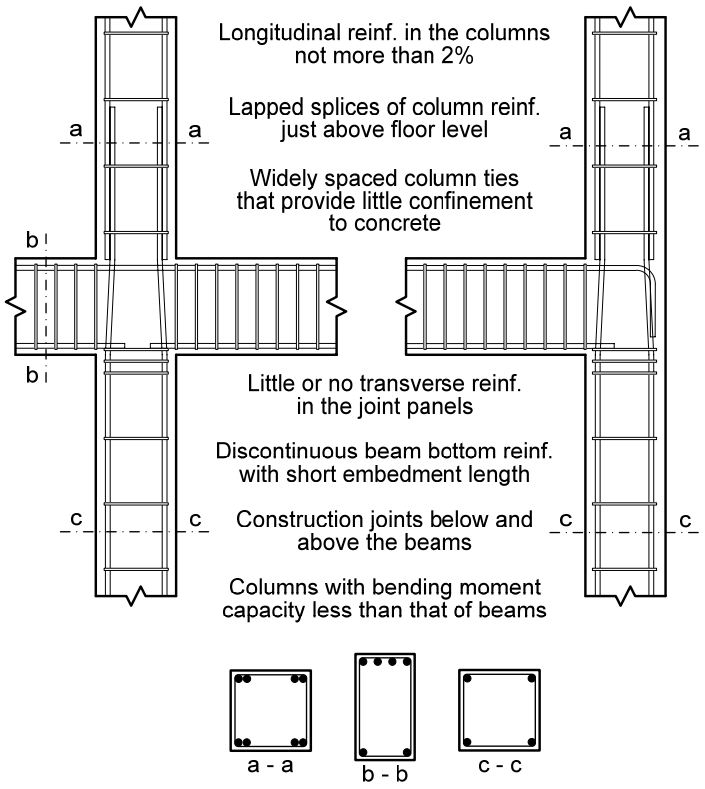

Figure 2.1 — Typical details in lightly reinforced concrete structures identified by Beres et al. [2.3]

2.4 PERFORMANCE OF NONSEISMICALLY DESIGNED BEAM-COLUMN JOINTS

Many catastrophic failures because of earthquakes (Japan, 1978; Algeria, 1980; Italy, 1980; Greece, 1981; Mexico, 1985; Taiwan, 1999; and Turkey, 1999 and 2002)(Figure 2.2) have shown the vulnerability of reinforced concrete (RC) joints built before seismic design codes were adopted or built without seismic considerations, even when such codes were in place [2.5-2.7].

Critical details of lightly reinforced RC frames were identified, and their effects on seismic behavior were studied by Pessiki et al. [2.8] and Beres et al. [2.3, 2.9-2.11]. Through their reviews of detailing manuals and design codes from the past five decades and their consultation with practicing engineers, they identified seven details, shown in

Figure 2.2 — Corner joint failure in 1999, İzmit/Turkey earthquake.
(Courtesy of National Information Service for Earthquake Engineering,
University of California, Berkeley)

Figure 2.1, typical and potentially critical to the safety of gravity load-designed (GLD) structures in an earthquake. Their experimental program included testing of 20 interior and 14 exterior full-scale beam-column joints under cyclic static loading, and shaketable tests on a 1/8-scale three-story building. No floor slabs were used in the beam-column joint tests; short transverse prestressed stub beams were used in some specimens. In interior joints having continuous beam bottom reinforcement, failure was due to the heavy damage in the joint and in the column in some cases and due to the beam pulling away from the joint in other cases (Figure 2.3a). The use of two No. 3 ties in the joint shifted the failure from the joint to the column splice region, with the damage being

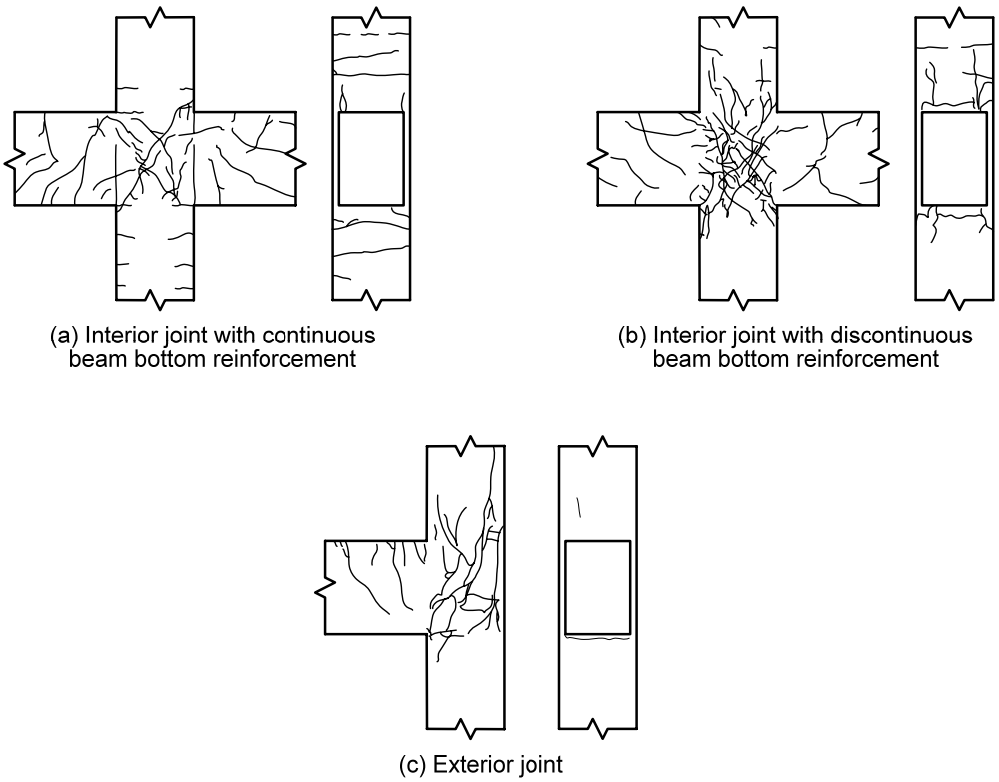

Figure 2.3 — Typical cracking patterns of non-seismically detailed joints observed by Beres et al. [2.10]

concentrated below the first column tie. Splitting cracks and loss of cover did not extend along the splice; however, loss of cover led to buckling of column bars in two specimens. Column bar size and arrangement did not affect the peak joint strength. In the case of discontinuous beam bottom reinforcement, cracks appeared in the embedment region, and later the cracks either merged with diagonal joint cracks or proceeded vertically (Figure 2.3b). The beam bars pulled out at approximately 2/3 of their yield stress. The pullout resistance was independent of the two bar sizes and the two column axial load levels examined. In the exterior joints, initial cracks around the embedment region proceeded diagonally toward the column bar splice region and extended downward to the bottom column, causing spalling of a large column piece and prying of the beam top bar (Figure 2.3c). An increase in column axial load resulted in an increase in peak strength (15 to 25%) of both interior and exterior joints, while it reduced strength degradation in exterior

specimens. It also delayed the onset of shear cracking and provided better confinement to embedded bars. The beneficial effect of transverse beams as suggested by ACI 352R-91 [2.12] was not supported by experiments using transverse stubs. The maximum experimental shear stresses (0.42 to 1.08 MPa [5 to 13 psi]) were 30 to 40% lower than the maximum capacities allowed by ACI 352R-91 [2.12] to be used in design (note that these ACI guidelines pertain to well detailed joints in new construction). The main conclusion from shaketable tests on the 1/8 scale building was that lightly reinforced RC structures are very flexible and may show significant P-Δ effects. Floor slabs played a major role in increasing the capacity of beams, thus leading to a soft story column failure.

The results of a comprehensive research program to experimentally and analytically evaluate the behavior of GLD structures, and to assess several retrofit alternatives, were published in the early 1990s [2.13-2.18].

Aycardi et al. [2.15] presented the results of unidirectional, quasistatic lateral load tests on one exterior and one interior 1/3-scale beam-column joint designed only for gravity loads. The specimens included a slab and transverse beams on both sides. The exterior subassemblage showed progressive damage starting in the beam, through pullout of discontinuous beam bottom bars, and later damage in the columns. A weak beam-strong column failure was evident with a maximum joint shear stress of 0.87 MPa (10.5 psi). The interior subassemblage had no joint transverse reinforcement and exhibited progressive damage only in the columns with little damage to the beams. A weak column-strong beam failure and a maximum joint shear stress of 1.04 MPa (12.5 psi) were observed. For both specimens, the maximum strength occurred between 2 and 3% drift.

The results of Aycardi et al. [2.15] were then used by Bracci et al. [2.16] to evaluate the seismic performance of a 1/3-scale three-story GLD model, previously tested by Beres et al. [2.11] at 1/8 scale. When tested on a shaketable, the 1/3-scale model showed an identical pattern of plastic hinges as the 1/8 scale model, while some dif-

ferences in base shear demand and story drifts were observed. Bracci et al. [2.16] stated that: "1) GLD structures were dominated by weak column-strong beam behavior; 2) their response can be predicted with adequate knowledge of component behavior; and 3) they can resist minor earthquakes without considerable damage, but moderate to severe earthquakes cause substantial sidesway deformations exceeding the recommended limits." Both studies [2.15, 2.16] concluded that simple retrofit techniques for the interior columns and beam-column joints could improve the hysteretic behavior and prevent formation of column failure mechanisms.

Kunnath et al. [2.17] performed inelastic time history analyses of three-, six-, and nine-story GLD buildings using a computer program. The effects of discontinuous beam bottom reinforcement, lack of joint shear reinforcement, and level of column and beam confinement were studied. Nonductile details were modeled through several simplifications at critical sections, and hysteretic behavior was obtained from previous tests of Aycardi et al. [2.15] and Pessiki et al. [2.19]. Four separate earthquake records and three separate degrading hysteretic behavior models were used. Kunnath et al. [2.17] concluded that buildings will survive moderate earthquakes with some repairable damage; however, they are susceptible to severe damage if subjected to strong ground motions. In the second part of this study, Kunnath et al. [2.18] used the same analysis tools to evaluate 16 separate detailing enhancements (for each building and each earthquake) including continuity or sufficient anchorage of beam bottom bars, transverse reinforcement in the joints, and additional confinement in the column and/ or beam hinge regions. When only continuity of beam bottom bars was provided, the restoration of beam capacity resulted in even more joint failures; damage shifted from beams to columns; and drifts increased. Hence, this enhancement alone was considered detrimental, especially in low-rise buildings, or in upper stories of high-rise buildings. Ensuring adequate joint strength led to a more uniform beam hinging and to a strong column-weak beam mechanism. Additional confinement in the hinge regions,

independent of other enhancements, was not effective in preventing nonductile failures. As expected, the combination of the three detailing strategies proved to yield the best benefits. In this case, when the beam hinging mechanism governed with a slight amount of column hinging in upper floors, the highest story shears and the smallest drifts were obtained.

Hakuto et al. [2.20] reported on the performance of three interior (O1, O4, and O5) and two exterior (O6 and O7) one-way† joints designed according to pre-1970s practice in New Zealand. The beam bottom bars were continuous through the interior joints, the beam stir ups were widely spaced, and the hooks of the longitudinal beam bars were bent out of the joint core in one of the exterior joints. In one interior joint with beams considerably stronger than the column, the failure was due to bond slippage along the longitudinal beam reinforcement in the joint core followed by joint shear failure. Those with stronger columns exhibited shear failure in the beam. As for the exterior joints with negligible transverse reinforcement, the beams hinged when the hooks of the beam bars were bent into the joint core, while the joint failed in shear when the hooks were bent out of the joint core.

Walker et al. [2.21] tested seven one-way interior joints without joint reinforcement. To study only the influences of joint shear stress demand and displacement history, their specimens departed from actual GLD buildings in that the beam bottom bars were continuous, the bond demand on beam bars was kept low, and strong column-weak beam was maintained. Two joint shear stress levels (0.75 and 1.29 MPa [9 and 15.5 psi]) and four different displacement histories were used. Within the context of performance-based engineering, five damage states were identified and correlated with story drift. The first joint cracks were observed at 0.5% drift and approximately 0.5 MPa (6 psi) shear stress. Yielding of beam bars occurred at 1.1 and

†A joint with no transverse beams or floor slab and loaded in its plane is called a "one-way joint" throughout this thesis. Note that in the Joint ACI-ASCE 352 Committee Report [2.5], a "one-way interior joint" is termed an exterior joint, and a "one-way exterior" is termed a corner joint.

1.5% drift for low and high joint shear demands, respectively, with no marked difference due to displacement history. Higher joint shear demand influenced the joint damage adversely. In the case of low shear demand, damage was initiated at the center of joint at 3% drift and the core was damaged at 4%, while these values were 2 and 3%, respectively, in the case of high shear demand. Damage to joint concrete was a function of both the number of cycles and drift amplitude. Final failure was due to significant loss of joint concrete followed by buckling of longitudinal column bars. It was also noted that full symmetric displacement cycles were more damaging than half-asymmetric cycles.

As part of an experimental study on one-way exterior joints with deficient detailing, Clyde and Pantelides [2.22] defined five levels of performance for two levels of column axial load, similar to those identified by Walker et al. [2.21] for interior joints. Based on the results of four cyclic joint tests, each level was defined in terms of story drift, crack width, and joint shear strength factor (γ used in joint shear stress expression). The crack patterns were very similar to those found previously for other exterior joint tests. In the case of higher column axial load, a 3 to 13% increase in γ and a 20% decrease in energy dissipation capacity were observed; the defined performance levels, with a few exceptions, were reached at smaller drifts, larger crack widths, and larger joint shear strength factors.

The aforementioned studies have all been conducted on test specimens with beams having approximately the same width as that of the columns. Attention was recently drawn by Li et al. [2.23, 2.24] to nonseismically detailed narrow beam-wide column joints. In the experimental part of their study [2.23], four one-way interior narrow beam-wide column joints were tested with the beams framing into the wide side of the rectangular column in two of the specimens. A strong column-weak beam criterion was satisfied for all specimens. The test variables were the amount of joint transverse reinforcement and the lap splice details for column and beam bars. All specimens exhibited severe joint diagonal cracking after testing. Li et al. [2.23] stated that “more

than 74% of the joint shear force can be carried by the diagonal concrete strut." Columns remained intact except for one specimen in which the lap splice above the joint failed. The lap splicing of the beam bottom bars within the joint did not worsen the performance, and it was suggested that no limitation should be put on the beam bar diameter in the case of wall like column joints. The addition of 15 and 24% of the joint transverse reinforcement required by NZS 3101:1995 [2.25] did not increase the strength but did improve the ductility and energy dissipation. In the analytical part of their investigation, Li et al. [2.24] used finite element analyses to study the effect of joint transverse reinforcement, column axial load, and bond condition on the behavior of narrow beam-wide column joints. The analytical predictions were satisfactory except that the pinching of the hysteresis loops observed in the experiments could not be captured analytically. The addition of joint reinforcement improved the behavior but did not prevent the eventual joint failure, and it did not improve the bond conditions for the beam and column bars. For the case in which the beams framed into the wide side of the column, an increase in the column axial load up to 40% of its axial load capacity was found to be beneficial. For wall-like joints, the results on the effect of column axial load were mixed.

In addition to the aforementioned studies, some experimental and analytical results pertaining to the behavior of nonseismically designed joints are also available in several publications in which the performance of a few (usually one or two) reference specimens were used as a basis for evaluating the improvements due to certain repair or strengthening methods [2.9, 2.13, 2.26-2.49]. The behaviors of these specimens were governed by one or a combination of the failure modes. For brevity, their performances are not discussed herein, but are evident from the implemented repair and strengthening methods that are reviewed in the following sections. The common damage modes that indicated the need for repair/strengthening were: 1) joint shear cracks and spalling of joint concrete; 2) cracks initiating at the joint embedment region, generally combining with the diagonal joint cracks, followed by pull ut of discontinuous beam bottom bars; 3)

growing of diagonal joint cracks toward the column bar splice region especially in the case of exterior joints; 4) spalling of concrete at the back of exterior joints, sometimes followed by prying of beam top bars with 90-degree hooks into the joint; 5) buckling of column bars due to loss of concrete in the joint region; and 6) column and/or limited beam yielding.

2.5 REPAIR AND STRENGTHENING TECHNIQUES FOR BEAM-COLUMN JOINTS

Research on the repair and strengthening of joints included epoxy repair, removal and replacement, reinforced or prestressed concrete jacketing, concrete masonry unit jacketing or partial masonry infills, steel jacketing and/or addition of external steel elements, and fiber-reinforced polymer (FRP) composite applications. Each technique required a different level of artful detailing and consideration of labor, cost, disruption of building occupancy, and range of applicability. The main objective of the research was to establish a strength hierarchy between the columns, beams, and joints so that seismic strength and ductility demands could be accommodated through ductile beam hinging mechanisms instead of column hinging or brittle joint shear failures. In gravity load-designed structures, where beams are often stronger than columns, strengthening the column is generally not sufficient by itself since the joint then becomes the next weakest link due to either lack of transverse reinforcement, discontinuous beam bottom reinforcement, or other nonductile detailing. Thus, the shear capacity and the effective confinement of joints must be improved. Achieving such an improvement is challenging in actual three-dimensional frames because of the presence of transverse beams and floor slab that limit the accessibility of the joint and because of the difficulties in developing the strength of externally placed reinforcements (that is, steel plates, FRP sheets, or rods) within the small area of the joint. At present, the techniques that have been tested either have not accounted for the three-dimensional geometry of the actual frame joints and are

applicable in only special cases, or they resulted in architecturally undesirable configurations with bulky members.

2.5.1 Epoxy Repair

Concrete structures have long been repaired using pressure injection of epoxy [2.50]; a relatively new method of epoxy repair is vacuum impregnation. French et al. [2.26] studied the effectiveness of both epoxy techniques to repair two one-way interior joints that were moderately damaged due to inadequate anchorage of continuous beam bars. For vacuum impregnation (Figure 2.4), epoxy inlet ports were located at the bottom of each beam and at the base of the column repair region. The vacuum was applied through three hoses attached at the top of the repair region in the column. Both repair techniques were successful in restoring over 85% of the stiffness, strength, and energy dissipation characteristics of the original specimens. Severe bond deterioration in the repaired joints occurred only one half-cycle earlier than in the original specimens. The main conclusion was that vacuum impregnation presents an effective means of repairing large regions of damage at once and that it can be modified for joints with fewer accessible sides.

Beres et al. [2.9] retested one of their deficiently detailed one-way interior joints (Figure 2.1) after repairing it by vacuum injection of methyl-methacrylate resin without removing the initially applied gravity load. The failure in both the original and repaired specimens was due to pullout of the embedded beam bottom bars and extensive diagonal cracks in the joint. Although the repair restored only 75% of the initial stiffness and 72% of the column shear capacity, the energy dissipation capacity remained almost unchanged due to a reduced rate of strength deterioration.

Filiatrault and Lebrun [2.27] reported on the performance of two one-way exterior joints, one with nonseismic detailing and one with closely spaced transverse reinforcement in the beam, column, and joint; each was repaired by epoxy pressure

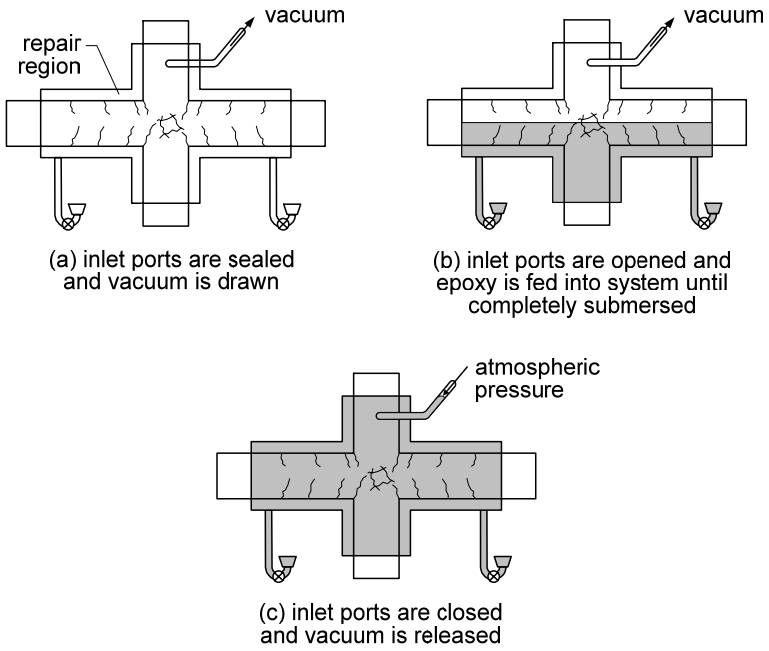

Figure 2.4 — Vacuum impregnation procedure applied by French et al. [2.26]

injection. Filiatrault and Lebrun [2.27] said that the repair procedure was particularly effective in improving the strength, stiffness, and the energy dissipation capacity of the nonseismically detailed specimen and that more pinching was observed in the hysteresis loops of the seismically detailed specimen after repair.

Karayannis et al. [2.28] studied the effects of joint reinforcement arrangement on the efficiency of epoxy repair by pressure injection. Eleven of the tested one-way exterior joint specimens were repaired by epoxy injection only and then retested. In these specimens, cracks were observed both at the joint region and at the beam end during the first cycles, but the failure was finally due to beam hinging. After repair, the specimens with two joint stirrups or column longitudinal bars crossed within the joint exhibited only beam flexural failure with serious fragmentation of concrete at the beam end and significant reduction in pinching of the hysteresis loops. The specimens with one joint stirrup, however, exhibited the same failure mode before and after repair. The increases in peak load and dissipated energy were 8 to 40% and 53 to 139%, respectively. The change in

stiffness varied between a 27% decrease and a 10% increase. The variations in performance were partially attributed to the variations in being able to inject epoxy successfully into the joint cracks.

The results of the epoxy repair applications on one-way joints have shown that the reliability of this technique in restoring the original characteristics of damaged joints is questionable. The bond around the reinforcing bars, once destroyed, does not seem to be completely restored by epoxy injection [2.51]. This is evidenced by the partial recovery of stiffness and by the pinching in the hysteresis loops. It is also clear that the effectiveness of the epoxy repair is limited by the access to the joint and that epoxy cannot be effectively introduced into the joints surrounded by transverse beams and floor slab. This limitation can possibly be overcome by further advances in the vacuum impregnation technique. A high level of skill is required for satisfactory execution of such techniques, and application may be limited by the ambient temperature [2.50]. General guidelines for using epoxy in the repair of concrete structures and for verifying their field performance can be found in references 50, 52, and 53, respectively.

2.5.2 Removal and Replacement

Partial or total removal and replacement of concrete is used for heavily damaged joints with crushed concrete, buckled longitudinal bars, or ruptured ties. Before the removal, the damaged structure must be temporarily supported to ensure stability. Depending on the amount of concrete removed, some additional ties or longitudinal reinforcement may be added [2.54]. Generally, high-strength, low- or nonshrink concrete is used for replacement. Special attention must be paid to achieving a good bond between the new and the existing concrete.

The experimental program conducted by Karayannis et al. [2.28] included six one-way exterior joint specimens that exhibited a concentrated damage in the joint and a loss of considerable amount of concrete in this region. This damage mode can be attrib-

uted to the joint not having any stirrups in two of the specimens and to the flexural strength ratio being very low (0.67) in the others. The joints were repaired by first recasting the missing part of the joint with a high-strength (83 MPa [12,100 psi]), low-shrink cement paste, then by epoxy injection into the surrounding cracks. The repair did not alter the failure mode of the specimens with one or no joint stirrups, although an increase of 39 to 71% in peak load, 15 to 39% in stiffness, and 19 to 34% in energy dissipation capacity was observed. The specimens with two joint stirrups, however, improved remarkably after repair and developed a beam hinge with no damage to the joint. On average, the peak load and the dissipated energy increased by 42 and 170%, respectively, while only 80% of the stiffness could be recovered.

Tsonos [2.29] repaired two identical half-scale, one-way exterior joints by removing the concrete in the entire joint region and part of the column ends, and replacing it with a high-strength (70 MPa [10,150 psi]), nonshrink mortar. One of the specimens was also provided with two additional horizontal joint ties. The repair resulted in significant increases in the strength, stiffness, and energy dissipation capacity, especially toward the end of the tests. After repair, the specimens exhibited the same failure mode that involved the formation of a beam hinge and damage concentration in this region only. Thus, Tsonos [2.29] concluded that the requirements on joint transverse reinforcement can be relaxed when high-strength mortar is used for the repair of heavily damaged joints.

Clearly, a beam-column joint with crushed concrete and buckled or ruptured reinforcement cannot be strengthened by any method without removing and replacing the damaged concrete. The aforementioned experiment results show that this technique can be used for strengthening, even by itself, if high-strength nonshrink concrete is used for replacement. This, however, relies on the assumption that the damaged joint is readily accessible, which is rarely the case in actual buildings, and shoring can be economically provided. Also, Lee et al. [2.30] stated that if only the beam end is repaired with this

technique, the high strength of the repair materials can cause the damage to move from the beam to the unrepaired joint and column.

2.5.3 Concrete Jackets

One of the earliest and the most common solutions for rehabilitation of concrete frames is to encase the existing column, along with the joint region, in new concrete with additional longitudinal and transverse reinforcement. The continuity of the added longitudinal bars through the joint requires opening the slab at the column corners (Figure 2.5a). The addition of the joint transverse reinforcement makes the process even more labor-intensive, in which case the beams are also cored, and in-place bending of the hooks is necessary.

Corazao and Durrani [2.55] strengthened three single (two exterior: ER, ES1R; one interior: IR) and two multi-joint (two-bay) subassemblages (CS2R, CS4R), some including a floor slab, by jacketing the column, the joint region, and sometimes a portion of the beam. Due to the difficulties experienced with in-place bending of the crosstie hooks in the joint region, the additional joint reinforcement was modified to a set of dowels with a hook. The strength, stiffness, and energy dissipation capacity of all three single-joint specimens were increased, except for the one-way exterior joint that dissipated less energy after jacketing. In two of these specimens, the damage was successfully moved away from the joint due to added beam bottom bars hooked both in the joint and at 25 cm (10 in.) from the column face. The retrofit was not as effective in improving the behavior of the multijoint specimens; the results were taken to indicate that jacketing of the columns alone was not adequate in restoring the performance without addressing the problem of load transfer between beams and columns.

In tests conducted by Alcocer and Jirsa [2.31] on four three-dimensional beam-column-slab subassemblages subjected to severe bidirectional loading, the need to drill holes through the beams for placing joint confinement reinforcement was eliminated by

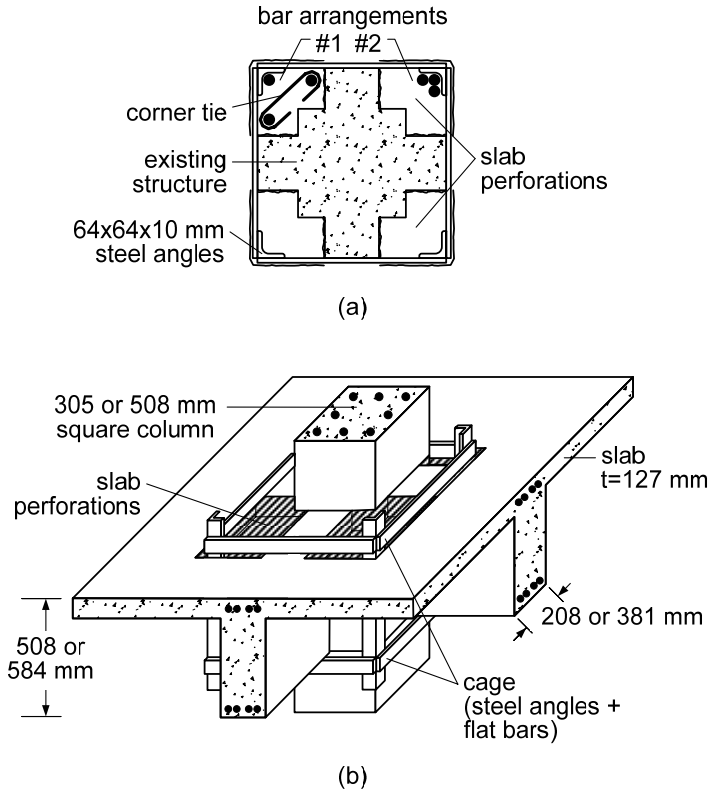

Figure 2.5 — Concrete jacketing technique studied by Alcocer and Jirsa [2.31]: (a) plan, and (b) perspective.

welding a structural steel cage around the joint (Figure 2.5b). The cage consisted of steel angles designed to resist the lateral expansion of the joint and flat bars connecting the angles. The studied variables were jacketing the columns only or both beams and columns, jacketing after or prior to first damage, and using bundles or distributed vertical reinforcement (Figure 2.5a) around the column. The critical section was within the jacket for the specimens with column jackets only, while the failure zone moved outside the cage when the beams were jacketed as well. It was reported that the steel cage and the corner ties confined the joint satisfactorily up to a 4% drift, at which time severe crushing and spalling occurred. Alcocer and Jirsa [2.31] recommended that the ACI 352R-76 [2.1] provisions on joint strength and bond could be used to proportion the jacket and that

distributed bars through the slab perforations should be preferred to bundles. The development of bundled bars can be a problem with smaller column beam strength ratios.

Another jacketing method employed post-tensioning of the additional column reinforcement placed in a high-strength concrete jacket and a reinforced concrete fillet built around the unreinforced beam-column joint (Figure 2.6a-c) [2.13, 2.14]. The bottom half of the first-story columns were conventionally jacketed with bonded longitudinal reinforcement and adequate transverse hoops to limit the strength enhancement due to post-tensioning and to ensure adequate energy dissipation in the event of an earthquake. Dimensions of the fillet were designed based on the required development length of the discontinuous beam bottom reinforcement and the desired beam hinge locations. As shown in Figure 2.6c, triangular segments of the slab were removed at the four corners of the column to permit placement of the fillets and vertical reinforcement, and all beams were drilled to place additional horizontal joint reinforcement. This method was first validated by Choudhuri et al. [2.13] by testing a 1/3-scale two-way interior beam-column-slab subassemblage previously tested by Aycardi et al. [2.15] without retrofit. Then, Bracci et al. [2.14] evaluated analytically and experimentally the application of this retrofit scheme to the columns of the 1/3-scale frame structure they had tested without retrofit [2.16], the results of which were summarized earlier in this chapter. In the analytical part, the structure was analyzed for four different alternatives: either the interior or all columns were strengthened, and the first-story columns had either partial or full base fixity. In the experimental part, only the interior columns were strengthened and provided with partial base fixity, and a series of shaketable tests were conducted on the frame structure. Both the subassemblage test and the shaketable tests showed that the original soft-story mechanism was avoided and that flexural hinges occurred at beam ends adjacent to the newly cast joint fillets with no noticeable damage to the columns.

The experimental program performed by Hakuto et al. [2.20] included testing of three one-way interior joints (R1, R2, and R3) with no joint reinforcement strengthened

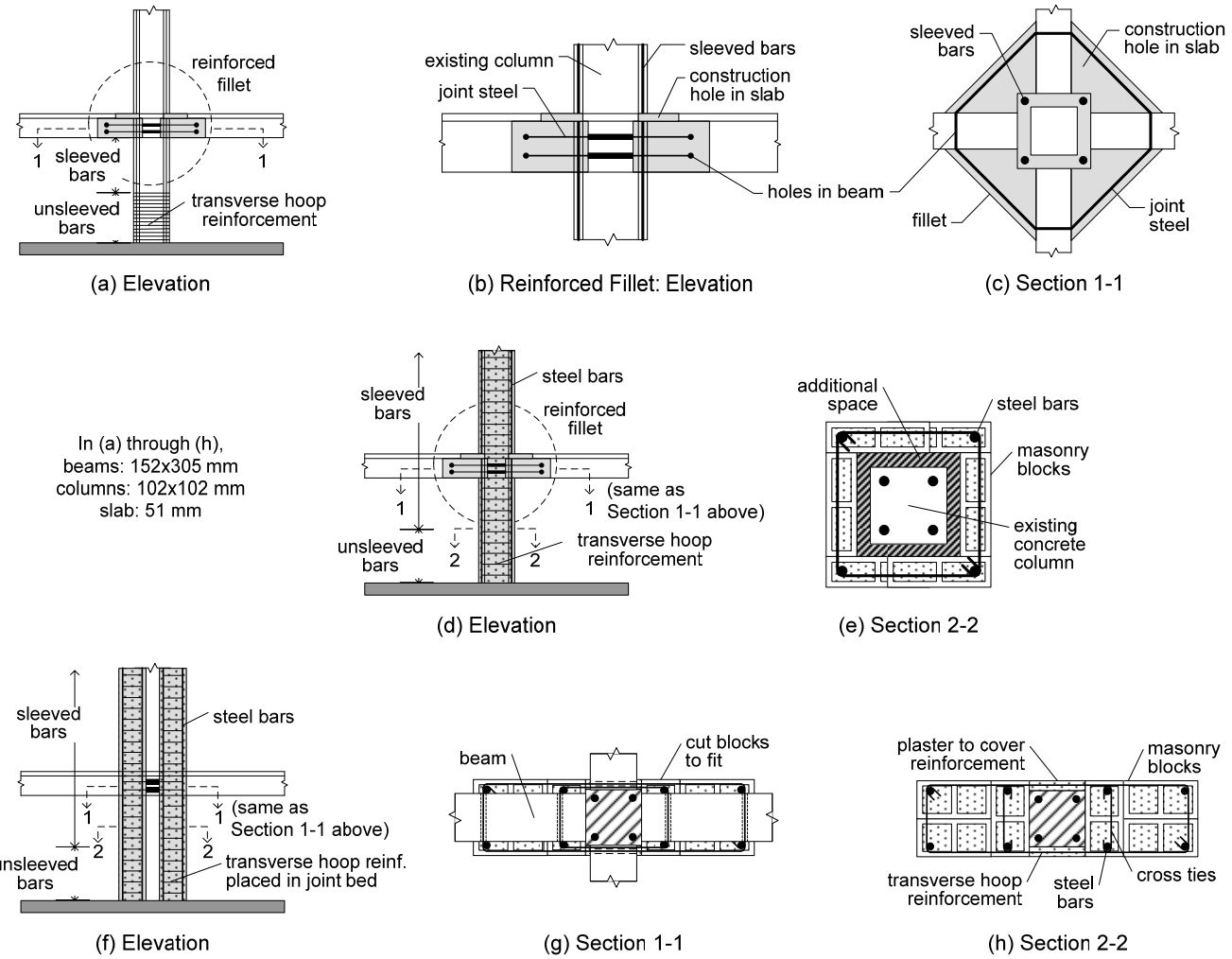

Figure 2.6 — Retrofit techniques studied by Bracci et al. [2.14]: (a, b, and c) prestressed concrete jacketing; (d and e) masonry block jacketing; and (f, g, and h) partial masonry infill.

with RC jackets. The specimen previously damaged in the joint region was strengthened by jacketing the beams, columns, and joint. The joint core was strength ned using plain circular hoops consisting of two U-shaped ties placed through holes drilled in the beams and welded in place. In the retrofit of the two specimens with no previous damage, the joint core was kept unreinforced, and one of them had a column jacket only. A stable and ductile response with beam plastic hinges was obtained except for the specimen with column jacket only, which underwent an early beam shear failure (at 0.7% drift). The major conclusions regarding the retrofits were that the addition of joint core hoops is very labor-intensive, but the hoops may not be required for one-way interior joints if the existing column is enlarged by jacketing so that the joint shear stress is reduced to less than 0.07.

Tsonos [2.56, 2.57] studied the effectiveness of RC jackets in cases where one or more sides of the columns and beam-column joints to be strengthened are inaccessible due to adjacent structures. Four one-way exterior joints with insufficient or no joint ties were repaired with three-sided high-strength (~60 MPa [8,700 psi]) concrete jackets [2.56], and another with no joint ties was repaired with a two-sided jacket [2.57]. Additional joint ties were placed by coring the beam, and short bars were placed in a transverse direction inside the hooks of the beam bars in the joint region to improve the anchorage of these bars. In the case of both two-sided and three-sided jacketing, the mode of failure before jacketing, which involved significant loss of joint concrete and damage at the column ends, was improved to formation of a beam hinge and buckling of beam bars after jacketing. The unjacketed rear side of the joints did not exhibit any distress. The hysteresis loops were remarkably improved in terms of peak load, stiffness, energy dissipation, and the amount of pinching.

An apparent disadvantage of concrete jacketing techniques is labor-intensive procedures such as perforating the floor slab, drilling through the beams, and sometimes in-place bending of the added joint transverse reinforcement. The need for drilling through the beams could be eliminated by welding a steel cage around the joint (Figure

2.5), but this results in poor appearance. Jacketing increases the member sizes, which reduces the available floor space and increases mass. The construction procedures also disrupt building occupants, which may well add to the overall cost of the rehabilitation. Finally, such jacketing techniques alter the dynamic characteristics of the building (for example, a 120% increase in first mode period and a 73% increase in base shear capacity was reported by Bracci et al. [2.14]). Changed dynamics may cause increased demands at unintended locations, and may require careful reanalysis. Nevertheless, concrete jacketing techniques did provide increased joint strength, shifted the failure to the beam, and increased overall lateral strength and energy dissipation.

2.5.4 Reinforced Masonry Blocks

Bracci et al. [2.14] analyzed (but did not test) strengthening using reinforced concrete masonry units (CMUs). The first method required the existing interior columns to be jacketed by CMUs, with additional longitudinal reinforcement within the corner cores extending continuously through the slabs and later post-tensioned (Figure 2.6d, e). Any space between the units and the existing column was then grouted. The shear capacity was increased by providing wire mesh in the mortar bed joints. A reinforced concrete fillet (Figure 2.6b, c) was built around the joints. In a second method, partial masonry infills reinforced with posttensioned vertical reinforcement were constructed on each side of existing columns as shown in Figure 2.6f-h. The exact number of units was governed by the development length of the discontinuous beam bottom reinforcement. The beam-column joints were strengthened in shear by wrapping with rectangular hoops passing through holes drilled in beams. Nonlinear dynamic analyses on the 1/ 3-scale, three-story GLD model [2.16], incorporating the results from previous component tests [2.15], showed that strong column-weak beam behavior was enforced and that adequate control of interstory drifts was achieved. For the case in which all columns in the model were strengthened, a beam hinging mechanism was dominant. When only interior col-

umns were strengthened, a predominant beam hinge mechanism was accompanied by some yielding in upper story exterior columns.

The same limitations mentioned previously for concrete jacketing also apply to CMU jacketing. In the case of partial masonry infills, an added functional disadvantage is an increased loss of internal space between the bays.

2.5.5 Steel Jackets and External Steel Elements

Various configurations of steel jackets, plates, or shapes have been used to increase the strength and ductility of deficient beam-column joints. Steel jackets consist of flat or corrugated steel plates, or rectangular or circular steel tubes prefabricated in parts and welded in place. The space between the jacket and RC frame is grouted with nonshrink or expansive cement mortar. Steel parts are often mechanically anchored to the concrete to improve confinement. Attaching plates to selected faces of the members using adhesives and bolts, and connecting these plates using rolled shapes (for example, angles) has also been attempted.

Corazao and Durrani [2.55] strengthened one exterior (ES2R) and one interior (IS1R) two way beam-column-slab subassemblage by bolting and epoxy-bonding external steel plates on each column face, welding steel angles to the plates, and by enlarging the joint region with a concrete fillet. As shown in Figure 2.7, the joint enlargement was similar to that used by Bracci et al. [2.14] (Figure 2.6c) except that the continuous joint hoops were replaced with dowels with a hook. The steel plates bonded at each face of the upper and lower columns were bolted to the old concrete near the joint and connected to each other by welded angles continuous through the slab. In the case of the interior joint, a plate was also bonded and bolted to the underside of the enlarged joint. For both specimens, cracking near the joint observed before retrofit was successfully moved to the end of the enlarged joint region after retrofit, and there was no evidence of damage in the column or its external reinforcement. The strength, initial

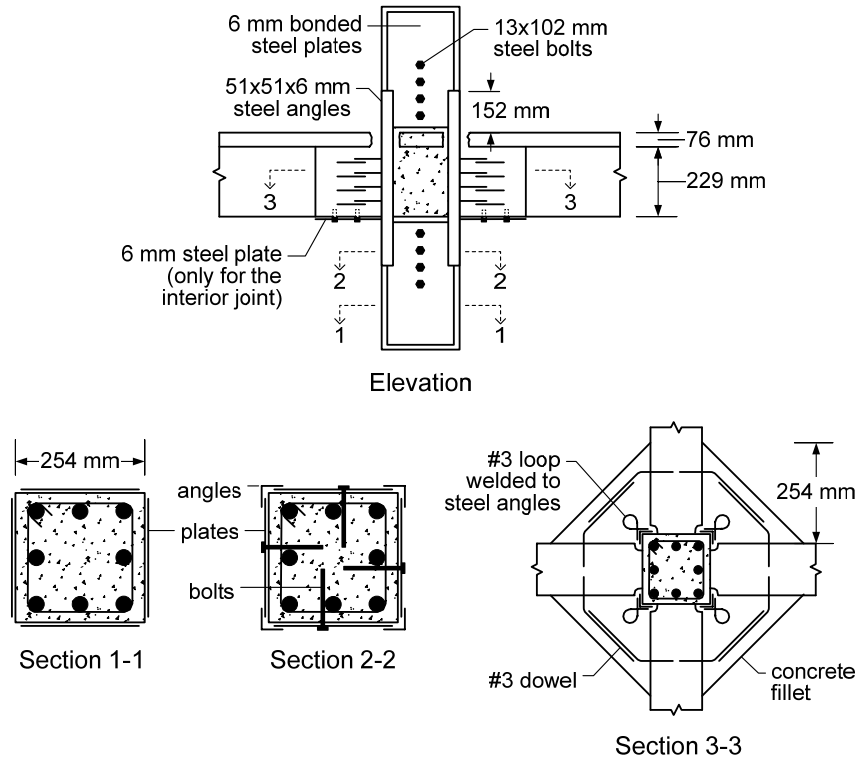

Figure 2.7 — External steel configurations studied by Corazao and Durrani [2.55].

stiffness, and energy dissipation of the exterior joint were increased by approximately 18, 12, and 2%, respectively. The corresponding increases for the interior joint were 21, 34, and 13%, respectively. The better improvement in the energy dissipation of the interior joint was attributed to the slippage between concrete and the steel plates of that joint.

Beres et al. [2.9] considered two different external plate configurations for strengthening one of their interior joints with discontinuous beam bottom reinforcement and for one of their exterior joints. To prevent pullout of the beam bottom bars, the interior joint was strengthened by bolting two steel channel sections to the underside of the beams and connecting them by two steel tie-bars running alongside the column (Figure 2.8a). The damage was transferred from the joint embedment zone to other parts of the joint; a 20% increase in peak strength, 10 to 20% increase in stiffness, and no significant change in energy dissipation were observed. The objective of the exterior joint

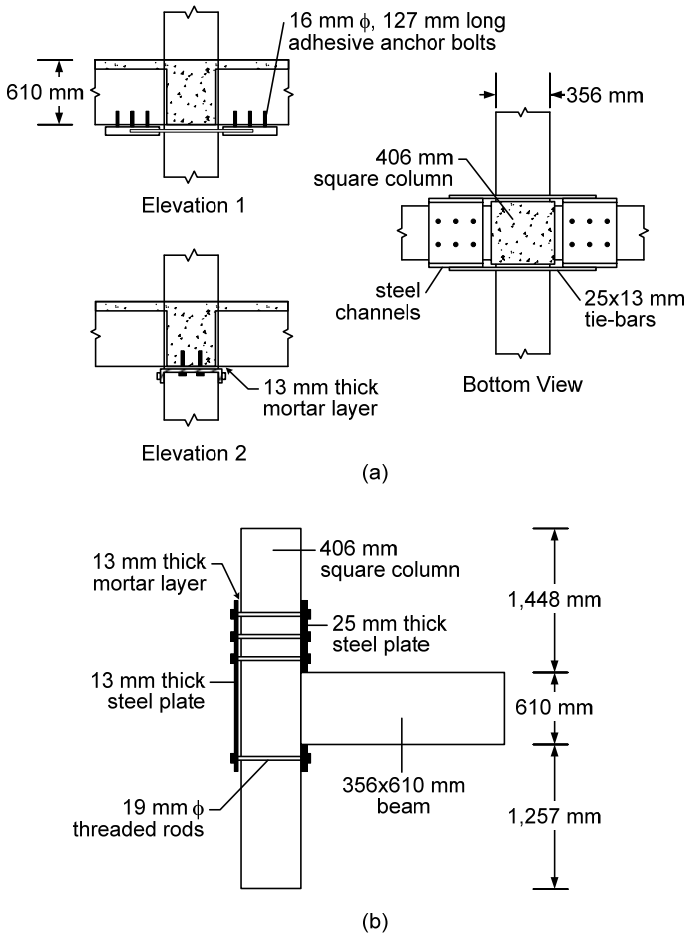

Figure 2.8 — External steel configurations studied by Beres et al. [2.9]

retrofit was to force the flexural hinges to form in the beam and to increase the joint confinement. External steel plates placed along the opposite faces of the upper and lower columns were connected with threaded rods (Figure 2.8b). This retrofit prevented the cracks from extending into the column bar splice region. A flexural hinge formed in the joint panel close to the beam, which was followed by the pullout of the beam bottom bars. The increase in the peak strength and the initial stiffness were 33 and 12%, respectively, with a higher rate of degradation than in the unstrengthened specimen. A notable increase in energy dissipation was observed in the final stages of loading.

Ghobarah et al. [2.32] and Biddah et al. [2.33] proposed the use of corrugated steel shapes to provide high out-of-plane stiffness. The grouted corrugated steel jacket

was intended to provide an early lateral confinement effect in the elastic range of the RC column as well as additional shear resistance in the column, beam, and joint. The cross-section of the corrugated steel plates and of the two-part jackets before and after installation are shown in Figure 2.9. In addition to the in-place welding, the joint jacket was also anchored to the concrete using two steel angles and anchor bolts (Figure 2.9a). A 20 mm (0.79 in.) gap was provided between the end of the beam jacket and the column face to minimize the flexural strength enhancement. Tests on four one-way exterior joints showed that the proposed system could change the joint shear failure mode to a ductile flexural mode in the beam when both the column and the beam were jacketed [2.32]. Effective confinement was achieved up to a 5% drift by increasing the ultimate compressive strain of concrete. Biddah et al. [2.33] added to this study by testing two exterior joint specimens with discontinuous beam bottom bars. One of them was a reference specimen, and the second was strengthened with a corrugated steel jacket around the column only in addition to two steel plates bolted to the beam and to the joint to prevent pullout of beam bottom bars. This strengthening system could not resist the bottom bar pullout observed in the reference specimen, and the bolts failed in shear; however, the system did provide an increase of approximately 38% in strength and 180% in energy dissipation capacity. A design methodology for calculating the required thicknesses of the corrugated steel jackets and the grout was also proposed [2.32].

The authors believe that, when compared with concrete and masonry jackets, the use of steel jackets can significantly reduce the construction time due to prefabrication. Disadvantages, however, such as the potential for corrosion, difficulty in handling the heavy steel plates, objectionable aesthetics in the case of corrugated steel shapes, and loss of floor space in the case of grouted steel tubes, cannot be overlooked. Steel jackets may result in excessive capacity increases, even where only confinement effect is intended, and create unexpected failure modes [2.34]. Even if these disadvantages are ignored, it seems difficult to apply these schemes to actual three-dimensional joints. The presence of

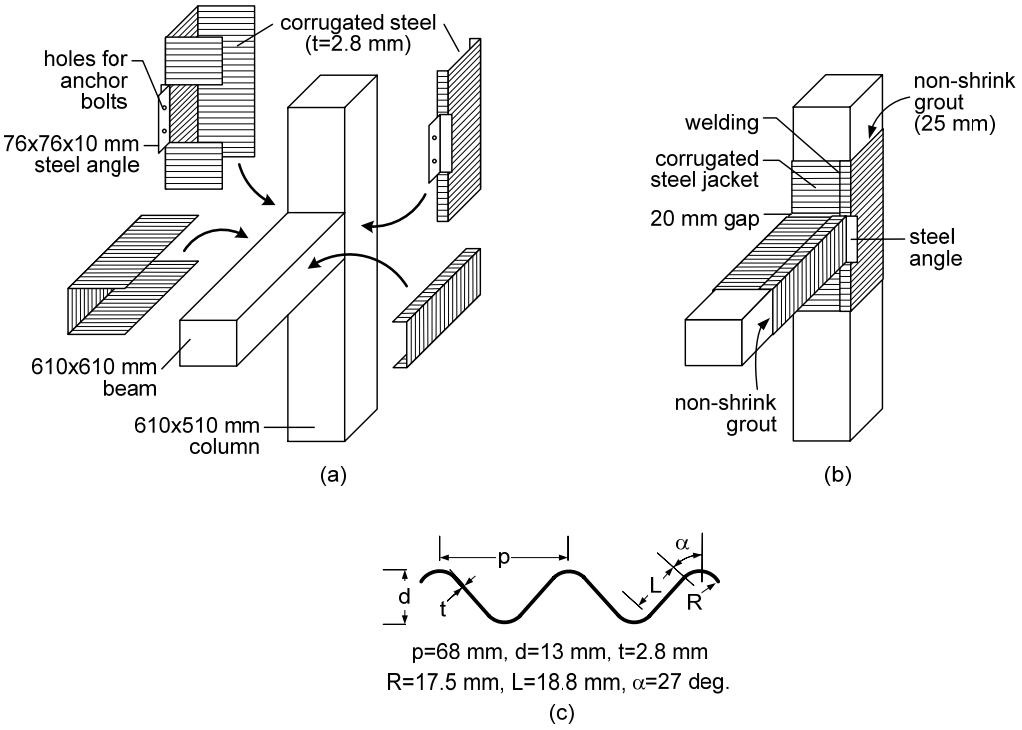

Figure 2.9 — Corrugated steel jacketing technique proposed by Ghobarah et al. [2.32] and Biddah et al. [2.33]: (a) before installation; (b) after installation; and (c) cross section of corrugated steel plates.

a floor slab, for instance, makes it difficult, if not unfeasible, to install beam jackets such as shown in Figure 2.9. Although different two-part corrugated steel jackets have been proposed [2.33] for interior, exterior, and corner joints with floor slab, there are no available data to validate their performance. Prestressing by preheating of externally attached steel straps in a repair scheme has been useful [2.58], but should not be relied on because it is difficult to control in the field.

2.5.6 Fiber-Reinforced Polymeric Composites

Since 1998, research efforts on upgrading existing beam-column joints have focused on the use of FRP composites in the form of epoxy-bonded flexible sheets, shop-manufactured strips, or near-surface-mounted rods. The relatively higher initial cost of FRPs is purportedly outweighed by their advantages such as high strength-weight ratios,

corrosion resistance, ease of application (including limited disruption to building occupancy), low labor costs, and no significant increase in member sizes [2.35, 2.36]. They are most attractive for their tailorability; the fiber orientation in each ply can be adjusted so that specific strengthening objectives such as increasing the strength only, confinement only, or both, can be achieved. An externally bonded FRP system requires that the concrete surface be thoroughly cleaned (all loose materials removed, and cracks epoxy-injected in damaged structures), a penetrating epoxy primer be applied, and each ply be placed between two coats of resin. Zureick and Kahn [2.59] postulated that the primer and the resin should only be applied when the ambient temperature is between 5 and 32 °C, the relative humidity is less than 90%, the concrete surface temperature is more than 2 °C above the dew point, and the concrete moisture content is no greater than 4%. They also suggested that the glass transition temperature of the resin should be at least 30 °C above the maximum operating temperature and that elapsed time between mixing and application of the first ply and between any two successive plies should be within a time period not exceeding the gel time of the resin.

At present, the literature on FRP-strengthened joints mainly consists of simplified two-dimensional tests [2.36, 2.37-2.45, 2.22] and an analytical study [2.35].

Prota et al. [2.40, 2.41] used CFRP rods in combination with externally bonded sheets (Figure 2.10a) to upgrade and test 11 one-way interior joints with three different levels of column axial load in an attempt to shift the failure first from the column to the joint, then from the joint to the beam. The CFRP rods were placed in epoxy-filled grooves prepared near the surface (Figure 2.10b). The failure modes could not be controlled as intended, and a ductile beam failure was not achieved. The Type 2 scheme moved the failure from the compression to the tension side of the column for low column axial load while, for high axial load, a combined column-joint failure occurred. The addition of CFRP rods as flexural reinforcement along the column (Type 3) led to a joint shear failure. When the joint panel was also strengthened (Type 4), the column-joint

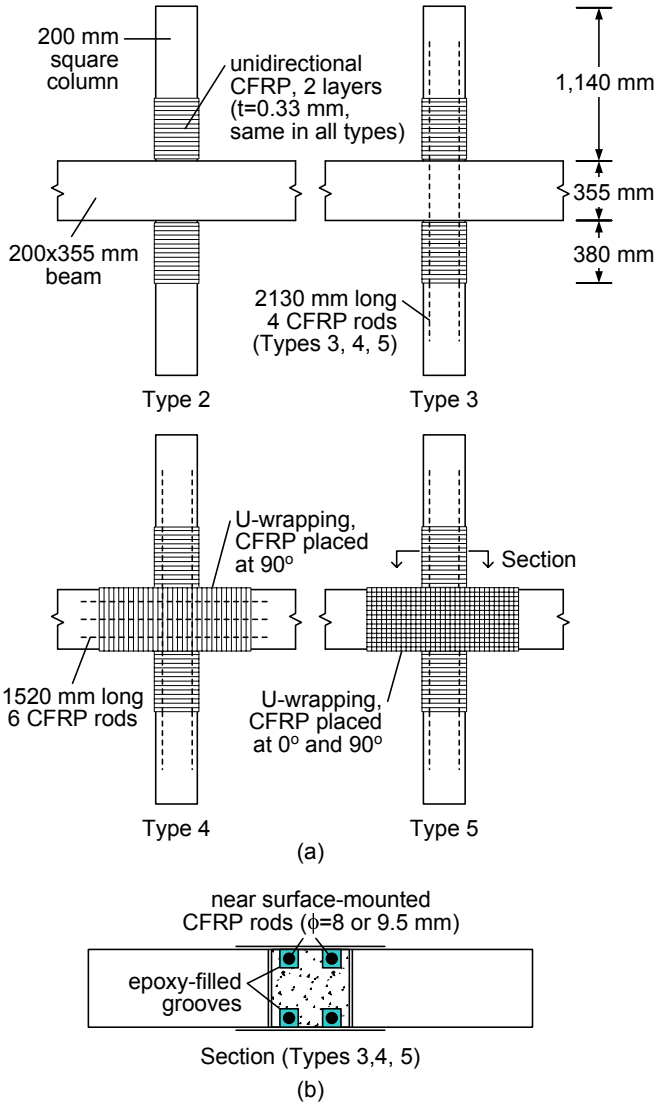

Figure 2.10 — Specimens strengthened with CFRP sheets and/or rods, tested by Prota et al. [2.40, 2.41]: (a) elevation, and (b) plan.

interface failed, which was attributed to termination of the FRP sheet reinforcement at that location to account for the presence of a floor system. The increases in strength were 7 to 33% for Type 2, 39 and 62% for Type 3, and 37 and 83% for Type 4. The changes in the maximum story drift for low and high column axial load were -11 and 25% for Type 2, 6 and -14% for Type 3, and 73 and 51% for Type 4, where negative values indicate loss of ductility. The Type 5 scheme with U-wrapping of the beam and joint resulted in a failure mode similar to that of Type 4.

Ghobarah and Said [2.36] tested four, one way exterior joints (Figure 2.11a), originally designed to fail in joint shear, with or without strengthening by unidirectional or bidirectional (±45 degrees) glass fiber-reinforced polymer (GFRP) sheets. Specimens T1R and T2R, previously damaged in the joint region and repaired, were provided with mechanical anchorage using steel plates and threaded rods core-drilled through the joint. While the GFRP sheet anchored through the joint in Specimen T1R was effective until it failed in tension, it provided no improvement in Specimen T4 due to lack of threaded-rod anchorage and the resulting early delamination. No debonding or joint shear cracking was observed in Specimen T2R; the failure was due to a beam plastic hinge. The placement of the diagonal unidirectional strips in Specimen T9 was facilitated by the triangular steel bars fitted at the four corners of the joint panel. This scheme could not prevent expansion of the joint concrete, which led to delamination and a simultaneous failure of the beam and joint. Overall, this study highlighted the importance of anchorage of composite sheets in developing the full fiber strength in a small joint area.

El-Amoury and Ghobarah [2.42] modified these GFRP schemes, as shown in Figure 2.11b, for strengthening joints with both inadequate anchorage of beam bottom bars and no hoop shear reinforcement. Both schemes resulted in an approximate 100% increase in load-carrying capacity; Specimens TR1 and TR2 dissipated three and six times the energy dissipated by the reference specimen, respectively. The failure of Specimen TR1 was due to complete debonding of the composites from the beam and column surfaces, and pullout of the beam bottom bars led by fracture of the weld around the bolt heads. In Specimen TR2, the use of two U-shaped steel plates eliminated debonding of the GFRP and reduced the strength degradation; this specimen eventually failed in joint shear.

As part of the experimental program conducted by Clyde and Pantelides [2.22], the performance of CFRP sheets on a single, one-way exterior joint was investigated. With the CFRP layout shown in Figure 2.12, the joint shear failure in the original

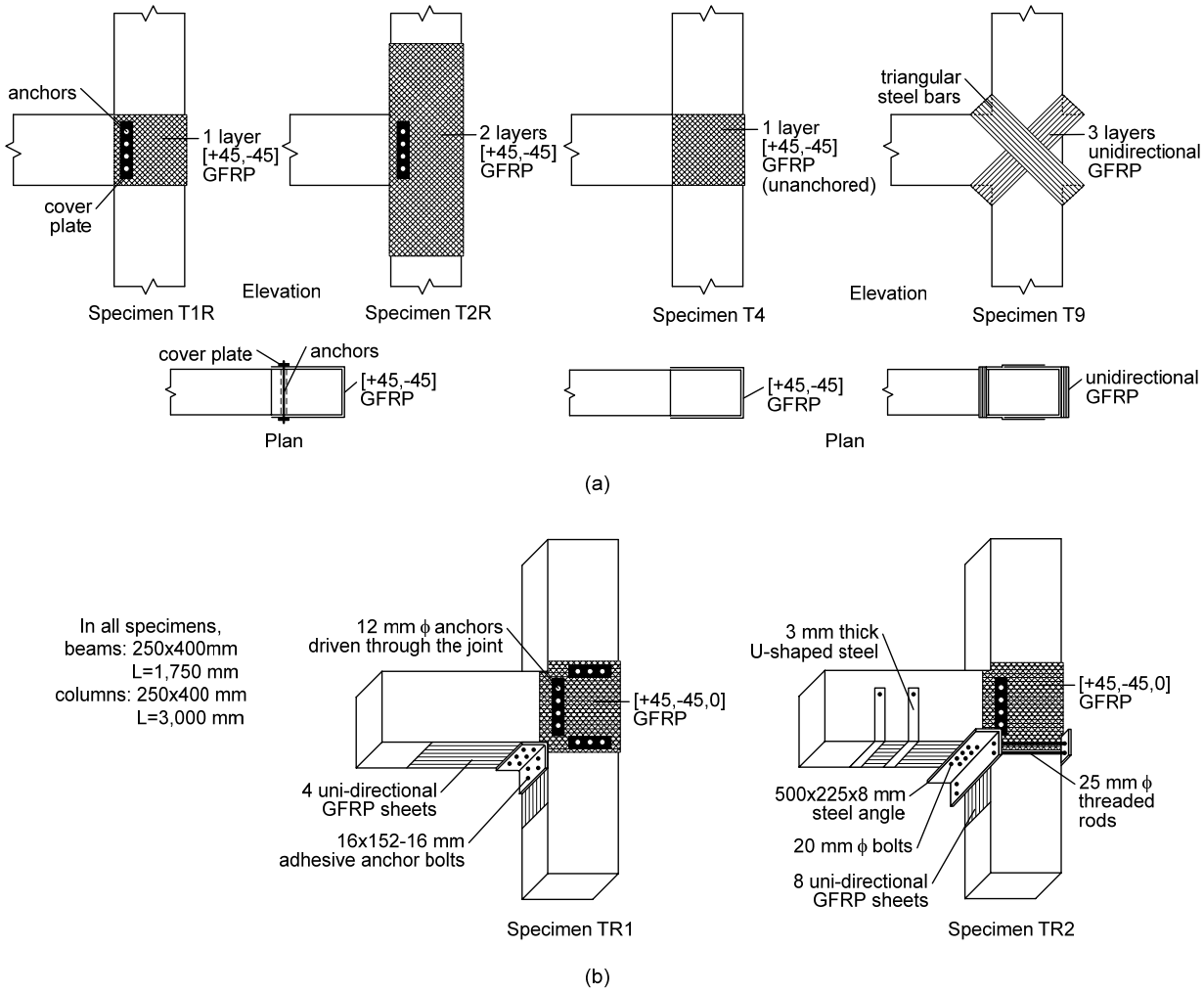

Figure 2.11 — Glass fiber-reinforced polymer-strengthened specimens tested by: Ghobarah and Said [2.36], and (b) El-Amoury and Ghobarah [2.42].

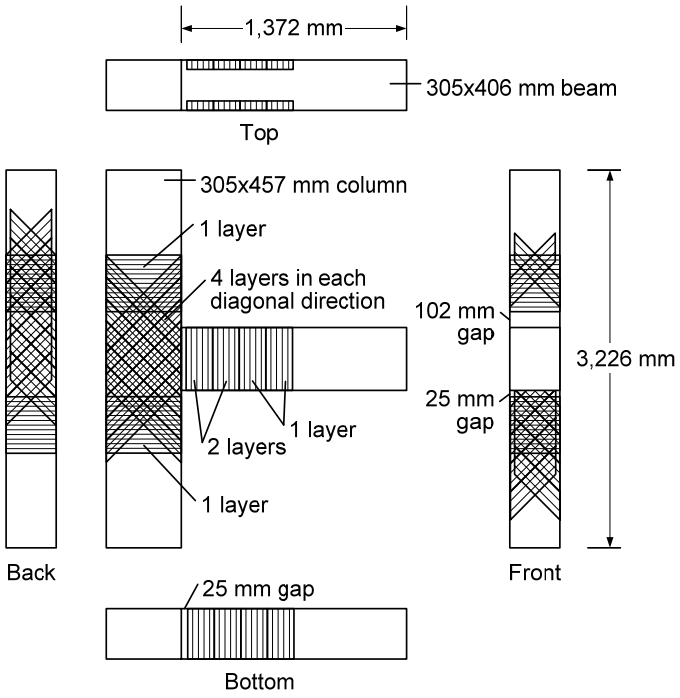

Figure 2.12 — Carbon fiber-reinforced polymer-strengthened specimen tested by Clyde and Pantelides [2.22].

specimens was shifted to the beam-column interface with minimal damage in the CFRP wrap. The increases in joint shear strength, maximum drift, and energy dissipation capacity were 5, 78, and 200%, respectively.

Antonopoulos and Triantafillou [2.35] analytically modeled FRP-strengthened joints based on the original model by Pantazopoulou and Bonacci [2.60]. The states of stress and strain at six stages of the response were numerically solved until concrete crushing or FRP failure due to fracture or debonding occurred. To validate their analytical model and determine the role of various parameters on the effectiveness of FRP, Antonopoulos and Triantafillou [2.43] also conducted 2/3-scale reverse-cycle tests on 18 exterior joints strengthened with various configurations of pultruded carbon strips and with flexible carbon or glass fiber sheets. The investigated variables were the following: area fraction and distribution of FRP, column axial load, internal joint reinforcement, initial damage, carbon versus glass fibers, sheets versus strips, and the

effect of transverse stub beams. All 18 specimens were designed to fail in joint shear both before and after strengthening so that the contribution of FRP to the joint shear capacity could be evaluated. Consequently, the failures were preceded by partial or complete debonding of composites (either at the unanchored ends or near the joint corners), leading to substantial pinching in the hysteresis loops. An increase in column axial load from 4 to 10% of its axial load capacity improved the strength increase from 65 to approximately 85% and the energy increase from 50 to 70%. The increase in stiffness varied in each loading cycle and reached values around 100%. The conclusions of this research highlighted the need for mechanical anchorage, better performance of flexible sheets over strips, the positive effect of increased column axial load on shear capacity of FRP-strengthened joints, better energy dissipation due to glass fibers than carbon fibers, increased effectiveness of FRP due to less internal joint reinforcement, and the negative effect of transverse stubs on the effectiveness of FRPs. Analytical predictions [2.35] of shear strength were found to be in good agreement with these experimental results as well as with the results of Gergely et al. [2.39].

The aforementioned survey of the literature indicates that externally bonded FRP composites can eliminate some of the important limitations (for example, difficulties in construction or increases in member sizes) of other strengthening techniques, and still improve the joint shear capacity and shift the failure towards ductile beam hinging mechanisms. Such improvements have been achieved even with low quantities of FRP by placing the fibers in ±45- degree directions in the joint region and by wrapping the member ends to clamp the ±45-degree sheets and increase the confinement. Most studies have shown that the behavior is dominated by debonding of the composites from the concrete surface, and have indicated the need for a thorough surface preparation as well as for reliable mechanical anchorage methods that would lead to effective joint confinement and full development of fiber strength. The authors believe that the development of such anchorage methods can possibly create a potential for FRP-

strengthened actual three-dimensional joints, which are yet to be tested. Though a high level of skill is not necessary, selection and application of FRP composites requires careful consideration of the environmental conditions (for example, temperature and humidity) present at the time of application and likely during the service life [2.59].

The following publications were also reviewed in this study but could not be incorporated in this chapter due to space limitations: Dogan et al. [2.46]; Shannag et al. [2.47]; Migliacci et al. [2.58]; Adin et al. [2.48]; Hoffschild et al. [2.34]; Gergely et al. [2.37, 2.39]; Pantelides et al. [2.38]; Pantelides and Gergely [2.49]; Tsonos and Stylianidis [2.44]; and Karayannis and Sirkelis [2.45]. A detailed review of these publications is presented elsewhere [2.61].

2.6 CONCLUSIONS

From the literature review on the performance, repair, and strengthening of nonseismically detailed RC beam-column joints presented in this chapter, the following conclusions were drawn:

1. The critical nonseismic joint details in existing RC structures have been well identified as shown in Figure 2.1; however, the investigation of their effects on seismic behavior have been limited to testing of isolated one-way joints (no floor slab, transverse beams, or bidirectional loads) to a very large extent, and 1/8- and 1/3-scale building models that may not accurately simulate the actual behavior of structural details;
2. Epoxy repair techniques have exhibited limited success in restoring the bond of reinforcement, in filling the cracks, and restoring shear strength in one-way joints, although some authors believe it to be inadequate and unreliable [2.54]. The authors believe that injection of epoxy into joints surrounded by floor members would be similarly difficult;
3. Concrete jacketing of columns and encasing the joint region in a reinforced fillet is an effective but the most labor-intensive strengthening method due to difficulties in plac-

ing additional joint transverse reinforcement. Welding an external steel cage around the joint instead of adding internal steel has also proven effective in the case of a three-dimensional interior joint test. These methods are successful in creating strong column-weak beam mechanisms, but suffer from considerable loss of floor space and disruption to building occupancy;

4. An analytical study showed that joint strengthening with reinforced masonry units can lead to desirable ductile beam failures and reduction of interstory drifts; however, no experimental data are available to validate their performance;
5. Grouted steel jackets tested to date cannot be practically applied in cases where floor members are present. If not configured carefully, such methods can result in excessive capacity increases and create unexpected failure modes. Externally attached steel plates connected with rolled sections have been effective in preventing local failures such as beam bottom bar pullout and column splice failure; they have also been successfully used in combination with a reinforced concrete fillet surrounding the joint;
6. Externally bonded FRP composites can eliminate some important limitations of other strengthening methods such as difficulties in construction and increases in member sizes. The shear strength of one-way exterior joints has been improved with ±45-degree fibers in the joint region; however, ductile beam failures were observed in only a few specimens, while in others, composite sheets debonded from the concrete surface before a beam plastic hinge formed. Reliable anchorage methods need to be developed to prevent debonding and to achieve full development of fiber strength within the small area of the joint, which can possibly lead to the use of FRPs in strengthening of actual three-dimensional joints; and
7. Most of the strengthening schemes developed thus far have a limited range of applicability, if any, either due to the unaccounted floor members (that is, transverse beams and floor slab) in real structures or to architectural restrictions. Experiments conducted

to date have generally used only unidirectional load histories. Therefore, the research in this area is far from complete, and a significant amount of work is necessary to arrive at reliable, cost-effective, and applicable strengthening methods. In developing such methods, it is important that testing programs be extended to include critical joint types (for example, corner) under bidirectional cyclic loads.

2.7 REFERENCES

[2.1] ACI-ASCE Committee 352 (1976). "Recommendations for design of beam-column joints in monolithic reinforced concrete structures (ACI 352R-76)." *ACI Journal Proceedings*, 73(7), 375-393.

[2.2] Standard Association of New Zealand (1982). *Code of practice for the design of concrete structures (NZS 3101:1982)*, Wellington, New Zealand.

[2.3] Beres, A., Pessiki, S. P., White, R. N., and Gergely, P. (1996). "Implications of experiments on the seismic behavior of gravity load designed RC beam-to-column connections." *Earthquake Spectra*, 12(2), 185-198.

[2.4] ACI-ASCE Committee 352 (2002). *Recommendations for design of beam-column connections in monolithic reinforced concrete structures (ACI 352R-02)*, American Concrete Institute, Farmington Hills, MI.

[2.5] Moehle, J. P., and Mahin, S. A. (1991). "Observations on the behavior of reinforced concrete buildings during earthquakes." *Earthquake-resistant concrete structures: Inelastic response and design*, SP-127, S. K. Ghosh, ed., American Concrete Institute, Farmington Hills, MI, 67-89.

[2.6] Sezen, H., Whittaker, A. S., Elwood, K. J., and Mosalam, K. M. (2003). "Performance of reinforced concrete buildings during the August 17, 1999 Kocaeli, Turkey earthquake, and seismic design and construction practise in Turkey." *Engineering Structures: The Journal of Earthquake, Wind and Ocean Engineering*, 25(1), 103-114.

[2.7] Erdik, M., Sesetyan, K., Demircioglu, M. B., Celep, U., Biro, Y., and Uckan, E. (2002). *Preliminary observations on the Sultandagi, Turkey, earthquake of February 3, 2002,* EERI Special Earthquake Report.

[2.8] Pessiki, S. P., Conley, C., White, R. N., and Gergely, P. (1990). "Seismic behavior of the beam column connection region in lightly-reinforced concrete frame structures." *Proceedings of Fourth U.S. National Conference on Earthquake Engineering*, Palm Springs, CA, (2), 707-716.

[2.9] Beres, A., El-Borgi, S., White, R. N., and Gergely, P. (1992). *Experimental results of repaired and retrofitted beam-column joint tests in lightly reinforced concrete frame buildings,* Technical report NCEER-92-0025, State University of New York at Buffalo, Buffalo, NY.

[2.10] Beres, A., Pessiki, S. P., White, R. N., and Gergely, P. (1991). "Seismic performance of existing reinforced concrete frames designed primarily for gravity loads." *Sixth Canadian Conference on Earthquake Engineering*, Toronto, Ontario, Canada, 655-662.

[2.11] Beres, A., White, R. N., Gergely, P., Pessiki, S. P., and El Attar, A. (1992). "Behavior of existing non-seismically detailed reinforced concrete frames." *Proceedings of the Tenth World Conference on Earthquake Engineering*, Balkema, Rotterdam, 3359-3363.

[2.12] ACI-ASCE Committee 352 (1992). *Recommendations for design of beam-column joints in monolithic reinforced concrete structures (ACI 352R-91 [reapproved 1997])*, American Concrete Institute, Farmington Hills, MI.

[2.13] Choudhuri, D., Mander, J. B., and Reinhorn, A. M. (1992). *Evaluation of seismic retrofit of reinforced concrete frame structures: Part I—Experimental performance of retrofitted subassemblages*, Technical report NCEER-92-0030, State University of New York at Buffalo, Buffalo, NY.

[2.14] Bracci, J. M., Reinhorn, A. M., and Mander, J. B. (1995). "Seismic retrofit of reinforced concrete buildings designed for gravity loads: Performance of structural model." *ACI Structural Journal*, 92(6), 711-723.

[2.15] Aycardi, L. E., Mander, J. B., and Reinhorn, A. M. (1994). "Seismic resistance of reinforced concrete frame structures designed only for gravity loads: Experimental performance of subassemblages." *ACI Structural Journal*, 91(5), 552-563.

[2.16] Bracci, J. M., Reinhorn, A. M., and Mander, J. B. (1995). "Seismic resistance of reinforced concrete frame structures designed for gravity loads: Performance of structural system." *ACI Structural Journal*, 92(5), 597-609.

[2.17] Kunnath, S. K., Hoffmann, G., Reinhorn, A. M., and Mander, J. B. (1995). "Gravity load-designed reinforced concrete buildings—Part I: Seismic evaluation of existing construction." *ACI Structural Journal*, 92(3), 343-354.

[2.18] Kunnath, S. K., Hoffmann, G., Reinhorn, A. M., and Mander, J. B. (1995). "Gravity load-designed reinforced concrete buildings—Part II: Evaluation of detailing enhancements." *ACI Structural Journal*, 92(4), 470-478.

[2.19] Pessiki, S. P., Conley, C. H., Gergely, P., and White, R. N. (1990). *Seismic behavior of lightly reinforced concrete column and beam-column joint details*, Technical report NCEER-90-0014, State University of New York at Buffalo, Buffalo, NY.

[2.20] Hakuto, S., Park, R., and Tanaka, H. (2000). "Seismic load tests on interior and exterior beam-column joints with substandard reinforcing details." *ACI Structural Journal*, 97(1), 11-25.

[2.21] Walker, S. G., Yeargin, C. M., Lehman, D. E., and Stanton, J. F. (2002). "Performance based seismic evaluation of existing joints." *Proceedings of the Seventh U.S. National Conference on Earthquake Engineering* (CD-ROM), Boston, MA.

[2.22] Clyde, C., and Pantelides, C. P. (2002). "Seismic evaluation and rehabilitation of R/C exterior building joints." *Proceedings of the Seventh U.S. National Conference on Earthquake Engineering* (CD-ROM), Boston, MA.

[2.23] Li, B., Wu, Y., and Pan, T. C. (2002). "Seismic behavior of nonseismically detailed interior beam-wide column joints—Part I: Experimental results and observed behavior." *ACI Structural Journal*, 99(6), 791-802.

[2.24] Li, B., Wu, Y., and Pan, T. C. (2003). "Seismic behavior of nonseismically detailed interior beam-wide column joints—Part II: Theoretical comparisons and analytical studies." *ACI Structural Journal*, 100(1), 56-65.

[2.25] Standard Association of New Zealand (1995). *The design of concrete structures (NZS 3101:1995)*, Wellington, New Zealand.

[2.26] French, C. W., Thorp, G. A., and Tsai, W. J. (1990). "Epoxy repair techniques for moderate earthquake damage." *ACI Structural Journal*, 87(4), 416-424.

[2.27] Filiatrault, A., and Lebrun, I. (1996). "Seismic rehabilitation of reinforced concrete joints by epoxy pressure injection technique." *Seismic rehabilitation of concrete structures*, SP-160, G. M. Sabnis, A. C. Shroff, and L. F. Kahn, eds., American Concrete Institute, Farmington Hills, MI, 73-92.

[2.28] Karayannis, C. G., Chalioris, C. E., and Sideris, K. K. (1998). "Effectiveness of RC beam-column connection repair using epoxy resin injections." *Journal of Earthquake Engineering*, 2(2), 217-240.

[2.29] Tsonos, A. G. (2001). "Seismic rehabilitation of reinforced concrete joints by the removal and replacement technique." *European Earthquake Engineering*, (3), 29-43.

[2.30] Lee, D. L. N., Wight, J. K., and Hanson, R. D. (1977). "Repair of damaged reinforced concrete frame structures." *Proceedings of the Sixth World Conference on Earthquake Engineering*, New Delhi, India, (3), 2486-2491.

[2.31] Alcocer, S.M., and Jirsa, J. O. (1993). "Strength of reinforced concrete frame connections rehabilitated by jacketing." *ACI Structural Journal*, 90(3), 249-261.

[2.32] Ghobarah, A., Aziz, T. S., and Biddah, A. (1997). "Rehabilitation of reinforced concrete frame connections using corrugated steel jacketing." *ACI Structural Journal*, 4(3), 283-294.

[2.33] Biddah, A., Ghobarah, A., and Aziz, T. S. (1997). "Upgrading of nonductile reinforced concrete frame connections." *Journal of Structural Engineering (ASCE)*, 123(8), 1001-1009.

[2.34] Hoffschild, T. E., Prion, H. G. L., and Cherry, S. (1995). "Seismic retrofit of beam-to-column joints with grouted steel tubes." *Recent developments in lateral force transfer in buildings*: *Thomas Paulay Symposium*, SP-157, N. Priestley, M. P. Collins, and F. Seible, eds., American Concrete Institute, Farmington Hills, MI, 397-425.

[2.35] Antonopoulos, C. P., and Triantafillou, T. C. (2002). "Analysis of FRP-strengthened RC beam-column joints." *Journal of Composites for Construction (ASCE)*, 6(1), 41-51.

[2.36] Ghobarah, A., and Said, A. (2002). "Shear strengthening of beam-column joints." *Engineering Structures: The Journal of Earthquake, Wind and Ocean Engineering*; 24(7), 881-888.

[2.37] Gergely, I., Pantelides, C. P., Nuismer, R. J., and Reaveley, L. D. (1998). "Bridge pier retrofit using fiber-reinforced plastic composites." *Journal of Composites for Construction (ASCE)*, 2(4), 165-174.

[2.38] Pantelides, C. P., Gergely, J., Reaveley, L. D., and Volnyy, V. A. (1999). "Retrofit of reinforced concrete bridges with carbon fiber reinforced polymer composites." *Fourth International Symposium for Fiber Reinforced Polymer Reinforcement for Reinforced Concrete Structures*, SP-188, C. W. Dolan, S. H. Rizkalla, and A. Nanni, eds., American Concrete Institute, Farmington Hills, MI, 441-453.

[2.39] Gergely, J., Pantelides, C. P., and Reaveley, L. D. (2000). "Shear strengthening of RCT-Joints using CFRP composites." *Journal of Composites for Construction (ASCE)*, 4(2), 56-64.

[2.40] Prota, A., Nanni, A., Manfredi, G., and Cosenza, E. (2001). "Selective upgrade of beam-column joints with composites." *Proceedings of the International Conference on FRP Composites in Civil Engineering*, Hong Kong.

[2.41] Prota, A., Manfredi, G., Nanni, A., and Cosenza, E. (2002). "Selective seismic strengthening of RC frames with composites." *Proceedings of the Seventh U.S. National Conference on Earthquake Engineering* (CD-ROM), Boston, MA.

[2.42] El-Amoury, T., and Ghobarah, A. (2002). "Seismic rehabilitation of beam-column joint using GFRP sheets." *Engineering Structures: The Journal of Earthquake, Wind and Ocean Engineering*, 24(11), 1397-1407.

[2.43] Antonopoulos, C. P., and Triantafillou, T. C. (2003). "Experimental investigation of FRP-strengthened RC beam-column joints." *Journal of Composites for Construction (ASCE)*, 7(1), 39-49.

[2.44] Tsonos, A. G., and Stylianidis, K. (2002). "Seismic retrofit of beam-to-column joints with high-strength fiber jackets." *European Earthquake Engineering*, 16(2), 56-72.

[2.45] Karayannis, C. G., and Sirkelis, G. M. (2002). "Effectiveness of RC beam-column connections strengthening using carbon-FRP jackets." *Proceedings of the Twelfth European Conference on Earthquake Engineering* (CD-ROM), London, PR 549.

[2.46] Dogan, E., Hill, H., and Krstulovic-Opara, N. (2000). "Suggested design guidelines for seismic retrofit with SIMCON and SIFCON." *High-performance fiber-reinforced concrete in infrastructural repair and retrofit*, SP-185, N.

Krstulovic-Opara, and Z. Bayasi, eds., American Concrete Institute, Farmington Hills, MI, 207-248.

[2.47] Shannag, M. J., Barakat, S., and Abdul-Kareem, M. (2002). "Cyclic behavior of HPFRC-repaired reinforced concrete interior beam-column joints." *Materials and Structures*, 35, 348-356.

[2.48] Adin, M. A., Yankelevsky, D. Z., and Farhey, D. N. (1993). "Cyclic behavior of epoxy-repaired reinforced concrete beam-column joints." *ACI Structural Journal*, 90(2), 170-179.

[2.49] Pantelides, C. P., and Gergely, J. (2002). "Carbon-fiber-reinforced polymer seismic retrofit of RC bridge bent: Design and in-situ validation." *Journal of Composites for Construction (ASCE)*, 6(1), 52-60.

[2.50] ACI Committee 224 (1993). *Causes, evaluation, and repair of cracks in concrete structures (ACI 224.1R-93 [reapproved 1998])*, American Concrete Institute, Farmington Hills, MI.

[2.51] Popov, E., and Bertero, V. V. (1975). "Repaired R/C members under cyclic loading." *Earthquake Engineering and Structural Dynamics*, (4), 129-144.

[2.52] ACI Committee 503 (1993). *Use of epoxy compounds with concrete (ACI 503R-93 [reapproved 1998])*, American Concrete Institute, Farmington Hills, MI.

[2.53] International Concrete Repair Institute (1999). "Guide for verifying field performance of epoxy injection of concrete cracks (Guideline No. 03734, Dec. 1998)." *Concrete repair manual*, published jointly by ICRI & ACI, Farmington Hills, MI, 607-616.

[2.54] UNDP/UNIDO PROJECT RER/79/015, UNIDO (1983). "Repair and strengthening of reinforced concrete, stone and brick-masonry buildings." *Building Construction under Seismic Conditions in the Balkan Regions*, Vienna, 5.

[2.55] Corazao, M., and Durrani, A. J. (1989). *Repair and strengthening of beam-to-column connections subjected to earthquake loading*, Technical report NCEER-89-0013, State University of New York at Buffalo, Buffalo, NY.

[2.56] Tsonos, A. G. (2001). "Seismic retrofit of R/C beam-to-column joints using local three-sided jackets." *European Earthquake Engineering*, (1), 48-64.

[2.57] Tsonos, A. G. (2002). "Seismic repair of exterior R/C beam-to-column joints using two sided and three-sided jackets." *Structural Engineering and Mechanics*, 13(1), 17-34.

[2.58] Migliacci, A., Antonucci, R., Maio, N. A., Napoli, P., Ferreti, S. A., and Via, G. (1983). "Repair techniques of reinforced concrete beam-column joints." *Proceedings of the IABSE Symposium on Strengthening of Building Structures—Diagnosis and Therapy*, International Association of Bridge and Structural Engineering (IABSE), Zurich, Switzerland, 355-362.

[2.59] Zureick, A., and Kahn, L. (2001). "Rehabilitation of reinforced concrete structures using fiber-reinforced polymer composites." *ASM Handbook*, ASM International, (21), 906-913.

[2.60] Pantazopoulou, S., and Bonacci, J. (1992). "Consideration of questions about beam-column joints." *ACI Structural Journal*, 89(1), 27-36.

[2.61] Engindeniz, M., Kahn, L. F., and Zureick, A. (2004). *Repair and strengthening of non-seismically designed RC beam-column joints: State-of-the-art*, Research report No. 04-4, Georgia Institute of Technology, Atlanta, GA. (available online at http://www.ce.gatech.edu/groups/struct/reports)

CHAPTER 3

ADEQUACY OF CORNER BEAM-COLUMN JOINTS IN PRE-1970 REINFORCED CONCRETE BUILDINGS

3.1 INTRODUCTION

This research experimentally addresses the adequacy of corner beam-column joints in nonseismically detailed reinforced concrete buildings typically found constructed before 1970. Two extensively instrumented full-scale corner beam-column-slab specimens representing design deficiencies and material properties typical of pre-1970 construction were subjected to a reverse-cycle bidirectional displacement history consisting of alternate and simultaneous cycles in the two primary frame directions. Interstory drift ratios of up to 1.9% were applied. Data from instrumentation were used to evaluate the damage modes, strength hierarchy, joint shear strength and joint shear stress-strain behavior, anchorage of reinforcing bars, and hysteretic behavior including the strength, stiffness and energy dissipation characteristics. Effects of the presence of floor members and bidirectional loading were emphasized. The joints were able to develop normalized joint shear stresses of up to $0.67\sqrt{MPa}$ in a primary direction during unidirectional loading, and up to $0.91\sqrt{MPa}$ in a 45-degree direction from the beam axes during bidirectional loading; however, the severity of damage and loss of stiffness and strength at relatively low drift levels indicated that such joints are not expected to survive drift ratios of around 2% typically envisioned to occur during design earthquakes. Although no comprehensive guidelines exist for estimating bidirectional joint shear strength, it was found that if an estimation were to be based on simultaneous occurrence of the FEMA 356-recommended strength factor (γ) of $0.50\sqrt{MPa}$ in both primary directions, it would still be conservative by 20-25%.

3.2 BACKGROUND

In the United States, guidelines for the design of reinforced concrete (RC) beam-column joints were first reported by the ACI-ASCE Committee 352 in 1976 [3.1]. Design and construction practices followed before 1976 resulted in reinforcement details in the joint regions shown in Figure 3.1a, which do not conform to the current seismic detailing requirements of ACI 318-05 [3.2] and the recommendations of ACI-ASCE 352R-02 [3.3]. The fact that these deficiencies jeopardize the safety of a large number of existing buildings around the world in the event of an earthquake (Figure 3.1b) creates an urgent need to establish the adequacy of nonseismically designed beam-column joints.

A comprehensive review of the technical literature on the performance of nonseismically designed RC beam-column joints was presented elsewhere [3.4] (Chapter 2). Experimental studies have been limited, to a large extent, to testing of one-way, planar joint specimens with no floor slab or transverse beams, and to 1/8- and 1/3-scale building models that may not accurately represent the full-scale behavior of structural details. Applied load histories consisted of unidirectional, in-plane cycles even when the presence of floor members was taken into account. The ACI-ASCE Committee 352 [3.3] recommended further research to establish the adequacy of older joints so that evaluation guidelines for building rehabilitation and methods of improving the performance of such joints could be developed. The committee also drew special attention to joint configurations that are likely to be subjected to bidirectional loading. The objective of the research reported in this chapter was to begin addressing this need as pertaining to the performance of corner beam-column joints subjected to bidirectional cyclic loading.

3.3 EXPERIMENTAL PROGRAM

The experimental program consisted of reverse-cycle quasi-static bidirectional loading of two full-scale corner beam-column-slab specimens that represented the part of the corner of a building isolated between two stories at the assumed inflection points in the case of

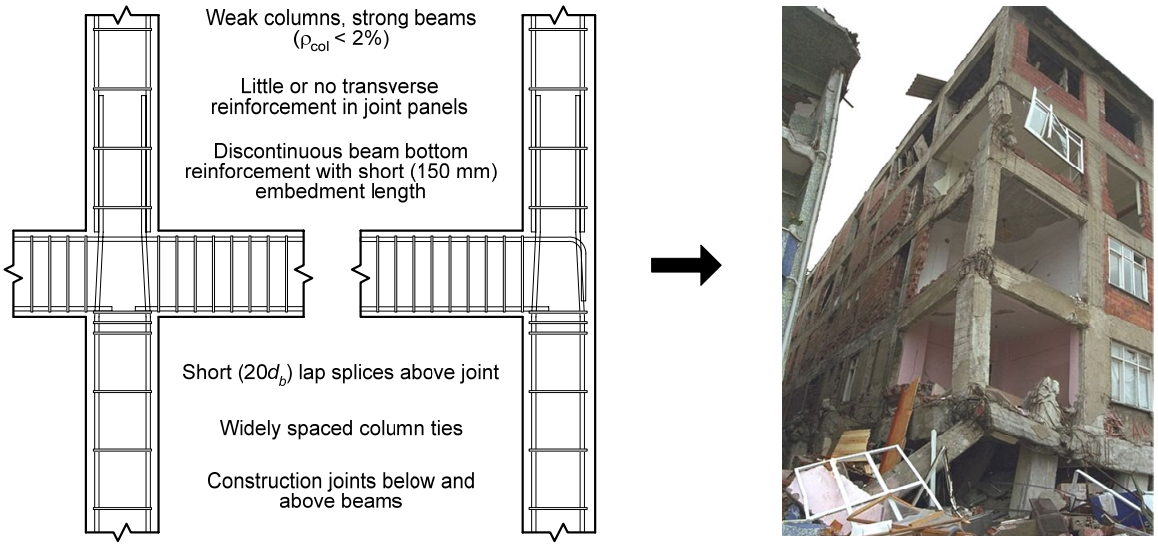

Figure 3.1 — (a) Typical deficiencies in nonseismically designed RC buildings identified by Beres et al. [3.5], and (b) Corner joint failure in 1999, İzmit, Turkey earthquake (Courtesy of NISEE, University of California Berkeley).

lateral loading. The specimens were designed according to the ACI 318-63 code [3.6] such that they represented the material properties (specified f_c'=21 MPa, Grade 280 reinforcing bars) and major deficiencies in reinforcement detailing typical of pre-1970 construction practice. The current strong column/weak beam criterion was intentionally violated using a target column-to-beam moment strength ratio ($\Sigma M_c/\Sigma M_b$) of approximately 0.9 in both principal directions. Other major deficiencies incorporated in the specimens were: (1) no joint shear reinforcements, (2) beam bottom bars with an embedment length of only 150 mm into the joint, and (3) a short ($20d_b$) and unconfined lap splice of column longitudinal bars just above floor level. The resulting overall dimensions and reinforcement details are shown in Figure 3.2. The specimens differed from each other only in the actual concrete properties. A summary of the material properties including those of the reinforcing bars is presented in Table 3.1.

The tests were conducted as shown in Figure 3.3. The top of the column was free to translate vertically, free to rotate in any direction, but was restrained laterally, thus

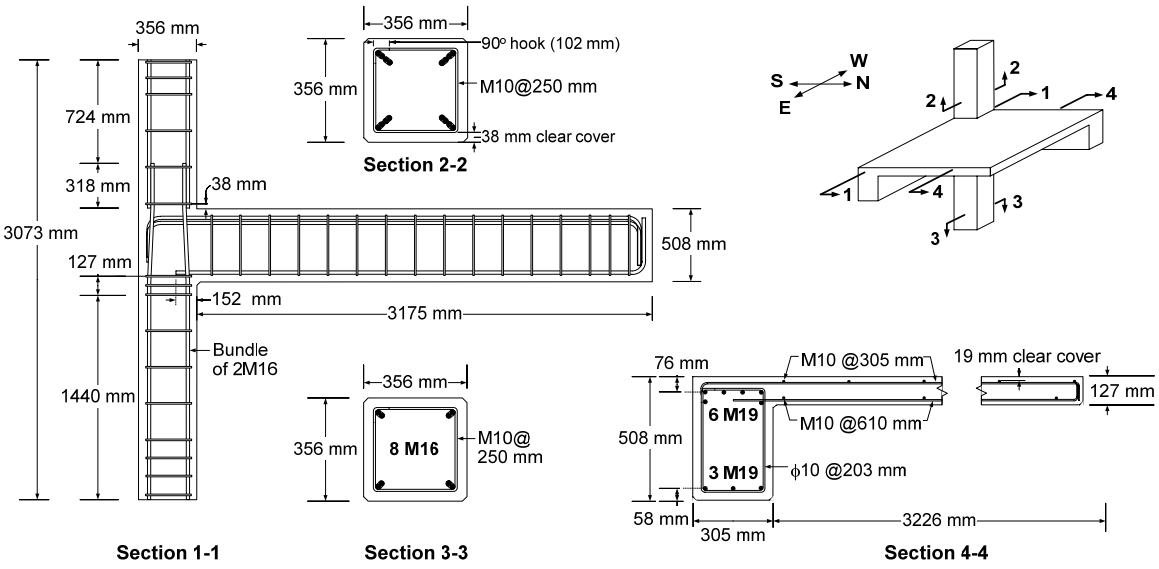

Figure 3.2 — Reinforcement details.

Table 3.1 — Material properties.

	Concrete					Reinforcing bars		
	Specimen 1		Specimen 2					
	Lift 1*	Lift 2	Lift 1	Lift 2		M10 (#3)	M16 (#5)	M19 (#6)
f_c' (MPa)	25.8	34.1	34.6	28.6	f_y (MPa)	367	352	315
E_c (GPa)	21.7	20.2	21.5	20.1	ε_y (με)	1740	1890	1620

* Each specimen was cast in two lifts resulting in a cold joint at the bottom of the upper column. Reported concrete properties are those measured on the test days.

simulating a condition with zero moments. The connection at the bottom of the column simulated a fixed support; the length of the lower column was designed such that an inflection point would form below the beam at a distance equal to the length of the upper column. Cyclic lateral loads were simulated by hydraulic actuators mounted vertically at the end of the beams, 3050 mm from the column centerline. The end of each beam had a connection simulating a zero-moment condition about all three major axes so that not only bending rotations but torsional rotations expected due to the presence of the slab

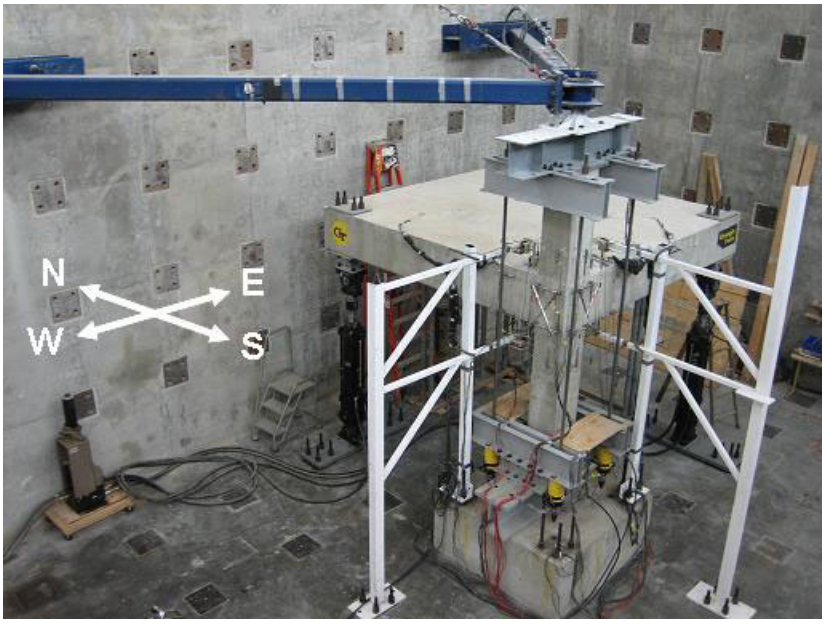

Figure 3.3 — Test setup.

were allowed.

The loading procedure simulated a cyclic lateral loading of a building carrying service gravity loads. Prior to the cyclic loading of the beams, a column axial load of 10% of the column's compressive load capacity was applied, and both beams were brought to a negative (downward) displacement level that resulted in a strong-axis beam moment comparable to that estimated to occur in the modeled frame building under service loads. The beams were then cycled around this deformed position at displacement levels corresponding to ±0.93%, ±1.40%, and ±1.87% interstory drift ratios as shown in Figure 3.4. To better analyze the effects of bidirectional loading, unidirectional loadings in the EW and then the NS directions were performed first. The applied displacement levels were selected as 1.0, 1.5, and 2.0 times the displacement at first yield (Δ_y) measured during the unidirectional loading of Specimen 1. Testing of Specimen 2 was terminated after the ±1.40% drift cycles (at point 9c in Figure 3.4) to represent a less severe damage level than Specimen 1 in the subsequent retrofit studies which are outside the scope of this chapter.

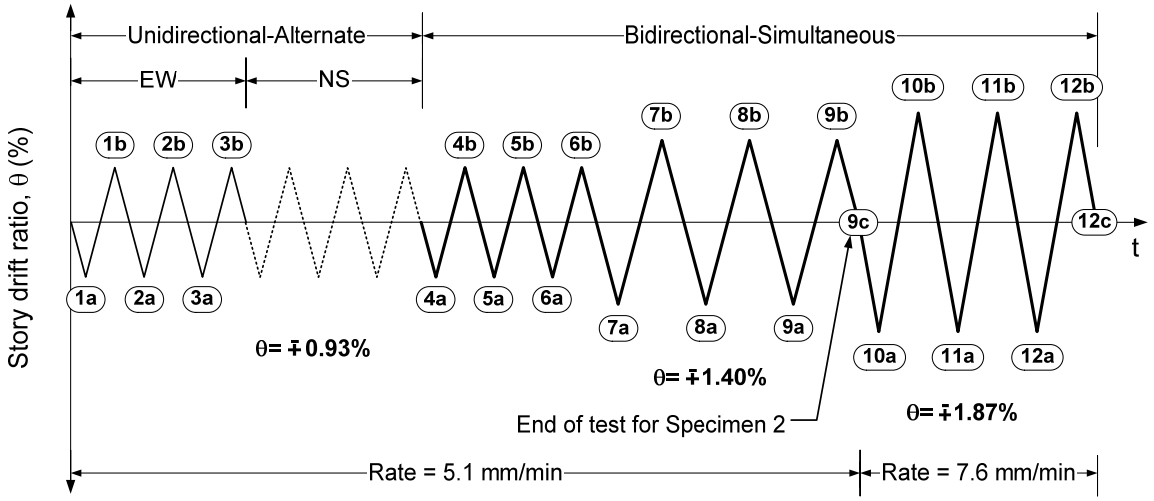

Figure 3.4 — Applied displacement history.

The specimens were instrumented to monitor: (1) strains in all column and beam bars at the column-joint and beam-joint interfaces; in a majority of the slab top and bottom bars at the beam-slab interfaces; in two beam top bars and all beam bottom bars within the joint; and in four column ties (all four legs) and one stirrup in each beam (two vertical legs) (Figure 3.5a-d); (2) joint shear strains, (3) relative rotations of the beams and columns with respect to the joint (Figure 3.5e), (4) global rotation and translation of the joint region with respect to a fixed reference frame (Figure 3.5e), (5) torsional rotation of the beams at the beam tips and near the column faces via two potentiometers at each location, (6) column shear forces via full-bridge strain gage configurations mounted on the reaction frame connected to the top of the column, and (7) column axial load via load cells mounted on each hydraulic jack at each corner of the column. All interior and exterior instrumentation was identical in the EW and NS directions.

Additional information on the experimental program is given in a previous publication [3.7] (Chapter 4).

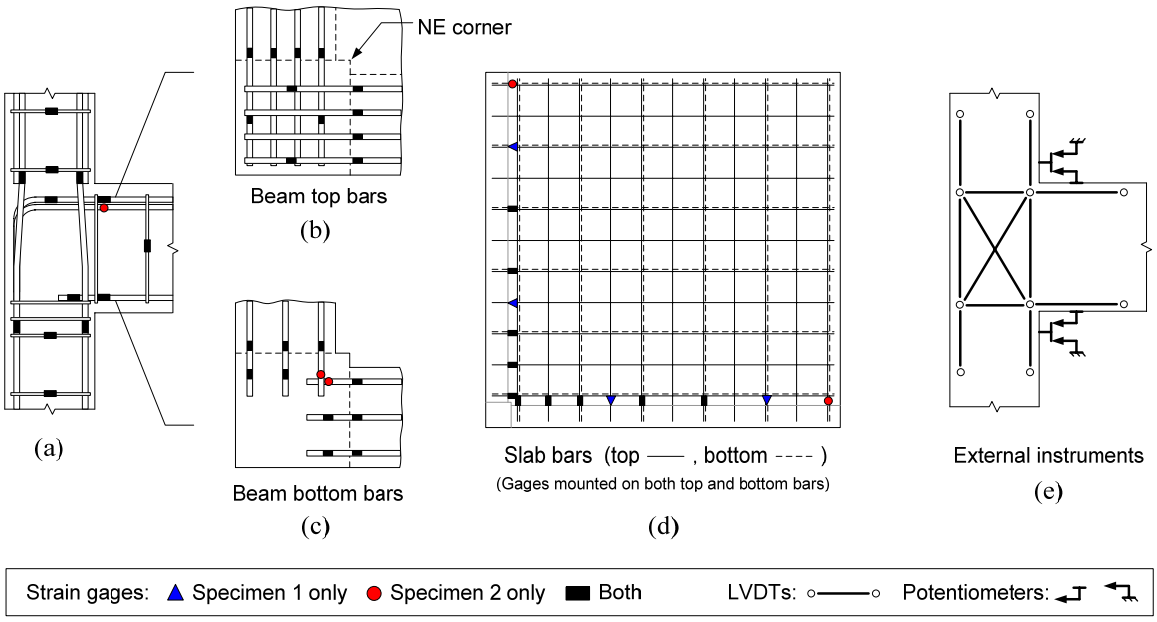

Figure 3.5 — Instrumentation.

3.4 FAILURE MECHANISMS

3.4.1 Damage Modes and Strength Hierarchy

The behavior of the specimens departed significantly from a seismically desirable ductile failure mechanism. The causes of failure were different for the negative (downward beam displacement) and positive (upward) directions of loading. For the negative direction, the behavior was dominated by a combination of: (1) yielding in the upper column bars at loads and displacements less than those causing yielding of the beam top bars, (2) joint shear cracking, and (3) propagation of joint cracks into the upper column splice region. For the positive direction, the poor response was solely due to the loss of anchorage of the beam bottom bars and the resulting inability to develop high positive moments in the beams at the column face. The state of damage in the specimens at the end of the test (at loading points 12c for Specimen 1 and 9c for Specimen 2) is shown in Figure 3.6. The maximum widths of cracks measured on the west face of the specimen at locations labeled in Figure 3.6 at different stages of loading are summarized in Table 3.2.

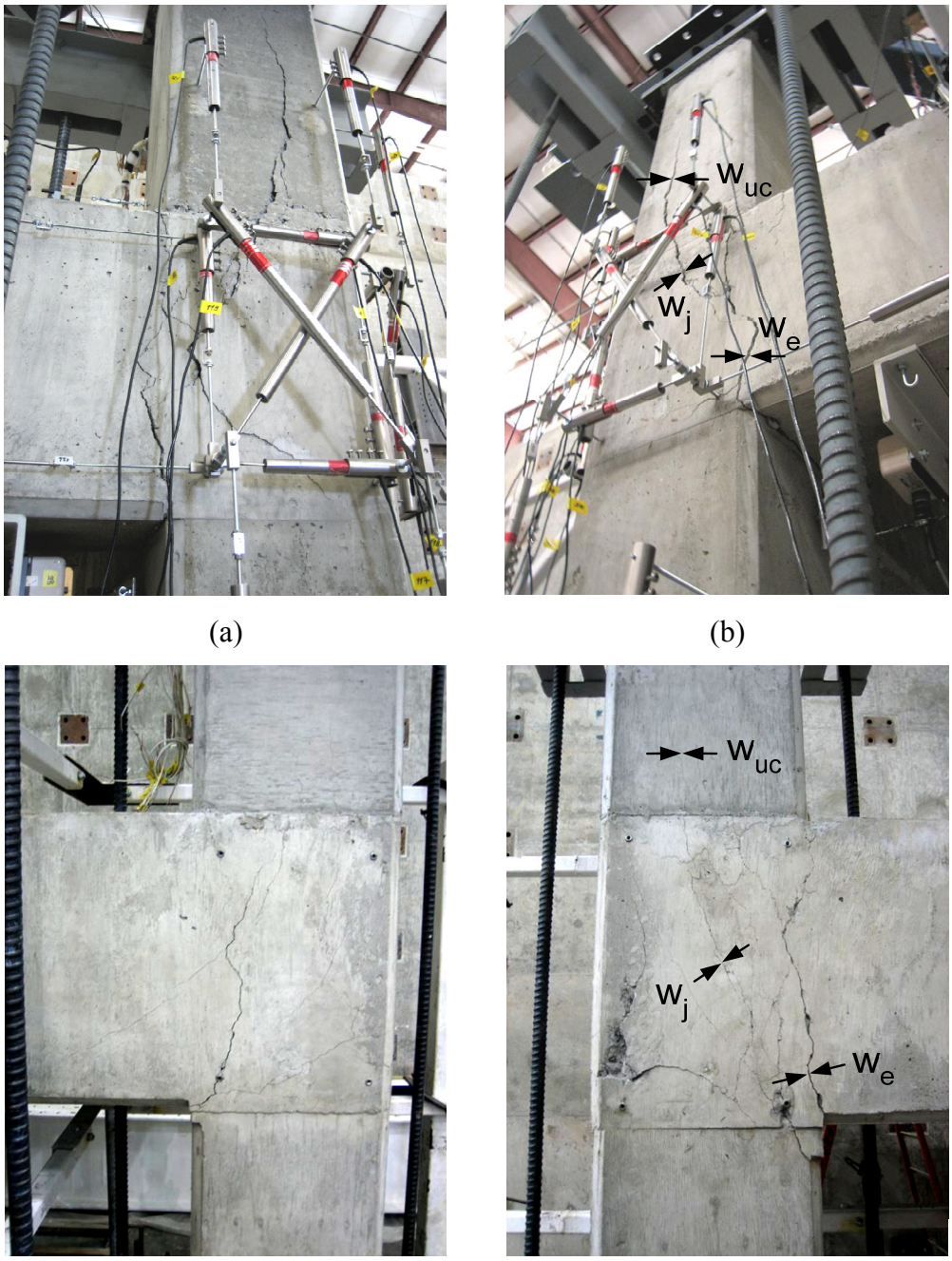

(a) (b)

(c) (d)

Figure 3.6 — Damage at the end of test on west and south faces: (a, b) Specimen 1, and (c, d) Specimen 2.

Table 3.2 — Maximum crack widths measured at the west face at different stages of loading.

Cycles	Drift	Specimen 1			Specimen 2		
		w_e (mm)	w_j (mm)	w_{uc} (mm)	w_e (mm)	w_j (mm)	w_{uc} (mm)
1 - 3	±0.93% Unidirectional	1.5	1.00	0.0	2.5	0.3	0.0
4 - 6	±0.93% Bidirectional	1.8	1.8	0.0	2.5	0.8	0.0
7 - 9	±1.40% Bidirectional	5.1	2.3	0.8	4.8	1.8	0.3
10 - 12	±1.87% Bidirectional	6.4	6.4	3.3	n/a	n/a	n/a

The smaller extent of damage in Specimen 2 is not only because this specimen was subjected to a smaller maximum drift level, it is also because it exhibited a less severe weak column/strong beam behavior than Specimen 1. In Specimen 1, the yield strain of the column reinforcing bars was reached as early as peak 1a at the inside (NE) corner of the upper column-joint interface, and significant yielding in this corner bar began after peak 4a. Specimen 1 beam bars did not yield throughout the test; the outermost beam top bars developed as high as 92% of their yield strain while the innermost bars developed only 43% of yield. In Specimen 2, the NE corner bar in the upper column had developed only 86% of its yield strain at peak 4a, and significant yielding began only after peak 7a. Yielding in the upper column was soon followed by limited beam yielding in two outer top bars in both EW and NS beams in Specimen 2. The innermost beam top bars developed strains ranging from 53 to 81% of their yield strain throughout the test. Yielding in the lower column NW bars was observed in Specimen 1 at peak 10a, but not in Specimen 2; however, the measured strain levels showed that it would probably be observed in Specimen 2 as well, had this specimen been subjected to that drift level.

The diagonal cracking in the joint region occurred in one direction, and not in the often observed “X” pattern, because the loss of anchorage of the beam bottom bars

prevented the development of high shears and the formation of the other diagonal crack (Figure 3.6b). Prying of the hooked beam top bars caused bulging of the sides of the joint up to 6.4 mm in Specimen 1 and 1.8 mm in Specimen 2. Such bulging took place after the beginning of the bidirectional cycles. The joint shear cracks propagated vertically into the upper column during the ±1.40% bidirectional drift cycles in both specimens. During the ±1.87% bidirectional drift cycles applied to Specimen 1, the width of joint shear cracks tripled, and it was clear that the cracks on the EW and NS faces were connected diagonally through the joint, forming a large triangular pyramid-shaped concrete block trying to separate from the outside corner of the column. The first tie along the column lap splice resisted this separation by developing strains as high as 1550 με in its S and W legs. The damage to the joint in Specimen 2 was slightly different in that a more distributed cracking pattern consisting of several cracks parallel to the diagonal was observed instead of one major crack as in Specimen 1.

Although the response of isolated joint specimens including those tested in this study should not be extrapolated to determine the extent of damage to, or the post-earthquake functionality of, an entire building, the aforementioned observations show that nonseismically designed RC frames are susceptible to severe damage even at relatively low interstory drift levels. When evaluated according to the FEMA 356 [3.8] guidelines summarized in Table 3.3, such frames cannot meet the Life Safety Performance Level at the limiting drift ratio of 2%. Based on the results of Specimen 1, one can also hypothesize that the Collapse Prevention Performance Level would not be met at the limiting drift ratio of 4%. This is because if Specimen 1 was subjected to a 4% drift, yielding in the beams could possibly be initiated; however, yielding in both the upper and lower columns would have progressed severely, and a large portion of the joint concrete and part of the upper column would have spalled off at the SW corner since this corner was already separated at the end of the ±1.87% drift cycles.

Table 3.3 — FEMA 356 Structural Performance Levels and damage in primary concrete frames.

	Structural Performance Levels		
	Immediate Occupancy (S-1)	Life Safety (S-3)	Collapse Prevention (S-5)
Damage	Minor hairline cracking. Limited yielding possible at a few locations. No crushing (strains below 0.003).	Extensive damage to beams. Spalling of cover and shear cracking (<3 mm width) for ductile columns. Minor spalling in nonductile columns. Joint cracks <3 mm wide.	Extensive cracking and hinge formation in ductile elements. Limited cracking and/or splice failure in some nonductile columns. Severe damage in short columns.
Drift	1% transient; negligible permanent	2% transient; 1% permanent	4% transient or permanent

3.4.2 Contributions to Total Drift

The displacements applied at the beam ends (Δ_b) can be divided into five contributions:

$$\Delta_b = \Delta^{be} + \Delta^{ce} + \Delta^{bj} + \Delta^{cj} + \Delta^{js} \tag{3.1}$$

where Δ^{be} and Δ^{ce} are caused by the elastic deformations of the beam and column, respectively; Δ^{bj} and Δ^{cj} are caused by the concentrated rotations of the beam and column with respect to the joint, respectively; and Δ^{js} is caused by joint shear strains. Δ^{bj} and Δ^{cj} may include contributions due to inelastic rotations at the beam-joint and column-joint interfaces, respectively, and/or rotations at these locations due to loss of anchorage of reinforcing bars (e.g. beam bottom bars, column lap splice). For a satisfactory seismic performance, Δ^{be} and Δ^{ce} are desirable, Δ^{cj} and Δ^{js} are to be avoided, and Δ^{bj} should be caused by yielding, and not the loss of anchorage, of beam bars.

The performances of the tested specimens were evaluated in this respect using the data from external instrumentation as explained in detail in Appendix D, which can be summarized as follows:

$$\Delta^{ce} + \Delta^{cj} = \theta_c^{tot}\left(L_b + \frac{b_c}{2}\right) \tag{3.2}$$

$$\Delta^{bj} = \theta_{bj} L_b \tag{3.3}$$

$$\Delta^{js} = \left(\gamma_2 L_b - \gamma_1 \frac{b_c}{2}\right) \tag{3.4}$$

$$\Delta^{be} = \Delta_b - \sum(\Delta^{ce} + \Delta^{cj} + \Delta^{bj} + \Delta^{js}) \tag{3.5}$$

where, θ_c^{tot} is the total column rotation, θ_{bj} is the beam concentrated rotation at the beam-joint interface; γ_1 and γ_2 are the vertical and horizontal joint shear strains, respectively; L_b is the beam length measured from the column face; and b_c is the column width. γ_1 and γ_2 were approximated as:

$$\gamma_1 = \gamma_s\left(\frac{h_j}{L_{lc} + L_{uc} + h_j}\right) \tag{3.6}$$

$$\gamma_2 = \gamma_s - \gamma_1 \tag{3.7}$$

where, γ_s is the measured joint shear strain; L_{lc} and L_{uc} are the lower and upper column lengths, respectively; and h_j is the joint height. θ_c^{tot} was determined from Equation (3.8):

$$\theta_c^{tot} = \theta_j - \gamma_2 \tag{3.8}$$

where θ_j is the total joint rotation measured with respect to a fixed frame.

The results of such an analysis, for example for the EW beam in Specimen 1, are presented in Figure 3.7. During the downward loading of the beam (Figure 3.7a), the contribution due to joint shear strains increased continuously from 12% in the first cycle to 66% in the last. As the test progressed, the beam started to pivot around the center of the joint which is evidenced by the decrease in the contributions due to beam flexure and beam concentrated rotation at the beam-joint interface. In the case of upward loading (Figure 3.7b), beam concentrated rotation contributed 52% of the total displacement in the first cycle which showed the loss of anchorage of the beam bottom bars and which quickly became the primary cause of beam end displacements. During upward loading to a drift of +1.40% (7b) and larger, the beam started to exhibit a rigid body motion about the beam-joint interface. The joint did not undergo shear deformations since the beam bottom bars could not sustain high tensile forces that would lead to significant joint shear stresses. Some negative contributions shown in Figure 3.7b can be attributed to the behavior where some of the cracks created during the downward loading of the beams did not close completely when the loading direction was reversed, and they caused permanent rotations.

3.4.3 Joint Shear Strength

3.4.3.1 Development of Joint Shear

The free-body diagrams of the slab, beams and joint for the negative loading direction are shown in Figure 3.8. As the beams were subjected to negative bending moments, the elongation at the top surfaces of the beams was transferred through in-plane shear (V_{s1}^{h}, V_{s2}^{h}) to the slab [3.9]. In the beams, the accumulation of these shear forces along the beam-slab interface was equilibrated by an increase in the compression at the bottom of the beam (C_{b1}, C_{b2}). In the slab, the shear forces along the interface with one beam result in an increase in tension in the slab longitudinal reinforcement anchored into

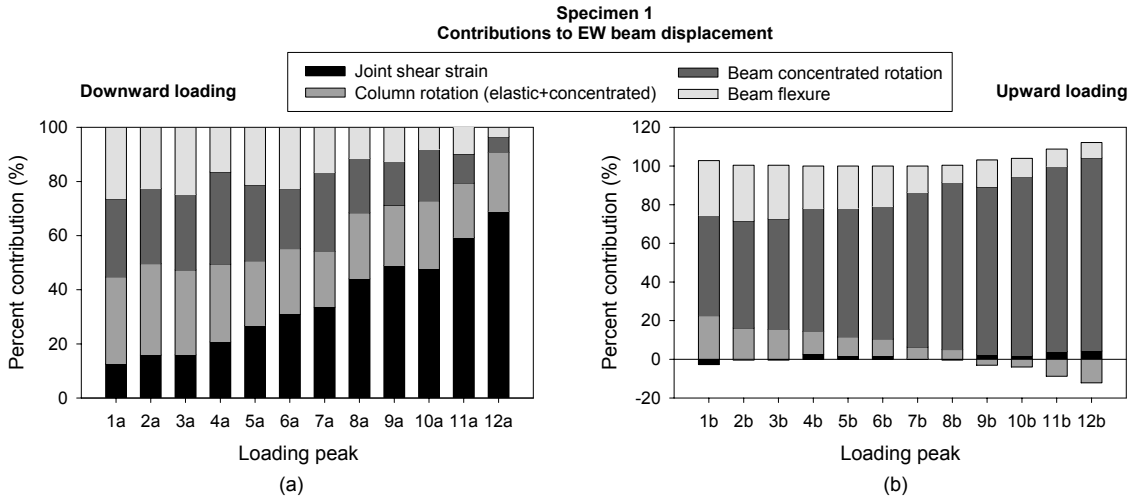

Figure 3.7 — Contributions to applied drift.

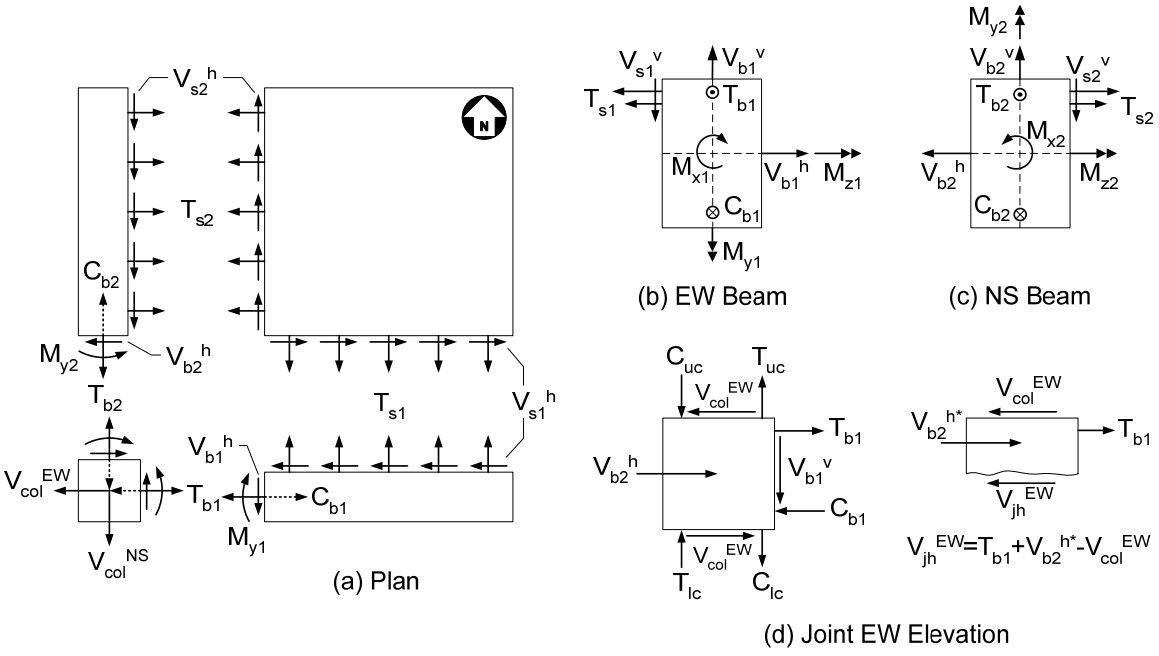

Figure 3.8 — Force transfer mechanisms between slab, beams and joint during downward loading. Subscripts 1 and 2 indicate forces associated with the EW and NS beams, respectively.

the other beam (T_{s1}, T_{s2}). The tension in the slab reinforcement caused torsion (M_{x1}, M_{x2}) as well as weak-axis bending (M_{y1}, M_{y2}) in the beams as shown in Figure 3.8b,c. Consequently, the beam sections at the column faces were subjected forces and moments about all three axes resulting in a complicated force distribution that must be transferred to the columns through the joint. Although it was not straightforward to determine how much shear was actually transferred through the joint; the following statements can be made:

- The horizontal shear force at the mid-height of the joint, for example in the EW direction, can be written as:

$$V_{jh}^{EW} = T_{b1} + V_{b2}^{h*} - V_{col}^{EW} \tag{3.9}$$

where T_{b1} is the total normal force on the tension side of the EW beam, V_{b2}^{h*} is the horizontal shear force carried by the part of the NS beam-joint interface above the joint mid-height, and V_{col}^{EW} is the column shear in the EW direction (Figure 3.8d).

From

$$V_{b2}^{h*} < V_{b2}^{h} = \sum T_{s2} \tag{3.10}$$

Equation (3.9) suggests that some part of the total tensile force carried by the slab longitudinal reinforcement ($\sum T_{s2}$) is transferred through the joint as shear. Equation (3.9) can be rewritten as:

$$V_{jh}^{EW} = \left(T_{b1} + T_{s2}^{*}\right) - V_{col}^{EW} \tag{3.11}$$

where T_{s2}^{*} represents the contribution of slab to joint shear.

- The tensile forces in the beam top bars are not only created by the strong-axis beam moments (M_{z1}, M_{z2}) but they are also affected by torsion (M_{x1}, M_{x2}) and weak-

axis bending (M_{y1}, M_{y2}) of the beams. While there is not a closed-form analytical solution for the strain distribution due to torsion in an L-shaped reinforced concrete section (i.e. part of the slab acting like a flange to the beam), torsion is known to induce tension in all longitudinal bars. Such an increase in T_{b1} results in an increase in joint shear.

3.4.3.2 Experimental Results

The variation of the normalized horizontal joint shear stress (τ'_{jh}) throughout the test was determined for the EW and NS directions separately, where

$$\tau'_{jh} = \frac{V_{jh}}{\sqrt{f'_c} b_j h_c} \tag{3.12}$$

b_j is the effective joint width as defined in ACI-ASCE 352R-02 [3.3], and h_c is the column depth. The normalized joint shear stress at a point during bidirectional loading (τ'^{b}_{jh}) was taken as:

$$\tau'^{b}_{jh} = \sqrt{\left(\tau'^{EW}_{jh}\right)^2 + \left(\tau'^{NS}_{jh}\right)^2} \tag{3.13}$$

In determining V_{jh} in Equation (3.12), the total normal force transferred to the joint on the tension side of the beam (T_b) was estimated via two different methods.

In the first method, T_b was estimated by using the strong-axis beam moments at the column face (M_z) and assuming a constant moment arm of *jd=0.875d* between the tension and compression resultants (i.e. $T_b = M_z / 0.875d$). The resulting τ'_{jh} values were plotted against the joint shear strain (γ_s) for both the EW and NS directions as presented in Figure 3.9, where γ_s for each joint panel was taken as the average of four values

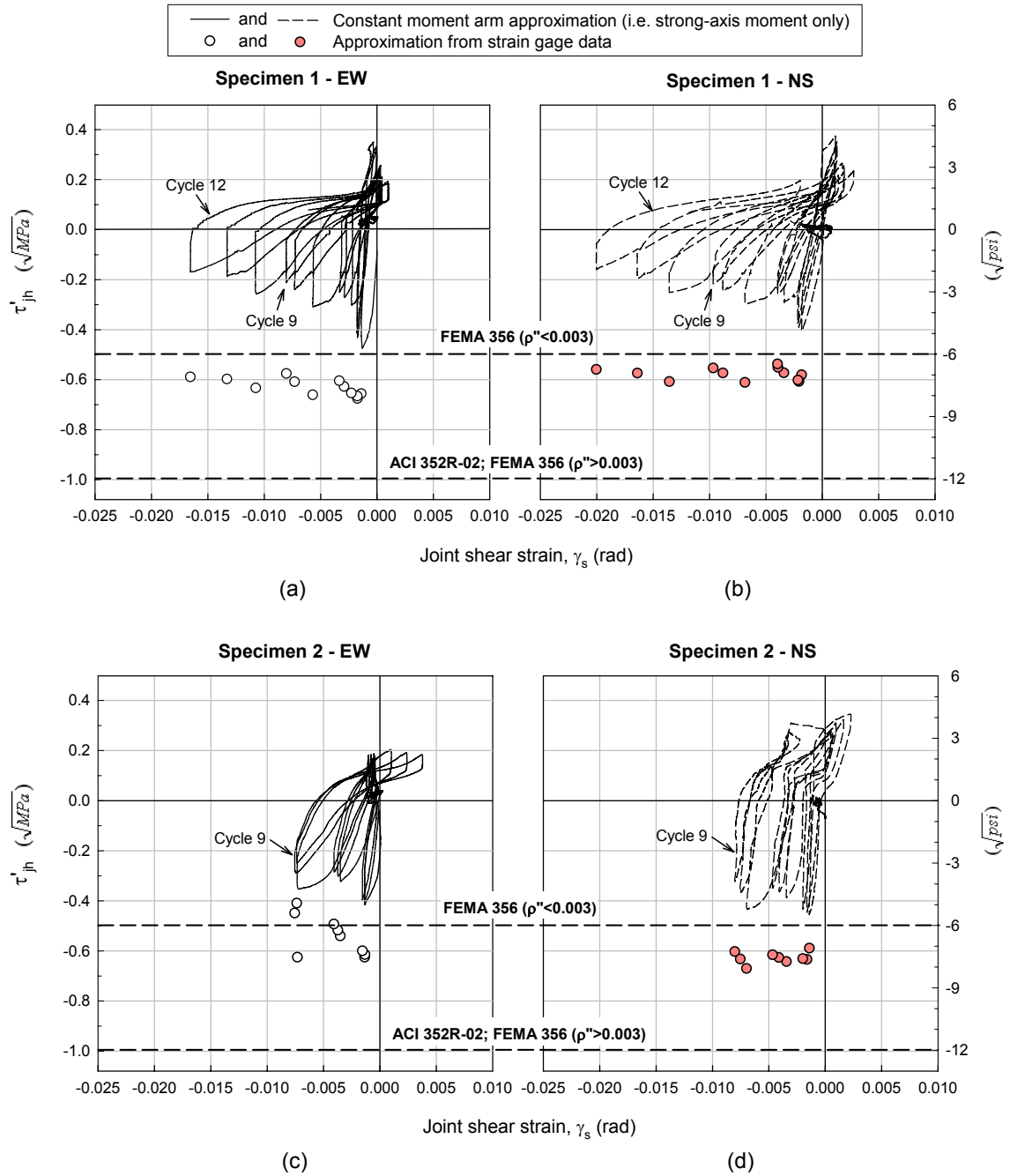

Figure 3.9 — Joint shear stress-strain hysteresis loops for (a, b) Specimen 1, and (c, d) Specimen 2, where $\rho''=0$.

obtained from the LVDT configuration in Figure 3.4e using plane-strain transformation. These curves correspond with the previous discussions in that significant softening and distortion of the joint during downward loading and the inability to mobilize high joint shear stresses during upward loading are clear. For the case of downward loading, the maximum normalized joint shear stress, also referred to as the joint shear strength factor γ, occurred during unidirectional loading as 0.47[†] for Specimen 1, and during the ±1.40% bidirectional drift cycles as 0.54 for Specimen 2. Specimen 1, during bidirectional loading, achieved a maximum value of 0.42. For upward loading, maximum values of 0.37 and 0.34 were obtained during the first cycle of unidirectional loading for Specimen 1 and Specimen 2, respectively, followed by a quick degradation in these values as the loss of anchorage of the beam bottom bars progressed. This method has been widely used for specimens without floor members; in the present case, however, it implicitly assumes that the resultant tension force at the beam-joint interface is created by strong-axis bending only. Other contributions to the tension in the beam longitudinal bars that are mentioned previously are not accounted for, resulting in an underestimation of shear carried by the joint.

In the second method, T_b was estimated as the sum of forces in longitudinal reinforcing bars on the tension side of the beam determined from the measured strains in these bars. The forces in three slab bars (two top, one bottom) within the effective width of the slab, which is discussed later in this chapter, were also included in T_b. The strains in the bars were converted to forces using the stress-strain curves which were obtained experimentally for various cyclic loading/unloading cases that were observed in the strain histories recorded during the tests. Such stress-strain curves obtained for #6 beam bars and for #3 slab bars are presented in detail in Appendix B. This method was used to

[†] The normalized joint shear stresses reported in the text are absolute values of those plotted in Figure 3.9 for consistency in their comparison with the current provisions later in this chapter.

determine τ'_{jh} at the downward loading peaks only, and not to develop the complete hysteretic variation of τ'_{jh}, due to damage to the strain gages on the beam bottom bars during upward loading as a result of progressive loss of anchorage of these bars. The resulting τ'_{jh} values obtained for the EW and NS directions are shown with circles on the plots in Figure 3.9. The vector sum of the values in the two directions as in Equation (3.13) resulted in maximum values (γ) of 0.90 and 0.91 for Specimen 1 and Specimen 2, respectively, both of which occurred during the ±1.40% bidirectional drift cycles. These values are 112% and 69% higher than those obtained for bidirectional loading via "constant moment arm approximation". This significant difference is primarily due to the fact that the beam bars transfer more forces to the joint than predicted based on the strong-axis beam moments only, and all contributions to these forces were directly accounted for by using the strain gage data. It was, however, implicitly assumed that the net normal force transferred to the joint by the upper half of the beam (T_b) consisted of forces in the beam and some slab longitudinal bars, and that no compressive forces existed in this region that would need to be subtracted from T_b leading to a possible reduction in the obtained τ'_{jh} values. In reality, the compressive forces have an unknown and irregular distribution over the cross-section due to the combination of moments about all three axes.

3.4.3.3 Comparison with the Current Provisions

The γ values obtained for the specimens were compared with those currently recommended by ACI-ASCE 352R-02 [3.3] and FEMA 356 [3.8] for use in calculating the shear strength of corner beam-column joints.

ACI-ASCE 352R-02 [3.3] requires that in designing joints with beams framing in from two perpendicular directions, joint shear strength be evaluated in each direction

independently. It is stated that for bidirectional loading, the design implicitly assumes an elliptical interaction diagram that becomes circular when both unidirectional strengths are equal (Sec. 4.3.1). It is also stated that such an interaction relationship was found to underestimate the bidirectional joint shear strength by 10 to 35%. For corner joints in frames designed according to the seismic requirements of ACI 318-02, it is required that the joint shear strength factor (γ) be taken as 1.00. The following observations were made when these provisions were compared with the normalized joint shear stresses obtained in this study by using strain gage data:

- The maximum bidirectional normalized joint shear stress obtained for the 0.93% drift cycles were 30% and 33% higher than those obtained for the unidirectional loading at the same drift level for Specimen 1 and Specimen 2, respectively. Although the shear stresses at a 0.93% drift level do not represent the actual strength of the joint, these results seem to agree with the commentary of ACI-ASCE 352R-02 that an assumed circular interaction diagram for bidirectional joint shear strength may underestimate the actual bidirectional strength by up to 35%.
- The small margin between the bidirectional γ values obtained for the tested specimens (0.90 and 0.91 for Specimen 1 and Specimen 2) and that assumed by ACI-ASCE 352R-02 [3.3] for seismically designed corner joints (γ=1.00) is because of the conservatism of ACI-ASCE 352R-02 [3.3] for bidirectional loading. It should not be taken to mean that the tested joints exhibited strengths almost equivalent to that of seismically designed corner joints. Although the normalized joint shear stresses in either primary direction did not exceed 0.67 in both specimens throughout the test, the joints suffered damage at relatively low interstory drift ratios. Given the observed failure mechanisms, the large contribution of joint shear deformations to interstory drift (Figure 3.7), and the severe degradation in hysteretic parameters as discussed in the following sections, it is clear that significant retrofit measures are needed to improve both stiffness and strength of such joints.

For use in seismic rehabilitation of existing concrete buildings, FEMA 356 [3.8] Sec.6.5.2.3 recommends the same γ value (1.00) for corner joints as ACI-ASCE 352R-02 [3.3] provided that the volumetric joint transverse reinforcement ratio (ρ'') is not less than 0.003. For little or no joint transverse reinforcement (ρ''<0.003), γ is reduced to 0.50. The case of bidirectional loading is not discussed; therefore, these provisions are not directly comparable to the experimental results in this study. Even so, the following observations were made:

- Considering that normalized joint shear stresses of up to 0.67 in Specimen 1 and 0.63 in Specimen 2 were developed during unidirectional loading even at a low drift ratio of ±0.93%, and that no transverse reinforcements were used in these specimens (i.e. ρ''=0), the γ value of 0.50 recommended by FEMA 356 [3.8] for ρ''<0.003 seems to be conservative.
- If FEMA 356 [3.8] were to assume a circular interaction diagram for bidirectional shear strength of non-code-conforming joints (ρ''<0.003) as ACI-ASCE 352R-02 [3.3] does for code-conforming joints, the measured strengths would have been significantly underestimated [for example, γ=0.50 (FEMA) versus 0.90 (measured) for Specimen 1]. Even if a square interaction diagram were used, it would still underestimate the measured strengths by 21% for Specimen 1 and by 22% for Specimen 2 [for example, $\gamma = 0.50\sqrt{2} = 0.71$ versus 0.90 (measured) for Specimen 1].

3.4.4 Anchorage of Reinforcing Bars

3.4.4.1 Beam Bottom Bars

For seismically resistant joints, bars terminating within the joint should be anchored in a confined core using a 90-degree standard hook with a development length

l_{dh} as defined in ACI-ASCE 352R-02 [3.3], Sec. 4.5.2.4[‡]. Using the measured material properties, l_{dh} corresponds to $10\,d_b$ for Specimen 1 and $8.7\,d_b$ for Specimen 2. The fact that the beam bottom bars in these specimens were anchored by only $8\,d_b$ (150 mm) into an unconfined joint without any hooks hindered the development of the bars in tension when the beams were loaded upwards.

The variation of strains in the NS beam bottom bars just outside the joint and at 76 mm into the joint is presented for both specimens in Figure 3.10. Significant decrease in strains or deviation of strains at these two locations from one another is taken to indicate loss of anchorage in a bar. The plots indicate that the loss of anchorage became dominant especially after the beginning of the bidirectional cycles and that it initiated first in the inner bars (gages g5, g6) and then in the middle bars (gages g3, g4). The outer bars (gages g1, g2) maintained their anchorage until the end of the ±1.40% bidirectional drift cycles in both specimens. The higher demand on the inner bars, as previously mentioned, is a result of the combined torsion and unsymmetric bending created due to the presence of the slab. In general, all bottom bars developed only about half of their yield capacity in both specimens, although the inner bar in Specimen 1 was able to develop up to three quarters of its yield capacity outside the joint during the unidirectional cycles. The strain gage mounted within the joint on the inner bar in Specimen 2 (gage g6 in Figure 3.10) indicated that this bar developed much higher strains within the joint than outside the joint and reached its yield strain. No satisfactory explanation is available for this phenomenon.

The loss of anchorage in the beam bottom bars resulted in inability to mobilize the positive moment capacity of the beam and significant loss of stiffness as seen in Figure 3.11, where the variation of the beam relative rotation with beam strong-axis moment at

[‡] l_{dh} defined in ACI-ASCE 352R-02 [3.2] is a combination of the anchorage requirements in ACI 318-02 [3.10] with modifications to reflect detrimental effects of load reversals, increase in stress under large deformations, etc.

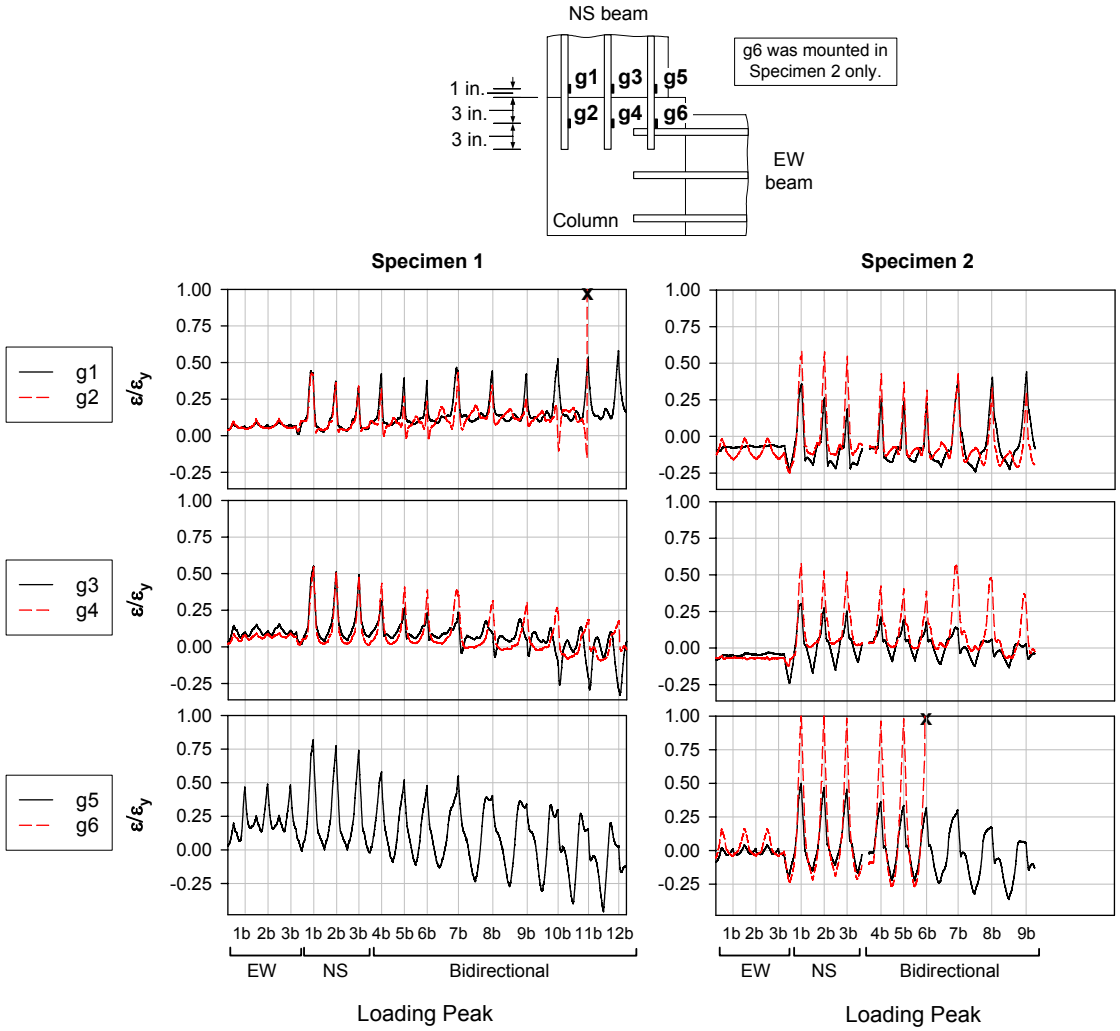

Figure 3.10 — Variation of strains in the NS beam bottom bars.

the NS column face is presented for Specimen 1. A significant drop in the positive moment that developed in the beam and deterioration of stiffness after the beginning of bidirectional loading is clear (peak 1b versus 4b). Only 47% of the beam's positive moment capacity M_n^+ was developed at peak 4b, where M_n^+ was estimated analytically by assuming perfect anchorage for all beam reinforcing bars. This ratio dropped to 32% at peak 12b although the magnitude of drift applied at this peak was twice that applied at peak 4b. The hysteretic degradation in stiffness is quantified later in this chapter.

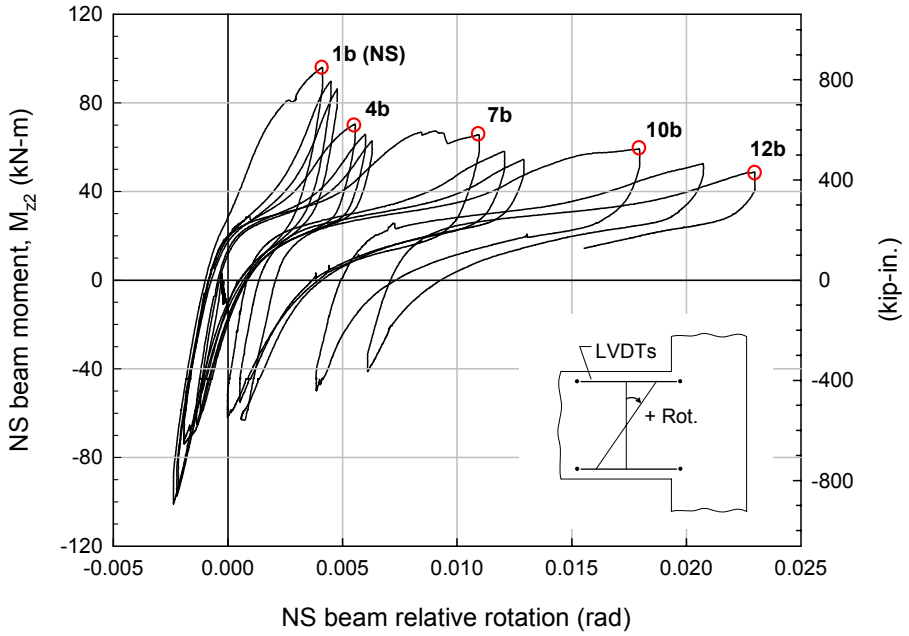

Figure 3.11 — Strong-axis moment versus relative rotation with respect to column for Specimen 1, NS beam.

3.4.4.2 Beam Top Bars

Beam top bars satisfied the ACI-ASCE 352R-02 [3.3] development recommendations partially in that they terminated in standard hooks and had an adequate development length l_{dh} of $13.7d_b$, but they were anchored in a joint core that was not confined with any transverse reinforcements and the concrete cover on bar extension beyond the hook was 38 mm compared to the required 51 mm. The lack of core reinforcement and cover could possibly have led to prying and anchorage loss. The tendency of these bars to prying was clear from a bulging of up to 6.4 mm observed in the joint panels in Specimen 1, most of which took place during the ±1.87% drift cycles. In Specimen 2, bulging was limited to 1.8 mm at the end of the ±1.40% drift cycles, but the tip of the outermost NS beam top bar was exposed due to spalling at the south face signaling the possibility of more damage at larger drift levels. The strains measured just outside the joint and at 178 mm into the joint (mid-width) were compared for the innermost and the outermost bars in each beam to assess any deterioration in anchorage along these bars. Such a comparison

was not possible for Specimen 1 due to damage to strain gages. In Specimen 2, these bars developed slightly higher strains outside the joint than at mid-width of the joint throughout the test with a consistent increase in strains at both locations with increased drift magnitude. There was no reason to believe that these bars lost anchorage in a way that would significantly affect the overall behavior of the specimens.

3.4.4.3 Column Longitudinal Bars

A major weakness related to anchorage was the lap splice of the column bars just above the joint. The lap was inadequate in length, $20d_b$ versus 38 to $44d_b$ required for a Class B tension splice; the lap was unconfined because the stirrup spacing s =254 mm versus required $s < d/4$ or 102 mm; and the lap splices were at locations where flexural yielding was expected, which is not permitted by ACI 318-05, Chapter 21 [3.2]. Column bars at the inside (NE) and outside (SW) corners were most vulnerable to anchorage loss due to bidirectional loading. Data from strain gages mounted at the upper column-joint interface on bars continuing from the lower column indicated that in both specimens, the SW (outside corner) bars lost their anchorage in the upper column partially during the ±0.93% bidirectional drift cycles and completely during the first ±1.40% drift cycle. In Specimen 1, this was later evidenced by the separation of a triangular pyramid-shaped concrete block from the column at this corner (Figure 3.12b) during the ±1.87% drift cycles. The bars in the NE (inside) corner of the upper column, which were reported previously to have undergone significant yielding, survived the first negative peak at 1.40% drift, but not the second negative peak, at which point the width of the flexural crack at this corner increased suddenly from 2.5 mm to up to 6.4 mm. This was accompanied by the separation of a 50 mm x 50 mm portion of the joint inside corner along the entire joint depth and spalling at this corner (Figure 3.12c,d), which left the column bar unprotected and led to loss of its anchorage through the joint. Loss of anchorage coupled with such section losses at the inside and outside corners resulted in

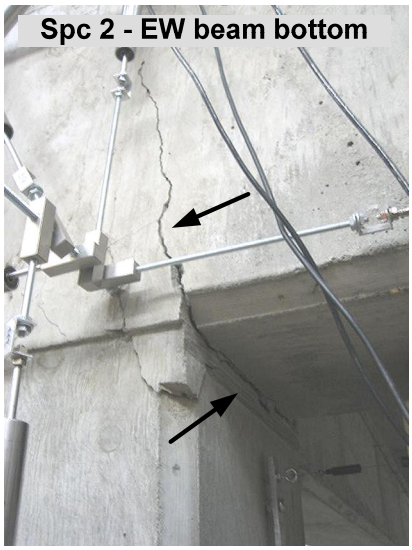

(a)

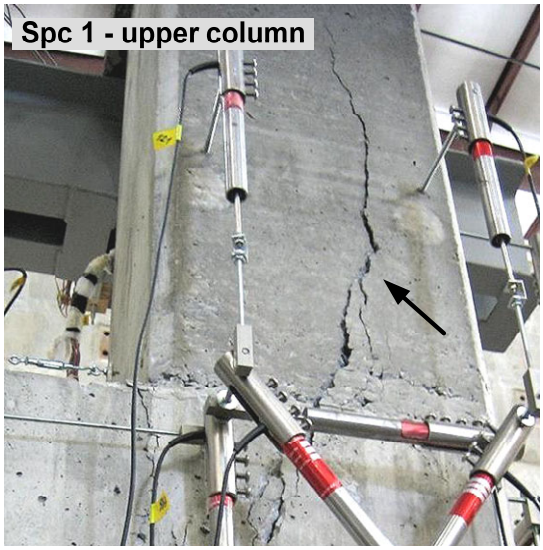

(b)

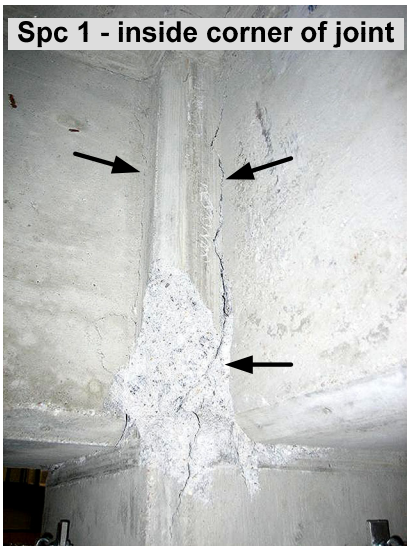

(c)

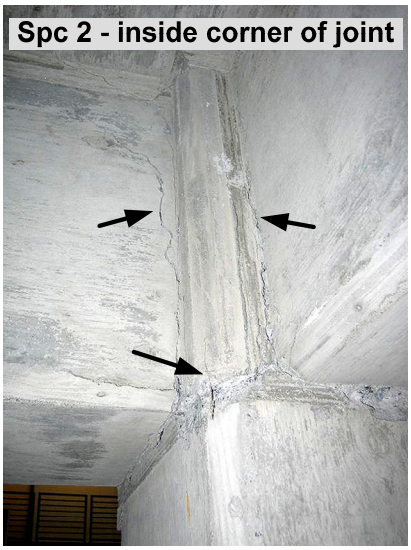

(d)

Figure 3.12 — Loss of anchorage of reinforcing bars.

severe reduction in the biaxial capacity of the column and lowered the already-low column-to-beam moment strength ratio as reported previously by Leon and Jirsa [3.11] for interior joints.

3.5 HYSTERETIC PERFORMANCE

The aforementioned failure mechanisms resulted in force-drift hysteretic curves characterized by lack of ductility due to severe degradation in stiffness, pinching, and loss of strength especially after the beginning of the bidirectional cycles. The curves obtained for both EW and NS beams in both specimens are presented in Figure 3.13a to Figure 3.13d. The curves are shifted from the horizontal line representing zero load due to the initial compressive (positive) loads on the actuators at the deformed position used as the reference level for cyclic loading. This deformed position is the "zero" drift datum.

The hysteretic response obtained for the upward loading of the EW beam in Specimen 2 (Figure 3.13c) is remarkably more deficient than others because this beam was loaded upwards accidentally prior to the test resulting in pull-out of the beam bottom bars. The maximum loads for both downward and upward loading occurred during the first unidirectional cycles. When the same drift level (±0.93%) was applied simultaneously in both directions, the peak loads decreased significantly, especially for Specimen 1 (Figure 3.13a, b), then the strength degraded more gradually. The ±1.87% bidirectional drift cycles, applied to Specimen 1 only, brought the level of degradation in all hysteretic parameters from "moderate" to "severe".

The peak-to-peak stiffness (K_p), defined as the slope of the line connecting the negative and positive peaks of a cycle, decreased by 79% from the first to the last (12^{th}) cycle for Specimen 1 as shown in Figure 3.14a, b. For Specimen 2, the decrease in K_p until the last (9^{th}) cycle was 52% for the NS direction. Such severe stiffness losses at relatively low bidirectional drift levels of 1.40% to 1.87% indicate that buildings with deficiencies similar to those incorporated in the tested specimens would have

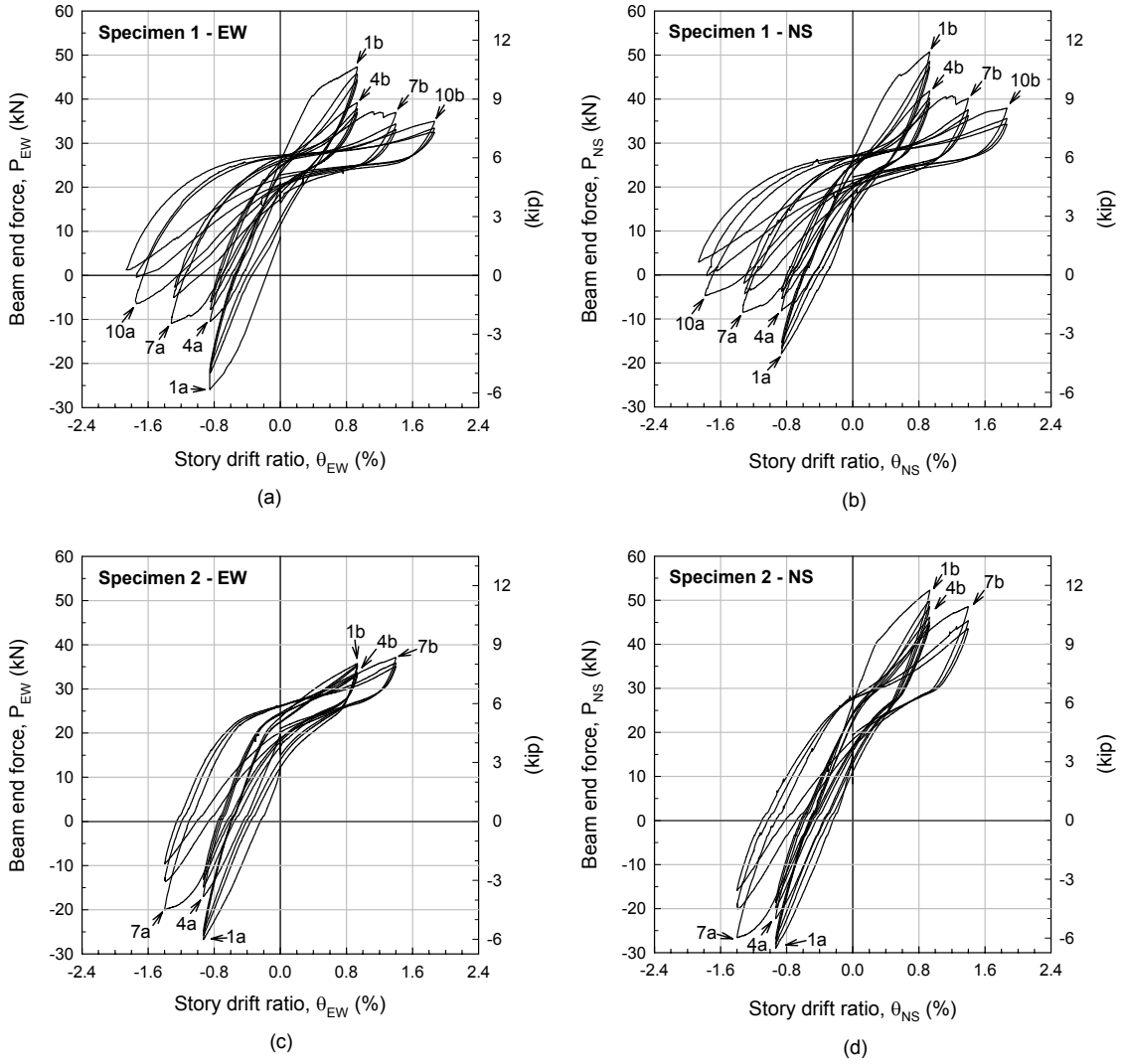

Figure 3.13 — Force-drift hysteresis loops for (a, b) Specimen 1, and (c, d) Specimen 2.

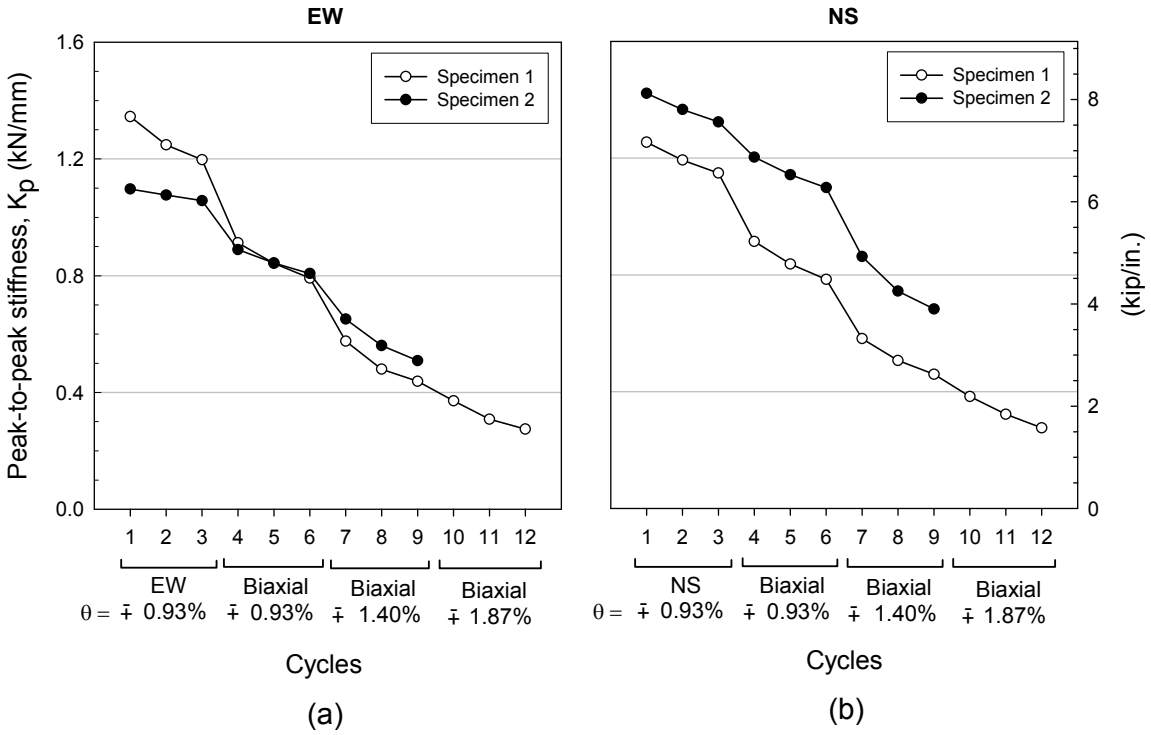

Figure 3.14 — Stiffness degradation in the (a) EW, and (b) NS direction.

significantly reduced interstory stiffness at the 2% drift levels typically envisioned to occur during design earthquakes.

Energy dissipation was evaluated by calculating the areas enclosed by the force-displacement curves in each cycle; their cumulative plots are presented in Figure 3.15a, b. As a result of the progressive increase in pinching and strength degradation, these plots showed no signs of good seismic energy dissipation capacity.

3.6 EFFECT OF FLOOR SLAB

The presence of the floor slab and the bidirectional nature of loading played a major role in the behavior of the specimens. In addition to the previously mentioned effects, the following are noted:

- The behaviors identified by other researchers [3.12] that the slab increases the joint shear stress input through several paths consisting of diagonal compression struts in the slab, torsion, and weak-axis bending of the transverse beam were confirmed. The

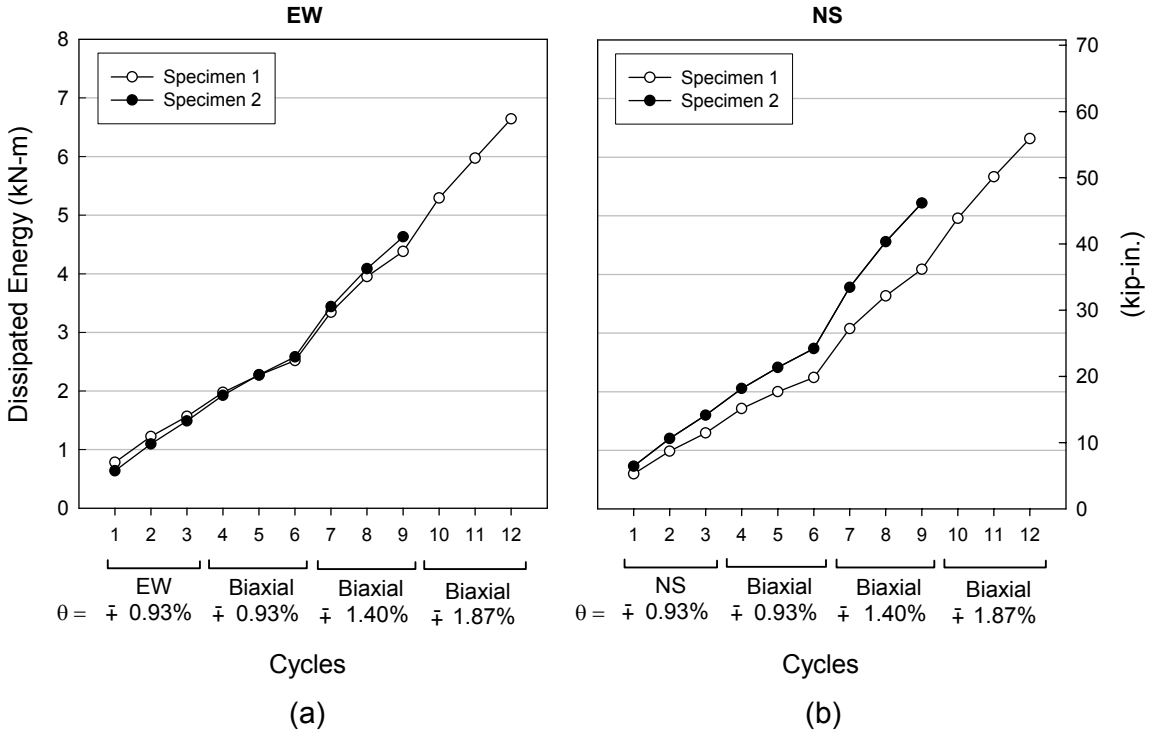

Figure 3.15 — Cumulative energy dissipation in the (a) EW, and (b) NS direction.

latter two mechanisms were mentioned in the previous sections. Forming of diagonal compression struts in the slab concrete was evident from the fact that all slab reinforcements in both directions (expect for a few bottom bars) remained in tension throughout the test regardless of the direction of beam moments. This, and a diagonal crack in the slab, which extended from the joint region to the opposite (NE) corner and through the thickness of the slab, indicated a principal tension force perpendicular to this crack and compressive forces parallel to it. Such a membrane action was attributed to the shear stresses developed at the beam-slab interfaces due to deformation compatibility between the slab and the beams [3.12].

- In the uncracked state of the slab, only two top bars and one bottom bar in the slab near the column in each direction were found to be effective as additional tension reinforcement to the beams. The strains in the NS beam and slab top bars at the first negative peak of each drift level are presented in Figure 3.16a. The slab

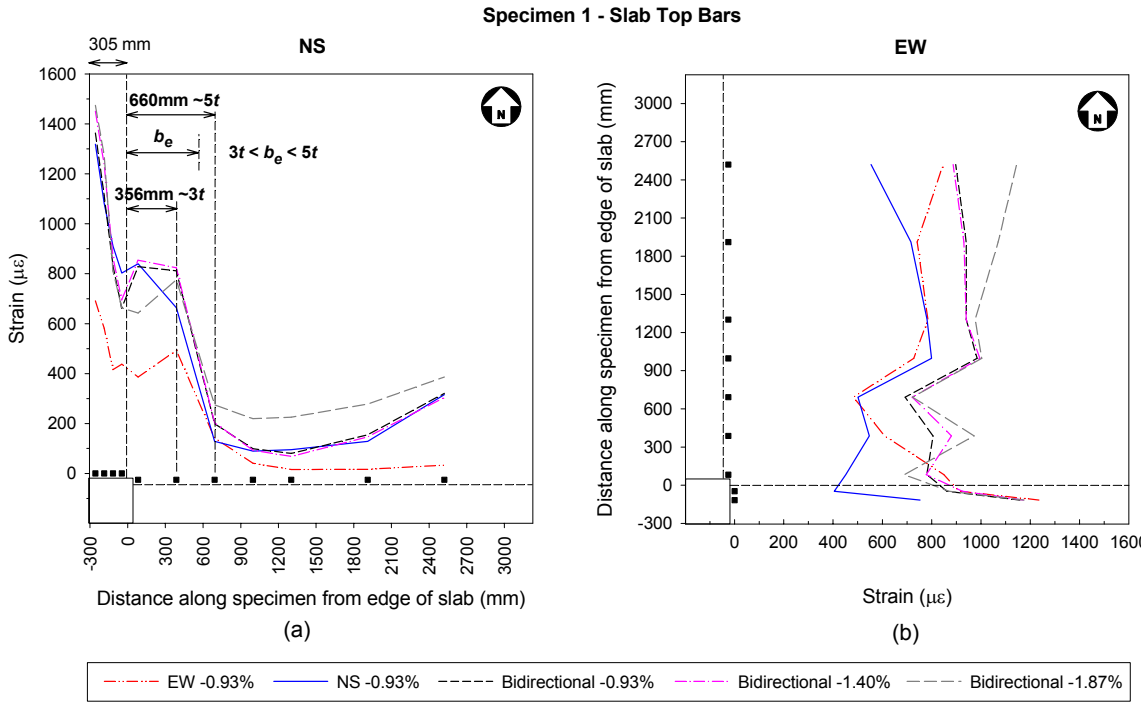

Figure 3.16 — Strains in the beam and slab top bars at the first negative peaks of each drift level for Specimen 1: (a) EW, and (b) NS directions.

reinforcement seemed to be effective up to a point between the second and third bars (i.e. 356 mm to 660 mm from the beam face), which was in reasonable agreement with the effective overhanging flange width (b_e) of 508 mm calculated according to the current specifications of ACI-ASCE 352R-02 [3.3], Sec. 3.3.2 and ACI 318-05 [3.2], Sec. 8.10.3 (i.e. $b_e \leq \min\{1/12$ times beam span, 6 times slab thickness, 1/2 times clear distance to next web$\}$). This was the case for the NS direction throughout the test, and no significant cracking was observed parallel to the EW beam that would change this strain distribution. Across the slab bars in the EW direction, a similar strain distribution was changed into a more uniform distribution when, at approximately 0.76% drift during the first unidirectional cycle in the EW direction, a crack formed at the NS beam-slab interface across the entire width and through the

thickness of the slab. After this, all slab bars became effective as shown in Figure 3.16b.

- The strain distributions across the slab did not change significantly when the loading was changed from unidirectional to bidirectional, or when the magnitude of the bidirectional drift was increased (Figure 3.16a). This indicated a reduction in the extent of slab participation when the slab was forced to develop a bidirectional membrane action. Damage in the column and the joint during bidirectional loading reduced their stiffness, so it required larger drifts to engage the same amount slab participation.
- Unsymmetric bending and torsional twist of the beams due to the presence of the slab had a major impact on the loss of anchorage of the beam bottom bars which was previously shown to cause severe stiffness losses. Even during the loading of only one beam (that is, excluding the adverse effects of bidirectional loading), the inner bottom bar in that beam was strained two to three times higher than the outer one. Such a distribution of strains, rather than an equal sharing between the three bars, worsened the bond of the inner bar, which lost its anchorage as soon as the bidirectional loading began. This increased the demand on the remaining two bars, and loss of anchorage and severe reductions in overall stiffness during subsequent cycles became unavoidable.

3.7 CONCLUSIONS

Two full-scale RC corner beam-column-slab specimens representing typical pre-1970 design were subjected to interstory drift ratios of up to 1.9% applied simultaneously in both primary directions. The results from these experiments showed that nonseismically designed corner beam-column joints are susceptible to severe damage at relatively low interstory drift levels. Localization of inelastic demands in the columns, joint shear failure, and loss of anchorage in beam bottom bars and in column lap splices led to severe

loss of stiffness and strength. Because of these undesirable failure mechanisms, the remarkable ductility inherent in Grade 40 reinforcing bars could not be mobilized, and no effective energy-dissipating mechanisms were developed.

Specifically, the following conclusions were drawn:

1. The behavior of a corner beam-column-slab joint subjected to bidirectional loading is significantly different from that observed in simplified unidirectional, planar exterior joint tests and analyses commonly found in the literature. The reduction in the biaxial capacity of the column due to anchorage and section losses at the inside (NE) and outside (SW) corners of the column, the increased and nonuniformly distributed strains in the beam bars due to forces created by the slab (e.g. torsion) and the resulting increase in the joint shear force should not be overlooked. The shear force transferred to the joint can be significantly larger than that predicted based only on the strong-axis beam moments and an assumed constant moment arm.
2. The resultant of joint shear forces simultaneously occurring in the two primary directions during bidirectional loading is larger than the shear force created in a primary direction by unidirectional loading at the same drift level. For a -0.93% drift, the maximum bidirectional shear force was 30 to 44% larger than the maximum unidirectional shear forces. An assumed elliptical (circular in the case of symmetry) interaction diagram for bidirectional loading would result in underestimation of the actual bidirectional joint shear strength.
3. Despite the lack of any joint transverse reinforcements (ρ''=0), the specimens were able to develop unidirectional normalized joint shear stresses of up to $0.67\sqrt{MPa}$ during loading in either primary direction, even at a low drift ratio of ±0.93%. The γ value of 0.50 specified by FEMA 356 [3.8] for use in estimating the shear strength of corner joints with little or no joint transverse reinforcement (ρ''<0.003) seems to be conservative. As for bidirectional loading, the obtained joint shear force resultants at

approximately 45 degrees from the beam axes indicated that, even if the bidirectional joint shear strength was estimated for simultaneous occurrence of the FEMA-recommended value in both primary directions (i.e. $\gamma = 0.50\sqrt{2} = 0.71$), the estimated strength would be conservative by 20 to 25%.

4. If the tested specimens were part of an actual RC building to be evaluated according to the FEMA 356 [3.8] guidelines (i.e. based on strength hierarchy and crack sizes), critical performance levels that assure the safety of the building and its occupants such as Life Safety at 2% drift or Collapse Prevention at 4% drift would not have been met. The observed loss of stiffness (up to 80%) and lack of an effective energy dissipation mechanism also support this conclusion.
5. There is a clear need to develop effective seismic retrofit schemes for columns and beam-column joints so that seismic demands can be met through ductile beam mechanisms. Retrofit measures should be taken also to delay/prevent the loss of anchorage of beam bottom bars. Given the inadequacy of the current state-of-the-art on strengthening of RC beam-column joints [3.3, 3.4], more tests on joints with all floor members are needed to develop techniques for improving the shear strength of seismically deficient joints. Such efforts must account for the possibility of loading in various directions. Bidirectional loading was shown in this chapter to have detrimental effects especially on the column, joint, and on the anchorage of the beam bottom bars.

3.8 REFERENCES

[3.1] ACI-ASCE Committee 352 (1976). "Recommendations for design of beam-column joints in monolithic reinforced concrete structures (ACI 352R-76)." *ACI Journal Proceedings*, 73(7), 375-393.

[3.2] ACI Committee 318 (2005). *Building code requirements for structural concrete (ACI 318-05) and commentary (318R-05)*, American Concrete Institute, Farmington Hills, MI.

[3.3] ACI-ASCE Committee 352 (2002). *Recommendations for design of beam-column connections in monolithic reinforced concrete structures (ACI 352R-02)*, American Concrete Institute, Farmington Hills, MI.

[3.4] Engindeniz, M., Kahn, L. F., and Zureick, A. (2005). "Repair and strengthening of reinforced concrete beam-column joints: State of the art." *ACI Structural Journal*, 102(2), 187-197.

[3.5] Beres, A., Pessiki, S. P., White, R. N., and Gergely, P. (1996). "Implications of experiments on the seismic behavior of gravity load designed RC beam-to-column connections." *Earthquake Spectra*, 12(2), 185-198.

[3.6] ACI Committee 318 (1963). *Building code requirements for reinforced concrete (ACI 318-63)*, American Concrete Institute, Detroit, MI.

[3.7] Engindeniz, M., Kahn, L. F., and Zureick, A. "Performance of an RC corner beam-column joint severely damaged under bidirectional loading and rehabilitated with FRP composites." *Seismic strengthening of concrete buildings using FRP composites,* American Concrete Institute, Farmington Hills, MI, Accepted April 2007, *In press.*

[3.8] FEMA (2000). *Prestandard and commentary for the seismic rehabilitation of buildings (FEMA 356)*, Federal Emergency Management Agency, Washington, D.C.

[3.9] French, C. W., and Moehle, J. P. (1991). "Effect of floor slab on behavior of slab-beam-column connections." *Design of beam-column joints for seismic resistance,* SP-123*,* J. O. Jirsa, ed., American Concrete Institute, Farmington Hills, MI, 225-258.

[3.10] ACI Committee 318 (2002). *Building code requirements for structural concrete (ACI 318-02) and commentary (318R-02)*, American Concrete Institute, Farmington Hills, MI.

[3.11] Leon, R. T., and Jirsa, J. O. (1986). "Bidirectional loading of R.C. beam-column joints." *Earthquake Spectra*, 2(3), 537-564.

[3.12] Pantazopoulou, S. J., and French, C. W. (2001). "Slab participation in practical earthquake design of reinforced concrete frames." *ACI Structural Journal*, 98(4), 479-489.

CHAPTER 4

PERFORMANCE OF AN RC CORNER BEAM-COLUMN JOINT SEVERELY DAMAGED UNDER BIDIRECTIONAL LOADING AND REHABILITATED WITH FRP COMPOSITES

4.1 INTRODUCTION

This chapter presents the performance of a full-scale reinforced concrete corner beam-column-slab specimen that was first severely damaged under bidirectional quasi-static loading, then rehabilitated and retested. The specimen was built using the pre-1970s construction practices including the use of low-strength materials (f_c'=3000 psi [21 MPa], Grade 40 reinforcing bars) and deficiencies in reinforcement detailing. The rehabilitation process consisted of: (1) epoxy injection, (2) addition of a bar within the clear cover of the column at the inside corner, and (3) external application of a multilayer composite system made of unidirectional carbon-epoxy layers placed at different orientations. The carbon fiber-reinforced polymeric system was heat-cured at a temperature of 80°±10°C (176°±18°F) for 6 hours. The performance was evaluated both before and after rehabilitation based on the progression of damage and the hysteretic behavior including the changes in the strength, stiffness, and energy dissipation characteristics. The results indicated that even a severely damaged corner joint can be effectively rehabilitated using CFRP to achieve a ductile beam failure mechanism. The joint was upgraded to withstand story drift ratios of up to 3.7% applied simultaneously in both directions.

4.2 BACKGROUND

Reinforced concrete (RC) buildings constructed with inadequate or no seismic considerations constitute a significant portion of the building stock in many countries. Many catastrophic failures during earthquakes have indicated the vulnerability of beam-column

joints in such buildings. In the U.S., buildings constructed before the adoption of the first design guidelines for RC beam-column joints in 1976 [4.1] typically have the following major deficiencies in the joint regions: (1) strong beams, weak columns, (2) little or no joint transverse reinforcement, (3) beam bottom reinforcements with short embedment length, (4) short lapped splices of column bars just above floor level, and (5) wide spacing of column ties [4.2].

The ACI-ASCE Committee 352 [4.3] recommended that the adequacy of these joints be established and that methods of improving their performance be developed. A detailed review of the technical literature shows that such efforts, in general, have been limited to testing of one-way joint specimens with no floor slab or transverse beams [4.4] (Chapter 2). As a result, most of the proposed strengthening schemes were not only geometrically inapplicable to actual frame joints, but they also did not account for force transfer mechanisms and damage modes created by the presence of floor members and bidirectional loading. In studies where such effects were considered, the improved performance of the strengthened specimens was shadowed by the labor-intensiveness and bulkiness of the proposed strengthening schemes (e.g. concrete jacketing).

Relative advantages and disadvantages of previously studied repair and strengthening techniques were presented elsewhere [4.4] (Chapter 2). Among these techniques, externally bonded fiber-reinforced polymeric (FRP) composite applications offer advantages over others including ease of construction, corrosion resistance, and no increase in member sizes and mass. FRP composites are most attractive for their tailorability; the fiber-orientation in each ply can be adjusted so that specific strengthening objectives such as increasing the strength only, confinement only, or both, can be achieved [4.5]. Tests conducted to date on joint specimens with no floor members have shown that FRP composites can be promising for achieving ductile failure mechanisms if debonding of composites from the concrete surface can be delayed or prevented. Use of FRPs in rehabilitation of actual three-dimensional frame joints,

however, requires testing with consideration of the presence of floor members and bidirectional loads. In addition, thermal properties such as the glass-transition temperature and rate of curing of the matrix systems used in rehabilitation should be assessed with respect to the operating temperatures that the rehabilitated structure is likely to face during its service life. Curing schedules so adjusted may also improve the bond between the composite systems and concrete [4.6].

4.3 RESEARCH SIGNIFICANCE

This research starts to answer "needed research" posed by ACI-ASCE Committee 352 "Design of Beam-Column Connections in Monolithic Reinforced Concrete Structures", and it demonstrates the efficacy of CFRP for RC beam-column joint rehabilitation.

4.4 EXPERIMENTAL PROGRAM

4.4.1 Specimen Design

A full-scale corner beam-column-slab specimen was designed using the pre-1970s construction practices including deficient detailing and low-strength materials (specified f'_c=3000 psi [21 MPa], Grade 40 reinforcing bars), and according to the ACI 318-63 code [4.7]. From a review of the failure modes observed in previous studies in the literature, a column-to-beam moment strength ratio ($\Sigma M_c/\Sigma M_b$) of approximately 0.9 was targeted in the design to ensure a failure mode involving damage to the joint. Such a design called for the overall dimensions and reinforcement details shown in Figure 4.1. The major deficiencies expected to dominate the behavior of the specimen were: (1) actual $\Sigma M_c/ \Sigma M_b$=0.86, (2) no joint shear reinforcements, (3) beam bottom bars with an embedment length of only 6 in. (150 mm) into the joint, (4) a short ($20d_b$) and unconfined lapped splice of column longitudinal bars just above floor level.

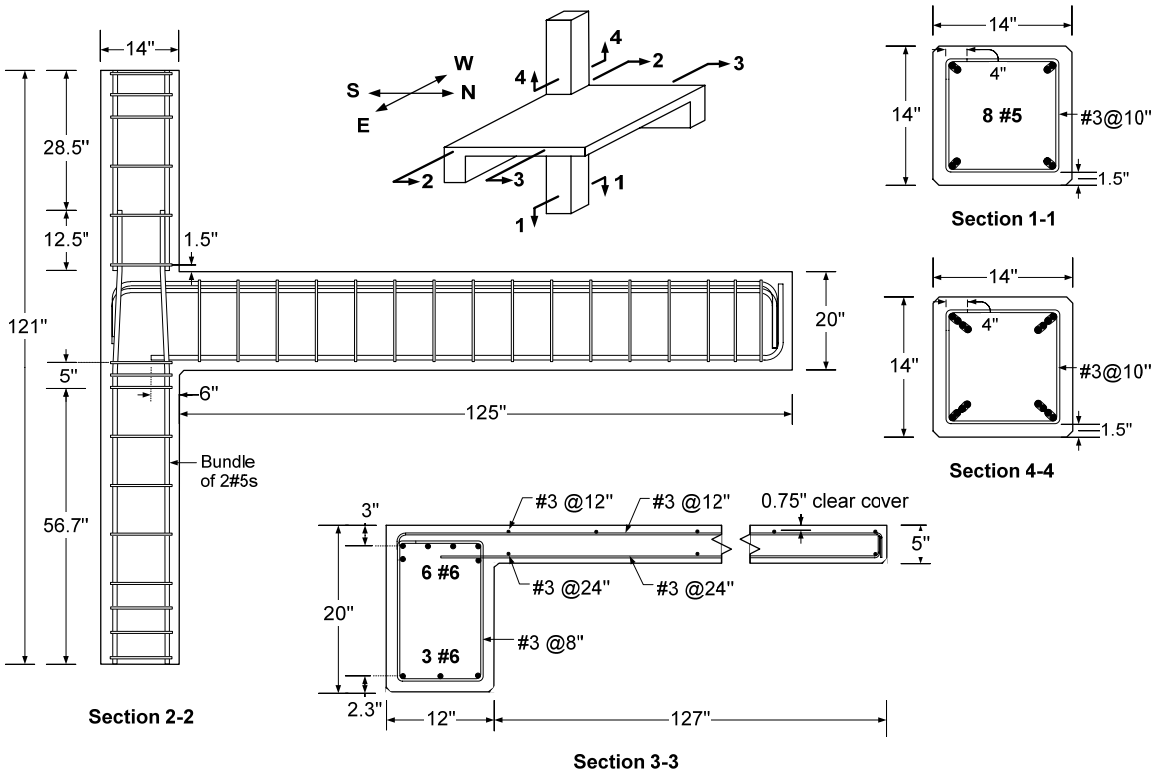

Figure 4.1 — Reinforcement details (1 in.=25.4 mm).

4.4.2 Material Properties

The specimen was cast in two lifts resulting in a cold joint at the bottom of the upper column. The average compressive strength of concrete (f'_c) for the first lift was 2880 psi (19.8 MPa) on the 28th day and 3740 psi (25.8 MPa) on both test days (i.e. before and after rehabilitation). For the second lift, f'_c was 3600 psi (24.8 MPa) on the 28th day and 4950 psi (34.1 MPa) on the test days. The reinforcements consisted of #3, #5, and #6 Grade 40 deformed bars with average yield strengths of 54 ksi (372 MPa), 52 ksi (358 MPa), and 46 ksi (317 MPa), respectively.

4.4.3 Test Setup

The specimen represents the part of the corner of a building isolated at the assumed inflection points (i.e. midspan of beams and columns) when the building is

subjected to lateral loads. The test setup is shown in Figure 4.2. The top of the column was connected to a universal joint that allowed rotation in any direction and vertical translation; only lateral translations were restrained. The bottom of the column was fixed to the strong floor; the length of the lower column was designed such that an inflection point would form below the beam at a distance equal to the length of the upper column. Cyclic lateral loads were simulated by hydraulic actuators mounted vertically at the end of the beams. In addition to the rotational releases at each end of the actuators about an axis perpendicular to the beams, a special fixture was used between the specimen and the actuators to permit torsional rotations expected due to the presence of the slab. The column axial load was applied using a fixture consisting of a DWYDAG rod running alongside each corner of the column and a hydraulic center-hole jack connected to each rod.

4.4.4 Instrumentation of the As-Built Specimen

The strains in the reinforcing bars were monitored at the joint-beam, joint-column, and beam-slab interfaces in both EW and NS directions using electrical resistance strain gages mounted on the bars (Figure 4.3a,b). Strain gages were also mounted on two outer beam bottom bars in each direction at 3 in. (76 mm) into the joint, two stirrups above and below the joint (all four legs), and on a beam stirrup (two vertical legs) as shown in Figure 4.3a. Joint shear strains and relative rotations of the beams and columns with respect to the joint were monitored using the LVDT configuration in Figure 4.3c on both S and W faces of the specimen. Additional measurement of the rotation of the beams with respect to the column was performed using string potentiometers mounted at the midwidth of the beam top and bottom surfaces (Figure 4.3c). Global rotations and translations of the joint region in both directions were measured with respect to a fixed reference frame using potentiometers (Figure 4.3c). Torsional rotations of each beam were monitored using potentiometers mounted on the inner and outer edges of the beam

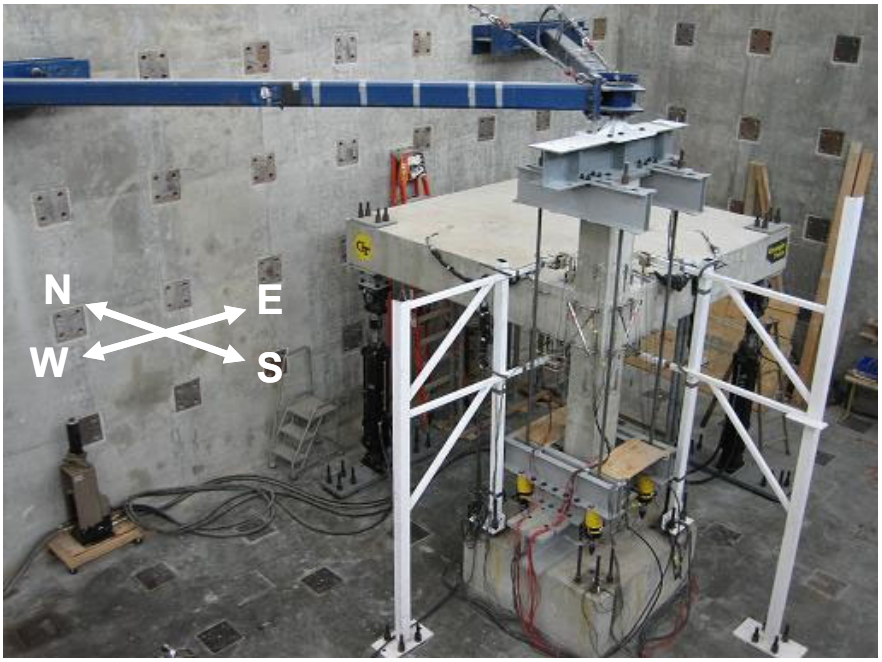

Figure 4.2 — Test setup.

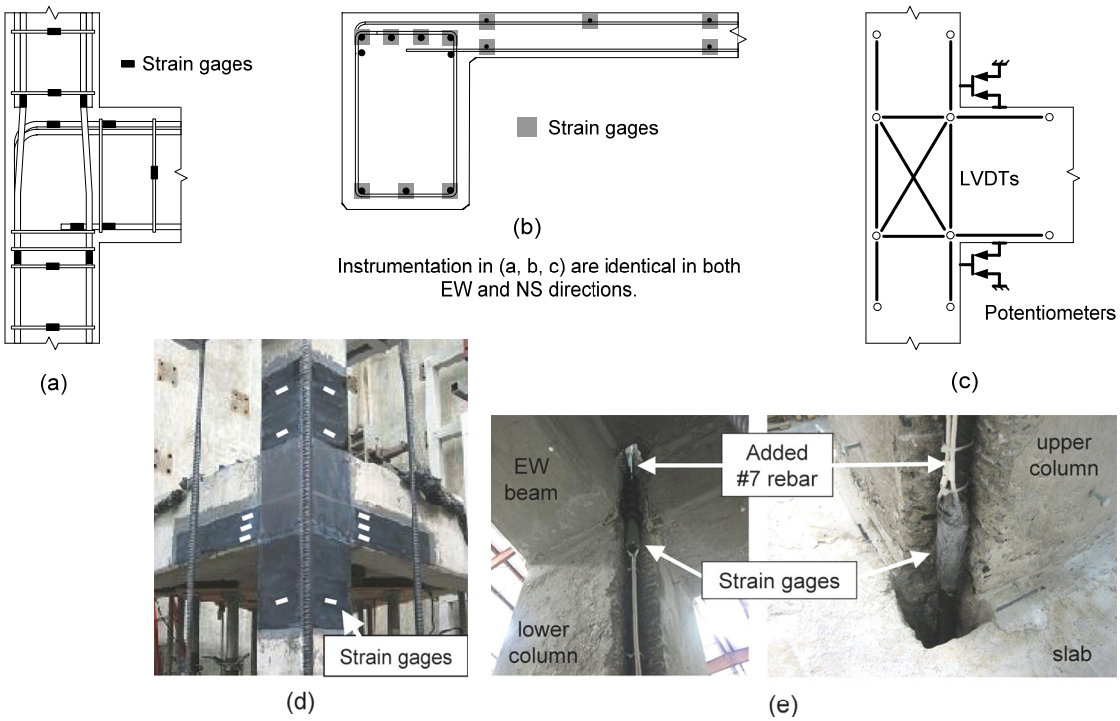

Figure 4.3 — Instrumentation.

bottom surface at the tip of the beam and at a section near the column faces. The column shear forces were monitored by full-bridge strain gage configurations mounted on each arm of the triangular reaction frame connected to the universal joint atop the column. The column axial load was monitored by a load cell mounted on each hydraulic jack at each corner of the column.

4.4.5 Loading Procedure

The loading procedure simulated a cyclic lateral loading of a building carrying service gravity loads. First, a column axial load of 10% of the column's compressive load capacity was gradually applied ($0.1P_o$=74 kip [330 kN]). Then, both beams were deflected downwards in a displacement-controlled mode until the strong-axis beam moments at the column faces were brought to a level that was estimated to occur in an actual frame building under service loads. The beams were then subjected to cyclic loading symmetrically around this deformed position in a displacement-controlled mode as shown in Figure 4.4.

The applied displacement history included unidirectional cyclic loading of EW and NS beams, respectively, at a displacement level of $\pm\Delta_y$, which was followed by bidirectional simultaneous cyclic loading of both beams at displacement levels $\pm\Delta_y$, $\pm1.5\Delta_y$, $\pm2.0\Delta_y$, and $\pm4.0\Delta_y$. The objective of the unidirectional loading was to compare the behavior of the specimen to that under biaxial loading in the later cycles. The displacement at first yield, Δ_y, was determined by continuously monitoring the strains in all column and beam critical sections during the first stage of loading. The first yield occurred in the upper column at the inside (NE) corner at a displacement of $\pm\Delta_y$=1.12 in. (28.5 mm) measured from the reference deformed position used for cyclic loading. As a result, the applied displacement levels corresponded to interstory drift ratios (θ) of ±0.93%, ±1.40%, ±1.87%, and ±3.73%. Three cycles were applied at each

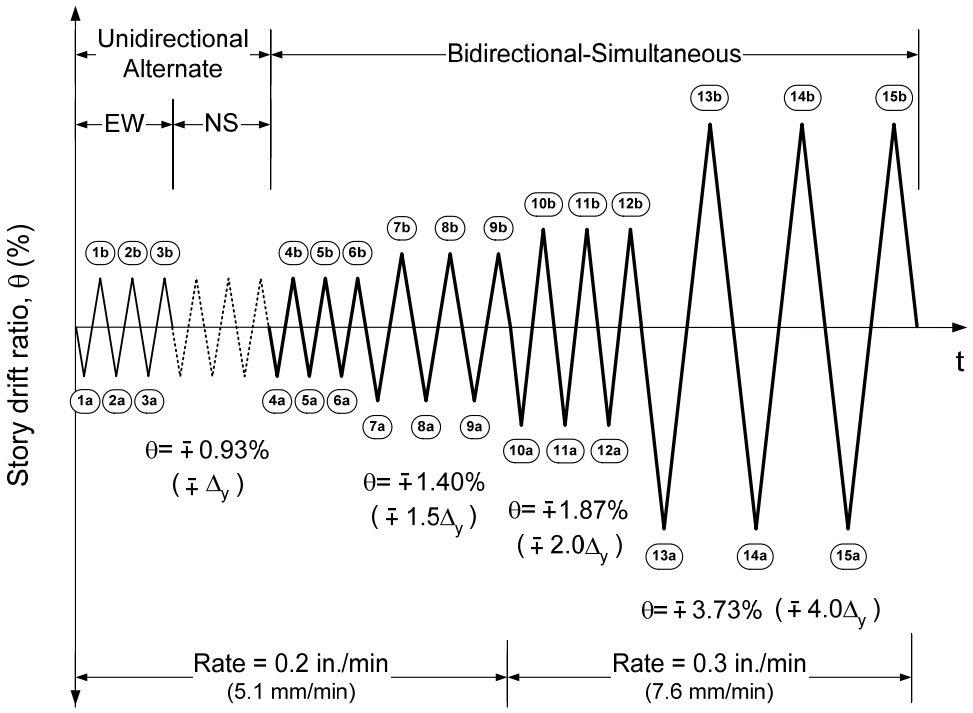

Figure 4.4 — Applied displacement history. Negative drift (downward beam displacement) causes tension at the top of the beams. Cycle 1 has negative peak 1a and positive peak 1b.

unidirectional or bidirectional drift level to determine cyclic degradation. A displacement rate of 0.2 in./min (5.1 mm/min) was used until the beginning of the ±1.87% drift cycles, at which point the rate was increased to 0.3 in./min (7.6 mm/min). The loading of the as-built specimen was terminated after the ±1.87% drift cycles upon achieving a severe level of damage, thus preventing the specimen to become unstable under the applied loading condition. After rehabilitation, the specimen was subjected to the entire displacement history.

The following terminology is used throughout this chapter: Positive direction for actuator displacements are upwards. A load step consists of moving to a certain drift level in one direction, then moving back to the reference position. A load cycle consists of a load step in the negative direction followed by another in the positive direction. A drift

level that is applied simultaneously in the EW and NS directions is referred to as a bidirectional drift.

4.5 PERFORMANCE OF THE AS-BUILT SPECIMEN

4.5.1 Overall Behavior

The behavior of the as-built specimen was dominated by a combination of four major damage modes:

1. Yielding in the upper column during the negative load steps. The first peak at -0.93% drift in the EW direction represents the first yield accompanied by wide flexural cracks at the inside (NE) corner of the upper column. The demand at this corner increased significantly during the bidirectional cycles, the width of the cracks reaching 0.1 in. (2.5 mm) and 0.25 in. (6.4 mm) at the first peaks at -1.40% and -1.87% drift, respectively. The first yield in the lower column also occurred at the first peak at -1.87% drift.
2. Slippage/pull-out of beam bottom bars during the positive load steps. Flexural cracks at the beam-column interfaces extending vertically from the bottom to the middepth of the beams reached a maximum width of 0.06 in. (1.5 mm) during the unidirectional cycles and 0.08 in. (2.0 mm), 0.2 in. (5.1 mm), and 0.31 in. (7.9 mm) at the +0.93%, +1.40%, and +1.87% bidirectional drift levels, respectively. The strain readings indicated that the bottom bars near the inside faces of the beams were subjected to larger tensile forces than those on the outside. Although the bars performed well during the unidirectional cycles, and the inner bars developed strains as high as 1360 με (ε_y=1660 με), they lost their anchorage gradually after the beginning of the bidirectional cycles. A comparison of strains just outside the joint with those at 3 in. (76 mm) into the joint indicated that, by the end of test, only the bars on the outside were left with a limited anchorage.

3. Joint shear cracking during the negative load steps. Figure 4.5 shows that diagonal cracking in the joint occurred in one direction only and not in the often recorded "X" manner, because the loss of anchorage of the beam bottom bars prevented the formation of the other diagonal crack. The maximum width of the joint shear cracks was 0.04 in. (1.0 mm) during the unidirectional cycles. During the bidirectional cycles, they not only opened wider in the plane of the joint panel, but they also exhibited bulging in the direction perpendicular to the surface due to rotation of the hooked beam top bars. At the second peak at -0.93% bidirectional drift, these cracks had joined those at the bottom of the beam and reached a width of 0.07 in. (1.8 mm) to 0.08 in. (2.0 mm).
4. Propagation of cracks into the upper column. At the first peak at -1.40% drift, the diagonal crack in the joint panel propagated vertically into the upper column forming a combined crack extending from the bottom of the beam into the upper column, exhibiting a bulging of up to 0.25 in. (6.4 mm) in the later cycles. At the end of the test, this crack measured 0.31 in. (7.9 mm) wide at the beam embedment region, 0.25 in. (6.4 mm) wide in the joint panel, and 0.125 in. (3.2 mm) in the upper column (Figure 4.5a, b). The cracks in EW and NS faces were connected through the joint at an angle of roughly 45 degrees, forming a large triangular prismlike concrete block trying to separate from the outside corner of the column. The two stirrups along the column lapped splice resisted this separation by developing strains as high as 1550 με in their S and W legs.

The maximum tensile strains achieved in the beam top bars provide a means of comparing the specimen's performance with a desirable ductile beam hinging mechanism. The strain measurements at the NS beam-column interface showed that while the outermost top bar developed 90% of its yield strain during the bidirectional cycles, the innermost top bar developed only 42%. A similar strain distribution was

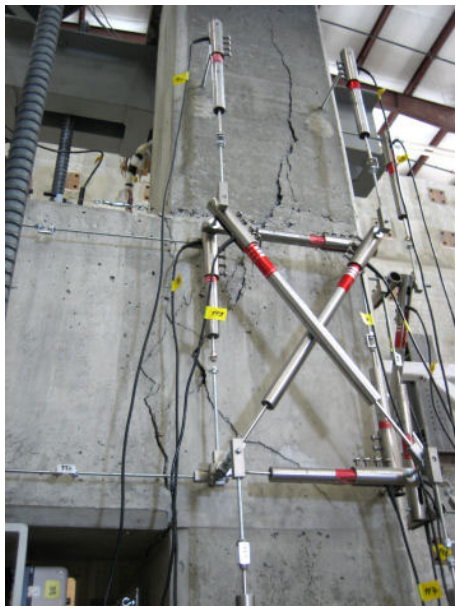

(a) West face

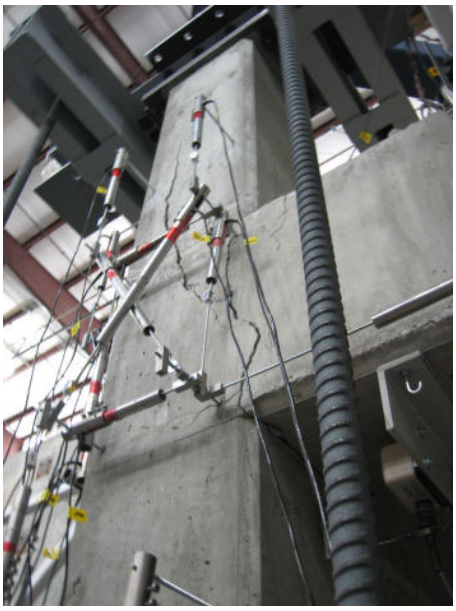

(b) South face

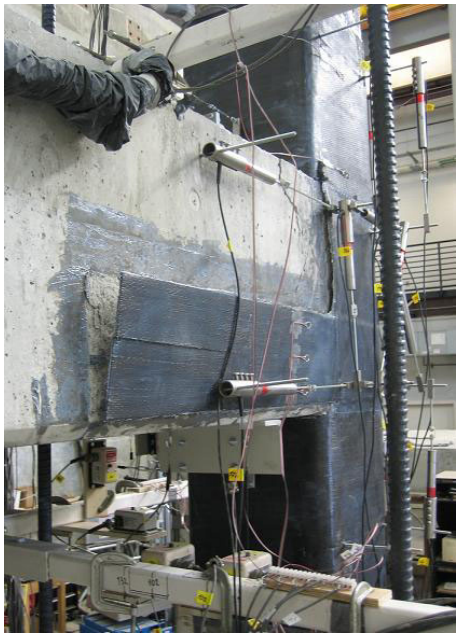

(c) West face

(d) South face

Figure 4.5 — Damage at the end of test: (a, b) before rehabilitation at cycle point 12a, and (c, d) after rehabilitation at cycle point 15a.

recorded at the EW beam-column interface. Such a strain distribution is attributed to combined unsymmetric bending and torsion in the beams due to the presence of the slab. The measured strain levels indicated that a significant strengthening of the column and the joint was needed to achieve yielding in all beam top bars.

Two major cracks were observed in the slab:

1. A flexural crack that formed in a direction parallel to the NS beam at 3.5 in. (89 mm) from the inside face of this beam and propagated across the entire width and through the thickness of the slab—This crack initiated during the EW unidirectional cycles and reached a maximum width of 0.02 in. (0.5 mm). Such a crack did not occur in the EW direction during the NS unidirectional cycles.
2. A diagonal crack at the bottom surface extending from the joint region to the opposite corner—This crack was located after completing the test and measured 0.04 in. (1.0 mm)-wide. It indicated the need for special diagonal reinforcement in the slab corners in line with the requirements of ACI 318-05, Section 13.3.6.

4.5.2 Hysteretic Behavior

The strength, stiffness, and energy dissipation characteristics of the specimen were evaluated through the force-drift hysteretic response, presented in Figure 4.6 for both EW and NS directions. The curves are shifted from the horizontal line representing zero load due to the initial loads on the actuators (EW=2.0 kip [8.9 kN], NS=2.7 kip [12.0 kN]) at the deformed position used as the reference level for cyclic loading. This deformed position is the “zero” drift datum. Positive load values indicate compression force in the hydraulic ram.

The peak loads measured in each cycle in both negative and positive loading directions are presented in Table 4.1. The maximum loads in both positive and negative directions occurred in the first unidirectional cycles. A significant decrease in the peak loads was observed at the beginning of the bidirectional cycles, then the strength

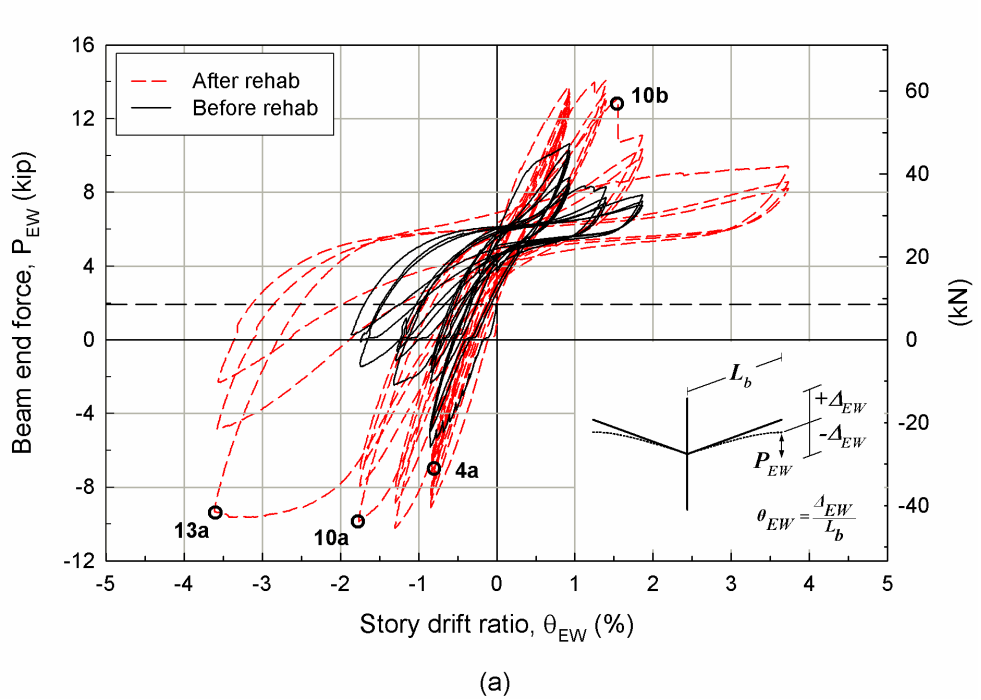

(a)

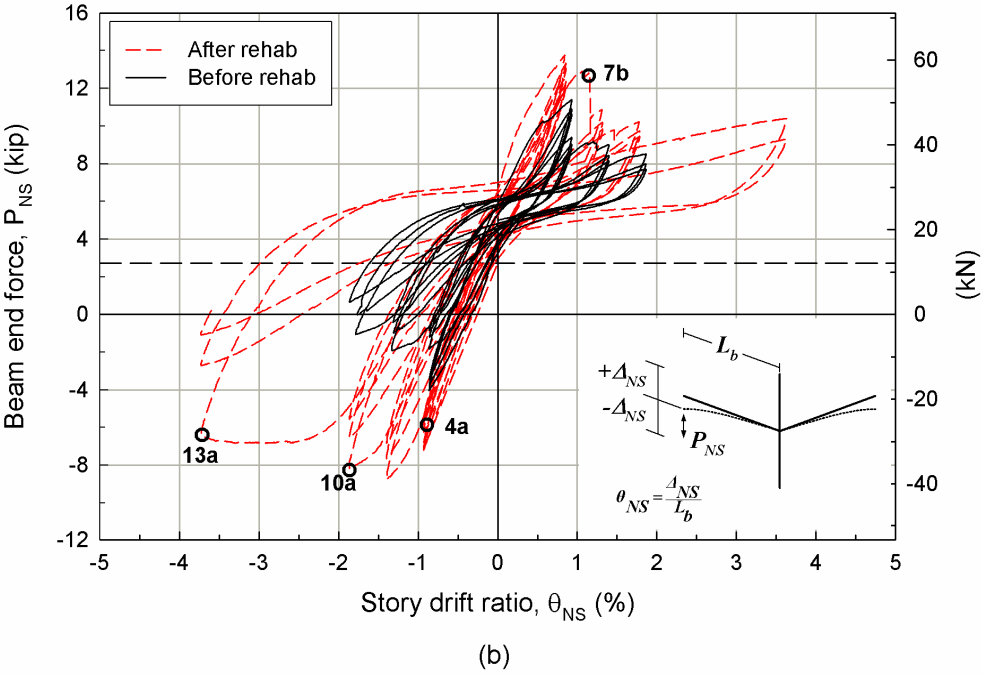

(b)

(4a) First yield in beams, (7b) Debonding of FRP strips on NS beam,
(10a) Extensive yielding in beams and first yield in column,
(10b) Debonding of FRP strips on EW beam, (13a) Joint failure

Figure 4.6 — Force-drift hysteresis loops: (a) EW, and (b) NS.

Table 4.1 — Peak Loads

		EW				NS			
		Before Rehab		After Rehab		Before Rehab		After Rehab	
Drift, θ	Cycle	$-P_{max}$ (kip)	$+P_{max}$ (kip)	$-P_{max}$ (kip)	$+P_{max}$ (kip)	$-P_{max}$ (kip)	$+P_{max}$ (kip)	$-P_{max}$ (kip)	$+P_{max}$ (kip)
EW ±0.93%	1	-5.83	10.64	-9.11	13.73	*		*	
	2	-4.97	10.28	-8.68	13.42				
	3	-4.62	9.98	-8.43	13.22				
NS ±0.93%	1	*		*		-4.03	11.40	-7.13	13.75
	2					-3.74	10.91	-7.20	13.33
	3					-3.46	10.64	-6.98	13.08
Biaxial ±0.93%	1	-2.35	8.79	-7.25	12.93	-1.84	9.40	-6.24	12.56
	2	-1.75	8.51	-6.89	12.54	-1.21	9.04	-5.87	12.20
	3	-1.35	8.29	-6.63	12.39	-0.85	8.80	-5.60	12.03
Biaxial ±1.40%	1	-2.46	8.31	-10.23	14.08	-1.91	9.02	-8.77	10.88
	2	-1.13	7.72	-8.86	13.39	-0.97	8.44	-7.65	10.20
	3	-0.61	7.45	-8.00	12.99	-0.42	8.14	-6.84	9.85
Biaxial ±1.87%	1	-1.45	7.86	-9.86	11.11	-1.06	8.53	-8.15	10.23
	2	-0.10	7.52	-7.97	10.35	-0.02	8.01	-6.55	9.75
	3	0.28	7.30	-6.99	9.92	0.66	7.71	-5.55	9.46
Biaxial ±3.73%	1	**		-9.63	9.43	**		-6.83	10.41
	2			-4.88	8.58			-2.71	9.32
	3			-2.31	8.21			-1.08	***

* Peak loads during the unidirectional cycles are reported for the direction of loading only.

** Testing of the as-built specimen was terminated after the ±1.87% bidirectional drift cycles.

*** $+P_{max}$ in this cycle could not be recorded due to a data acquisition problem.

1 kip = 4.448 kN

degraded more gradually. Both the overall and cyclic strength degradation was more pronounced in the negative direction as a result of the progressive damage in the joint panel and in the upper column.

Significant degradation in stiffness and pinching of the curves were dominant throughout the hysteresis loops. The peak-to-peak stiffness K_p, defined as the slope of the line connecting the peak of a negative load step to that of the next positive load step, decreased continuously as shown in Figure 4.7. An 80% decrease in K_p from the first cycle to the last cycle was observed in the EW direction; the decrease in K_p in the NS direction was 78%. The degradation in stiffness was more significant after the beginning of the bidirectional cycles.

The energy dissipated by the specimen was calculated as the area enclosed by the force-displacement curves. Cumulative plots of the dissipated energy in both EW and NS directions are presented in Figure 4.8. Although the total energy increased continuously, the increase was not proportional to the increase in the applied displacements due to the combined effects of increased pinching and strength degradation.

The plot of the joint shear stress factor (γ) versus the joint shear strain (γ_s) is presented in Figure 4.9, where $\gamma = V_{jh} / \sqrt{f_c'} b_j h_c$ as defined in ACI 352R-02, Sec. 4.3.1. The horizontal joint shear force (V_{jh}) was determined as the difference between the column shear force and the total tensile normal force (T_b) acting on the beam-joint interface. T_b was estimated by assuming a constant moment-arm of *jd=0.875d* between the tension and compression resultants at this section (i.e. $T_b = M_z$ */0.875d*). γ_s for each joint panel was taken as the average of four joint shear strain estimates obtained from the LVDT configuration in Figure 4.3c. The resulting γ versus γ_s plots were in line with all previous discussions in that significant softening and distortion of the joint during the negative load steps was clear. Maximum shear stresses were in the negative direction, the

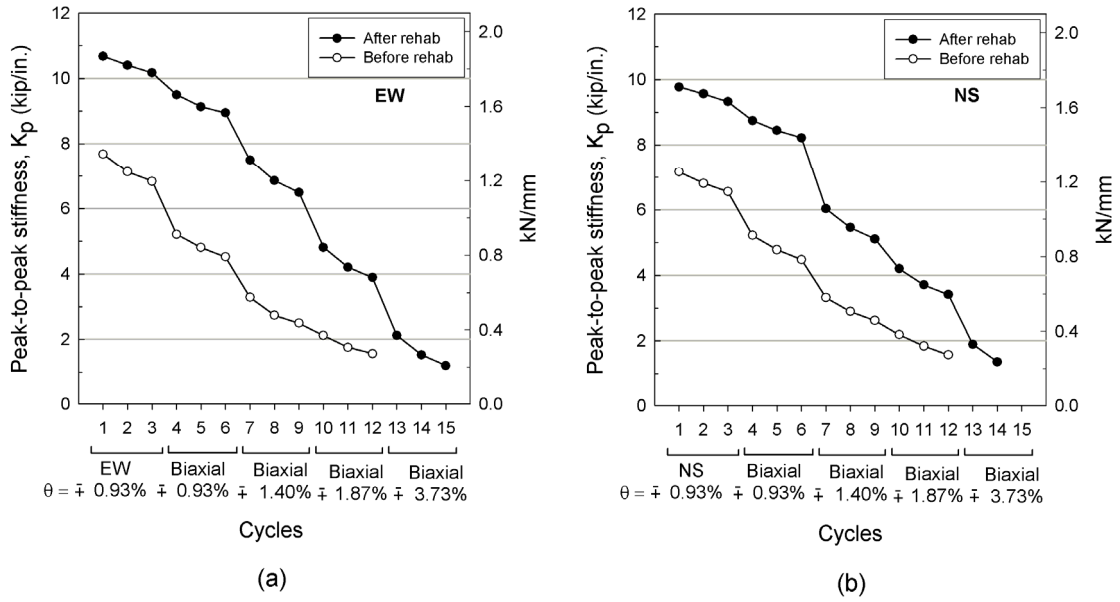

Figure 4.7 — Stiffness degradation: (a) EW, and (b) NS.

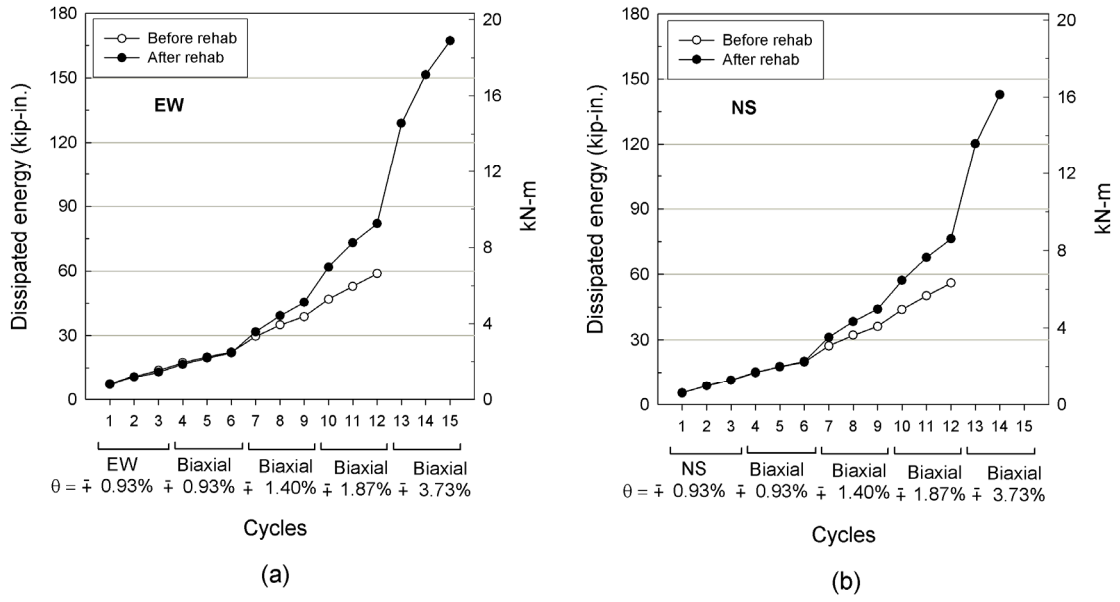

Figure 4.8 — Cumulative dissipated energy: (a) EW, and (b) NS.

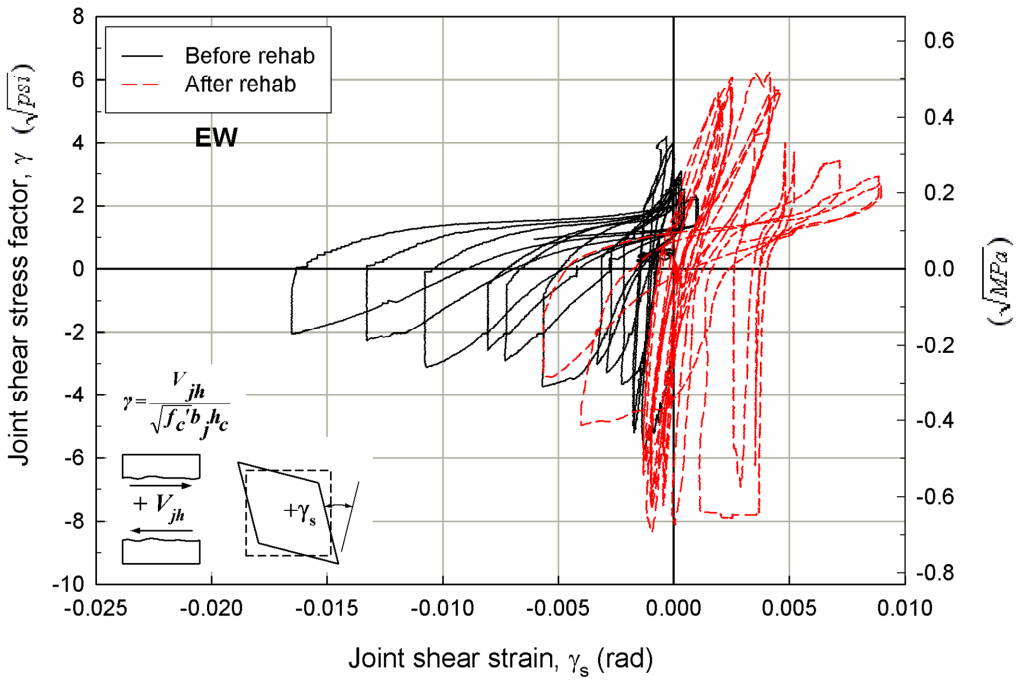

(a)

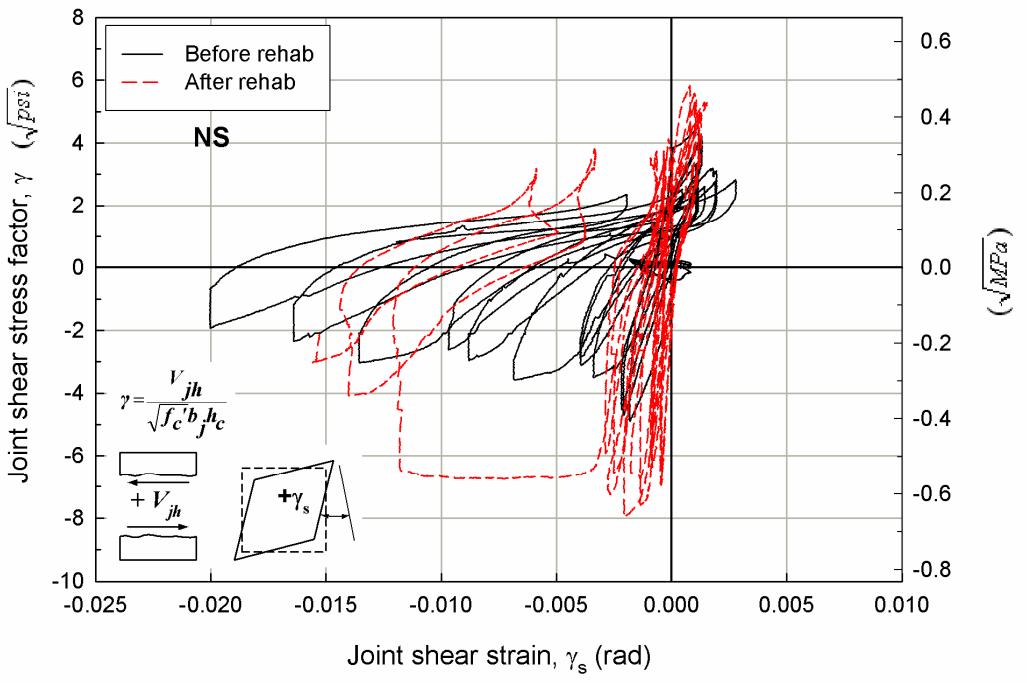

(b)

Figure 4.9 — Joint shear stress-strain hysteresis loops: (a) EW, and (b) NS.

γ factor being $5.7\sqrt{psi}$ ($0.47\sqrt{MPa}$) and $4.9\sqrt{psi}$ ($0.41\sqrt{MPa}$) for the EW and NS directions, respectively. For the positive loading direction, maximum γ values of $4.2\sqrt{psi}$ ($0.35\sqrt{MPa}$) and $4.5\sqrt{psi}$ ($0.37\sqrt{MPa}$) were obtained for the EW and NS directions.

The shear capacity of the joint may be underestimated by the use of the "constant moment-arm approximation" because of the unaccounted contributions to the tensile forces in the beam bars. Data not included here for brevity suggests that torsion, for instance, increases the tensile forces in all the beam bars. Even so, this method can be used to compare the joint shear strength before and after rehabilitation.

4.6 REHABILITATION PROCEDURE

All rehabilitation steps were performed at the deformed position used as reference for cyclic loading. The specimen was first repaired by pressure-injection of a high-strength, high-modulus, low-viscosity epoxy that filled all cracks larger than 0.01 in. (0.3 mm) [Figure 4.10a]. The injection of approximately 2 gal. (7.6 L) of epoxy confirmed the severity of damage in the specimen.

4.6.1 Strengthening Design and Application

The specimen was strengthened to achieve improvements in the following areas: (1) flexural strength of the column, (2) joint shear strength, (3) beam bottom bar anchorage, (4) column end confinement, and (5) flexural strength at the SW corner of the slab. Strengthening in all areas except (1) was performed using a 9 oz/yd^2 (300 g/m^2) unidirectional carbon fabric impregnated with a high-strength, high-modulus epoxy matrix using a hand-layup technique. During the preliminary design of the experiment, tensile properties of the carbon-epoxy system were taken as those reported by the manufacturer (i.e. tensile strength P_u^{CFRP} =2100 lb/in./layer [370 N/mm/layer], ultimate

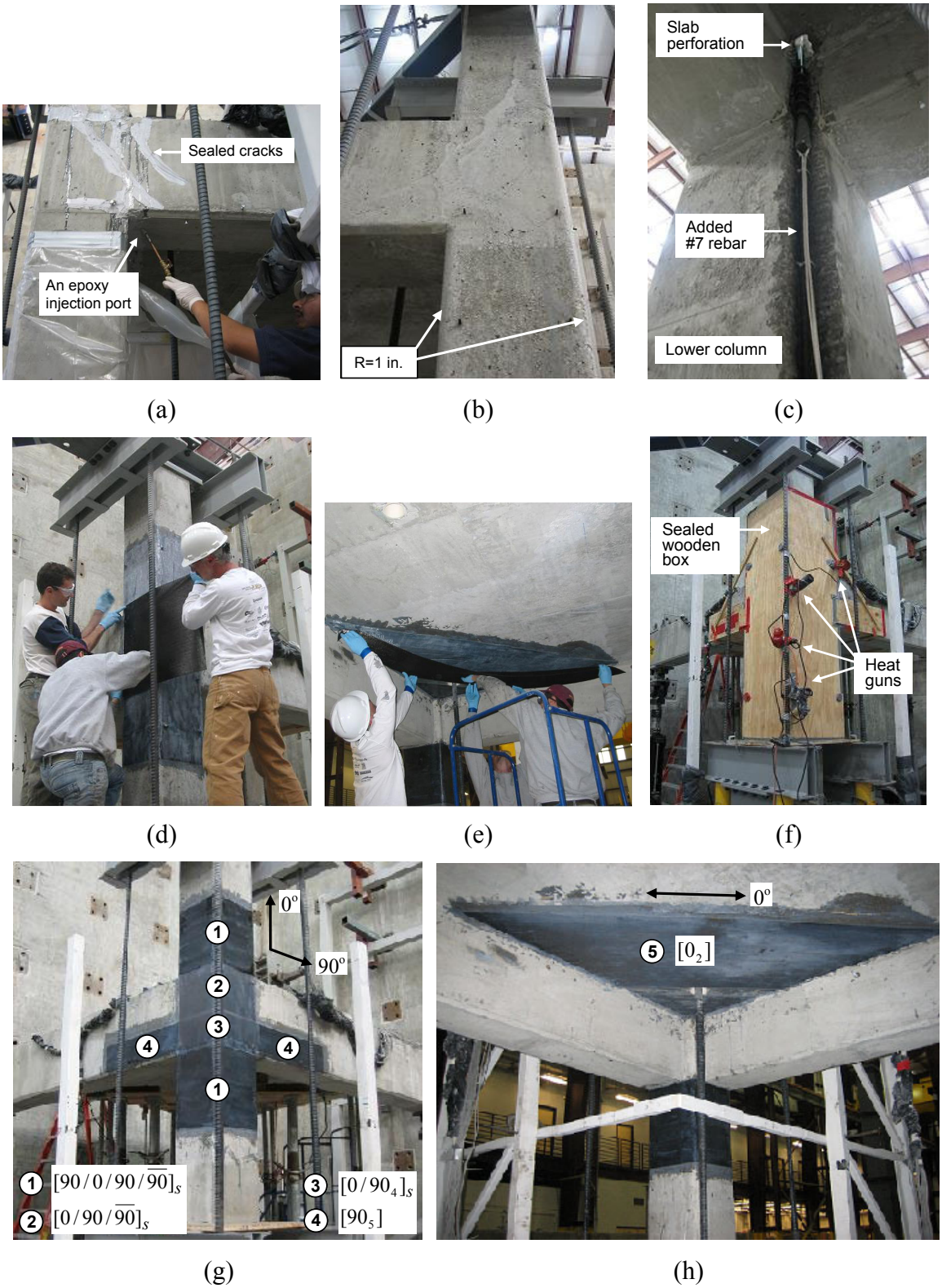

Figure 4.10 — Rehabilitation process: (a, b) epoxy injection and surface preparation, (c) addition of a #7 reinforcing bar, column inside corner, (d, e) CFRP application on column and bottom of slab, (f) heat-curing of CFRP, and (g, h) finished look.

strain ε_u^{CFRP}=1.00%, thickness t=0.020 in./layer [0.5 mm/layer]). The properties attained in the actual application were examined by testing coupons cut from a single-layer plate (i.e. witness plate) made using the same technique and curing schedule (see next section) as that used in rehabilitating the specimen. The witness plate contained 42% fibers by weight, which corresponded to a fiber volume ratio of approximately 34% assuming a 4% void volume in the system. Based on 10 coupon tests, the following average values were obtained: P_u^{CFRP}=2930 lb/in./layer (510 N/mm/layer), ε_u^{CFRP}=1.52%, and t=0.027 in./layer (0.7 mm/layer).

The following approach was taken in the design and application of strengthening in each area:

1. **Flexural strength of the column.** The higher force demand on the inside corner of the upper column required addition of flexural reinforcement along the entire height of the column and continuous through the slab. The amount of existing column longitudinal reinforcement (2#5) at this corner was doubled by removing a 2 in. x 2 in. (50 mm x 50 mm) portion of the column corner including a perforation in the slab, adding a #7 bar (f_y=65 ksi [448 MPa]) (Figure 4.10c), and recasting the corner with a polymer-modified, cementitious mortar (f'_c=7200 psi [49.6 MPa] on the test day).

2. **Joint shear strength.** The maximum horizontal joint shear force ($V_{jh}^{\max}$) that could develop was estimated by assuming yielding of all beam top bars and the three slab bars within 20 in. (510 mm) (ACI 318-05 [4.8], Sec. 8.10.3) next to the beams:

$$V_{jh}^{\max} = \sum A_s f_y - V_{col} = 6\left(A_s f_y\right)_{\#6} + 3\left(A_s f_y\right)_{\#3} - \frac{M_n^-}{L_b} 1.25 \qquad (4.1)$$

where M_n^- is the negative moment capacity of the beam, L_b is the beam length measured from column face, and 1.25 is the ratio of the beam end load to column

shear (V_{col}) analytically determined for this test setup using the measured material properties. Three layers of CFRP oriented perpendicular to the longitudinal axis of the column (90 degrees) were required to resist this force according to Equation 4.2:

$$n_{jh} = \frac{V_{jh}^{\max}}{h_j P_u^{CFRP}} \tag{4.2}$$

where n_{jh} is the number of layers, h_j is the height of the joint covered with CFRP (20 in. [510 mm]), and P_u^{CFRP} is the average tensile strength (lb/in./layer) of CFRP (n_{jh}=2.62=3). An additional two layers oriented at 0 degree (parallel to the column) were provided to resist the vertical component of the principal tension force in the joint panel. All layers were extended into the upper and lower columns by a distance equal to the height of the confined regions at the column ends. All five layers were applied on the S and W faces of the specimen only.

3. **Beam bottom bar anchorage.** Although the demand was larger on the bottom bars near the inside faces of the beams than on those near the outside faces, for ease of construction, an attempt was made to improve the positive moment capacity of the beams by providing CFRP reinforcement on the outside faces only. CFRP strips were placed around the SW corner of the joint such that the strips extended 28 in. (710 mm) on to the beams measured from the beam-column interfaces ("Area 4" in Figure 4.10g). The number of layers (n_s) was selected such that the load capacity of the strips would be equivalent to that of all three bottom bars at yield:

$$n_s = \frac{\sum A_s f_y}{w_s P_u^{CFRP}} = \frac{3\left(A_s f_y\right)_{\#6}}{w_s P_u^{CFRP}} \tag{4.3}$$

The width of the strips (w_s), preferred to be less than half the beam depth to avoid an undesirable increase in the negative moment capacity of the beams, was arbitrarily

selected as 7 in. (180 mm); this resulted in n_s=4.13=5. An anchorage length of 28 in. (710 mm) was selected so that the distance from the tip of the beam bottom bars to the end of the strips would be equivalent to the development length of these bars according to ACI 318-05, Sec.12.15.

4. **Column end confinement.** The CFRP used for confinement of the column ends was designed per ACI 440.2R-02, Sec. 11.3 such that the effective usable compressive strain in concrete would be equivalent to that provided by the hoop reinforcement required by ACI 318-05, Sec. 21.4.4. This approach called for two layers (90 degrees) of wrapping at the column ends over a length of 18 in. (460 mm) ["Area 1" in Figure 4.10g]. Wrapping the column ends also provides an effective means of anchorage for the layers extended from the joint onto the columns as well as for the column longitudinal bar added in the NE corner.
5. **SW corner of the slab.** A 48 in. x 48 in. (1220 mm x 1220 mm) triangular portion of the bottom surface was strengthened with two layers of CFRP to increase the flexural strength to an extent required by ACI 318-05, Sec. 13.3.6. The fibers in both layers were oriented in the NW-SE direction ("Area 5" in Figure 4.10h). Strengthening at the top surface was deemed unnecessary due to limited cracking in this region.

It is to be noted that the use of the manufacturer's reported nominal CFRP properties in the design and rounding up of the resulting numbers of required layers (e.g. n_{jh}, n_s) to whole numbers led to the use of a few more layers of CFRP than what would be used if the properties attained in the actual application were known. For instance, the as-attained properties would lead to n_{jh}=2 (instead of 3) and n_s=3 (instead of 5); the efficacy of such a configuration is to be studied in subsequent experiments.

4.6.2 Curing of CFRP

Our differential scanning calorimetry (DSC) tests conducted on the matrix system used for the FRP system showed that room temperature-cured Sikadur 330 US epoxy had glass transition temperature (T_g) values of 49°C (122°F) and 56°C (133°F) after 9 and 60 days, respectively. This raised a concern about the mobility of the epoxy molecular chain structure in an operating temperature range that is often encountered in the vast majority of regions around the world. It is often recommended that the FRP system have a T_g of 10°C (18°F) to 30°C (54°F) higher than the operating temperature [4.9-4.11].

To achieve an acceptable degree of molecular cross-linking, the matrix system was heat-cured at 80°C (176°F) for a duration of 3 hours or more. DSC results indicated that, after 3 hours, the T_g was increased to 70°C (158°F). Subsequently, all areas of the specimen that were strengthened with CFRP were heat-cured at a temperature of 80°±10°C (176°±18°F) for 6 hours instead of 3 hours, an arbitrary decision that was based on the fact that part of the heat would be absorbed by concrete. Heat-curing was performed by building a sealed, insulated wooden box around the region, and then heating the enclosed region with four adjustable heat guns (Figure 4.10f). DSC tests conducted on samples taken from the FRP system after the completion of the test program resulted in T_g values between 63°C (145°F) and 65°C (149°F).

4.6.3 Layup Sequence

The CFRP layers were stacked in a sequence that would result in a symmetric layup in all areas. A symmetric layup was necessary to: (1) prevent curvatures during heat-curing that could cause early debonding from the concrete surface, and (2) eliminate the extension-bending coupling that would result in difficulties associated with the determination of the tensile properties of the FRP system. The final stacking sequences in all areas are shown in Figure 4.10g, h.

4.6.4 Instrumentation of the Rehabilitation Components

The strains in the added #7 bar at sections above and below the beams were monitored using two strain gages at each section (Figure 4.3e). The strains in the FRP strips bonded on each beam were monitored using three strain gages mounted on the strips at a section 4 in. (102 mm) away from the beam-joint interface (Figure 4.3d). These gages were evenly spaced with the bottom one being at the level of the beam bottom bars. Strain gages were also mounted on the column end wraps at the midwidth of the column at the first and second stirrup levels above the joint and at the third stirrup level below the joint (Figure 4.3d).

4.7 PERFORMANCE AFTER REHABILITATION

4.7.1 Overall Behavior

After rehabilitation, the poor behavior of the as-built specimen was improved to a desirable strong column-weak beam behavior. The initiation of damage was delayed until the beginning of the bidirectional cycles, and the damage modes leading to the failure of the specimen started to occur only after the ±1.87% drift cycles. Improvements in performance are summarized below in reference to the damage modes that dominated the behavior of the specimen before rehabilitation:

1. **Onset and progression of bar yielding.** The first yield was delayed until the first peak at -0.93% bidirectional drift at which point yielding occurred in both beams and in the slab. The second beam top bars from outside in both beams and a slab top bar parallel to the NS near the column yielded, the outermost beam top bars just reached their yield strain (ε_y =1660 με), and the strains in the other beam top bars ranged from 1230 με to 1330 με. The flexural cracks near the top of both beams measured 0.02 in. (0.5 mm) wide. At the first peak at -1.40% drift, the two outer beam top bars in each beam and two slab top bars near the column parallel to each beam had yielded; the other beam top bars had just reached their yield strain. The flexural cracks near the top

of the beams measured 0.07 in. (1.8 mm) and 0.05 in. (1.3 mm) wide for the EW and NS beams. The #7 bar added in the NE corner of the column reached its yield strain (ε_y =2490 με) in the upper column at the first peak at -1.87% drift at which point all beam top bars except for the innermost NS beam top bar had yielded, and the cracks in the EW and NS beams were 0.15 in. (3.8 mm) and 0.08 in. (2.0 mm) wide. During the ±1.87% and ±3.73% drift cycles, the EW beam underwent more damage than the NS beam, and the strains in the beam bars increased more rapidly than in the column bars as drift increased. At the first peak at -3.73% drift, the EW beam underwent severe spalling. The innermost NS beam top bar did not yield throughout the test but developed strains as high as 1490 με. While the NS beam top bars that did yield developed strains as high as 14,080 με, the demand on the column was limited to a maximum strain of 5250 με in the added #7 bar in the upper column and spalling of the inside corner of the joint near the first negative peak at -3.73% drift.

2. **Beam bottom bar anchorage.** The FRP strips bonded on the beams ("4" in Figure 4.10g) prevented the distress from concentrating at the column face. At the third peak at +0.93% bidirectional drift, distress consisted of 0.01 in. (0.3 mm)-wide flexural cracks at the bottom surfaces of the beams distributed over a distance of 50 in. (1270 mm) from the column face, and cracks at the beam-column interface measuring 0.01 in. (0.3 mm)-wide under the FRP strips and 0.04 in. (1.0 mm)-wide near the inside corner of the column. At the first peak at +1.40% drift, a complete debonding of the FRP strips on the NS beam took place suddenly, initiating at the beam-column interface and moving along the beam. The FRP strips developed a maximum strain of 4570 με at the level of the beam bottom bars. The strips on the EW beam were debonded over a distance of 10 in. (250 mm) from the beam-column interface, and complete debonding did not occur until the first peak at +1.87% drift. A maximum strain of 3920 με was developed in these EW strips. After debonding of the FRP strips, the

beams lost much of their improved behavior in positive bending. A thin layer of concrete attached to the debonded strips indicated the need for better anchorage schemes for these strips so the resulting interfacial and normal stresses can be maintained by the concrete.

3. **Joint shear capacity.** The problem of joint shear failures prior to ductile failure of the beams was resolved. Although very small portions of the FRP system in the joint ("2" and "3" in Figure 4.10g) started to debond near the beam-joint interfaces during the ±1.87% drift cycles, the failure of the joint required a drift of -3.73%, at which point the beams had undergone significant yielding and damage. The failure of the joint involved crushing of the joint core and separation of the FRP system with large pieces of the joint concrete attached to it. This indicated a remarkable performance of the FRP system in maintaining the bond to concrete until the failure of the joint concrete.
4. **Column end confinement.** No significant signs of damage were observed at the column ends throughout the test. The tendency of the upper column to expand just above the joint was prevented by the FRP wrap which developed strains as high as 9730 με and 6880 με at the first stirrup level in the W and S faces, respectively, at the third peak at -3.73% drift. At this point, the W leg of the first stirrup above the joint had just yielded (ε_y=1960 με), and the other legs had developed strains up to 1720 με. The strains measured at the second stirrup level 11.5 in. (290 mm) above the slab indicated that there was no tendency of the column to expand.

The epoxy-injected cracks in the slab did not reopen but new cracks formed next to them and at other locations. At the bottom surface, a diagonal crack with a maximum width of 0.05 in. (1.3 mm) formed between the edge of the triangular FRP-strengthened region and the outer corner, which was accompanied by two other cracks extending from the corners of the triangular region in a direction parallel to the diagonal. At the top sur-

face, flexural cracks formed near both EW and NS beam-slab interfaces across the entire width of the slab (width $\leq$ 0.03 in. [0.8 mm]). Additional flexural cracks formed in both directions away from the beams with widths up to 0.02 in. (0.5 mm).

4.7.2 Hysteretic Behavior

The hysteretic behavior of the specimen before and after rehabilitation are compared in Figure 4.6 through Figure 4.9 and in Table 4.1.

The strong column-weak beam behavior manifested itself in the force-drift hysteresis loops (Figure 4.6) as increases in the negative peak loads that were maintained until the first peak at -3.73% drift, after which deflection the peak loads decreased due to significant damage in the beams. The maximum negative loads were increased by 57% and 70% for the EW and NS beams, respectively, when compared with those obtained for the as-built specimen. For the positive loading direction, up to 40% and 27% increases in the maximum loads were achieved for the EW and NS beams, respectively, until the FRP strips on the side of the beams debonded. Debonding of the strips are marked "7b" and "10b" on the hysteretic plots in Figure 4.6. Percent increases in the peak loads were calculated with respect to the initial loads on the actuators at the deformed position used as reference for cyclic loading, represented by horizontal dashed lines in Figure 4.6.

The increases in peak-to-peak stiffness (K_p) during the bidirectional cycles ranged from 82 to 160% for the EW direction and from 68 to 117% for the NS direction (Figure 4.7). Unlike in the as-built specimen, much of the initial stiffness was maintained through the bidirectional cycles especially until bedonding of the FRP strips on the beams.

The increase in the amount of energy dissipated by the specimen after the onset of yielding in the beams is clearly observed in Figure 4.8. Until the end of the ±1.87% drift cycles, where loading of the as-built specimen was terminated, the rehabilitated specimen dissipated 39% and 37% more energy in the EW and NS directions, respectively. During

the ±3.73% drift cycles, the amount of the dissipated energy was doubled; a majority of this energy was dissipated during the first cycle where a complete ductile failure of the beams was achieved.

The shear stress-strain behavior of the joint was improved significantly toward a desirable "rigid joint" behavior (Figure 4.9). Notable distortion of the joint occurred only after crushing of the joint concrete at the first peak at -3.73% drift. The maximum joint shear stress factors (γ) of $8.3\sqrt{psi}$ ($0.69\sqrt{MPa}$) and $8.0\sqrt{psi}$ ($0.66\sqrt{MPa}$) obtained for the negative loading direction for the EW and NS directions represent increases of 46% and 63% over the values obtained for the as-built specimen. As previously discussed, the actual shear strength of the joint may be underestimated by the "constant moment-arm approximation" used in determining the reinforcing bar tensile forces at the beam-joint interfaces. For example, another estimate of γ can be obtained for the load state where all the EW beam top bars and two slab top bars near this beam have yielded. Assuming that the second layer of beam top reinforcements have also yielded (not instrumented), and not considering any strain hardening, a γ value of approximately $10.8\sqrt{psi}$ ($0.90\sqrt{MPa}$) was obtained. Such a γ value is very close to that recommended by the ACI 352R-02 for use in the design of new corner joints that have members required to dissipate energy through reversals of deformation into the inelastic range (i.e. Type 2 joints: $\gamma = 12\sqrt{psi}$ [$1.00\sqrt{MPa}$]).

4.8 CONCLUSIONS

The following conclusions were drawn from the experimental results presented in this chapter:

1. The behavior of a nonseismically designed reinforced concrete corner beam-column joint was dominated by a combination of column bar yielding, joint shear failure, and loss of anchorage of beam bottom bars.

2. Consideration of bidirectional loading and presence of all floor members revealed damage modes that may be overlooked in two-dimensional tests and analyses (e.g. larger demands on the inside corner of the column and on the beam bottom bars near the inside faces of the beams).
3. Even a severely damaged corner joint was efficiently rehabilitated to meet the strong column-weak beam criterion through easy-to-implement procedures such as the addition of a reinforcing bar within the clear cover of the column and the bonding of a CFRP system that was heat-cured in place.
4. Development of the positive moment capacity of the beam needs improvement. CFRP strips bonded on the outside faces of the beams were effective in anchoring the beam bottom bars, and they developed the yield stress in the exterior bar in the EW beam. But the full ductile capacities of the exterior bars were not developed, and the interior bottom bars were not brought to yield. Improvement in the anchorage of these CFRP strips and/or additional strengthening near the interior beam bottom bars may be needed.
5. Heat-curing of the composite system in place provided an effective means for achieving a full cure of the epoxy matrix quickly and for increasing the glass-transition temperature to values above the maximum operating temperature. While a superior composite-concrete bond was also achieved for the current specimen, additional data are necessary to evaluate the contribution of heat-curing to this performance.

The scope of this chapter was limited to discussion of the global behavior of the specimen. A more detailed investigation of the internal force transfer mechanisms that led to this global behavior will be the subject of a future publication.

4.9 REFERENCES

[4.1] ACI-ASCE Committee 352 (1976). "Recommendations for design of beam-column joints in monolithic reinforced concrete structures (ACI 352R-76)." *ACI Journal Proceedings*, 73(7), 375-393.

[4.2] Beres, A., Pessiki, S. P., White, R. N., and Gergely, P. (1996). "Implications of experiments on the seismic behavior of gravity load designed RC beam-to-column connections." *Earthquake Spectra*, 12(2), 185-198.

[4.3] ACI-ASCE Committee 352 (2002). *Recommendations for design of beam-column connections in monolithic reinforced concrete structures (ACI 352R-02)*, American Concrete Institute, Farmington Hills, MI.

[4.4] Engindeniz, M., Kahn, L. F., and Zureick, A. (2005). "Repair and strengthening of reinforced concrete beam-column joints: State of the art." *ACI Structural Journal*, 102(2), 187-197.

[4.5] ACI Committee 440.2 (2002). *Guide for the design and construction of externally bonded FRP systems for strengthening concrete structures (ACI 440.2R-02)*, American Concrete Institute, Farmington Hills, MI.

[4.6] Ferrier, E. (1999). "Composite-concrete interface behavior under thermo-stimulated creep and fatigue loading. Application to estimated calculation of RC beam durability." Ph.D. thesis, L'Université Claude Bernard Lyon 1, Lyon, France. (In French)

[4.7] ACI Committee 318 (1963). *Building code requirements for reinforced concrete (ACI 318-63)*, American Concrete Institute, Detroit, MI.

[4.8] ACI Committee 318 (2005). *Building code requirements for structural concrete (ACI 318-05) and commentary (318R-05)*, American Concrete Institute, Farmington Hills, MI.

[4.9] Zureick, A., and Kahn, L. (2001). "Rehabilitation of reinforced concrete structures using fiber-reinforced polymer composites." *ASM Handbook*, ASM International, (21), 906-913.

[4.10] The Composite Materials Handbook-MIL 17 (2002). *Guidelines for characterization of structural materials*, V. 1, published jointly by Technomic Publishing Co., Inc, and Materials Sciences Corporation in cooperation with ASTM, Lancaster, PA.

[4.11] AFGC (2003). *Repairing and strengthening of structures in concrete by means of composite materials – Interim recommendations*, French Association of Civil Engineering, Paris, France. (In French)

CHAPTER 5

EFFICACY OF CFRP FOR SEISMIC RETROFIT OF PRE-1970 RC CORNER BEAM-COLUMN JOINTS WITH MODERATE OR SEVERE DAMAGE

5.1 INTRODUCTION

This chapter presents the results of an experimental investigation examining the efficacy of carbon fiber-reinforced polymer (CFRP) composites for retrofitting nonseismically designed reinforced concrete corner beam-column joints with moderate or severe damage. Two full-scale corner beam-column-slab specimens, identically designed using materials and detailing deficiencies typical of pre-1970 construction, were first subjected to reverse-cycle bidirectional loading, then repaired and strengthened using a combination of epoxy injection, addition of a steel reinforcing bar within the clear cover at the column inside corner, and external bonding of multiple layers of CFRP which were heat-cured in-situ. Improvements in seismic behavior were evaluated in terms of failure mechanisms, joint shear stress-strain behavior, and changes in strength, stiffness and energy dissipation characteristics. The results indicated that failure modes that dominated the behavior of the as-built specimens such as column bar yielding, joint shear failure, and loss of anchorage in beam bottom bars and in column bar splice region can be effectively prevented or delayed until after beam hinging. Even a severely damaged corner joint was upgraded to withstand bidirectional normalized joint shear stresses (i.e. $[(\tau_{jh}{}'^{EW})^2+(\tau_{jh}{}'^{NS})^2]^{1/2}$) of up to $1.29\sqrt{MPa}$, interstory drift ratios of up to 2.4% without significant shear deformations and up to 3.7% without joint shear failure.

5.2 BACKGROUND

Deficiencies in beam-column joints in reinforced concrete (RC) buildings constructed with inadequate or no seismic considerations pose a significant threat to the safety of these structures as evidenced by many earthquakes. The fact that special provisions for seismic design were not included in the ACI 318 Building Code until 1971 [5.1] and no specific design guidelines existed for beam-column joints until 1976 [5.2] manifests itself in many catastrophic failures (Figure 5.1). Reinforced concrete structures designed primarily for gravity loads were found to have significant deficiencies including: (1) weak columns (longitudinal reinforcement ratio less than 2%), strong beams, (2) no joint transverse reinforcements, (3) insufficient anchorage length (150 mm) of beam bottom bars, (4) short lap-splices ($20d_b$) of column bars just above floor level, and (5) wide spacing of column ties [5.3].

A comprehensive review of the state-of-the-art on the repair and strengthening of RC beam-column joints [5.4] (Chapter 2) showed that efforts in this area have yet to account for the presence of all floor members and severity of bidirectional loading, and to develop strengthening schemes that can eliminate the limitations (e.g. laborious and massive operations) of conventional techniques (e.g. concrete jacketing). ACI-ASCE Committee 352 found the available information scarce, and recommended further research [5.5].

Externally bonded fiber-reinforced polymeric (FRP) composites have shown great potential for retrofitting reinforced concrete structures. Because of this, various international organizations drafted guidelines to facilitate implementation of this technology in construction. Examples include *fib* Bulletin 14 [5.6], ACI 440.2R-02 [5.7], CAN/CSA-S806 [5.8], AFGC [5.9], and CNR-DT 200 [5.10]. These guidelines do not cover strengthening of beam-column joints. Tests conducted to date on numerous planar beam-column joint specimens (i.e. joints with no floor slab or transverse beams) have indicated the potential for achieving ductile failure mechanisms by strengthening with

Figure 5.1 — Corner beam-column joint failure in the 1999 İzmit, Turkey earthquake.

FRPs. Development of design guidelines for FRP-strengthening of actual frame joints, however, require testing on specimens with realistic 3D frame geometries subjected to severe load histories. Joint types that are likely to be subjected to bidirectional loading need to be investigated [5.5].

The objective of this research was to experimentally investigate the efficacy of carbon fiber-reinforced polymer (CFRP) composites for repair and strengthening of pre-1970 RC corner beam-column joints. The adequacy of such joints when subjected to moderate or severe bidirectional loading in their as-built condition is presented in detail in Chapter 3. The focus of this chapter is on the improvements in the behavior after retrofit, although a summary of the behavior prior to retrofit also is presented for completeness.

5.3 EXPERIMENTAL PROGRAM

Two full-scale corner beam-column-slab specimens were built to represent part of the corner of a building isolated at the inflection points (i.e. midspan of beams and columns) which were assumed to form when the building is subjected to lateral loads. The specimens were designed according to ACI 318-63 [5.11]; the current strong column/weak beam criterion was intentionally violated (target $\Sigma M_c/\Sigma M_b=0.90$); and

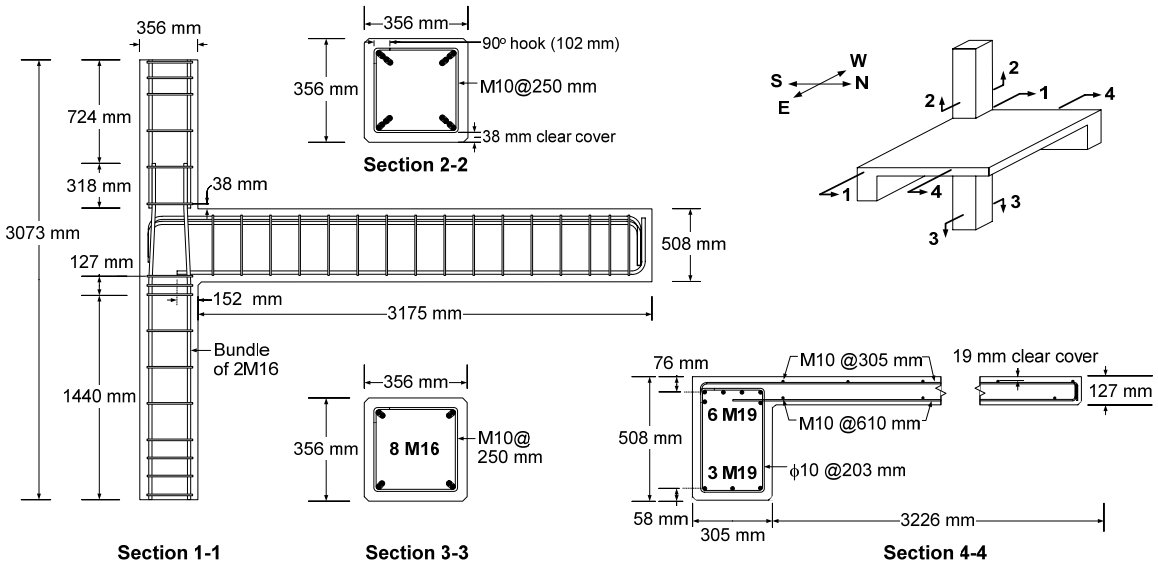

Figure 5.2 — Reinforcement details.

material properties (f_c'=21 MPa, f_y=280 MPa) typical of the pre-1970 construction practice were specified. In addition, the following detailing deficiencies were incorporated: (1) no joint shear reinforcement, (2) short (150 mm) embedment of beam bottom bars into the joint, and (3) a short and unconfined lap-splice of column bars just above floor level. Such a design resulted in the overall dimensions and reinforcement details shown in Figure 5.2. The average compressive strength of concrete (f_c') used for the lower column, beams and slab was 25.8 MPa for Specimen 1 and 34.6 MPa for Specimen 2 on the test days; f_c' for the upper columns of specimens 1 and 2 was 34.1 MPa and 28.6 MPa, respectively. The average yield strengths of the reinforcing bars were 367 MPa, 352 MPa, and 315 MPa for M10 (#3), M16 (#5), and M19 (#6) bars, respectively. Monotonic tension tests on the reinforcing bars indicated a remarkable ductility in these bars (Figure 5.3) and a potential for improved energy dissipation if this ductility could be mobilized in the strengthened specimens.

Tests were conducted in the setup shown in Figure 5.4a, which simulated a fixed support at the bottom of the column and a hinge (rotations in any direction and vertical translation are released, lateral translations are restrained) atop the column. Reverse-cycle

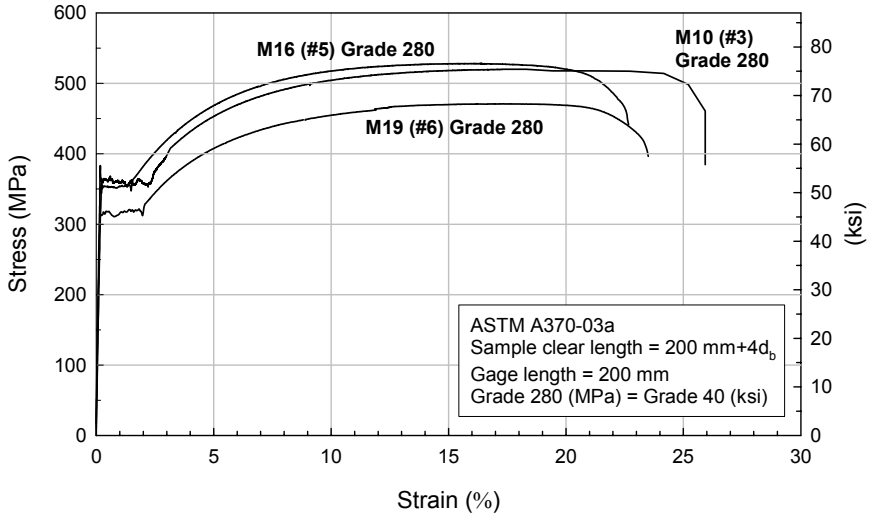

Figure 5.3 — Ductility of the Grade 280 reinforcing bars.

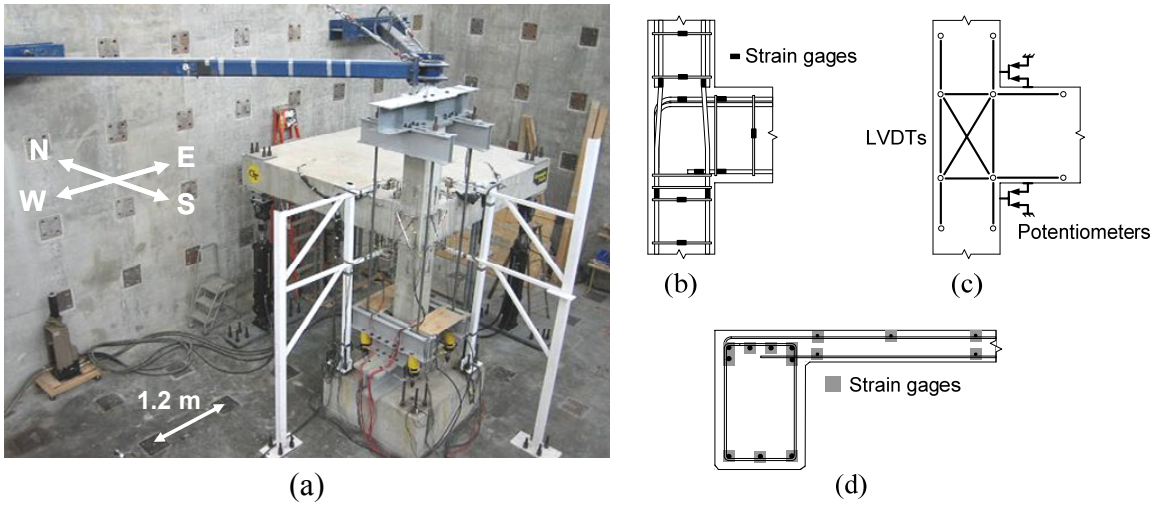

Figure 5.4 — (a) Test setup, and (b,c,d) instrumentation of the as-built specimens, identical in EW and NS directions.

loads were applied with hydraulic actuators mounted vertically at the end of the beams, 3050 mm from the column centerline, in such a way that rotations about all three major axes (i.e. including torsion) were allowed. A separate fixture consisting of four DWYDAG bars and four center-hole jacks was used to apply the axial load on the column.

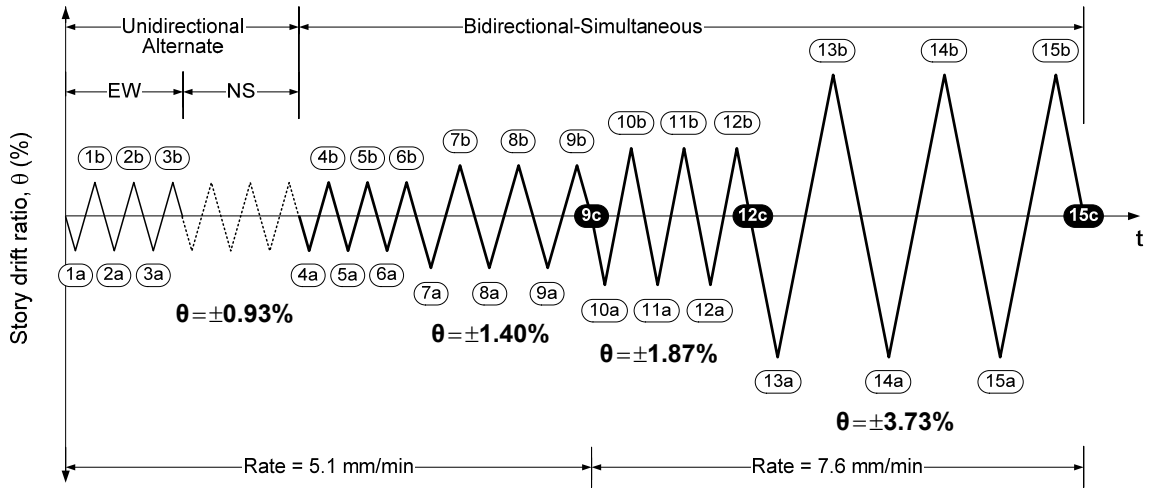

Figure 5.5 — Applied displacement history. Downward beam displacement is considered negative drift. End of test is point 12c for Specimen 1 and point 9c for Specimen 2 in their as-built condition, and point 15c for both specimens after retrofit.

An extensive instrumentation layout consisting of 160 data acquisition channels was used, the details of which are presented in Appendix B for brevity. Part of this layout pertaining to the discussions in this chapter is shown in Figures 5.4b-d.

The effect of service gravity loads likely to be present at the time a building is subjected to lateral loads was accounted for by first applying a column axial load of 10% of the column's compressive load capacity, and then displacing both beams downwards until the strong-axis beam moments at the column faces were brought to a level that was estimated to occur in an actual frame building under service loads. A reverse-cycle displacement history was then applied around this deformed position as shown in Figure 5.5. The unidirectional loading in the EW and NS directions at the beginning of the test were performed to better study the effects of bidirectional loading in the later cycles. The applied displacement levels correspond to 1.0, 1.5, 2.0, and 4.0 times the displacement at first yield (Δ_y) observed in Specimen 1. In the as-built condition, Specimen 1 and Specimen 2 were subjected to maximum interstory drift ratios (θ) of ±1.87% (until point 12c in Figure 5.5) and ±1.40% (until point 9c), respectively, to represent different levels

of damage prior to retrofit. After retrofit, both specimens were subjected to the entire displacement history (i.e. up through θ=3.73%).

5.4 BEHAVIOR OF THE AS-BUILT SPECIMENS

The behavior of both specimens before strengthening was dominated by damage modes and hysteretic characteristics that would clearly be detrimental to the strength and stability of an actual building. A detailed interpretation of results from testing of the as-built specimens is presented in Chapter 3. A summary of the major findings from that study is presented below to allow direct comparisons with the behavior after retrofit later in this chapter.

5.4.1 Damage Mechanisms and Strength Hierarchy

Specimen 1 exhibited significant yielding at the inside (NE) corner of the upper column after peak 4a, some yielding in the lower column after peak 10a, but no yielding in the beams throughout the test with the maximum strains in the beam top bars ranging from $0.43\varepsilon_y$ to $0.92\varepsilon_y$ (ε_y=1620με). During downward loading, column yielding was accompanied by joint shear cracking, large shear rotations, and bulging in the joint. A large portion of the bulging and widening of the joint shear cracks took place during the ±1.87% drift cycles. When the beams were loaded upwards, the loss of anchorage of beam bottom bars was solely responsible for the poor behavior as discussed in detail in Chapter 3. Such bond failure was why the cracking in the joint panels was along one diagonal only, and not in the often observed "X" pattern. At the end of the ±1.87% drift cycles (end of Specimen 1 as-built test), a major crack occurred extending from the beam bottom bar embedment region, diagonally through the joint and vertically into the upper column lap splice region on the S face. The crack was connected to a similar crack on the W face diagonally through the joint, forming a large triangular pyramid-shaped concrete block trying to separate from the outside corner of the column (Figure 5.6a,b), which was

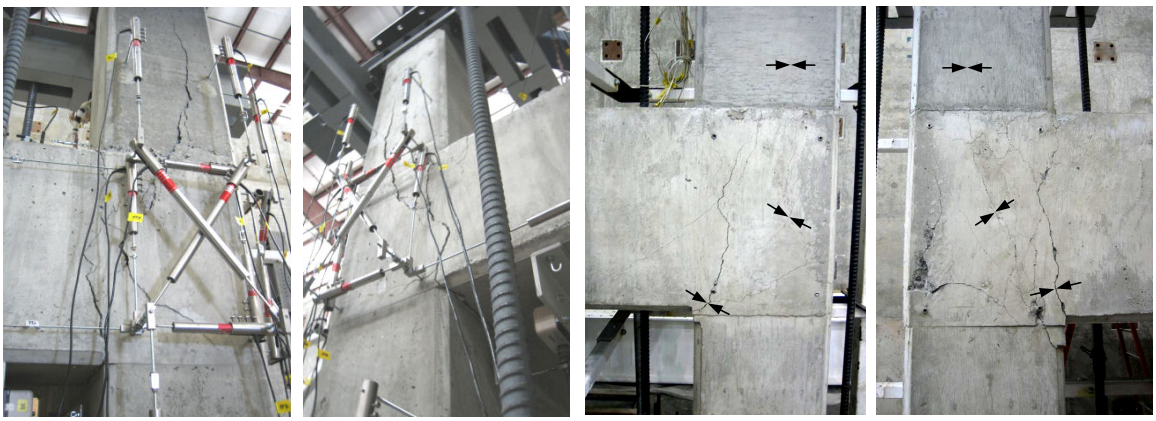

(a) (b) (c) (d)

Figure 5.6 — Damage modes before retrofit: (a, b) Specimen 1, and (c, d) Specimen 2.

considered severe damage.

Specimen 2 exhibited a similarly deficient behavior with slight differences in the damage mechanism indicating a less severe weak column/strong beam behavior than Specimen 1 because significant yielding in the upper column did not begin until peak 7a, and it was soon followed by limited yielding (up to $1.28\,\varepsilon_y$) in two outer beam top bars in both beams. The limited yielding in these beam top bars, which experienced larger demand due to the combined effects of torsion and unsymmetric bending, should not be taken to indicate "beam yielding" because four other top bars in each beam did not reach their yield strain. The joint panels exhibited a distributed cracking consisting of several cracks parallel to the diagonal instead of one major crack. The state of damage after the ±1.40% drift cycles (end of Specimen 2 as-built test) is shown in Figure 5.6c,d, which was considered moderate damage.

5.4.2 Hysteretic Behavior

The aforementioned damage mechanisms resulted in force-drift hysteretic curves characterized by lack of ductility due to severe degradation in stiffness, pinching, and loss of strength especially after the beginning of the bidirectional cycles. The curves

obtained for the NS beam, for example, in both specimens are shown with solid lines in Figure 5.7. The curves are shifted from the horizontal line representing zero load due to the initial compressive (positive) loads on the actuators at the deformed position used as the reference level for cyclic loading. This deformed position is the "zero" drift datum.

The peak-to-peak stiffness (K_p), defined as the slope of the line connecting the negative and positive peaks of a cycle, decreased by 78% from the first to the last (12^{th}) cycle for Specimen 1. For Specimen 2, the decrease in K_p until the last (9^{th}) cycle was 52%. No effective energy dissipation mechanisms were developed because of the progressive increase in pinching and strength degradation.

5.4.3 Joint Shear Strength

The plot of the normalized joint shear stress factor (τ'_{jh}) versus joint shear strain (γ_s), is perhaps the best means to evaluate the adequacy of the joint, where $\tau'_{jh} = V_{jh} \Big/ \sqrt{f'_c}\, b_j h_c$ as defined in ACI-ASCE 352R-02 [5.5], and γ_s was taken as the average of four estimates obtained from the LVDT configuration in Figure 5.4c using plane-strain transformation. Determination of the total horizontal shear force transferred through the joint (V_{jh}), however, is a complex phenomenon due to forces and moments about all three axes at the beam-joint interfaces due to the presence of the slab and bidirectional loading. When V_{jh} was approximated by considering the contribution of the strong-axis beam bending moment (M_z) only and assuming a constant moment arm (*jd*), as commonly done for planar joint specimens in the literature (e.g. $V_{jh} = M_z / jd - V_{col} = M_z / 0.875d - V_{col}$), the hysteretic curves shown with solid lines in Figure 5.8a and Figure 5.8c were obtained for the NS direction for Specimen 1 and Specimen 2, respectively. These curves indicated maximum τ'_{jh} values of 0.47 and 0.54

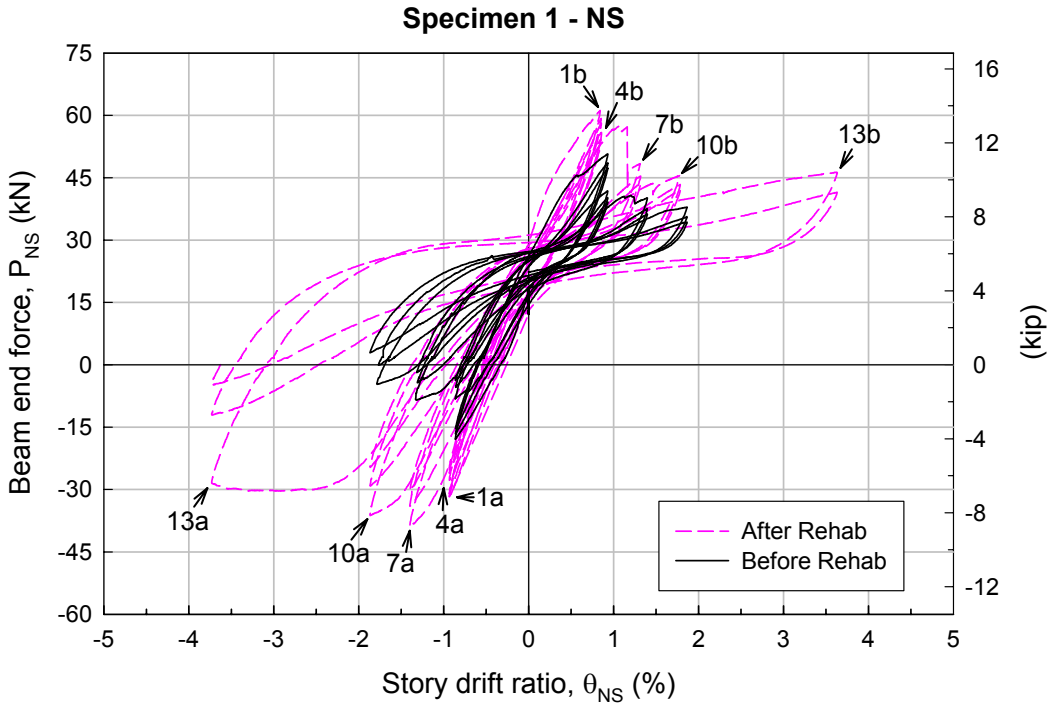

(a)

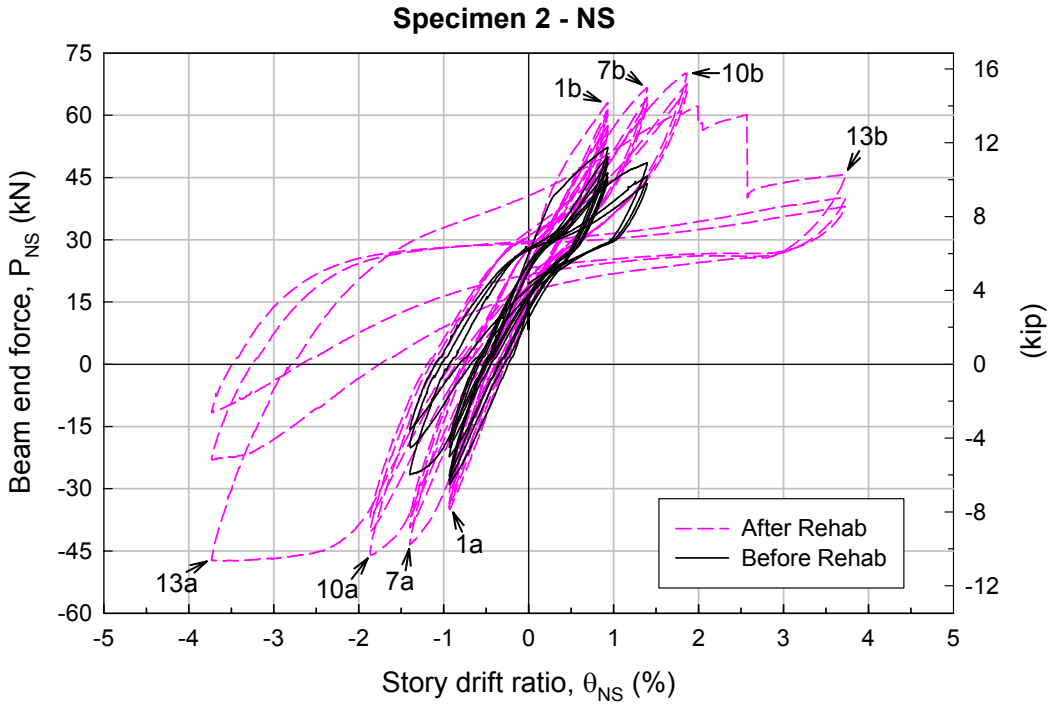

(b)

Figure 5.7 — Force-drift hysteretic response in the NS direction before and after retrofit: (a) Specimen 1, and (b) Specimen 2.

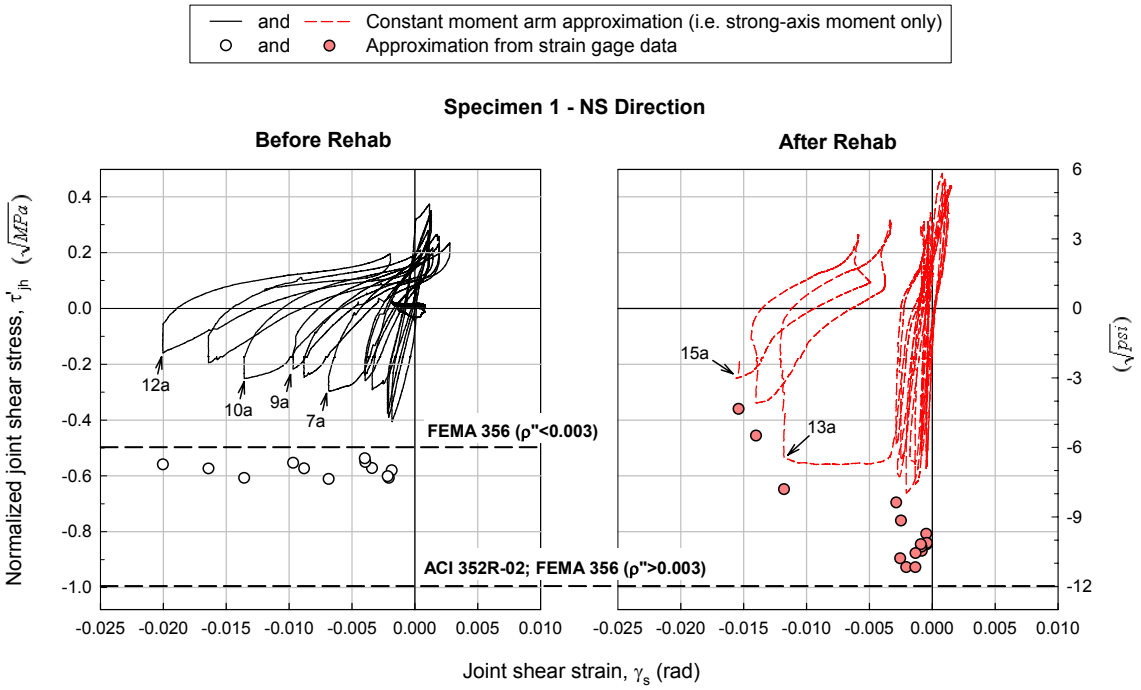

Figure 5.8 — Joint shear stress-strain hysteresis loops obtained for the NS direction before and after retrofit: (a, b) Specimen 1, and (c, d) Specimen 2.

($\sqrt{MPa}$) for downward loading of Specimen 1 and Specimen 2, respectively. These values, however, underestimate the shear carried by the joint since the increase in the tension in the beam longitudinal bars due to forces other than the strong-axis bending moment (e.g. torsion) is not considered. In a second, more accurate approach, forces in each longitudinal bar on the tension side of the beam were determined from strain gage data, and the total normal tensile force (T_b) applied to the joint at the beam-joint interface was taken as their sum (i.e. instead of $T_b = M_z / jd$). Forces in three slab bars within the effective width of the slab were also included in T_b. Strains were converted to forces using the stress-strain curves developed for the M19 (#6) beam bars and the M10 (#3) slab bars for various cyclic loading/unloading cases observed in the strain histories recorded during the tests. The resulting τ'_{jh} values, which are shown with circles in Figure 5.8a,c at the downward loading peaks, are significantly higher than those obtained by the first, approximate method, especially at the bidirectional loading peaks. This is because the beam bars transferred significantly larger forces to the joint than predicted based on the strong-axis beam moments only, and all contributions to these forces were directly accounted for in the strain gage data. The maximum τ'_{jh} values obtained by this method were 0.61 for Specimen 1 and 0.64 for Specimen 2. These values are well below the value of γ=1.00 recommended by ACI-ASCE 352R-02 [5.5] for use in calculating the strength of well-detailed corner joints in seismic regions. This, coupled with the excessive joint shear deformations observed in Figure 5.8a [$(\gamma_s)_{max}$=-0.020 rad] and in Figure 5.8c [$(\gamma_s)_{max}$=-0.008 rad], indicate the need for significant shear strengthening of the joint to achieve an ideal "rigid" joint behavior. The fact that the vector sum of the τ'_{jh} values simultaneously occurring in the EW and NS directions resulted in a maximum value of 0.86 for Specimen 1 and 0.91 for Specimen 2, and that these values are close to

the ACI-ASCE 352R-02-recommended value of γ=1.00, is because of the conservatism of the ACI-ASCE 352R-02 [5.5] in assuming a circular interaction diagram for the case of bidirectional loading (Chapter 3), not because the tested specimens exhibited behaviors comparable to those of well-detailed joints.

5.5 RETROFIT: PROCEDURE AND TEST RESULTS

The specimens were retrofitted while in their deformed position used as reference for reverse-cycle loading. Both specimens were repaired first by injecting a high-strength, high-modulus, low-viscosity epoxy that filled all cracks larger than 0.3 mm. The epoxy injection was followed by strengthening procedures directed at improving: (1) flexural strength of the column, (2) joint shear strength, (3) beam bottom bar anchorage, (4) column confinement, and (5) flexural strength at the SW corner of the slab (performed for Specimen 1 only). All objectives except (1) were pursued using a multi-layer carbon-epoxy system that was tailored from a 300 g/m^2 unidirectional carbon fabric and applied using a hand lay-up technique. The design of this system was based on the manufacturer's reported nominal CFRP properties (i.e. tensile strength P_u^{CFRP}=370 N/mm/layer, ultimate strain ε_u^{CFRP}=1.00%, thickness t=0.5 mm/layer). Tests were conducted on coupons cut from a single-layer witness plate made during the actual application to validate manufacturer's data; these coupon tests resulted in the following average properties: P_u^{CFRP}=510 N/mm/layer, ε_u^{CFRP}=1.52%, t=0.7 mm/layer. First, Specimen 1 was retrofitted and retested. Strengthening of Specimen 2 was designed in light of the findings from the Specimen 1 retest.

5.5.1 Specimen 1

5.5.1.1 Strengthening

All strengthening steps performed for Specimen 1 including the design approach, application, and instrumentation were previously presented in detail in Chapter 4 [5.12].

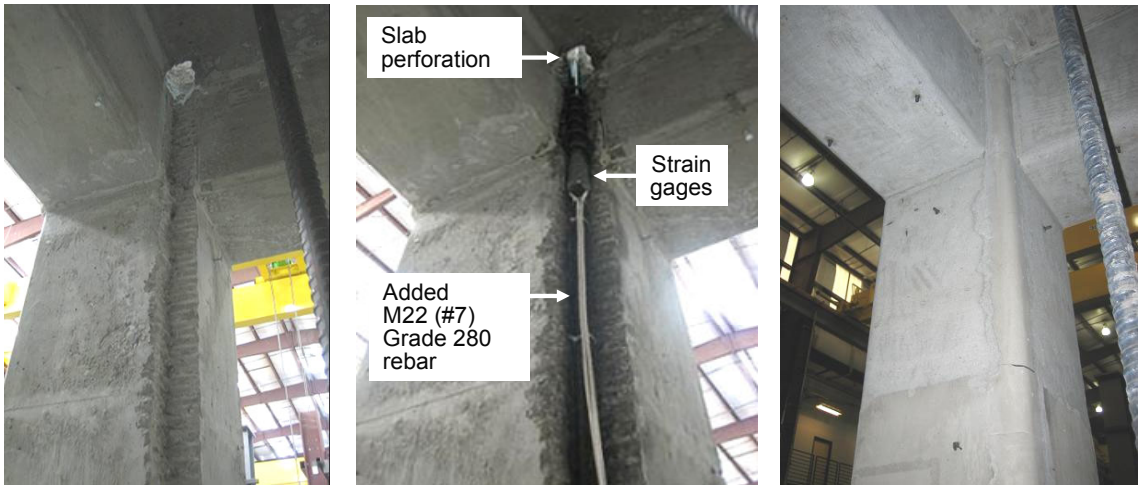

(a) (b) (c)

Figure 5.9 — Flexural strengthening of the column.

The presentation herein is limited to an overview of the entire process:

Flexural strength of the column: To prevent the localized yielding at the inside (NE) corner of the column, a 50 mm x 50 mm portion of this corner (clear cover) was removed along the entire height including a perforation in the slab (Figure 5.9a); a M22 (#7) bar (f_y=445 MPa) was added (Figure 5.9b); and this corner was recast with a polymer-modified cementitious mortar (f_c'=49.6 MPa on test day) (Figure 5.9c). The resulting cover was 20 mm.

Joint shear strength: Three layers of CFRP oriented at 90° (perpendicular to column axis) and two layers at 0° were used to resist the maximum possible horizontal and vertical joint shear forces, respectively, based on flexural yielding of the beam bars. All layers were applied on the S and W faces only and extended onto the columns until the end of the confined regions (460 mm).

Beam bottom bar anchorage: Five layers of 180 mm-wide CFRP strips were placed around the SW corner of the joint and extended onto both beams (Areas 3 and 4 in Figure 5.10). The distance from the tip of the beam bottom bars within the joint to the end of the strips was equivalent to the development length of these bars (i.e. 860 mm).

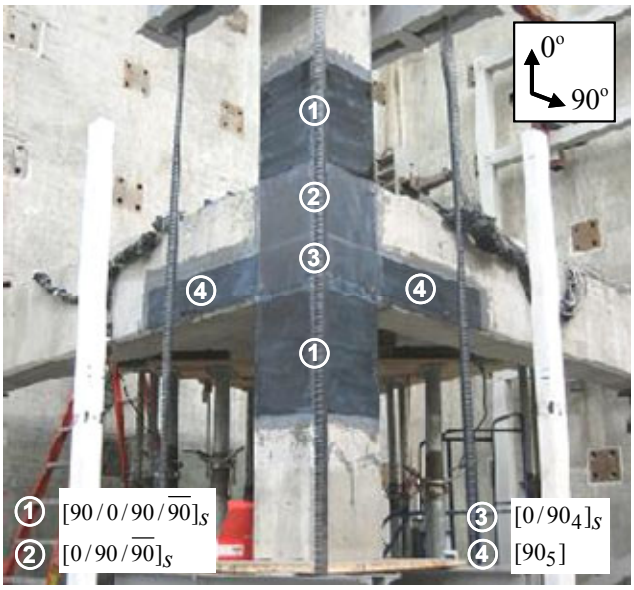

Figure 5.10 — CFRP strengthening scheme applied to Specimen 1.

The load capacity of the strips was equal to that of all three beam bottom bars at yield.

Column confinement: Two 90° CFRP layers were used to wrap the columns over a height of 460 mm below and above the joint (Area 1 in Figure 5.10). The design of the wrap was based on a target effective usable compressive strain in concrete equivalent to what would be provided by the steel hoop reinforcements required by ACI 318-05, Sec. 21.4.4 [5.13] for confining column ends.

SW corner of the slab: Because of the large diagonal crack at the bottom surface of the slab which extended from the SW to the NE corner, two layers of CFRP were placed perpendicular to this crack at the SW corner over a 1220 mm x 1220 mm triangular area to increase the flexural strength to an extent required by ACI 318-05, Sec. 13.3.6 [5.13].

CFRP layers were stacked in a sequence that would result in a symmetric lay-up in all areas as shown in Figure 5.10. All CFRP-applied areas were heat-cured at 80°C for 6 hours following the application to quickly achieve the full-cure of the epoxy. Differential scanning calorimetry (DSC) tests conducted on samples taken from the CFRP system after the completion of the test program indicated that the epoxy had a

glass-transition temperature (T_g) of 65°C. The thermal cure was also expected to improve the bond between the composite system and concrete.

5.5.1.2 Performance after Retrofit

The hierarchy of strength between the beams, column and joint was successfully changed. During downward loading of the beams, major events characterizing the failure occurred in the following order:

1. At peak 4a, yielding in the beam and slab reinforcement including two outer top bars in each beam and a slab top bar next to the NS beam,
2. At peak 7a, yielding in the other beam top bars and in two slab top bars next to each beam,
3. At peak 10a, yielding in the M22 (#7) bar added in the NE corner of the upper column,
4. At peak 13a, crushing of the joint core and separation of the CFRP system with large pieces of joint concrete attached to it. At the time of joint crushing, extensive yielding in two outer top bars in each beam (up to $8.7\varepsilon_y$) occurred and concrete spalled (Figure 5.11b). Moderate yielding in the added M22 column bar (up to $2.2\varepsilon_y$) and spalling of the inside corner of the joint (Figure 5.11c) had occurred.

A similar success was achieved only to a limited extent during upward loading. The CFRP strips bonded on the side of the beams performed well initially in anchoring the beam bottom bars, but debonded suddenly first in the NS direction at peak 7b (ε_{max}=4570 με, Figure 5.11a), then in the EW direction at peak 10b (ε_{max}=3920 με, Figure 5.11b). The full yield capacities of the beam bottom bars could not be developed.

The favorable change to beam yielding before column yielding was also evident from the change in the contributions to the beam displacements from different deformation mechanisms. An analysis of data from the external instruments as explained

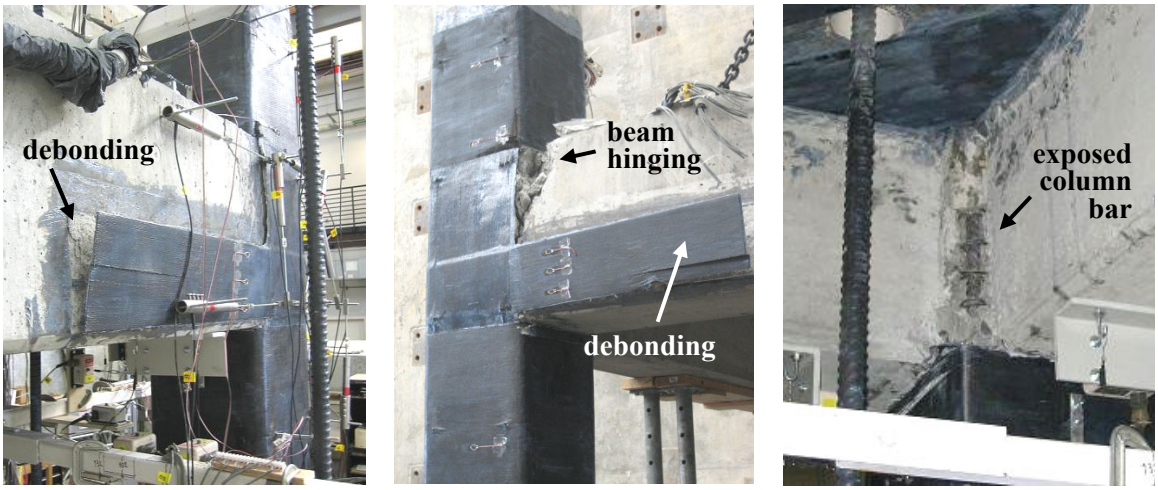

(a) (b) (c)

Figure 5.11 — Damage modes of Specimen 1 after retrofit: (a) W face, (b) S face, and (c) joint inside corner.

in detail in Appendix D indicated that for the downward loading of the EW beam, for example, displacements caused by joint shear rotation constituted up to 66% of the total beam displacement before retrofit (Figure 5.12a), while the corresponding contribution after retrofit remained under 16% (Figure 5.12b). The achievement of beam hinging after retrofit resulted in a considerable increase in the displacements due to beam concentrated rotation which constituted 63% of the total beam displacement toward the end of the test (Figure 5.12b). For the upward loading of the same beam, the contribution due to beam concentrated rotation, which was dominant before retrofit due to loss of beam bottom bar anchorage (Figure 5.12c), was reduced initially, but increased later upon debonding the CFRP strips bonded on the side of the beams (Figure 5.12d). Some negative contributions shown in Figure 5.12 are due to the behavior where some of the cracks created during loading in one direction did not close when the direction of loading was reversed, and they caused permanent rotations.

The hysteretic response was improved significantly, as seen in Figure 5.7a for the NS direction, especially for the case of downward loading. The increase in the peak loads

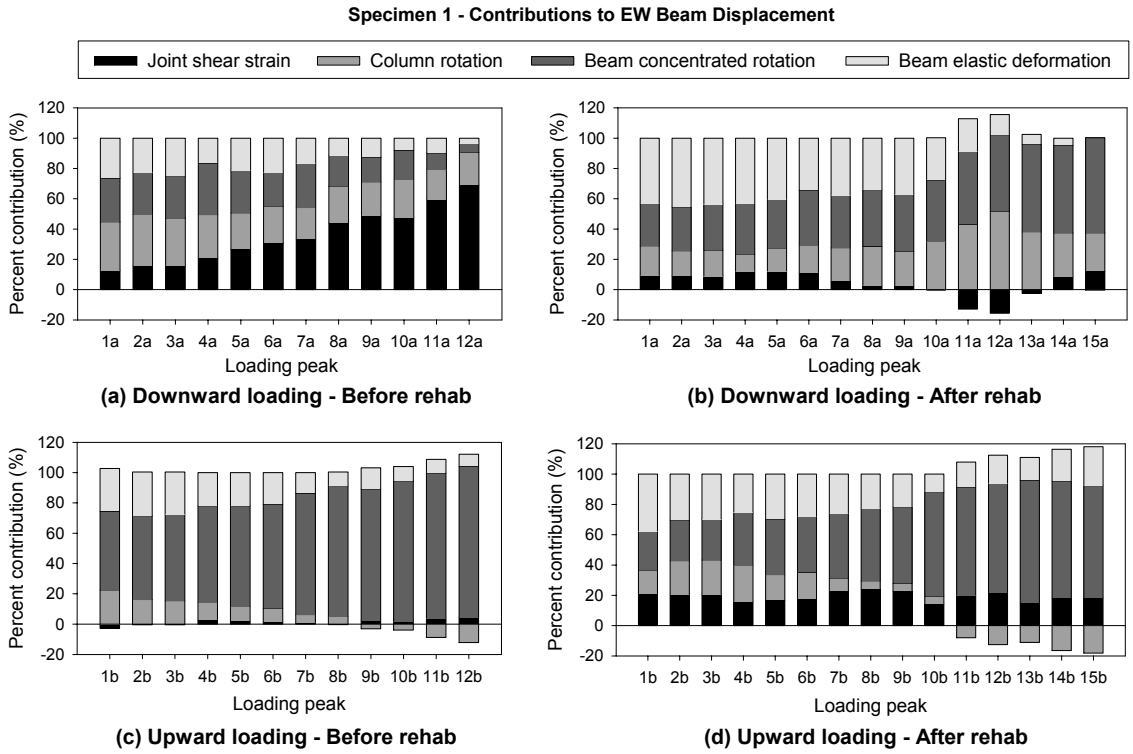

Figure 5.12 — Contributions to Specimen 1, EW beam displacement.

at the applied displacement peaks resulted in an increase in peak-to-peak stiffness during the bidirectional cycles ranging from 68 to 117% (Figure 5.13a). The cummulative energy that had been dissipated by the end of the test was 2.85 times that dissipated by the as-built specimen (Figure 5.13b). A similarly improved response was obtained for the EW direction except that the increase in positive peak loads was maintained for three more cycles due to delayed debonding of the CFRP strips on the EW beam.

The shear stress-strain behavior of the joint after retrofit is presented in Figure 5.8b for the NS direction. The joint was upgraded to sustain normalized joint shear stresses (τ'_{jh}) of up to 0.93 in a primary frame direction and 1.29 (vector sum) in a 45-degree direction from the beam axes under bidirectional loading. These values represent a 52% increase from those obtained before strengthening and indicate that the joint could sustain, simulatenously in both primary frame directions, joint shear stresses that are very

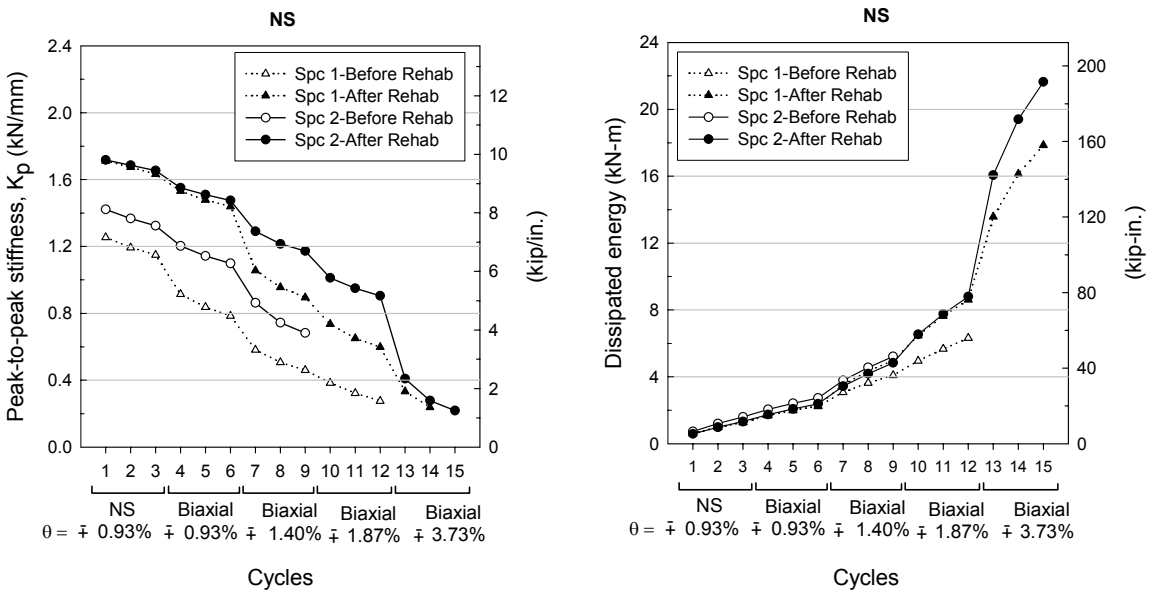

Figure 5.13 — (a) Stiffness degradation, and (b) cumulative energy dissipation in the NS direction.

close to the recommended strength of seismically designed corner joints (γ=1.00$\sqrt{MPa}$) [5.5]. The joint remained "rigid" with the joint shear strains (γ_s) being within ±0.004 rad up to an interstory drift ratio of approximately -2.4% (toward peak 13a). After this point, γ_s increased rapidly; however, even at the peak drift ratio of -3.7% (peak 13a), the bidirectional joint shear strength remained comparable to the maximum obtained for the as-built condition of the joint. Such drift levels are much larger than those envisioned to occur during design earthquakes (i.e. ~2%), and therefore, indicates the efficacy of the applied CFRP scheme. On the other hand, the inability to develop the full positive moment capacity of the beams, and consequently, the shear strength of the joint during upward loading, indicated the need for improvement in this area.

5.5.2 Specimen 2

5.5.2.1 Strengthening

In strengthening Specimen 2, the objectives were to maintain the improvements achieved in Specimen 1 in the case of downward loading and to develop a larger portion of the beams' positive moment capacity in the case of upward loading. The following steps were taken:

1. Strengthening schemes applied to Specimen 1 for improving the column flexural strength, joint shear strength, and column end confinement were identically applied to Specimen 2.
2. To further delay or prevent debonding of the CFRP strips used for improving the anchorage of beam bottom bars, two additional measures were taken:
   a) The extension length of these strips onto the beams was increased from 710 mm to 2080 mm measured from the column faces (Areas 4 and 5 in Figure 5.14). This length was obtained by determining the point along the span corresponding to the cracking moment M_{cr}^{+} under factored loads, and extending the strips past this point by a distance equal to the development length (l_{df}) of the strips according to the proposed revisions to ACI 440.2 [5.7].
   b) Considering the fact that debonding of the strips in Specimen 1 initiated near the beam-column interfaces, two layers of U-wrapping were used at the beam ends to provide a clamping effect for these strips. U-wrapping was provided continuously over a length of 970 mm from the column face, a length over which transverse steel reinforcement is required by ACI 318-05, Sec. 21.4.4.4 [5.13] for confining member ends (Areas 5 and 6 in Figure 5.13). In order to maintain a symmetric CFRP lay-up in all strengthened areas as in Specimen 1, an additional two layers of U-wrapping were applied to the concrete surface prior to application of the axial beam strips.

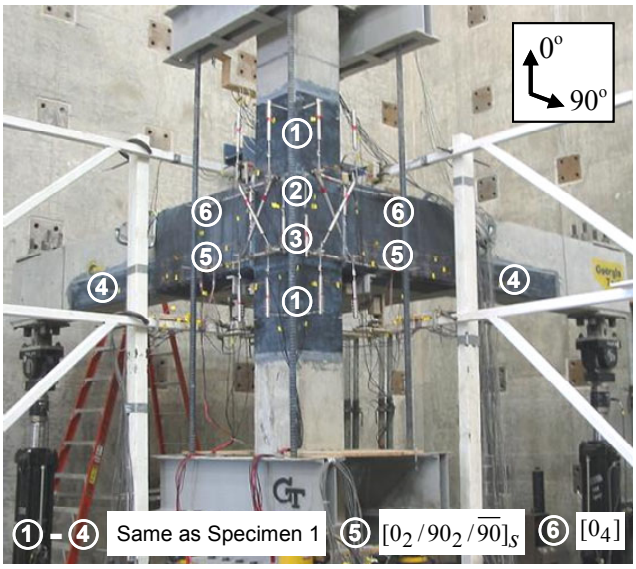

Figure 5.14 — CFRP strengthening scheme applied to Specimen 2.

CFRP strengthening at the SW corner of the slab bottom surface in Specimen 1 was found to not have a significant effect on the behavior, and therefore, was not used in Specimen 2. Curing of the CFRP system was performed with the same schedule used for Specimen 1 (6 hours at 80°C). A finished view of Specimen 2 after retrofit is shown in Figure 5.14.

5.5.2.2 Performance after Retrofit

Specimen 2 surpassed Specimen 1 in achieving an acceptable seismic behavior in that not only the hierarchy of strength was successfully shifted, but also the inelastic demands were met by the beams only. No yielding was observed in the columns. The following order of events characterized the failure:

1. Initiation of yielding in the outer beam top bars (two in EW, three in NS) at peak 1a of unidirectional loading in each direction (up to $1.16\,\varepsilon_y$) and at peak 4a of bidirectional loading (up to $1.25\,\varepsilon_y$),

2. At peak 7a, yielding in five of six beam top bars in each beam with extensive yielding in the outermost EW bar (up to $6.57\varepsilon_y$),
3. At peaks 7b through 9b, debonding of CFRP strips on the EW beam within 280 mm from the column face (Area 5 in Figure 5.14),
4. At peak 10a, yielding in all beam top bars, extensive yielding in two bars in the EW beam (up to $9.93\varepsilon_y$) and in three bars in the NS beam (up to $13.25\varepsilon_y$), partial debonding of CFRP in the joint panels (Area 2) and of the upper portion of U-wraps near the column faces (Area 6),
5. At peaks 10b and 11b, debonding of the strips on the NS beam within 50 mm from the column face (Area 5) and progression of debonding on the EW beam (Areas 5 and 6),
6. At peak 13a, crushing of the upper outside corners of the beams and separation of large blocks of concrete attached to the U-wraps (Figure 5.15a,c), and progression of debonding in the EW joint panel,
7. At approximately 2.6% drift level toward peak 13b, rupture of the CFRP strips at the NS column face accompanied by complete debonding of these strips within the joint panels and within 480 mm from the column faces (Figure 5.15a,b).

The maximum strain developed in the CFRP strips at the beam bottom bar level was 6540 με at the initiation of debonding and 10,000 με (in the NS strip) at rupture. The strain in the added M22 (#7) column bar did not exceed $0.94\varepsilon_y$ (at peak 13a) throughout the test.

The force-drift hysteretic response was superior to not only that of the as-built Specimen 2 (Figure 5.7b) but to that of the retrofitted Specimen 1 (Figure 5.7a) as well. When compared with the latter, the maximum negative and positive loads were 22% and 15% higher, respectively, for the NS direction. The peak-to-peak stiffness of both retrofitted specimens were comparable in the first six cycles, but the delayed

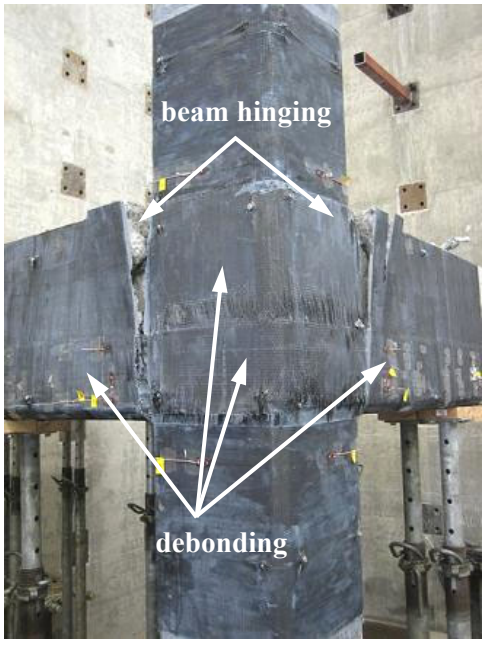

(a)

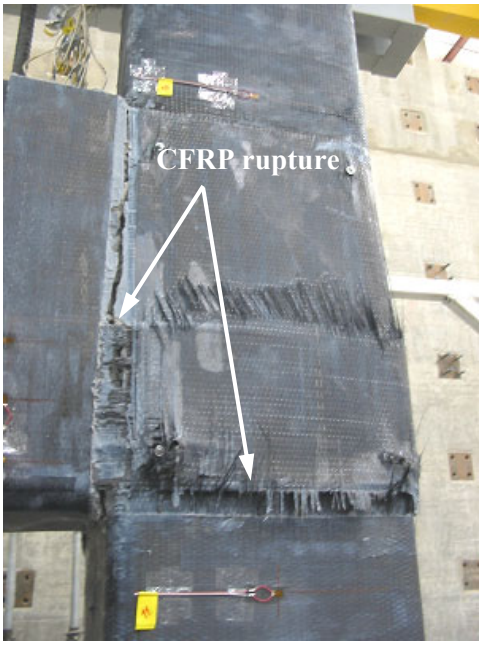

(b)

(c)

(d)

Figure 5.15 — Damage modes of Specimen 2 after retrofit: (a) perspective view of beam hinging and CFRP debonding, (b) CFRP rupture, (c) beam hinge close-up, and (d) cracking under CFRP at the NS beam hinge.

debonding/rupture of the CFRP strips in Specimen 2 provided an additional average increase of 27% in cycles 7 through 9, and 45% in cycles 10 through 12 (Figure 5.13a). The mobilization of the ductile capacities of all beam top bars until the end of their yield plateaus, manifested especially in the 13th cycle in Figure 5.7b, led to an additional 21% increase in the dissipated energy in the NS direction compared to that dissipated by Specimen 1 after retrofit (Figure 5.13b).

The maximum normalized joint shear stresses (τ'_{jh}) developed in the EW and NS directions occurred simultaneously at peak 7a as 0.73 and 0.77, respectively, resulting in a vector sum of 1.06 (Figure 5.8d). The fact that these values were lower than those obtained for Specimen 1 (Figure 5.8b), by no means indicates that strengthening of Specimen 2 was less successful, because: (1) although a more substantial yielding was observed in the beams in Specimen 2 than in Specimen 1, this did not result in a larger joint shear force due to the remarkable length of the yield plateau (from 1620 με to 18,100 με) of the Grade 280 M19 (#6) bars; and (2) when normalized with a higher $\sqrt{f'_c}$ for Specimen 2, the maximum joint shear stress resulted in lower τ'_{jh} values. Therefore, the joint shear strength improvement in Specimen 2 was still significant. In addition, the joint in Specimen 2 exhibited an improvement over that in Specimen 1 in that the CFRP strips on the side of the beams helped mobilize the joint in resisting upward beam loads; positive joint shear strains were developed consistently, reaching 0.01 rad prior to the rupture of these strips.

The variation of contributions from different deformation mechanisms to the applied beam displacements is shown for the NS beam in Figure 5.16 for both before and after retrofit. For the case of downward loading, favorable changes in the deformation characteristics after retrofit previously noted for Specimen 1 such as vanishing of the joint shear strain contribution and the increase in the contribution due to beam

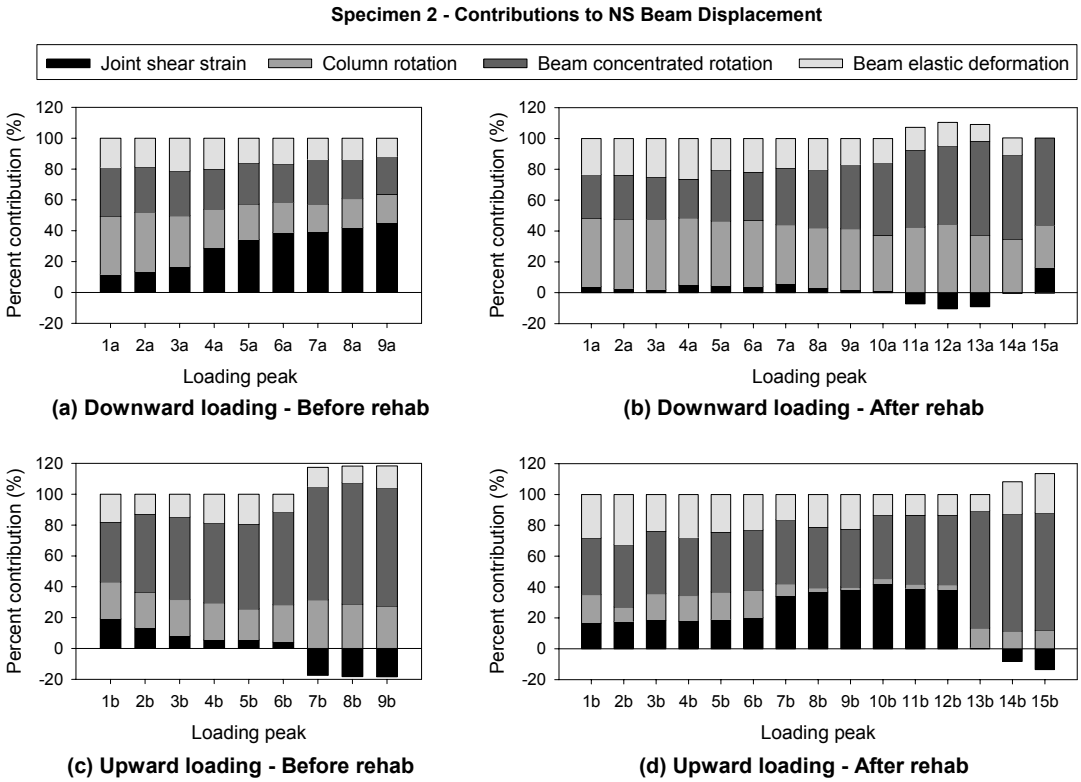

Figure 5.16 — Contributions to Specimen 2, NS beam displacement.

concentrated rotation were also observed for Specimen 2. Two additional changes were also noted. First, during downward loading, the "rigid" behavior of the joint led to an increase in the contributions due to total column rotations (elastic plus concentrated). Although no yielding was observed in the column bars during the test, it would have been preferable if the rigidity of the retrofitted joint led to further increase in the beam rotations than what was observed. Second, for the case of upward loading, the improvement in the anchorage and confinement of the CFRP strips bonded on the side of the beams led to an increase in the force transferred to the joint, and consequently, in the beam displacements caused by joint shear strain more than that observed for Specimen 1. While an increase in joint shear deformations may seem to be seismically undesirable, this is in fact an improvement in the present case considering that no resistance was provided by the joint before retrofit due to pull-out of beam bottom bars.

5.6 CONCLUSIONS

The results from these experiments showed that, in spite of their elastic nature and brittle failure modes, CFRPs can lead to increases in both strength and ductility of pre-1970 RC corner beam-column joints by preventing or delaying failure mechanisms that would otherwise precede formation of beam yielding/hinging mechanisms. Adverse effects of early column yielding, joint shear failure and loss of anchorage in beam bottom bars and in column lap splices observed in the as-built specimens were effectively prevented or delayed in the retrofitted specimens, even though the specimens were subjected to either moderate or severe damages prior to retrofit.

The remarkable ductility inherent in the Grade 280 reinforcing bars typically found in older buildings can be mobilized if they are adequately anchored in the beams. This was the case the beam top bars, especially in Specimen 2, during downward loading. During upward loading, however, CFRP strips can only compensate the loss of strength but not the loss of ductility caused by beam bottom bar pull-out, because these bars cannot develop their full ductile capacity within a 150 mm embedment length regardless of how long the failure of the CFRP strips is delayed. The CFRP strengthening scheme resulted in an acceptable seismic performance and survived interstory drift ratios in excess of those envisioned to occur in design earthquakes. Further improvements in ductility in the case of upward loading should be investigated.

The joints were upgraded to withstand normalized 45-degree bidirectional joint shear stresses of up to $1.29\sqrt{MPa}$ in Specimen 1 and $1.06\sqrt{MPa}$ in Specimen 2. These values indicate that joint shear strength levels comparable to those of well-detailed RC corner beam-column joints according to ACI-ASCE 352R-02 [5.5] ($\gamma = 1.00\sqrt{MPa}$) were achieved.

5.7 REFERENCES

[5.1] ACI Committee 318 (1971). *Building code requirements for reinforced concrete (ACI 318-71)*, American Concrete Institute, Farmington Hills, MI.

[5.2] ACI-ASCE Committee 352 (1976). "Recommendations for design of beam-column joints in monolithic reinforced concrete structures (ACI 352R-76)." *ACI Journal Proceedings*, 73(7), 375-393.

[5.3] Beres, A., Pessiki, S. P., White, R. N., and Gergely, P. (1996). "Implications of experiments on the seismic behavior of gravity load designed RC beam-to-column connections." *Earthquake Spectra*, 12(2), 185-198.

[5.4] Engindeniz, M., Kahn, L. F., and Zureick, A. (2005). "Repair and strengthening of reinforced concrete beam-column joints: State of the art." *ACI Structural Journal*, 102(2), 187-197.

[5.5] ACI-ASCE Committee 352 (2002). *Recommendations for design of beam-column connections in monolithic reinforced concrete structures (ACI 352R-02)*, American Concrete Institute, Farmington Hills, MI.

[5.6] *fib* (2001). *Externally bonded FRP reinforcement for RC structures,* Bulletin 14, International Federation for Structural Concrete, Lausanne, Switzerland.

[5.7] ACI Committee 440.2 (2002). *Guide for the design and construction of externally bonded FRP systems for strengthening concrete structures (ACI 440.2R-02)*, American Concrete Institute, Farmington Hills, MI.

[5.8] CAN/CSA-S806 (2002). *Design and construction of building components with fibre-reinforced polymers*, Canadian Standards Association, Toronto, Ontario, Canada.

[5.9] AFGC (2003). *Repair and strengthening of structures in concrete by means of composite materials – Interim recommendations*, French Association of Civil Engineering, Paris, France. (in French)

[5.10] CNR-DT 200 (2004). *Guide for the design and construction of externally bonded FRP systems for strengthening existing structures*, Italian National Research Council, Rome, Italy.

[5.11] ACI Committee 318 (1963). *Building code requirements for reinforced concrete (ACI 318-63)*, American Concrete Institute, Detroit, MI.

[5.12] Engindeniz, M., Kahn, L. F., and Zureick, A. "Performance of an RC corner beam-column joint severely damaged under bidirectional loading and rehabilitated with FRP composites." *Seismic strengthening of concrete buildings using FRP composites,* American Concrete Institute, Farmington Hills, MI, Accepted April 2007, *In press*.

[5.13] ACI Committee 318 (2005). *Building code requirements for structural concrete (ACI 318-05) and commentary (318R-05)*, American Concrete Institute, Farmington Hills, MI.

[5.14] FEMA (2000). *Prestandard and commentary for the seismic rehabilitation of buildings (FEMA 356)*, Federal Emergency Management Agency, Washington, D.C.

CHAPTER 6

CFRP-RETROFIT OF UNDAMAGED PRE-1970 RC CORNER BEAM-COLUMN JOINTS WITH MODERATE OR LOW CONCRETE STRENGTH

6.1 INTRODUCTION

This research experimentally investigated the efficacy of carbon fiber-reinforced polymer (CFRP) composites for seismic strengthening of pre-1970 reinforced concrete corner beam-column joints with moderate- and low-strength concrete ($f_c^{'}$=33.9 MPa and 15.4 MPa). Two full-scale corner beam-column-slab specimens were designed with strength hierarchy and reinforcement details that represented pre-1970 construction and were in contrast to the current capacity design philosophy. Each was first retrofitted with the addition of a steel reinforcing bar within the clear cover at the column inside corner and was then strengthened with multiple layers of CFRP. The specimens were subjected to a reverse-cycle bidirectional displacement history up to an interstory drift ratio of ±3.73%. The effectiveness of pre- versus post-damage retrofit was examined by comparing the performance to that of a previously reported moderately-damaged-then-retrofitted specimen. The results indicated that a seismically acceptable strength hierarchy and a bidirectional joint shear strength larger than that of code-conforming corner joints can be achieved with CFRP retrofit. While pre-damage retrofit did not provide significant additional improvements in the overall hysteretic behavior and in the joint shear capacity compared to post-damage retrofit, strengthening prior to damage helped the joint to maintain much of its improved shear capacity through larger drift cycles (up to 3.73%). A joint constructed with low-strength concrete was also effectively strengthened; however, the reduced overall structural stiffness caused by the lower modulus concrete may

possibly lead to structural collapse before the improved joint strength could be fully mobilized.

6.2 BACKGROUND

Earthquakes around the world are constant reminders of the inadequacy of pre-1970 reinforced concrete (RC) buildings which lack the seismic resistance obtained by the current capacity design philosophy and the reinforcement details that provide ductility. Beams that frame into weaker columns through unreinforced beam-column joints cannot develop yielding/hinging mechanisms, and structural failures may be initiated due to column hinging, joint shear failures, or a combination of both. Inadequate anchorage of reinforcements at critical locations (e.g. beam bottom bars with 6 in. straight anchorage into the joint and column bars with only $20d_b$ lap-splice length at the floor level) prevent the members from developing their full flexural capacities under lateral loading. Such deficiencies cause beam-column joint failures as illustrated in Figure 6.1a and call for effective techniques for both pre- and post-earthquake retrofit of such joints.

Fiber-reinforced polymer (FRP) composites have exhibited great potential for seismic strengthening of beam-column joints in studies conducted since the late 1990's where significant data were obtained for FRP-retrofitted planar joint specimens (i.e. joints with no transverse beams or floor slab) subjected to unidirectional loads [6.1-6.7]. Promising results from such two-dimensional tests have recently led to more realistic testing of FRP-strengthened beam-column joints even as part of complete, full-scale framed structures [6.8-6.10]. Balsamo et al. [6.8] used multi-directional carbon FRP (CFRP) composites to restore the original properties of a unidirectionally loaded, damaged, two-bay, four-story, code-conforming RC structure by increasing the deformation capacity of the columns and the shear capacity of the joints and walls. Much

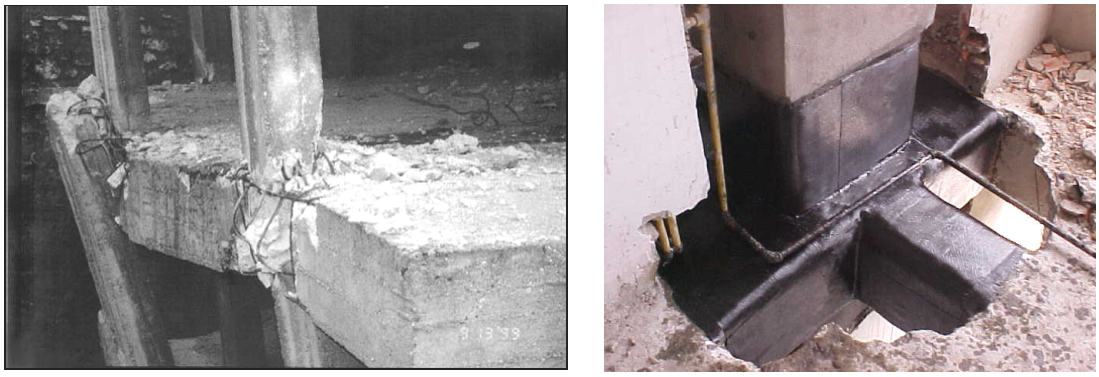

(a) (b)

Figure 6.1 — (a) Beam-column joint damage in 1999 İzmit, Turkey earthquake [6.1], and (b) a CFRP retrofit implemented in construction with massive operations [Jorge Rendón, personal communication, 2007].

of the intended improvements could not be achieved due to failure at the foundation. Pampanin et al. [6.9] retrofitted an initially damaged, planar, three-bay, three-story, RC frame representative of pre-1970 Italian construction using unidirectional CFRP composites. A "partial retrofit" was employed where exterior joint regions were strengthened for both joint shear and column flexure while interior regions were strengthened for column flexure only. Such a retrofit scheme helped delay the strength degradation until 2.0% drift (compared to 1.6% before strengthening), but pinching and lack of energy dissipation persisted. Di Ludovico et al. [6.10] conducted bidirectional pseudo-dynamic tests on a 3D, three-story, torsionally unbalanced RC structure representative of early-1970s Greek construction before and after a "light intervention" using multi-directional glass FRP (GFRP) composites. The retrofit was limited to confinement of all column ends, shear strengthening of only corner joints, and shear strengthening of a wall-type column. The maximum displacement and the energy dissipation of the structure were doubled, and the target peak ground acceleration of 0.3g was survived without significant damage.

While the aforementioned studies have begun addressing the effects of actual 3D frame geometry and bidirectional loading on FRP-strengthening of beam-column joints,

the effects of damage prior to retrofit have yet to be addressed. Additional testing is also necessary to facilitate the development of design guidelines for FRP-strengthening of beam-column joints which are not covered comprehensively in the currently available guidelines [6.11-6.15].

The objective of this research was to experimentally investigate the efficacy of CFRP composites for both pre- and post-earthquake retrofit of pre-1970 RC corner beam-column joints without significant removal of existing concrete such as that shown in Figure 6.1b. The improvements in the behavior of severely or moderately damaged corner beam-column joints after CFRP retrofit (Specimen 1 and Specimen 2) were presented in detail in Chapter 5. This chapter focuses on whether further improvements could be achieved if CFRP retrofit were performed prior to any damage (Specimen 3) and on the extent of improvements that could be achieved if the joint were undamaged but the concrete strength were significantly lower (Specimen 4).

Although the performance of moderately-damaged-then-retrofitted Specimen 2 is not repeated here in detail, comparisons between Specimen 3 and Specimen 2 allow determination of the effects of damage prior to retrofit since both were cast from the same concrete batch and were retrofitted using identical schemes. Having been retrofitted in their undamaged state but representing different levels of concrete strength, Specimen 4 and Specimen 3 allow determination of the effects of low concrete strength.

6.3 EXPERIMENTAL PROGRAM

Corner joints in a typical pre-1970 RC frame building were simulated by building two full-scale beam-column-slab specimens designed according to ACI 318-63 [6.16] with typical pre-1970 reinforcement detailing deficiencies. The beams and columns were terminated at the points of contraflexure that form during lateral loading of a building. The current capacity design approach was intentionally violated by targeting a column-to-beam moment strength ratio of 0.9. No joint shear reinforcements were used (Figure

6.2a). Beam bottom bars were anchored by only 150 mm ($8d_b$) embedment into the joint, and column bars lap-spliced just above the joint had an anchorage length of only 318 mm ($20d_b$). The only difference between the specimens (3 and 4) was in the concrete properties. Specimen 3 represented a joint with moderate-strength concrete (f_c'=33.9 MPa) while Specimen 4 represented a lower concrete strength (f_c'=15.4 MPa); the concrete properties attained on the day of testing are shown in Figure 6.2b. The reinforcing bars had yield strengths ranging from 317 to 367 MPa and were characterized by the remarkable length of their yield plateaus (Figure 6.2b).

Tests were conducted in a setup shown in Figure 6.2c where the base of the column had a fixed support, and the top of the column had a pin support with free vertical translation. Prior to retrofit, service gravity load effects were simulated by applying a compressive column axial load equal to 10% of the column's capacity, and by displacing both beams downwards until the strong-axis bending moment at the column face was similar to that estimated for an actual building under service loads. After retrofit, cyclic lateral loads were simulated by quasistatic reverse-cycle loading of the beams in the vertical direction at the end of each beam, 3000 mm from the column centerline. The actuator-to-beam connections allowed free rotation around all three major axes (i.e. including torsion). The applied displacement history consisted of alternate unidirectional loading of up to 0.93% interstory drift in the primary frame directions followed by simultaneous loading in both directions up to 3.73% drift simulating lateral loading of a building at 45 degrees from the primary axes (Figure 6.2d).

A total of 160 internal plus external instruments were used to monitor strain distributions in the beam, column, and slab-to-beam interfaces, strains in stirrups near the joint, joint shear strains, global movement of the joint in space, relative movement of the beams and columns with respect to the joint, beam twist, column axial load, and beam and column shear forces. All details of the experimental program that are not covered

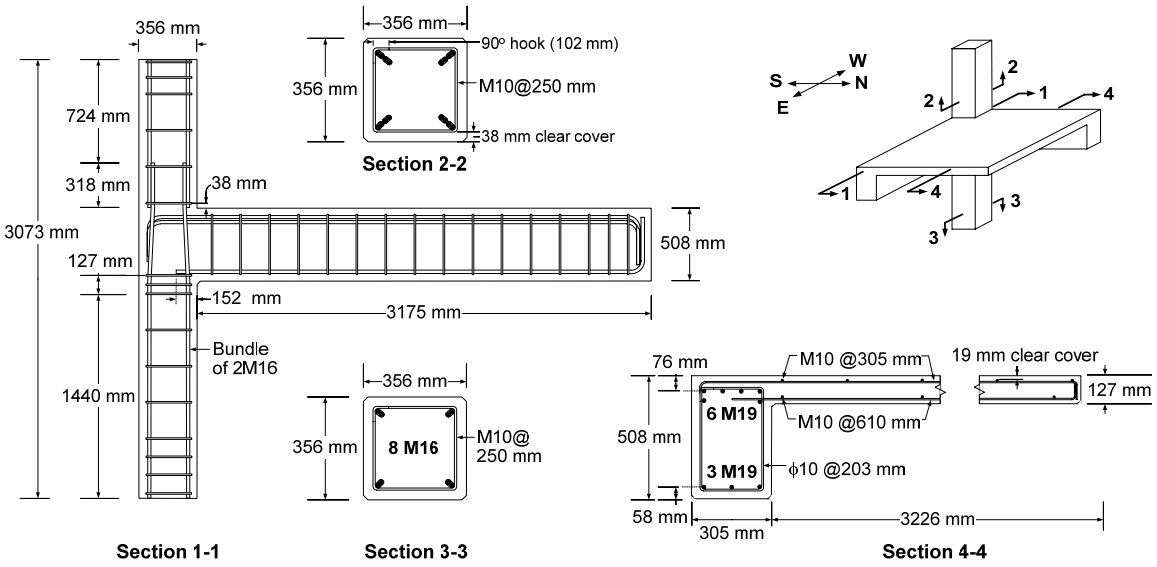

(a)

Concrete

	Specimen 3		Specimen 4	
	Lift 1	Lift 2	Lift 1	Lift 2
$f_c^{'}(MPa)$	33.9	27.9	15.4	26.1
$E_c(GPa)$	23.4	22.3	20.0	22.3

Reinforcing bars

	M10 (#3)	M16 (#5)	M19 (#6)
$f_y(MPa)$	367	352	315
Yield plateau (με)	1740-24,720	1890-13,250	1620-18,070

(b)

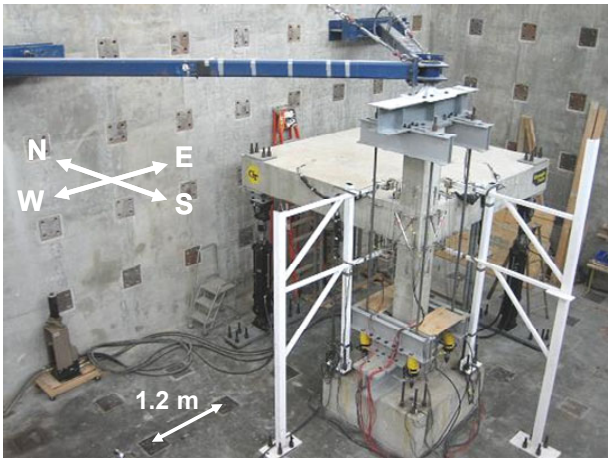

(c)

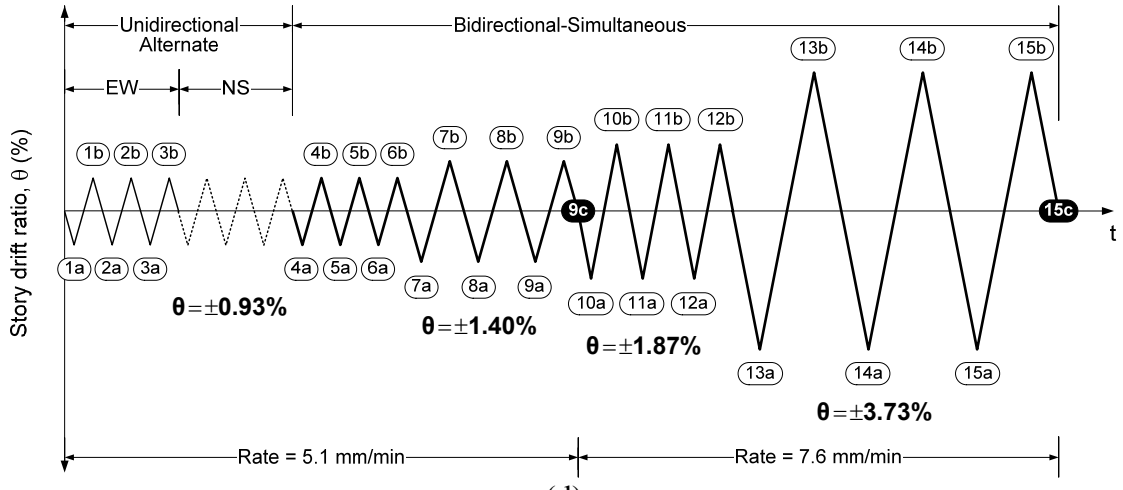

(d)

Figure 6.2 — (a) Reinforcement details, (b) test setup and primary frame directions, (c) concrete and reinforcing bar properties, and (d) applied displacement history.

herein for brevity are presented in Appendix B.

6.4 RETROFIT PROCEDURE

The retrofit was performed in two steps: (1) addition of a steel reinforcing bar within the column clear cover at the inside (NE) corner along the entire column height to delay/prevent localized column yielding at this corner that was observed in previous tests on specimens without strengthening (Chapter 3), and (2) external bonding of a multi-layer CFRP composite system aimed at improving the joint shear strength, positive moment capacity of the beam (i.e. beam bottom bar anchorage), and confinement of the column and beam ends. Step 1 was performed by removing a 50 mm x 50 mm portion of the column inside corner including a perforation in the slab, adding a M22 (#7) Grade 420 (f_y=445 MPa) reinforcing bar, and by recasting this corner with a polymer-modified cementitious mortar ($f_c^{'}$=49.6 MPa). In Step 2, the CFRP system was tailored from a relatively light (300 g/m^2) unidirectional carbon fabric for ease of application around the joint corner. The CFRP design was based on the following "design values" reported by the manufacturer: tensile strength P_u^{CFRP}=370 N/mm/layer, ultimate strain ε_u^{CFRP}=1.00%, and thickness t=0.5 mm/layer. The CFRP system used for Specimen 3 consisted of the following layup as illustrated in Figure 6.3:

- Three layers of CFRP oriented at 90° (perpendicular to column axis) and two layers at 0° were used on the S and W faces of the joint (areas 3, 4, 5 in Figure 6.3) to resist the maximum joint shear that was estimated to occur at flexural yielding of all beam top bars; these sheets were extended onto the columns until the end of the confined regions (area 1).
- Five layers of 180 mm-wide CFRP strips were placed around the SW corner of the joint and extended onto both beams 2080 mm measured from the column face (areas 3, 5, 4 in Figure 6.3). The total load capacity of the five strips was made equal to that

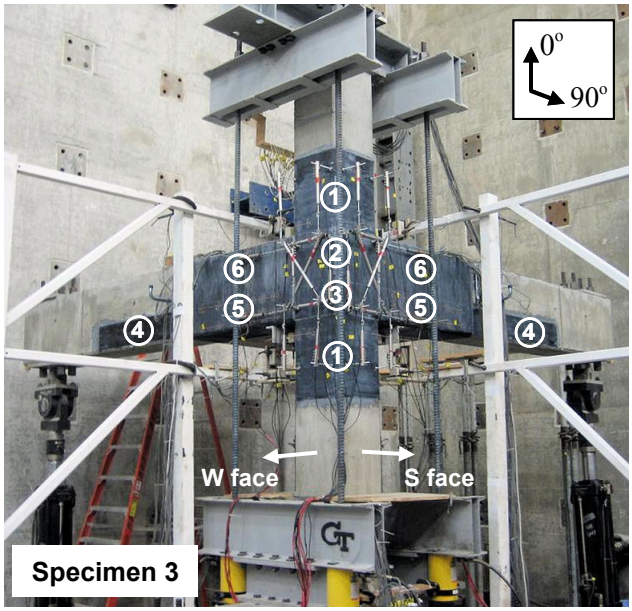

Figure 6.3 — CFRP strengthening scheme applied to Specimen 3.

of all three beam bottom bars at yield. The extension length of 2080 mm was obtained by determining the point along the span corresponding to the cracking moment under factored loads and extending the strips past this point by a distance equal to the development length of the strips according to the proposed revisions to ACI 440.2 [6.17]. To delay/prevent debonding of the five strips near the beam-joint interfaces, the beams were U-wrapped over the strips with two layers of CFRP over a length of 970 mm from the column face, a length over which transverse steel reinforcement is required by ACI 318-05, Sec. 21.4.4.4 [6.18] for confining member ends (areas 5 and 6 in Figure 6.3).

- Two 90° layers of CFRP were used to wrap the column ends over a height of 460 mm above and below the joint (area 1 in Figure 6.3). The wraps were designed to provide an effective usable strain in concrete that would be achieved had the columns been confined by steel hoop reinforcements required by ACI 318-05, Sec. 21.4.4 [6.18]. These wraps also served as additional anchorage for both the column reinforcing bar

added at the inside corner and for the CFRP sheets extended from the joint panels onto the columns.

The details of all design calculations are presented in Appendix E. All CFRP layers were applied in one session in a stacking sequence that would result in a symmetric layup in all areas as shown in Figure 6.3. All CFRP-applied areas were heat-cured at 80±10°C for 6 hours following the application to quickly achieve the full-cure of the epoxy resin and to increase its glass-transition temperature; this curing schedule was selected based on the differential scanning calorimetry tests conducted on the resin prior to the application as presented in detail in Appendix B. To confirm that the aforementioned "design properties" of CFRP could be attained in actual application, a single-layer witness plate was made during the application and subjected to the same heat-curing schedule. Ten coupons were cut from this plate and tested, resulting in average values of P_u^{CFRP}=510 N/mm/layer, ε_u^{CFRP}=1.52%, and t=0.7 mm/layer as presented in Appendix B.

The CFRP scheme presented in this section was for Specimen 3. Reconsideration of this scheme for the specimen with low concrete strength (Specimen 4) is presented later in this chapter.

6.5 ROLE OF NO INITIAL DAMAGE ON THE EFFICACY OF RETROFIT: SPECIMEN 3 VERSUS SPECIMEN 2

As mentioned previously, Specimens 3 was cast from the same concrete batch and received the same retrofit scheme as Specimen 2, and the only difference between the two specimens was that Specimen 3 was retrofitted in its undamaged state.

The repair of Specimen 2 by epoxy injection followed by retrofit using the procedure described in Section 6.4 provided major improvements in its performance when compared to that obtained for its as-built condition. Such improvements were presented in detail in Chapter 5 and included the following:

- The failure mechanisms before retrofit were column bar yielding, joint shear cracking, and anchorage loss of beam bottom bars and column lap-splices; these mechanisms prevented the development of beam hinges. Retrofit shifted failure to a strong column/weak beam mechanism where all beam top bars were able to develop their ductile capacities, column bars did not yield, and the joint exhibited a "rigid" behavior up to a 2.4% drift.
- The maximum bidirectional normalized joint shear stress $\tau_{jh}^{'b}$ (i.e. $[\tau_{jh}^{'EW} + \tau_{jh}^{'NS}]^{1/2}$) developed by the joint was increased from $0.91\sqrt{MPa}$ before retrofit to $1.06\sqrt{MPa}$ after retrofit which is larger than the value of γ=1.00 recommended by ACI-ASCE 352R-02 [6.19] for use in calculating the strength of well-detailed corner joints in seismic regions.
- The increase in the peak loads at the applied displacement peaks resulted in an increase in peak-to-peak stiffness ranging from 21% to 25% during the unidirectional cycles and from 29% to 72% during the bidirectional cycles (Figure 6.4a).
- The specimen exhibited effective energy dissipation after retrofit as shown in Figure 6.4b due to the mobilization of the entire yield plateaus of all beam top bars.
- A good CFRP-to-concrete bond was achieved; the CFRP beam strips placed around the joint, for example, developed strains as high as 6540 με at the initiation of debonding and developed their full capacity (i.e. rupture) at ultimate as shown in Figure 6.5a,b.

The same retrofit scheme when applied to the undamaged Specimen 3 was slightly more effective in improving certain performance parameters, but not to an extent that emphasized the benefit of pre-damage retrofit over post-damage retrofit as presented below.

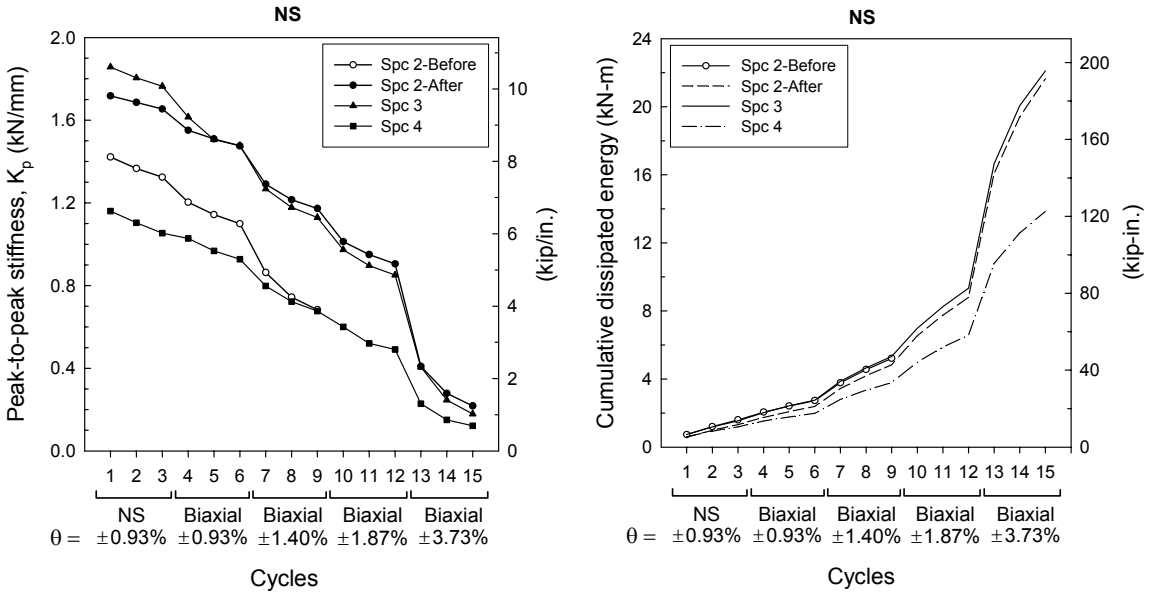

Figure 6.4 — Variation of (a) peak-to-peak stiffness, and (b) cumulative dissipated energy in the NS direction.

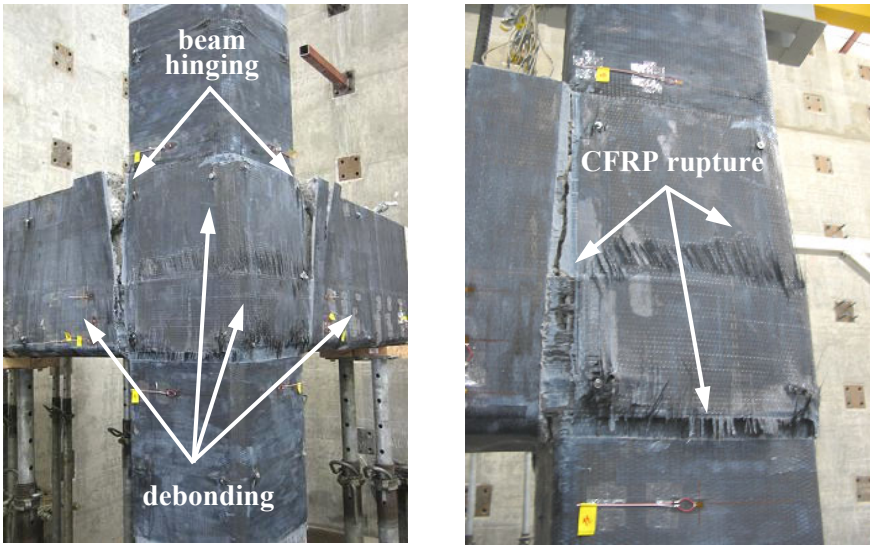

Figure 6.5 — Damage in Specimen 2 after retrofit: (a) perspective view of beam hinging and CFRP debonding/rupture, (b) CFRP rupture close-up.

6.5.1 Damage Mechanisms and Strength Hierarchy

The following order of events characterized the failure of Specimen 3:

1. At peak 1a of unidirectional loading in each direction, initiation of beam bar yielding with strains in five of six beam top bars ranging from 0.96 to 1.2 ε_y in the EW beam and from 0.95 to 1.1 ε_y in the NS beam, and yielding in the first NS slab top bar up to 1.36 ε_y (the gages on the first slab top and bottom bars were not available).
2. At peak 5a, shear cracking in the upper column inside (NE) corner above the CFRP-wrapped portion.
3. At peak 7a (-1.40% drift), yielding in all NS beam top bars (up to 1.43 ε_y), in five EW beam top bars (up to 1.76 ε_y), and in two NS slab top bars (up to 1.26 ε_y), initiation of yielding in the upper column NE corner both in the lap-spliced bars (1.65 ε_y) and in the added M22 (#7) bar (1.02 ε_y), and separation of the M22 column bar from the un-wrapped portion of the upper column.
4. At peaks 7b through 9b, partial debonding of EW beam CFRP strips (area 5 in Figure 6.3) within 400 mm from the column face and debonding of the NS beam strips within 100 mm from the column face.
5. At peak 10a (-1.87% drift), yielding in all top bars in both beams with extensive yielding in the outer bars (up to 11.3 ε_y in EW beam, 5.7 ε_y in NS), loss of anchorage of the added M22 column corner bar (ε_{max}=1.12 ε_y) and debonding of the upper column wrap at the NE corner (area 1), and debonding of the beam U-wraps near the column faces (area 6).
6. At peak 10b, debonding of the EW beam strips within the joint (area 3) and of the NS beam strips within 300 mm from the column face (area 5).

7. Toward peak 13a, strain hardening in three EW beam top bars (up to $14.4\varepsilon_y$) and in two NS beam top bars (up to $14.0\varepsilon_y$), yielding in the second EW slab top bar ($1.16\varepsilon_y$), and progression of yielding in the lap-spliced column bars at the NE corner; at approximately -2.5% drift, rapid increase in joint shear deformations and loss of anchorage in the outer beam top bars and in the column lap-splice; at peak 13a, up to 7 mm-wide flexural and torsional cracks on the beam top surfaces (Figure 6.6c,d), debonding of beam U-wraps within 250 mm from the column faces (Figure 6.6a), and yielding of reinforcement in the lower column (1.05 to $1.47\varepsilon_y$).
8. Between +2.3 to 3.4% drift toward peak 13b, transverse splitting/rupture of the EW beam CFRP strips at the column face (area 5), debonding of all CFRP sheets in both joint panels (areas 2 and 3), rupture of the strips at the SW corner, and debonding of the NS strips within 600 mm from the column face (area 5) (Figure 6.6a,b).

The average maximum strains across the width of the CFRP beam strips at the beam-column interfaces were 5880 με and 5230 με for the EW and NS beams, respectively, with the strains at the beam bottom bar level being 6480 με and 5820 με. The average strain in the strips near the end of the beam U-wraps did not exceed 1370 με throughout the test. The maximum strain in the fiber-direction of the beam U-wraps was 1460 με. The upper column wrap provided confinement by developing an average strain of 3590 με on both outside faces, while such a confinement demand on the lower column wrap was limited (ε_{max}=490 με).

The differences between the aforementioned failure mechanism and that previously observed for the case of post-damage retrofit (i.e. Specimen 2) were limited to the following:

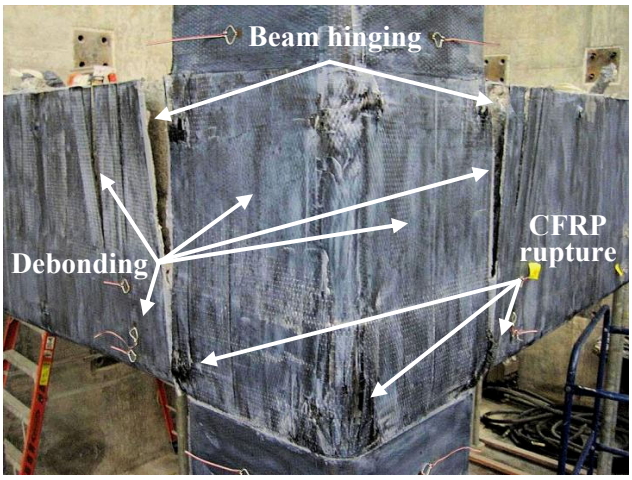

(a)

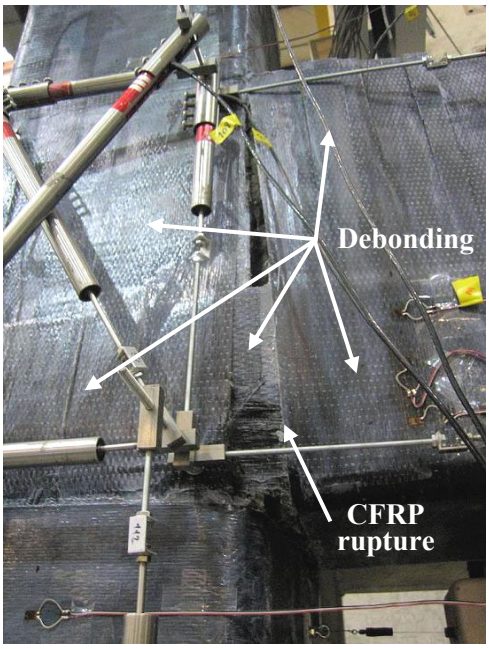

(b)

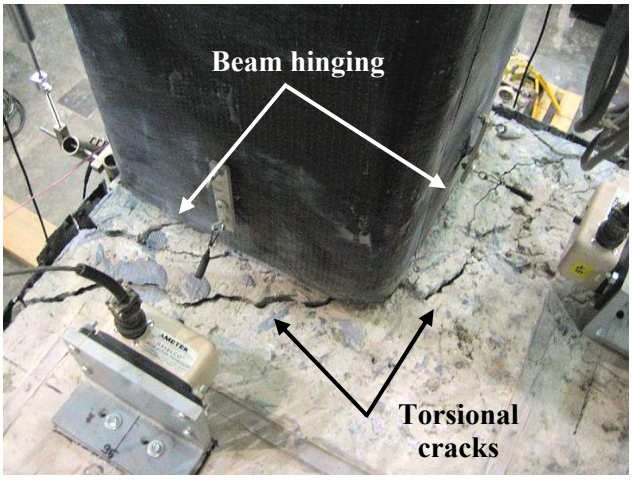

(c)

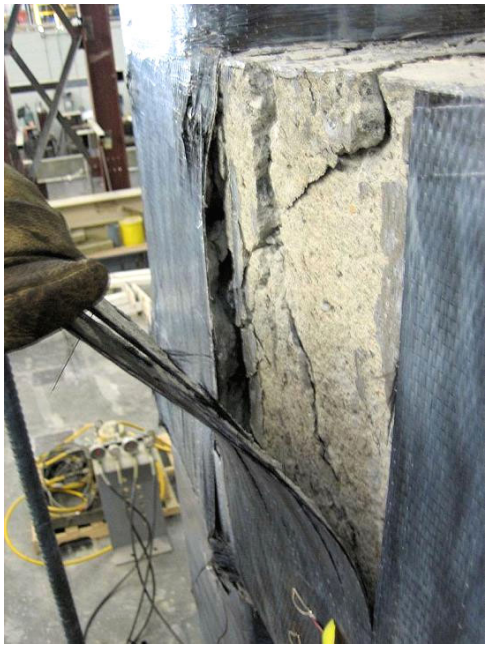

(d)

Figure 6.6 — Damage modes of Specimen 3: (a) perspective view of beam hinges and CFRP rupture, (b) rupture of EW beam CFRP strip, (c) top view of beam hinges (slab SW corner), and (d) cracking under CFRP at the EW beam hinge.

- The CFRP beam strips in Specimen 3 did not maintain their bond to concrete as well as those in Specimen 2, and significant debonding had taken place along both beams and within joint S face before the CFRP failure described in Step 8 above. The rupture of CFRP occurred only at the SW joint corner and at the beam-column interfaces to a limited extent, not along the entire perimeter of the strips within the joint as in Specimen 2 (Figure 6.5). Even so, the peak loads were not significantly affected.
- The CFRP sheets on the part of the joint panels above the strips survived peak 13a unlike those in Specimen 2, and debonded simultaneously with the beam strips as described in Step 8 above.
- The stiffness of the undamaged joint zone in Specimen 3 increased the demand on the columns compared to Specimen 2. The upper column wrap developed strains 1.5 times higher than Specimen 2 and debonded partially; the un-wrapped portion of the upper column developed shear cracks which led to the separation of the added M22 column rebar; and the lower column bars at the three outside corners yielded at peak 13a.

Such differences in the failure mechanisms did not translate into major differences in the hysteretic performance parameters as presented in the following sections.

6.5.2 Hysteretic Behavior

The force-drift hysteretic response of Specimen 3, for example in the NS direction, is presented in Figure 6.7. This response indicated two differences from that of Specimen 2 after retrofit:

- Additional average increases of 10% in the downward peak loads and 6% in the upward peak loads during the first three (unidirectional) cycles were obtained. This initial increase in the peak loads resulted in an 8% increase in the initial stiffness and 7% in the stiffness in cycles 2 and 3, as shown in Figure 6.4a. Such an increase in the initial stiffness when compared to a specimen that was damaged and epoxy-injected

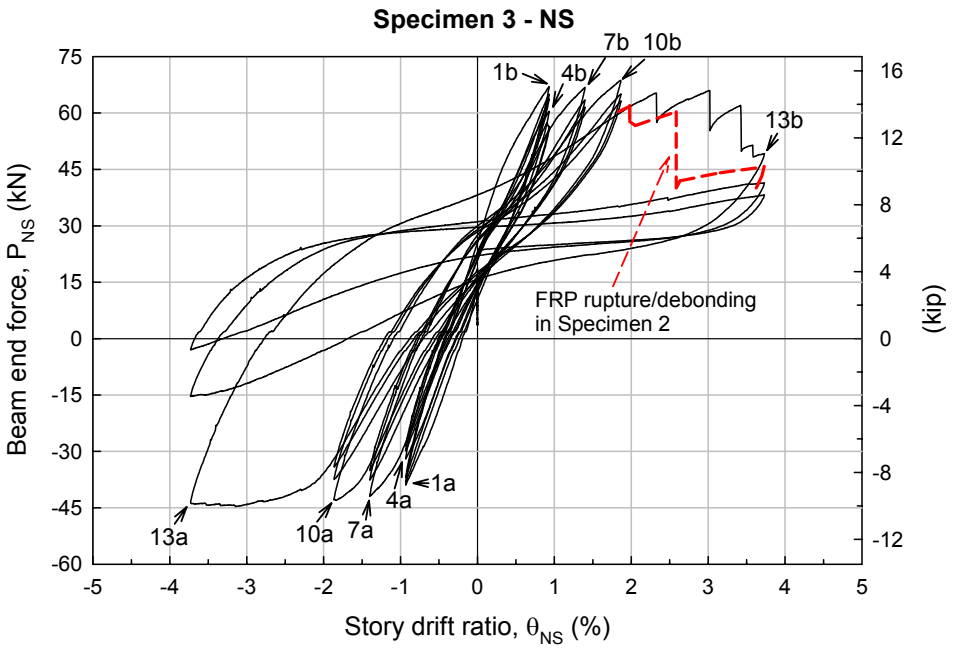

Figure 6.7 — Force-drift hysteretic response of Specimen 3 in the NS direction.

prior to retrofit was predicted, since epoxy injection cannot be expected to restore 100% of the original properties. In fact, epoxy injection was more effective than expected; the stiffness throughout the bidirectional cycles was almost identical in both specimens (Figure 6.4a).

- Although debonding of CFRP in Specimen 3 was accompanied by less CFRP rupture than in Specimen 2 (Figure 6.5 versus Figure 6.6a,b), debonding was more progressive and less sudden in Specimen 3. Failure of the CFRP beam strips and joint sheets in the NS direction, for instance, took place progressively between 2.3% and 3.4% drift toward peak 13b, which was manifested in the force-drift plot in Figure 6.7 as a less rapid strength degradation during cycle 13 as compared to Specimen 2. (The upper portion of cycle 13 obtained for Specimen 2 was superimposed on this plot for comparison.) However, Specimen 3 had only a 2% increase in the cumulative dissipated energy than Specimen 2 as shown in Figure 6.4b.

Such changes in hysteretic performance were not taken to indicate any significant advantages of pre-damage retrofit over post-damage retrofit.

6.5.3 Joint Shear Strength

The variation of normalized joint shear stress (τ'_{jh}) and joint shear strain (γ_s) in Specimen 3 and Specimen 2 is compared in Figure 6.8 where $\tau'_{jh} = V_{jh} \Big/ \sqrt{f'_c}\, b_j h_c$ as defined in ACI-ASCE 352R-02 [6.19] and γ_s was taken as the average of four estimates obtained from an LVDT configuration mounted on the joint panels, the details of which are presented in Appendix B. The hysteretic degradation in joint shear strength and stiffness was examined by estimating the horizontal joint shear force V_{jh} by considering the strong-axis beam bending moment (M_z) only and assuming a constant moment arm (*jd=0.875d*) as commonly done for planar specimens found in the literature (i.e. $V_{jh} = M_z / 0.875d - V_{col}$). The resulting curves, which are presented for the NS direction in Figure 6.8 with solid and dashed lines, indicated that an almost "rigid" joint behavior was achieved for both specimens during downward loading in the first 12 cycles and up to approximately -2.5% drift toward peak 13a. During upward loading, Specimen 3 exhibited smaller joint shear strains indicating the higher stiffness of the previously-undamaged Specimen 3. The τ'_{jh} values obtained by the "constant moment arm approximation" were not taken to represent the actual shear stresses carried by the joint since this method does not account for forces transferred to the joint other than the strong-axis beam moment. As previously presented in Chapter 3, torsional forces in the beam that are created due to the presence of the slab and bidirectional loading significantly increase the joint shear. All forces were taken into account using forces in each beam top bar and in the slab bars within the effective width. Forces were determined by using the strain gage data and the cyclic stress-strain curves experimentally developed

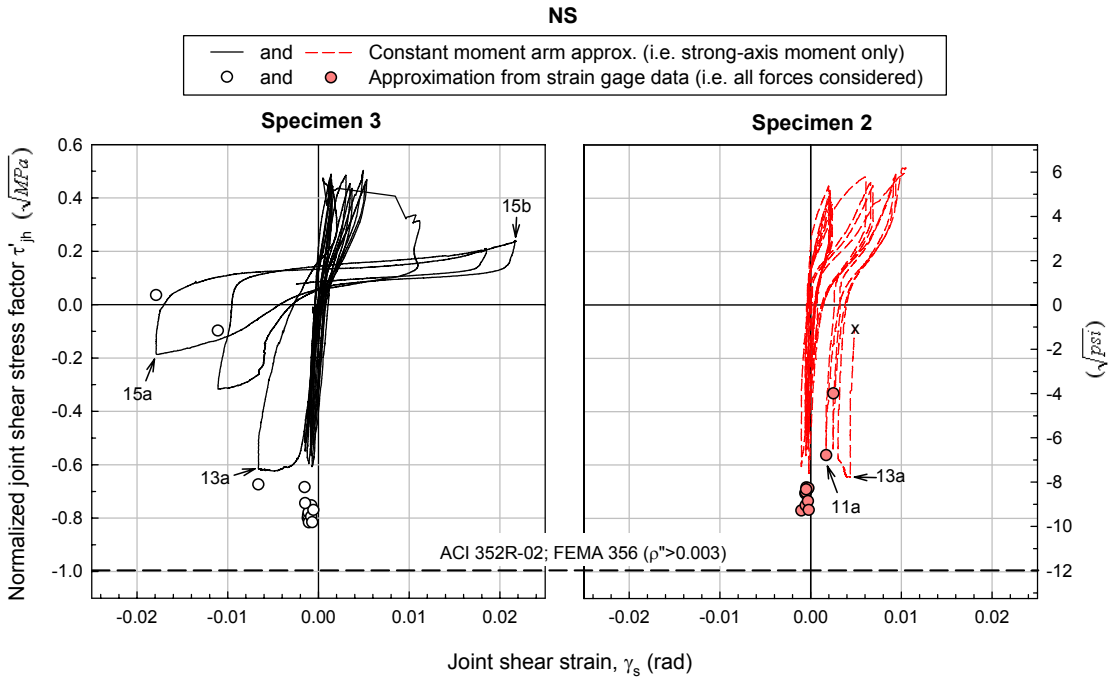

Figure 6.8 — Joint shear stress-strain hysteresis loops obtained for the NS direction: (a) Specimen 3 versus (b) Specimen 2-after retrofit.

for the bars for various loading-unloading patterns observed in the recorded strain histories. The sum of these forces were then taken as the total normal tensile force (T_b) applied to the joint at the beam-joint interface (i.e. instead of $T_b = M_z / jd$). The τ'_{jh} values obtained by this method at the downward loading peaks are shown for the NS direction in Figure 6.8 with circles. These values were higher for Specimen 3 by 12% in cycles 1 to 6 and by 5% in cycles 7 to 10; moreover, Specimen 3 maintained much of its improved joint shear strength through cycle 13 unlike Specimen 2 which lost much of its after cycle 10. In the EW direction, Specimen 3 developed similarly higher τ'_{jh} values than Specimen 2 by 24% in cycles 1 to 6 and by 8% in cycle 7; the joint in Specimen 3 survived cycle 13 but that in Specimen 2 lost much of its strength after cycle 7. The maximum bidirectional normalized joint shear stress $\tau'^{b}_{jh} = (\tau'^{EW}_{jh} + \tau'^{NS}_{jh})^{1/2}$, which

occurred at peak 7a (-1.40% drift) as $1.06\sqrt{MPa}$ for Specimen 2 and which was larger than the ACI-ASCE 352R-02-recommended value of γ=1.00, was further improved to $1.15\sqrt{MPa}$ and occurred at a larger drift level for Specimen 3 (at peak 10a, -1.87% drift). Specimen 3 exhibited a τ'^{b}_{jh} value of $1.03\sqrt{MPa}$ even at peak 13a (-3.73% drift), while the maximum τ'^{b}_{jh} for Specimen 2 after its peak was $0.90\sqrt{MPa}$ at peak 10a (-1.87% drift). These results indicated that, although not significantly manifested in the aforementioned force-drift responses, the fact that Specimen 3 was undamaged before retrofit helped the joint to withstand larger shear stresses and larger drift levels.

6.6 EFFICACY OF RETROFIT IN THE CASE OF LOW CONCRETE STRENGTH: SPECIMEN 4 VERSUS SPECIMEN 3

The compressive strength of concrete (f'_c) in the lower column, beams, and slab in Specimen 4 was less than half of that in Specimen 3 on the test day (Lift 1 in Figure 6.2b). The lower strength required that the strength hierarchy between the members and possible failure modes for the as-built condition of Specimen 4 be re-examined. Such a large reduction in f'_c was expected to affect the strength hierarchy as follows:

1. Negative moment capacity of the beams was reduced by only 5% while the moment capacity of the lower column at the applied axial load level ($0.1\,P_o$) was reduced by 26%. There was no significant change in the upper column strength because f'_c in Lift 2 was much higher. The column-to-beam strength ratio reduced from 1.05 in Specimen 3 to 0.94 in Specimen 4 and suggested that the flexural demand on the column could increase.
2. Shear strengths of the lower column, beams, and joint were reduced by approximately 33% due to the reduction in $\sqrt{f'_c}$. Considering the shear forces developed in Specimen 3, this was not expected to pose a problem for the beams. For the columns,

reduction in the shear strength was expected to be critical if peak loads were to be comparable to those in Specimen 3. Most importantly, the joint was not expected to withstand as high of joint shear forces and survive as high of drift levels as in Specimen 3.

3. Anchorage of reinforcing bars was significantly reduced due to low $\sqrt{f_c'}$. This was expected to cause earlier pull-out of beam bottom bars and possibly the loss of anchorage of beam top bars which are developed in a joint that was expected to undergo more damage due to reduced shear strength.

6.6.1 Reconsideration of the CFRP Retrofit

Although the column-to-beam flexural strength ratio was reduced in Specimen 4 due to low f_c', no additional measures were taken to improve the column's flexural strength so that the two specimens could be compared directly. Column flexural strengthening consisted of adding a M22 (#7) steel reinforcing bar at the inside (NE) column corner as previously described for Specimen 3. Different components of the CFRP scheme were re-considered as follows:

CFRP joint sheets: Although the reduced shear strength of the joint may seem to require an increased amount of CFRP in the joint panels, it is noted that the amount used in the initial design was based on the maximum joint shear force that could develop during beam hinging. Using more CFRP was not expected to provide additional strength because strength would be limited by the bond to concrete. Therefore, the CFRP layout in the joint panels was kept unchanged.

CFRP beam strips: These strips developed their rupture strength between +2.5% and +3.4% drift in Specimen 3 and helped achieve the design goal of obtaining a positive moment capacity that was at least half of the negative moment capacity. To delay the rupture and possibly survive the +3.73% drift at peak 13b, the use of additional layers of

CFRP strips seemed to be needed. On the other hand, the CFRP-to-concrete bond that was already expected to be worse due to low $f_c^{'}$ could be further reduced if the CFRP thickness was increased because added force could lead to earlier debonding and eventually to a poorer performance than that of Specimen 3. As a result, the number of layers and width of CFRP beam strips were kept unchanged from Specimen 3. As for their extension length along the beams, the length past the U-wrapped portion of the beams (area 4 in Figure 6.3) was omitted in Specimen 4 (Figure 6.9) since such an extension was found to be ineffective based on the strain readings in this portion of the strips in both Specimen 3 and Specimen 2.

CFRP beam U-wraps: Although better confinement of the CFRP beam strips would be desirable due to the poorer CFRP-to-concrete bond expected in Specimen 4, there was no reason to believe that further confinement could be provided by increasing the number of layers of beam U-wraps considering that there was not a large demand on these wraps in both Specimen 3 and Specimen 2 (ε_{max}=1110-1460 με). The layout of beam U-wraps was therefore kept unchanged from Specimen 3.

CFRP column wraps: The design approach for the column wraps (i.e. provide confinement equivalent to what would be provided by steel hoops required by ACI 318-05, Sec. 21.4.4 [6.18]) called for only one layer of CFRP (a reduction from two layers) in Specimen 4 due to reduced $f_c^{'}$. Even so, the second layer was still used to compensate the aforementioned reduction in the column's shear strength. Given the shear cracking and separation of the added M22 column bar in the un-wrapped portion of the upper column in Specimen 3, this upper part was also wrapped in Specimen 4 using one layer of CFRP (area 7 in Figure 6.9).

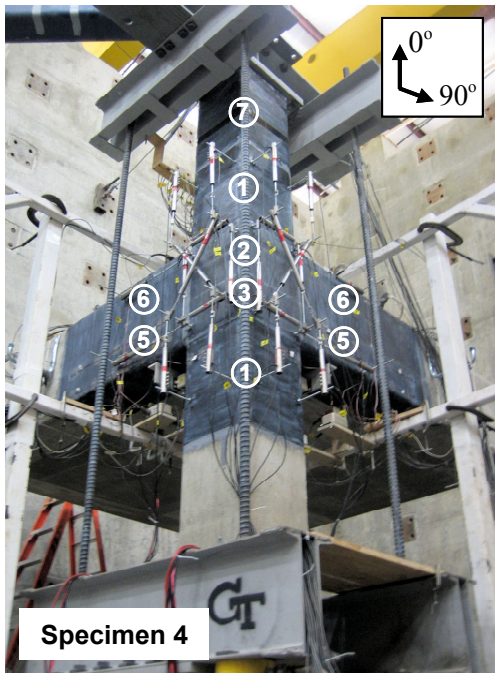

Stacking sequences

	Specimens 2 and 3	Specimen 4
①	$[90/0/90/\overline{90}]_S$	same
②	$[0/90/\overline{90}]_S$	same
③	$[0/90_4]_S$	same
④	$[90_5]$	deleted
⑤	$[0_2/90_2/\overline{90}]_S$	same
⑥	$[0_4]$	same
⑦	N/A	[90]

Figure 6.9 — Modified CFRP strengthening scheme for Specimen 4.

6.6.2 Damage Mechanisms and Strength Hierarchy

As expected, the moment capacity of the beams could not be fully mobilized, and a ductile beam hinging mechanism could not be achieved. Yielding occurred first in two slab top bars near each beam during the unidirectional cycles. Then, at peak 7a of the bidirectional cycles, yielding occurred in two NS beam top bars and in the added M22 column bar. Yielding in the EW beam did not occur until peak 13a (in two bars up to $1.38\,\varepsilon_y$) at which point yielding in the NS beam was still limited (in two bars up to $1.66\,\varepsilon_y$), but yielding in the added M22 column bar had progressed ($3.1\,\varepsilon_y$). Although large flexural cracks were formed on the beam top surfaces near the column faces (Figure 6.10b), the strains in beam top bars did not indicate a ductile beam hinge with yielding of all beam top bars in either beam throughout the test, and the maximum strains in four of the six top bars that did not yield in each beam ranged between 0.61 and $0.96\,\varepsilon_y$. This may indicate some loss of anchorage of beam top bars, although such an anchorage loss

was not observed in the strain gage data. The developed beam moments were not high enough to result in high column moments that would cause yielding in the original (M16) column bars; the strains in these bars did not exceed $0.72\varepsilon_y$ in the upper column and $0.70\varepsilon_y$ in the lower column. Instead, much of the demand was on the joint. Despite the significantly reduced concrete shear strength due to low $f_c^{'}$, the joint performed well. Complete debonding of the CFRP sheets in the joint panels did not occur until peak 13a, although the NS beam strips within the joint (W face of area 3 in Figure 6.9) had debonded at peak 8b and the sheets in the joint areas above the beam strips (area 2) had partially debonded at peak 11b. In contrast to an expected poor CFRP-to-concrete bond, the behavior of the CFRP beam strips was controlled by a debonding/rupture mechanism similar to that observed for Specimen 3. Failure of the strips was characterized by debonding within 100 to 200 mm from the column faces at peak 8b, partial rupture at the NS column face at peak 10b, propagation of debonding over 500 mm from the column faces until peak 13a, and simultaneous rupture at the EW and NS column faces and at the SW joint corner at +2.7% drift toward peak 13b (Figure 6.10a). The maximum average strain across the width of the strips was 7260 με near the EW column face with the strain at the beam bottom bar level being 9420 με. Achievement of such high strain levels and rupture indicated that low $f_c^{'}$ did not affect the CFRP-to-concrete bond and nor did it cause earlier debonding as previously thought. It is believed that drift levels larger than 2.7% could have been survived had additional CFRP beam strips been used.

The view of the joint region after the removal of CFRP and loose concrete after the test is shown in Figure 6.10d. As seen, most of the damage was sustained by the joint; the top and bottom corners of the beams were also crushed; but the columns did not undergo significant damage.

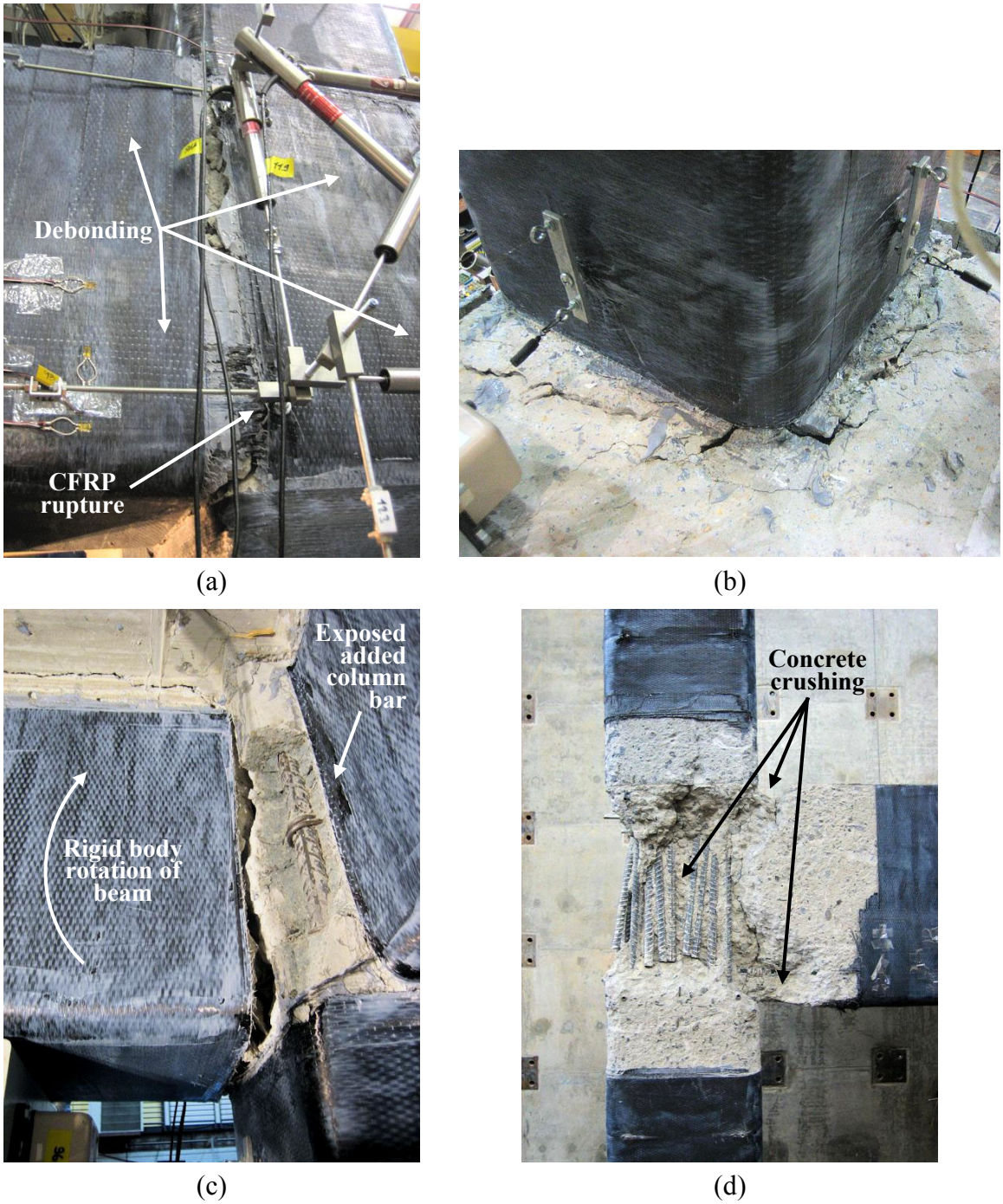

Figure 6.10 — Damage modes of Specimen 4: (a) CFRP rupture/debonding, (b) beam bottom bar pull-out, (c) exposed column bar at joint inside corner and upward rigid body rotation of beam, and (d) joint region after removal of CFRP and loose concrete.

6.6.3 Hysteretic Behavior

The force-drift hysteretic response, presented in Figure 6.11 for the NS direction, indicated that the behavior of Specimen 4 was dominated by a significantly lower stiffness than that of Specimen 3, which resulted in lower peak loads at the applied displacement peaks. The reduction in peak-to-peak stiffness (K_p) was proportional to $\sqrt{f_c'}$. K_p was not only 32 to 44% lower than that of Specimen 3 throughout the test, it was also 15 to 20% lower than that of the unretrofitted Specimen 2 in the first six cycles (Figure 6.4a). The hysteretic energy dissipation was similarly lower, with the cumulative amount at the end of the test being 37% lower than that of Specimen 3 (Figure 6.4b).

Other than such reductions in peak loads, stiffness, and energy dissipation, the overall shape of the hysteretic curves was similar to that of Specimen 3 for downward loading. Although yielding in the beams was limited to only a few bars and occurred only up to $1.66\varepsilon_y$, the hysteretic curves indicated a "pseudo ductility" toward peak 13a similar to that observed for previous specimens that exhibited significant beam hinging. Such pseudo ductility in Specimen 4 could be in part due to two characteristics of low-strength concrete. First, low-strength concretes exhibit a compressive stress-strain curve with a more gradual descending portion and a larger ultimate strain ($\varepsilon_{cu} > 0.003$) [6.20]. This may have led to some ductility during crushing of concrete at the beam bottom and within the joint panel (Figure 6.10d). Second, low-strength concretes may exhibit larger lateral strains (i.e. expansion). This may have increased the effectiveness of CFRP confinement of the joint in increasing both strength and ductility of the concrete. In addition to such characteristics of low-strength concrete, the pseudo ductility could also be due to the progressive debonding of CFRP as also observed by Moon [6.21].

For upward loading, the peak loads were similarly reduced, and another difference from Specimen 3 was in the envelope of cycle 13; that of Specimen 3 is

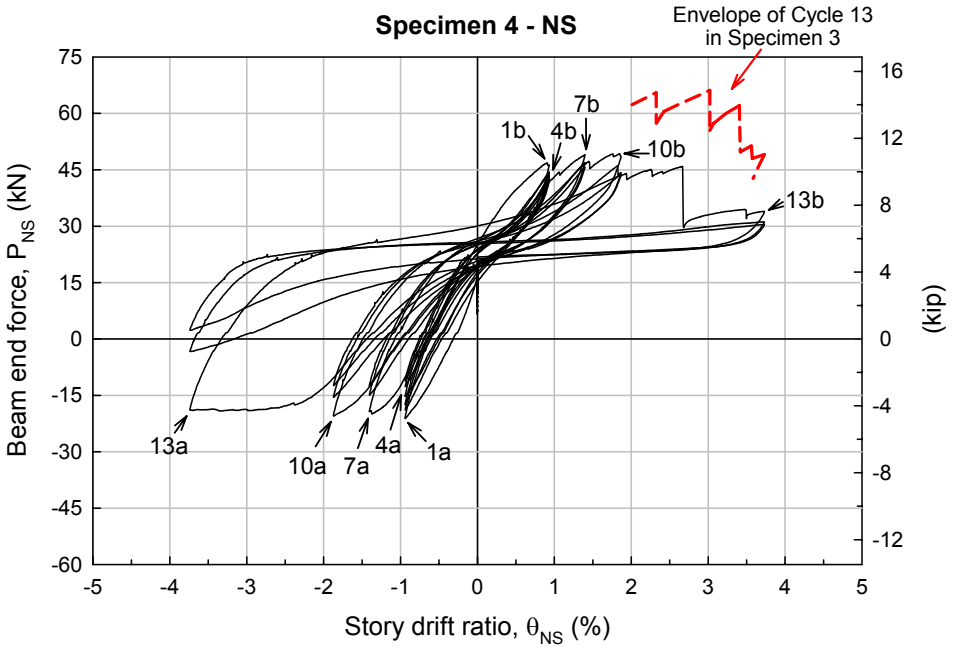

Figure 6.11 — Force-drift hysteretic response of Specimen 4 in the NS direction.

superimposed on Figure 6.11 for comparison. As seen, the load carrying capacity was not lost progressively between +2.3 and +3.4% drift as in Specimen 3, but it was lost suddenly at +2.7% drift with simultaneous rupture of the CFRP beam strips at the EW and NS column faces and at the SW corner of the joint. As previously mentioned, the use of additional CFRP beam strips could have delayed the CFRP rupture and improved the performance further.

6.6.4 Joint Shear Strength

Although the beam top bars in Specimen 4 did not undergo significant yielding (only two bars in each beam up to $1.66\varepsilon_y$, other bars between 0.61 and $0.96\varepsilon_y$), the maximum shear force induced in the joint V_{jh}^{max} (obtained from strain gage data) was only 17% less than that in Specimen 3. Such a reduction in V_{jh}^{max} was less than the reduction in $\sqrt{f_c'}$ between the two specimens, leading to larger normalized joint shear

stresses ($\tau'_{jh} = V_{jh} / \sqrt{f'_c} b_j h_c$) in Specimen 4 as presented in Figure 6.12 as an example for the EW direction. At peak 13a, τ'_{jh} values reached the ACI-ASCE-recommended level of γ=1.00$\sqrt{MPa}$ simultaneously in both EW (0.98$\sqrt{MPa}$) and NS (1.02$\sqrt{MPa}$) directions resulting in a maximum bidirectional normalized joint shear stress (τ'^{b}_{jh}) of 1.41$\sqrt{MPa}$ at approximately 45 degrees. This τ'^{b}_{jh} value was larger than those obtained for all other specimens in this project reported herein and in Chapter 5 and indicated the effectiveness of the applied CFRP scheme even in the case of low-strength concrete.

While CFRP retrofit clearly improved the joint shear strength, identification of the mechanisms through which this improvement occurred is not straightforward. CFRP may have contributed directly by carrying part of the joint shear force, indirectly by confining the joint and hence increasing the strength and ductility of the joint concrete, or by a combination of both. Regardless of the mechanism, the retrofitted joint shear capacity can be expressed as the sum of that of the unretrofitted/unconfined joint concrete (V_c) and all contributions of CFRP (V_{CFRP}) as follows:

$$\begin{aligned} V_{jh} &= V_c + V_{CFRP} \\ &= \gamma \sqrt{f'_c} b_j h_c + V_{CFRP} \end{aligned} \tag{6.1}$$

Although the first term in Equation (6.1) was lower for Specimen 4 due to low concrete strength, this specimen developed larger normalized joint shear stresses than Specimen 3 indicating that the larger joint shear strain demand on the concrete due to its lower elastic (E_c) and shear (G_c) moduli was met by the CFRP. Larger strains induced higher forces in the CFRP resulting in a larger total force resistance; that is, CFRP became more effective in improving the joint strength in the case of low concrete strength.

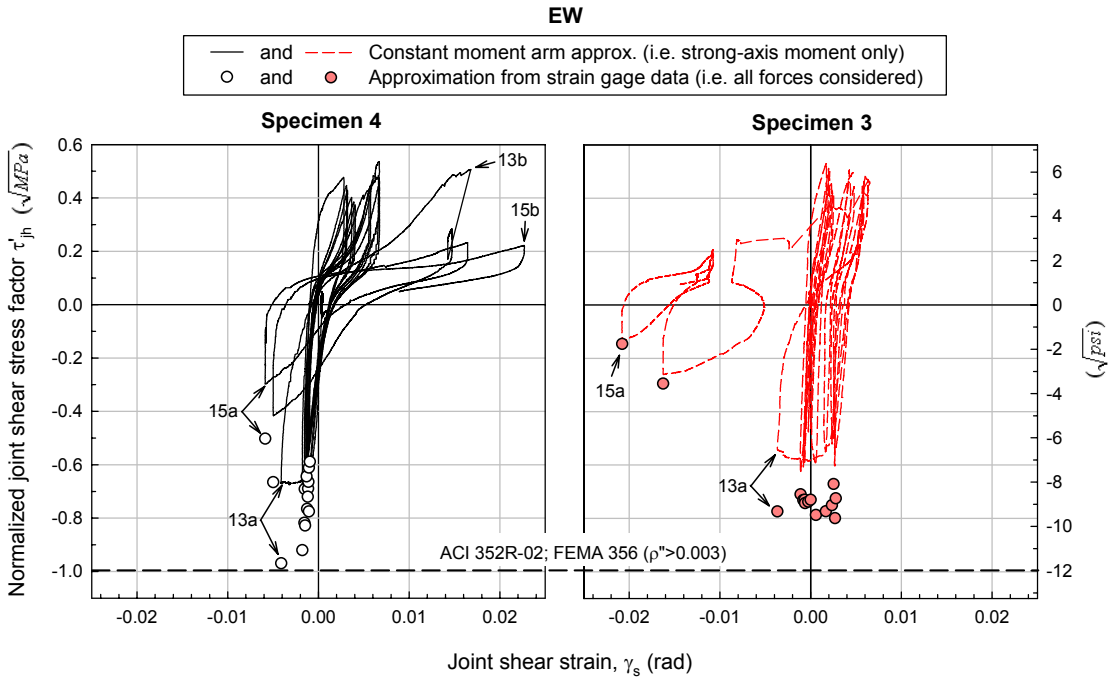

Figure 6.12 — Joint shear stress-strain hysteresis loops obtained for the EW direction: (a) Specimen 4 versus (b) Specimen 3.

The improvement in joint shear strength was evaluated in this thesis in terms of the total joint shear capacity (V_{jh}) and not by determining the separate contributions in Equation (6.1). The total capacity approach is analogous to that used in the design of well-detailed joints [6.19] where the total joint shear capacity is determined by a single shear strength factor (γ) and not by quantifying the contribution of concrete and joint transverse reinforcement separately. An attempt to quantify the CFRP contribution to strength of joints with varying concrete strength will be presented in a future publication.

6.7 CONCLUSIONS

For the specimen with moderate-strength concrete, a seismically desirable strength hierarchy was achieved where extensive yielding in the beam top bars preceded the onset of yielding in the column bars. The maximum obtained bidirectional normalized joint shear stress was larger than the γ factor recommended by ACI-ASCE 352R-02 [6.19] for

determining the shear strength of seismically designed corner joints ($\left(\tau'^{b}_{jh}\right)_{max}=1.15\sqrt{MPa}$ versus $\gamma=1.00\sqrt{MPa}$). While such improvements indicated the efficacy of CFRP retrofit for upgrading as-built pre-1970 corner joints, they were not considered significantly superior to those obtained previously for a moderately-damaged-then-retrofitted specimen. What was superior in the case of pre-damage retrofit, however, was that the joint maintained much of its improved strength until after a -3.73% drift peak unlike the loss of strength during the ±1.87% drift cycles in the case of post-damage retrofit.

Low concrete strength did not hinder the efficacy of CFRP for improving the joint shear strength but it did cause a significant reduction in the overall stiffness of the specimen which prevented the development of a ductile beam hinge mechanism. When compared to the specimen with moderate concrete strength, the CFRP-to-concrete bond was not any worse; complete debonding of the joint sheets did not occur any earlier; and rupture of the beam strips was still achieved. The initial peak-to-peak stiffness of the specimen, however, was even lower than that of an unretrofitted specimen with moderate-strength concrete by 18%.

To evaluate the adequacy of the obtained improvements, further testing and analysis of complete frame structures are needed. More invasive techniques may be required to increase the stiffness in cases of such low concrete strengths.

6.8 REFERENCES

[6.1] Said, A. M., and Nehdi, M. L. (2004). "Use of FRP for RC frames in seismic zones: Part I. Evaluation of FRP beam-column joint rehabilitation techniques." *Applied Composite Materials*, 11(4), 205-226.

[6.2] Ghobarah, A., and Said, A. (2002). "Shear strengthening of beam-column joints." *Engineering Structures: The Journal of Earthquake, Wind and Ocean Engineering*; 24(7), 881-888.

[6.3] El-Amoury, T., and Ghobarah, A. (2002). "Seismic rehabilitation of beam-column joint using GFRP sheets." *Engineering Structures: The Journal of Earthquake, Wind and Ocean Engineering*, 24(11), 1397-1407.

[6.4] Clyde, C., and Pantelides, C. P. (2002). "Seismic evaluation and rehabilitation of R/C exterior building joints." *Proceedings of the Seventh U.S. National Conference on Earthquake Engineering* (CD-ROM), Boston, MA.

[6.5] Antonopoulos, C. P., and Triantafillou, T. C. (2003). "Experimental investigation of FRP-strengthened RC beam-column joints." *Journal of Composites for Construction (ASCE)*, 7(1), 39-49.

[6.6] Prota, A., Nanni, A., Manfredi, G., and Cosenza, E. (2004). "Selective upgrade of underdesigned reinforced concrete beam-column joints using carbon fiber-reinforced polymers." *ACI Structural Journal*, 101 (5), 699-707.

[6.7] Ghobarah, A., and El-Amoury, T. (2005). "Seismic rehabilitation of deficient exterior concrete frame joints." *Journal of Composites for Construction (ASCE)*, 9(5), 408-416.

[6.8] Balsamo, A., Colombo, A., Manfredi, G., Negro, P., and Prota, A. (2005). "Seismic behavior of a full-scale RC frame repaired using CFRP laminates." *Engineering Structures*, 27(5), 769-780.

[6.9] Pampanin, S., Bolognini, D., and Pavese, A. (2007). "Performance-based seismic retrofit strategy for existing reinforced concrete frame systems using fiber-reinforced polymer composites, *Journal of Composites for Construction (ASCE)*, 11(2), 211-226.

[6.10] Di Ludovico, M., Prota, A., Manfredi, G., and Cosenza, E. (2008). "Seismic strengthening of an under-designed RC structure with FRP." *Earthquake Engineering and Structural Dynamics*, 37(1), 141-162.

[6.11] *fib* (2001). *Externally bonded FRP reinforcement for RC structures, Bulletin 14*, International Federation for Structural Concrete, Lausanne, Switzerland.

[6.12] ACI Committee 440.2 (2002). *Guide for the design and construction of externally bonded FRP systems for strengthening concrete structures (ACI 440.2R-02)*, American Concrete Institute, Farmington Hills, MI.

[6.13] ISIS Canada (2001). *Strengthening reinforced concrete structures with externally-bonded fibre reinforced polymers*, Design Manual No. 4, The Canadian Network of Centres of Excellence on Intelligent Sensing for Innovative Structures, Winnipeg, Manitoba, Canada.

[6.14] AFGC (2003). *Repair and strengthening of concrete structures by means of composite materials – Interim recommendations*, French Association of Civil Engineering, Paris, France. (In French)

[6.15] CNR-DT 200 (2004). *Guide for the design and construction of externally bonded FRP systems for strengthening existing structures*, Italian National Research Council, Rome, Italy.

[6.16] ACI Committee 318 (1963). *Building code requirements for reinforced concrete (ACI 318-63)*, American Concrete Institute, Detroit, MI.

[6.17] ACI Committee 440.2 (2007). *Guide for the design and construction of externally bonded FRP systems for strengthening concrete structures (ACI 440.2R-02 in revision)*, American Concrete Institute, Farmington Hills, MI.

[6.18] ACI Committee 318 (2005). *Building code requirements for structural concrete (ACI 318-05) and commentary (318R-05)*, American Concrete Institute, Farmington Hills, MI.

[6.19] ACI-ASCE Committee 352 (2002). *Recommendations for design of beam-column connections in monolithic reinforced concrete structures (ACI 352R-02)*, American Concrete Institute, Farmington Hills, MI.

[6.20] MacGregor, J. G. (1997). *Reinforced Concrete – Mechanics and Design*, 3rd edition, Prentice Hall, Upper Saddle River, NJ.

[6.21] Moon, F. L. (2004). "Seismic strengthening of low-rise unreinforced masonry structures with flexible diaphragms." Ph.D. thesis, Georgia Institute of Technology, Atlanta, GA.

CHAPTER 7

CONCLUSIONS AND RECOMMENDATIONS

7.1 CONCLUSIONS

The major conclusions drawn from the results of a series of experiments conducted on full-scale RC corner beam-column-slab joints both before and after retrofit with CFRP composites are presented below in three groups.

General

- Experimental modeling of all floor members (i.e. transverse beam and slab) and the use of bidirectional loading resulted in damage modes and force transfer mechanisms that were overlooked in simplified unidirectional, planar exterior joint tests commonly found in the literature. Future design and analyses of corner joints should not overlook (1) the reduction in the biaxial capacity of the column due to anchorage and section losses at the inside (NE) and outside (SW) corners, (2) the increased and nonuniformly distributed strains in the beam bars due to forces created by the slab (e.g. torsion, weak-axis bending), and (3) the resulting increase in the horizontal joint shear force.
- As a result of the internal forces created due to the presence of the slab, beam top bars transferred significantly larger forces to the joint than predicted based only on the strong-axis beam moments and based on an assumed constant moment arm as typically done for two-dimensional joint specimens. Larger top bar forces were evident from analyses based on the strain histories of all beam top bars and on experimentally developed cyclic stress-strain curves for these bars. While such an increased demand on the beam top bars does not necessarily increase the maximum possible joint shear force due to the remarkable length of the yield plateaus of Grade

40 reinforcing bars, the larger bar forces cause joint shear cracking and large interstory drift ratios to occur at lateral load levels lower than predicted by unidirectional analyses.

Adequacy of As-built Pre-1970 RC Corner Joints

- Pre-1970 RC corner beam-column joints are susceptible to severe damage even at drift levels lower than those envisioned to occur during typical design earthquakes (i.e. ~2%). The lack of the strength hierarchy and reinforcement details required by the current capacity design philosophy results in seismically undesirable failure modes such as yielding of column reinforcement, joint shear failure, loss of anchorage of beam bottom bars, and failure of column lap-splices which lead to severe loss of stiffness and strength. No effective energy dissipation mechanisms can be developed.
- Buildings with such joints may be prone to significant second order effects and eventual loss of vertical load carrying capacity due to rapid loss of lateral stiffness and large joint shear deformations. Under cyclic loading with a maximum interstory drift ratio of ±1.9%, 78 to 80% of the initial stiffness was lost, and 69 to 83% of the drifts were caused by joint shear deformations.
- If the tested specimens were part of an actual RC building to be evaluated according to the FEMA 356 [7.1] guidelines (i.e. based on strength hierarchy, distribution of damage, and crack sizes) the Life Safety Performance Level at 2% drift and the Collapse Prevention Performance Level at 4% drift would not have been met.
- Bidirectional loading plays a significant role in the observed response, and should be considered in structure evaluation. A significant drop in peak loads and stiffness, and a more rapid propagation of damage was observed as soon as the loading direction was changed from unidirectional to 45-degree bidirectional.

- The joint shear strength factor of $\gamma = 0.50\sqrt{MPa}$ recommended by FEMA 356 [7.1] for estimating the shear strength of non-code-conforming ($\rho'' < 0.003$) corner joints is conservative. Despite the lack of any joint transverse reinforcements ($\rho'' = 0$), the specimens were able to develop normalized joint shear strength factors up to $0.67\sqrt{MPa}$ in the primary frame directions. Moreover, such joint shear factors could be developed in both directions simultaneously, reaching a maximum vector sum of $0.91\sqrt{MPa}$. Joint shear strength factor for bidirectional loading, which was not addressed by FEMA 356 [7.1], can be taken as $0.50\sqrt{2} = 0.71\sqrt{MPa}$ (i.e. square interaction diagram) until further increase is justified by additional experimental data.
- There is a clear need for effective retrofit for columns and beam-column joints of pre-1970 RC buildings. Retrofit schemes should include measures to delay/prevent the loss of anchorage of beam bottom bars; such anchorage failure was responsible for much of the loss in overall stiffness.

Efficacy of Retrofit

- Strength hierarchy, deformation mechanisms, stiffness, and energy dissipation characteristics of pre-1970 RC corner beam-column joints were improved efficiently by easy-to-implement procedures such as epoxy injection (in case of prior damage), addition of a steel reinforcing bar within the clear cover of the column, and external bonding of a CFRP system for increasing joint shear strength, column confinement, and beam positive moment capacity (i.e. anchorage of beam bottom bars).
- Such joints can be retrofitted using the scheme developed in this study to achieve ductile beam hinge mechanisms and rigid joint behavior up to interstory drift ratios of at least 2.4%, even in cases of severe existing damage, provided that concrete strength is not too low to provide adequate lateral stiffness and reinforcement anchorage. While joint specimens with concrete strengths of 26 MPa and higher were retrofitted

efficiently in this study, one specimen with 15 MPa concrete exhibited significantly lower stiffness and no beam plastic hinging. In cases of such low-strength concrete, more invasive techniques may be necessary to improve the overall structural stiffness and anchorage of beam reinforcing bars (e.g. additional column flexural strengthening, full-wrapping of beam ends).

- Regardless of the level of existing damage and concrete strength, the shear strength factor (γ) of all retrofitted joints surpassed the design strength factor for seismically designed, code-conforming corner beam-column joints according to ACI-ASCE 352R-02 [7.2] as presented in Figure 7.1. CFRP contributed to joint shear strength for all concrete strengths, and joint shear strength became a less critical parameter as concrete strength decreased. The efficacy of retrofit may be controlled by stiffness rather than strength of the retrofitted structure in cases of low-strength concrete.
- Post-earthquake retrofit of moderately damaged corner joints was as effective as pre-earthquake retrofit for achieving a strong column/weak beam behavior. Repair by epoxy injection prior to strengthening was effective in restoring much of the original properties of damaged joints.
- The improvement in joint shear strength was similar for both pre- and post-earthquake retrofit; however, much of the improved strength was maintained through larger drift levels (up to 3.7%) only in the case of pre-earthquake retrofit.
- The loss of beam positive moment capacity and reduction in overall strength and stiffness caused by beam bottom bar pull-out were mitigated by bonding CFRP strips on the beam outside faces at the beam bottom bar level provided that the strips were adequately anchored by beam U-wrapping.
- In-situ heat-curing of the composite system provided an effective means to achieve full cure of the resin system quickly and to increase the glass-transition temperature to values above the maximum operating temperature.

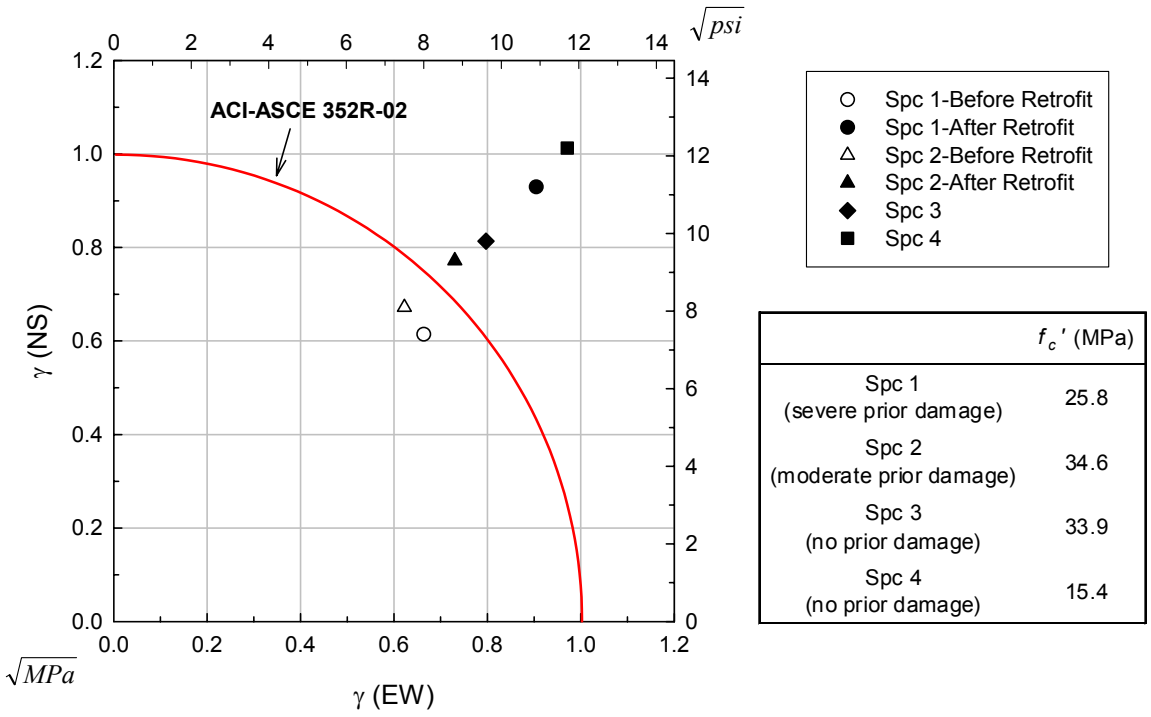

Figure 7.1 — Bidirectional joint shear strength: CFRP-retrofitted specimens versus code-conforming, seismically designed corner beam-column joints.

7.2 DESIGN RECOMMENDATIONS

In light of the above-listed findings from testing of the CFRP retrofit design strategies, the following design recommendations are made:

- For seismic strengthening of corner beam-column joints, the use of CFRP composites deserves major consideration.
- Epoxy injection should be used to restore much of the original properties of the joint even if the existing damage is severe.
- The number of CFRP layers needed in the joint panels to ensure beam hinging prior to joint failure is recommended to be determined by assuming that the joint shear force corresponding to beam hinging is to be carried by CFRP only and by assuming a uniform horizontal stress distribution in CFRP across the joint depth. CFRP lay-ups should provide strength in both horizontal and vertical directions (e.g. 0°/90°, ±45°)

to resist the diagonal principal stresses in the joint panel. The sheets bonded on the joint panels should be extended onto the columns so that CFRP-wrapping of the column ends for confinement can also serve as anchorage for the joint sheets.

- The confinement provided by CFRP-wrapping of the columns should be at least equivalent to that provided by steel hoop reinforcements required by ACI 318-05, Chp. 21 [7.3] in terms of both the maximum usable compressive strain of confined concrete ($\varepsilon_{cc}^{'}$) and the length over which confinement is provided. Equations given by ACI 440.2R-02 [7.4] can be used to determine $\varepsilon_{cc}^{'}$ for both CFRP-wrapping and confinement by steel hoops.
- Horizontal CFRP strips should be bonded around the outside corner of the joint and extended onto the beams at the beam bottom bar level to provide a beam positive moment capacity of at least half the negative moment capacity. The maximum load capacity of the strips should be equal to half the capacity of all beam top bars at yield, and the contribution of beam bottom bars should be considered negligible. The beam ends should be U-wrapped over a distance in which transverse confinement steel is required by ACI 318-05, Chp. 21 [7.3] so that the full rupture strength of the CFRP strips can be developed. Extension of the strips past this U-wrapped portion is not necessary.
- To eliminate long curing times, to increase the glass-transition temperature of the resin, and to improve the CFRP-to-concrete bond, in-situ heat-curing of the composite system is recommended. Selection of heat-curing schedules should be based on extensive thermal analysis of samples using techniques such as differential scanning calorimetry and dynamic mechanical analysis, and on pull-off tests to ensure adequate CFRP-to-concrete bond.

- A symmetric lay-up in all CFRP-applied areas is recommended in order to not cause curvatures in the composite sheets and initiation of early debonding during heat-curing.

7.3 FUTURE RESEARCH

This research demonstrated the efficacy of CFRP composites for retrofitting pre-1970 RC corner beam-column joints based on testing four full-scale beam-column-slab subassemblages. To further advance the state-of-the-art in this area and to facilitate the transition from research to implementation in construction, additional research in the following areas is recommended:

- Complete frame structures should be tested to confirm the efficacy of joint retrofit schemes developed based on subassemblage tests. Testing of both two- and three-dimensional frame structures has been initiated in Europe during the course of this study as summarized in Appendix A; such studies should be continued.
- Different approaches for identifying retrofit design targets and quantifying and detailing FRP retrofit components should be studied. The mechanisms through which FRP contributes to joint behavior should be identified (e.g. direct contribution through load-carrying, indirect contribution through confinement), and comprehensive design equations should be developed to quantify each contribution for different FRP lay-ups.
- Methods of improving the ductility of beams under positive moments (i.e. beam bottom bars in tension) should be investigated since simultaneous beam yielding at the opposite sides of a frame would further enhance the energy dissipation capacity.
- The effect of in-situ heat-curing of the composite system on the composite-to-concrete bond should be further investigated. Different heat-curing schedules should be studied to minimize the labor and application time required to achieve the full cure of the resin, obtain a glass-transition temperature that is acceptable for the service

environment, and to ensure an adequate composite-to-concrete bond. Practical heat-curing systems should be developed to facilitate field applications.

7.4 REFERENCES

[7.1] FEMA (2000). *Prestandard and commentary for the seismic rehabilitation of buildings (FEMA 356)*, Federal Emergency Management Agency, Washington, D.C.

[7.2] ACI-ASCE Committee 352 (2002). *Recommendations for design of beam-column connections in monolithic reinforced concrete structures (ACI 352R-02)*, American Concrete Institute, Farmington Hills, MI.

[7.3] ACI Committee 318 (2005). *Building code requirements for structural concrete (ACI 318-05) and commentary (318R-05)*, American Concrete Institute, Farmington Hills, MI.

[7.4] ACI Committee 440.2 (2002). *Guide for the design and construction of externally bonded FRP systems for strengthening concrete structures (ACI 440.2R-02)*, American Concrete Institute, Farmington Hills, MI.

APPENDIX A

THE STATE OF THE ART — CONTINUED (2004-2008)

The publications pertaining to the strengthening of RC beam-column joints using FRP composites available at the initiation of the present study were reviewed in Chapter 2. These studies demonstrated the great potential of FRPs for achieving desirable ductile failure mechanisms and have led to further testing to improve some of the developed schemes and to investigate their effectiveness on full-scale, complete frame structures. This appendix presents a review of the archival publications that have become available during the course of this study, where strengthening of RC beam-column joints with FRP composites was studied specifically or as part of global strengthening schemes developed for complete frame structures. As previously mentioned, the lack of comprehensive guidelines on the selection of design objectives, quantification of the required amount of FRP for each objective, and on detailing prevents wider acceptance and implementation of this technology in joint strengthening. Therefore, in the following reviews, special attention is paid to such design aspects as allowed by the reported details.

Said and Nehdi [A.1] re-evaluated the efficacy of the strengthening schemes studied earlier by Ghobarah and Said [1.30] (Figure 1.9a) by comparing their performance to that of a well-designed joint (J1) that conformed to the requirements of the Canadian building code CSA A23.3-94 [A.2]. Said and Nehdi [A.1] concluded that although the strengthening schemes significantly improved the performance of joints built prior to the 1970s, even the most successfully strengthened specimen T2R (Figure 1.9a), which exhibited a beam-hinging mechanism, did not meet the performance of the code-conforming specimen J1. This conclusion, however, was based on the entire hysteretic curves obtained up to interstory drift ratios of approximately 6.0%, 7.6% and

8.2% for the FRP-strengthened specimens, and 9% for the code-conforming specimen. The author believes that these drift ratios are unrealistically high for the purposes of such a comparison. In fact, the FRP-strengthened specimen T2R met the performance level of the code-conforming specimen J1 in terms of peak load, peak-to-peak stiffness and energy dissipation up to a drift ratio of approximately 4.5% which is larger than the limiting drift ratio of 4% for the Collapse Prevention Performance Level according to FEMA 356 [A.3]. Such a performance by this FRP strengthening scheme should not be underrated. Its limited range of applicability to real structures due to presence of floor members, however, cannot be overlooked.

Ghobarah and El-Amoury [A.5] continued their earlier efforts [1.30, 1.37] to develop strengthening schemes for preventing bond-slip/pull-out of beam bottom bars with inadequate anchorage length of 150 mm into the joint found in pre-1970 RC construction. Two series of one-way exterior joint specimens were tested under quasistatic cyclic loading, where each series consisted of a control specimen and two specimens strengthened without prior damage. In Series 1, the beam bottom bars were anchored in a joint confined with four #3 stirrups, while in Series 2, the joint was unconfined and shear-deficient. To focus on beam bottom bar failure, a strong column/weak beam criterion was satisfied in both series in contrast to a typical pre-1970 design. In the control specimen in Series 1, beam bottom bars were able to yield before losing anchorage at $2\Delta_y$ (Δ_y=beam yield displacement). The first attempt to prevent this failure was to bond CFRP sheets to beam bottom face, which were extended onto the column. The sheets were anchored to the column at the corner with a triangular steel plate (Figure A.1a). This scheme was not effective; the CFRP developed a maximum strain of only 2700με, and then debonded from the concrete surface and ruptured under the steel plate at the beam-column corner. In the second attempt, the corner of the steel anchor plate was rounded, and the plate was anchored by steel bolts welded to the beam and

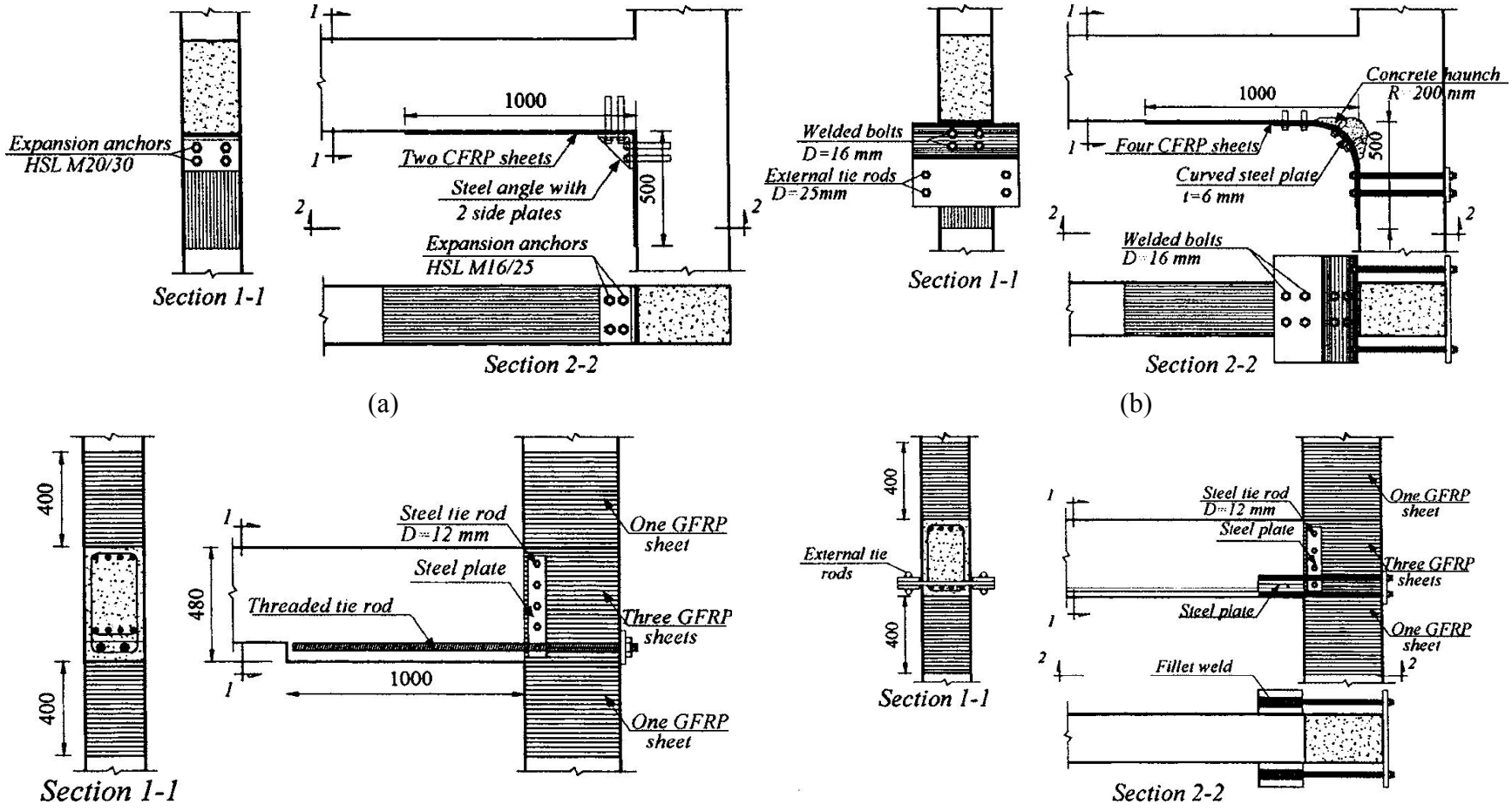

Figure A.1 — Strengthening schemes studied by Ghobarah and El-Amoury [A.5].

column bars and by external threaded rods connected to a bearing plate at the back of the column (Figure A.1b). Debonding and rupture of the CFRP sheets were effectively prevented, and a ductile beam failure was achieved until the welds of the anchor bolts in the curved portion fractured at $4\Delta_y$. In Series 2, where the behavior of the control specimen was due to joint shear failure during downward loading and beam bottom bar pullout during upward loading, GFRP sheets were used for strengthening joints and confining columns, and steel threaded rods were used to improve beam bottom bar anchorage. In one case, threaded rods were extended through the holes drilled in the column and encased in new concrete at the beam end (Figure A.1c). U-shaped steel ties were used along the beam to improve their anchorage. Yielding of these rods was achieved, and an equal yield moment capacity was obtained in both positive and negative directions; however, these rods lost function when the interface between the new and old concrete failed at $1.5\Delta_y$. In another case, threaded rods were welded to steel plates which were welded to the beam bottom bars; the rods were externally connected to a bearing plate at the back of the column (Figure A.1d). Although aesthetically less desirable, this proved to be the most effective scheme in this study. A symmetric and stable hysteretic behavior with reduced pinching was obtained up to $6\Delta_y$ at which point the threaded rods fractured. Ten times more energy was dissipated compared to the control specimen. The GFRP sheets in the joint panel remained effective throughout the test with no signs of debonding.

Balsamo et al. [A.6] and Di Ludovico et al. [A.7] conducted bidirectional pseudo-dynamic tests on a full-scale, three-dimensional, torsionally unbalanced, three-story reinforced concrete frame structure (Figure A.2a, b) before and after a "light intervention" using GFRP composites. The structure represented typical Greek construction practices in the early 1970s with smooth reinforcing bars, no joint transverse reinforcements, lap-spliced column bars at floor levels ($l_{ls} \sim 33\, d_b$), unconfined columns

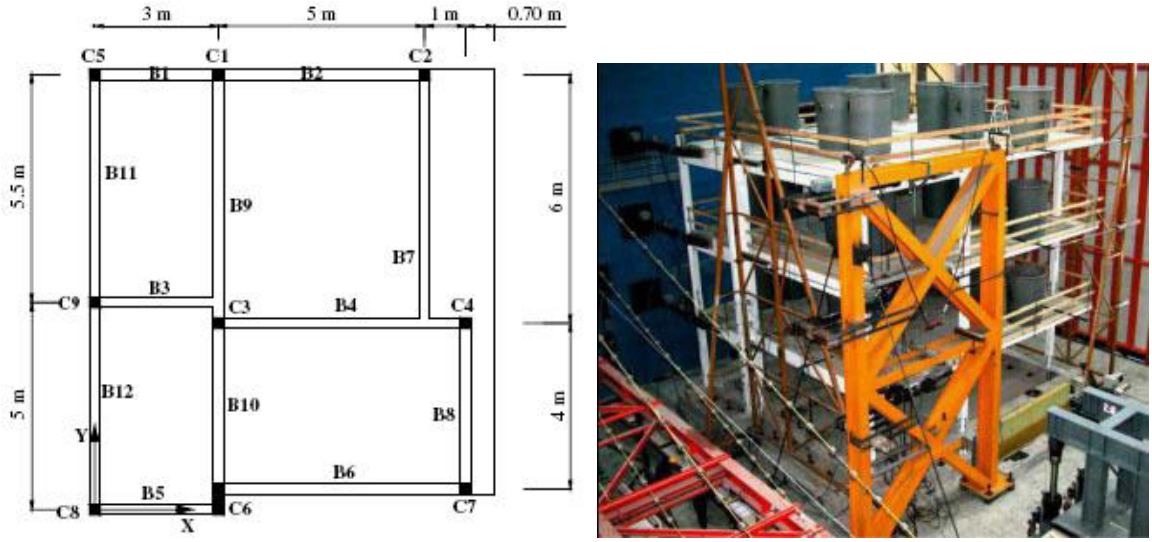

(a) (b)

(c) (d) (e)

Figure A.2 — Retrofit of a full-scale, torsionally unbalanced RC structure by Balsamo et al. [A.6] and Di Ludovico et al. [A.7]: (a) floor plan, (b) test setup, (c) confinement of column ends, (d) strengthening of corner joints, and (e) shear strengthening of the wall-type column.

and beams, f_y=300 MPa, and f_c'=25 MPa. When subjected to a ground motion record with the peak ground acceleration (PGA) scaled to 0.2g, which was applied in a manner that maximized torsional effects, the as-built structure suffered major damage including crushing of concrete at the ends of columns at all stories. Following an assessment based on nonlinear static pushover analysis and capacity spectrum approach, the design of the retrofit scheme was targeted at increasing the displacement capacity of the structure by at least 48% so that the frame would survive a PGA of 0.3g. All column ends were confined (Figure A.2c) and the corner joints were strengthened for shear (Figure A.2d). Only the wall-type column C6 was wrapped along its entire height to increase its shear capacity (Figure A.2e). A change in the strength hierarchy was not intended with such a "light intervention". Column confinement was provided with two layers of a unidirectional, 900g/m^2 GFRP system, the required amount of which was quantified based on the calculated increase in the ultimate compressive strain of concrete and the assumption that increasing the ultimate rotation capacity at the hinge regions to at least twice that of the original member would be necessary. The length of the confined regions was selected as approximately twice the effective plastic hinge length calculated according to Eurocode 8 [A.8]. The shear strengthening design for corner joints was performed by: (1) calculating the shear capacity of the as-built joints based on an equation in Ordinance 3431 [A.9] that takes into account the effect of column axial load and limits the principal tensile stress in exterior joints to $0.3\sqrt{f_c'}$ MPa, (2) selecting the design target joint shear strength as 2.5 times that calculated in Step 1, the reason for which was not explicitly stated, and (3) determining the required amount of FRP according to an approach proposed by Antonopoulos and Triantafillou [A.10] which was previously reviewed in Chapter 2. Two layers of a 1140 g/m^2, multidirectional (0, 90, ±45) GFRP system were used for this purpose. These layers were extended onto the beams 200 mm and U-wrapped (Figure A.2d), but the layers were not extended onto the columns to avoid a reduction in the

rotation capacity of the columns. Retesting of the structure indicated that the retrofit measures did not significantly change the performance of the structure in terms of strength, maximum displacement, or energy dissipation at the previously used PGA level of 0.2g except for the elimination of damage. At the target PGA level of 0.3g, the strength remained unchanged; however, the maximum displacement and the dissipated energy were successfully doubled without significant damage.

Balsamo et al. [A.11] also studied the effectiveness of CFRP composites in restoring the original structural properties of a full-scale, three-dimensional, four-story reinforced concrete structure (Figure A.3a, b) which was initially damaged under pseudo-dynamic unidirectional (along the axis of symmetry) loading up to 1.5 times the "design earthquake." The structure did not represent poor design or detailing practices as in similar studies; one of the frames in the structure was designed according to Eurocode 8 [A.8], and the other was designed according to a deformation-based method. The behavior of the as-built structure was controlled by the shear failure of the shear walls, and damage was also observed at the base of the first-story columns and at the interior beam-wall and beam-column joints in the first two stories. The repair consisted of epoxy injection and the application of the CFRP scheme shown in Figure A.3b with the aim of restoring the original structural properties by increasing the deformation capacity of the columns and the shear capacity of the joints and walls. The CFRP scheme consisted of unidirectional, bidirectional (0, 90), and multidirectional (0, 90, ±45) carbon fabrics. Different fabrics were used on similar components to compare the effectiveness of different layups, which are not detailed here for brevity. The target for joint strengthening was to increase the shear capacity of all joints by at least 25%, the reason for which was not specified. The approach proposed by Antonopoulos and Triantafillou [A.10] was used for this purpose. The sheets placed on the joints were extended onto both the columns and beams by 200 mm. The column confinement was expected to increase the column flexural strength by up to 10% and its ultimate curvature by more than 100% without an

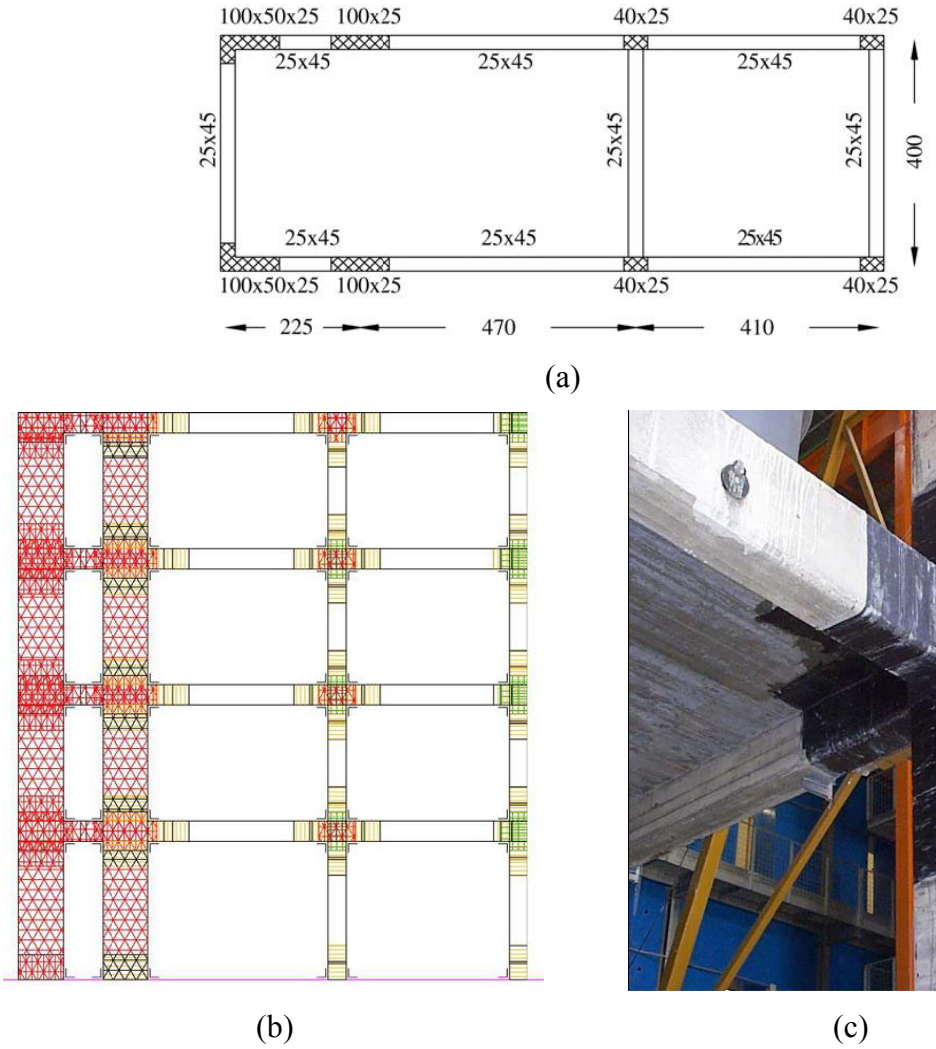

Figure A.3 — Repair of a full-scale RC structure by Balsamo et al. [A.11]: (a) floor plan, (b) CFRP scheme, and (c) finished look of a corner joint.

explicitly stated design target. The column ends were confined over a length of 750 mm (3 times the smaller column width), and the wall ends were confined over 550 mm (2.2 times the smaller wall width). The beams were U-wrapped over a length of at least 400 mm (0.9 times the beam depth) (Figure A.3c). When retested, the structure did not attain the intended improvements because of failures at the column/wall-foundation interfaces. Lower stiffness, no significant increase in the maximum base shear and no change in the total dissipated energy were observed. Overall, these tests highlighted the need for careful examination of the foundations in retrofit efforts.

Pampanin et al. [A.12] studied the predictability of the sequence of failure events in CFRP-strengthened beam-column joints by developing capacity-demand curves for the beam, column and joint within M-N (moment-axial load) performance domains. In developing these curves, each limit state was converted to equivalent column moments (M) at that state. The equivalent curves for the joint were based on simplified analytical models for joint strength degradation (rotational spring within a concentrated plasticity approach) as a function of joint shear deformation and principal tensile stresses in the panel zone. This methodology was validated by quasistatic cyclic testing of interior and exterior one-way beam-column joint specimens and planar, three-story, three-bay frames with and without CFRP strengthening. All test specimens and frames were 2/3-scale and designed according to 1939 Italian code [A.13] with smooth reinforcing bars, no joint transverse reinforcements, lap-spliced column bars at floor levels, and widely spaced column ties. Unlike similar studies, the column axial load was varied in the specimen tests as a linear function of the applied lateral load to simulate more accurately the actual stress level in the joint during lateral cyclic sway of a frame building. In their as-built condition, exterior joint specimens failed due to combined joint shear and beam bar slippage within the joint; interior joint specimen failed due to concentration of damage in the column; and the planar three-bay frame exhibited a behavior similar to that observed in the one-way joint specimens. An attempt to achieve a strong column/weak beam strength hierarchy at the interior joints was deemed unfeasible without major interventions; therefore, a "partial retrofit" was adopted, where all columns were strengthened for flexure; all exterior joints were strengthened for shear to achieve beam hinging; but shear strengthening of interior joints consisted only of CFRP strips placed continuously along the column for flexural strengthening. A unidirectional CFRP system was used. The resulting strengthening schemes for the specimens are shown in Figure A.4a,b, which were also applied to a frame system (Figure A.4c). The specific design approaches for quantification and detailing of CRFP were not reported. The experimental

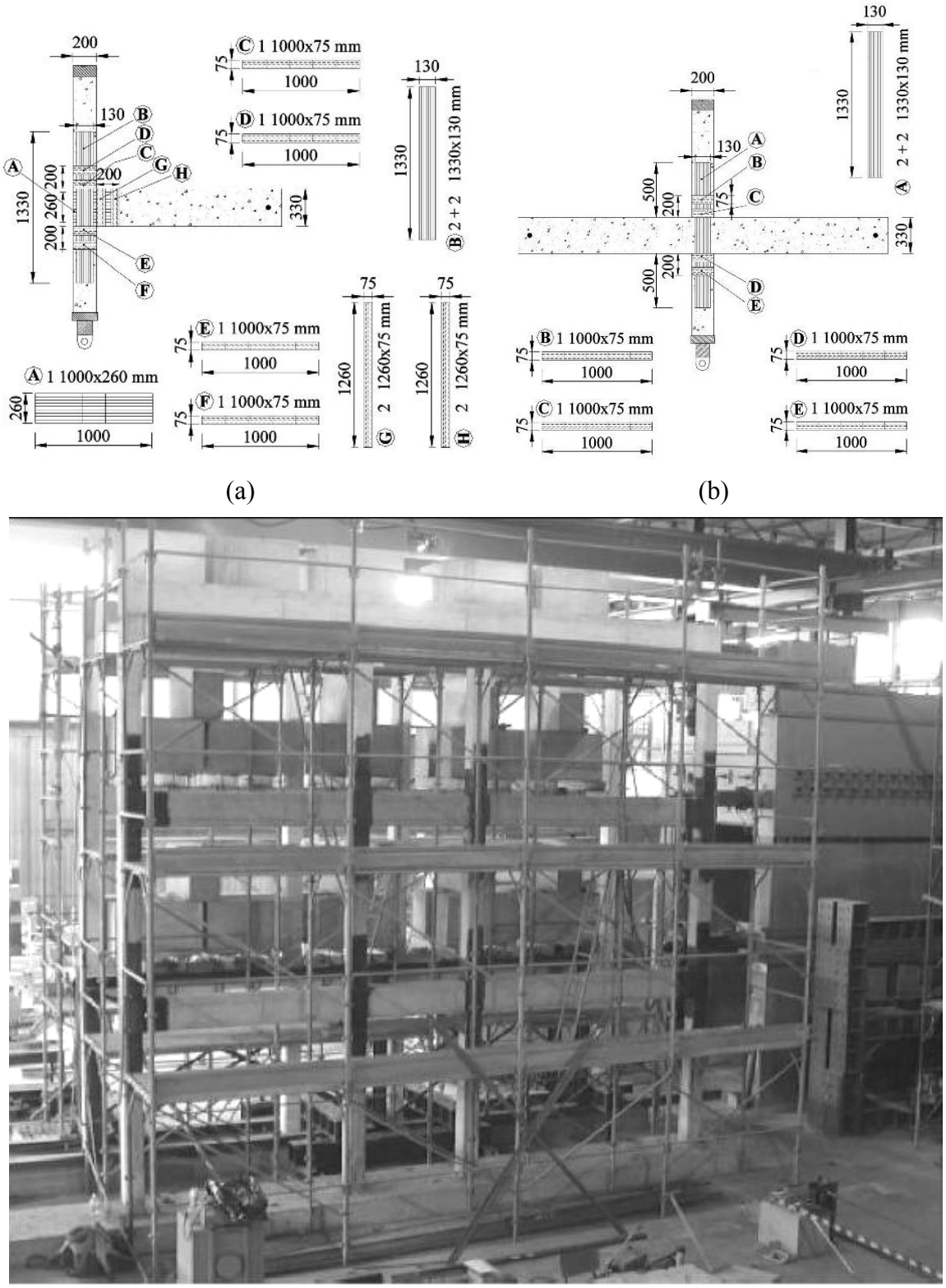

(a) (b)

(c)

Figure A.4 — CFRP-strengthened (a, b) specimens and (c) frame tested by Pampanin et al. [A.12]

results showed that the exterior joint specimens were improved in all hysteretic parameters without any strength degradation up to 3.5% drift and exhibited beam hinging. The improvement in interior joint specimens, however, was limited to some increase in strength with no signs of increased ductility. CFRP strips bonded along the columns continuously through the joint for column flexural strengthening debonded and could only postpone column flexural damage. Strengthening of the test frame with the same schemes used on exterior and interior joint specimens did not seem to alter the behavior of the frame significantly. The strength degradation in the test frame was delayed until 2.0% drift (compared to 1.6% before strengthening), but pinching and lack of energy dissipation persisted.

REFERENCES

[A.1] Said, A. M., and Nehdi, M. L. (2004). "Use of FRP for RC frames in seismic zones: Part I. Evaluation of FRP beam-column joint rehabilitation techniques." *Applied Composite Materials*, 11(4), 205-226.

[A.2] CSA A23.3-94 (1994). *Design of concrete structures*, Canadian Standards Association, Rexdale, Ontario, Canada.

[A.3] FEMA (2000). *Prestandard and commentary for the seismic rehabilitation of buildings (FEMA 356)*, Federal Emergency Management Agency, Washington, D.C.

[A.4] B.R.S. Ingenieros C.A. <http://www.brsingenieros.com.ve> (December 2007).

[A.5] Ghobarah, A., and El-Amoury, T. (2005). "Seismic rehabilitation of deficient exterior concrete frame joints." *Journal of Composites for Construction (ASCE)*, 9(5), 408-416.

[A.6] Balsamo, A., Manfredi, G., Mola, E., Negro, P., and Prota, A. (2005). "Seismic rehabilitation of a full-scale RC structure using GFRP laminates, *SP-230: 7th international symposium on fiber-reinforced (FRP) polymer reinforcement for concrete structures*, American Concrete Institute, Farmington Hills, MI, 1325-1344.

[A.7] Di Ludovico, M., Prota, A., Manfredi, G., and Cosenza, E. (2008). "Seismic strengthening of an under-designed RC structure with FRP." *Earthquake Engineering and Structural Dynamics*, 37(1), 141-162.

[A.8] European Standard, EN 1998-3, Eurocode 8 (2003). *Design of structures for earthquake resistance, Part 3: Strengthening and repair of buildings*, Doc. CEN/TC250/SC8/N343, Draft No. 3, European Committee for Standardization, Brussels, Belgium.

[A.9] Ordinance n. 3431 (2005). *General criteria for seismic classification of national territory and technical guidelines for structures in seismic zones*, Presidenza del Consiglio dei Ministri, Rome, Italy. (in Italian)

[A.10] Antonopoulos, C. P., and Triantafillou, T. C. (2002). "Analysis of FRP-strengthened RC beam-column joints." *Journal of Composites for Construction (ASCE)*, 6(1), 41-51.

[A.11] Balsamo, A., Colombo, A., Manfredi, G., Negro, P., and Prota, A. (2005). "Seismic behavior of a full-scale RC frame repaired using CFRP laminates." *Engineering Structures*, 27(5), 769-780.

[A.12] Pampanin, S., Bolognini, D., and Pavese, A. (2007). "Performance-based seismic retrofit strategy for existing reinforced concrete frame systems using fiber-reinforced polymer composites, *Journal of Composites for Construction (ASCE)*, 11(2), 211-226.

[A.13] Regio Decreto (1939). 16 November-XVIII, n. 2228. (in Italian)

APPENDIX B

DETAILS OF THE EXPERIMENTAL PROGRAM

B.1 MATERIAL PROPERTIES

B.1.1 Concrete

The specimens were cast using normal weight concrete with a specified compressive strength of f_c'=3000 psi (20.7 MPa). Each specimen was cast in two lifts resulting in a cold joint at the floor level. For both Lift 1 and Lift 2 concrete, three compression tests were conducted on the 28th day and on each test day to determine f_c' according to ASTM C 39/C 39M-04a [B.1], and three separate tests were conducted to determine the modulus (E_c) according to ASTM C469-02 [B.2]. All tests were conducted on 6 in. x 12 in. cylinder samples. The averages of the measured properties including the unit weight (w_c) are presented in Table B.1. The time elapsed between the test days before and after strengthening was short enough to not cause changes in concrete properties.

Table B.1 — Average measured concrete properties.

		Specimen 1		Specimen 2		Specimen 3		Specimen 4	
		Lift 1	Lift 2	Lift 1	Lift 2	Lift 1	Lift 2	Lift 1	Lift 2
f_c' (psi)	28th day	2880	3600	3540	2820	3540	2820	1110	2820
	Test days	3740	4950	5010	4140	4910	4040	2230	3790
E_c (ksi)	28th day	2520	2920	2520	2240	2520	2240	1720	2240
	Test days	3140	2930	3120	2920	3400	3230	2900	3230
w_c (lb/ft^3)		144	146	143	146	143	146	135	146

B.1.2 Reinforcing Bars

Two series of tests were conducted on the reinforcing bars. In the first series, the stress-strain curves under monotonic tensile loading were obtained according to ASTM A370-03a, Annex 9 [B.3] up to ultimate (i.e. break) for the #3, #5, and #6 Grade 40 reinforcing bars and up to 85 ksi stress (due to capacity of testing machine) for the #7 Grade 60 bars used for flexural strengthening of the column during retrofit. The average values of parameters characterizing the stress-strain curves for each bar size are tabulated in Table B.2, and typical curves are presented in Figure B.1. The number of samples used for obtaining each reported average value is shown in parentheses in Table B.2.

The second series of tests were conducted to characterize the stress-strain curves of the #6 beam bars and the #3 slab bars under various cases of cyclic loading so that the forces transferred to the joint during the beam-column joint tests could be determined. These cyclic rebar tests were conducted after reviewing the strain histories recorded during the beam-column joint tests and identifying the main loading-unloading mechanisms. For the #6 bars, obtaining the stress-strain curves presented in Figure B.2 to Figure B.7 was found sufficient to determine the forces in all beam top bars throughout the tests. For the #3 bars, only the curve presented in Figure B.8 was obtained, and the general findings from the tests on #6 bars were utilized. Test parameters such as sample length, loading and unloading rates, and instrumentation are listed below each figure.

Table B.2 — Average measured reinforcing bar properties under monotonic tensile loading.

	Grade 40			Grade 60
	#3	#5	#6	#7**
f_y (ksi)	53.2 (9)*	51.1 (9)	45.7 (9)	64.6 (3)
ε_y (με)	1740 (6)	1890 (6)	1620 (6)	2310 (3)
E_s (ksi)	30,780 (6)	26,870 (6)	28,190 (6)	27,970 (3)
f_y' (ksi)	55.1 (4)	52.9 (5)	47.7 (13)	-
ε_{sh} (με)	24,720 (6)	13,250 (6)	18,070 (6)	4600 (3)
f_u (ksi)	74.8 (8)	77.2 (8)	68.6 (9)	-
f_u' (ksi)	57.3 (8)	63.2 (8)	56.5 (9)	-
ε_u (με)	259,240 (5)	224,980 (4)	257,830 (6)	-

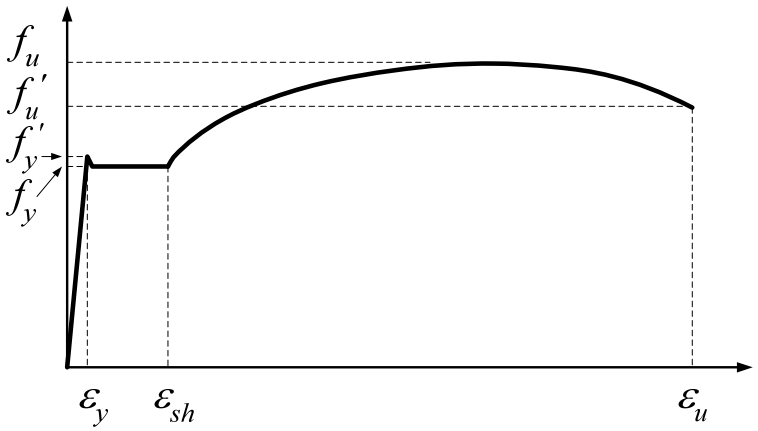

Test Method: ASTM A370-03a, Annex 9 [B.3]

Sample Clear Length = 8 in. + $4d_b$

* Numbers in parentheses indicate the number of test samples used to obtain the reported average.

** #7 bars were used only for flexural strengthening of the column during retrofit.

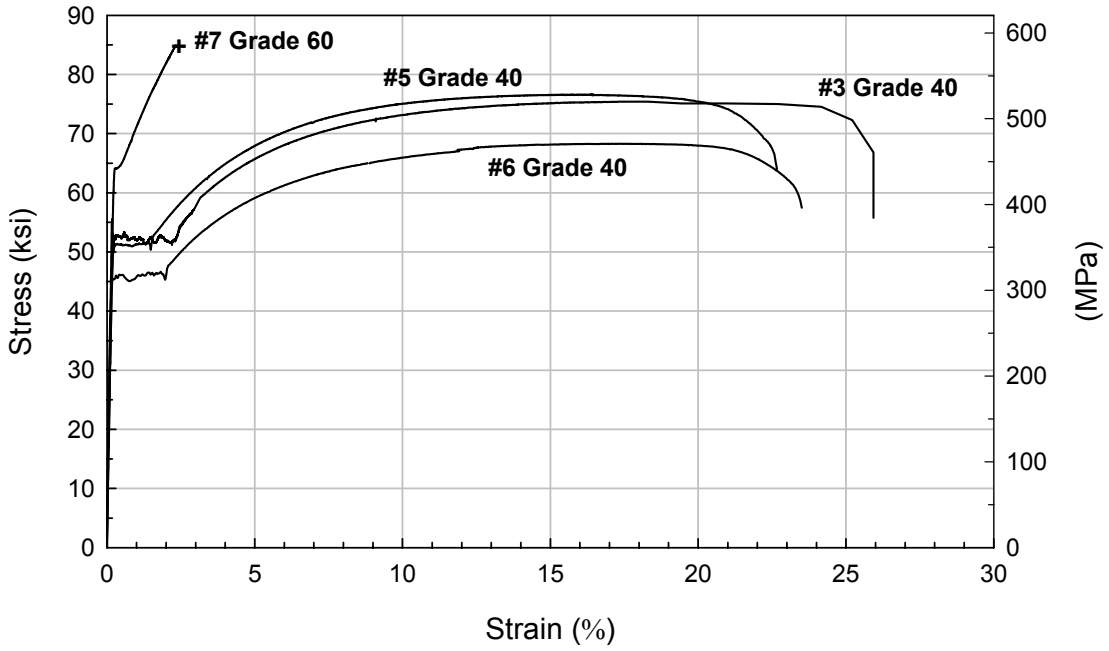

Sample clear length = 8 in. + $4d_b$, Instrumentation: LVDT over 8 in. gage length, Loading: 0.005 in./min

Figure B.1 — Monotonic tensile stress-strain behavior of the reinforcing bars. (Note: #7 bars were not loaded to ultimate)

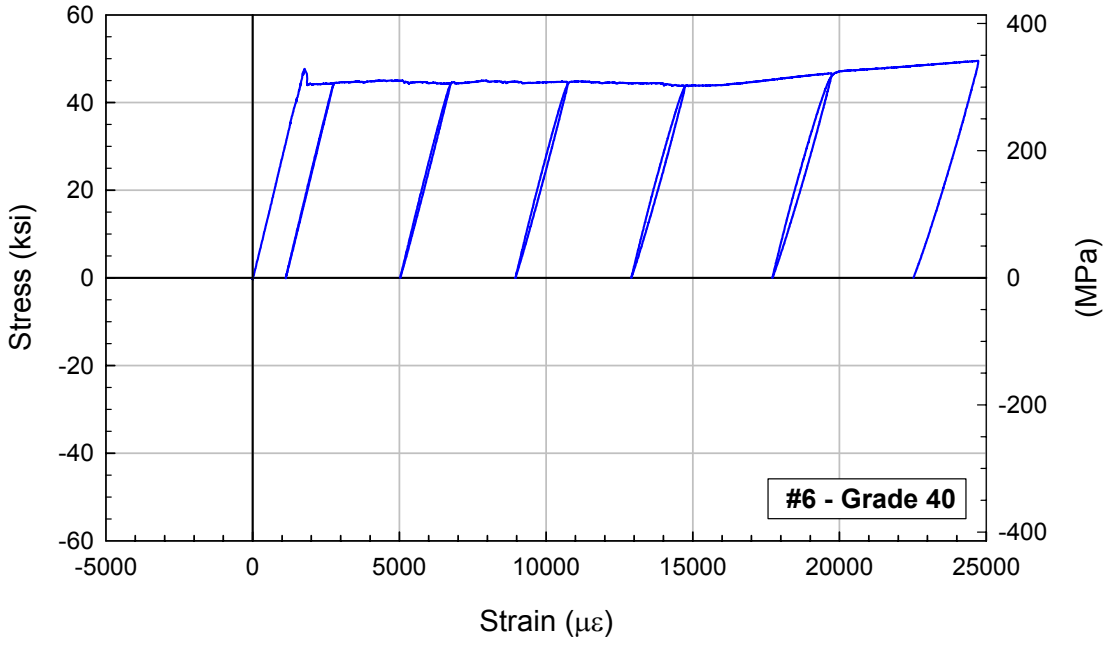

Sample clear length = 2 in. + $4d_b$, Instrumentation: extensometer with 2 in. gage length, Loading: 1000 με/min, Unloading: -10,000 lb/min

Figure B.2 — Cyclic stress-strain behavior of #6 reinforcing bars – Case 1.

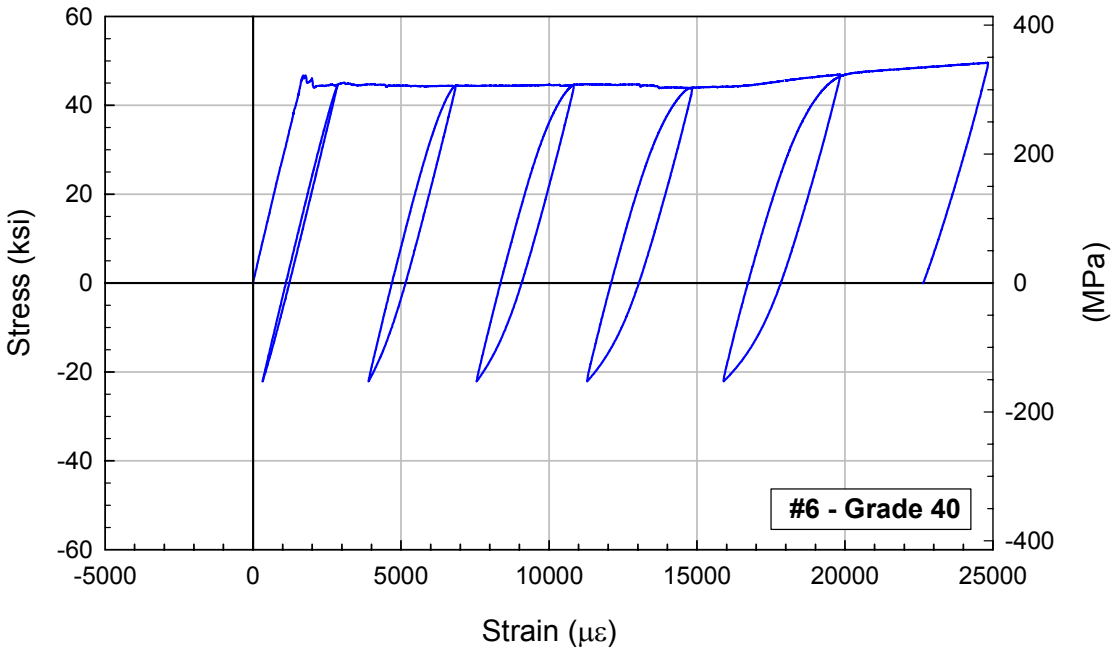

Sample clear length = 2 in. + 4d_b, Instrumentation: extensometer with 2 in. gage length, Positive loading: 1000 με/min, Negative loading: -10,000 lb/min

Figure B.3 — Cyclic stress-strain behavior of #6 reinforcing bars – Case 2.

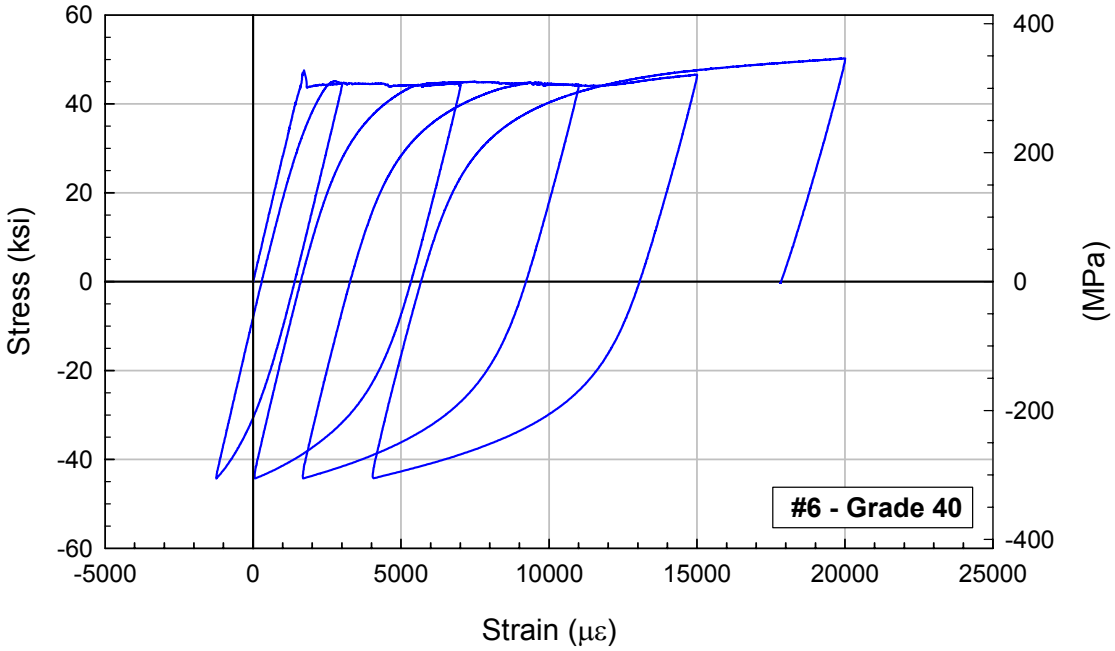

Sample clear length = 2 in. + 4d_b, Instrumentation: extensometer with 2 in. gage length, Positive loading: 1000 με/min, Negative loading: -10,000 lb/min

Figure B.4 — Cyclic stress-strain behavior of #6 reinforcing bars – Case 3.

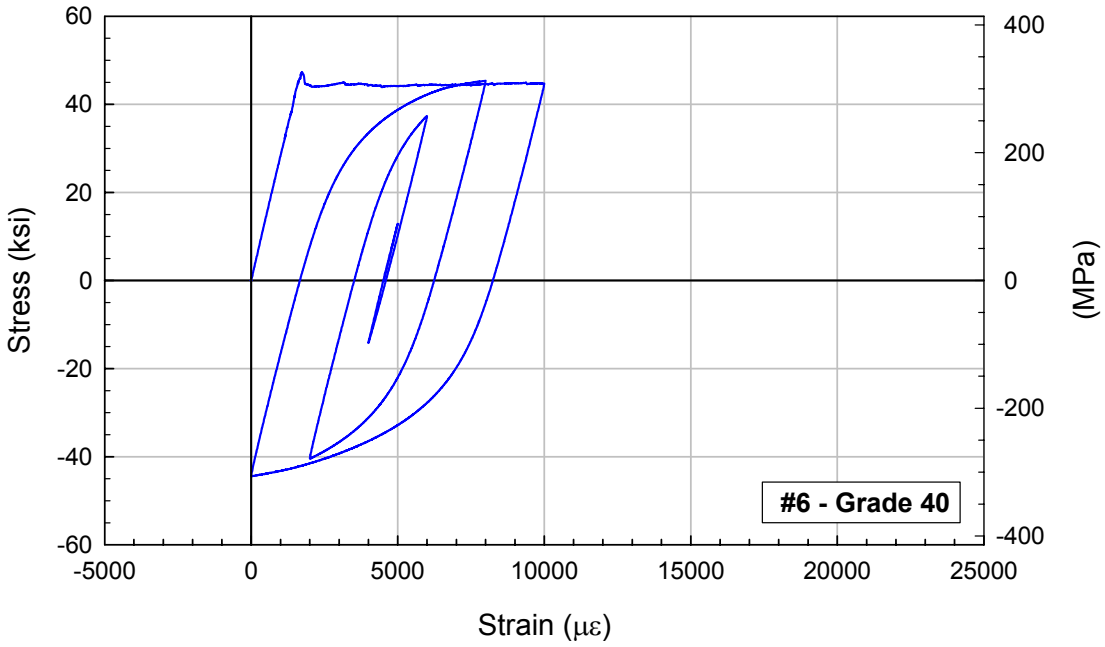

Sample clear length = 2 in. + 4d_b, Instrumentation: extensometer with 2 in. gage length, Loading: ±1000 με/min

Figure B.5 — Cyclic stress-strain behavior of #6 reinforcing bars – Case 4.

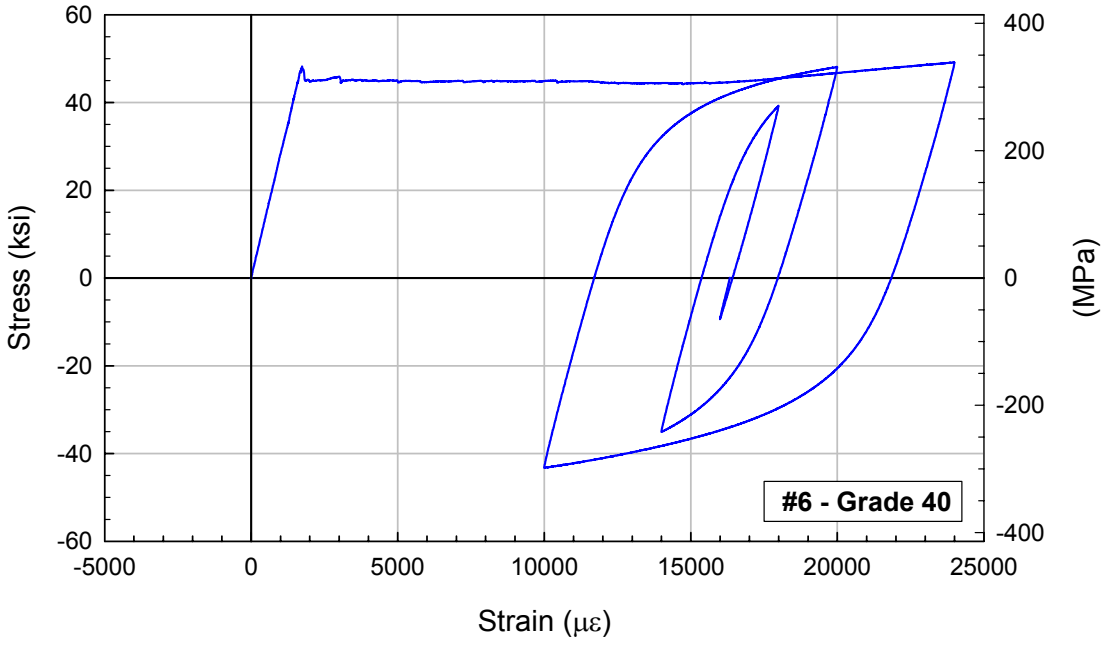

Sample clear length = 2 in. + 4d_b, Instrumentation: extensometer with 2 in. gage length, Loading: ±1000 με/min

Figure B.6 — Cyclic stress-strain behavior of #6 reinforcing bars – Case 5.

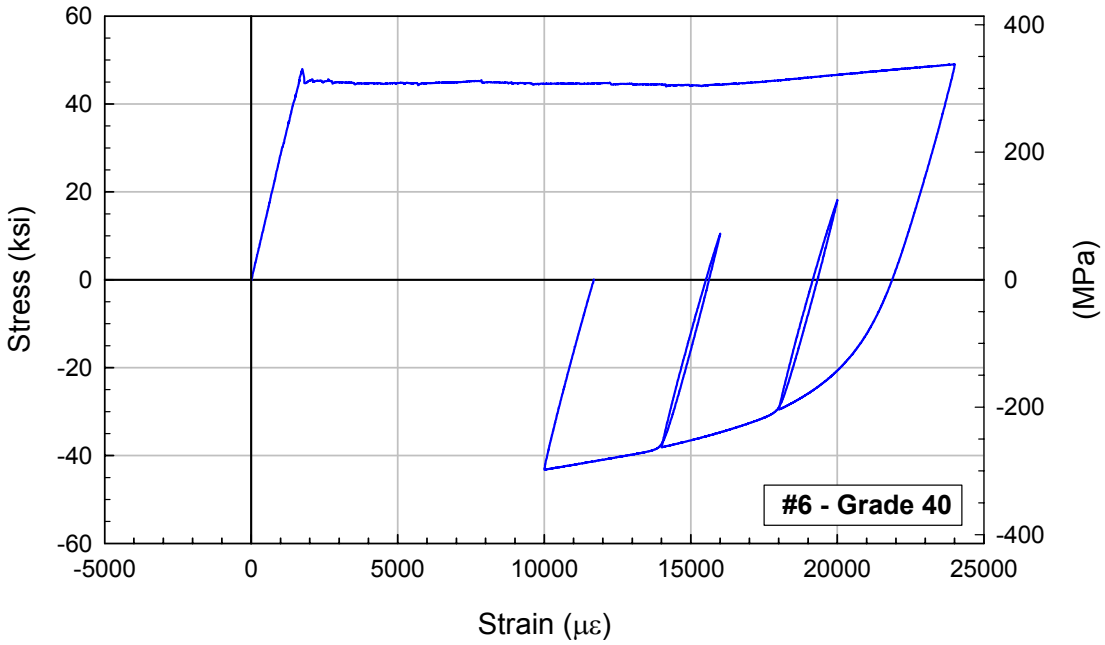

Sample clear length = 2 in. + 4d_b, Instrumentation: extensometer with 2 in. gage length, Loading: ±1000 με/min

Figure B.7 — Cyclic stress-strain behavior of #6 reinforcing bars – Case 6.

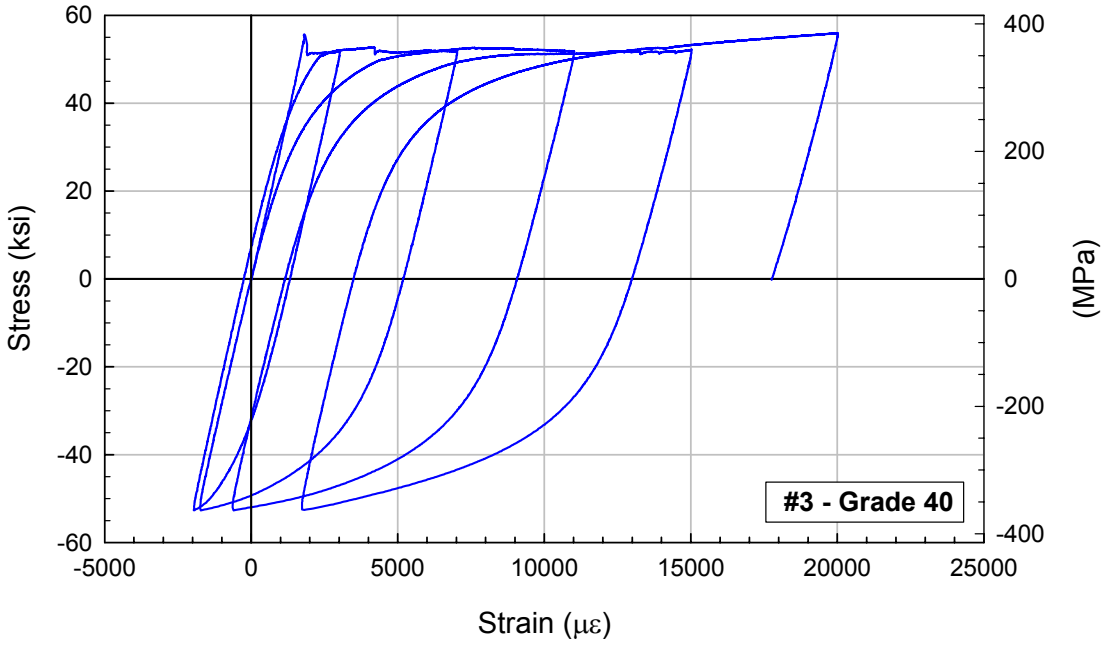

Sample clear length = 1 in. + 4d_b, Instrumentation: extensometer with 1 in. gage length, Positive loading: 1000 με/min, Negative loading: -2500 lb/min

Figure B.8 — Cyclic stress-strain behavior of #3 reinforcing bars.

B.1.3 Carbon Fiber-Reinforced Polymer (CFRP)

All CFRP strengthening schemes tested in this study were tailored from a 9 oz/yd^2 unidirectional carbon fabric impregnated with a high-modulus, high-strength epoxy resin. The material properties of the fabric and resin reported by the manufacturer are presented in Figure B.9. Additional tests conducted on these materials are presented below.

B.1.3.1 Thermal Properties of Resin

As with most impregnating resins commonly used for external bonding of FRP composites to concrete structures, the thermal property of the resin reported by the manufacturer (i.e. heat deflection temperature=50°C after 7 days at a temperature of 23°C and 50% relative humidity) raised a concern about the mobility of the molecular chain structure in high operating temperature ranges that are often encountered around the world. Another point of interest was the rate of cure, since in many rehabilitation projects it would be desirable to cure the resin as quickly as possible. To address such concerns, a series of differential scanning calorimetry (DSC) tests were conducted according to ASTM D 3418 [B.4] on resin samples that were subjected to two different curing schedules. In one case, test samples were taken from a witness plate that was kept at 23±2°C, and DSC tests were conducted on day 1, 2, 4, 9, and 63 (5 samples on each day) after making the witness plate. Typical DSC output thermograms obtained on each day (Figure B.10a) indicated a slow rate of cure and an average glass-transition temperature (T_g) of only 56°C after 63 days. In another case, test samples were taken from a witness plate that was first subjected to a temperature of 80±4°C for 6 hours, then kept at 23±2°C. The results from DSC tests conducted on day 1, 2, 4, and 9, which are presented in Figure B.10b, indicated that curing of the resin had been completed (i.e. vanishing of the area under the right hand side of the curves) after 6 hours of exposure to 80±4°C, and that T_g was 70°C. The variation of T_g with time is presented in Figure B.11 for both room-temperature cure and for heat-cure.

Typical Data

Storage Conditions	Store dry at 40°-95°F (4°-35°C)
Color	Black
Primary Fiber Direction	0° (unidirectional)
Weight per Square Yard	9.0 oz. (300 g/m²)
Cured Laminate Properties (Design Values)	
Tensile Strength	1.05 x 10^5 psi (724 MPa)
Modulus of Elasticity	8.2 x 10^6 psi (56,500 MPa)
Elongation at Break	1.0%
Thickness	0.02 in. (0.51 mm)
Strength per Inch Width	2,100 lbs./layer (9.3 kN)
Fiber Properties	
Tensile Strength	550,000 psi (3,793 MPa)
Tensile Modulus	34 x 10^6 psi (234,000 MPa)
Elongation	1.5%
Density	0.065 lbs/in³ (1.8 g/cc)

(a) SikaWrap Hex® 117C fabric

Typical Data *(Material and curing conditions @ 73°F (23°C) and 50% R.H.)*

Shelf Life	2 years in original, unopened container.
Storage Conditions	Store dry at 40°-95°F (4°-35°C). **Condition material to 65°-75°F (18°-24°C) before using.**
Color	Light gray.
Mixing Ratio	Component 'A' : Component 'B' = 4 : 1 by weight
Consistency	Non-sag paste.
Pot Life	57 minutes (325 ml)
Tack Free Time	4-5 hours
Heat Deflection Temperature (ASTM D-648)	
7 day [fiber stress loading=264 psi (1.8 MPa)	120°F (50°C)

Mechanical Properties

Compressive Properties (ASTM D-695), psi (MPa)

	40°F (4°C)	60°F (16°C)	73°F (23°C)	90°F (32°C)
8 hour	-	-	-	8,000 (55.2)
1 day	-	8,100 (55.8)	10,700 (73.7)	10,600 (73.1)
3 day	8,100 (55.8)	11,200 (77.2)	11,100 (76.5)	11,000 (75.8)
7 day	11,200 (77.2)	11,600 (80.0)	11,200 (77.2)	11,800 (81.3)
14 day	12,500 (86.2)	12,400 (85.5)	11,800 (81.3)	11,900 (82.0)

Tensile Strength (ASTM D-638)	**7 day**	4,900 psi (33.8 MPa)
Elongation @ Break (ASTM D-638)	**7 day**	1.9%
Flexural Strength (ASTM D-790)	**7 day**	8,800 psi (60.6 MPa)
Flexural Modulus (ASTM D-790)	**7 day**	5.06 x 10^5 psi (3,489 MPa)

(b) Sikadur® 330 US resin

Figure B.9 — Fabric and resin properties reported by the manufacturer [B.5].

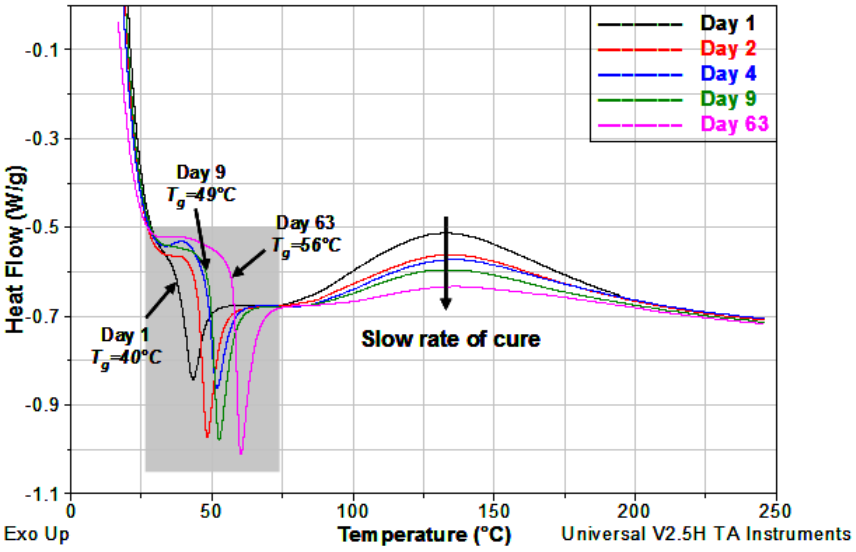

(a) Room temperature cure (23±2°C)

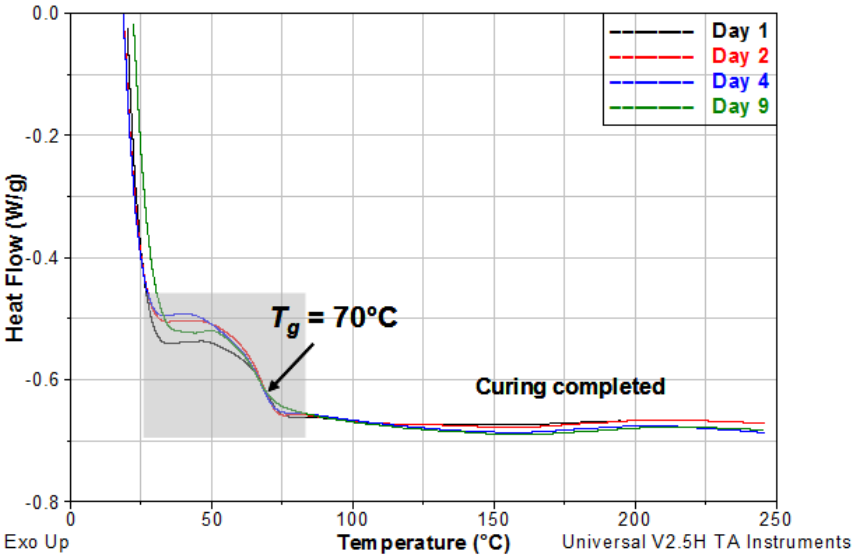

(b) Heat cure (80±4°C for 6 hours)

Figure B.10 — Glass-transition temperature (T_g) and rate of curing of the epoxy resin based on DSC thermograms.

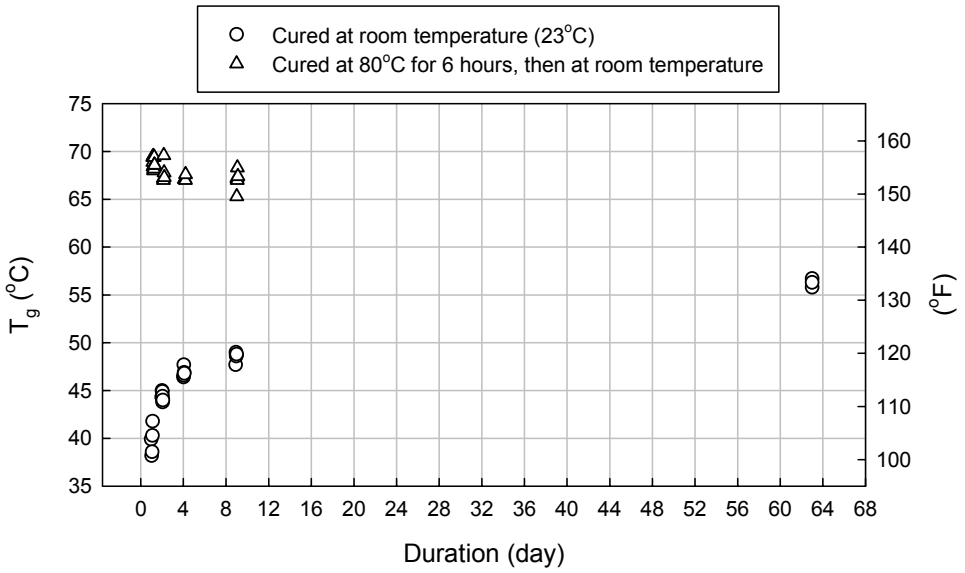

Figure B.11 — Variation of the glass-transition temperature (T_g) of the epoxy resin with time.

Heat-curing at 80°C for 6 hours improved the thermal properties of the resin as intended and was considered applicable in actual construction.

B.1.3.2 Tensile Strength of CFRP Sheets

Tensile strength of the CFRP sheets used in strengthening of the specimens may be different from the "design values" reported by the manufacturer (maximum load P_u^{CFRP}=2100 lb/in./layer, maximum strain ε_u^{CFRP}=1.0% in Figure B.9a) because of the uncertainties associated with the hand-layup process and because the CFRP systems were heat-cured in this study. To determine the properties attained in actual application, a single-layer, 24 in. x 24 in. witness plate was made during the retrofit of Specimen 1 using the same technique that was used for the specimen. The witness plate contained 41.9% fibers by weight which corresponded to a fiber volume ratio of 33.6% assuming a 4% void volume in the system based on previous experience in similar applications. The plate was first subjected to the same heat-curing schedule applied to the specimen (i.e. 80°C for 6 hours), then kept at room temperature (23°C) until testing (after 37 days). Ten

coupons were cut from the plate, prepared, and tested according to ASTM D 3039/D 3039M-00 [B.6] using an MTS hydraulic testing machine. The coupon dimensions are shown in Figure B.12a. Phenolic tabs with tapered ends were used at the coupon ends to uniformly distribute the gripping pressure. The strain was measured using an extensometer with a 1 in. gage length up to a strain of 0.7% at which point the extensometer was removed. The strain at ultimate (ε_u^{CFRP}) was approximated by linear extrapolation of the measured portion of the load-deformation curves up to the maximum measured load. The obtained load-deformation curves are presented in Figure B.12b, and the results for all coupons are presented in Table B.3. The following average values were obtained: P_u^{CFRP}=2930 lb/in./layer, and ε_u^{CFRP}=1.52%. It was found that the use of the "design values" reported by the manufacturer (i.e. P_u^{CFRP}=2100 lb/in./layer, ε_u^{CFRP}=1.00%) was safe, although those values would result in several more layers of CFRP than what would be called for if the properties that can be attained in the actual strengthening application were used.

B.1.3.3 Elastic Constants of CFRP Sheets

For use in analytically determining the elastic constants of all CFRP layups designed for retrofit in Appendix E, the effective elastic constants of a single-layer unidirectional CFRP (lamina) were calculated using the rule of mixture:

$$E_{11} = E_f V_f + E_m V_m \tag{B.1}$$

$$E_{22} = \frac{E_f E_m}{E_f V_m + E_m V_f} \tag{B.2}$$

$$\nu_{12} = \nu_f V_f + \nu_m V_m \tag{B.3}$$

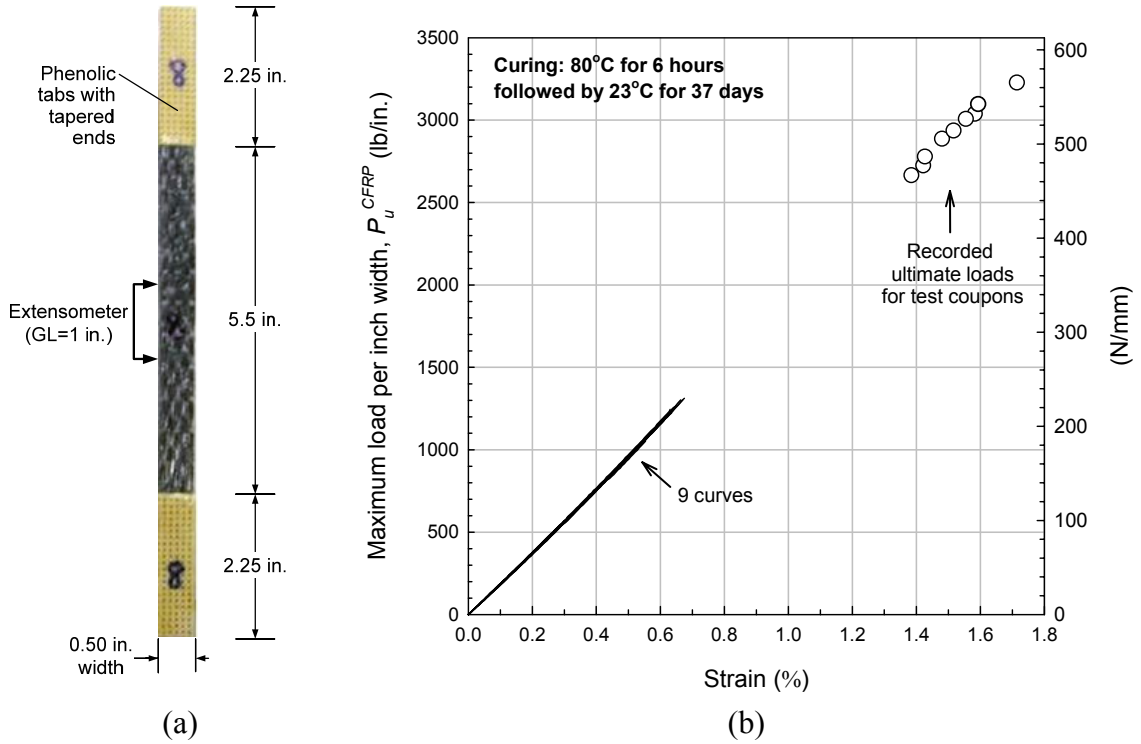

(a) (b)

Figure B.12 — Tensile coupon tests: (a) coupon dimensions, and (b) load-strain curves.

Table B.3 — Results of tension tests on coupons cured at 80±4°C for 6 hours.

Coupon	Width[a] (in.)	Thickness[a] (in.)	Max load (lb/in.)	Max strain (%)	Axial stiffness (lb/in.)
1	0.545	0.027	3230	1.71	188,890
2	0.550	0.027	3040	1.58	192,410
3	0.554	0.027	2890	1.48	195,270
4	0.537	0.027	3010	1.56	192,950
5[b]	~~0.545~~	~~0.028~~	~~2210~~	~~1.19~~	~~185,710~~
6	0.520	0.026	2940	1.52	193,420
7	0.541	0.028	2720	1.42	191,550
8	0.530	0.027	2670	1.38	193,480
9	0.530	0.027	3100	1.59	194,970
10	0.533	0.027	2780	1.43	194,410
Average	0.538	**0.027**	**2930**	**1.52**	**193,040**
COV (%)	2.0	1.9	6.3	6.8	1.0%

[a] The reported width and thickness are the averages of three values measured at different locations along the length.

[b] Coupon 5 was an outlier and was removed from the data set.

$$G_{12} = \frac{G_f G_m}{G_f V_m + G_m V_f} \tag{B.4}$$

where E_{11} and E_{22} are the longitudinal and transverse moduli, ν_{12} is the Poisson's ratio, and G_{12} is the shear modulus of the lamina; E_f, ν_f, and G_f are the elastic modulus, Poisson's ratio, and shear modulus of the carbon fiber, respectively; E_m, ν_m, and G_m are the elastic modulus, Poisson's ratio, and shear modulus of the epoxy resin, respectively; and V_f and V_m are the volume ratio of fibers and resin in the lamina, respectively [B.7]. The following values were reported by the manufacturer: E_f=34,000 ksi, E_m=258 ksi. For other parameters, typical values for carbon fibers and epoxy resin were assumed: ν_f=0.20, G_f=2000 ksi, ν_m=0.35, and $G_m = E_m / 2(1+\nu_m)$=96 ksi. The fiber volume ratio (V_f) was determined from:

$$V_f = \frac{1 - V_v}{1 + \frac{\delta_f}{W_f} \cdot \frac{W_m}{\delta_m}} = \frac{1 - 0.04}{1 + \frac{112.3 lb/ft^3}{0.419} \cdot \frac{0.581}{84 lb/ft^3}} = 33.6\% \tag{B.5}$$

where V_v is the volume of voids; δ_f and δ_m are the density of the fibers and resin, respectively; and W_f and W_m are the weight ratios of the fibers and resin in the lamina, respectively. A void volume of 4% was assumed based on previous experience in similar hand-layup applications. W_f and W_m were determined from the amount of resin used for making a witness plate. The resin volume ratio (V_m) was then obtained as:

$$V_m = 1 - V_f - V_v = 1 - 0.336 - 0.04 = 62.4\% \tag{B.6}$$

Finally, from Equations B.1 through B.4, the elastic constants of the lamina were obtained as: E_{11}=11,720 ksi, E_{22}=414 ksi, ν_{12}=0.285, and G_{12}=151 ksi.

B.2 REINFORCEMENT DETAILS

All specimens had identical reinforcement details which are presented in Figures B.13 through B.18.

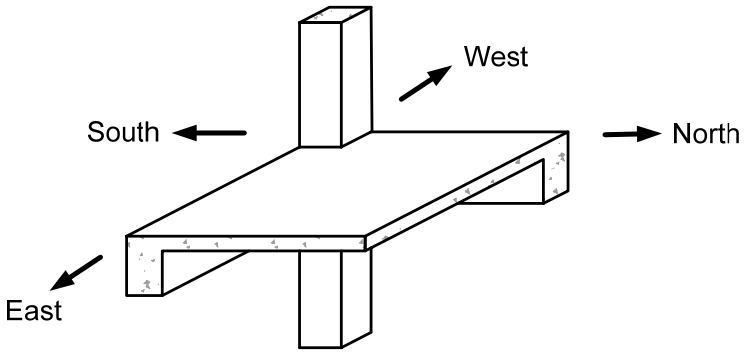

Figure B.13 — Primary frame directions.

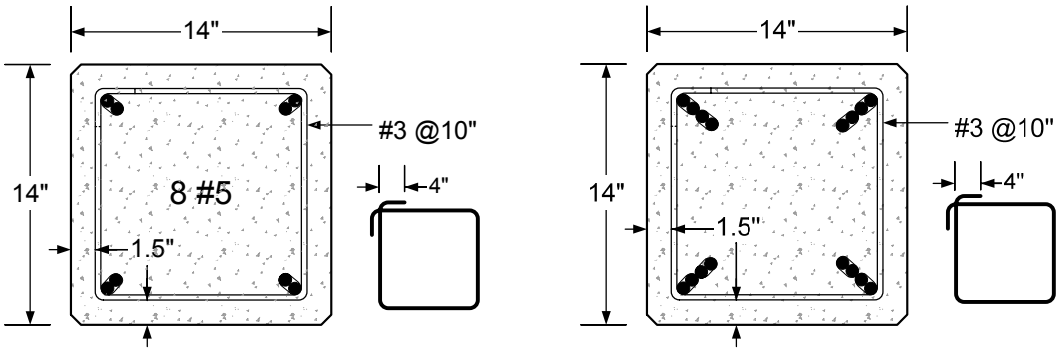

(a) Lower column (b) Upper column lap splice region

Figure B.14 — Column longitudinal reinforcements.

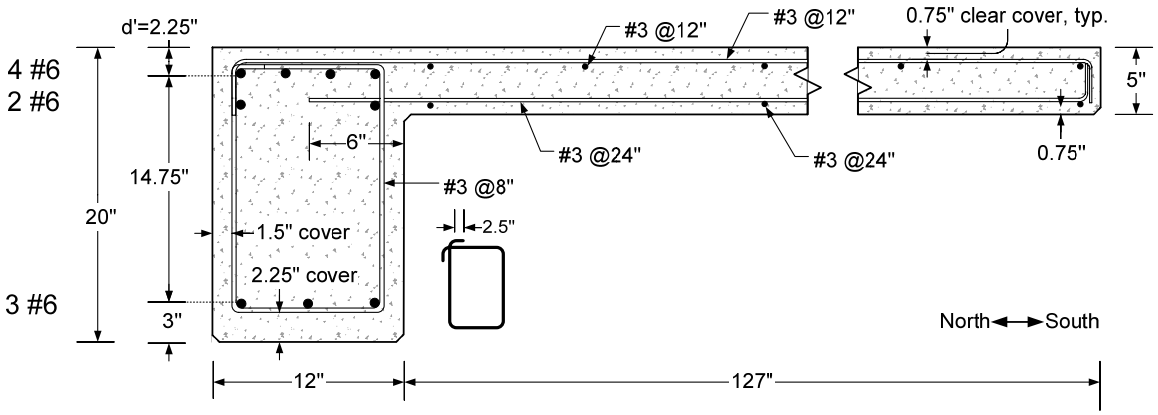

(a) EW beam

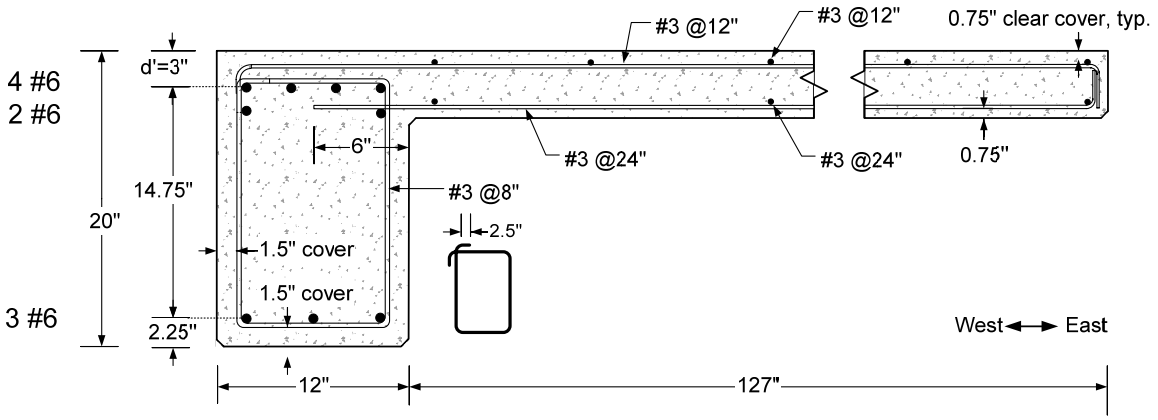

(b) NS beam

Figure B.15 — Beam longitudinal reinforcements.

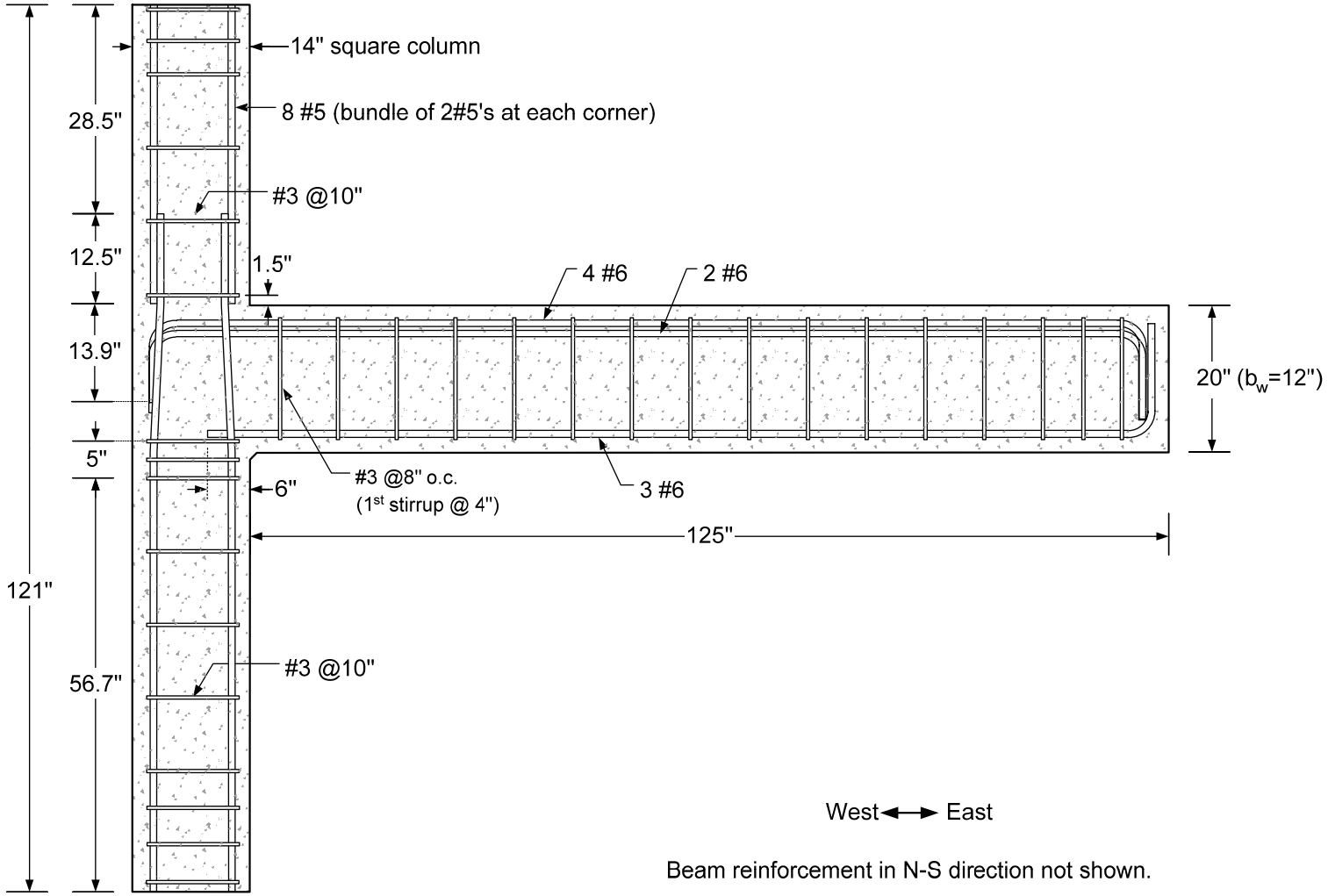

Figure B.16 — Transverse reinforcements in the EW direction (identical in the NS direction).

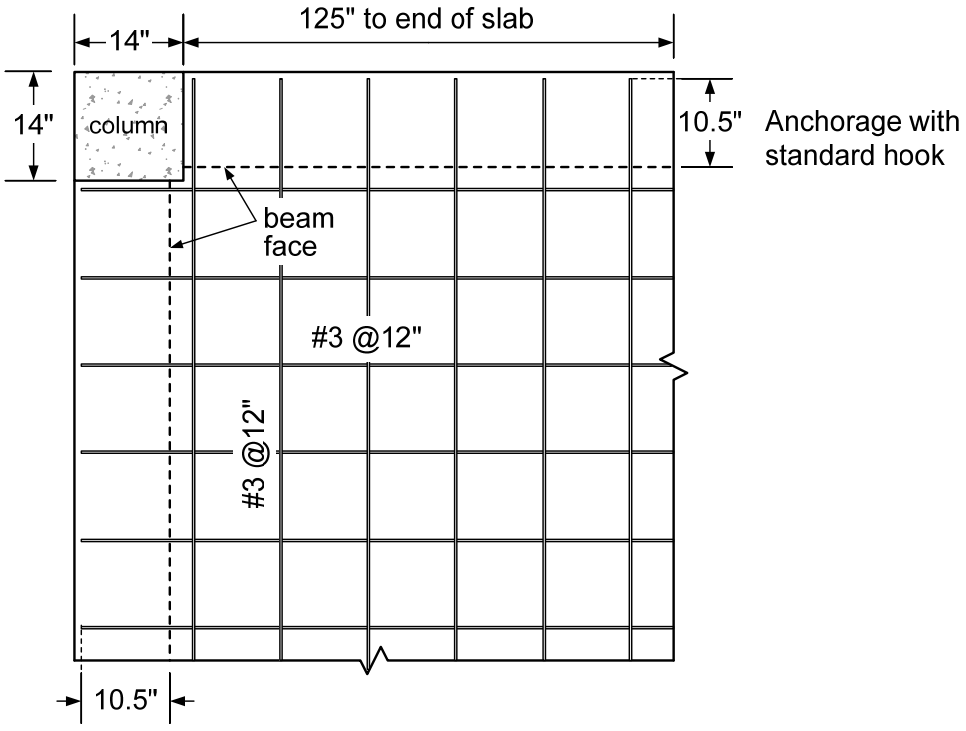

(a) Top layer

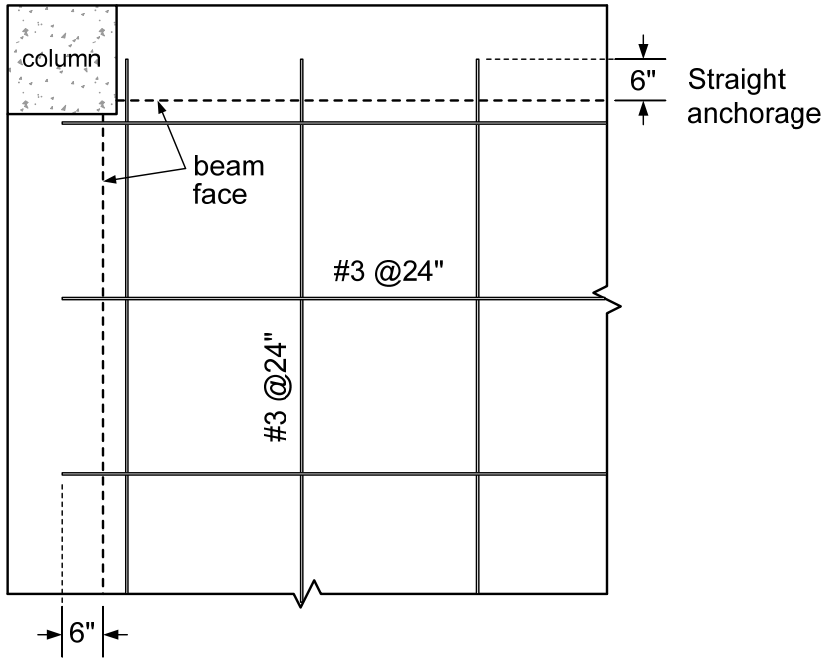

(b) Bottom layer

Figure B.17 — Slab reinforcements.

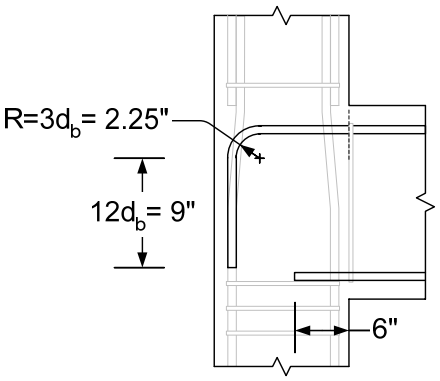

(a) Beam top and bottom bars

(b) View of beam bottom bars in the joint

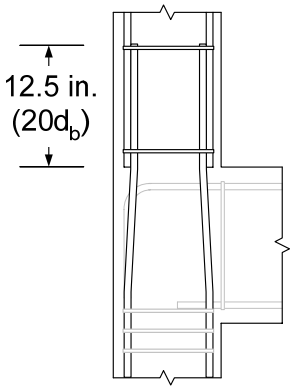

(c) Column lap-splice

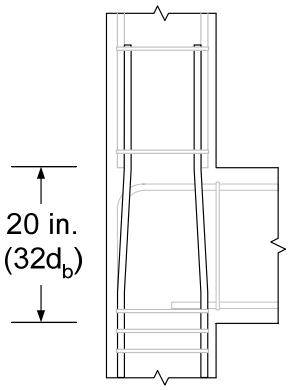

(d) Column bars passing through the joint

Figure B.18 — Critical reinforcement anchorages.

B.3 TEST SETUP

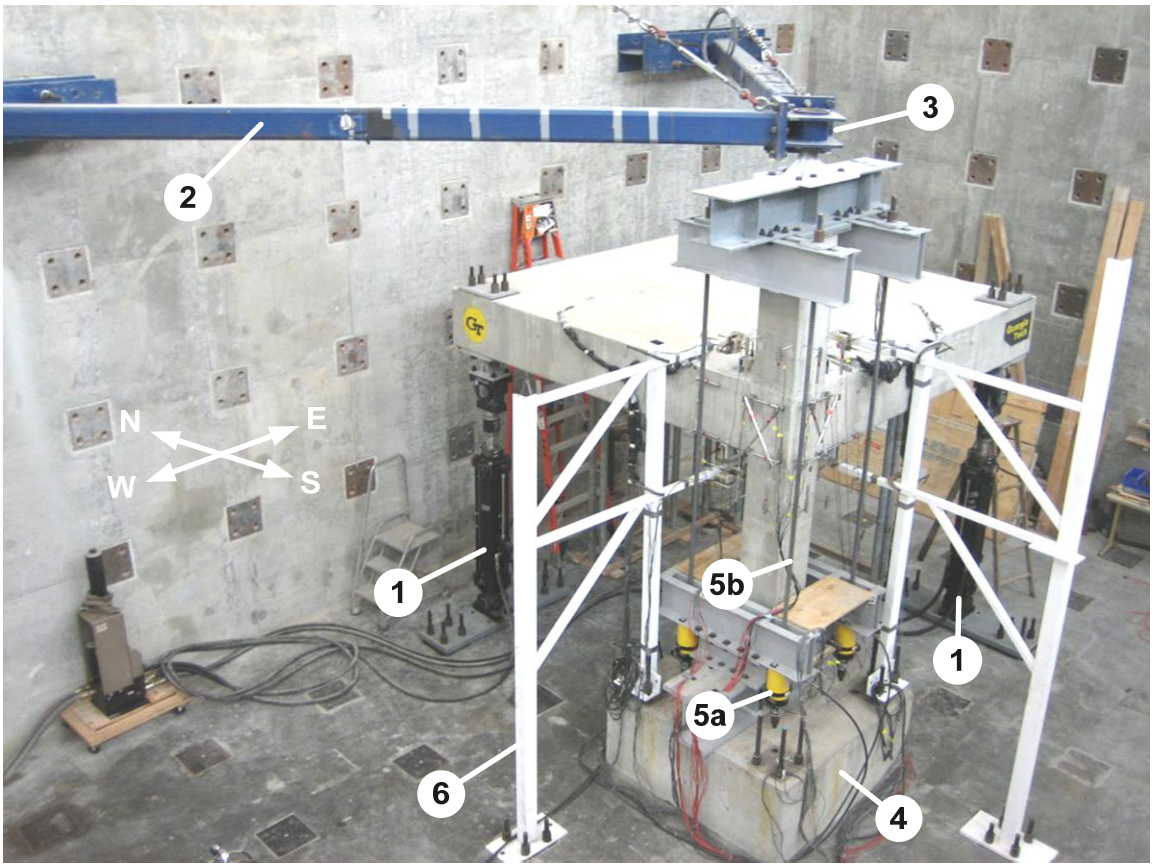

(1) Actuators, (2) Reaction frame, (3) Universal joint (3-D pin support), (4) Fixed support, (5) Application of column axial load: (5a) Center-hole hydraulic jacks, (5b) DWYDAG bars, (6) Fixed reference frame

Figure B.19 — Components of test setup.

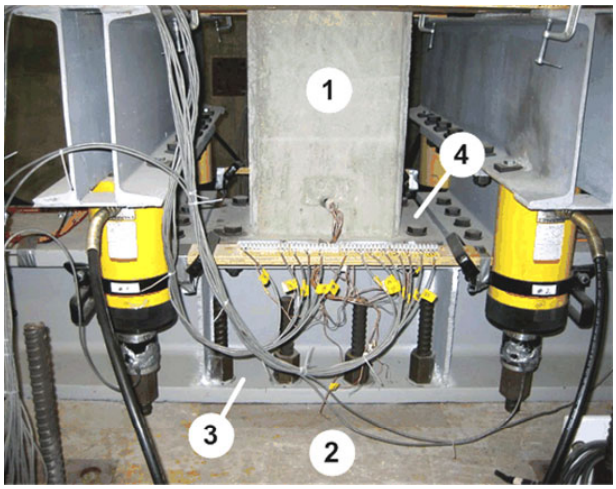

(a) Column base during test

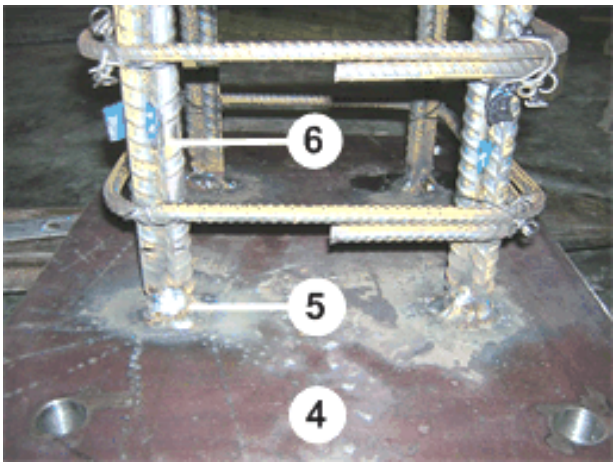

(b) Column cage-to-base plate connection

(1) Column, (2) Concrete block post-tensioned to strong floor, (3) Steel beam post-tensioned to concrete block, (4) Base plate bolted to steel beam, (5) Weld, (6) Column longitudinal bars

Figure B.20 — Fixed support at the bottom of column.

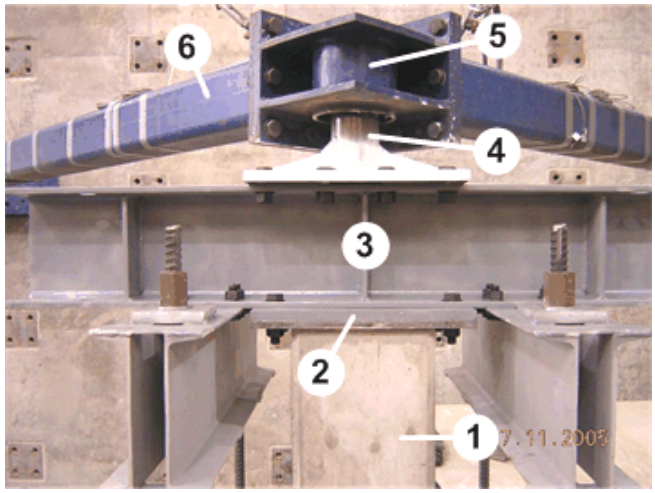

(a) Overall view

(1) Column, (2) Top steel plate with 4#5 reinforcing bars welded to it which are lap-spliced onto column longitudinal bars, (3) Steel beam bolted to column top steel plate, (4) Steel shaft welded on a steel plate bolted to the steel beam, (5) Steel cylindrical housing with spherical plain bearing

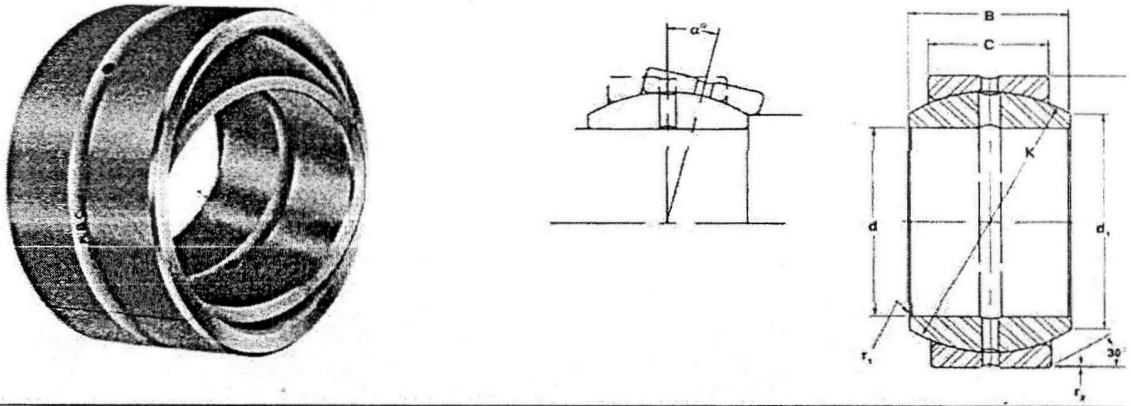

Part Number		d Inside Diameter			D Outside Diameter			B Inner Ring Width +0.000 -0.005	C Outer Ring Width +0.000 -0.005	K Sphere Dia. (REF)	Unmounted Diametral Clearance	d1 Shaft Shoulder Dia.	α Tilt Angle ❶ (deg)
Open	Sealed	Nom.	Max.	Min.	Nom.	Max.	Min.						
B80-9L	B80-9LSS	5	5.0000	4.9990	7 3/4	7.7500	7.7488	4.375	3.750	7.190	0.005/0.009	5.703	7

(b) Detail of spherical plain bearing in the universal joint [B.8]

Figure B.21 — Universal joint at the top of the column. Allows rotation in any direction and vertical translation.

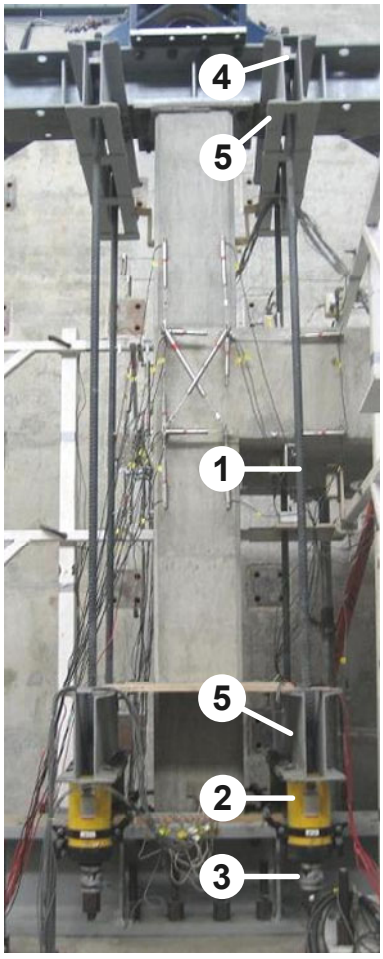

(a) Column elevation

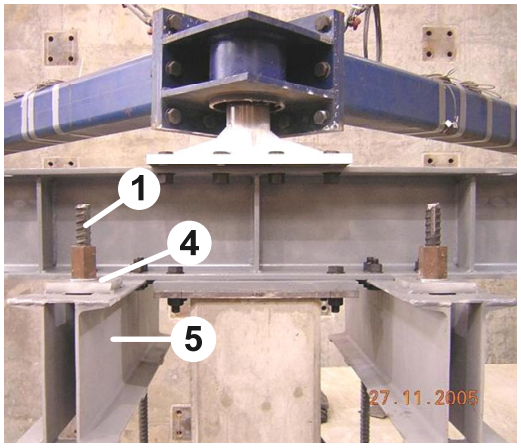

(b) Column top detail

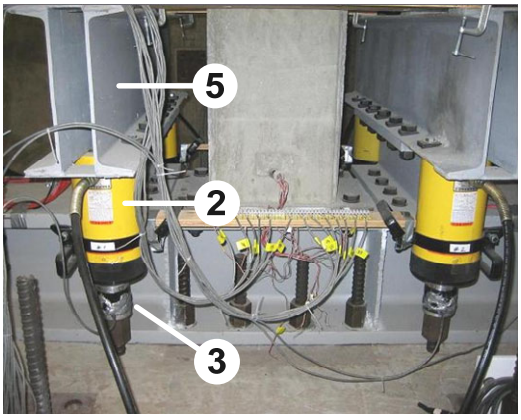

(c) Column bottom detail

(1) DWYDAG rods at each corner, (2) Center-hole hydraulic jacks (all jacks connected in parallel to the same pump), (3) Load cells, (4) Steel bearing plates, (5) Steel channels connected to the column top and bottom supports.

Figure B.22 — Application of column axial load.

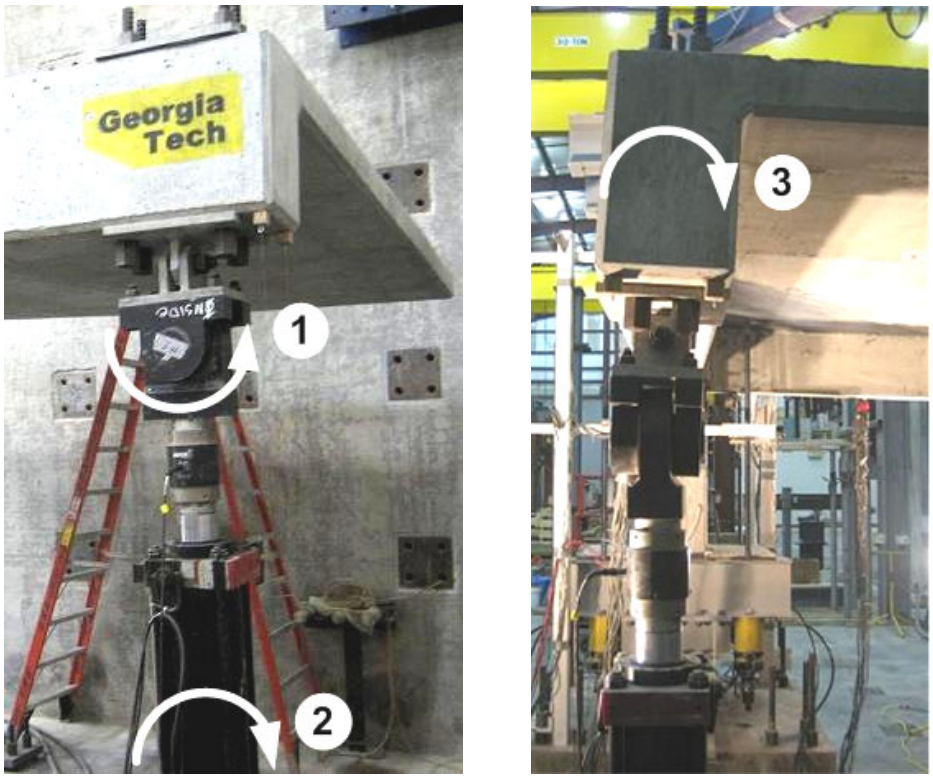

(a) Front view

(b) Side view and extent of torsional rotations during test

(1) Free rotation in bending direction at top, (2) Free rotation in bending direction at base, (3) Free torsional rotation.

Figure B.23 — Actuator-to-beam connections.

B.4 INSTRUMENTATION OF THE AS-BUILT SPECIMENS

B.4.1 Strain in Reinforcing Bars

The strains in the reinforcing bars were monitored by mounting 350Ω electrical resistance strain gages at locations shown in Figure B.24 and Figure B.25. The gage locations were symmetrical in the EW and NS directions. After testing of Specimen 1, four changes were made in strain-gaging of the other specimens: (1) the second layer of beam top reinforcing bars were also instrumented to better estimate the joint shear force, (2) the beam bottom bars on the inside were instrumented within the joint as well to better assess the larger demand on these bars compared to others, (3) the arrangement of strain gages in the slab was changed slightly to reduce the number of gages and still determine the strain distribution across the entire slab width, and (4) column longitudinal bars were also instrumented at the column base to check if the intended fixity at the column base was achieved.

At each strain gage location, the reinforcing bar was first ground smooth over a length of approximately 2 in.; the gage was mounted and wired; and the gage was sealed by a thin layer of polyurethane for water protection followed by a 0.25 in.-thick layer of silicone caulk for impact protection during concrete casting. The reduction in the concrete-to-reinforcing bar bond at the strain gage locations was assumed to not significantly affect the strains developed in the bars. The lead cables of the strain gages were routed along the reinforcing bars in small groups and taken out of the specimen at locations as close to the gages as possible to minimize the effect of the cables to the bond of the reinforcing bars.

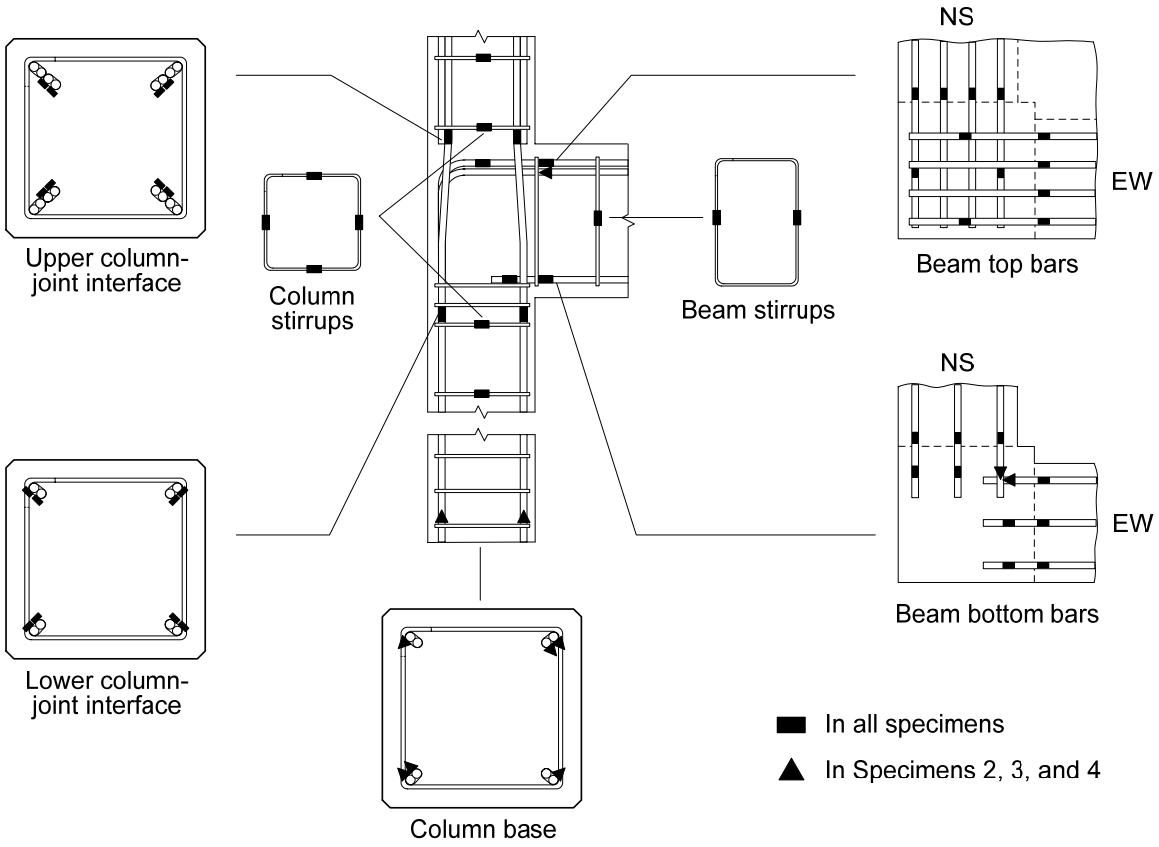

Figure B.24 — Strain gages mounted on the beam and column reinforcing bars.

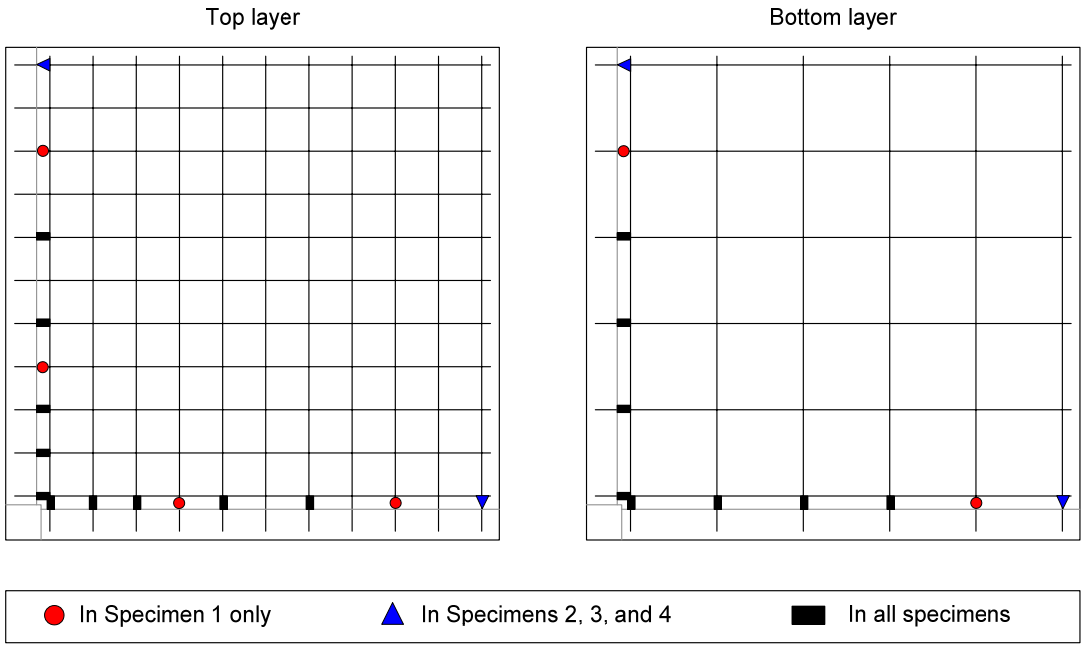

Figure B.25 — Strain gages mounted on the slab reinforcing bars.

B.4.2 Joint Shear Strain

Joint shear strains were monitored by using an LVDT configuration shown in Figure B.26 on both the EW and NS joint panels and by using a plane-strain transformation as in Equation (B.7):

$$\gamma_{xz} = \frac{\varepsilon_\varphi - \varepsilon_x \cos^2 \varphi - \varepsilon_z \sin^2 \varphi}{\sin \varphi \cos \varphi} \tag{B.7}$$

where, γ_{xz} is the shear strain, ε_x and ε_z are the strains in the x (horizontal) and z (vertical) directions, respectively, and ε_φ is the strain in an arbitrary third (diagonal) direction with an angle of φ measured counterclockwise from the x axis. For each joint panel, four estimates of the joint shear strain were obtained by forming triangular strain rosettes in the joint panel and by using the law of cosines (i.e. plane strain transformation) as follows:

$$\varepsilon_i = \frac{\Delta L_i}{L_i} \tag{B.8}$$

$$(\gamma_{xz})_1 = \frac{\varepsilon_6 - \varepsilon_1 \cos^2 \varphi - \varepsilon_4 \sin^2 \varphi}{-\sin \varphi \cos \varphi} \tag{B.9}$$

$$(\gamma_{xz})_2 = \frac{\varepsilon_5 - \varepsilon_1 \cos^2 \varphi - \varepsilon_2 \sin^2 \varphi}{\sin \varphi \cos \varphi} \tag{B.10}$$

$$(\gamma_{xz})_3 = \frac{\varepsilon_5 - \varepsilon_3 \cos^2 \varphi - \varepsilon_4 \sin^2 \varphi}{\sin \varphi \cos \varphi} \tag{B.11}$$

$$(\gamma_{xz})_4 = \frac{\varepsilon_6 - \varepsilon_3 \cos^2 \varphi - \varepsilon_2 \sin^2 \varphi}{-\sin \varphi \cos \varphi} \tag{B.12}$$

where, ΔL_i, L_i, and ε_i are the measured change in gage length, initial gage length and the resulting strain obtained from the i^{th} LVDT in Figure B.26a. An average of these

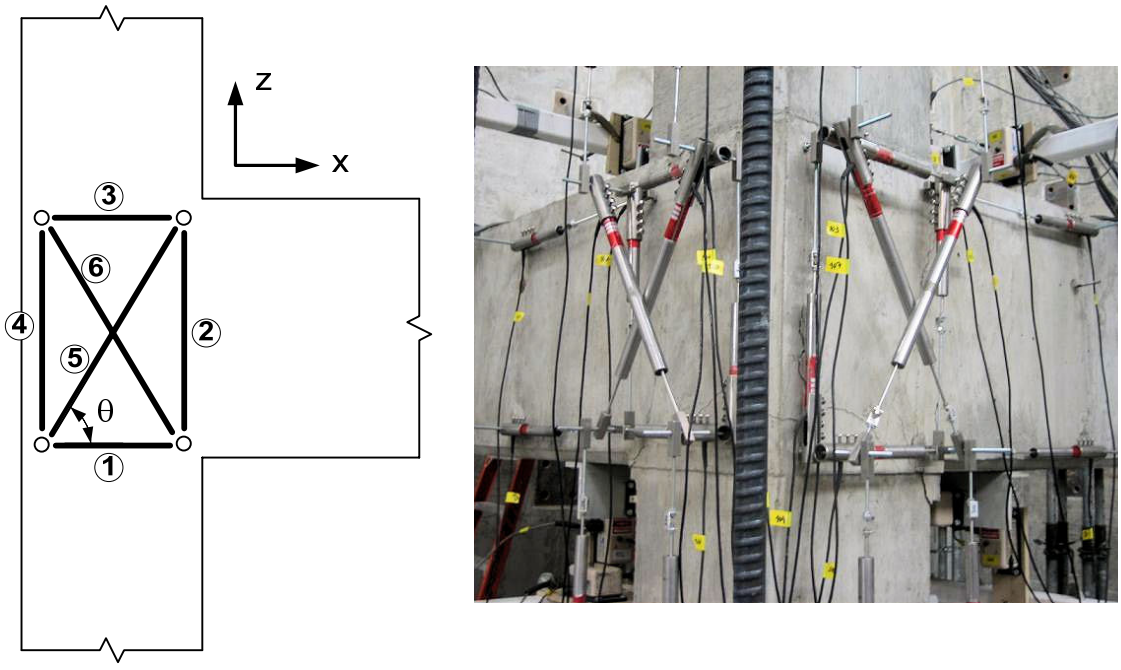

(a) (b)

Figure B.26 — LVDT layout for joint shear strain measurement. NS on left, EW on right.

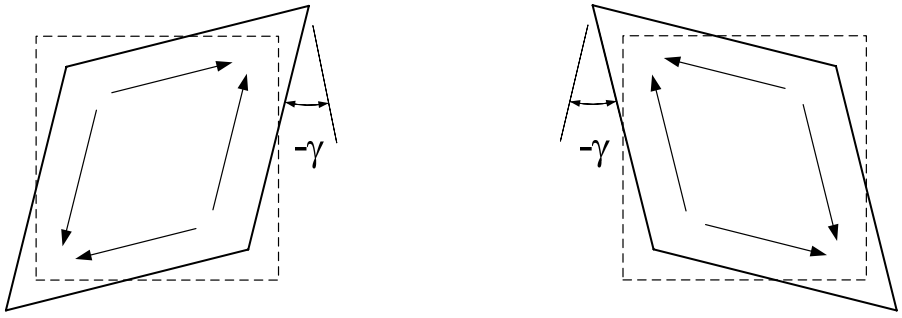

(a) EW (b) NS

Figure B.27 — Sign conventions for joint shear strain. Downward loading shown.

estimates was then used as the joint shear strain (Equation B.13).

$$\gamma_s = \frac{(\gamma_{xz})_1 + (\gamma_{xz})_2 + (\gamma_{xz})_3 + (\gamma_{xz})_4}{4} \tag{B.13}$$

It is to be noted that forming of four other strain rosettes by using LVDTs (3, 4, 6), (1, 2, 6), (1, 4, 5), and (2, 3, 5) results in the same average.

The sign convention for shear strains was selected to be consistent with the direction of loading (i.e. negative shear strains during downward loading) as shown in Figure B.27.

The LVDTs were mounted on the specimens using threaded rods which were connected to the coupling nuts placed in the specimens prior to concrete casting (Figure B.26b). The coupling nuts were anchored 6 in. into the specimens with threaded rods connected at their other ends.

B.4.3 Joint Global Rotation in Space

Global rotation of the joint in space (θ_j) was monitored with respect to a fixed reference frame in both the EW and NS directions using two potentiometers horizontally connected to the upper and lower columns at their mid-width and at a distance *a* (6 in.) above and below the joint, respectively, as shown in Figure B.28. The potentiometer readings were adjusted to account for the effect of deformations within the *a* distances above and below the joint as presented in detail in Appendix D, Sec. D.2, and θ_j was finally obtained as:

$$\theta_j = \frac{x + 2\gamma_s a}{h_j + 2a} \tag{B.14}$$

where *x* is the difference between the two potentiometer readings, γ_s is the joint shear strain obtained as explained in Sec. B.4.2, and h_j (20 in.) is the joint height.

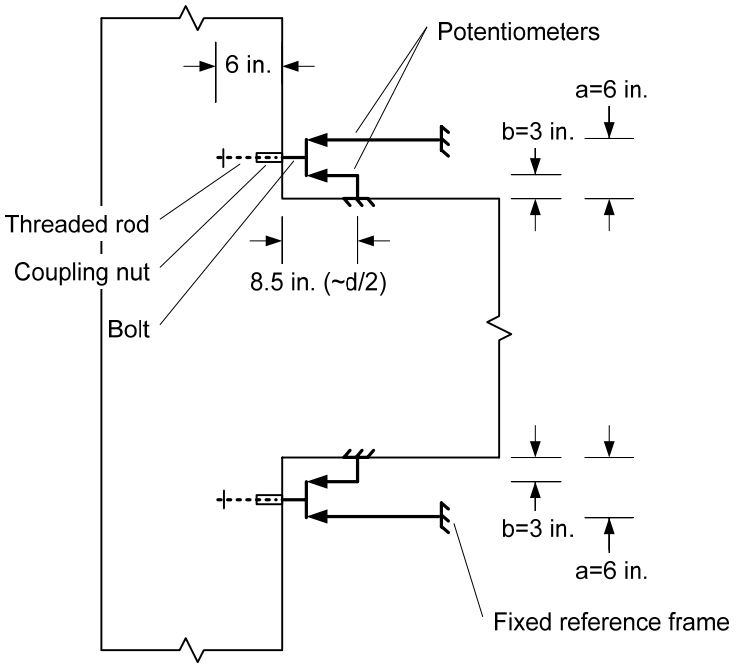

Figure B.28 — Measurement of beam relative rotations (identical in EW and NS directions).

B.4.4 Beam Relative Rotation with Respect to Joint

Relative rotation of the beams with respect to the joint (θ_{bj}) was monitored using two potentiometers which were fixed on the beam top and bottom surfaces at a distance equal to half the beam effective depth (i.e. *d/2*=8.5 in.) and horizontally connected to the upper and lower columns as shown in Figure B.28. The potentiometers were connected to the specimen at mid-width of the columns and at a distance *b* (3 in.) above and below the joint, respectively. The potentiometer readings were adjusted to account for the effect of deformations within the *b* distances above and below the joint as presented in detail in Appendix D, Sec. D.3, and θ_{bj} was finally obtained as:

$$\theta_{bj} = \frac{y - 2\gamma_s b}{h_j + 2b} \tag{B.15}$$

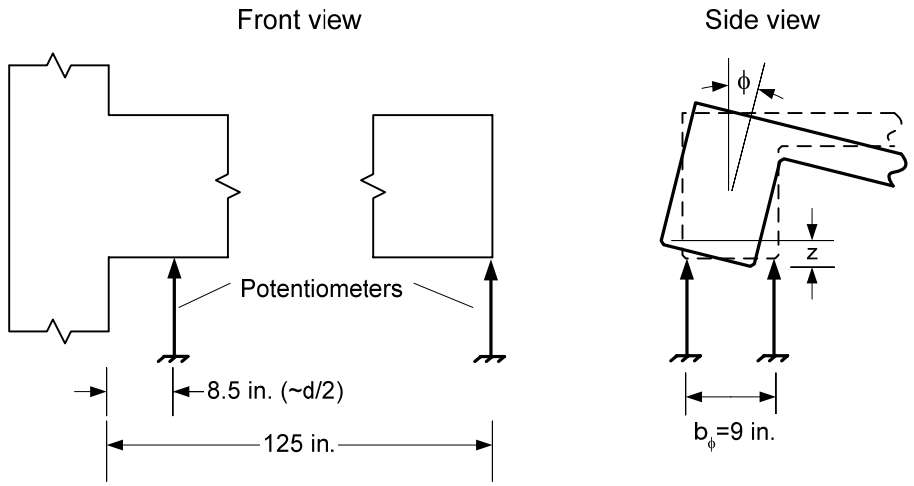

Figure B.29 — Measurement of beam torsional rotations (identical in EW and NS directions).

where *y* is the difference between the two potentiometer readings, γ_s is the joint shear strain obtained as explained in Sec. B.4.2, and h_j (20 in.) is the joint height.

B.4.5 Beam Torsional Rotation

Beam torsional rotation (ϕ_t) was monitored at both ends of the beams using two potentiometers at each location which were vertically connected to the soffit of the beams near the inside and outside edges, as shown in Figure B.29. ϕ_t was determined from:

$$\phi_t = \frac{z}{b_\phi} \tag{B.16}$$

where *z* is the difference between the two potentiometer readings and b_ϕ (9 in.) is the distance between the potentiometers.

B.4.6 Column Shear Force

The column shear force in the EW and NS directions were monitored by mounting electrical resistance strain gages to form a Wheatstone bridge at midspan of both tubular steel beams of the triangular reaction frame atop the column. The

Wheatstone bridges were formed by mounting a 350Ω electrical resistance strain gage on each face of the tubular beams. The force in each tubular beam (P_t) was determined according to the following equation provided by Dally et al. [B.9]:

$$P_t = CV_{out} = \frac{2AE_s}{S_g \cdot (1+\nu_s) \cdot V_{in}} V_{out} \tag{B.17}$$

where C is the calibration constant; A is the cross-sectional area of the tube; E_s and ν_s are the modulus of elasticity and Poisson's ratio of steel, respectively; S_g is the gage factor of the strain gages; V_{in} is the input voltage applied to the Wheatstone bridge; and V_{out} is the output voltage. The forces obtained by this method were confirmed by also monitoring the axial strain in one of the steel beams using strain gages mounted on both vertical faces. The resultant of the forces (vector sum) in the steel beams was divided into two components in the EW and NS directions which were taken as the column shear forces in these directions.

B.4.7 Column Axial Load

The fixture used for application of the column axial load was previously shown in Figure B.22. The force in each DWYDAG rod was monitored by placing a center-hole load cell between the hydraulic jack and the end nut at each corner, and the sum of the forces in all four rods was taken as the column axial load. Each load cell was made by mounting a Wheatstone bridge on a cylindrical aluminum block with a center hole. Each load cell was calibrated by using a hydraulic testing machine prior to the actual beam-column joint tests to determine the calibration constant C (Equation B.17).

B.5 INSTRUMENTATION OF THE RETROFIT COMPONENTS

Additional instrumentation used after retrofit consisted of strain gages mounted on the retrofit components to monitor: (1) the strain in the added #7 column reinforcing bar just

below and just above the joint with two strain gages at each location, (2) the variation of strain in the fiber direction across the width and along the length of the CFRP strips bonded at the bottom of the outside faces of the beams, (3) the strain in the CFRP beam U-wraps in the fiber direction near and away from the column face, and (4) the strain in the CFRP column wraps in the fiber direction near and away from the column-joint interfaces. The layout of strain gages on the CFRP systems were modified slightly in light of the findings as the test program progressed. The location and orientation of all strain gages on the CFRP systems are shown in Figure B.30 for all specimens on a generic CFRP scheme (i.e. not all shaded areas were covered with CFRP in all specimens).

B.6 LOADING

B.6.1 Simulation of Service Gravity Load Effects

The forces in corner joints that are likely to be present due to service gravity loads at the time a building is subjected to lateral loads were simulated in the specimens prior to cyclic loading of the beams as described below.

The column was assumed to be carrying a compressive axial load (P_{col}) equivalent to approximately 10% of its capacity (i.e. $0.1P_o$) due to service gravity loads. Such an axial load was applied to the specimens while the beams were in their initial level position using four hydraulic jacks placed at the corners of the column as previously shown in Figure B.22. Although the jacks were connected in parallel to a single electrical pump, differences between the loads applied at each corner were unavoidable, and P_{col} was taken as the sum of forces at four corners. While no attempts were made to accurately simulate the fluctuation in P_{col} due to overturning effects in an actual building subjected to lateral loading, it was not also intended to keep it constant during the tests, and variation of P_{col} during beam cyclic loading was allowed. P_{col} was not re-adjusted

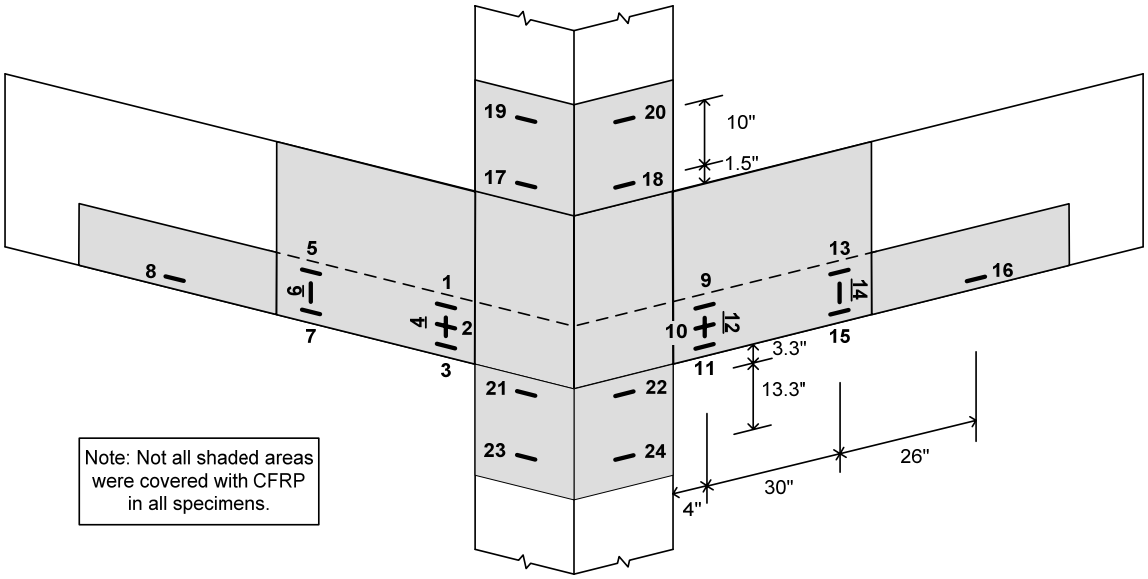

Gage locations in the horizontal direction:

- 1-4, and 9-12 are 4 in. away from the column face
- 5-7, and 13-15 are 34 in. from the column face
- 8 and 16 are 60 in. from the column face
- 17-24 are at mid-width of the column

Gage locations in the vertical direction:

- 3, 7, 8, 11, 15, and 16 are at the beam bottom bar level (Figure B.15)
- 2, 4, 6, 10, 12, and 14 are on the centerline of the CFRP strips
- 1, 5, 9, and 13 are symmetrical within the CFRP strips with respect to 3, 7, 11, and 15, respectively
- 17 and 18 are at the first stirrup level above the joint
- 19 and 20 are at the second stirrup level above the joint
- 21 and 22 are at the second stirrup level below the joint
- 23 and 24 are at the third stirrup level below the joint

	Strain gages																							
	1	2	3	4	5	6	7	8	9	10	11	12	13	14	15	16	17	18	19	20	21	22	23	24
Specimen 1	x	x	x						x	x	x						x	x	x	x			x	x
Specimen 2	x		x	x	x	x	x	x	x		x	x	x	x	x	x	x	x			x	x		
Specimen 3	x		x	x	x		x		x		x	x	x		x		x	x			x	x		
Specimen 4	x		x	x	x		x		x		x	x	x		x		x	x			x	x		

Figure B.30 — Strain gages mounted on the CFRP sheets.

unless a major loss of pressure in the jacks occurred, which was the case only for Specimen 4 where P_{col} was restored to $0.1P_o$ at the end of the ±1.40% interstory drift cycles. The axial loads in the upper and lower columns at all loading peaks in all tests can be found in tables presented in Appendix C.

After the application of the column axial load, both beams were displaced downwards until the major-axis beam bending moments at the column faces were approximately -170 kip-in. This moment level was determined by assuming a dead load (*DL*) of 100 psf, a live load (*LL*) of 50 psf, by using a service load combination of $w = 1.0DL + 0.25LL$, and by approximating the beam moment at the exterior column face of a continuous frame as $M_z = w\left(L'\right)^2 / 16$ where L' is the beam span length (the specimens simulated a span length of L'=20 ft). The contribution of the weight of the slab to the beam moment at the column face was considered by assuming a triangular load distribution on the beams. Downward displacement of the beams was performed in a displacement-controlled mode for safety reasons which resulted in some differences in the column-face moments, although both beams were displaced by an equal amount. This was attributed to the initial deviation of the beam horizontal axes from the "perfect horizontal" position. It is to be noted that the loads on the actuators at the end of this procedure were still compressive (upward) because of the beams' tendency to deflect more due to the weight of the slab in a single-curvature mode. Larger deflections under self-weight were not allowed in these tests, since such deflections would have resulted in forces in the joint region that are unlike those in an actual building where the beams deflect in a double-curvature mode. Simulation of the service gravity load beam moments using this procedure was performed before testing of Specimen 1 and Specimen 2 before retrofit, and for Specimen 3 and Specimen 4. This procedure was not performed before re-testing of Specimen 1 and Specimen 2 after retrofit; the reference beam positions in these tests were taken as those at the end of the first tests before retrofit.

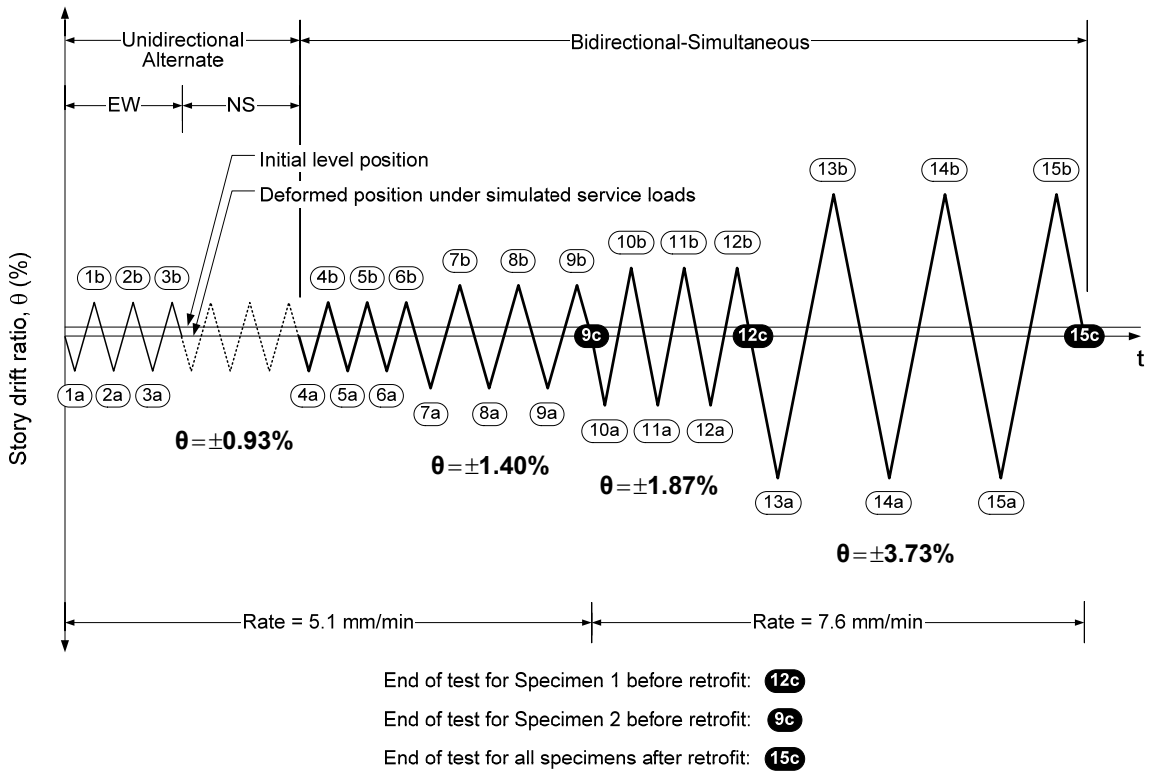

Figure B.31 — Applied displacement history.

B.6.2 Simulation of Cyclic Lateral Loading

Cyclic lateral loading was simulated by cyclic vertical loading of the beams symmetrically around the deformed position under simulated service loads as shown in Figure B.31. The boundary conditions at the actuator ends were previously described in Figure B.23. All tests were conducted in a pre-programmed displacement-controlled mode using MTS Model 661.23E-01 hydraulic actuators with a TestStar controller. The applied displacement levels correspond to 1.0, 1.5, 2.0, and 4.0 times the displacement at first yield of the upper column NE corner bar in Specimen 1 before retrofit. Testing of Specimen 1 and Specimen 2 were terminated at points 12c and 9c on the applied displacement history, respectively, to represent different levels of damage prior to retrofit.

B.7 DATA ACQUISITION

All instrument readings were set to zero while the specimens were in their initial undeformed (shored) position. Data were acquired at a rate of 1 scan/second using MEGADAC 3415AC data acquisition systems with TCS software. The instrumentation layout summarized in Section B.4 resulted in up to 160 channels of instruments, which forced the use of two data acquisition systems. The systems were operated independently, and the acquired data were synchronized after the tests using the shared outputs from actuator loads and displacements. The instruments were used at the following resolutions: strain gages: ±1.19 με; LVDTs: ±0.000126 in.; potentiometers: ±0.000642 in.; column load cells: ±3.9 lb; load cells on the reaction frame: ±2.9 lb; actuator loads: ±1.56 lb; actuator displacements: ±0.000469 in.

B.8 REFERENCES

[B.1] ASTM C 39/C 39M-04a (2004). *Standard test method for compressive strength of cylindrical concrete specimens*, ASTM International, West Conshohocken, PA.

[B.2] ASTM C 469-02 (2002). *Standard test method for static modulus of elasticity and Poisson's ratio of concrete in compression,* ASTM International, West Conshohocken, PA.

[B.3] ASTM A 370-03a (2003). *Standard test methods and definitions for mechanical testing of steel products,* ASTM International, West Conshohocken, PA.

[B.4] ASTM D 3418-99 (1999). *Standard test method for transition temperatures of polymers by differential scanning calorimetry,* ASTM International, West Conshohocken, PA.

[B.5] Sika Corporation (2003). <http://www.sikaconstruction.com/con/con-prod/htm> (February 2008).

[B.6] ASTM D 3039/D 3039M-00 (2000). *Standard test method for tensile properties of polymer matrix composite materials,* ASTM International, West Conshohocken, PA.

[B.7] Mallick, P. K. (1993). *Fiber-reinforced composites–Materials, manufacturing, and design*, 2nd edition, Marcel Dekker, Inc., New York, NY.

[B.8] Green, T. P. (2000). "Behavior of full-scale partially-restrained composite beam-to-column T-stub and shear tab connections under cyclic loading." MS thesis, Georgia Institute of Technology, Atlanta, GA.

[B.9] Dally, J. W., Rilay, W. F., and McConnell, K. G. (1993). "Force, torque, and pressure measurements." *Instrumentation for engineering measurements – 2nd edition*, John Wiley & Sons, Inc.

APPENDIX C

SUMMARY OF TEST RESULTS

This appendix is a collection of the results from all six tests, some of which were not presented in the preceding chapters for brevity. Plots that are similar to those presented in the preceding chapters to supplement certain discussions are presented here for all tests and for both primary frame directions (i.e. EW and NS). For each test, the following are presented consecutively:

- Observed damage modes,
- Force-drift hysteretic curves,
- Joint shear stress-strain hysteretic curves,
- Variation of peak-to-peak stiffness,
- Variation of cumulative dissipated energy,
- Strain distribution in the slab reinforcing bars,
- Percent contributions of joint, column, and beam deformation mechanisms to applied interstory drifts,
- Variation of strain in the CFRP sheets,
- A tabular summary of values of major parameters characterizing the behavior.

C.1 SPECIMEN 1 BEFORE RETROFIT

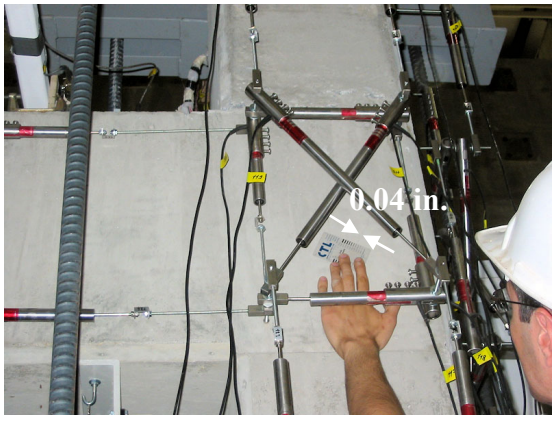

(a) NS joint panel at peak 2a
(-0.93% unidirectional drift)

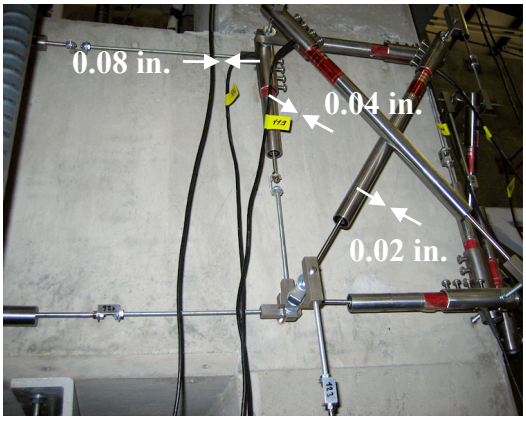

(b) NS joint panel at peak 4a
(-0.93% bidirectional drift)

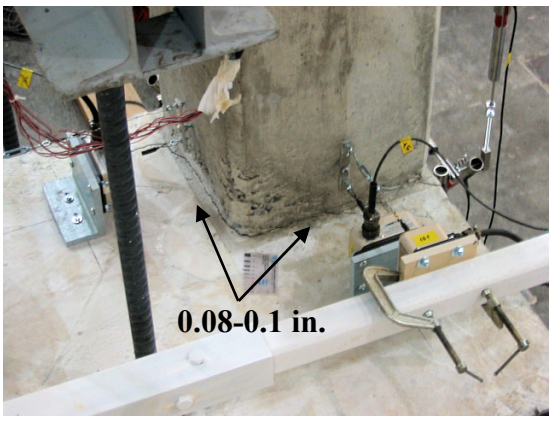

(c) Upper column NE corner at peak 4a
(-0.93% bidirectional drift)

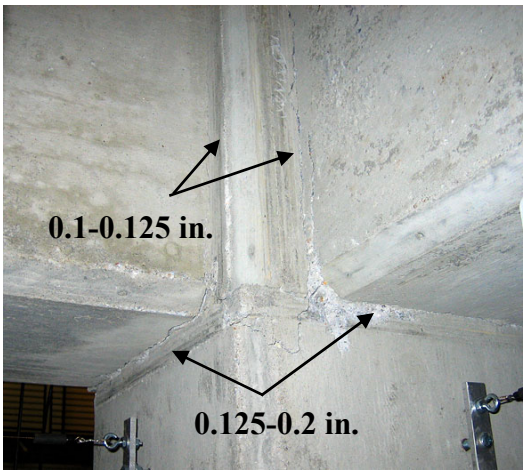

(d) Joint NE corner at peak 7b
(+1.40% bidirectional drift)

Figure C.1 — Damage modes – Specimen 1 before retrofit.

Views during and at the end of the last cycle: Cycle 12 (±1.87% bidirectional drift)

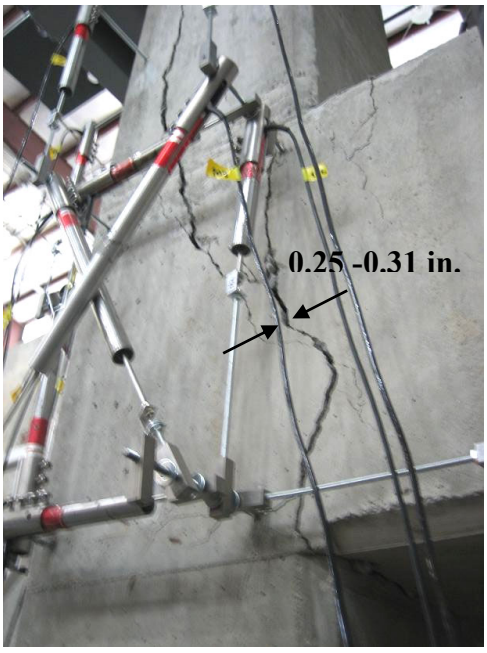

(e) EW joint panel

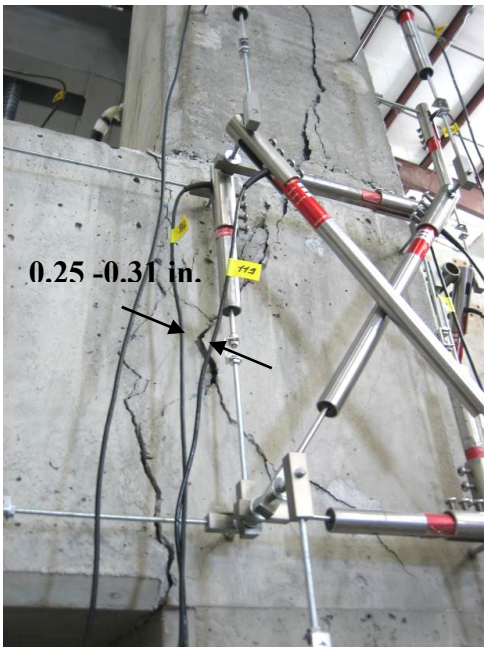

(f) NS joint panel

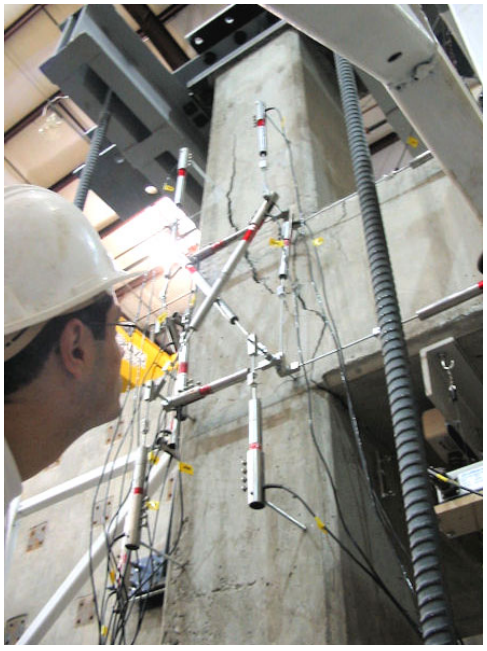

(g) EW elevation

(h) Joint NE corner

Figure C.1 — Continued.

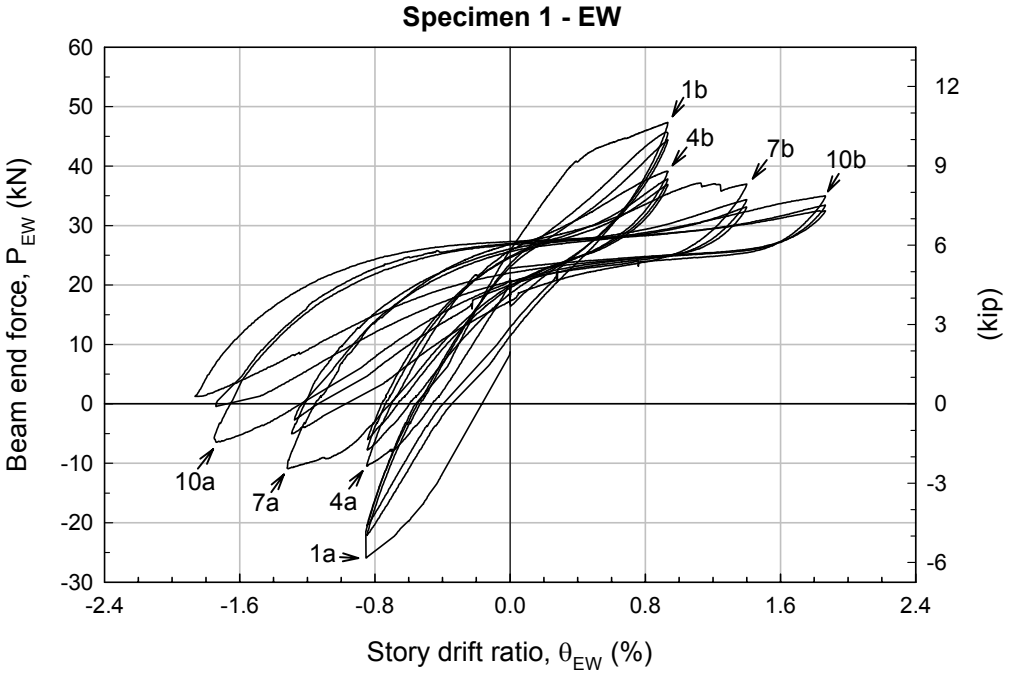

(a)

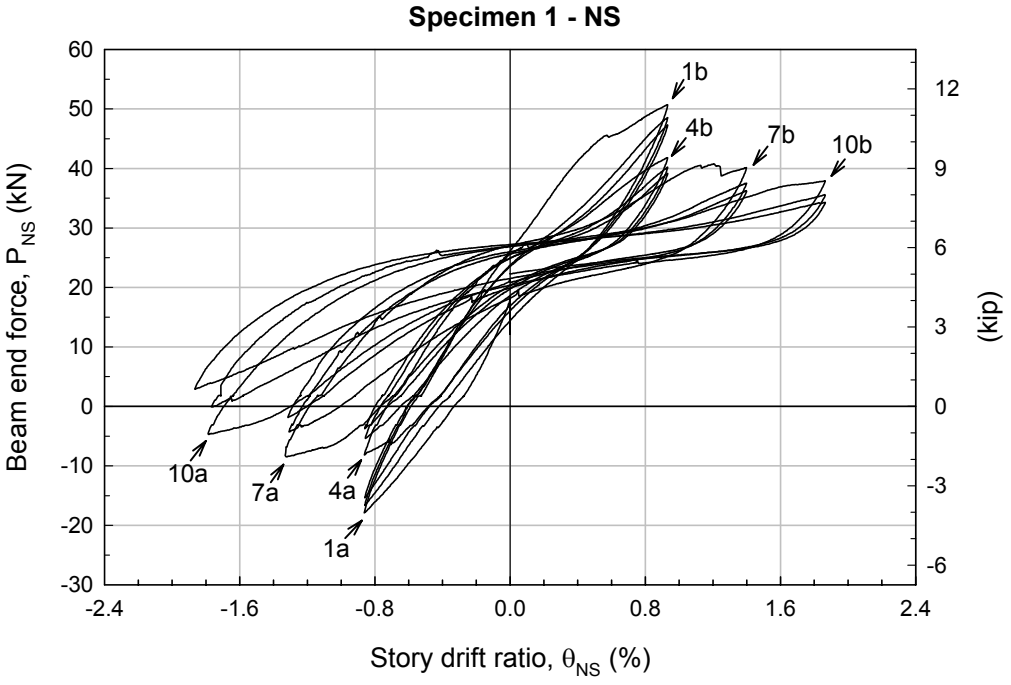

(b)

Figure C.2 — Force-drift hysteretic curves – Specimen 1 before retrofit: (a) EW, and (b) NS direction.

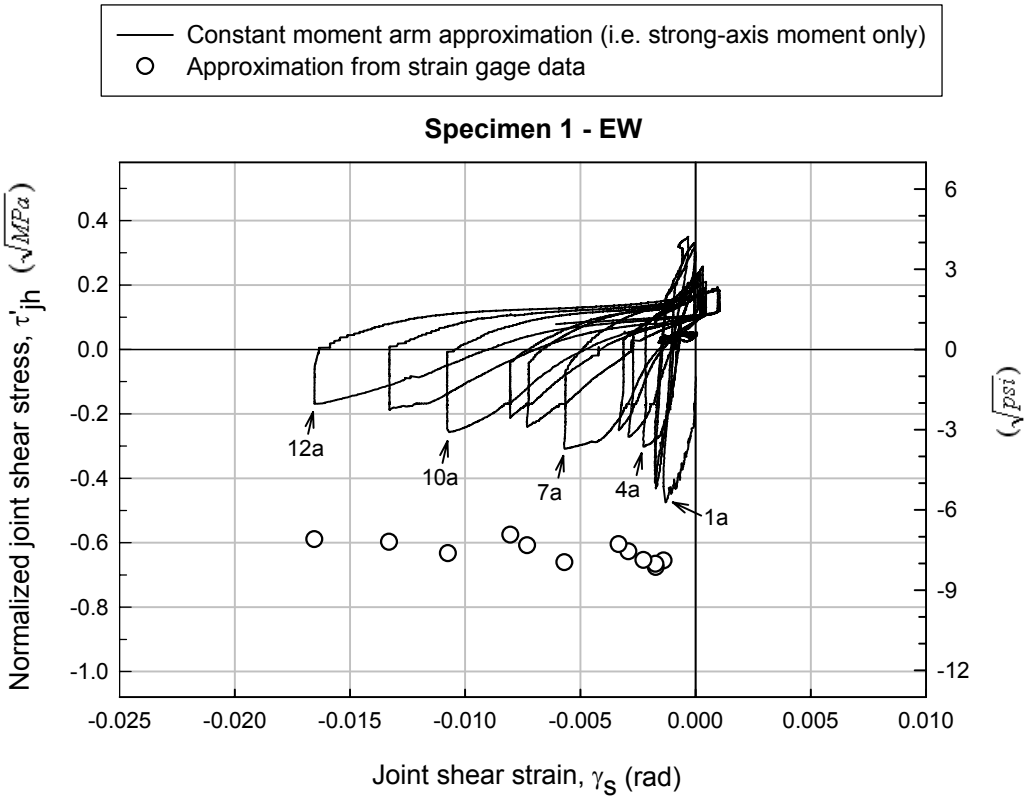

(a)

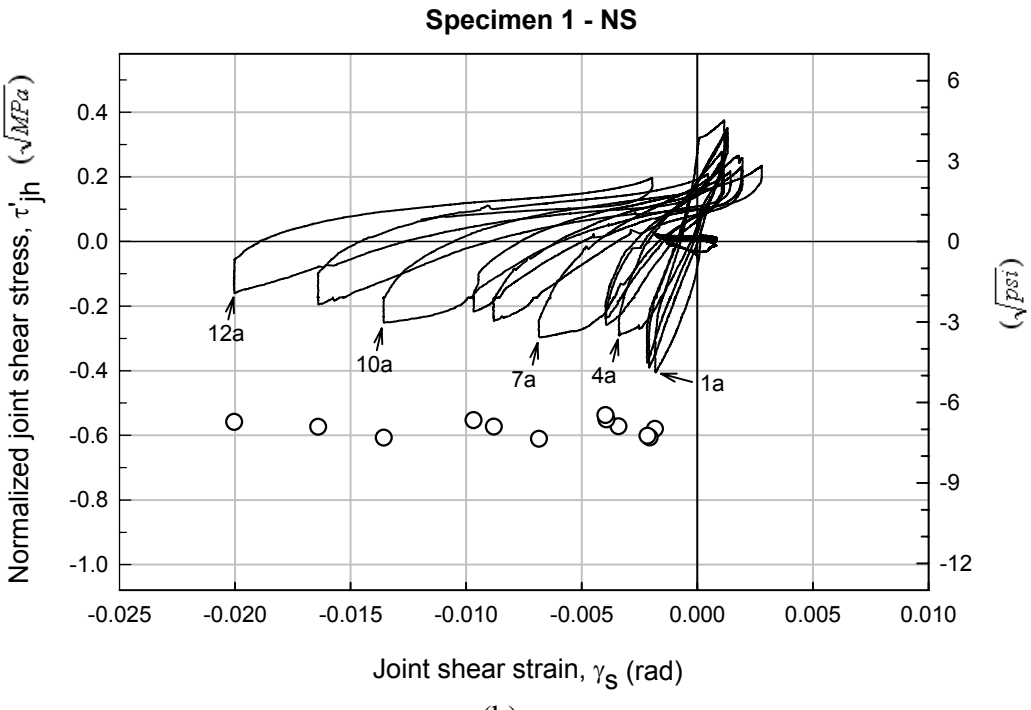

(b)

Figure C.3 — Joint shear stress-strain hysteretic curves – Specimen 1 before retrofit: (a) EW, and (b) NS direction.

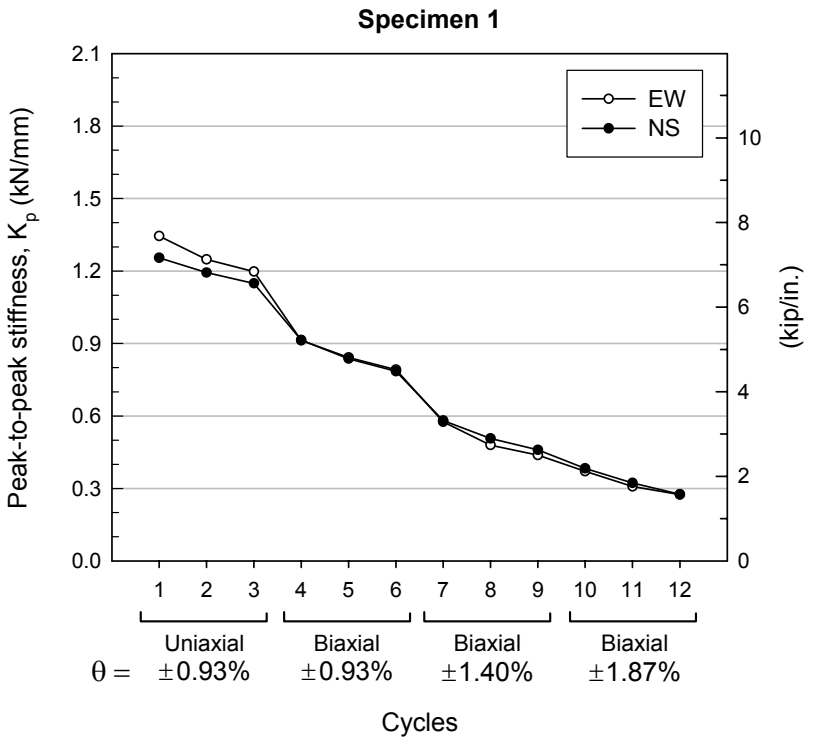

Figure C.4 — Variation of peak-to-peak stiffness – Specimen 1 before retrofit.

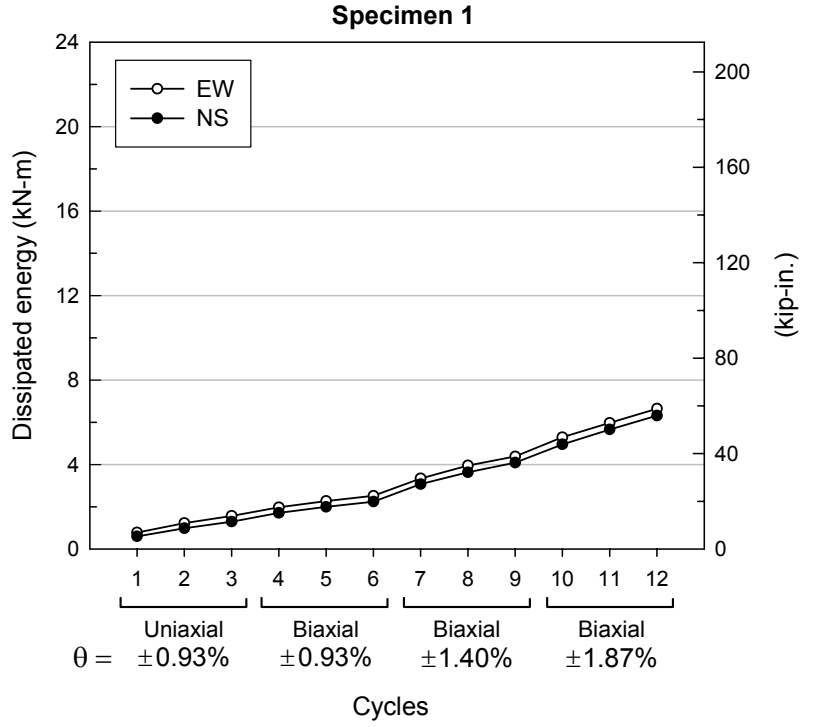

Figure C.5 — Variation of cumulative dissipated energy – Specimen 1 before retrofit.

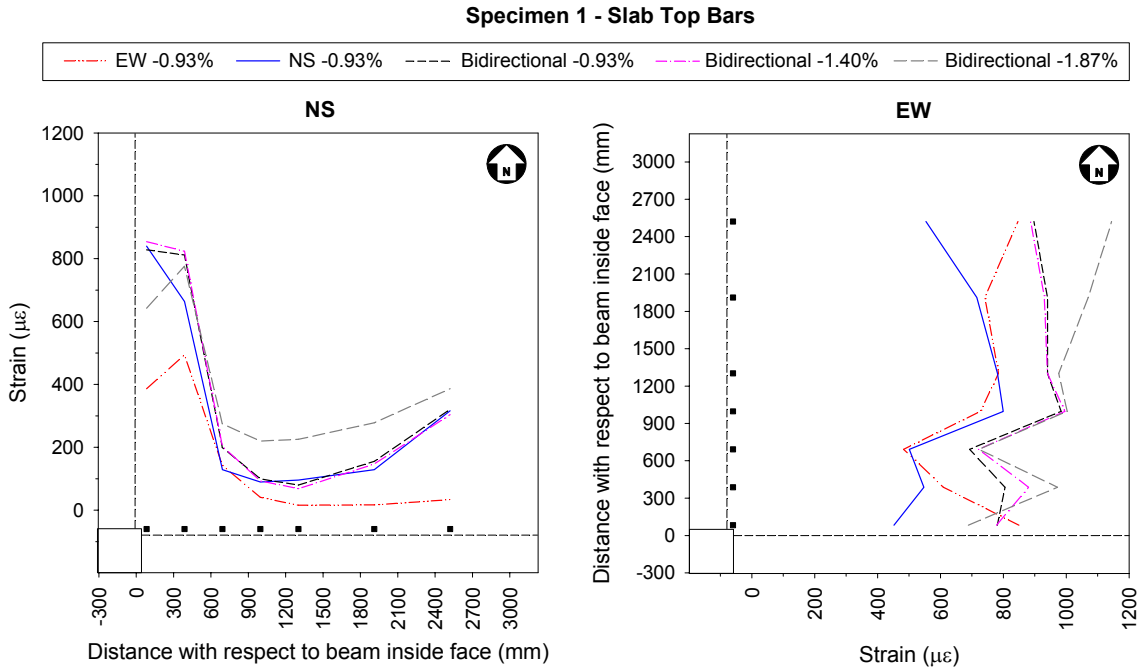

(a)

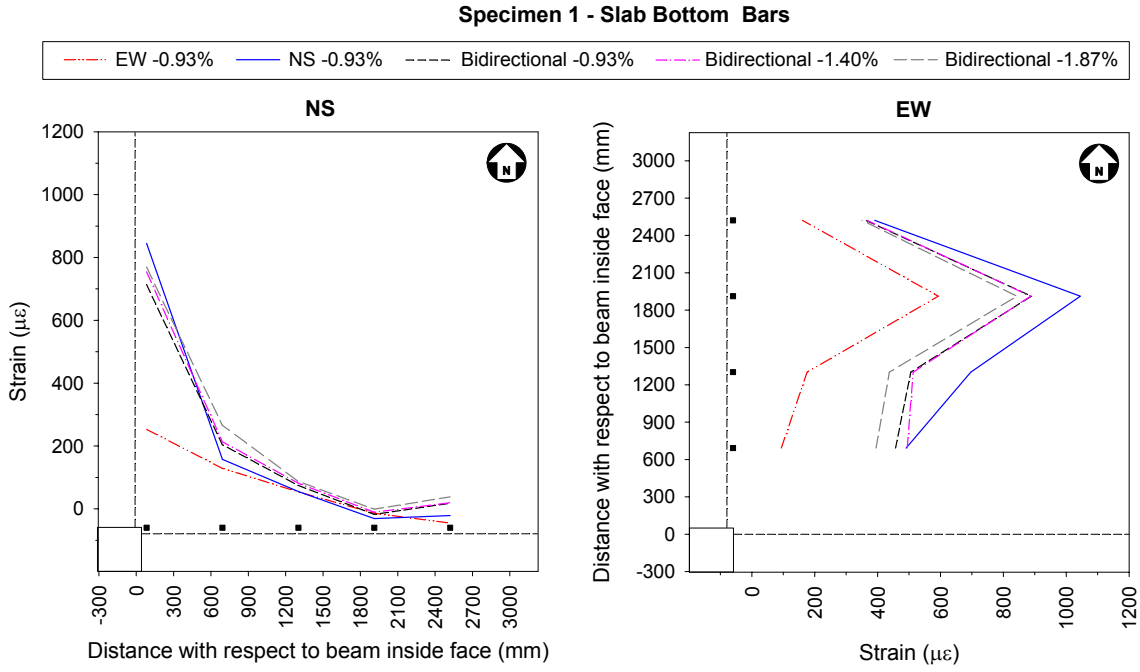

(b)

Figure C.6 — Strains in the slab bars at the first peak of downward loading at each drift level – Specimen 1 before retrofit: (a) top bars, and (b) bottom bars.

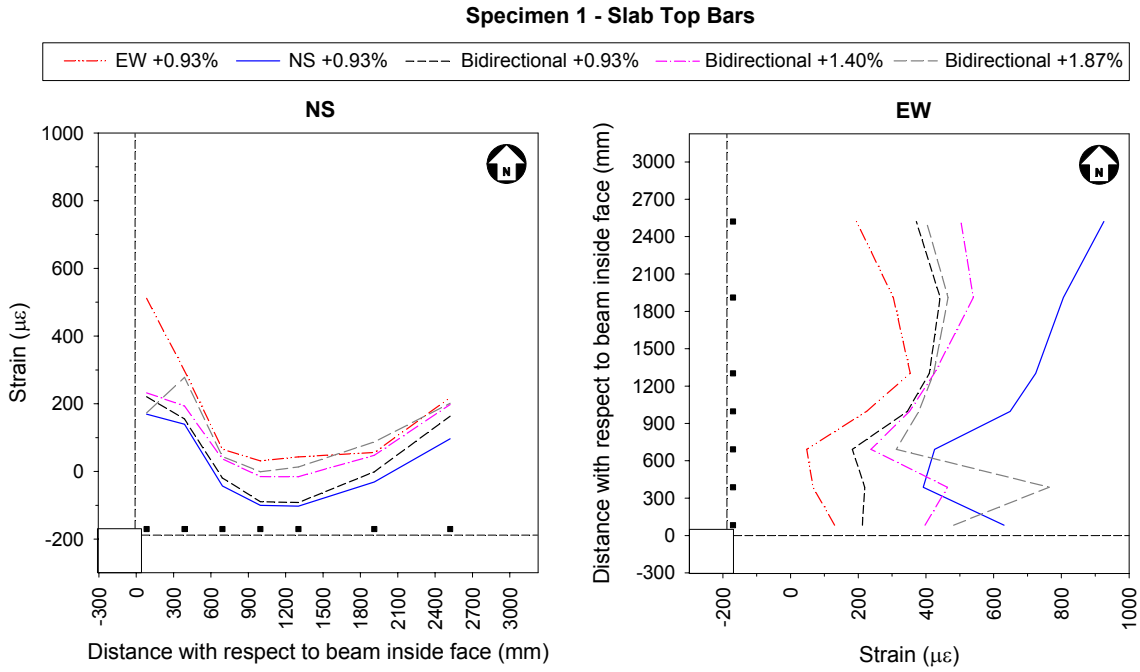

(a)

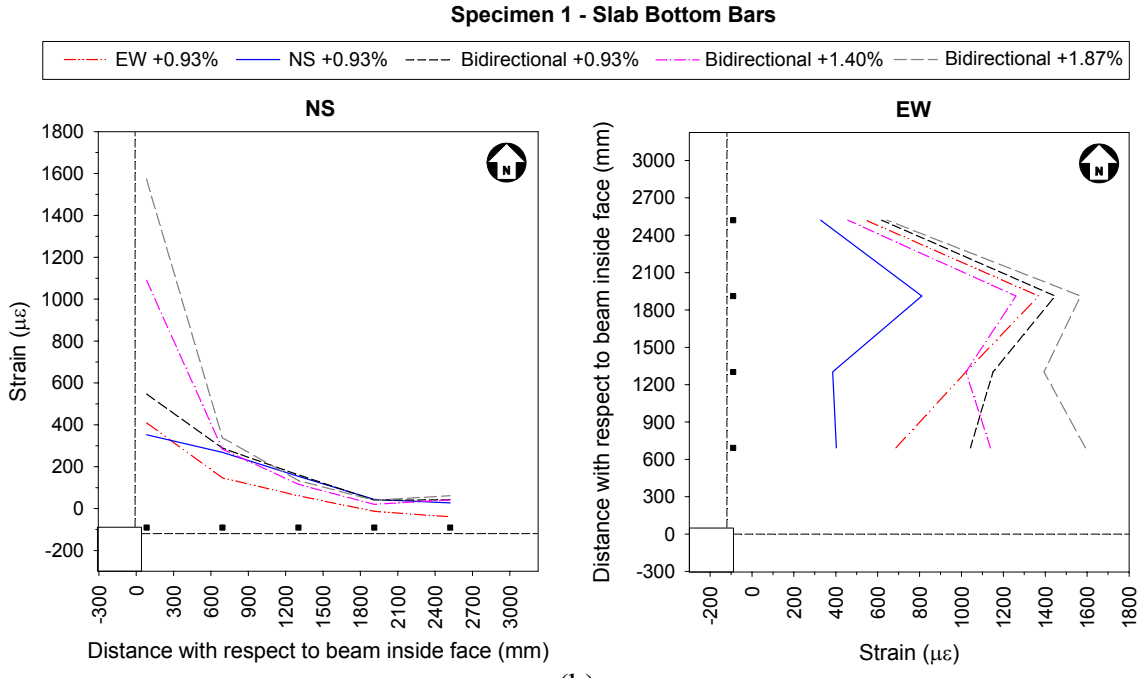

(b)

Figure C.7 — Strains in the slab bars at the first peak of upward loading at each drift level – Specimen 1 before retrofit: (a) top bars, and (b) bottom bars.

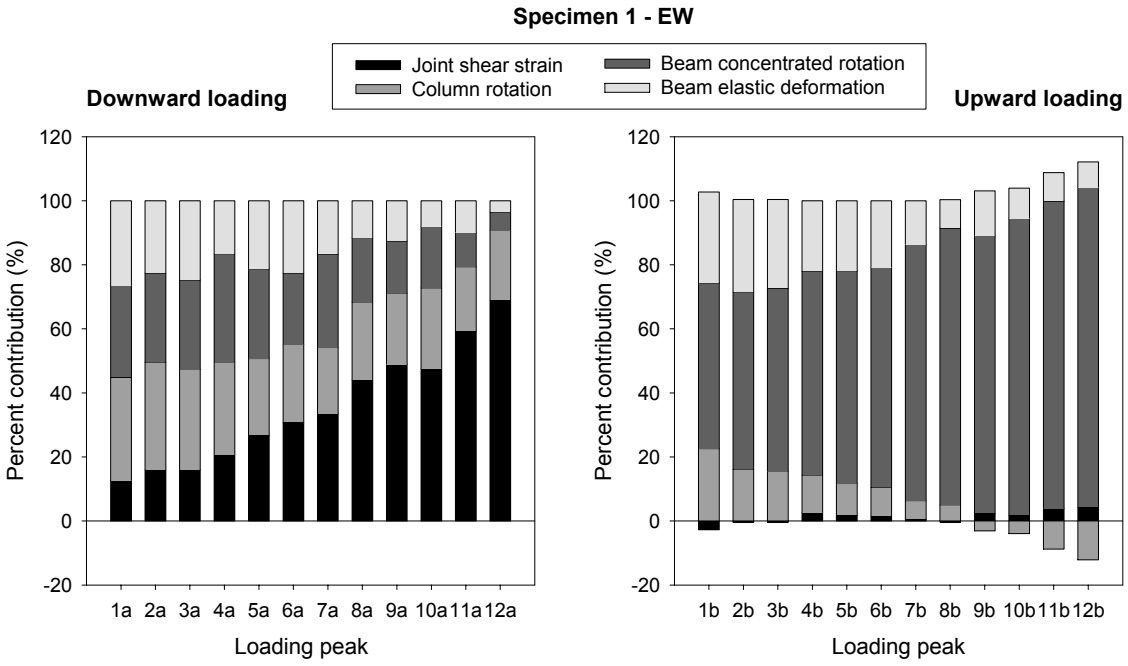

(a)

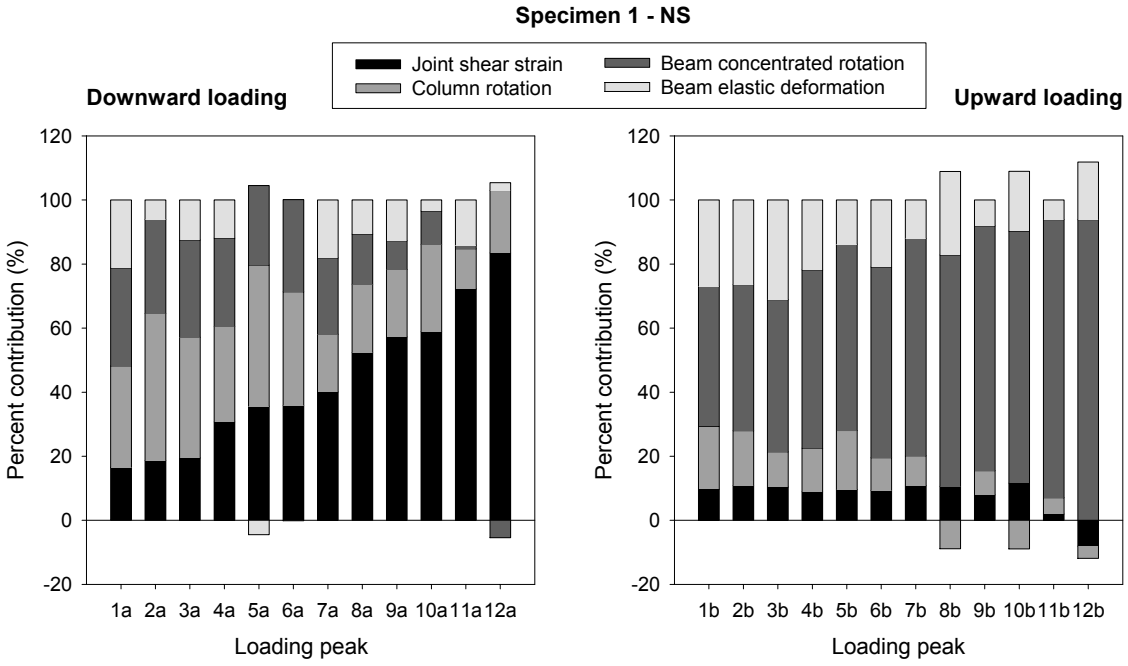

(b)

Figure C.8 — Percent contributions to applied interstory drift – Specimen 1 before retrofit: (a) EW, and (b) NS direction.

Table C.1 — Summary of test results – Specimen 1 before retrofit, EW direction.

Loading Peak	Δ_b (in.)	θ (%)	P (kip)	V_{col} (kip)	$P_{u.col}$ (kip)	$P_{l.col}$ (kip)	V_{jh} (kip)	τ'_{jh} ($\sqrt{psi}$)	V_{jh}^{sg} (kip)	τ'^{sg}_{jh} ($\sqrt{psi}$)	γ_s (rad)	K_p (kip/in.)	E^i (kip-in.)	E^{tot} (kip-in.)
0	0.000	0.00	1.96	-2.85	-71.6	-66.9	-11.5	-1.0	-	-	0.000000	-	-	-
1a	-1.025	-0.85	-4.82	-7.82	-76.9	-77.9	-57.0	-5.1	-87.9	-7.9	-0.001392	7.68	6.9	6.9
1b	1.118	0.93	10.58	4.28	-68.3	-54.3	46.6	4.2	-	-	-0.000329			
2a	-1.016	-0.85	-4.97	-8.05	-75.4	-76.4	-58.0	-5.2	-90.6	-8.1	-0.001731	7.13	3.9	10.8
2b	1.120	0.93	10.23	4.08	-67.0	-53.1	44.2	4.0	-	-	-0.000048			
3a	-1.017	-0.85	-4.61	-7.72	-74.5	-74.9	-55.6	-5.0	-89.3	-8.0	-0.001741	6.84	3.0	13.9
3b	1.117	0.93	9.94	3.88	-66.0	-52.3	42.1	3.8	-	-	-0.000051			
4a	-1.017	-0.85	-2.29	-5.88	-75.4	-79.5	-40.1	-3.6	-87.6	-7.9	-0.002267	5.21	3.6	17.5
4b	1.121	0.93	8.79	2.86	-64.1	-45.9	34.4	3.1	-	-	0.000319			
5a	-1.015	-0.85	-1.73	-5.52	-74.4	-77.4	-36.3	-3.3	-84.1	-7.6	-0.002919	4.81	2.6	20.1
5b	1.119	0.93	8.47	2.52	-62.7	-45.2	32.3	2.9	-	-	0.000225			
6a	-1.009	-0.84	-1.28	-5.28	-73.7	-75.7	-33.2	-3.0	-81.1	-7.3	-0.003344	4.52	2.2	22.3
6b	1.118	0.93	8.24	2.33	-61.7	-44.7	30.7	2.8	-	-	0.000202			
7a	-1.581	-1.32	-2.39	-5.70	-80.6	-84.8	-41.1	-3.7	-88.6	-8.0	-0.005694	3.29	7.3	29.6
7b	1.678	1.40	8.26	2.52	-63.4	-46.2	30.7	2.8	-	-	0.000101			
8a	-1.547	-1.29	-1.05	-5.11	-78.9	-80.8	-31.7	-2.8	-81.5	-7.3	-0.007315	2.74	5.4	35.0
8b	1.678	1.40	7.70	1.87	-61.0	-44.9	27.1	2.4	-	-	-0.000064			
9a	-1.529	-1.27	-0.55	-4.80	-77.0	-77.9	-28.2	-2.5	-77.1	-6.9	-0.008040	2.50	3.8	38.8
9b	1.676	1.40	7.39	1.46	-59.3	-43.9	25.2	2.3	-	-	0.000429			
10a	-2.102	-1.75	-1.28	-5.10	-80.2	-82.5	-33.4	-3.0	-84.8	-7.6	-0.010750	2.12	8.1	46.8
10b	2.239	1.87	7.82	2.00	-60.4	-44.1	27.9	2.5	-	-	0.000448			
11a	-2.089	-1.74	-0.03	-4.33	-76.6	-76.6	-24.8	-2.2	-80.1	-7.2	-0.013305	1.76	6.0	52.9
11b	2.239	1.87	7.50	1.53	-58.6	-43.1	25.9	2.3	-	-	0.000955			
12a	-2.235	-1.86	0.30	-4.16	-74.0	-73.0	-22.6	-2.0	-79.0	-7.1	-0.016546	1.57	5.9	58.8
12b	2.235	1.86	7.25	1.25	-57.7	-42.8	24.3	2.2	-	-	0.001041			

Table C.2 — Summary of test results – Specimen 1 before retrofit, NS direction.

Loading Peak	Δ_b (in.)	θ (%)	P (kip)	V_{col} (kip)	$P_{u.col}$ (kip)	$P_{l.col}$ (kip)	V_{jh} (kip)	τ'_{jh} ($\sqrt{psi}$)	V_{jh}^{sg} (kip)	τ'^{sg}_{jh} ($\sqrt{psi}$)	γ_s (rad)	K_p (kip/in.)	E^i (kip-in.)	E^{tot} (kip-in.)
0	0.000	0.00	2.74	-2.24	-71.6	-66.9	-6.7	-0.6	-	-	0.000000	-	-	-
1a	-1.032	-0.86	-3.93	-7.10	-73.4	-73.2	-53.8	-4.8	-77.8	-7.0	-0.001833	7.16	5.3	5.3
1b	1.118	0.93	11.38	4.36	-66.4	-50.9	50.2	4.5	-	-	0.001163			
2a	-1.030	-0.86	-3.69	-6.96	-72.7	-72.1	-52.0	-4.7	-81.4	-7.3	-0.002063	6.81	3.4	8.7
2b	1.116	0.93	10.85	3.97	-65.0	-49.8	46.7	4.2	-	-	0.001300			
3a	-1.032	-0.86	-3.45	-6.76	-72.1	-71.2	-50.4	-4.5	-80.7	-7.2	-0.002159	6.56	2.7	11.5
3b	1.118	0.93	10.61	3.75	-64.3	-49.3	45.2	4.1	-	-	0.001248			
4a	-1.033	-0.86	-1.78	-5.36	-75.4	-79.5	-38.8	-3.5	-76.8	-6.9	-0.003406	5.22	3.7	15.1
4b	1.118	0.93	9.40	2.89	-64.1	-45.9	37.3	3.3	-	-	0.001064			
5a	-1.028	-0.86	-1.20	-4.96	-74.4	-77.4	-34.6	-3.1	-73.8	-6.6	-0.003932	4.78	2.6	17.7
5b	1.118	0.93	9.00	2.54	-62.7	-45.2	34.7	3.1	-	-	0.001155			
6a	-1.031	-0.86	-0.78	-4.66	-73.7	-75.7	-31.7	-2.8	-72.1	-6.5	-0.003975	4.48	2.1	19.8
6b	1.117	0.93	8.75	2.36	-61.7	-44.7	33.0	3.0	-	-	0.001117			
7a	-1.593	-1.33	-1.75	-5.19	-80.6	-84.8	-38.7	-3.5	-81.9	-7.4	-0.006853	3.32	7.4	27.2
7b	1.675	1.40	8.97	2.67	-63.4	-46.2	34.3	3.1	-	-	0.001944			
8a	-1.566	-1.30	-0.90	-4.64	-78.9	-80.8	-32.6	-2.9	-76.8	-6.9	-0.008809	2.89	4.9	32.1
8b	1.677	1.40	8.40	2.17	-61.0	-44.9	30.7	2.8	-	-	0.001908			
9a	-1.575	-1.31	-0.36	-4.33	-77.0	-77.9	-28.7	-2.6	-74.2	-6.7	-0.009680	2.62	4.0	36.2
9b	1.675	1.40	8.08	1.91	-59.3	-43.9	28.6	2.6	-	-	0.001431			
10a	-2.145	-1.79	-1.03	-4.68	-80.2	-82.5	-33.6	-3.0	-81.4	-7.3	-0.013566	2.19	7.7	43.9
10b	2.236	1.86	8.47	2.19	-60.4	-44.1	31.2	2.8	-	-	0.002787			
11a	-2.116	-1.76	0.05	-4.18	-76.6	-76.6	-25.7	-2.3	-76.9	-6.9	-0.016402	1.84	6.3	50.1
11b	2.238	1.87	7.98	1.76	-58.6	-43.1	28.0	2.5	-	-	0.000472			
12a	-2.236	-1.86	0.69	-3.60	-74.0	-73.0	-21.3	-1.9	-74.9	-6.7	-0.020037	1.57	5.8	55.9
12b	2.235	1.86	7.65	1.47	-57.7	-42.8	25.9	2.3	-	-	-0.001944			

C.2 SPECIMEN 1 AFTER RETROFIT

Views during and at the end of the last cycle: Cycle 15 (±3.73% bidirectional drift)

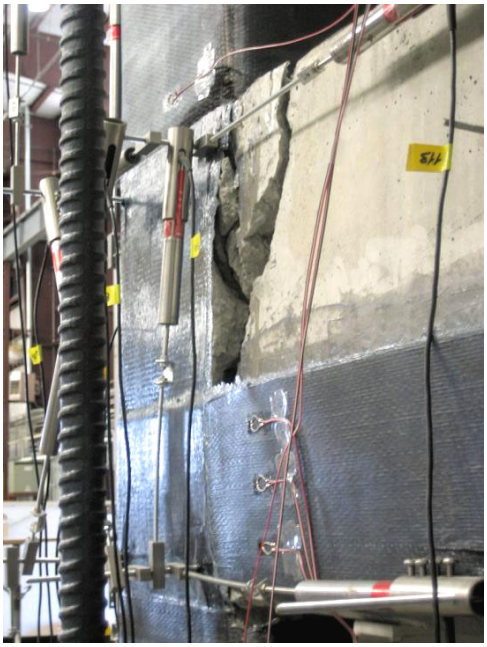

(a) EW beam hinge

(b) EW beam CFRP strips

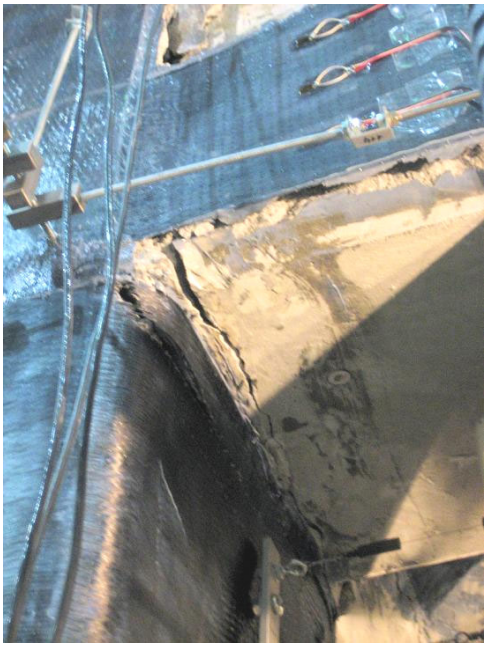

(c) EW beam bottom

(d) Joint NE corner

Figure C.9 — Damage modes – Specimen 1 after retrofit.

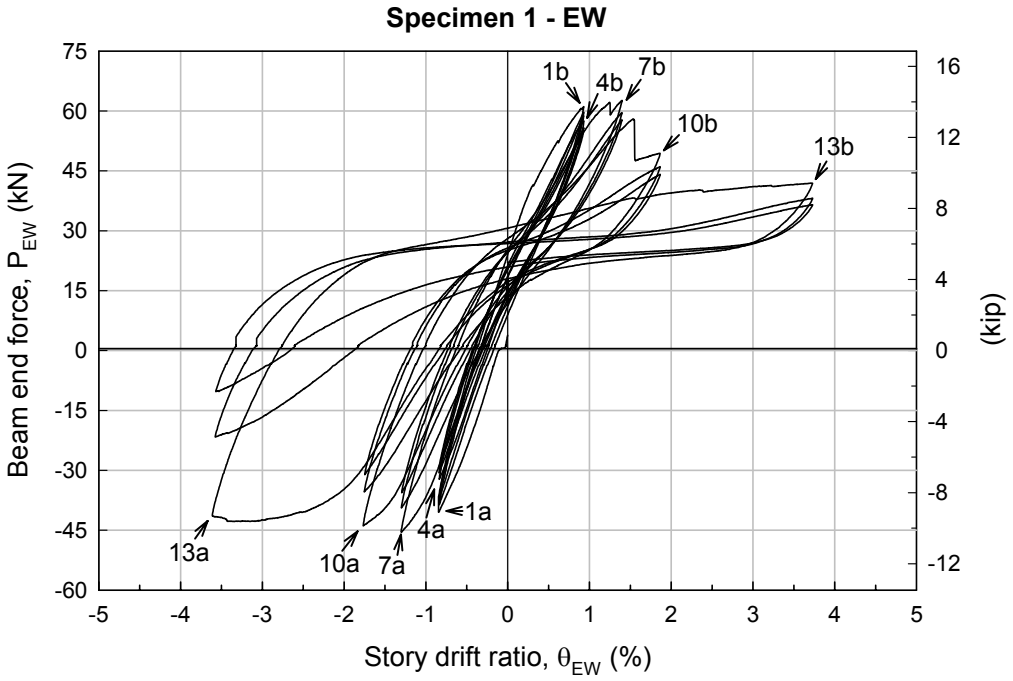

(a)

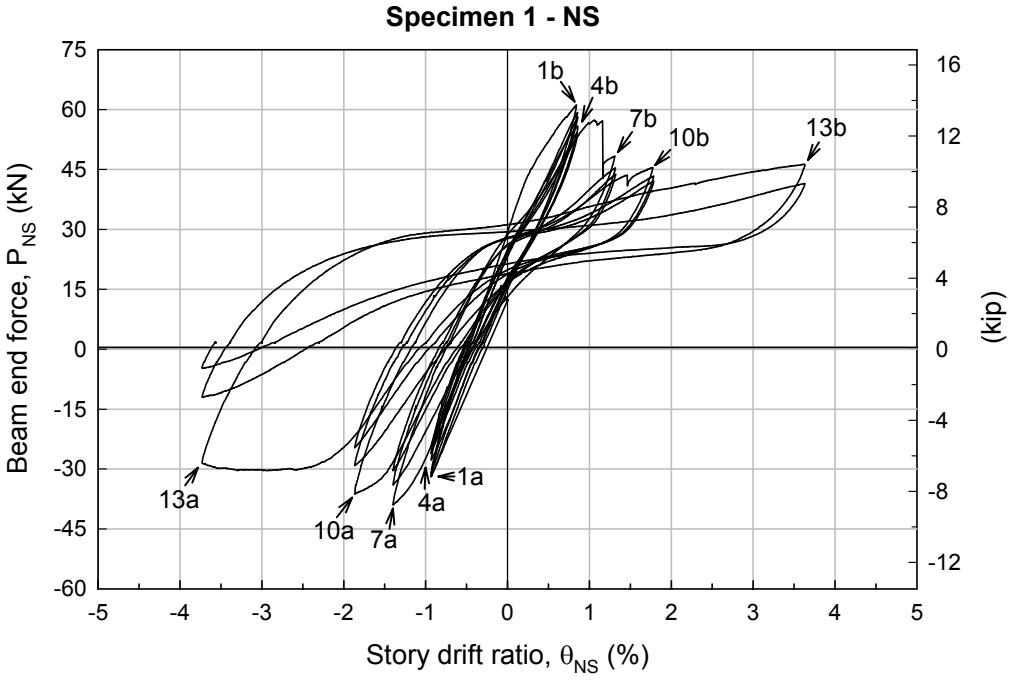

(b)

Figure C.10 — Force-drift hysteretic curves – Specimen 1 after retrofit: (a) EW, and (b) NS direction.

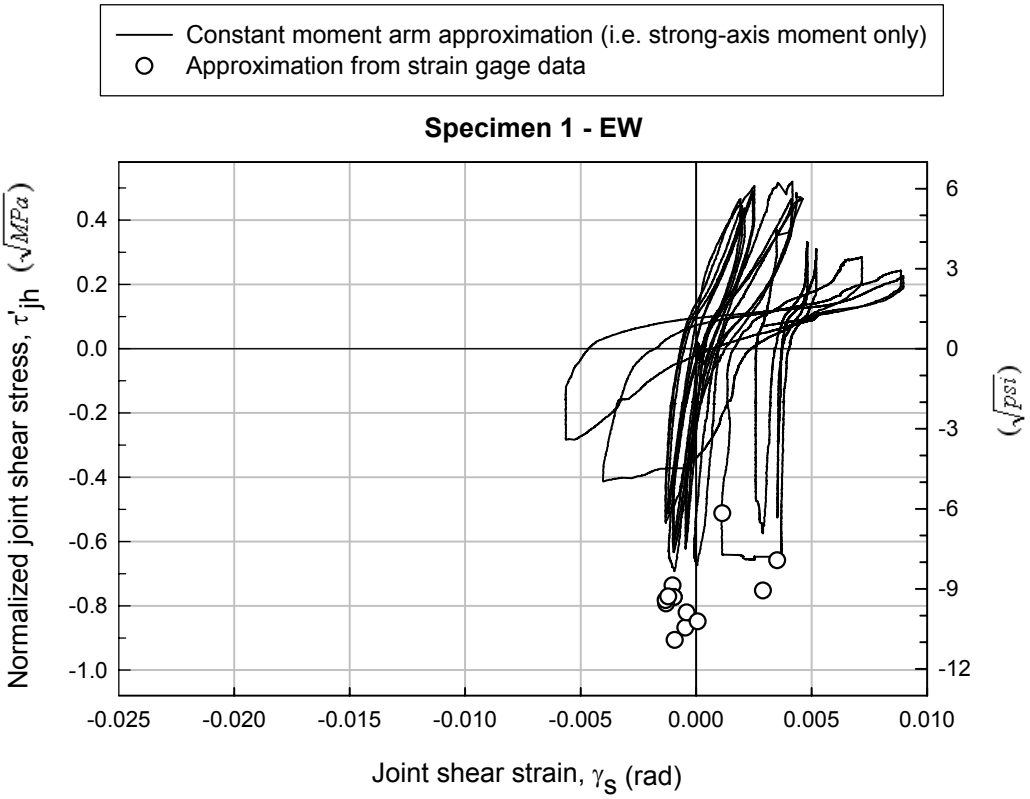

(a)

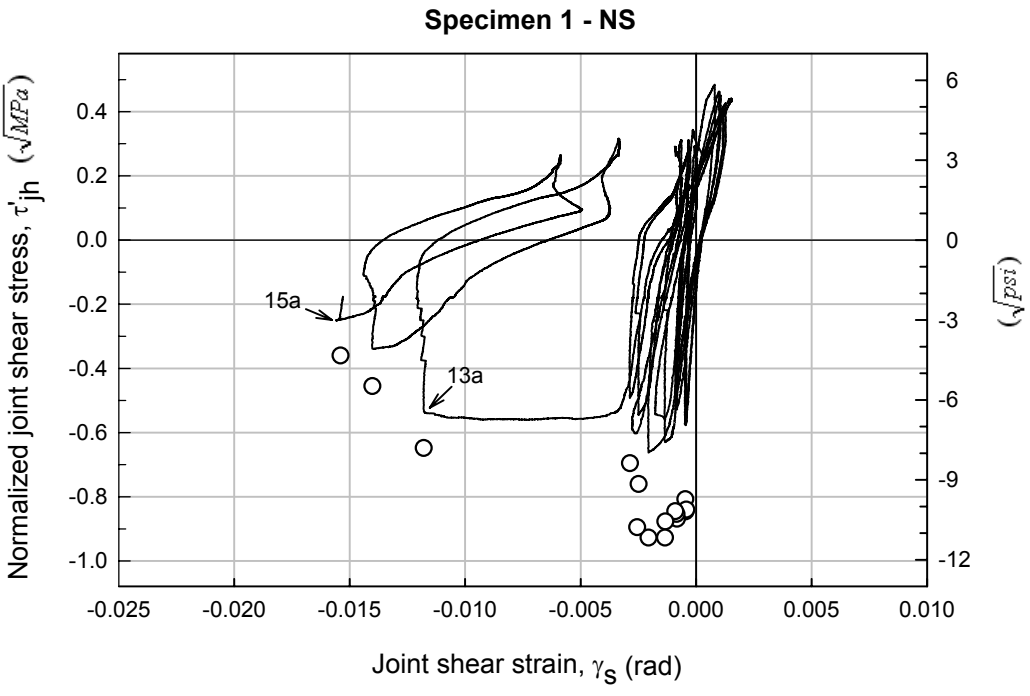

(b)

Figure C.11 — Joint shear stress-strain hysteretic curves – Specimen 1 after retrofit: (a) EW, and (b) NS direction.

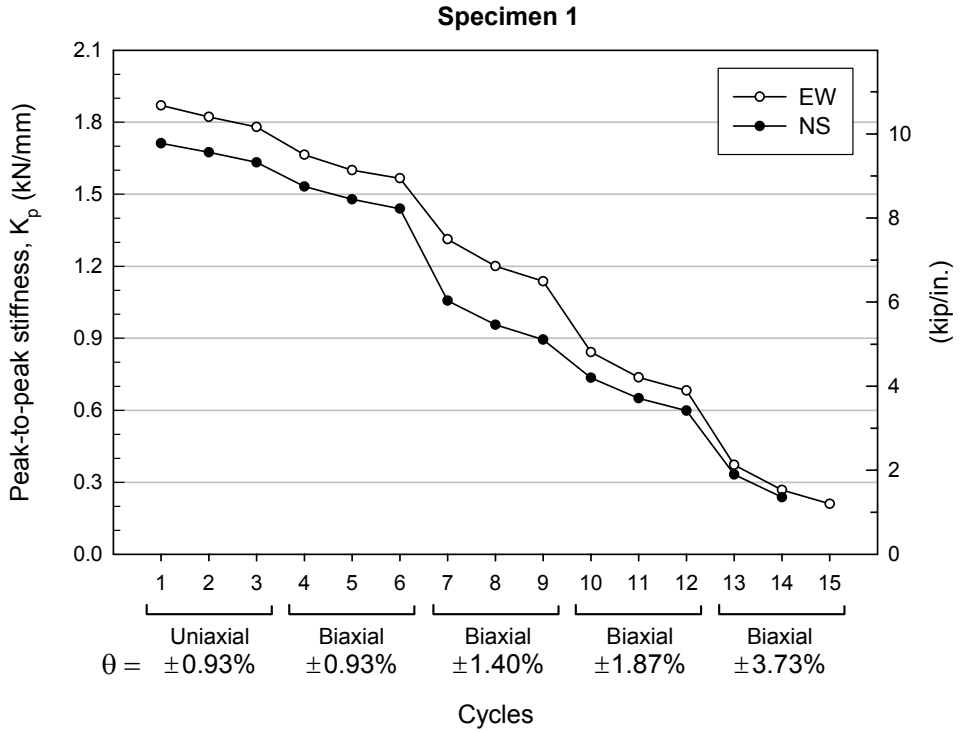

Figure C.12 — Variation of peak-to-peak stiffness – Specimen 1 after retrofit.

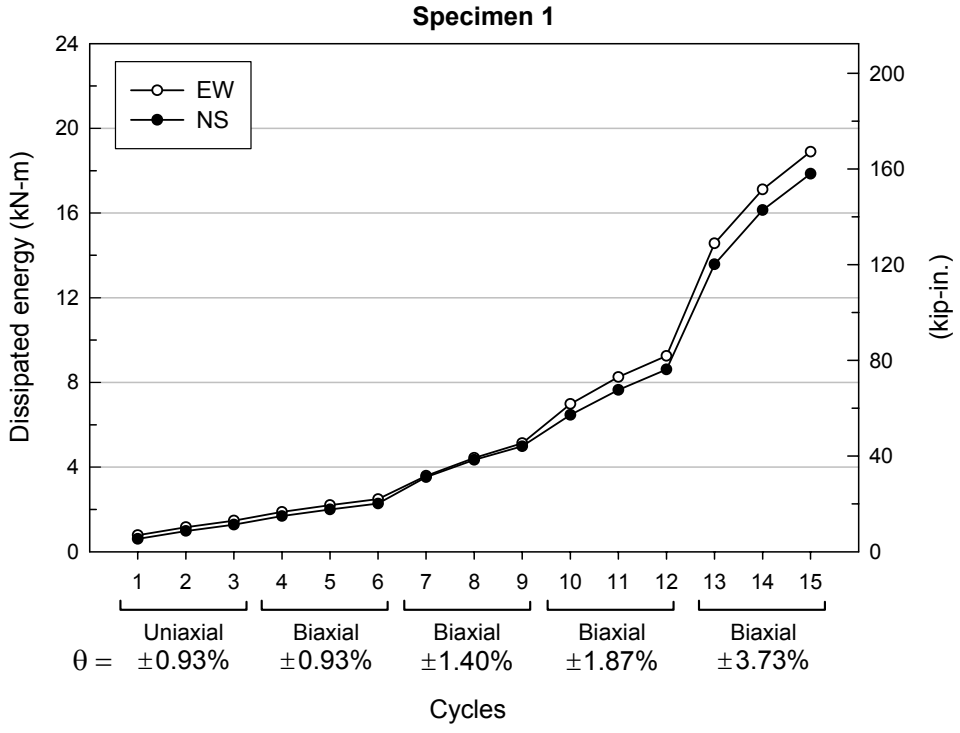

Figure C.13 — Variation of cumulative dissipated energy – Specimen 1 after retrofit.

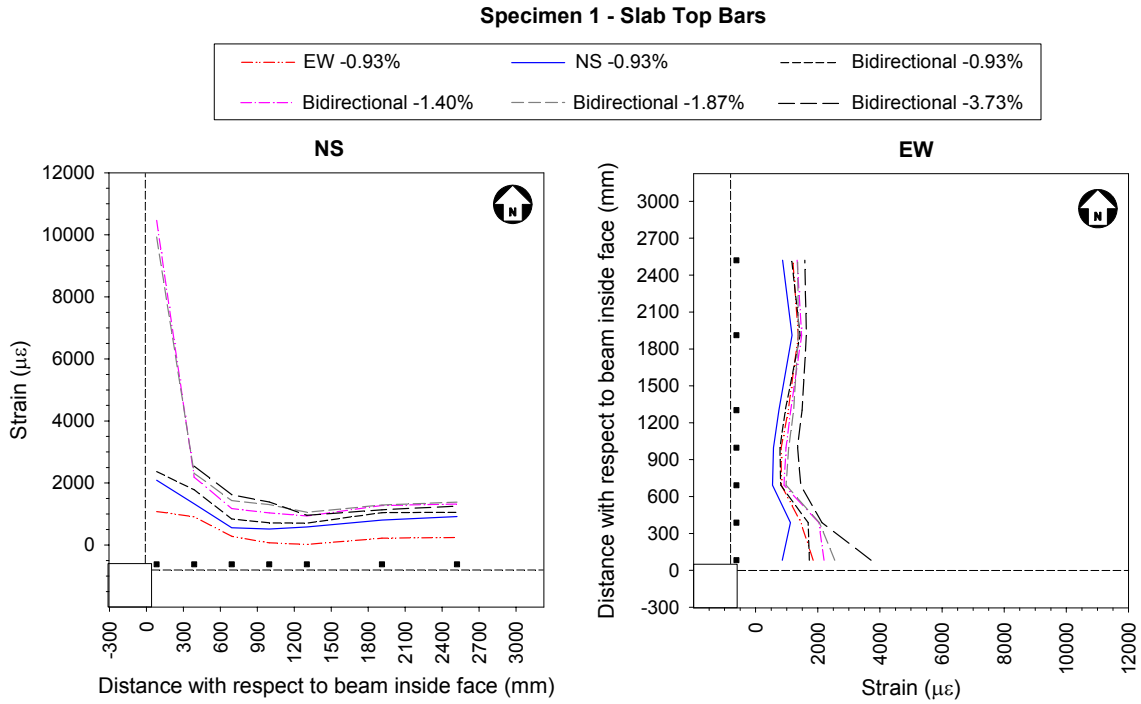

(a)

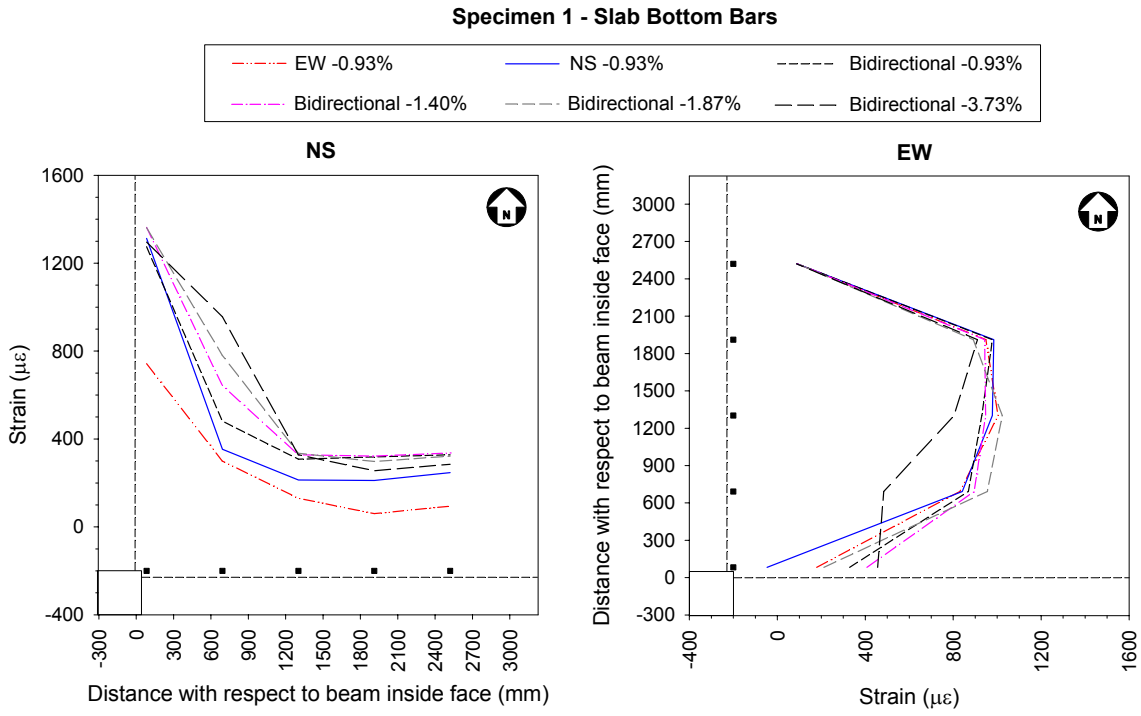

(b)

Figure C.14 — Strains in the slab bars at the first peak of downward loading at each drift level – Specimen 1 after retrofit: (a) top bars, and (b) bottom bars.

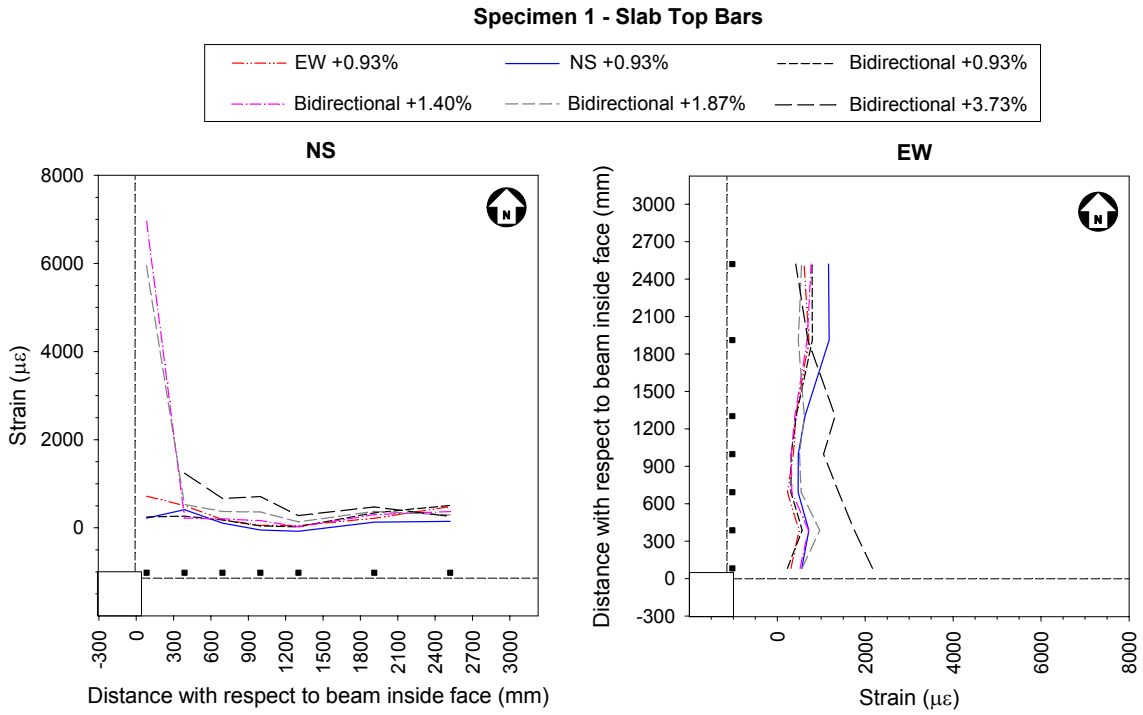

(a)

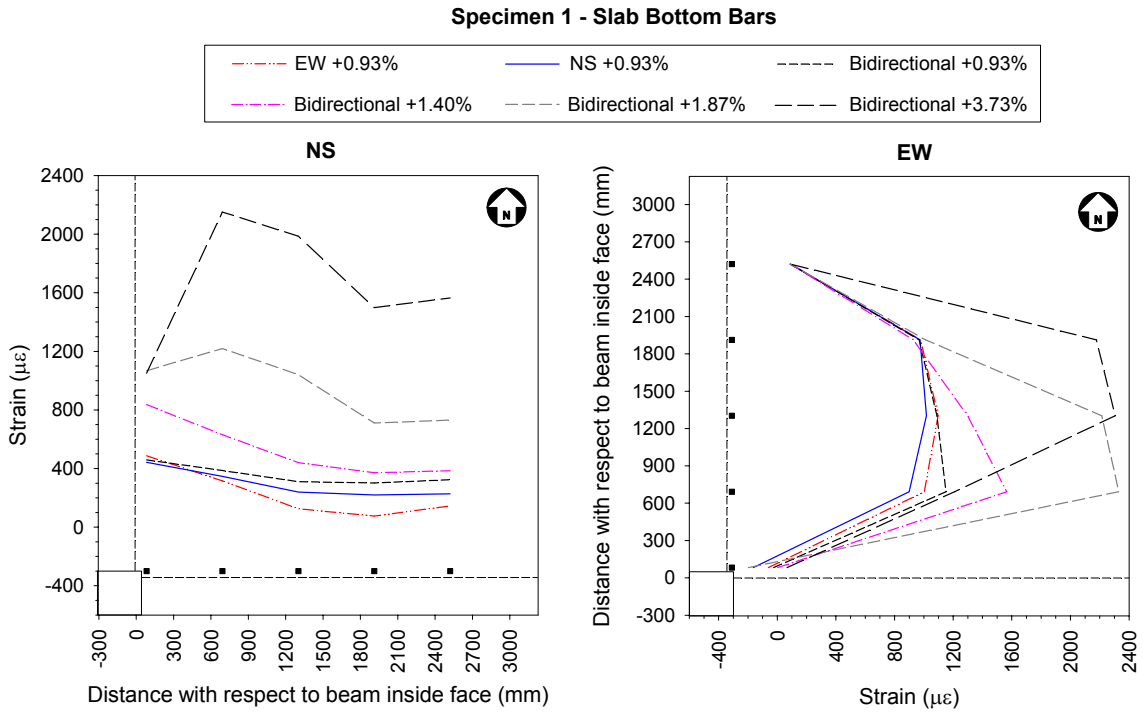

(b)

Figure C.15 — Strains in the slab bars at the first peak of upward loading at each drift level – Specimen 1 after retrofit: (a) top bars, and (b) bottom bars.

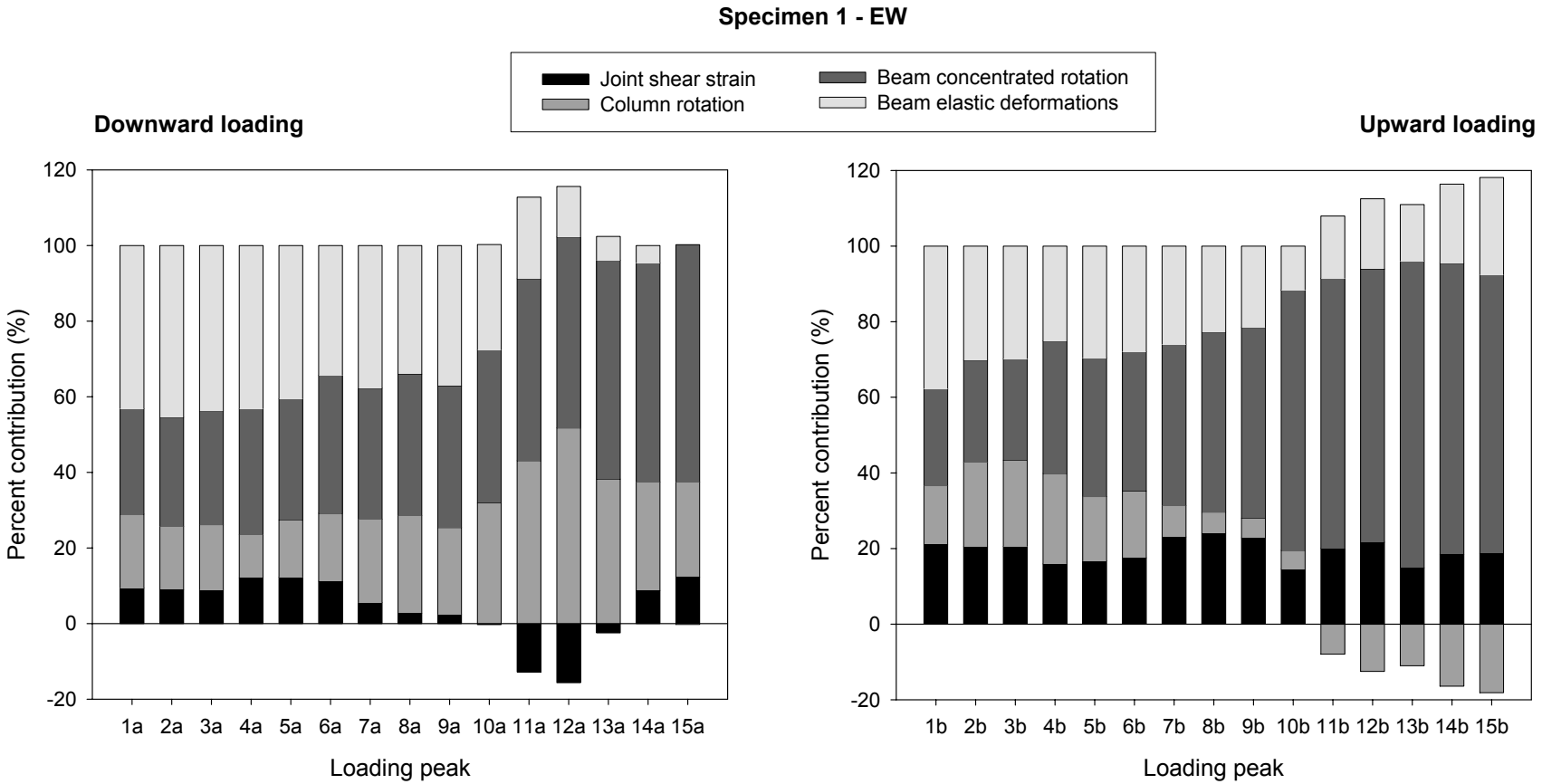

Figure C.16 — Percent contributions to applied interstory drift – Specimen 1 after retrofit, EW direction.

(Note: A similar plot for the NS direction could not be developed due to malfunctioning of an instrument.)

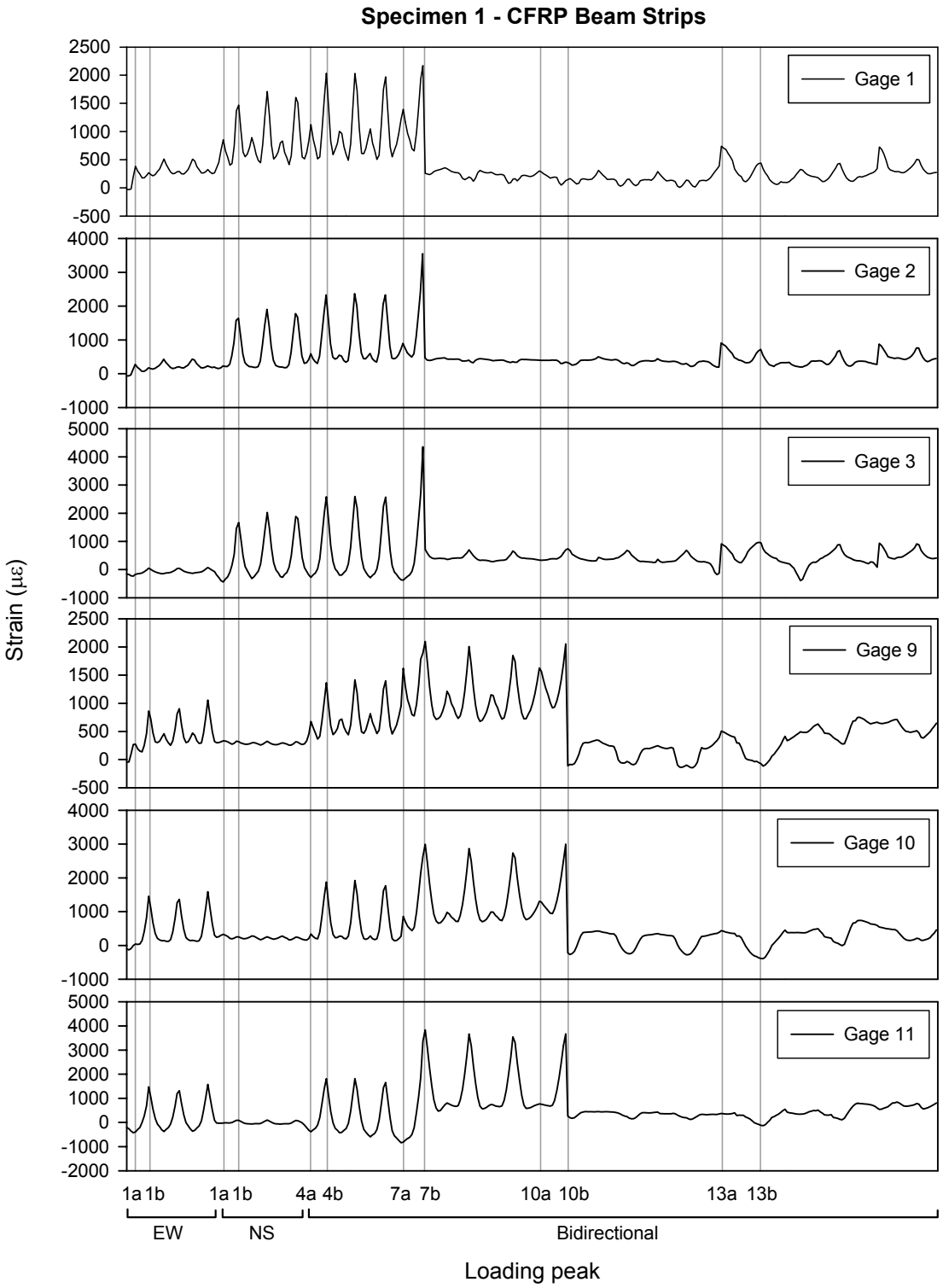

Figure C.17 — Strains in the CFRP beam strips – Specimen 1:
Gages 1, 2, 3: NS beam near column face; Gages 9, 10, 11: EW beam near column face.
(Gage locations and orientations are shown in Figure B.30.)

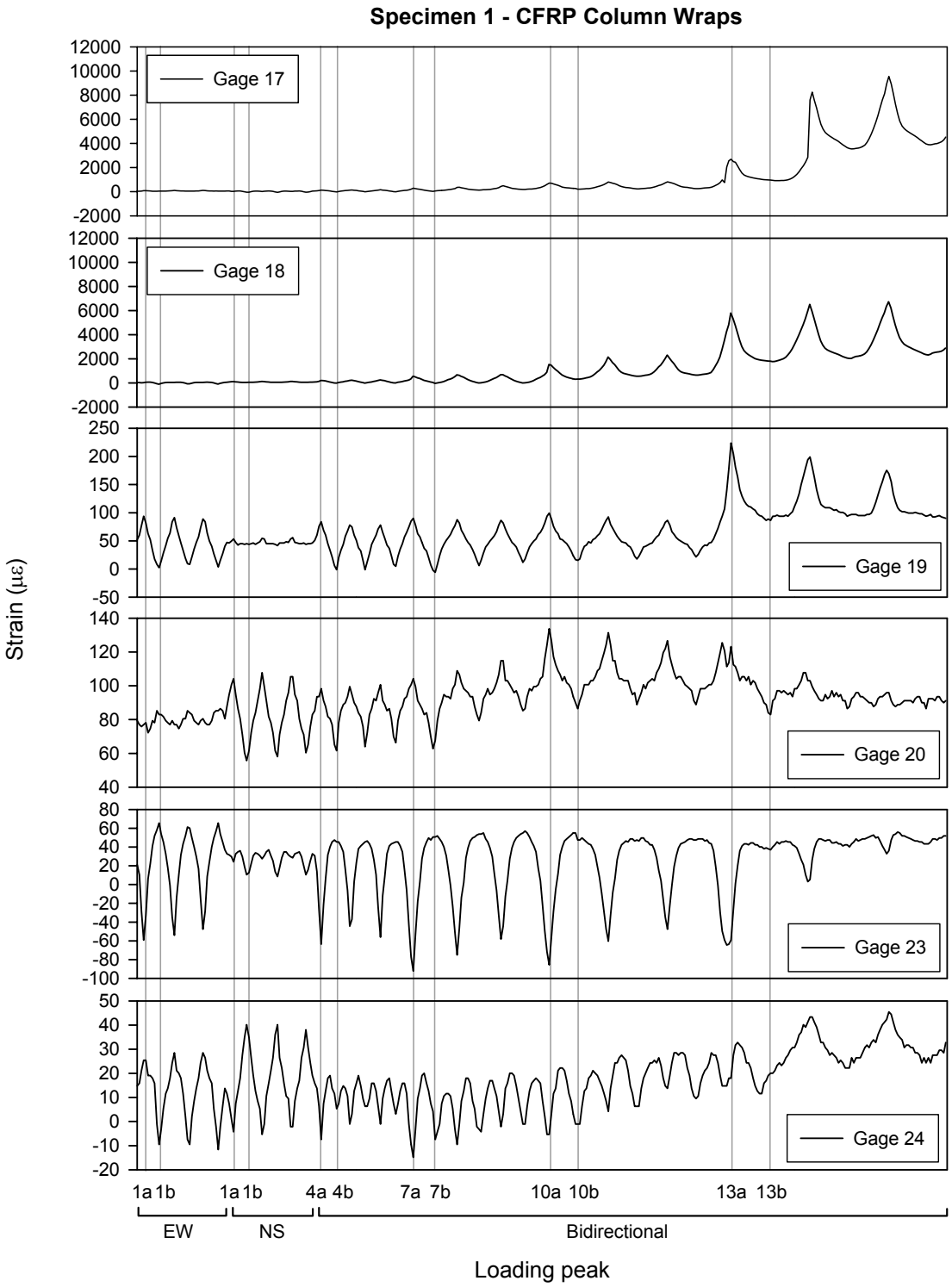

Figure C.18 — Strains in the CFRP column wraps – Specimen 1:
Gages 17, 18: Upper column, 1st stirrup level; Gages 19, 20: Upper column, 2nd stirrup level; Gages 23, 24: Lower column, 2nd stirrup level.
(Gage locations and orientations are shown in Figure B.30.)

Table C.3 — Summary of test results – Specimen 1 after retrofit, EW direction.

Loading Peak	Δ_b (in.)	θ (%)	P (kip)	V_{col} (kip)	$P_{u.col}$ (kip)	$P_{l.col}$ (kip)	V_{jh} (kip)	τ'_{jh} ($\sqrt{psi}$)	V_{jh}^{sg} (kip)	τ'^{sg}_{jh} ($\sqrt{psi}$)	γ_s (rad)	K_p (kip/in.)	E^i (kip-in.)	E^{tot} (kip-in.)
0	0.000	0.00	0.86	-3.89	-74.6	-72.7	-18.7	-1.7	-	-	0.000000	-	-	-
1a	-1.013	-0.84	-8.23	-11.07	-79.9	-87.0	-79.2	-7.1	-98.8	-8.9	-0.001023	10.68	6.9	6.9
1b	1.116	0.93	13.65	6.86	-75.4	-60.5	67.3	6.0	-	-	0.002525			
2a	-1.001	-0.83	-8.57	-11.47	-79.5	-87.0	-81.3	-7.3	-103.7	-9.3	-0.000970	10.40	3.3	10.3
2b	1.117	0.93	13.37	6.60	-74.9	-60.3	65.5	5.9	-	-	0.002456			
3a	-1.009	-0.84	-8.37	-11.27	-79.0	-86.3	-80.1	-7.2	-103.7	-9.3	-0.000968	10.17	2.7	13.0
3b	1.115	0.93	13.15	6.45	-74.5	-60.1	64.0	5.7	-	-	0.002463			
4a	-1.002	-0.83	-7.20	-10.06	-81.7	-95.1	-72.6	-6.5	-106.3	-9.6	-0.001305	9.50	3.7	16.6
4b	1.117	0.93	12.83	6.15	-74.9	-49.6	61.8	5.6	-	-	0.001911			
5a	-1.002	-0.83	-6.82	-9.80	-81.1	-93.7	-70.0	-6.3	-104.9	-9.4	-0.001324	9.14	2.9	19.5
5b	1.114	0.93	12.45	5.95	-74.3	-49.8	59.1	5.3	-	-	0.002003			
6a	-1.007	-0.84	-6.60	-9.65	-80.7	-92.9	-68.5	-6.2	-103.4	-9.3	-0.001213	8.95	2.5	22.0
6b	1.116	0.93	12.35	5.85	-74.0	-49.7	58.4	5.2	-	-	0.002103			
7a	-1.560	-1.30	-10.11	-12.24	-87.8	-106.5	-92.0	-8.3	-121.5	-10.9	-0.000930	7.50	9.8	31.7
7b	1.677	1.40	14.03	7.67	-76.6	-51.8	69.4	6.2	-	-	0.004161			
8a	-1.557	-1.30	-8.75	-11.32	-86.8	-103.1	-82.8	-7.4	-116.4	-10.5	-0.000466	6.85	7.5	39.2
8b	1.673	1.39	13.29	7.05	-75.3	-51.9	64.4	5.8	-	-	0.004324			
9a	-1.552	-1.29	-7.92	-10.76	-85.6	-100.3	-77.2	-6.9	-110.1	-9.9	-0.000411	6.49	6.1	45.3
9b	1.678	1.40	12.95	6.76	-74.4	-51.7	62.1	5.6	-	-	0.004119			
10a	-2.116	-1.76	-9.80	-12.06	-91.1	-109.0	-89.9	-8.1	-113.8	-10.2	0.000064	4.81	16.4	61.7
10b	2.234	1.86	11.03	5.10	-75.1	-53.9	49.2	4.4	-	-	0.003476			
11a	-2.103	-1.75	-7.97	-11.13	-88.5	-103.1	-77.2	-6.9	-100.9	-9.1	0.002889	4.21	11.3	73.0
11b	2.234	1.86	10.27	4.61	-72.8	-52.8	43.9	3.9	-	-	0.004812			
12a	-2.094	-1.74	-6.91	-10.44	-86.4	-98.8	-70.0	-6.3	-88.3	-7.9	0.003508	3.90	8.8	81.8
12b	2.233	1.86	9.84	4.14	-71.5	-52.3	41.1	3.7	-	-	0.005196			
13a	-4.332	-3.61	-9.27	-12.51	-97.0	-112.6	-85.5	-7.7	-68.7	-6.2	0.001131	2.13	47.1	128.9
13b	4.471	3.73	9.35	3.86	-76.4	-56.7	37.6	3.4	-	-	0.007162			
14a	-4.285	-3.57	-4.75	-9.75	-85.8	-93.2	-54.6	-4.9	-	-	-0.004032	1.53	22.5	151.5
14b	4.474	3.73	8.53	2.97	-72.2	-54.4	32.3	2.9	-	-	0.008881			
15a	-4.275	-3.56	-2.22	-8.06	-79.1	-82.3	-37.4	-3.4	-	-	-0.005652	1.20	15.7	167.2
15b	4.475	3.73	8.18	2.53	-69.7	-61.1	30.1	2.7	-	-	0.008973			

Table C.4 — Summary of test results – Specimen 1 after retrofit, NS direction.

Loading Peak	Δ_b (in.)	θ (%)	P (kip)	V_{col} (kip)	$P_{u.col}$ (kip)	$P_{l.col}$ (kip)	V_{jh} (kip)	τ'_{jh} ($\sqrt{psi}$)	V_{jh}^{sg} (kip)	$\tau'_{jh}{}^{sg}$ ($\sqrt{psi}$)	γ_s (rad)	K_p (kip/in.)	E^i (kip-in.)	E^{tot} (kip-in.)
0	0.000	0.00	-	-1.32	-74.6	-72.7	-	-	-	-	-	-	-	-
1a	-1.113	-0.93	-6.98	-8.87	-79.1	-83.4	-75.7	-6.8	-108.3	-9.7	-0.000471	9.78	5.4	5.4
1b	1.010	0.84	13.67	6.91	-74.8	-57.2	64.3	5.8	-	-	0.000793			
2a	-1.118	-0.93	-7.19	-8.87	-78.8	-83.1	-77.4	-7.0	-113.4	-10.2	-0.000457	9.56	3.2	8.6
2b	1.027	0.86	13.28	6.58	-74.0	-56.7	61.8	5.6	-	-	0.001010			
3a	-1.117	-0.93	-6.93	-8.71	-78.4	-82.3	-75.5	-6.8	-112.7	-10.1	-0.000427	9.32	2.6	11.3
3b	1.029	0.86	13.01	6.39	-73.6	-56.5	60.0	5.4	-	-	0.001063			
4a	-1.118	-0.93	-6.22	-7.93	-81.7	-95.1	-70.8	-6.4	-116.5	-10.5	-0.000830	8.75	3.6	14.9
4b	1.030	0.86	12.46	5.87	-74.9	-49.6	56.5	5.1	-	-	0.001272			
5a	-1.116	-0.93	-5.79	-7.62	-81.1	-93.7	-67.7	-6.1	-114.5	-10.3	-0.000853	8.44	2.8	17.7
5b	1.016	0.85	12.09	5.61	-74.3	-49.8	54.1	4.9	-	-	0.001189			
6a	-1.118	-0.93	-5.57	-7.47	-80.7	-92.9	-66.2	-5.9	-113.3	-10.2	-0.000913	8.22	2.4	20.1
6b	1.024	0.85	11.97	5.52	-74.0	-49.7	53.3	4.8	-	-	0.001152			
7a	-1.676	-1.40	-8.67	-9.64	-87.8	-106.5	-88.1	-7.9	-124.3	-11.2	-0.002067	6.03	11.1	31.2
7b	1.572	1.31	10.81	4.78	-76.6	-51.8	45.6	4.1	-	-	-0.000137			
8a	-1.675	-1.40	-7.55	-8.87	-86.8	-103.1	-80.2	-7.2	-120.0	-10.8	-0.002552	5.46	7.2	38.4
8b	1.579	1.32	10.10	4.18	-75.3	-51.9	41.1	3.7	-	-	-0.000354			
9a	-1.675	-1.40	-6.77	-8.38	-85.6	-100.3	-74.6	-6.7	-117.6	-10.6	-0.001339	5.11	5.7	44.0
9b	1.585	1.32	9.81	3.94	-74.4	-51.7	39.2	3.5	-	-	-0.000071			
10a	-2.236	-1.86	-8.09	-9.18	-91.1	-109.0	-84.0	-7.6	-124.3	-11.2	-0.001349	4.20	13.1	57.2
10b	2.128	1.77	10.14	4.29	-75.1	-53.9	41.2	3.7	-	-	-0.000645			
11a	-2.238	-1.86	-6.55	-8.16	-88.5	-103.1	-73.1	-6.6	-101.9	-9.2	-0.002489	3.71	10.5	67.6
11b	2.140	1.78	9.65	3.90	-72.8	-52.8	38.1	3.4	-	-	-0.000265			
12a	-2.236	-1.86	-5.48	-7.44	-86.4	-98.8	-65.5	-5.9	-93.3	-8.4	-0.002868	3.42	8.5	76.2
12b	2.140	1.78	9.37	3.74	-71.5	-52.3	36.2	3.2	-	-	-0.000347			
13a	-4.475	-3.73	-6.36	-7.98	-97.0	-112.6	-71.8	-6.4	-86.9	-7.8	-0.011796	1.90	44.0	120.1
13b	4.357	3.63	10.32	5.02	-76.4	-56.7	41.8	3.8	-	-	-0.003369			
14a	-4.472	-3.73	-2.63	-5.79	-85.8	-93.2	-44.9	-4.0	-61.1	-5.5	-0.014018	1.36	22.7	142.8
14b	4.356	3.63	9.26	4.08	-72.2	-54.4	35.1	3.1	-	-	-0.005888			
15a	-4.475	-3.73	-1.00	-4.92	-79.1	-82.3	-33.1	-3.0	-48.3	-4.3	-0.015400	-	-	-
15b	-	-	-	3.56	-69.7	-61.1	-	-	-	-	-			

C.3 SPECIMEN 2 BEFORE RETROFIT

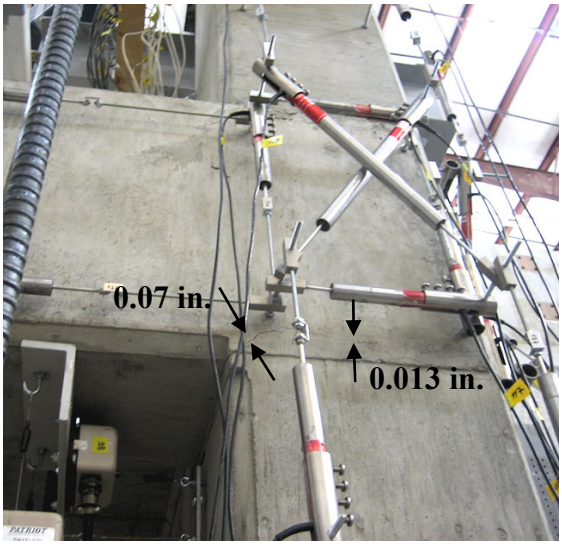

(a) NS joint panel at peak 2b
(+0.93% unidirectional drift)

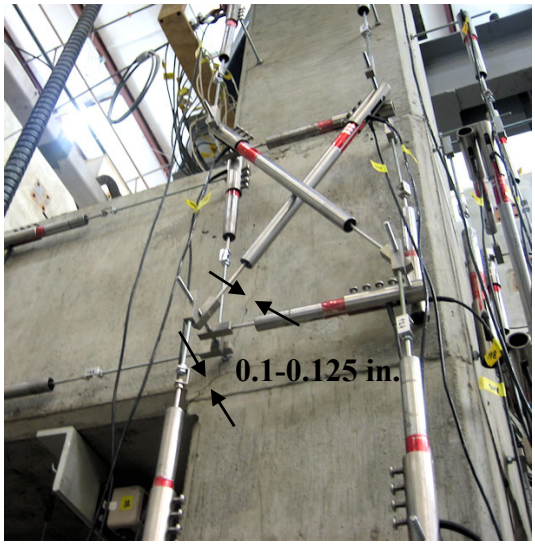

(b) NS joint panel at peak 5b
(+0.93% bidirectional drift)

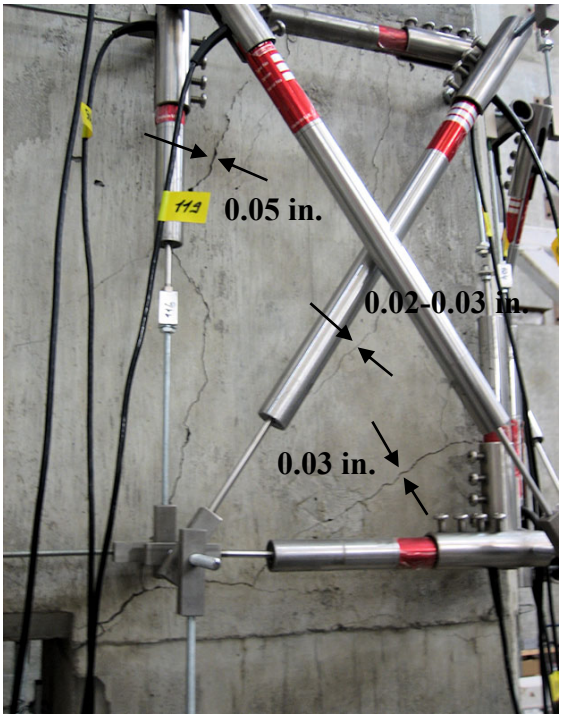

(c) NS joint panel at peak 8a
(-1.40% bidirectional drift)

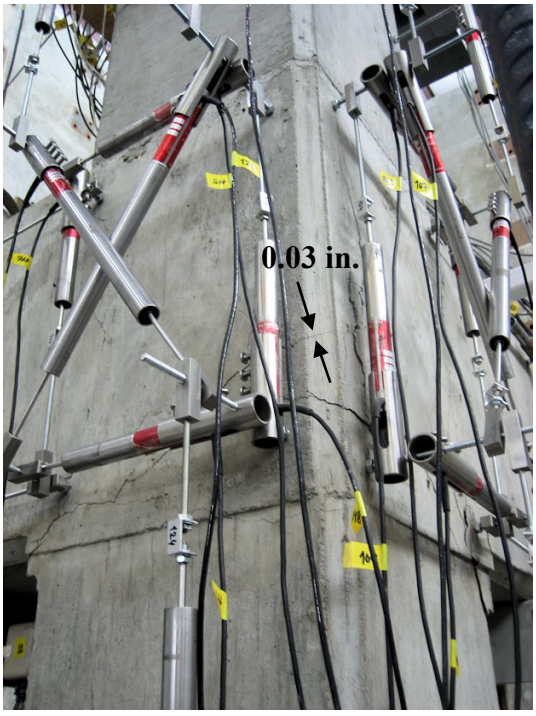

(d) SW joint corner at peak 8a
(-1.40% bidirectional drift)

Figure C.19 — Damage modes – Specimen 2 before retrofit.

Views during and at the end of the last cycle: Cycle 9 (±1.40% bidirectional drift)

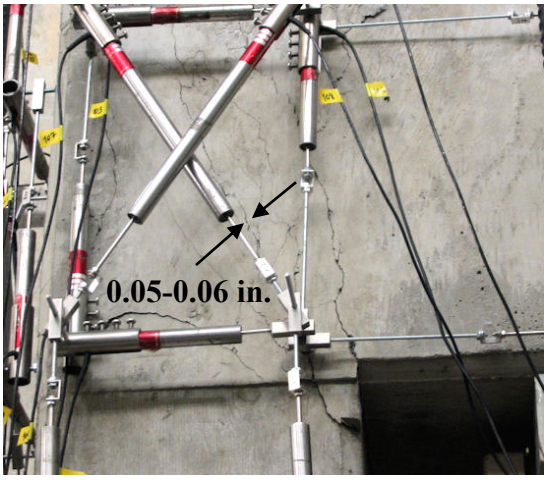

(e) EW joint panel (downward loading)

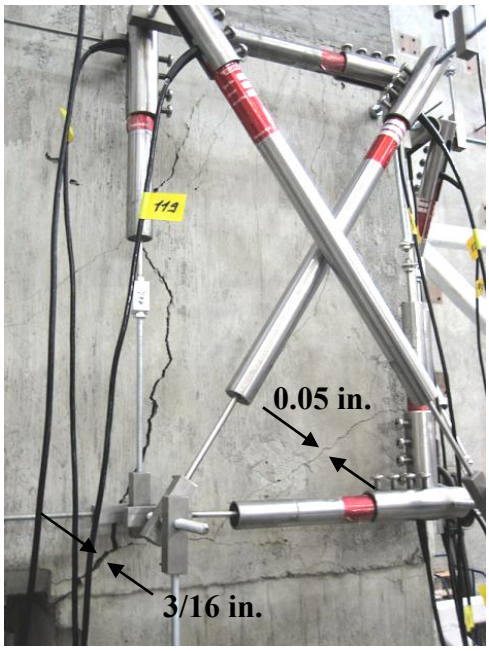

(f) NS joint panel (upward loading)

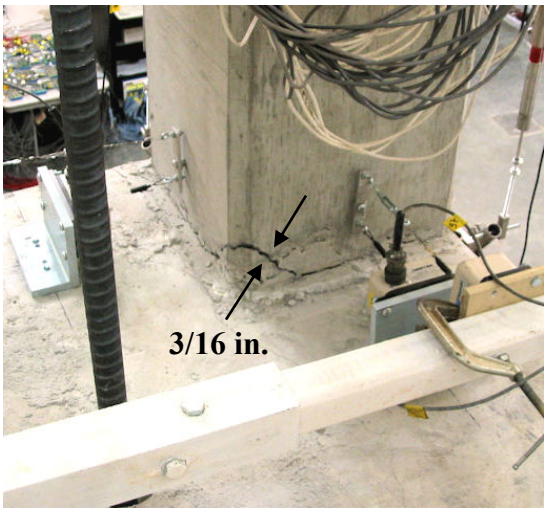

(g) Upper column NE corner

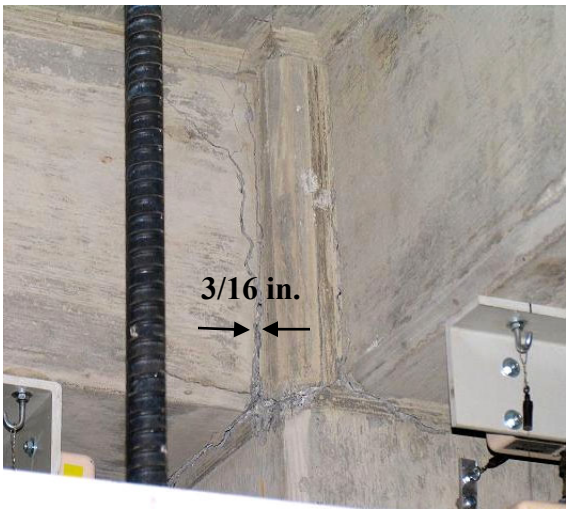

(h) Joint NE corner

Figure C.19 — Continued.

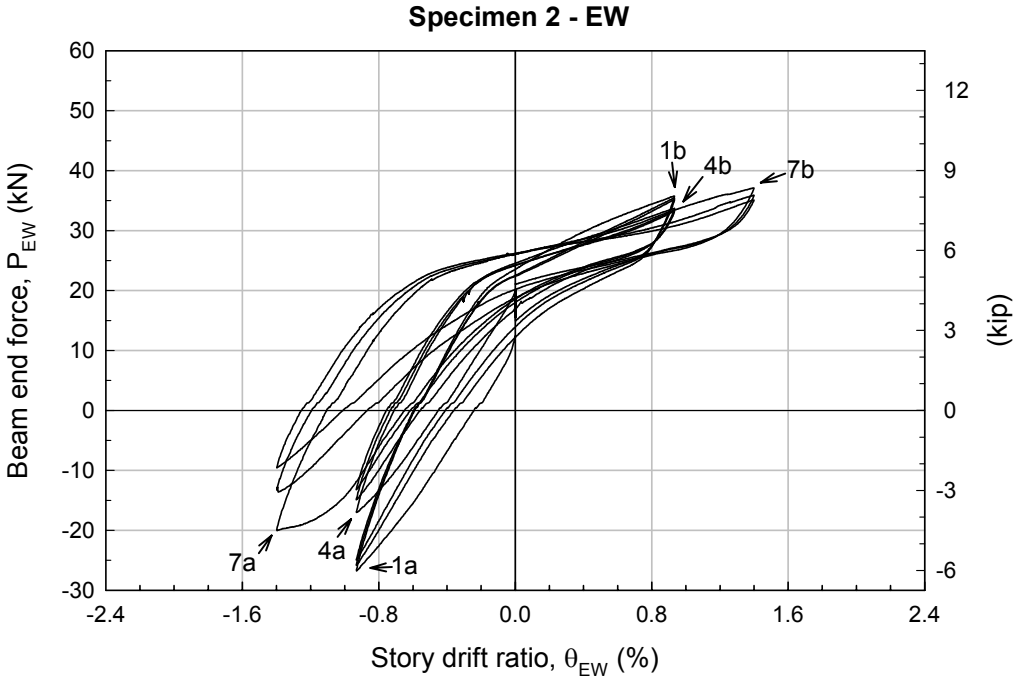

(a)

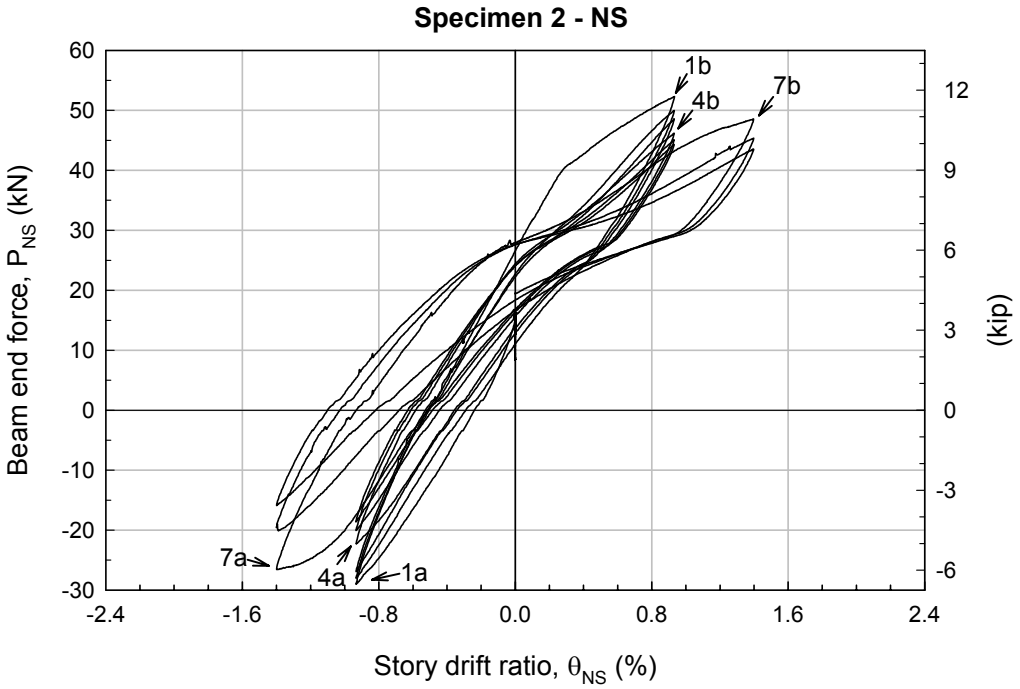

(b)

Figure C.20 — Force-drift hysteretic curves – Specimen 2 before retrofit: (a) EW, and (b) NS direction.

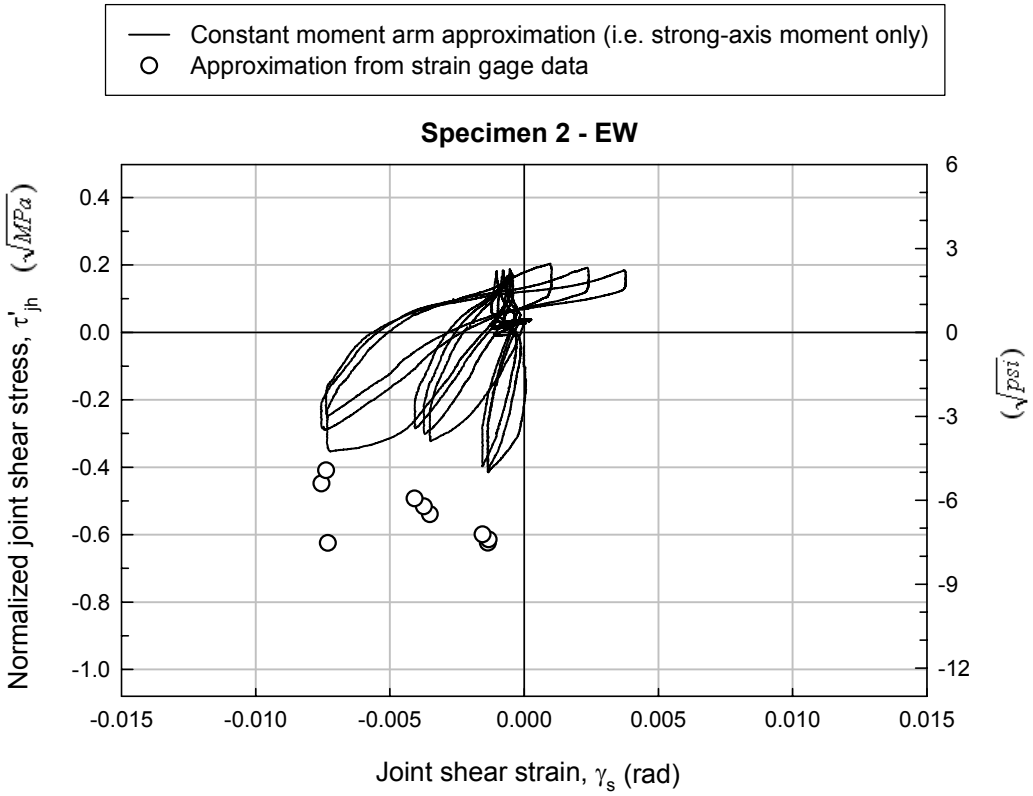

(a)

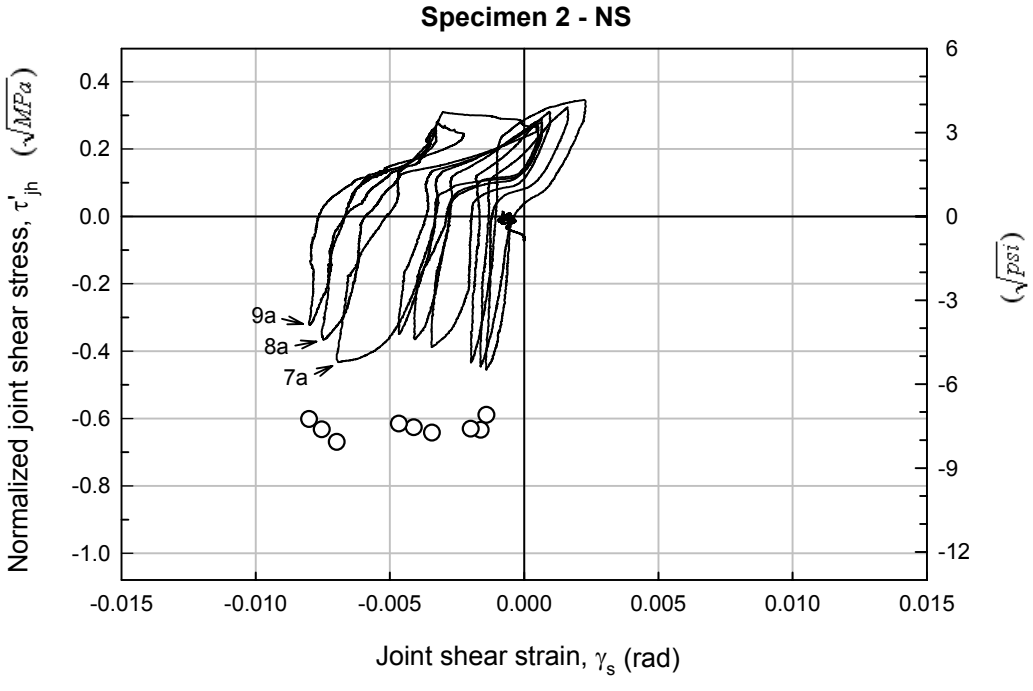

(b)

Figure C.21 — Joint shear stress-strain hysteretic curves – Specimen 2 before retrofit: (a) EW, and (b) NS direction.

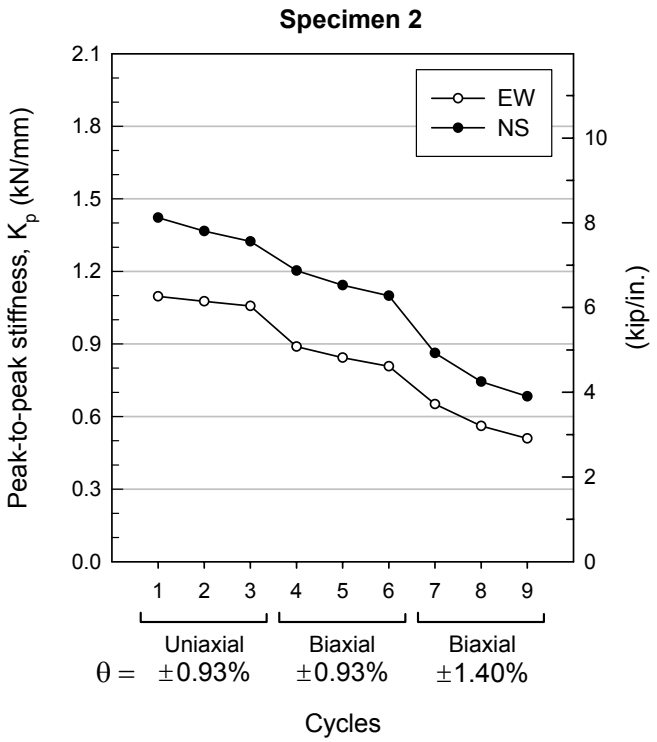

Figure C.22 — Variation of peak-to-peak stiffness – Specimen 2 before retrofit.

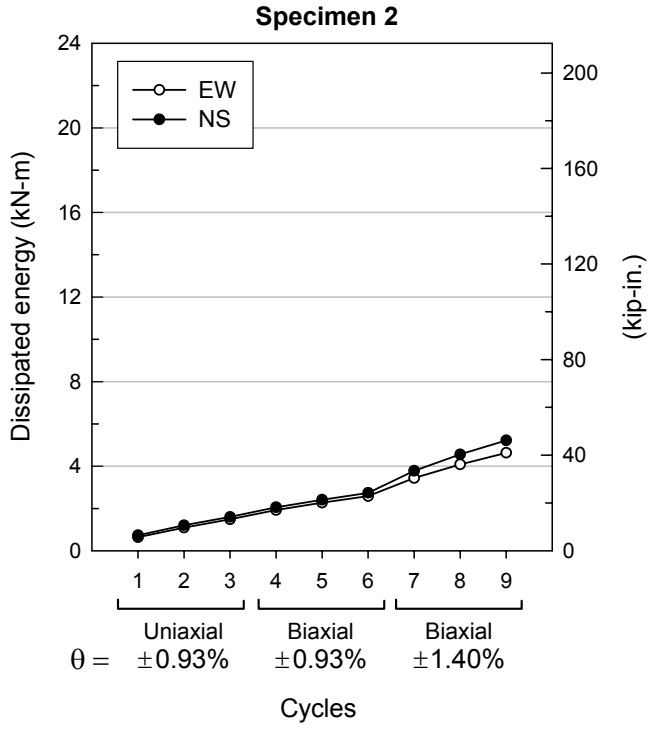

Figure C.23 — Variation of cumulative dissipated energy – Specimen 2 before retrofit.

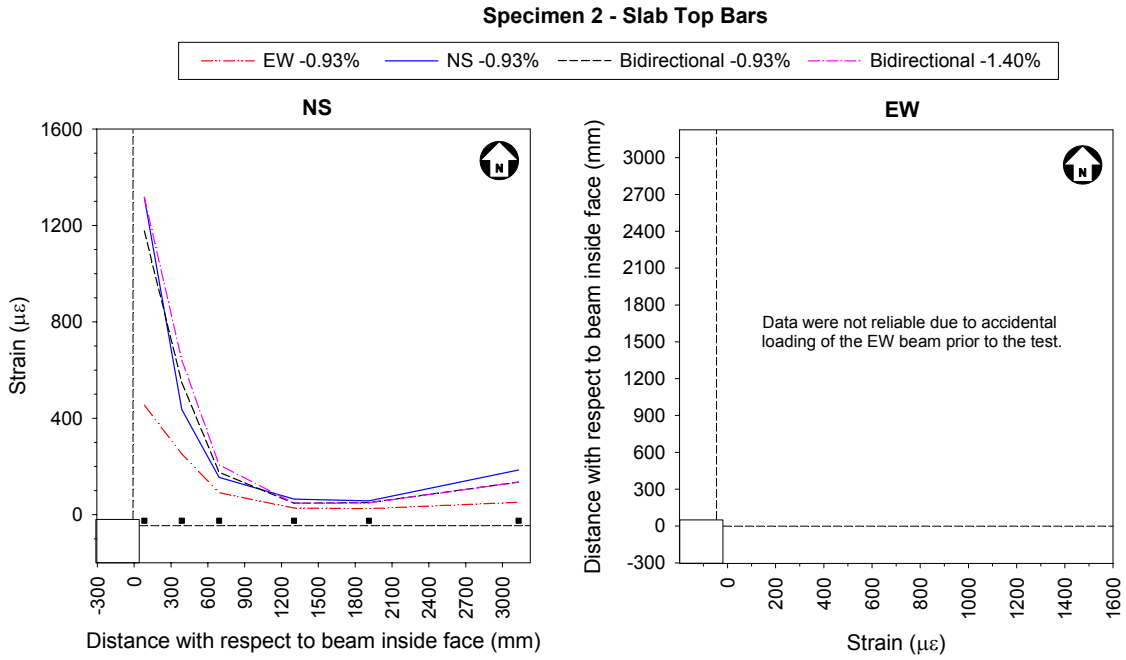

(a)

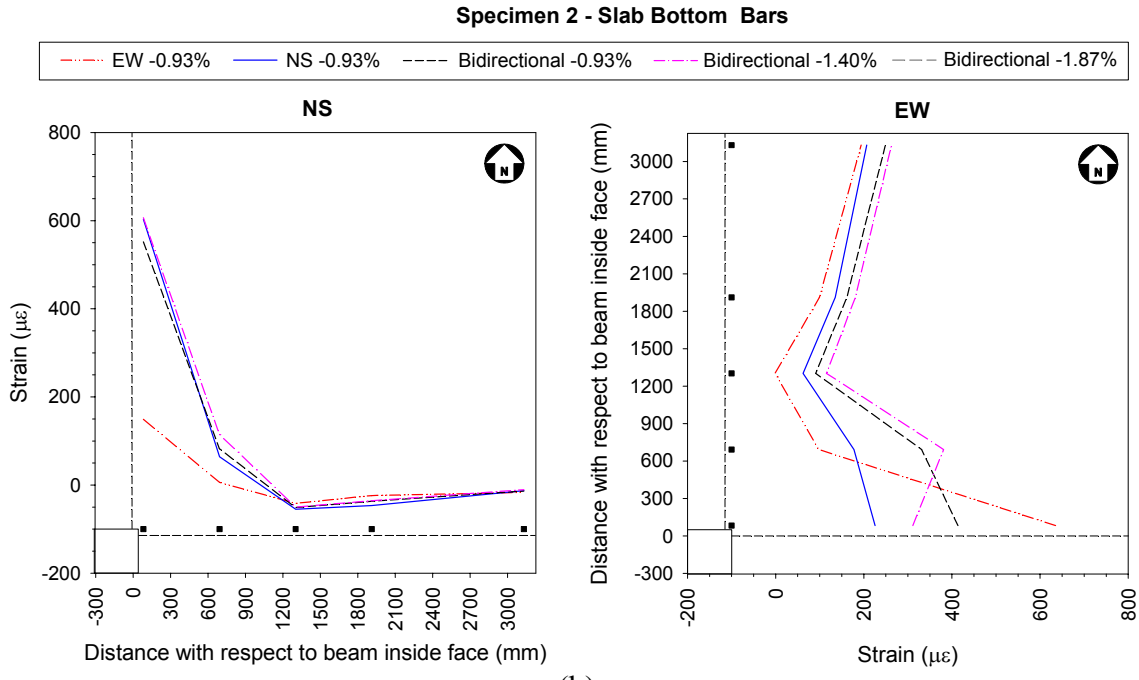

(b)

Figure C.24 — Strains in the slab bars at the first peak of downward loading at each drift level – Specimen 2 before retrofit: (a) top bars, and (b) bottom bars.

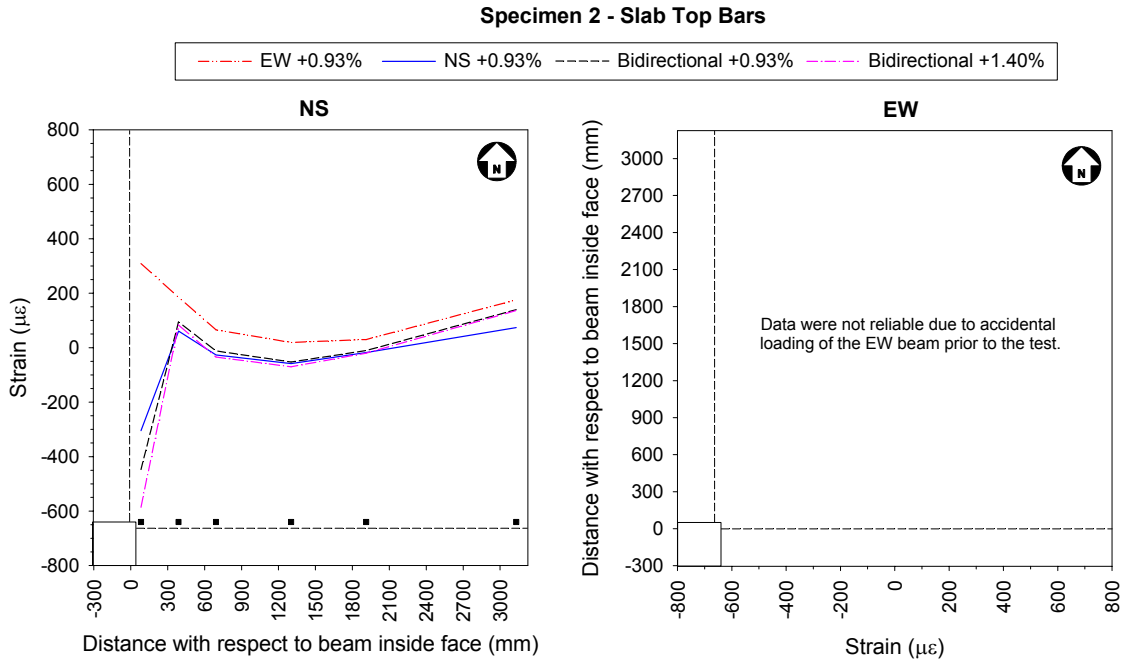

(a)

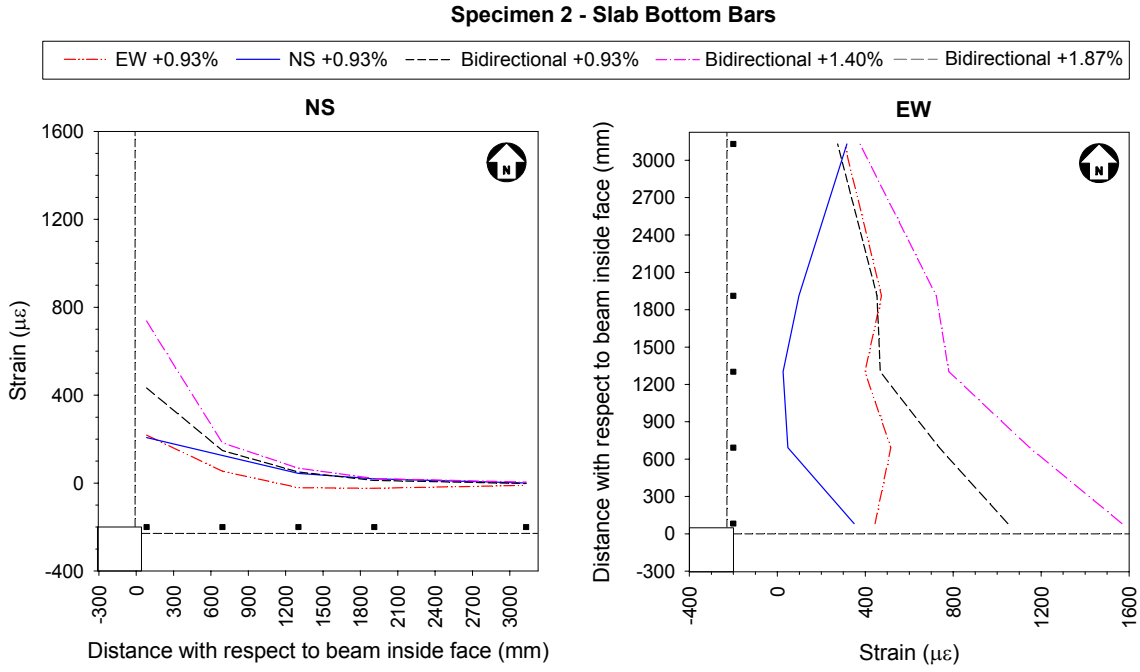

(b)

Figure C.25 — Strains in the slab bars at the first peak of upward loading at each drift level – Specimen 2 before retrofit: (a) top bars, and (b) bottom bars.

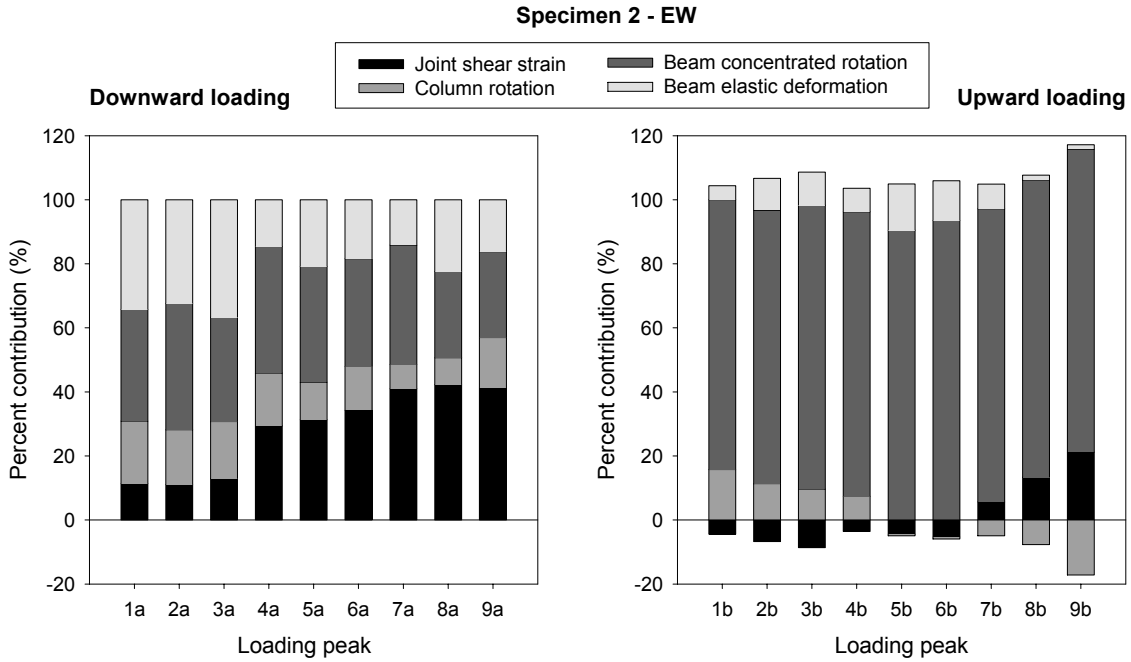

(a)

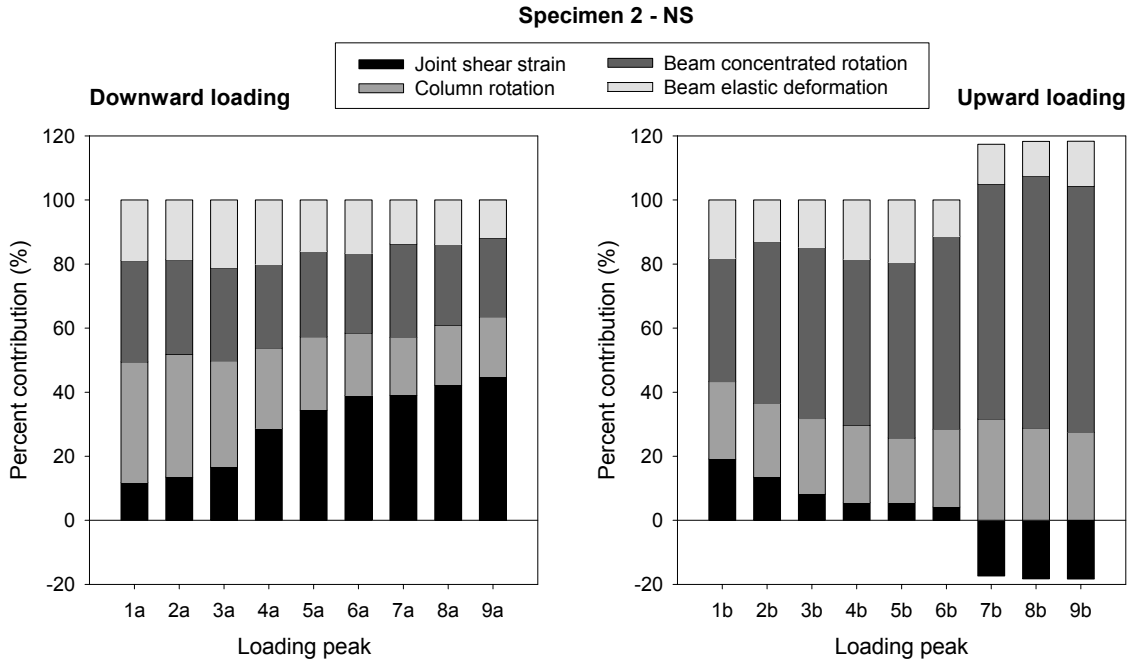

(b)

Figure C.26 — Percent contributions to applied interstory drift – Specimen 2 before retrofit: (a) EW, and (b) NS direction.

(The accidental upward loading of the EW beam prior to the test as mentioned previously is to be noted.)

Table C.5 — Summary of test results – Specimen 2 before retrofit, EW direction.

Loading Peak	Δ_b (in.)	θ (%)	P (kip)	V_{col} (kip)	$P_{u.col}$ (kip)	$P_{l.col}$ (kip)	V_{jh} (kip)	τ'_{jh} ($\sqrt{psi}$)	V_{jh}^{sg} (kip)	τ'^{sg}_{jh} ($\sqrt{psi}$)	γ_s (rad)	K_p (kip/in.)	E^i (kip-in.)	E^{tot} (kip-in.)
0	0.000	0.00	2.79	-1.89	-80.2	-75.5	-6.2	-0.48	-	-	0.000000	-	-	-
1a	-1.113	-0.93	-5.88	-9.18	-85.0	-88.3	-63.6	-4.94	-96.9	-7.5	-0.001354	6.26	5.7	5.7
1b	1.118	0.93	7.99	2.44	-76.5	-65.1	28.8	2.23	-	-	-0.000531			
2a	-1.115	-0.93	-5.72	-9.14	-82.9	-85.6	-62.4	-4.84	-95.4	-7.4	-0.001325	6.15	4.0	9.7
2b	1.118	0.93	7.89	2.32	-74.9	-63.5	28.1	2.18	-	-	-0.000808			
3a	-1.113	-0.93	-5.50	-8.97	-81.8	-84.1	-61.0	-4.74	-93.0	-7.2	-0.001550	6.04	3.5	13.2
3b	1.119	0.93	7.87	2.31	-73.9	-62.3	28.0	2.17	-	-	-0.001038			
4a	-1.114	-0.93	-3.70	-7.19	-84.4	-93.1	-49.4	-3.83	-83.8	-6.5	-0.003513	5.08	3.9	17.0
4b	1.117	0.93	7.52	1.36	-71.8	-54.0	26.2	2.04	-	-	-0.000433			
5a	-1.112	-0.93	-3.22	-6.96	-83.3	-90.9	-46.0	-3.57	-80.1	-6.2	-0.003737	4.82	3.1	20.1
5b	1.115	0.93	7.42	1.29	-70.7	-53.3	25.6	1.99	-	-	-0.000529			
6a	-1.112	-0.93	-2.81	-6.67	-82.3	-89.2	-43.2	-3.36	-76.5	-5.9	-0.004084	4.61	2.7	22.9
6b	1.114	0.93	7.36	1.23	-69.8	-52.5	25.2	1.95	-	-	-0.000638			
7a	-1.663	-1.39	-4.15	-7.28	-90.5	-100.3	-52.6	-4.08	-97.0	-7.5	-0.007314	3.72	7.6	30.4
7b	1.664	1.39	8.14	2.00	-72.2	-53.4	30.3	2.35	-	-	0.001012			
8a	-1.664	-1.39	-2.70	-6.53	-87.6	-94.4	-42.5	-3.30	-69.6	-5.4	-0.007552	3.20	5.7	36.2
8b	1.665	1.39	7.89	1.81	-69.9	-52.0	28.6	2.22	-	-	0.002395			
9a	-1.665	-1.39	-1.87	-6.03	-85.0	-90.2	-36.9	-2.86	-63.5	-4.9	-0.007377	2.91	4.8	41.0
9b	1.666	1.39	7.73	1.63	-68.2	-50.9	27.6	2.14	-	-	0.003794			

Table C.6 — Summary of test results – Specimen 2 before retrofit, NS direction.

Loading Peak	Δ_b (in.)	θ (%)	P (kip)	V_{col} (kip)	$P_{u.col}$ (kip)	$P_{l.col}$ (kip)	V_{jh} (kip)	τ'_{jh} ($\sqrt{psi}$)	V_{jh}^{sg} (kip)	τ'^{sg}_{jh} ($\sqrt{psi}$)	γ_s (rad)	K_p (kip/in.)	E^i (kip-in.)	E^{tot} (kip-in.)
0	0.000	0.00	1.93	-4.51	-80.2	-75.5	-10.7	-0.83	-	-	0.000000	-	-	-
1a	-1.114	-0.93	-6.39	-10.18	-83.9	-86.8	-69.8	-5.42	-91.4	-7.1	-0.001408	8.12	6.4	6.4
1b	1.112	0.93	11.60	3.44	-75.6	-59.7	52.7	4.09	-	-	0.002288			
2a	-1.113	-0.93	-6.15	-9.95	-83.2	-85.4	-68.1	-5.29	-98.4	-7.6	-0.001614	7.80	4.2	10.6
2b	1.114	0.93	11.14	3.07	-73.7	-58.2	49.7	3.86	-	-	0.001605			
3a	-1.115	-0.93	-5.93	-9.84	-82.3	-84.1	-66.6	-5.17	-97.8	-7.6	-0.001990	7.56	3.5	14.2
3b	1.113	0.93	10.81	2.82	-72.5	-57.2	47.6	3.69	-	-	0.000980			
4a	-1.116	-0.93	-4.91	-8.92	-84.4	-93.1	-59.5	-4.62	-99.6	-7.7	-0.003434	6.87	4.0	18.2
4b	1.114	0.93	10.29	2.37	-71.8	-54.0	44.3	3.44	-	-	0.000657			
5a	-1.116	-0.93	-4.40	-8.64	-83.3	-90.9	-55.9	-4.34	-97.2	-7.5	-0.004116	6.53	3.2	21.4
5b	1.113	0.93	10.05	2.14	-70.7	-53.3	42.7	3.31	-	-	0.000660			
6a	-1.115	-0.93	-4.03	-8.43	-82.3	-89.2	-53.2	-4.13	-95.5	-7.4	-0.004664	6.28	2.8	24.2
6b	1.111	0.93	9.85	1.94	-69.8	-52.5	41.4	3.22	-	-	0.000496			
7a	-1.666	-1.39	-5.66	-9.29	-90.5	-100.3	-65.1	-5.05	-104.0	-8.1	-0.006978	4.93	9.2	33.4
7b	1.663	1.39	10.67	2.80	-72.2	-53.4	46.5	3.61	-	-	-0.003100			
8a	-1.667	-1.39	-4.11	-8.43	-87.6	-94.4	-53.8	-4.18	-98.2	-7.6	-0.007539	4.25	6.9	40.3
8b	1.663	1.39	9.98	2.19	-69.9	-52.0	42.2	3.27	-	-	-0.003262			
9a	-1.668	-1.39	-3.35	-7.80	-85.0	-90.2	-48.5	-3.77	-93.4	-7.3	-0.008014	3.90	5.8	46.2
9b	1.664	1.39	9.59	1.86	-68.2	-50.9	39.7	3.08	-	-	-0.003277			

C.4 SPECIMEN 2 AFTER RETROFIT

Views during and at the end of the last cycle: Cycle 15 (±3.73% bidirectional drift)

(a) Perspective

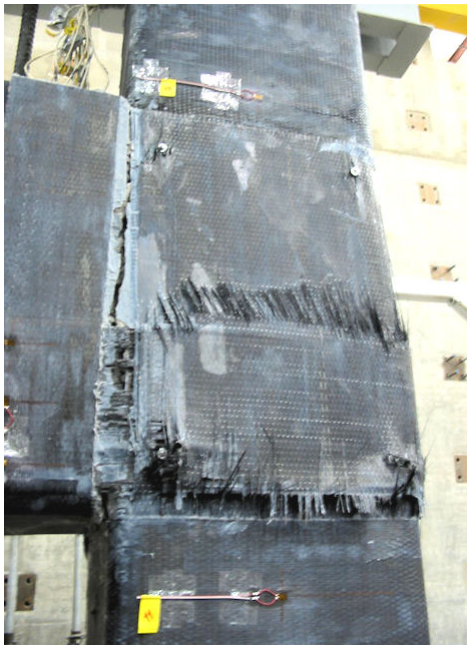

(b) NS joint panel

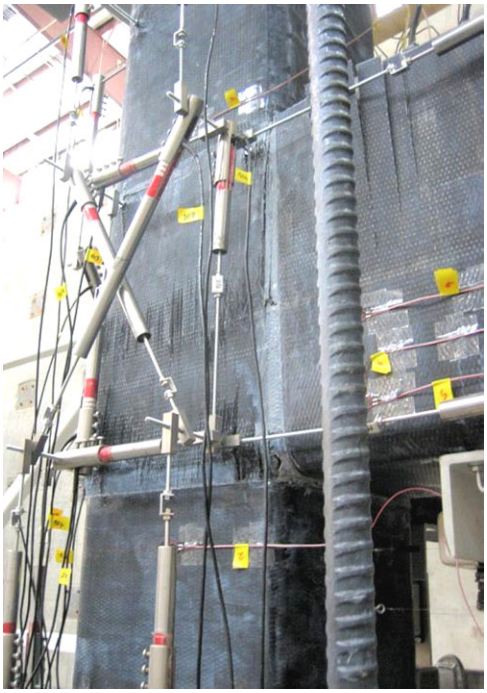

(c) EW joint panel

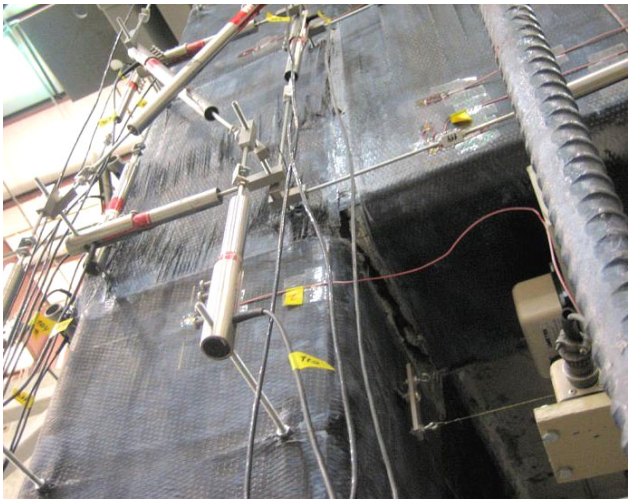

(d) EW beam bottom

Figure C.27 — Damage modes – Specimen 2 after retrofit.

Views during and at the end of the last cycle: Cycle 15 (±3.73% bidirectional drift)

(e) NS beam hinge top view

(f) NS beam hinge

(g) Upper column E face

(h) Extent of joint rotation

Figure C.27 — Continued.

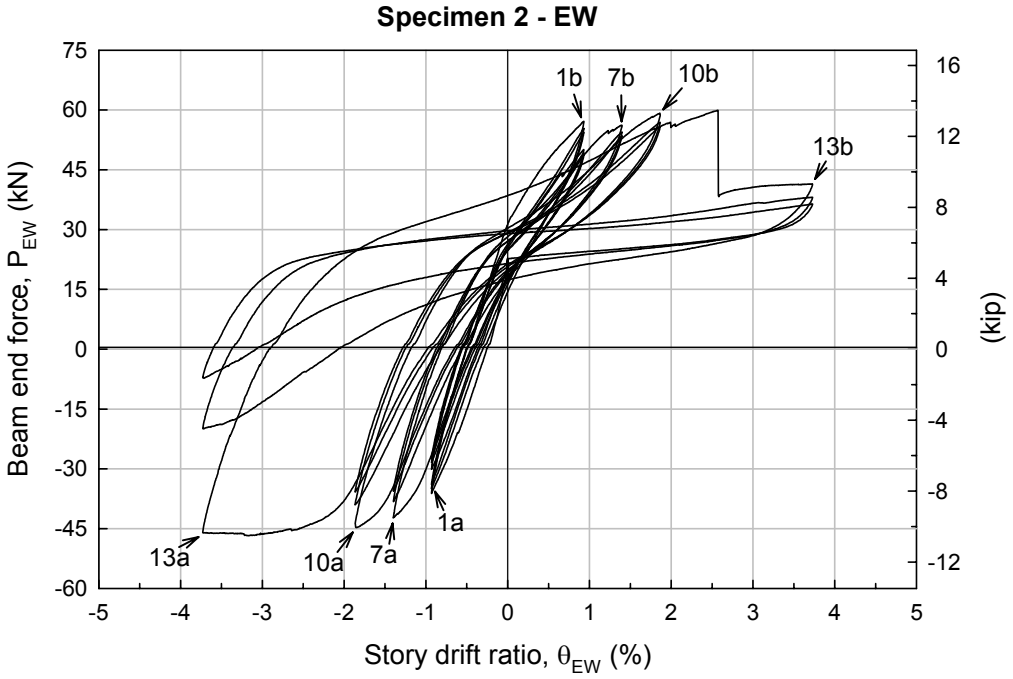

(a)

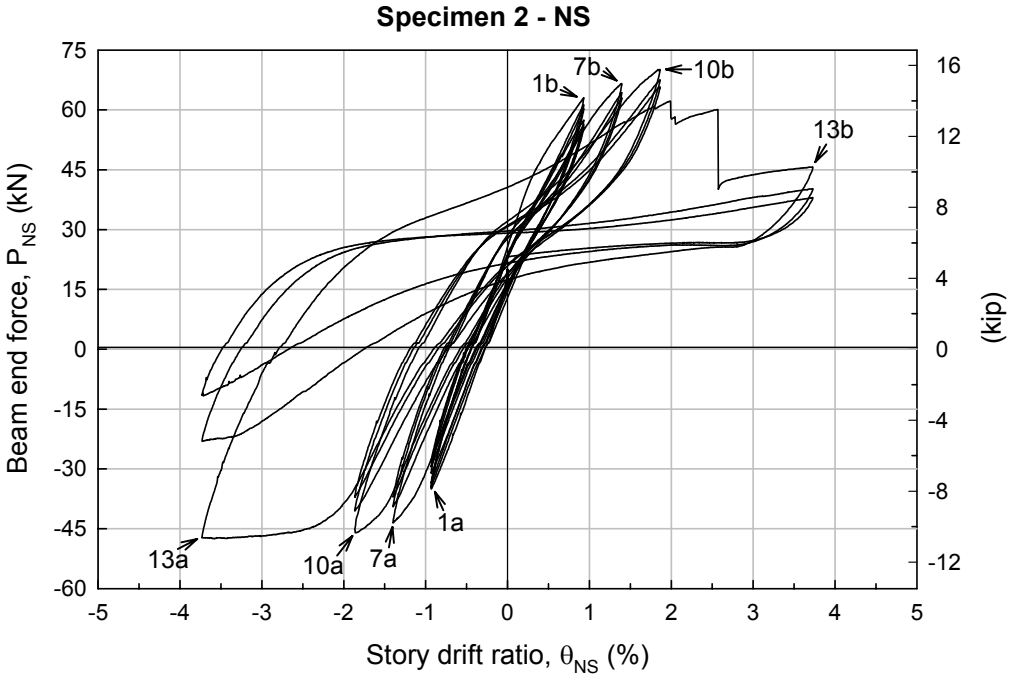

(b)

Figure C.28 — Force-drift hysteretic curves – Specimen 2 after retrofit: (a) EW, and (b) NS direction.

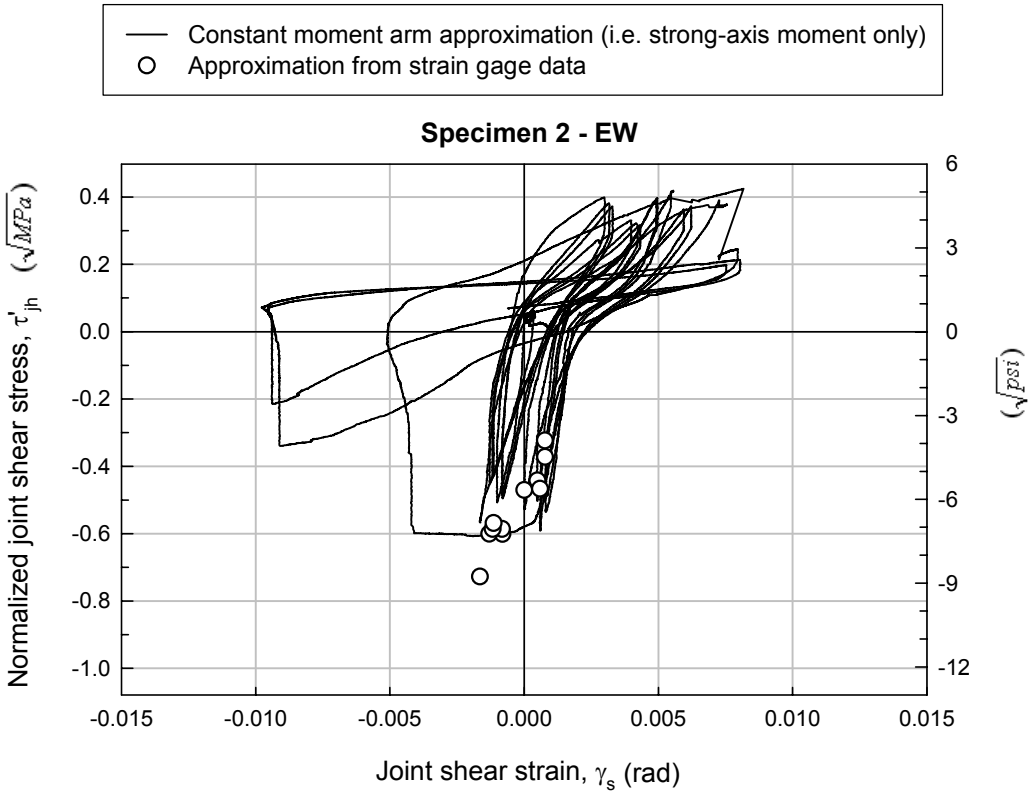

(a)

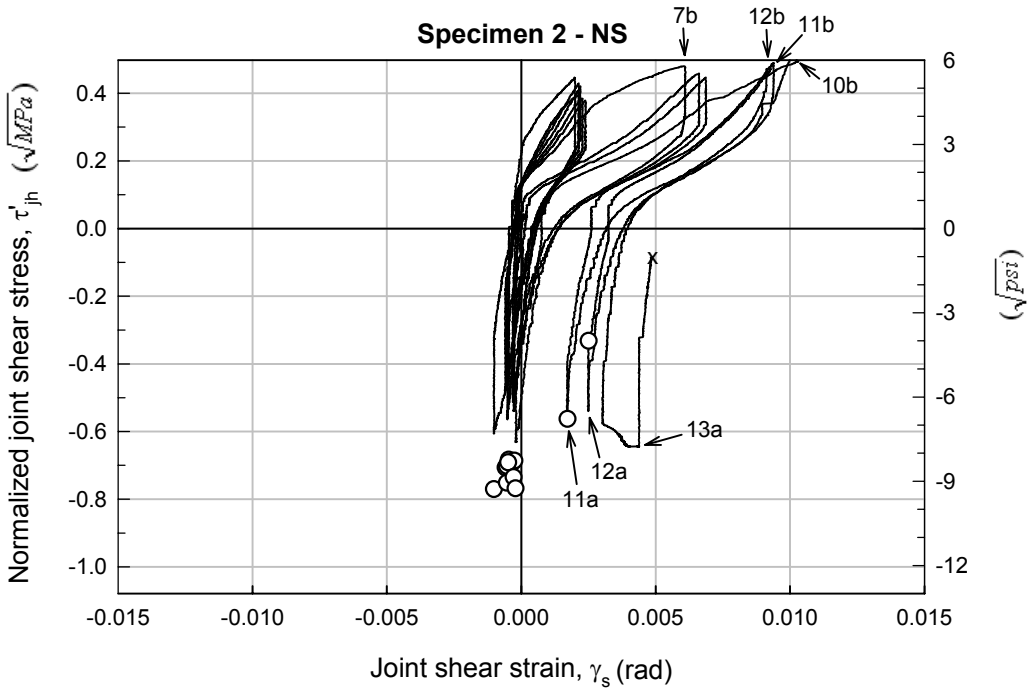

(b)

Figure C.29 — Joint shear stress-strain hysteretic curves – Specimen 2 after retrofit: (a) EW, and (b) NS direction.

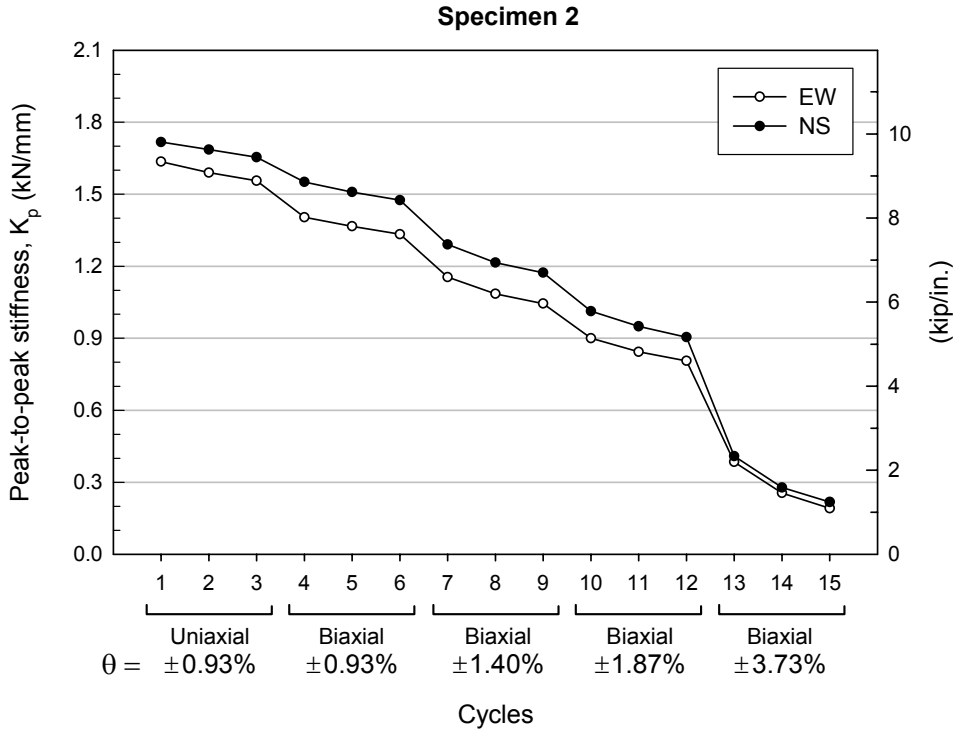

Figure C.30 — Variation of peak-to-peak stiffness – Specimen 2 after retrofit.

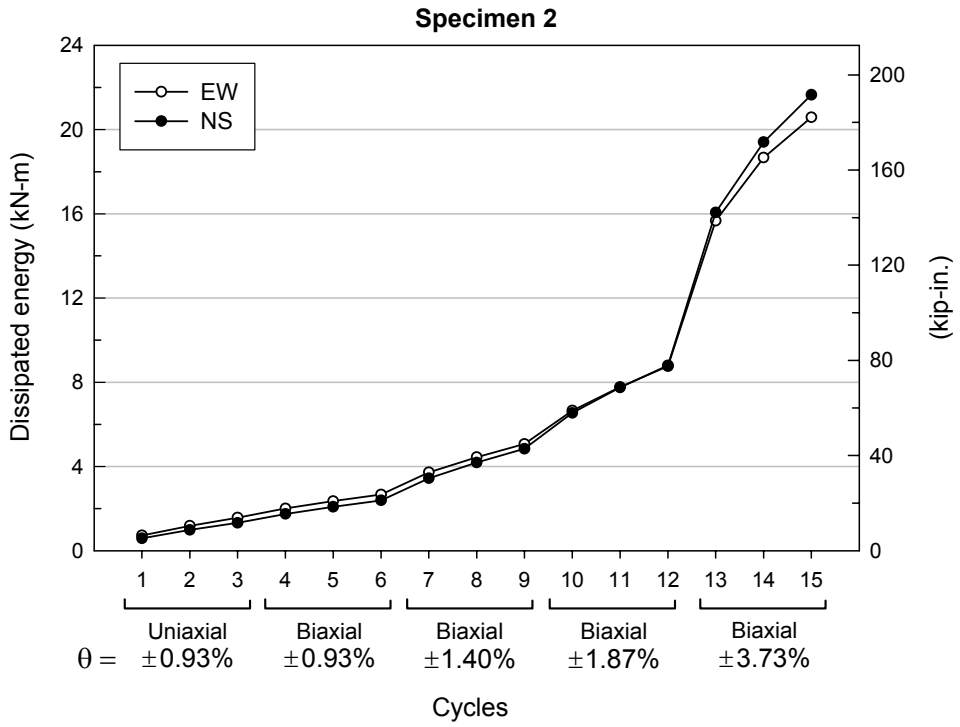

Figure C.31 — Variation of cumulative dissipated energy – Specimen 2 after retrofit.

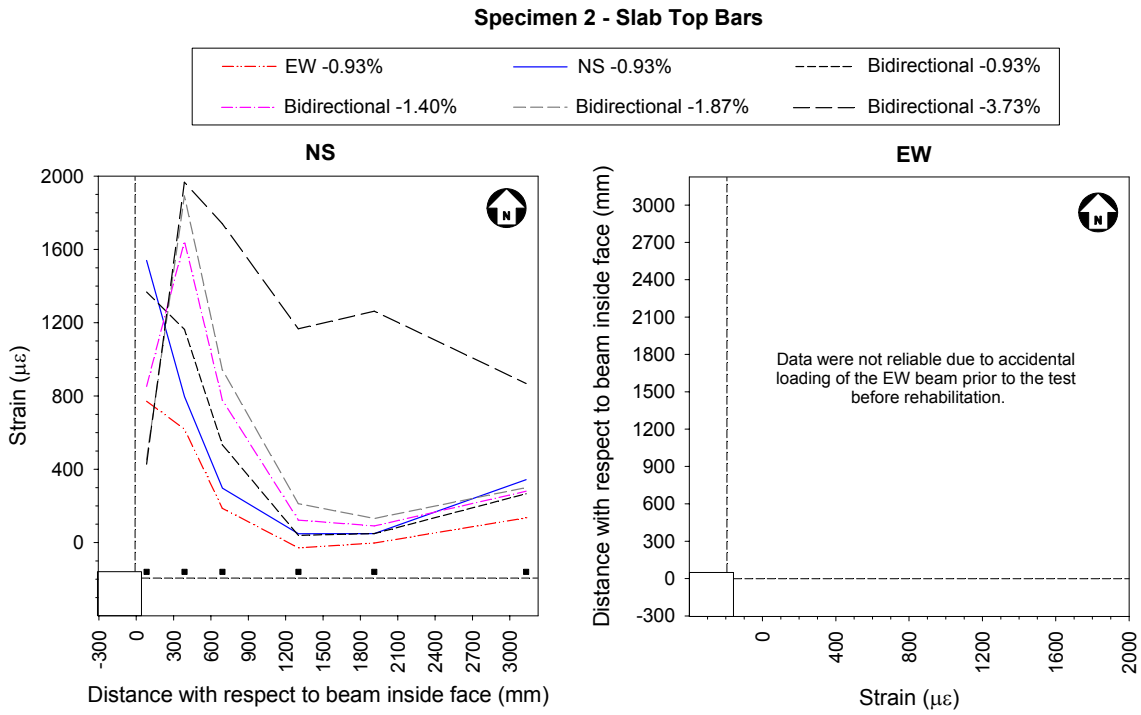

(a)

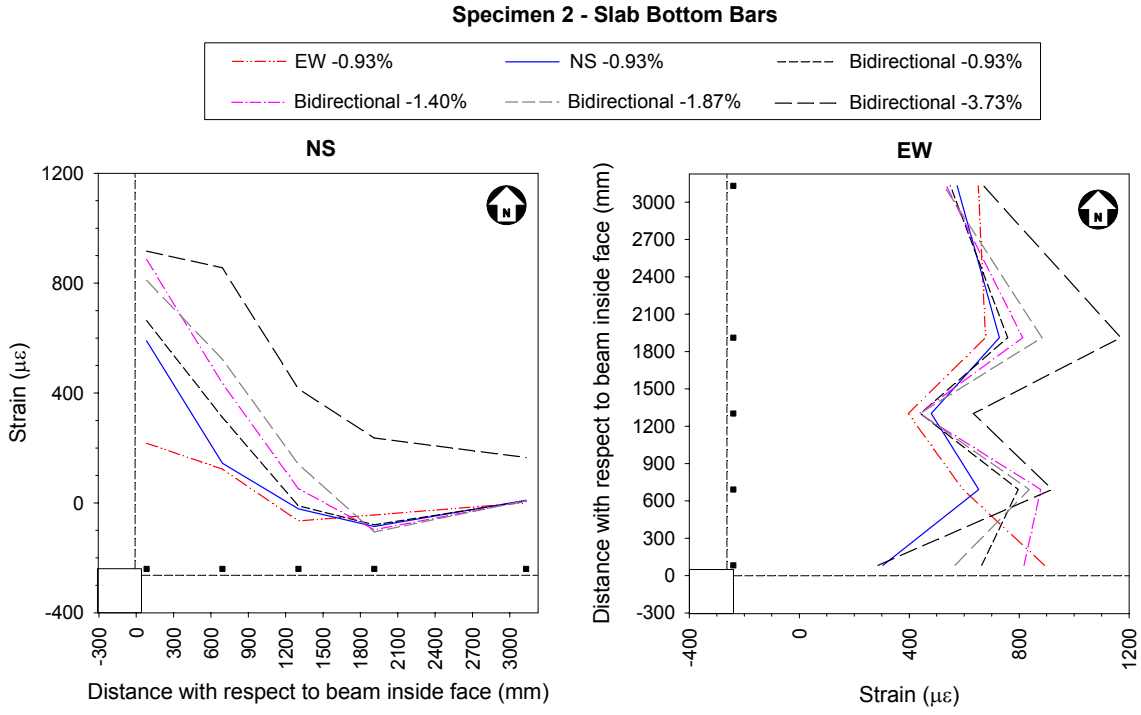

(b)

Figure C.32 — Strains in the slab bars at the first peak of downward loading at each drift level – Specimen 2 after retrofit: (a) top bars, and (b) bottom bars.

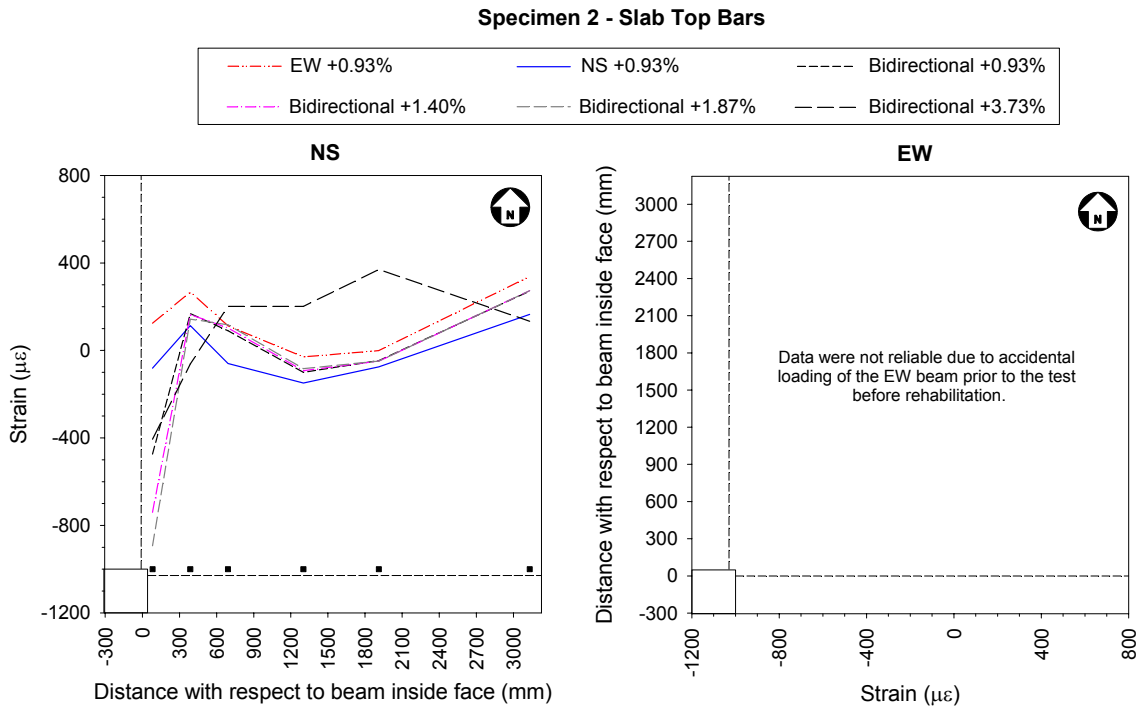

(a)

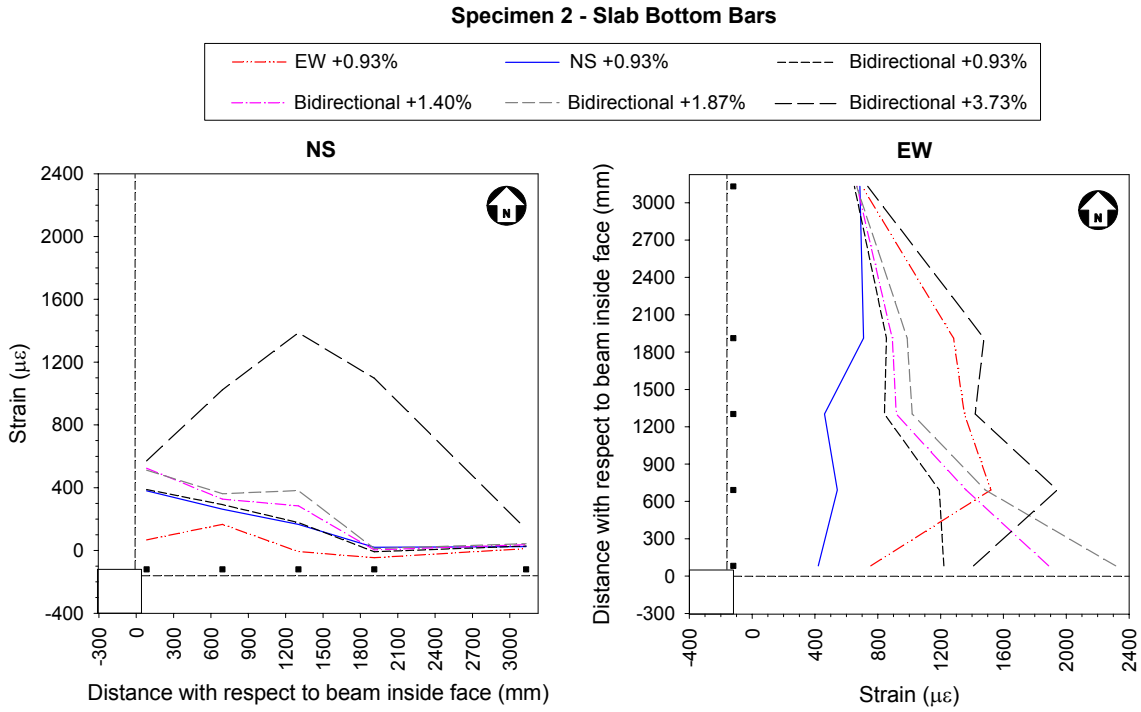

(b)

Figure C.33 — Strains in the slab bars at the first peak of upward loading at each drift level – Specimen 2 after retrofit: (a) top bars, and (b) bottom bars.

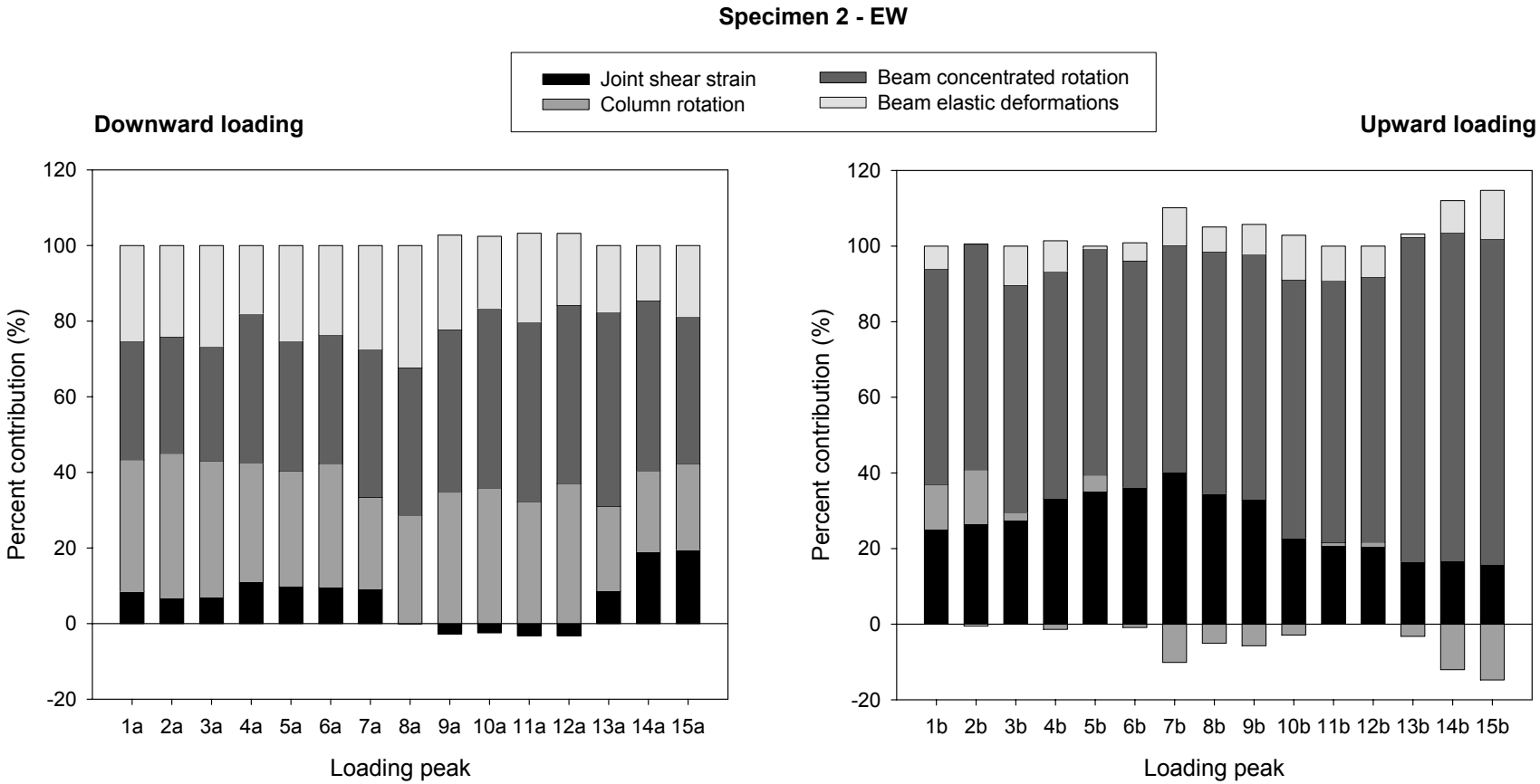

Figure C.34 — Percent contributions to applied interstory drift – Specimen 2 after retrofit, EW direction.

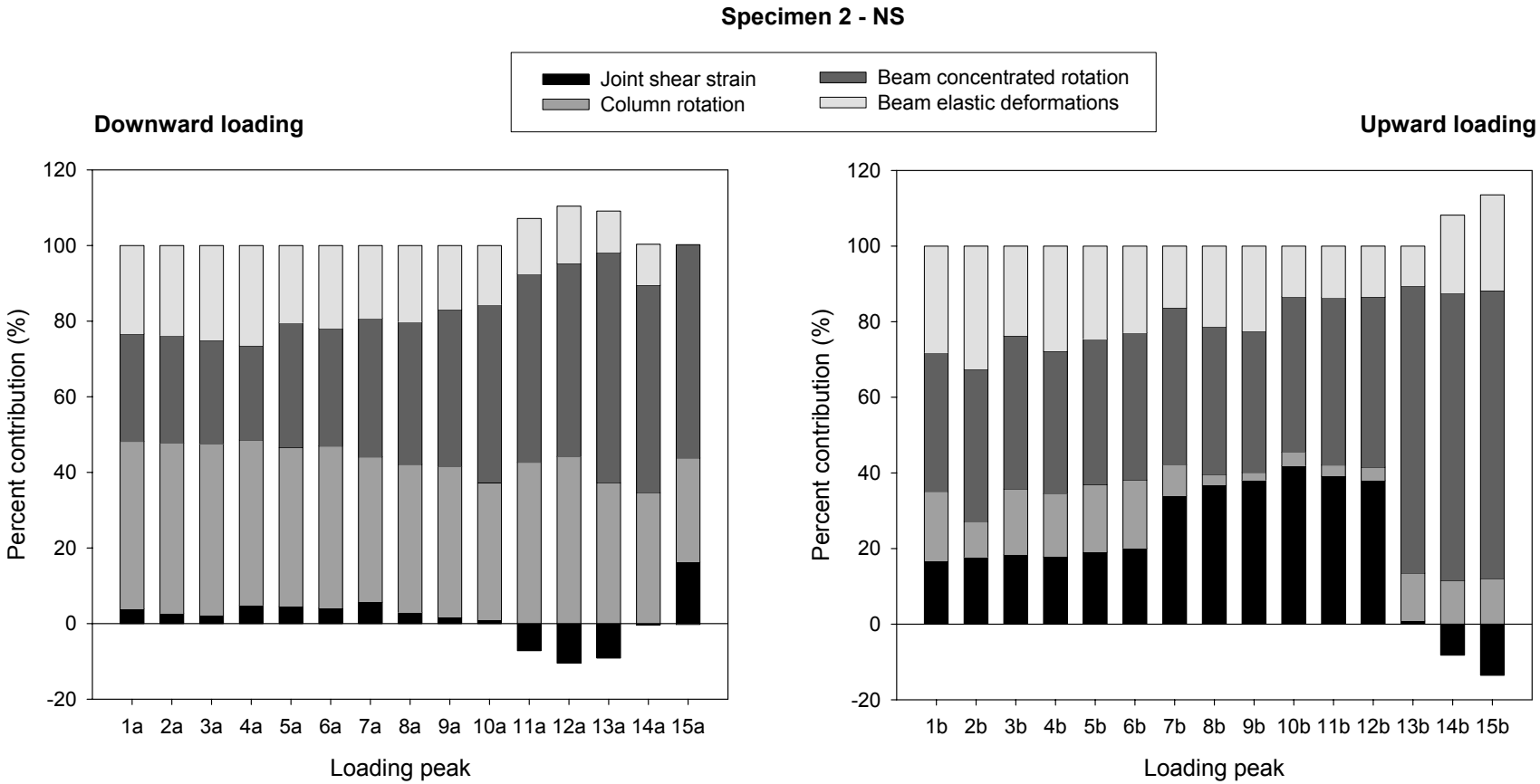

Figure C.35 — Percent contributions to applied interstory drift – Specimen 2 after retrofit, NS direction.

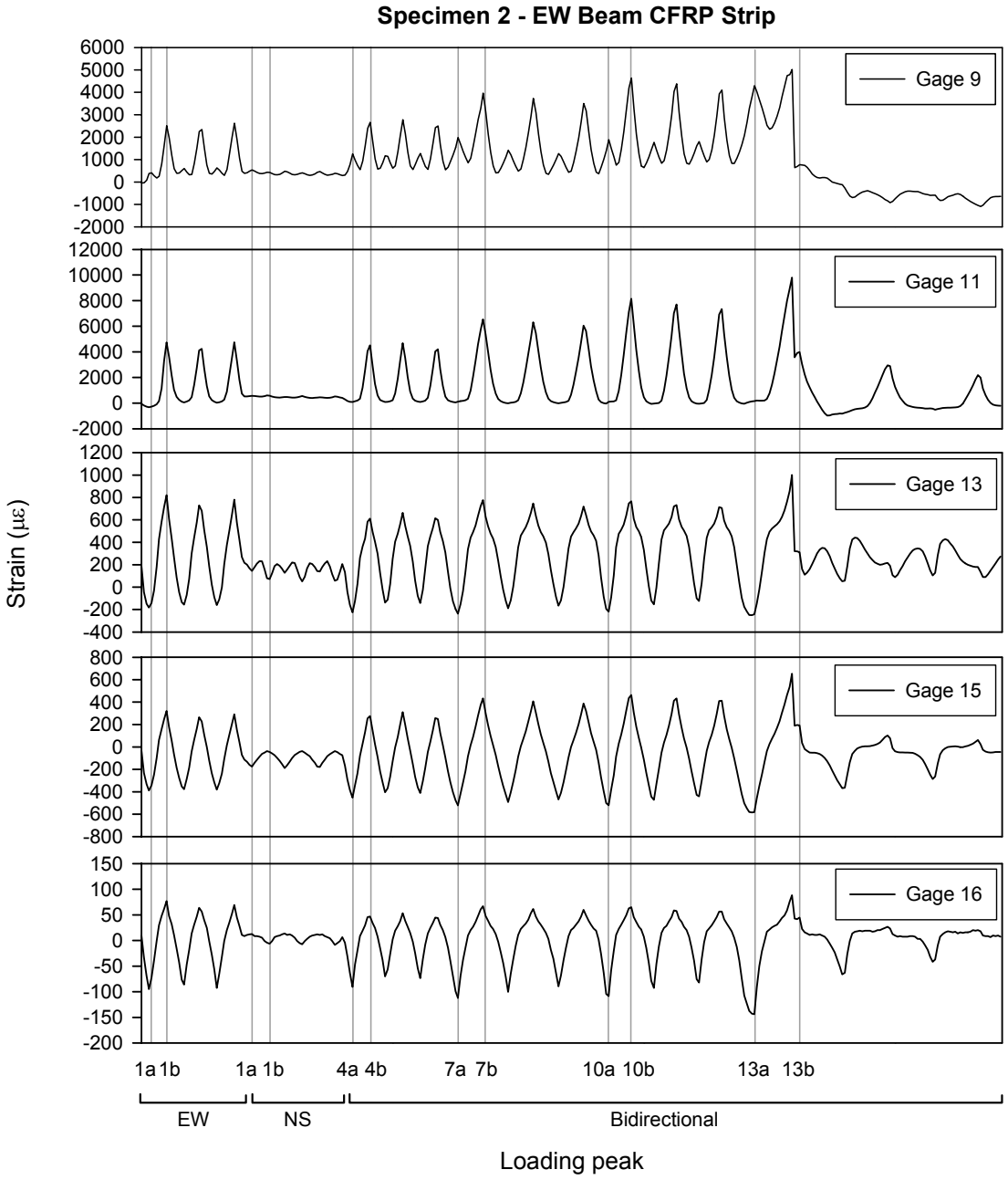

Figure C.36 — Strains in the CFRP beam strips – Specimen 2, EW beam:
Gages 9, 11: near column face; Gages 13, 15: near end of U-wrap;
Gage 16: near end of strip. (Gage locations and orientations are shown in Figure B.30.)

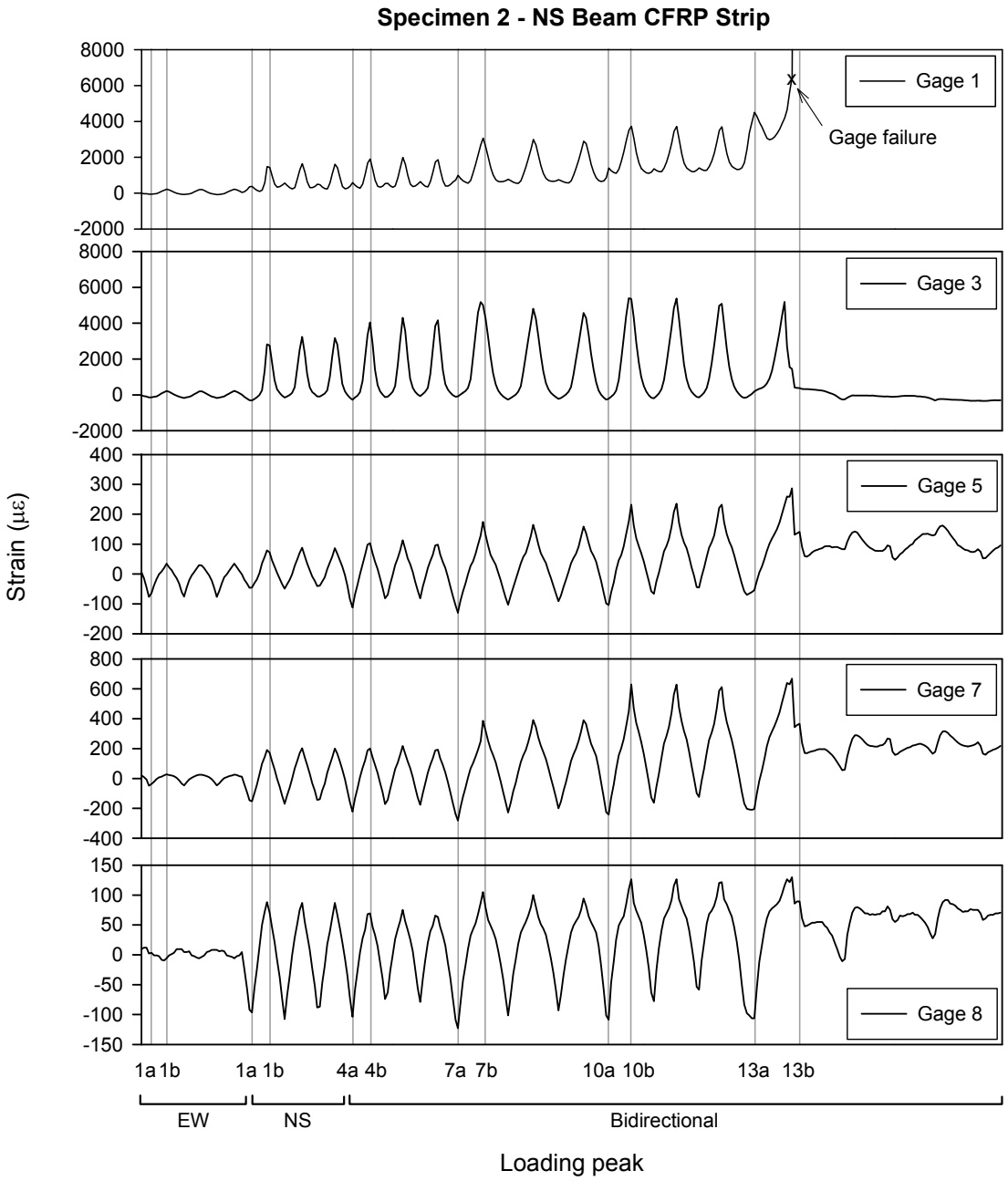

Figure C.37 — Strains in the CFRP beam strips – Specimen 2, NS beam:
Gages 1, 3: near column face; Gages 5, 7: near end of U-wrap;
Gage 8: near end of strip. (Gage locations and orientations are shown in Figure B.30.)

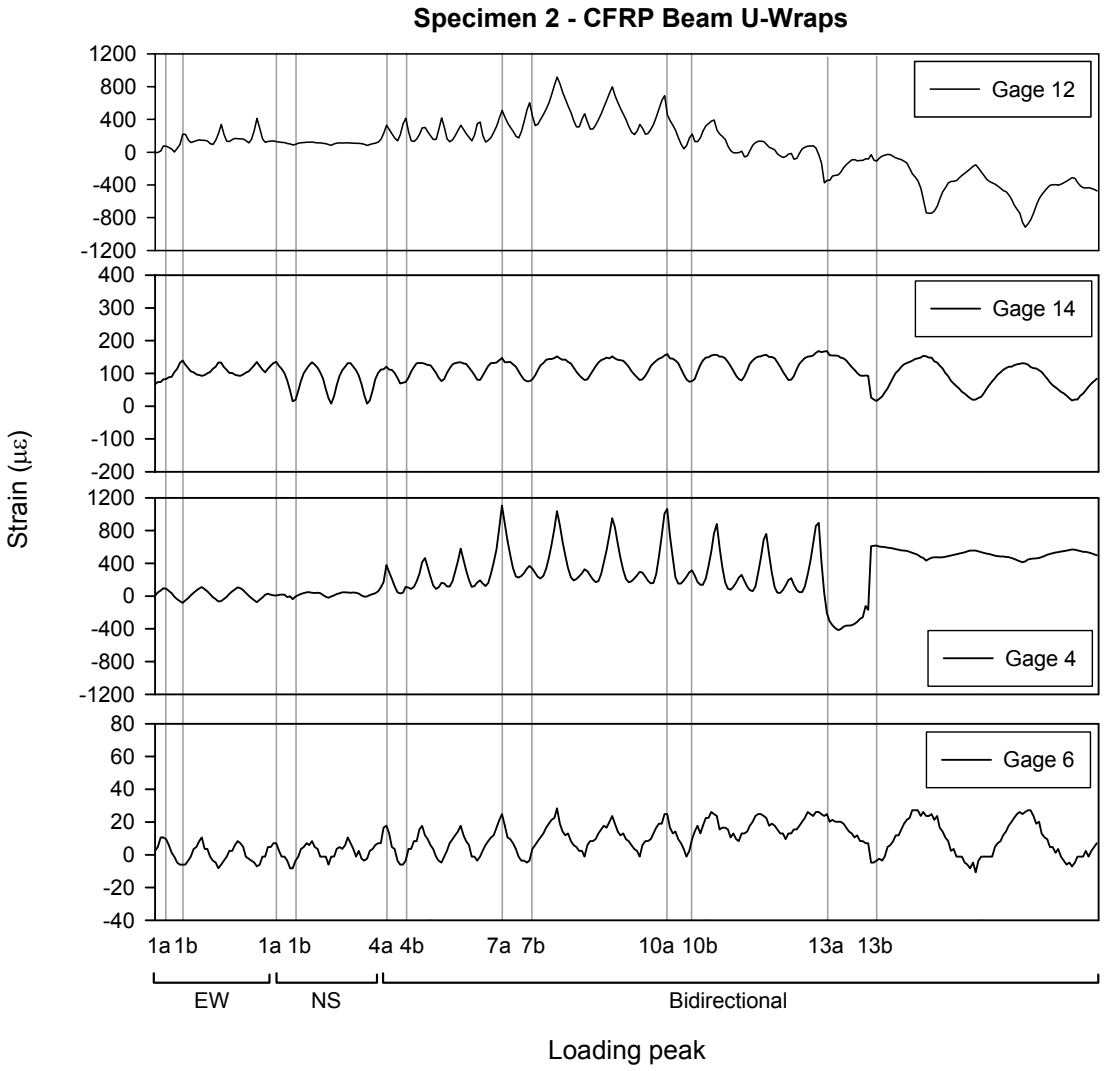

Figure C.38 — Strains in the CFRP beam U-wraps – Specimen 2:
EW beam: Gage 12 (near column face), Gage 14: near end of U-wrap;
NS beam: Gage 4 (near column face), Gage 6: near end of U-wrap.
(Gage locations and orientations are shown in Figure B.30.)

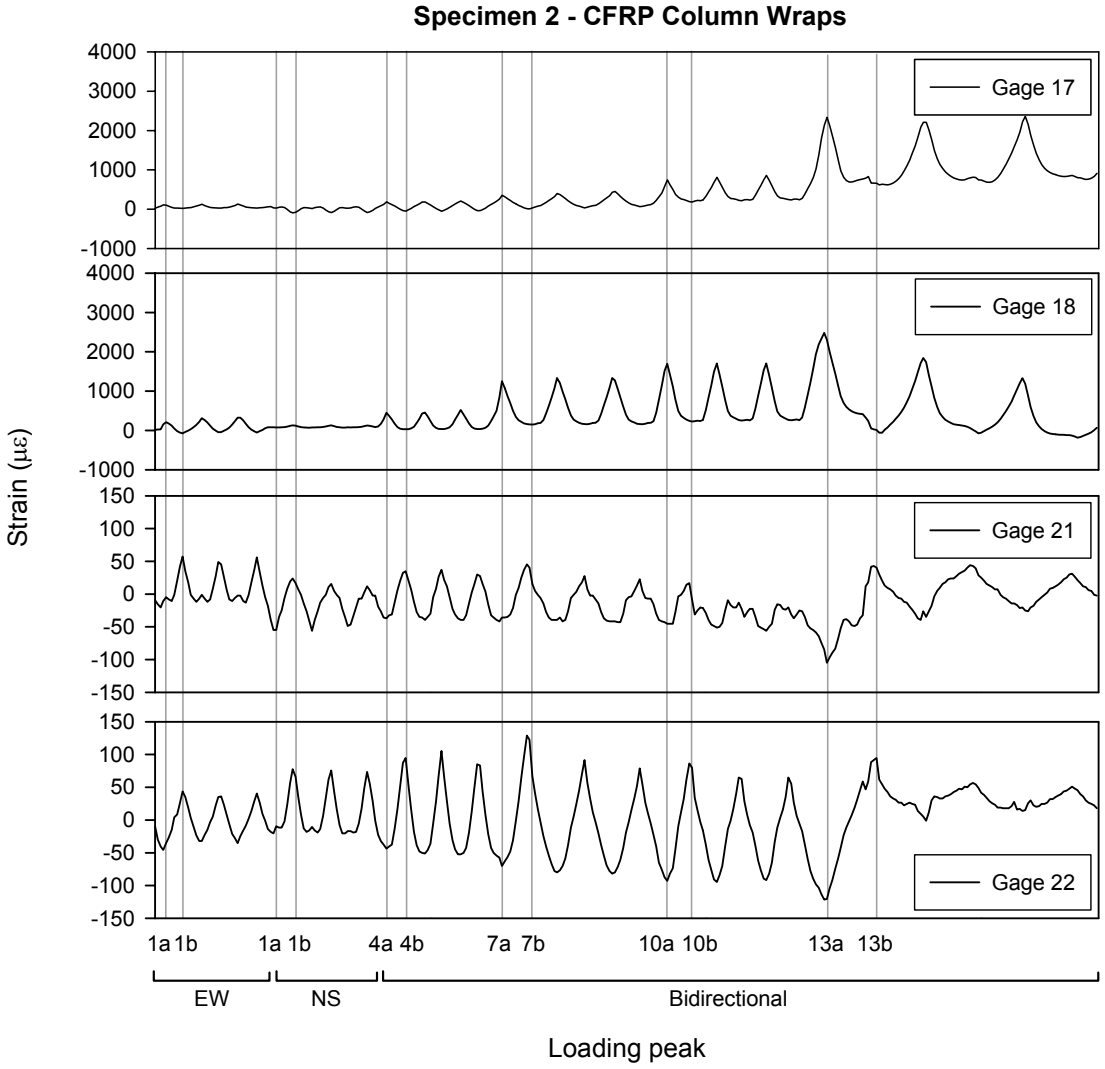

Figure C.39 — Strains in the CFRP column wraps – Specimen 2:
Gages 17, 18: Upper column, 1st stirrup level; Gages 21, 22: Lower column, 1st stirrup level. (Gage locations and orientations are shown in Figure B.30.)

Table C.7 — Summary of test results – Specimen 2 after retrofit, EW direction.

Loading Peak	Δ_b (in.)	θ (%)	P (kip)	V_{col} (kip)	$P_{u.col}$ (kip)	$P_{l.col}$ (kip)	V_{jh} (kip)	τ'_{jh} ($\sqrt{psi}$)	V_{jh}^{sg} (kip)	$\tau'_{jh}{}^{sg}$ ($\sqrt{psi}$)	γ_s (rad)	K_p (kip/in.)	E^i (kip-in.)	E^{tot} (kip-in.)
0	0.000	0.00	4.67	-0.67	-80.5	-71.9	6.7	0.52	-	-	0.000000	-	-	-
1a	-1.114	-0.93	-7.99	-10.67	-85.1	-89.8	-77.8	-6.04	-91.2	-7.1	-0.001020	9.34	6.4	6.4
1b	1.116	0.93	12.70	6.01	-79.3	-62.1	61.0	4.73	-	-	0.002999			
2a	-1.117	-0.93	-7.81	-10.61	-82.3	-86.6	-76.5	-5.94	-93.2	-7.2	-0.000805	9.08	4.1	10.5
2b	0.931	4486	0.00	5.66	-76.9	-60.1	58.7	4.56	-	-	0.003171			
3a	-1.114	-0.93	-7.52	-10.41	-80.7	-84.5	-74.6	-5.79	-90.9	-7.1	-0.000826	8.89	3.4	13.9
3b	1.118	0.93	12.21	5.59	-75.6	-58.9	57.7	4.48	-	-	0.003293			
4a	-1.112	-0.93	-6.60	-9.23	-83.1	-96.5	-68.9	-5.35	-93.2	-7.2	-0.001302	8.02	3.9	17.8
4b	1.113	0.93	11.13	4.59	-75.2	-51.4	50.4	3.91	-	-	0.003980			
5a	-1.116	-0.93	-6.33	-9.05	-82.1	-94.9	-67.0	-5.20	-91.0	-7.1	-0.001173	7.80	3.1	20.8
5b	1.116	0.93	10.99	4.52	-74.3	-50.7	49.4	3.84	-	-	0.004206			
6a	-1.111	-0.93	-6.01	-8.77	-81.1	-93.4	-65.0	-5.04	-88.2	-6.9	-0.001139	7.62	2.7	23.6
6b	1.114	0.93	10.84	4.38	-73.4	-50.1	48.4	3.76	-	-	0.004329			
7a	-1.674	-1.39	-9.42	-11.69	-87.7	-106.8	-87.4	-6.79	-112.9	-8.8	-0.001646	6.59	9.3	32.9
7b	1.676	1.40	12.54	5.89	-77.4	-50.0	59.8	4.64	-	-	0.007236			
8a	-1.673	-1.39	-8.46	-10.92	-85.8	-103.0	-81.1	-6.29	-73.0	-5.7	0.000003	6.20	6.4	39.3
8b	1.677	1.40	12.18	5.65	-75.7	-49.1	57.4	4.45	-	-	0.006224			
9a	-1.674	-1.40	-7.88	-10.49	-84.4	-100.5	-77.2	-5.99	-68.5	-5.3	0.000495	5.96	5.6	44.9
9b	1.678	1.40	11.99	5.45	-74.5	-48.3	56.1	4.36	-	-	0.005919			
10a	-2.231	-1.86	-9.70	-11.84	-89.7	-109.4	-89.4	-6.94	-72.4	-5.6	0.000590	5.14	14.0	58.9
10b	2.231	1.86	13.06	6.27	-77.9	-49.2	63.5	4.93	-	-	0.005463			
11a	-2.233	-1.86	-8.66	-11.05	-87.4	-105.0	-82.4	-6.40	-57.7	-4.5	0.000777	4.82	9.9	68.8
11b	2.233	1.86	12.69	5.95	-75.8	-48.0	61.0	4.73	-	-	0.004947			
12a	-2.235	-1.86	-8.00	-10.58	-85.3	-101.6	-78.0	-6.05	-50.2	-3.9	0.000772	4.60	8.7	77.5
12b	2.234	1.86	12.48	5.78	-74.1	-47.0	59.5	4.62	-	-	0.004926			
13a	-4.470	-3.73	-10.21	-13.09	-94.2	-114.9	-91.9	-7.14	-	-	-0.004095	2.20	61.1	138.6
13b	4.475	3.73	9.27	3.27	-69.4	-49.9	37.6	2.92	-	-	0.007949			
14a	-4.472	-3.73	-4.44	-9.65	-76.9	-86.4	-52.4	-4.07	-	-	-0.009118	1.46	26.6	165.2
14b	4.473	3.73	8.49	2.35	-61.8	-44.4	32.7	2.53	-	-	0.008044			
15a	-4.471	-3.73	-1.52	-7.67	-66.2	-70.2	-32.6	-2.53	-	-	-0.009386	1.09	16.9	182.2
15b	4.476	3.73	8.14	1.87	-58.2	-41.5	30.5	2.37	-	-	0.007520			

Table C.8 — Summary of test results – Specimen 2 after retrofit, NS direction.

Loading Peak	Δ_b (in.)	θ (%)	P (kip)	V_{col} (kip)	$P_{u.col}$ (kip)	$P_{l.col}$ (kip)	V_{jh} (kip)	τ'_{jh} ($\sqrt{psi}$)	V_{jh}^{sg} (kip)	τ'^{sg}_{jh} ($\sqrt{psi}$)	γ_s (rad)	K_p (kip/in.)	E^i (kip-in.)	E^{tot} (kip-in.)
0	0.000	0.00	3.94	-2.28	-80.5	-71.9	2.7	0.21	-	-	0.000000	-	-	-
1a	-1.119	-0.93	-7.73	-10.93	-82.2	-85.8	-79.5	-6.17	-106.1	-8.2	-0.000465	9.81	5.2	5.2
1b	1.118	0.93	14.12	5.54	-76.0	-56.9	69.0	5.35	-	-	0.001994			
2a	-1.117	-0.93	-7.70	-10.82	-81.4	-84.8	-79.4	-6.16	-107.2	-8.3	-0.000321	9.63	3.6	8.7
2b	1.119	0.93	13.77	5.28	-74.8	-55.9	66.7	5.18	-	-	0.002137			
3a	-1.118	-0.93	-7.55	-10.75	-80.5	-83.7	-78.3	-6.08	-106.5	-8.3	-0.000253	9.45	3.0	11.7
3b	1.119	0.93	13.54	5.05	-73.8	-55.1	65.2	5.06	-	-	0.002205			
4a	-1.115	-0.93	-6.86	-10.08	-83.1	-96.5	-73.6	-5.71	-109.7	-8.5	-0.000585	8.86	3.7	15.4
4b	1.115	0.93	12.76	4.35	-75.2	-51.4	60.2	4.68	-	-	0.002133			
5a	-1.115	-0.93	-6.53	-9.94	-82.1	-94.9	-71.2	-5.52	-108.9	-8.5	-0.000539	8.62	3.0	18.4
5b	1.115	0.93	12.59	4.13	-74.3	-50.7	59.2	4.60	-	-	0.002277			
6a	-1.115	-0.93	-6.27	-9.79	-81.1	-93.4	-69.3	-5.38	-107.3	-8.3	-0.000486	8.42	2.7	21.1
6b	1.114	0.93	12.41	3.97	-73.4	-50.1	58.0	4.51	-	-	0.002405			
7a	-1.677	-1.40	-9.70	-12.29	-87.7	-106.8	-93.5	-7.26	-119.6	-9.3	-0.001019	7.37	9.3	30.4
7b	1.676	1.40	14.87	6.06	-77.4	-50.0	73.9	5.73	-	-	0.006110			
8a	-1.673	-1.39	-8.75	-11.58	-85.8	-103.0	-86.8	-6.74	-116.6	-9.1	-0.000535	6.94	6.6	37.0
8b	1.677	1.40	14.41	5.66	-75.7	-49.1	70.9	5.50	-	-	0.006616			
9a	-1.674	-1.40	-8.24	-11.26	-84.4	-100.5	-83.2	-6.46	-114.1	-8.9	-0.000287	6.70	5.8	42.8
9b	1.678	1.40	14.13	5.43	-74.5	-48.3	69.1	5.37	-	-	0.006865			
10a	-2.232	-1.86	-10.04	-12.53	-89.7	-109.4	-95.9	-7.45	-119.2	-9.3	-0.000211	5.78	15.1	57.9
10b	2.231	1.86	15.60	6.55	-77.9	-49.2	78.7	6.11	-	-	0.010037			
11a	-2.235	-1.86	-9.01	-11.81	-87.4	-105.0	-88.6	-6.88	-87.3	-6.8	0.001717	5.43	10.7	68.6
11b	2.233	1.86	15.07	6.16	-75.8	-48.0	75.2	5.84	-	-	0.009384			
12a	-2.235	-1.86	-8.29	-11.29	-85.3	-101.6	-83.5	-6.48	-51.5	-4.0	0.002506	5.17	9.3	77.9
12b	2.236	1.86	14.70	5.86	-74.1	-47.0	72.9	5.66	-	-	0.009116			
13a	-4.472	-3.73	-10.50	-12.91	-94.2	-114.9	-99.1	-7.69	-	-	0.004376	2.33	64.3	142.2
13b	4.475	3.73	10.22	2.49	-69.4	-49.9	43.6	3.39	-	-	0.000402			
14a	-4.475	-3.73	-5.14	-9.41	-76.9	-86.4	-60.8	-4.72	-	-	0.000167	1.59	29.5	171.7
14b	4.471	3.73	8.95	1.45	-61.8	-44.4	35.4	2.75	-	-	-0.003941			
15a	-4.472	-3.73	-2.51	-7.69	-66.2	-70.2	-42.1	-3.27	-	-	-0.007824	1.25	19.9	191.6
15b	4.475	3.73	8.52	1.06	-58.2	-41.5	32.6	2.53	-	-	-0.006504			

C.5 SPECIMEN 3

Views during and at the end of the last cycle: Cycle 15 (±3.73% bidirectional drift)

(a) EW beam-joint interface

(b) EW beam bottom

(c) Joint NE corner

(d) EW and NS beam bottoms

Figure C.40 — Damage modes – Specimen 3.

Views during and at the end of the last cycle: Cycle 15 (±3.73% bidirectional drift)

(e) Slab SW corner

(f) Upper column NE corner

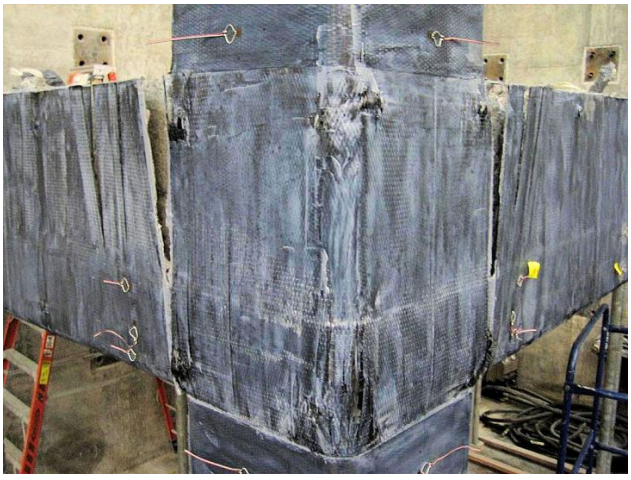

(g) Perspective

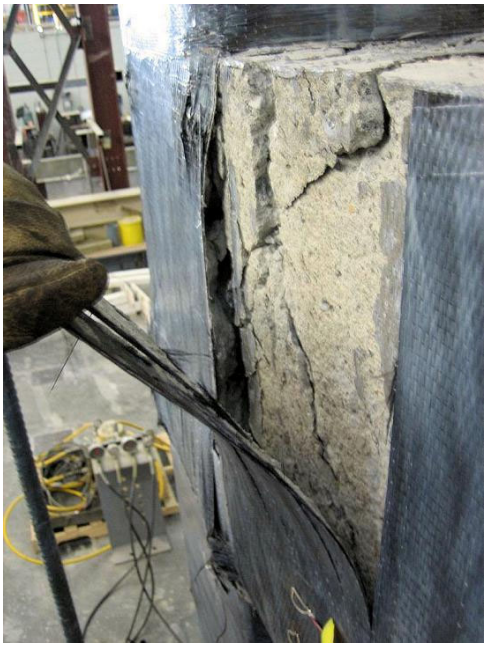

(h) EW beam hinge

Figure C.40 — Continued.

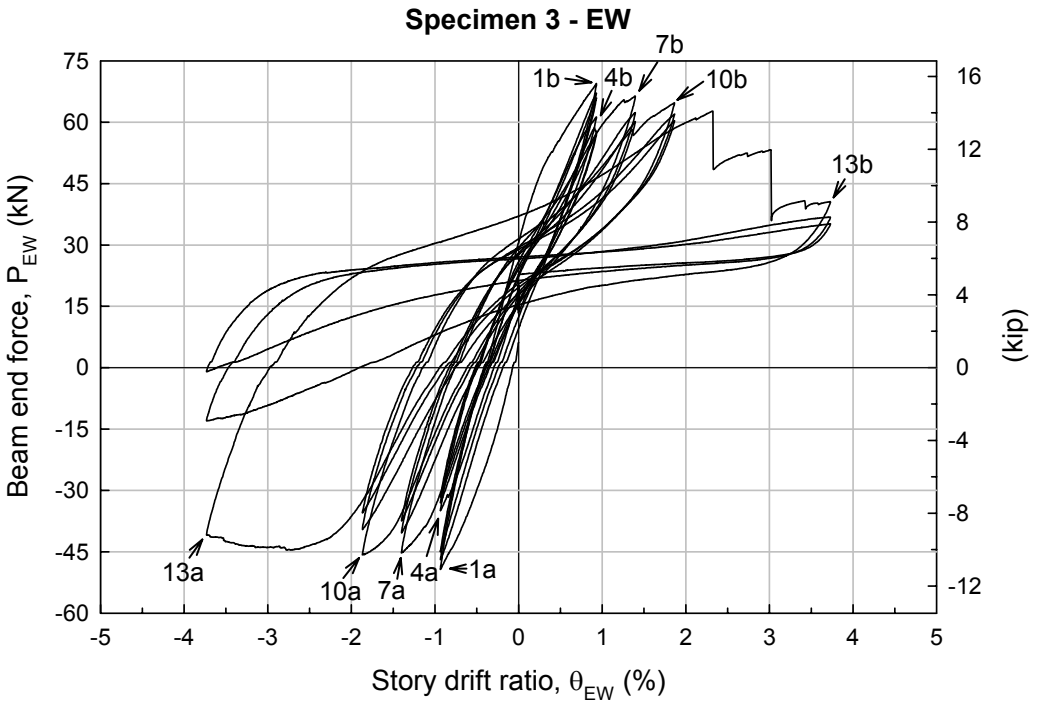

(a)

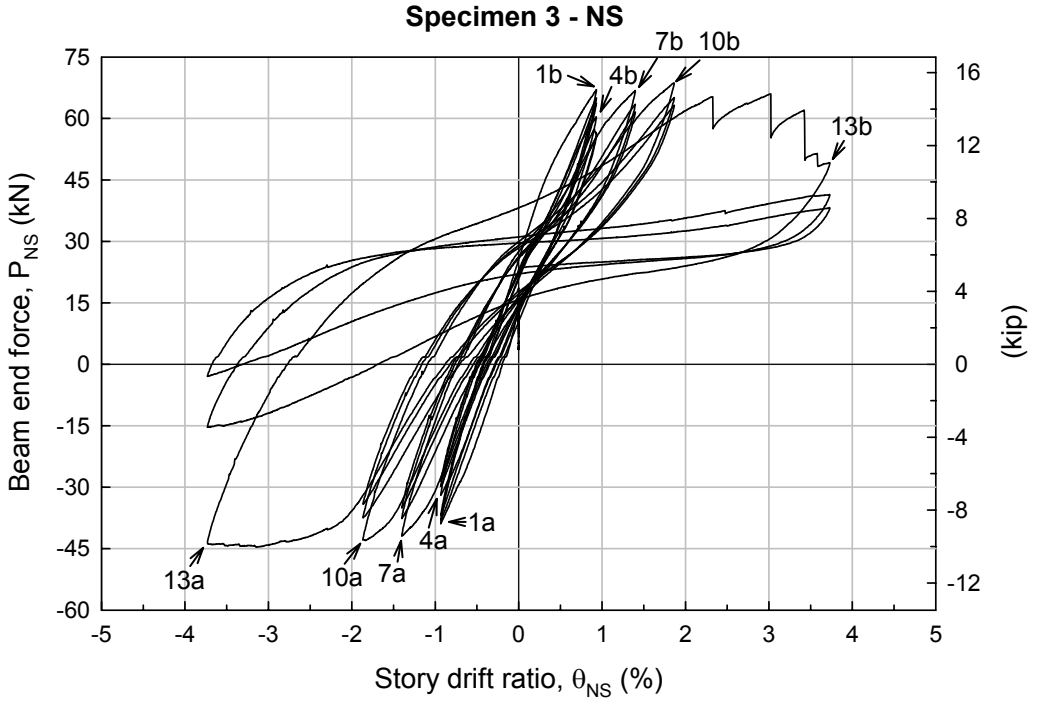

(b)

Figure C.41 — Force-drift hysteretic curves – Specimen 3:
(a) EW, and (b) NS direction.

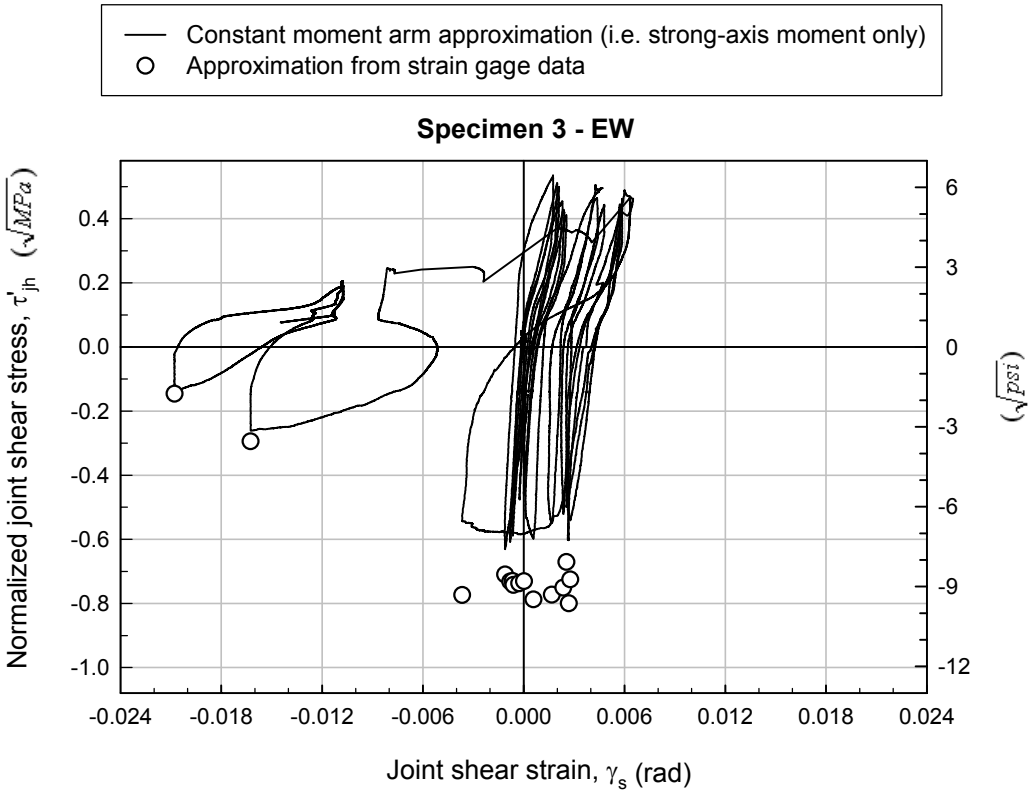

(a)

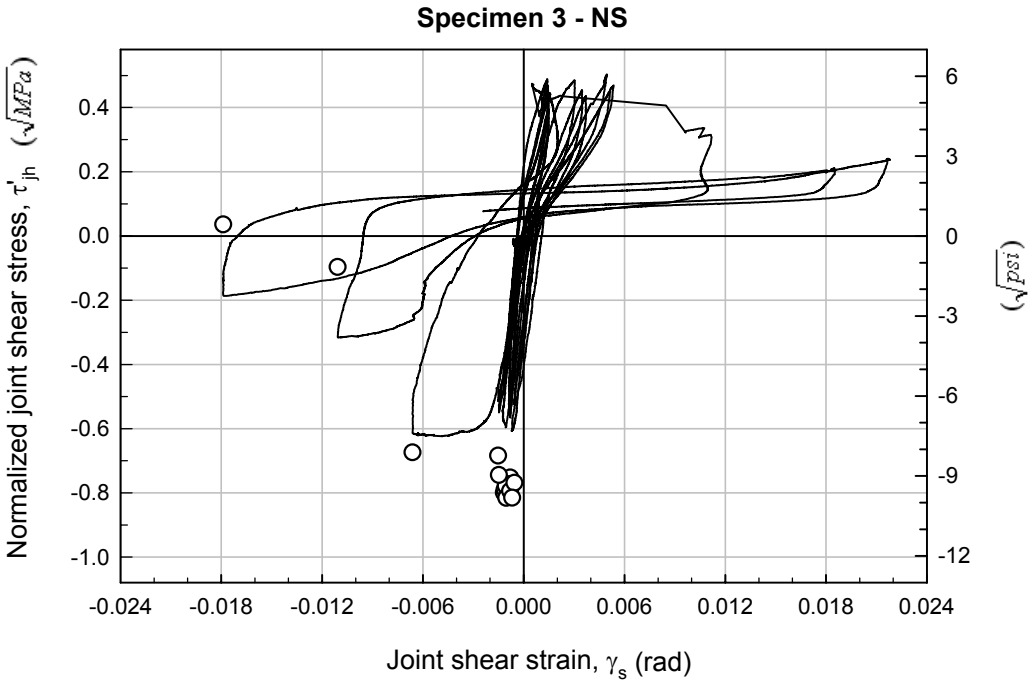

(b)

Figure C.42 — Joint shear stress-strain hysteretic curves – Specimen 3: (a) EW, and (b) NS direction.

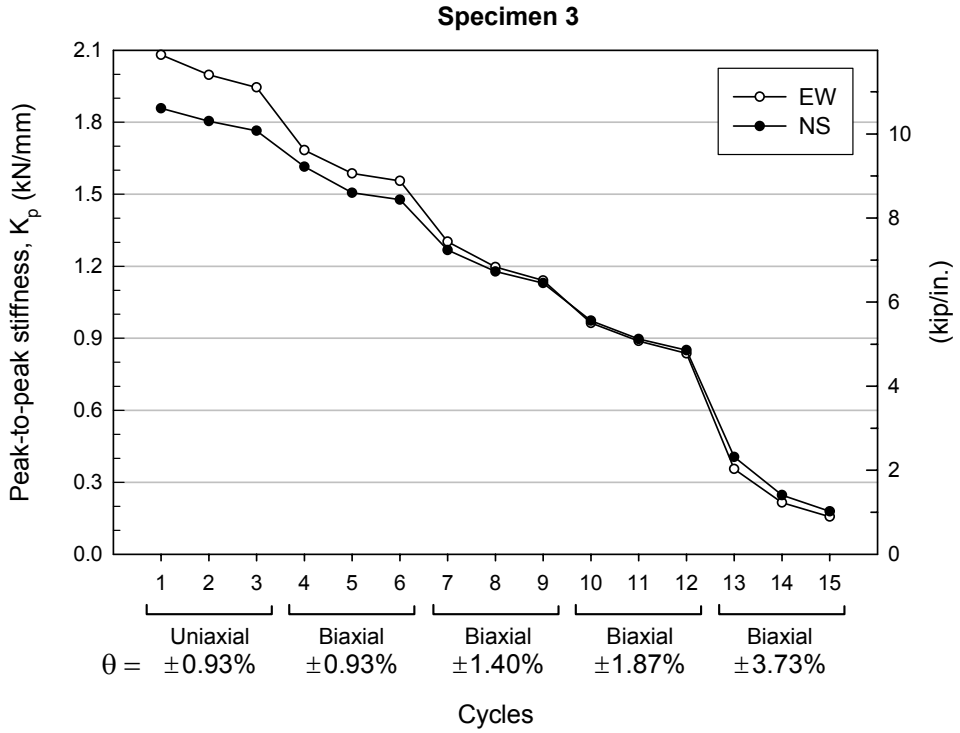

Figure C.43 — Variation of peak-to-peak stiffness – Specimen 3.

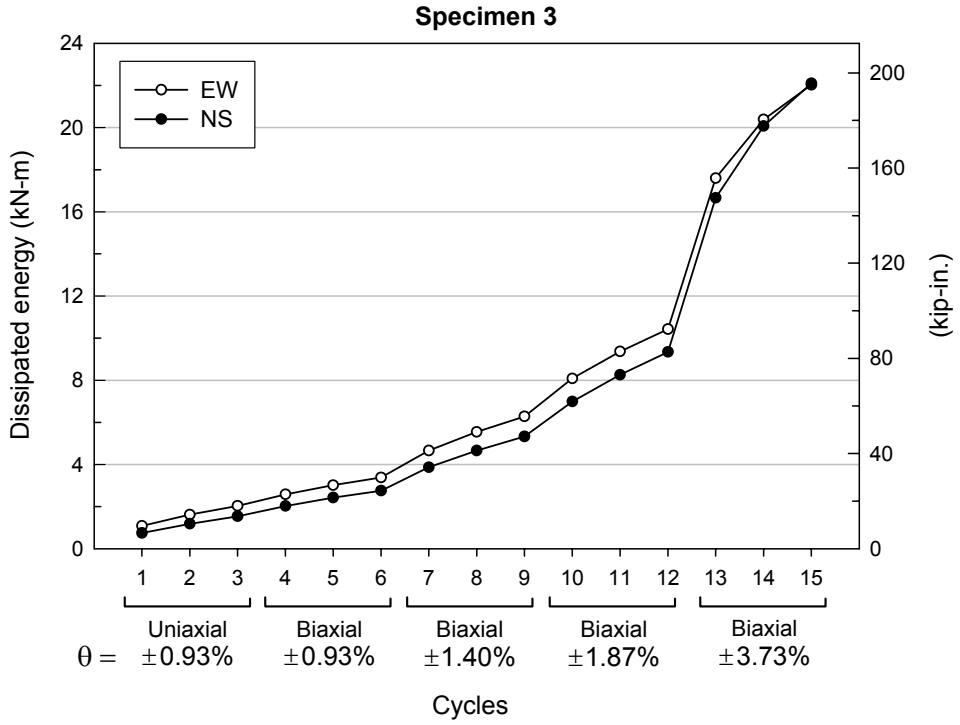

Figure C.44 — Variation of cumulative dissipated energy – Specimen 3.

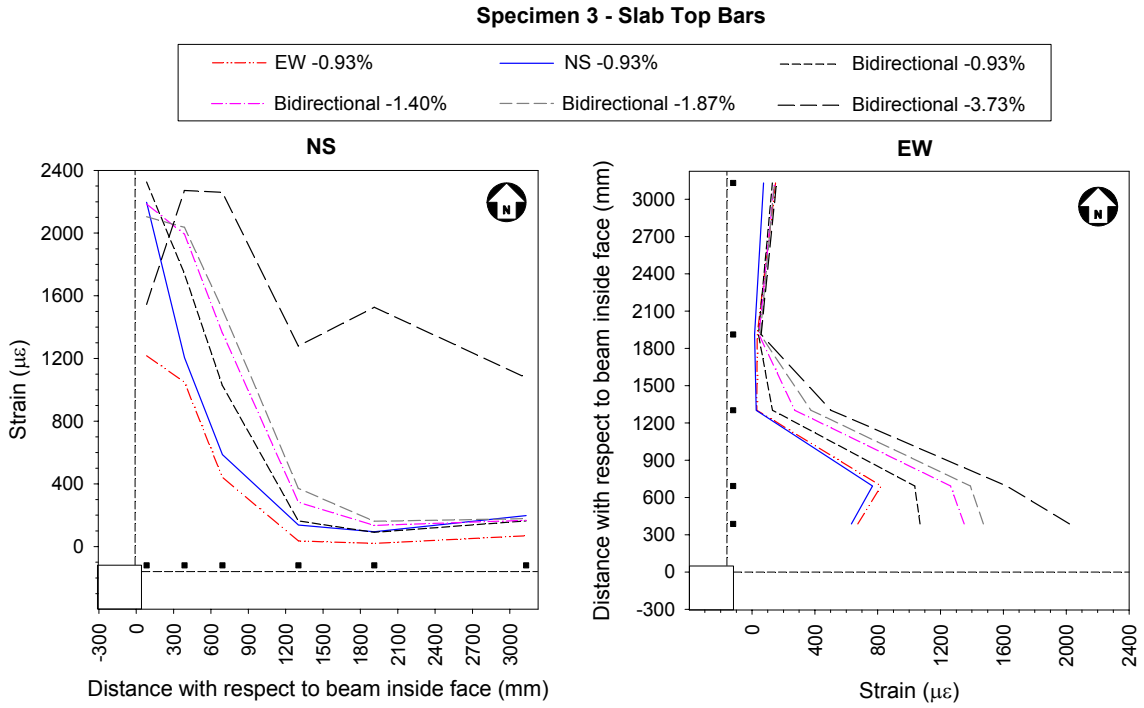

(a)

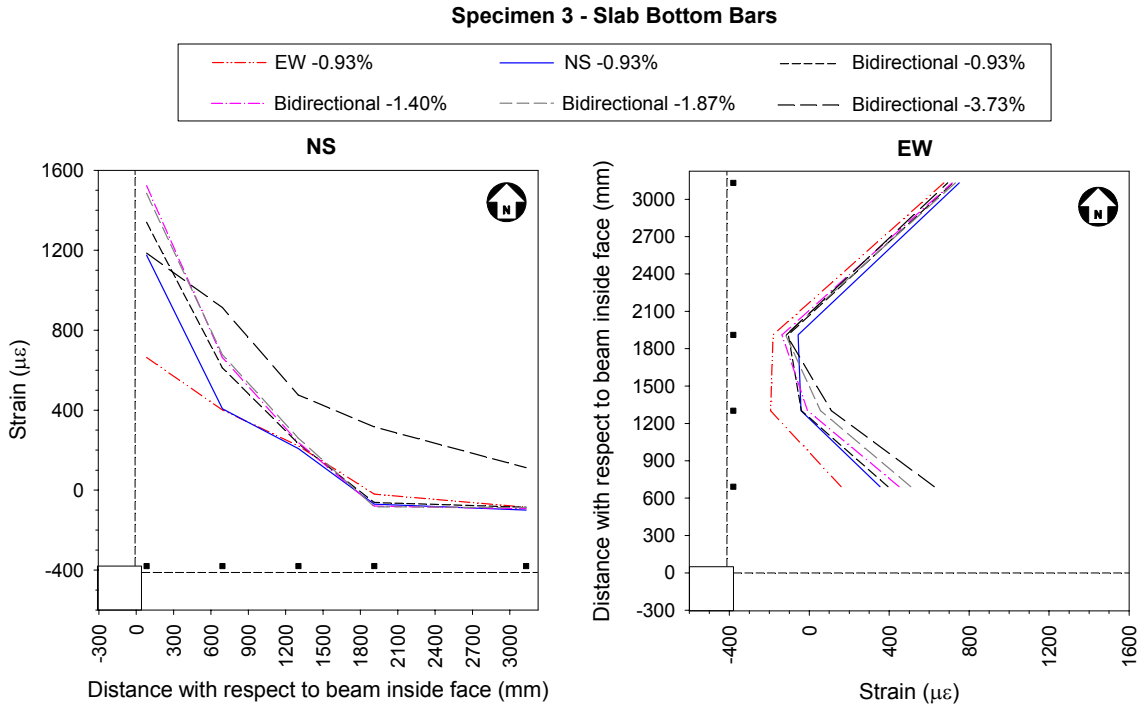

(b)

Figure C.45 — Strains in the slab bars at the first peak of downward loading at each drift level – Specimen 3: (a) top bars, and (b) bottom bars.

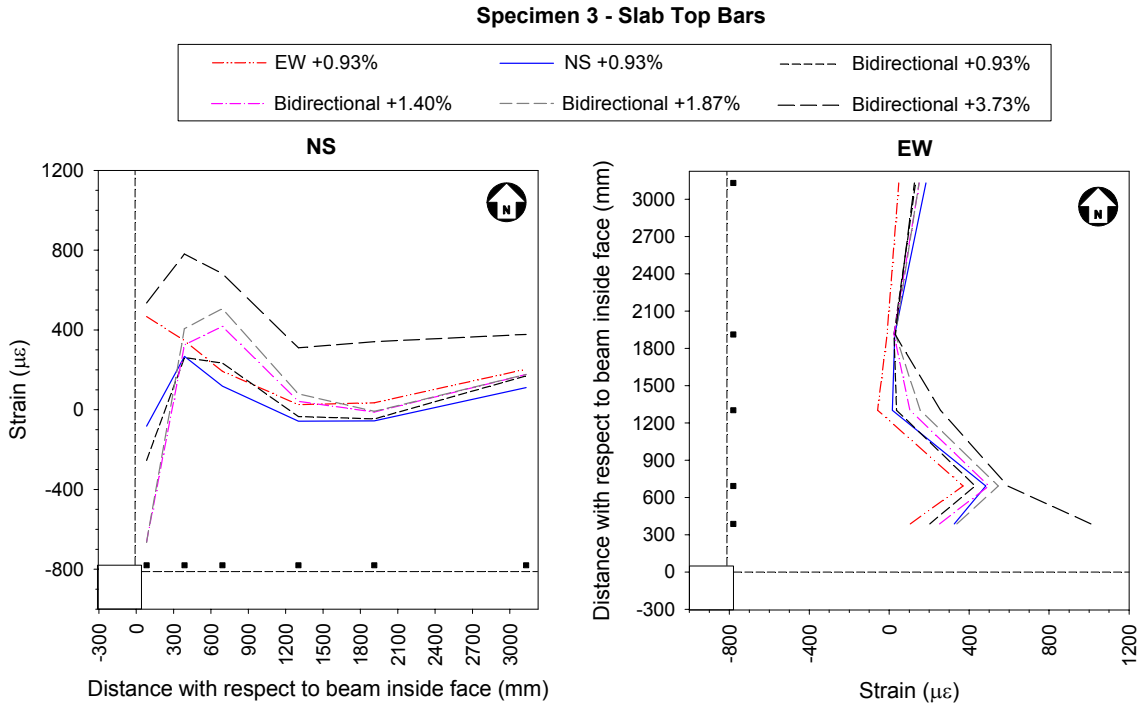

(a)

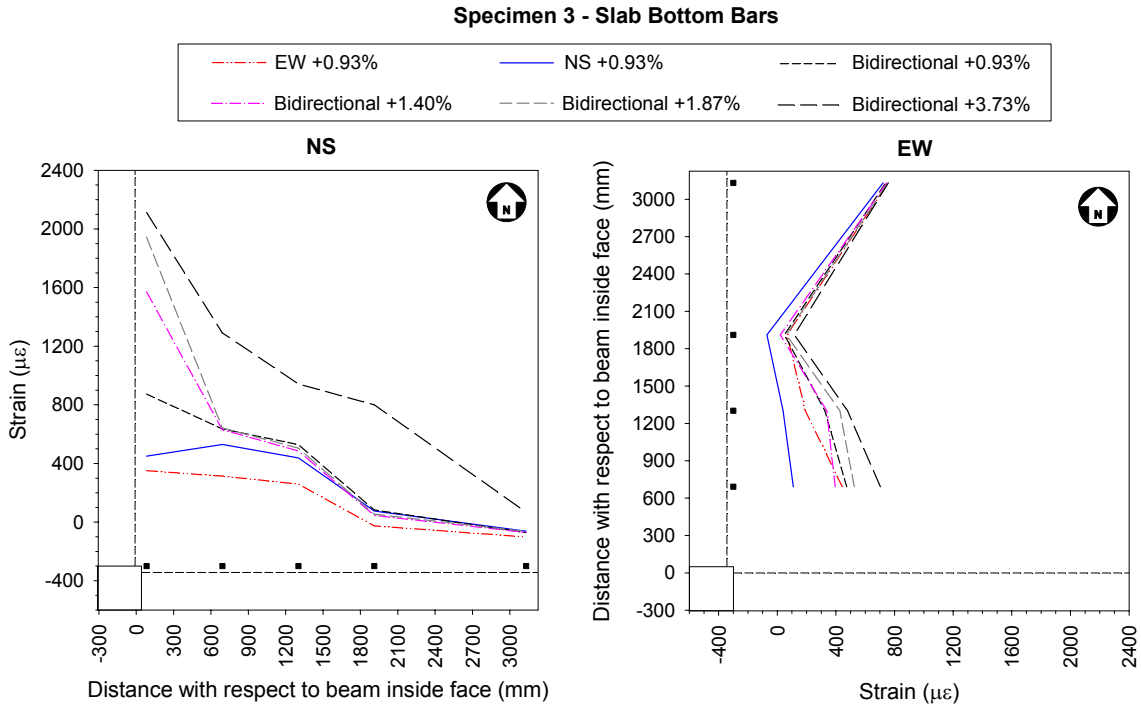

(b)

Figure C.46 — Strains in the slab bars at the first peak of upward loading at each drift level – Specimen 3: (a) top bars, and (b) bottom bars.

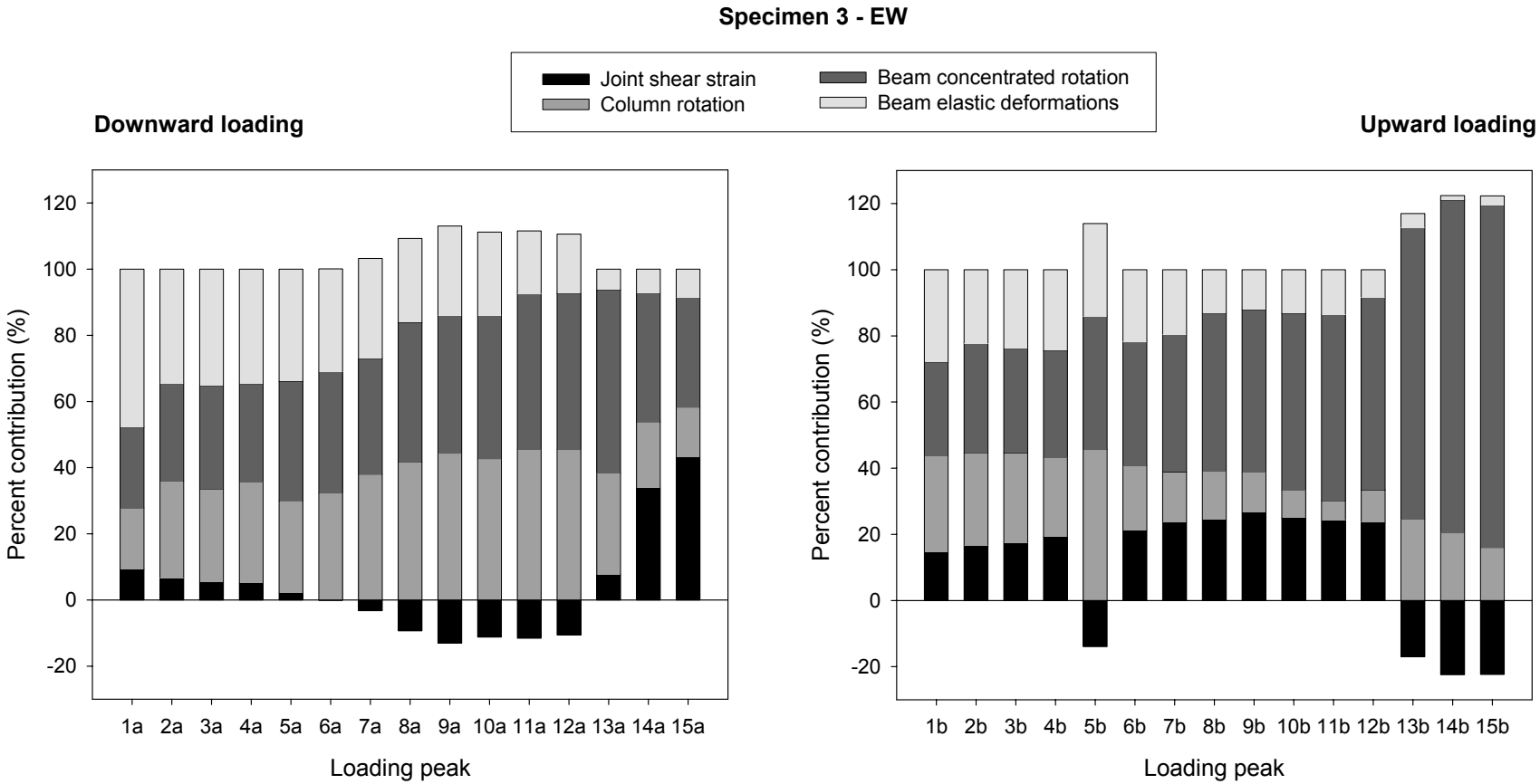

Figure C.47 — Percent contributions to applied interstory drift – Specimen 3, EW direction.

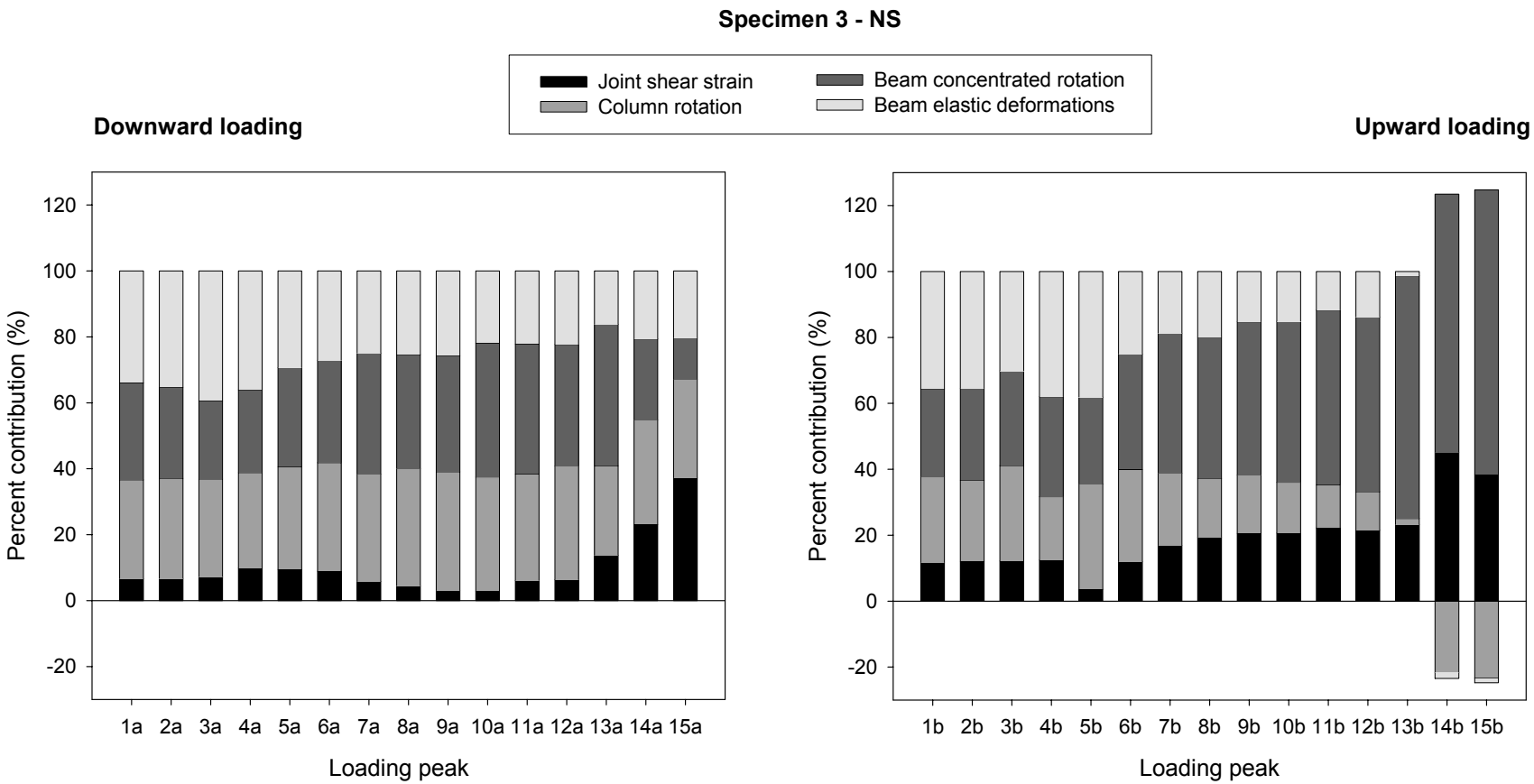

Figure C.48 — Percent contributions to applied interstory drift – Specimen 3, NS direction.

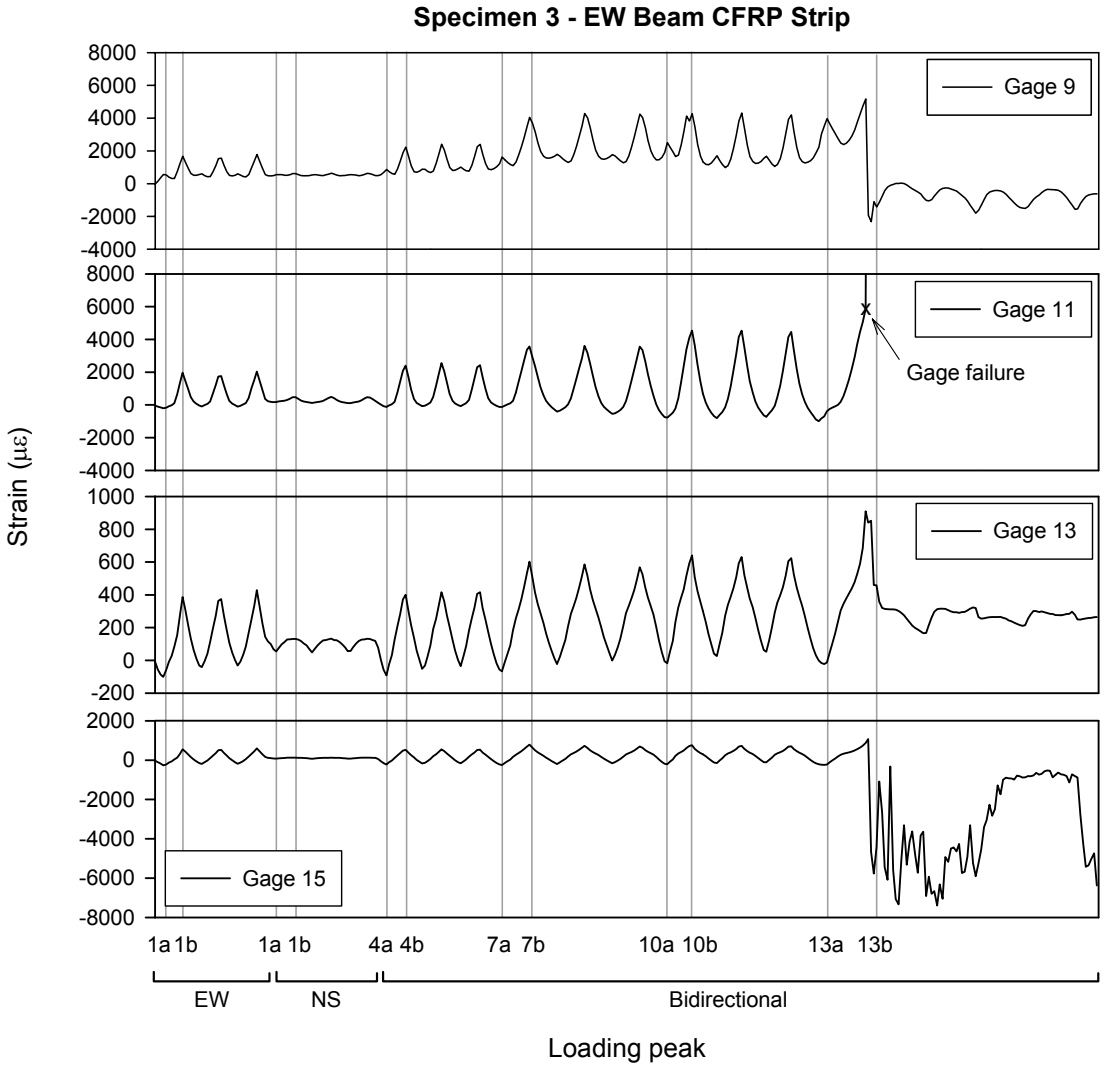

Figure C.49 — Strains in the CFRP beam strips – Specimen 3, EW beam:
Gages 9, 11: near column face; Gages 13, 15: near end of U-wrap.
(Gage locations and orientations are shown in Figure B.30.)

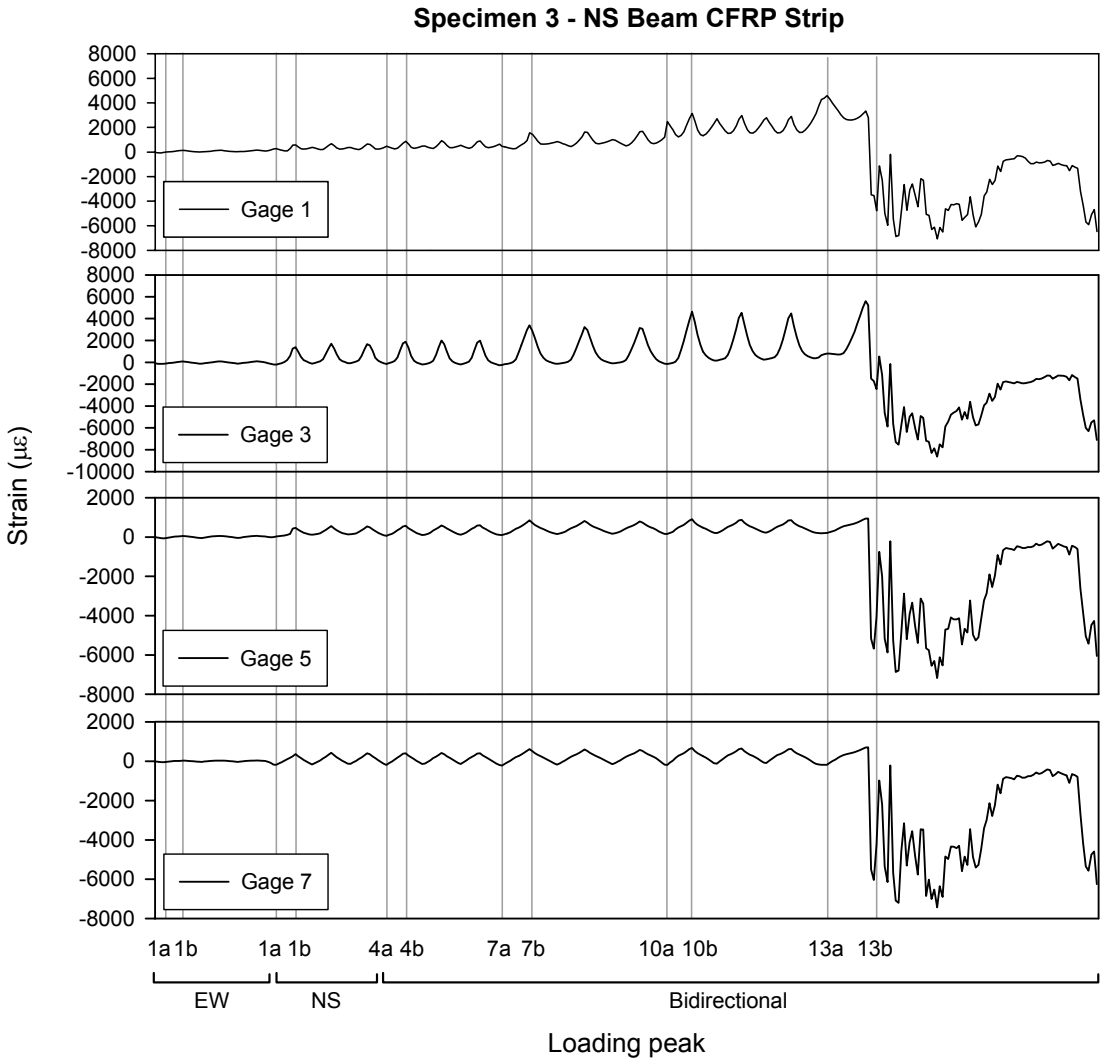

Figure C.50 — Strains in the CFRP beam strips – Specimen 3, NS beam:
Gages 1, 3: near column face; Gages 5, 7: near end of U-wrap.
(Gage locations and orientations are shown in Figure B.30.)

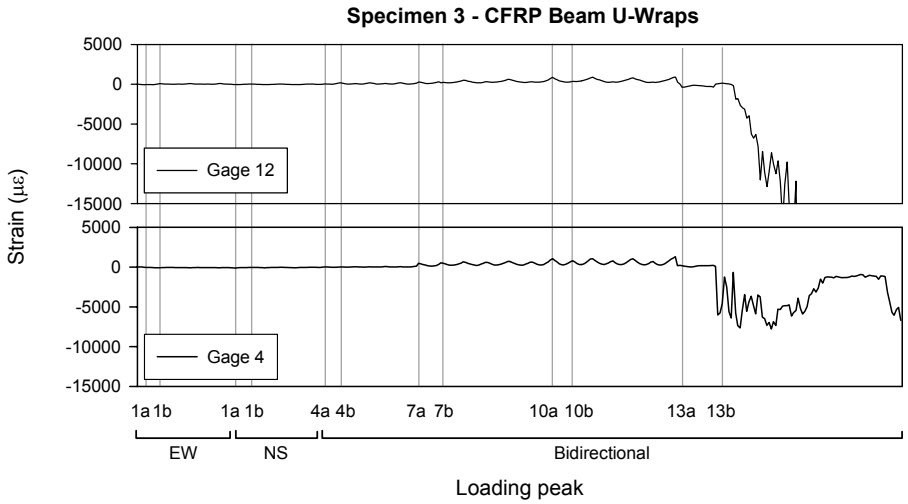

Figure C.51 — Strains in the CFRP beam U-wraps – Specimen 3:
Gages 12: EW beam, near column face; Gage 4: NS beam, near column face.
(Gage locations and orientations are shown in Figure B.30.)

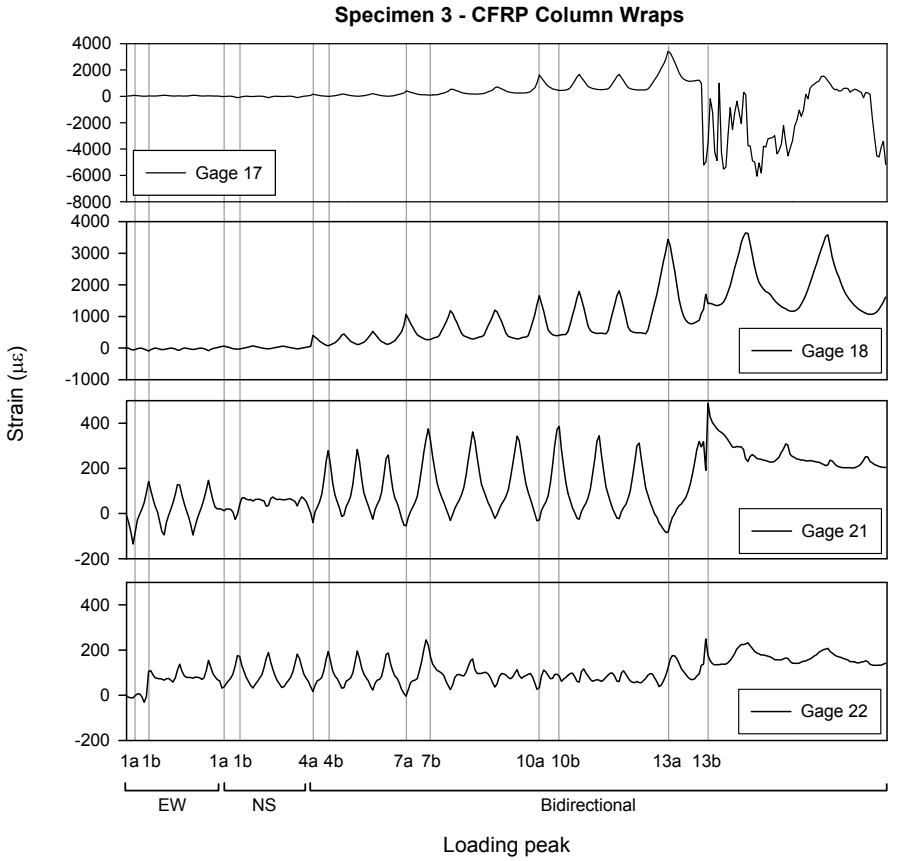

Figure C.52 — Strains in the CFRP column wraps – Specimen 3:
Gages 17, 18: Upper column, 1st stirrup level; Gages 21, 22: Lower column, 1st stirrup level. (Gage locations and orientations are shown in Figure B.30.)

Table C.9 — Summary of test results – Specimen 3, EW direction.

Loading Peak	Δ_b (in.)	θ (%)	P (kip)	V_{col} (kip)	$P_{u.col}$ (kip)	$P_{l.col}$ (kip)	V_{jh} (kip)	τ'_{jh} ($\sqrt{psi}$)	V_{jh}^{sg} (kip)	τ'^{sg}_{jh} ($\sqrt{psi}$)	γ_s (rad)	K_p (kip/in.)	E^i (kip-in.)	E^{tot} (kip-in.)
0	0.000	0.00	1.38	-5.23	-81.5	-79.3	-13.5	-1.06	-	-	0.000000	-	-	-
1a	-1.118	-0.93	-11.03	-14.61	-87.5	-96.0	-96.5	-7.57	-109.1	-8.6	-0.001108	11.88	9.6	9.6
1b	1.117	0.93	15.52	6.91	-81.6	-62.8	81.5	6.39	-	-	0.001745			
2a	-1.117	-0.93	-10.45	-14.24	-83.8	-91.3	-92.6	-7.26	-112.4	-8.8	-0.000804	11.40	4.7	14.3
2b	1.114	0.93	14.99	6.57	-78.2	-59.8	77.8	6.10	-	-	0.001998			
3a	-1.119	-0.93	-10.07	-13.89	-81.4	-88.3	-90.1	-7.06	-112.2	-8.8	-0.000654	11.11	3.7	18.0
3b	1.115	0.93	14.75	6.31	-76.1	-57.8	76.2	5.98	-	-	0.002097			
4a	-1.118	-0.93	-7.75	-11.28	-82.2	-97.1	-75.4	-5.91	-114.1	-8.9	-0.000614	9.62	4.8	22.8
4b	1.116	0.93	13.73	5.16	-74.0	-46.7	69.6	5.46	-	-	0.002310			
5a	-1.118	-0.93	-7.34	-11.10	-81.0	-94.9	-72.6	-5.69	-113.2	-8.9	-0.000265	9.06	3.8	26.7
5b	1.115	0.93	12.89	4.49	-72.2	-46.7	63.9	5.01	-	-	0.002412			
6a	-1.119	-0.93	-7.08	-10.85	-79.7	-93.2	-70.9	-5.56	-112.2	-8.8	0.000010	8.88	3.2	29.9
6b	1.117	0.93	12.78	4.45	-70.5	-45.3	63.1	4.95	-	-	0.002538			
7a	-1.679	-1.40	-10.10	-12.85	-88.8	-108.3	-91.4	-7.17	-121.0	-9.5	0.000585	7.44	11.3	41.2
7b	1.673	1.39	14.83	6.16	-75.6	-45.8	77.0	6.04	-	-	0.004267			
8a	-1.675	-1.40	-8.95	-12.05	-86.8	-104.0	-83.6	-6.55	-118.8	-9.3	0.001676	6.83	7.9	49.1
8b	1.673	1.39	13.94	5.41	-72.7	-44.6	70.9	5.56	-	-	0.004368			
9a	-1.679	-1.40	-8.38	-11.67	-84.6	-100.9	-79.8	-6.25	-115.3	-9.0	0.002352	6.51	6.5	55.6
9b	1.674	1.40	13.46	5.04	-69.8	-42.6	67.7	5.31	-	-	0.004791			
10a	-2.235	-1.86	-10.16	-12.87	-90.5	-110.2	-91.8	-7.20	-122.8	-9.6	0.002687	5.50	16.0	71.6
10b	2.232	1.86	14.42	5.77	-71.0	-41.3	74.3	5.83	-	-	0.005994			
11a	-2.237	-1.86	-8.83	-11.96	-86.5	-103.7	-82.8	-6.49	-111.4	-8.7	0.002774	5.07	11.3	82.9
11b	2.233	1.86	13.85	5.32	-68.6	-40.2	70.4	5.52	-	-	0.005853			
12a	-2.233	-1.86	-7.84	-11.43	-83.5	-99.0	-75.9	-5.95	-103.1	-8.1	0.002538	4.78	9.4	92.3
12b	2.235	1.86	13.52	5.07	-65.9	-38.2	68.1	5.34	-	-	0.005714			
13a	-4.475	-3.73	-9.13	-13.93	-103.4	-122.3	-83.1	-6.51	-118.9	-9.3	-0.003663	2.03	63.5	155.7
13b	4.470	3.73	9.02	2.14	-67.3	-47.3	36.9	2.89	-	-	-0.008152			
14a	-4.472	-3.73	-2.79	-10.57	-80.4	-86.5	-39.2	-3.07	-45.3	-3.5	-0.016262	1.23	24.7	180.4
14b	4.471	3.73	8.21	1.70	-55.4	-38.0	31.2	2.45	-	-	-0.010767			
15a	-4.474	-3.73	-0.15	-9.04	-64.7	-65.5	-21.0	-1.65	-22.4	-1.8	-0.020780	0.89	14.5	194.9
15b	4.472	3.73	7.85	1.29	-49.0	-32.6	28.9	2.26	-	-	-0.010723			

Table C.10 — Summary of test results – Specimen 3, NS direction.

Loading Peak	Δ_b (in.)	θ (%)	P (kip)	V_{col} (kip)	$P_{u.col}$ (kip)	$P_{l.col}$ (kip)	V_{jh} (kip)	τ'_{jh} ($\sqrt{psi}$)	V_{jh}^{sg} (kip)	$\tau'_{jh}{}^{sg}$ ($\sqrt{psi}$)	γ_s (rad)	K_p (kip/in.)	E^i (kip-in.)	E^{tot} (kip-in.)
0	0.000	0.00	0.81	-4.85	-81.5	-79.3	-19.1	-1.50	-	-	0.000000	-	-	-
1a	-1.118	-0.93	-8.65	-11.63	-80.7	-85.9	-86.0	-6.74	-115.6	-9.1	-0.000799	10.61	6.6	6.6
1b	1.118	0.93	15.07	6.26	-75.6	-56.1	75.1	5.89	-	-	0.001407			
2a	-1.116	-0.93	-8.46	-11.51	-79.8	-84.5	-84.6	-6.63	-119.2	-9.3	-0.000806	10.31	3.9	10.5
2b	1.118	0.93	14.55	5.89	-74.2	-55.1	71.7	5.63	-	-	0.001450			
3a	-1.117	-0.93	-8.23	-11.32	-78.6	-83.1	-83.0	-6.51	-118.8	-9.3	-0.000872	10.07	3.2	13.6
3b	1.114	0.93	14.25	5.66	-72.6	-53.9	69.7	5.47	-	-	0.001458			
4a	-1.117	-0.93	-7.09	-10.29	-82.2	-97.1	-75.1	-5.89	-122.8	-9.6	-0.001183	9.22	4.3	17.9
4b	1.118	0.93	13.52	5.06	-74.0	-46.7	65.0	5.10	-	-	0.001494			
5a	-1.119	-0.93	-6.63	-9.91	-81.0	-94.9	-72.0	-5.65	-121.3	-9.5	-0.001139	8.60	3.5	21.5
5b	1.114	0.93	12.57	4.35	-72.2	-46.7	58.8	4.61	-	-	0.001457			
6a	-1.118	-0.93	-6.42	-9.85	-79.7	-93.2	-70.4	-5.52	-119.6	-9.4	-0.001074	8.44	2.9	24.4
6b	1.118	0.93	12.45	4.22	-70.5	-45.3	58.1	4.55	-	-	0.001436			
7a	-1.679	-1.40	-9.36	-12.04	-88.8	-108.3	-91.1	-7.14	-125.4	-9.8	-0.001043	7.24	9.8	34.2
7b	1.676	1.40	14.92	6.23	-75.6	-45.8	74.0	5.81	-	-	0.003038			
8a	-1.674	-1.39	-8.33	-11.26	-86.8	-104.0	-83.9	-6.58	-122.0	-9.6	-0.000810	6.73	7.1	41.2
8b	1.675	1.40	14.19	5.65	-72.7	-44.6	69.4	5.44	-	-	0.003481			
9a	-1.679	-1.40	-7.87	-10.95	-84.6	-100.9	-80.6	-6.32	-118.2	-9.3	-0.000556	6.45	5.9	47.2
9b	1.675	1.40	13.77	5.38	-69.8	-42.6	66.5	5.22	-	-	0.003691			
10a	-2.236	-1.86	-9.53	-12.15	-90.5	-110.2	-92.3	-7.24	-125.2	-9.8	-0.000685	5.56	14.7	61.8
10b	2.235	1.86	15.33	6.64	-71.0	-41.3	76.6	6.01	-	-	0.004955			
11a	-2.235	-1.86	-8.36	-11.37	-86.5	-103.7	-84.0	-6.59	-114.3	-9.0	-0.001471	5.12	11.3	73.1
11b	2.235	1.86	14.53	6.02	-68.6	-40.2	71.5	5.60	-	-	0.005338			
12a	-2.232	-1.86	-7.57	-10.86	-83.5	-99.0	-78.3	-6.14	-105.1	-8.2	-0.001523	4.86	9.6	82.7
12b	2.237	1.86	14.14	5.73	-65.9	-38.2	68.9	5.40	-	-	0.005162			
13a	-4.475	-3.73	-9.77	-12.39	-103.4	-122.3	-93.9	-7.37	-103.5	-8.1	-0.006620	2.32	64.8	147.4
13b	4.472	3.73	10.95	3.68	-67.3	-47.3	47.7	3.74	-	-	0.011158			
14a	-4.471	-3.73	-3.36	-8.48	-80.4	-86.5	-47.9	-3.76	-14.9	-1.2	-0.011077	1.41	30.2	177.6
14b	4.472	3.73	9.24	2.45	-55.4	-38.0	36.5	2.86	-	-	0.021689			
15a	-4.471	-3.73	-0.60	-6.77	-64.7	-65.5	-28.2	-2.21	5.5	0.4	-0.017886	1.02	18.0	195.6
15b	4.475	3.73	8.54	1.86	-49.0	-32.6	32.0	2.51	-	-	0.018483			

C.6 SPECIMEN 4

Views during and at the end of the last cycle: Cycle 15 (±3.73% bidirectional drift)

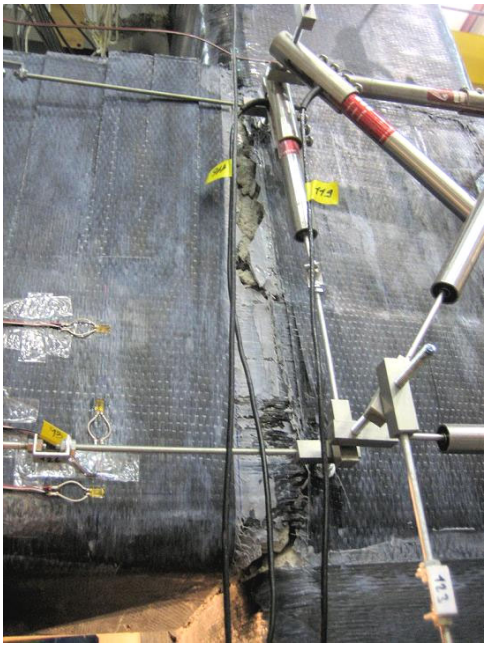

(a) NS beam-joint interface

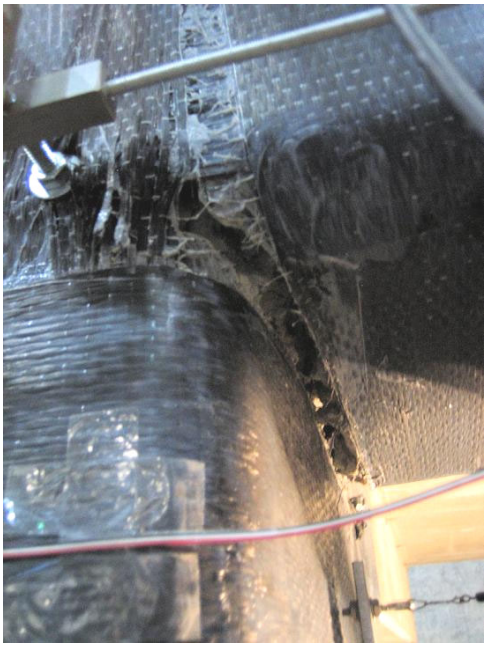

(b) EW beam bottom

(c) Joint NE corner

(d) Joint SW corner

Figure C.53 — Damage modes – Specimen 4.

Views during and at the end of the last cycle: Cycle 15 (±3.73% bidirectional drift)

(e) EW beam end

(f) Slab SW corner

(g) Joint after removal of CFRP

(h) Joint after removal of loose concrete

Figure C.53 — Continued.

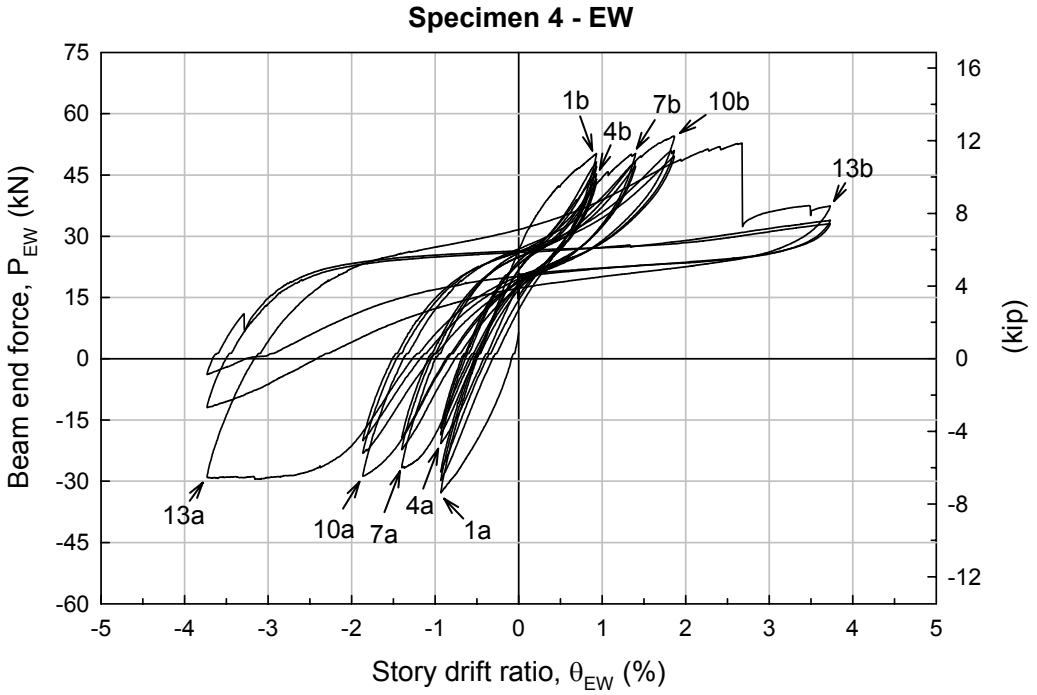

(a)

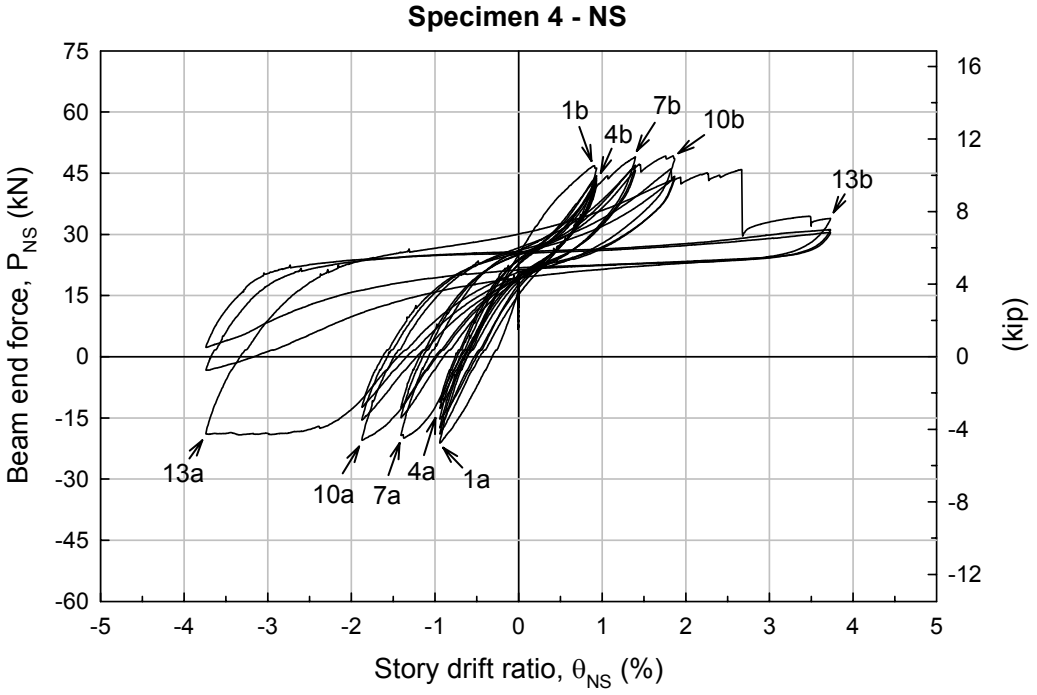

(b)

Figure C.54 — Force-drift hysteretic curves – Specimen 4:
(a) EW, and (b) NS direction.

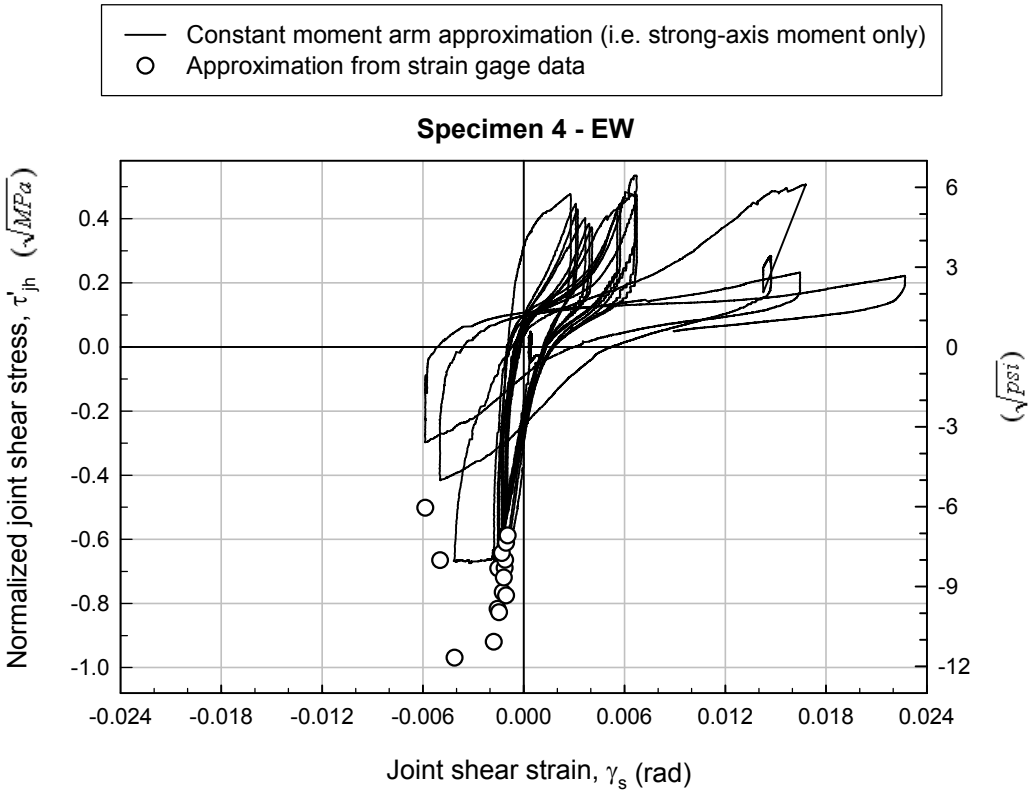

(a)

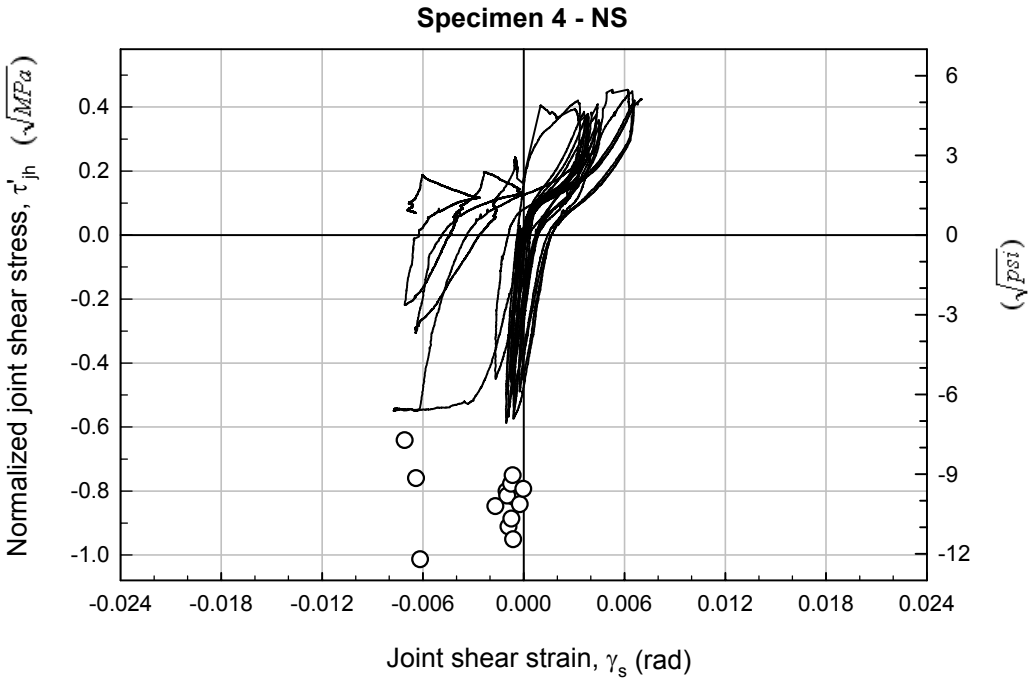

(b)

Figure C.55 — Joint shear stress-strain hysteretic curves – Specimen 4: (a) EW, and (b) NS direction.

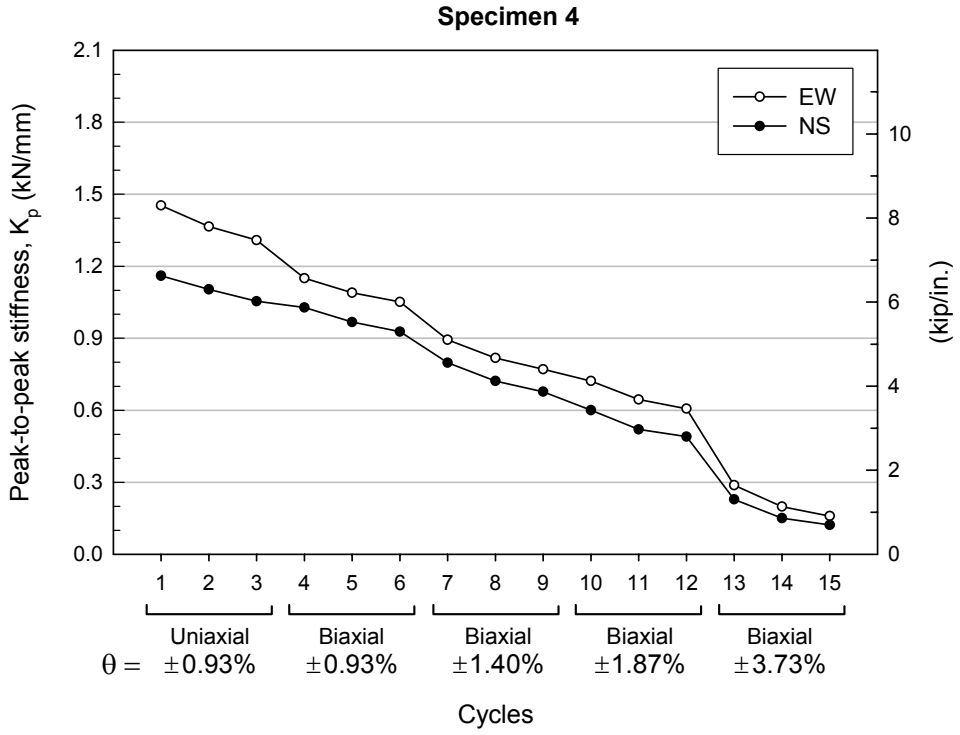

Figure C.56 — Variation of peak-to-peak stiffness – Specimen 4.

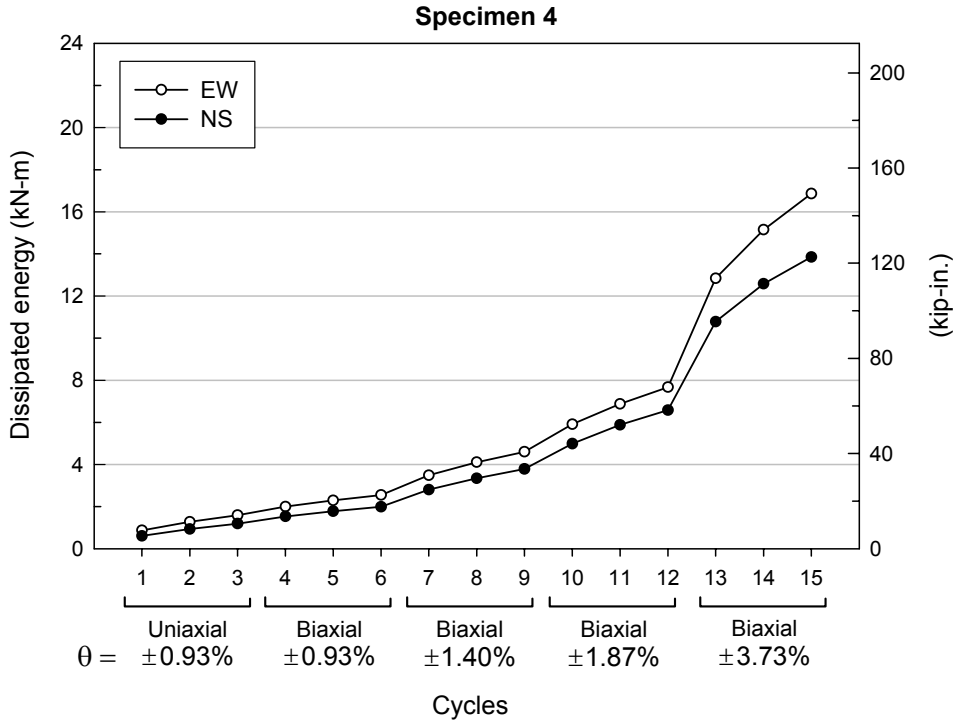

Figure C.57 — Variation of cumulative dissipated energy – Specimen 4.

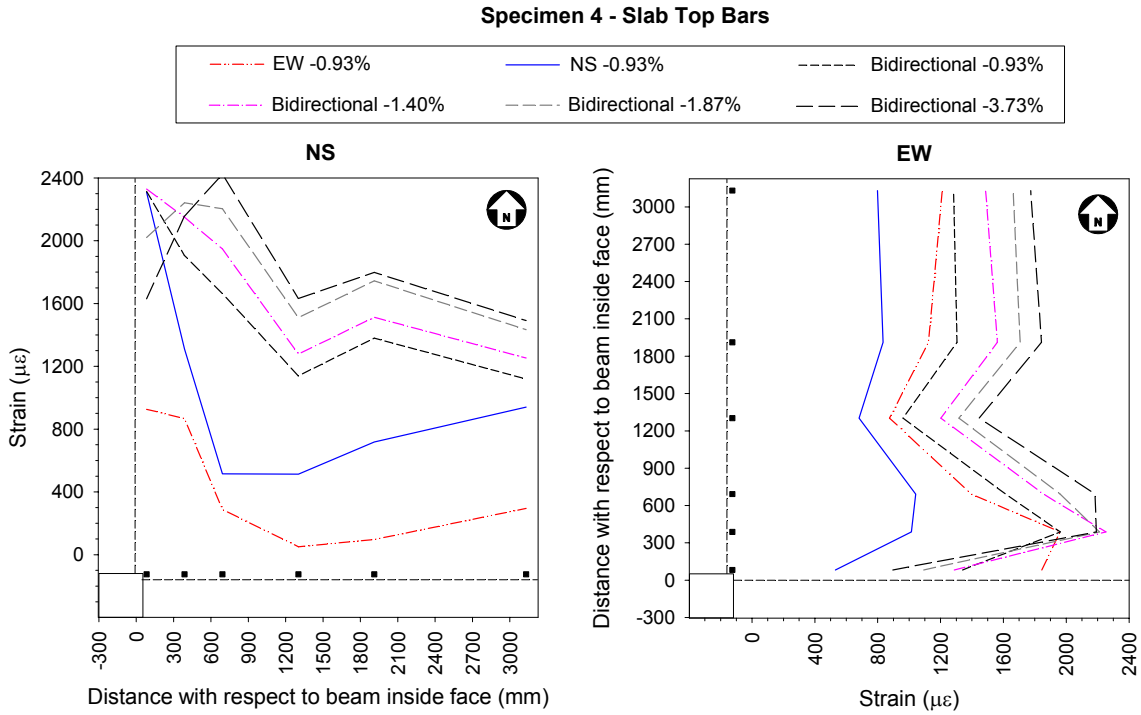

(a)

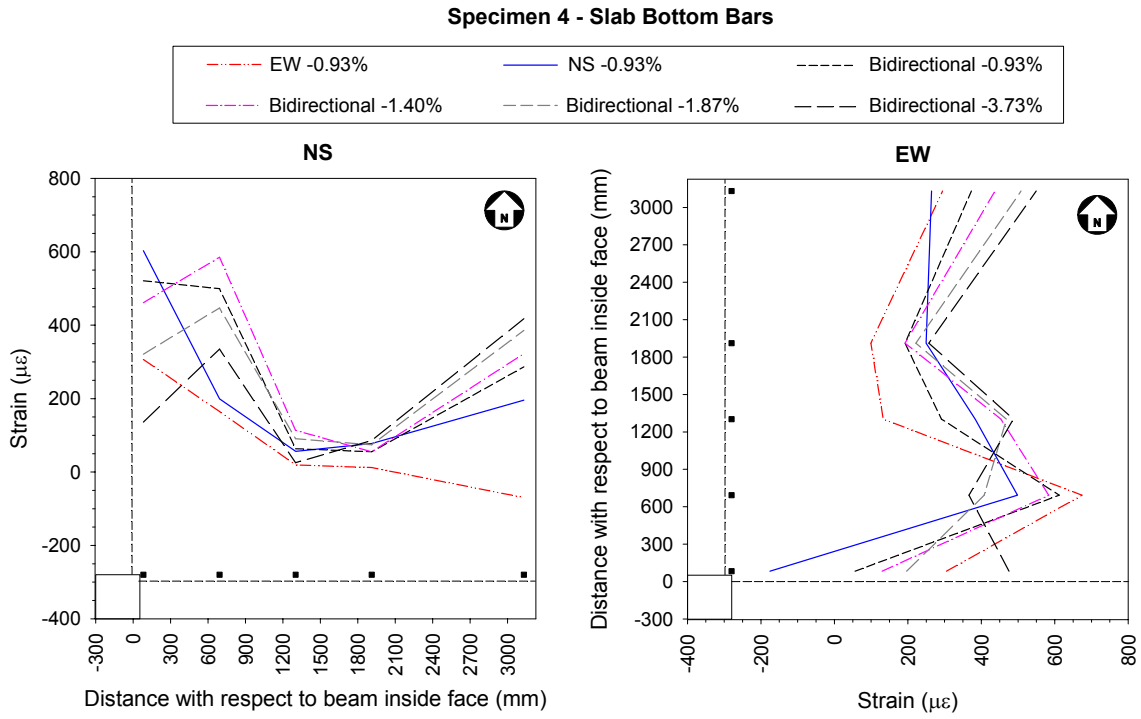

(b)

Figure C.58 — Strains in the slab bars at the first peak of downward loading at each drift level – Specimen 4: (a) top bars, and (b) bottom bars.

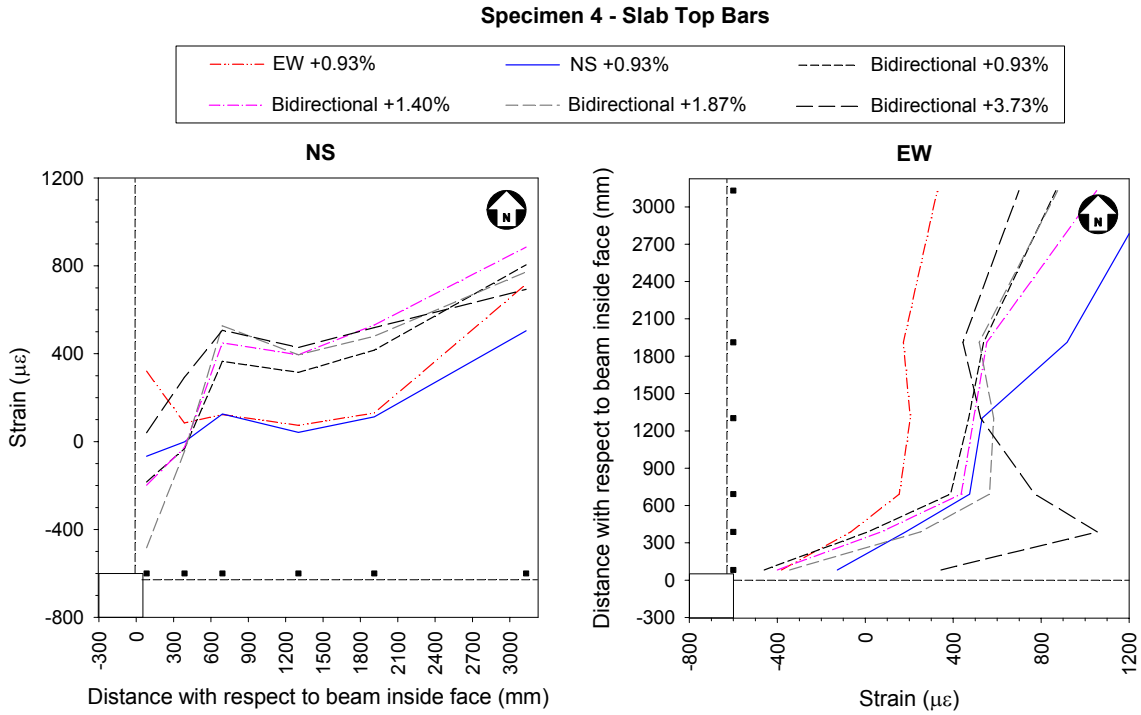

(a)

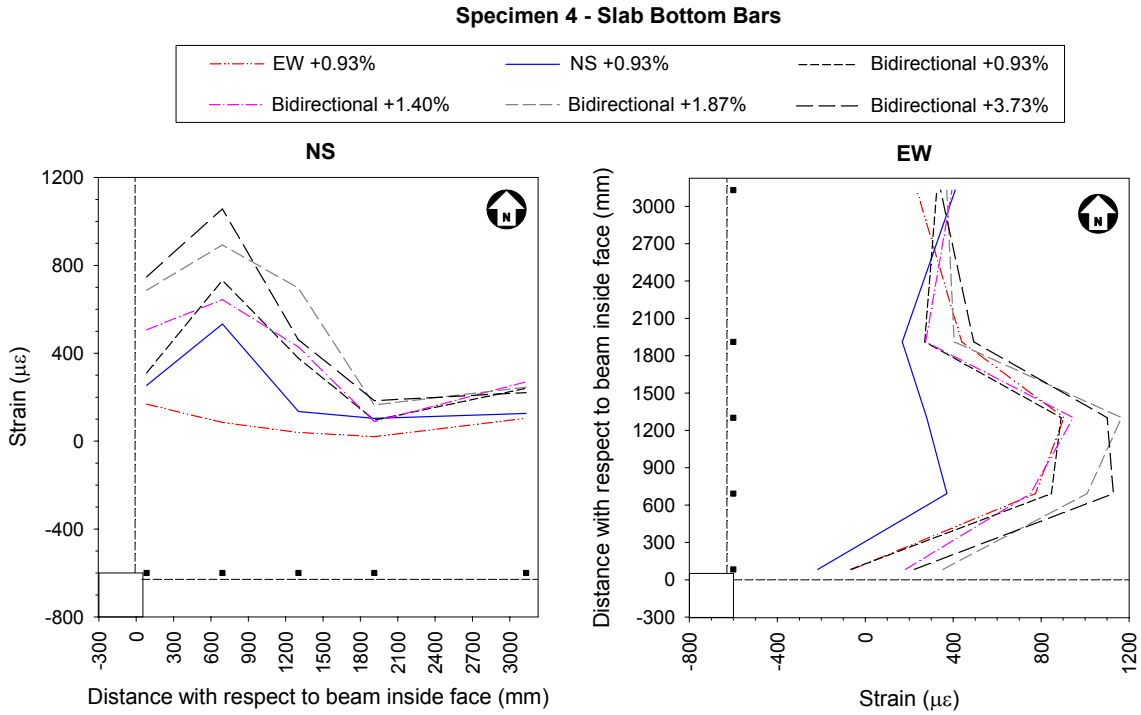

(b)

Figure C.59 — Strains in the slab bars at the first peak of upward loading at each drift level – Specimen 4: (a) top bars, and (b) bottom bars.

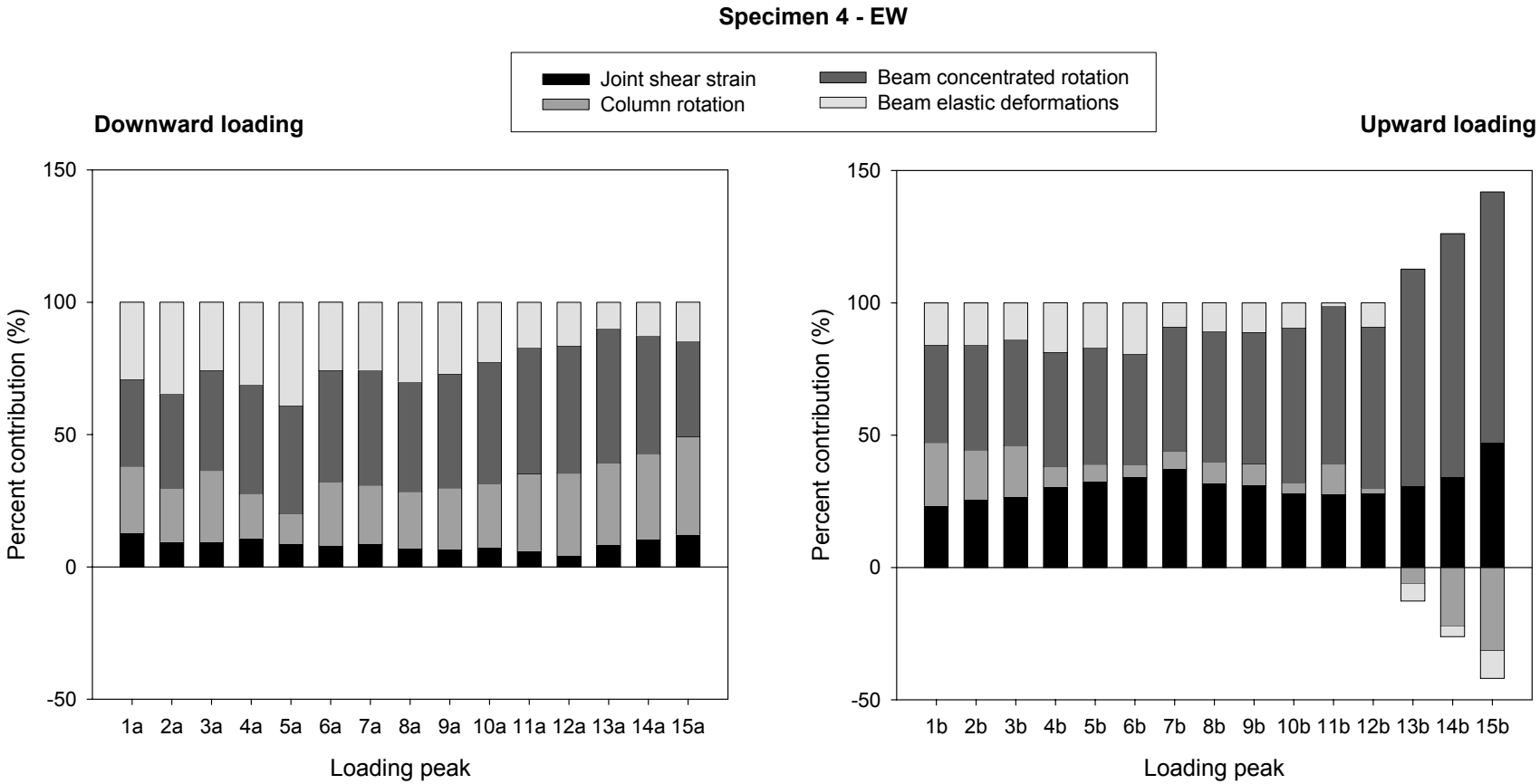

Figure C.60 — Percent contributions to applied interstory drift – Specimen 4, EW direction.

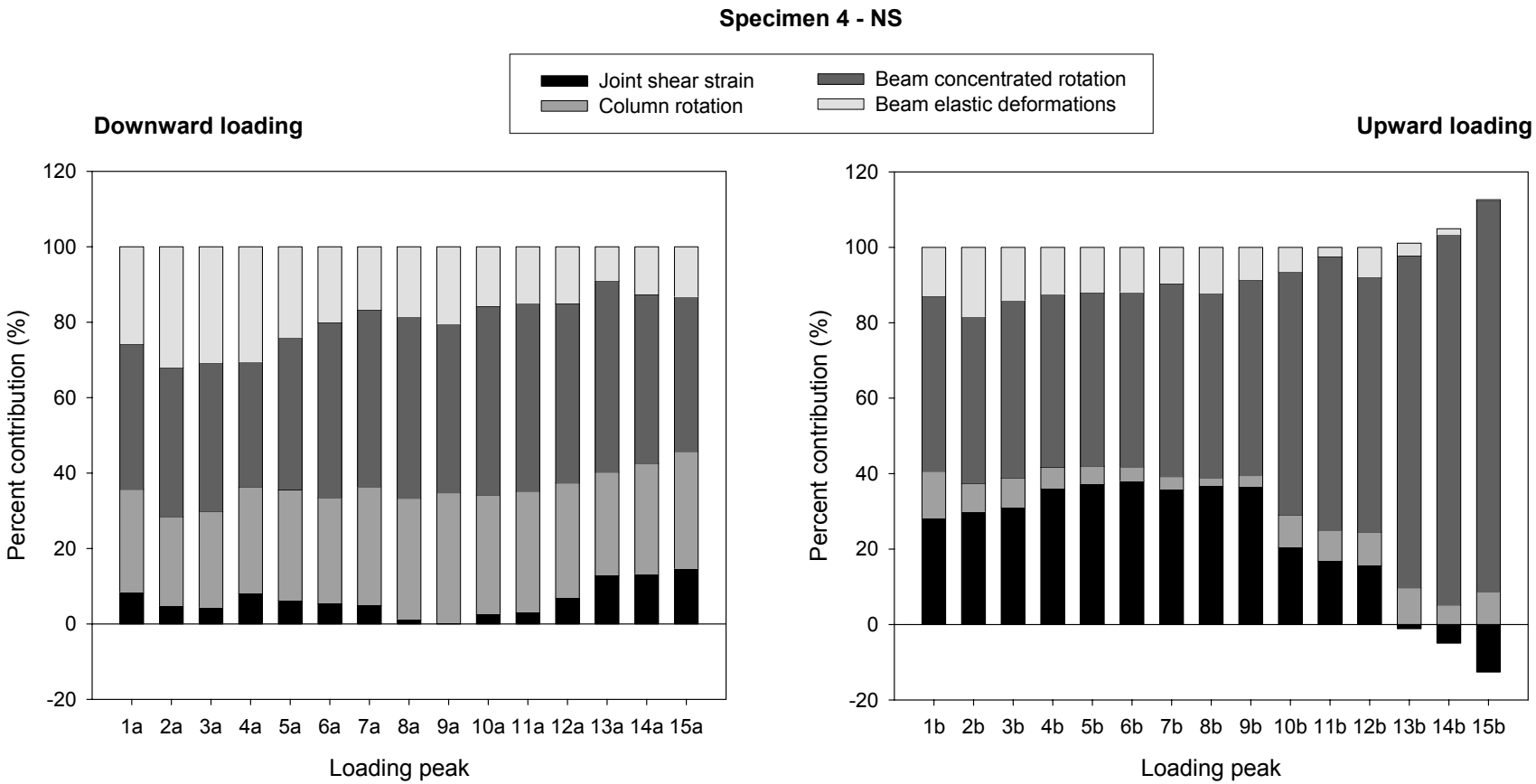

Figure C.61 — Percent contributions to applied interstory drift – Specimen 4, NS direction.

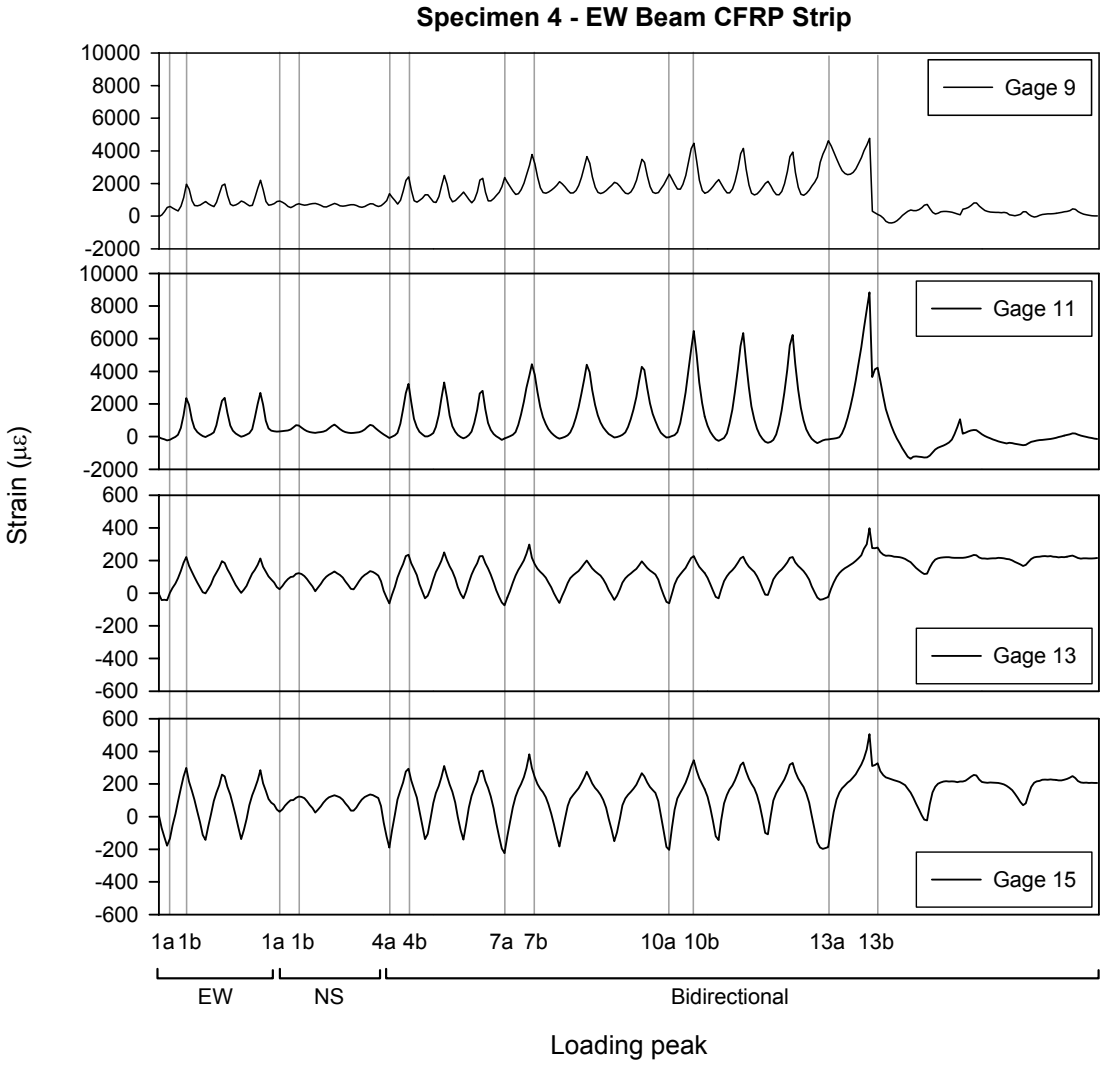

Figure C.62 — Strains in the CFRP beam strips – Specimen 4, EW beam:
Gages 9, 11: near column face; Gages 13, 15: near end of U-wrap.
(Gage locations and orientations are shown in Figure B.30.)

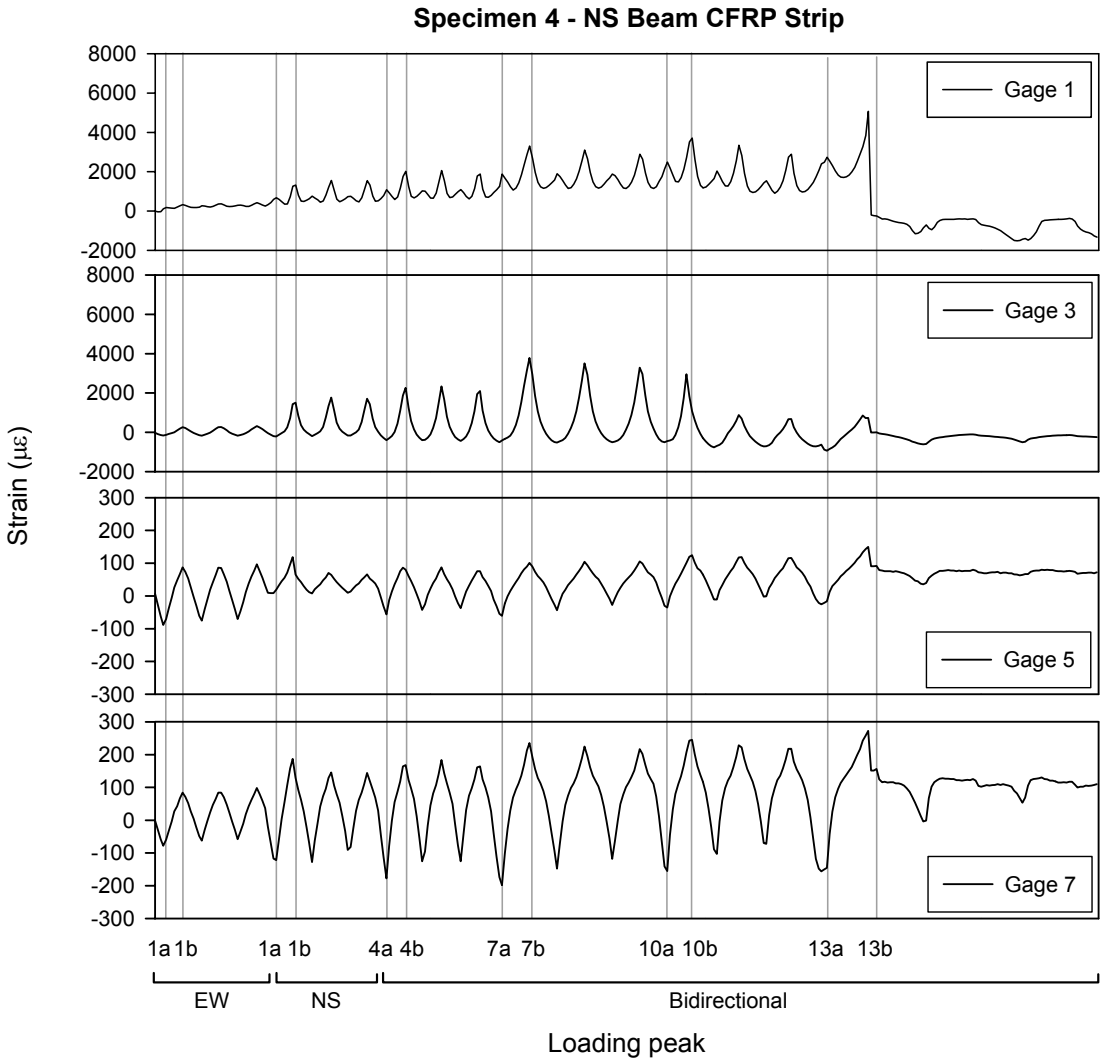

Figure C.63 — Strains in the CFRP beam strips – Specimen 4, NS beam:
Gages 1, 3: near column face; Gages 5, 7: near end of U-wrap.
(Gage locations and orientations are shown in Figure B.30.)

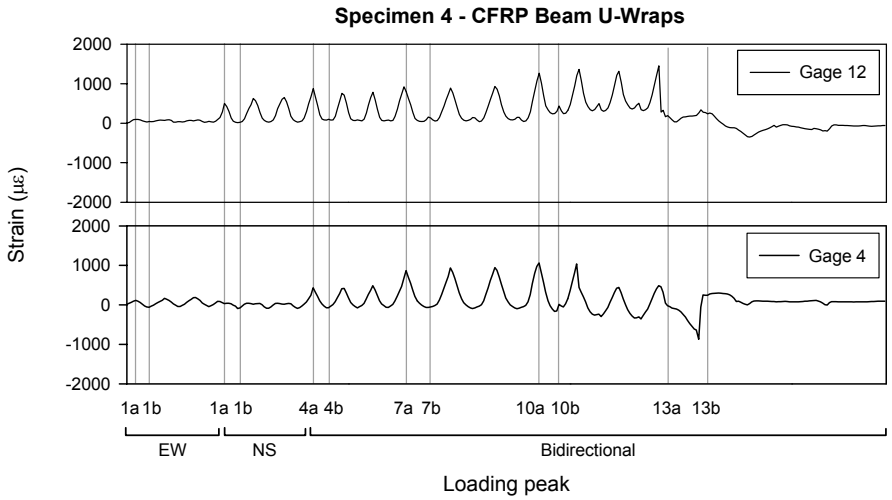

Figure C.64 — Strains in the CFRP beam U-wraps – Specimen 4:
Gages 12: EW beam, near column face; Gage 4: NS beam, near column face.
(Gage locations and orientations are shown in Figure B.30.)

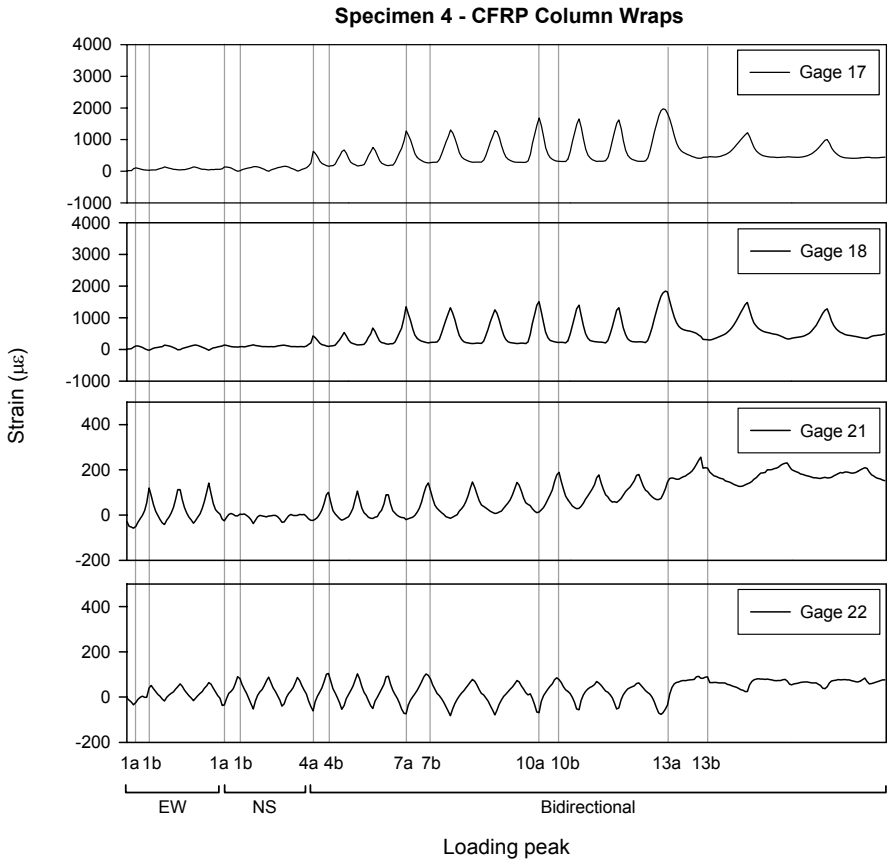

Figure C.65 — Strains in the CFRP column wraps – Specimen 4:
Gages 17, 18: Upper column, 1st stirrup level; Gages 21, 22: Lower column, 1st stirrup level. (Gage locations and orientations are shown in Figure B.30.)

Table C.11 — Summary of test results – Specimen 4, EW direction.

Loading Peak	Δ_b (in.)	θ (%)	P (kip)	V_{col} (kip)	$P_{u.col}$ (kip)	$P_{l.col}$ (kip)	V_{jh} (kip)	τ'_{jh} ($\sqrt{psi}$)	V_{jh}^{sg} (kip)	τ'^{sg}_{jh} ($\sqrt{psi}$)	γ_s (rad)	K_p (kip/in.)	E^i (kip-in.)	E^{tot} (kip-in.)
0	0.000	0.00	1.44	-1.19	-55.9	-52.8	-17.0	-1.98	-	-	0.000000	-	-	-
1a	-1.115	-0.93	-7.32	-8.04	-61.1	-65.9	-75.4	-8.78	-71.6	-8.3	-0.001514	8.30	7.7	7.7
1b	1.117	0.93	11.21	6.84	-54.1	-39.0	48.8	5.68	-	-	0.002805			
2a	-1.115	-0.93	-6.60	-7.56	-57.7	-61.5	-70.6	-8.22	-71.4	-8.3	-0.001138	7.80	3.6	11.3
2b	1.118	0.93	10.80	6.46	-51.0	-36.2	46.0	5.36	-	-	0.003088			
3a	-1.116	-0.93	-6.18	-7.25	-54.7	-57.9	-67.8	-7.89	-68.8	-8.0	-0.001105	7.47	2.8	14.1
3b	1.118	0.93	10.51	6.23	-47.8	-33.0	44.1	5.13	-	-	0.003220			
4a	-1.115	-0.93	-4.58	-5.84	-47.4	-55.4	-57.3	-6.66	-66.6	-7.8	-0.001302	6.57	3.6	17.7
4b	1.116	0.93	10.07	5.96	-38.2	-18.4	41.0	4.77	-	-	0.003675			
5a	-1.114	-0.93	-4.06	-5.49	-44.2	-51.1	-53.7	-6.25	-63.3	-7.4	-0.001048	6.22	2.6	20.3
5b	1.117	0.93	9.83	5.78	-35.1	-15.7	39.4	4.58	-	-	0.003909			
6a	-1.113	-0.93	-3.74	-5.28	-41.0	-47.2	-51.5	-6.00	-60.9	-7.1	-0.000951	6.01	2.3	22.6
6b	1.116	0.93	9.64	5.64	-31.9	-12.9	38.1	4.43	-	-	0.004082			
7a	-1.673	-1.39	-5.85	-7.15	-43.2	-53.3	-65.4	-7.61	-84.6	-9.8	-0.001548	5.10	8.3	30.9
7b	1.675	1.40	11.24	7.05	-32.0	-9.8	48.8	5.68	-	-	0.006714			
8a	-1.675	-1.40	-4.89	-6.54	-37.3	-45.6	-58.9	-6.85	-79.3	-9.2	-0.001251	4.67	5.5	36.3
8b	1.674	1.39	10.75	6.64	-26.8	-5.5	45.5	5.30	-	-	0.005740			
9a	-1.671	-1.39	-4.22	-6.06	-32.0	-39.0	-54.3	-6.32	-74.5	-8.7	-0.001185	4.40	4.4	40.7
9b	1.673	1.39	10.50	6.41	-22.3	-1.5	43.9	5.10	-	-	0.005572			
10a	-2.231	-1.86	-6.27	-7.47	-70.3	-81.1	-68.2	-7.93	-95.2	-11.1	-0.001779	4.12	11.6	52.3
10b	2.235	1.86	12.14	8.05	-59.1	-36.1	54.7	6.36	-	-	0.006720			
11a	-2.232	-1.86	-5.05	-6.64	-66.2	-74.6	-59.9	-6.98	-85.7	-10.0	-0.001464	3.68	8.5	60.8
11b	2.235	1.86	11.39	7.41	-56.3	-35.0	49.6	5.77	-	-	0.006628			
12a	-2.233	-1.86	-4.39	-6.18	-64.1	-71.2	-55.4	-6.45	-80.3	-9.3	-0.001054	3.47	7.1	67.9
12b	2.236	1.86	11.10	7.22	-55.1	-34.1	47.6	5.54	-	-	0.006717			
13a	-4.471	-3.73	-6.37	-8.40	-67.5	-78.1	-68.0	-7.92	-100.4	-11.7	-0.004112	1.64	45.8	113.7
13b	4.473	3.73	8.33	5.03	-52.6	-36.7	28.7	3.34	-	-	0.014731			
14a	-4.471	-3.73	-2.58	-5.85	-55.0	-58.3	-42.3	-4.92	-68.9	-8.0	-0.004978	1.13	20.4	134.1
14b	4.474	3.73	7.57	4.27	-48.9	-34.3	23.7	2.76	-	-	0.016443			
15a	-4.473	-3.73	-0.79	-4.65	-48.5	-48.7	-30.2	-3.51	-52.0	-6.0	-0.005860	0.91	15.2	149.2
15b	4.470	3.73	7.36	3.92	-47.2	-33.1	22.5	2.61	-	-	0.022716			

Table C.12 — Summary of test results – Specimen 4, NS direction.

Loading Peak	Δ_b (in.)	θ (%)	P (kip)	V_{col} (kip)	$P_{u.col}$ (kip)	$P_{l.col}$ (kip)	V_{jh} (kip)	τ'_{jh} ($\sqrt{psi}$)	V_{jh}^{sg} (kip)	τ'^{sg}_{jh} ($\sqrt{psi}$)	γ_s (rad)	K_p (kip/in.)	E^i (kip-in.)	E^{tot} (kip-in.)
0	0.000	0.00	1.70	-2.55	-55.9	-52.8	-14.5	-1.68	-	-	0.000000	-	-	-
1a	-1.126	-0.94	-4.65	-6.39	-52.1	-53.5	-60.0	-6.99	-82.9	-9.6	-0.001027	6.63	5.4	5.4
1b	1.106	0.92	10.15	4.60	-45.3	-30.6	41.0	4.77	-	-	0.003350			
2a	-1.124	-0.94	-4.20	-6.10	-49.5	-50.2	-56.8	-6.61	-84.8	-9.9	-0.000590	6.30	2.9	8.3
2b	1.118	0.93	9.94	4.39	-42.9	-28.3	39.7	4.62	-	-	0.003598			
3a	-1.125	-0.94	-3.83	-5.86	-47.2	-47.5	-54.2	-6.31	-82.8	-9.6	-0.000531	6.02	2.2	10.5
3b	1.118	0.93	9.67	4.24	-40.4	-26.1	37.8	4.40	-	-	0.003729			
4a	-1.128	-0.94	-3.42	-5.46	-47.4	-55.4	-51.4	-5.98	-84.4	-9.8	-0.000983	5.87	3.0	13.6
4b	1.117	0.93	9.76	4.26	-38.2	-18.4	38.5	4.48	-	-	0.004327			
5a	-1.126	-0.94	-2.83	-5.00	-44.2	-51.1	-47.3	-5.51	-80.5	-9.4	-0.000757	5.53	2.2	15.7
5b	1.119	0.93	9.57	4.09	-35.1	-15.7	37.3	4.34	-	-	0.004480			
6a	-1.127	-0.94	-2.51	-4.94	-41.0	-47.2	-44.9	-5.22	-77.7	-9.0	-0.000655	5.30	1.9	17.6
6b	1.116	0.93	9.37	3.96	-31.9	-12.9	35.9	4.18	-	-	0.004567			
7a	-1.685	-1.40	-4.32	-6.30	-43.2	-53.3	-57.6	-6.70	-94.4	-11.0	-0.000903	4.56	7.2	24.8
7b	1.679	1.40	11.02	5.32	-32.0	-9.8	46.6	5.42	-	-	0.006468			
8a	-1.684	-1.40	-3.35	-5.73	-37.3	-45.6	-50.6	-5.89	-87.1	-10.1	-0.000233	4.12	4.8	29.6
8b	1.675	1.40	10.49	4.95	-26.8	-5.5	43.1	5.02	-	-	0.006607			
9a	-1.685	-1.40	-2.76	-5.42	-32.0	-39.0	-46.3	-5.39	-82.2	-9.6	-0.000022	3.87	3.9	33.5
9b	1.675	1.40	10.24	4.69	-22.3	-1.5	41.5	4.83	-	-	0.006556			
10a	-2.245	-1.87	-4.54	-6.60	-70.3	-81.1	-59.0	-6.86	-98.5	-11.5	-0.000626	3.43	10.6	44.1
10b	2.237	1.86	10.82	5.06	-59.1	-36.1	45.4	5.29	-	-	0.004939			
11a	-2.245	-1.87	-3.43	-5.83	-66.2	-74.6	-51.2	-5.95	-91.8	-10.7	-0.000736	2.97	7.9	52.0
11b	2.238	1.86	9.89	4.33	-56.3	-35.0	39.4	4.58	-	-	0.004050			
12a	-2.245	-1.87	-2.75	-5.39	-64.1	-71.2	-46.3	-5.38	-87.8	-10.2	-0.001682	2.80	6.2	58.2
12b	2.239	1.87	9.81	4.29	-55.1	-34.1	38.8	4.51	-	-	0.003773			
13a	-4.483	-3.74	-4.15	-6.84	-67.5	-78.1	-55.7	-6.49	-104.9	-12.2	-0.006167	1.31	37.2	95.4
13b	4.472	3.73	7.54	2.85	-52.6	-36.7	23.7	2.76	-	-	-0.000531			
14a	-4.487	-3.74	-0.73	-4.46	-55.0	-58.3	-31.4	-3.66	-78.7	-9.2	-0.006405	0.86	15.9	111.3
14b	4.477	3.73	6.98	2.34	-48.9	-34.3	20.2	2.35	-	-	-0.002372			
15a	-4.487	-3.74	0.52	-3.61	-48.5	-48.7	-22.6	-2.63	-66.4	-7.7	-0.007089	0.70	11.3	122.6
15b	4.470	3.72	6.77	2.04	-47.2	-33.1	19.0	2.20	-	-	-0.006057			

APPENDIX D

CONTRIBUTIONS TO TOTAL INTERSTORY DRIFT

Data obtained from external instrumentation were used to approximate the contributions of the joint, column, and beam deformations to the applied beam end displacements. The objective was to obtain a satisfactory understanding of the deformation characteristics before and after retrofit, and not to perform a rigorous analysis. In developing the equations and schematics during this procedure, several assumptions were made which are mentioned in the following sections. The results, which are presented in detail in Appendix C, served the intended purpose but should not be taken as "exact" quantification of the actual contributions.

The displacements applied at the beam loaded ends (Δ_b) were divided into five contributions:

$$\Delta_b = \Delta^{be} + \Delta^{ce} + \Delta^{bj} + \Delta^{cj} + \Delta^{js} \tag{D.1}$$

where Δ^{be} and Δ^{ce} were caused by the elastic deformations of the beam and column, respectively; Δ^{bj} and Δ^{cj} were caused by the concentrated rotations of the beam and column with respect to the joint, respectively; and Δ^{js} was caused by joint shear strains. Δ^{bj} and Δ^{cj} may include contributions due to inelastic rotations at the beam-joint and column-joint interfaces, respectively, and/or rotations at these locations due to loss of anchorage of reinforcing bars (e.g. beam bottom bars, column lap splice). It was originally planned to quantify Δ^{bj}, Δ^{cj}, and Δ^{js} using the data from external instrumentation and to estimate Δ^{be} and Δ^{ce} analytically, using an approach similar to that of Leon [D.1]. Details of such instrumentation were presented in Appendix B.

Δ^{bj} and Δ^{js} were quantified as intended. Data from instrumentation that was used to monitor the concentrated column rotation (θ_{cj}), however, did not allow determination of Δ^{cj} as intended. As a result, the sum of Δ^{ce} and Δ^{cj} were quantified as the contribution due to "total column rotation" using the data from another set of instruments. The remaining contribution Δ^{be} was then determined as the difference between the sum of all other contributions and the total applied displacement (Δ_b) without an attempt to analytically estimate displacements which would not be straightforward especially after the onset of damage due to changes in the member stiffnesses and in the boundary conditions between them.

D.1 CONTRIBUTION DUE TO JOINT SHEAR STRAIN

The total joint shear strain (γ_s) consists of changes in the angle of both horizontal and vertical sides of the joint, and thus, can be expressed as:

$$\gamma_s = \gamma_1 + \gamma_2 \tag{D.2}$$

where γ_1 and γ_2 are the horizontal and vertical joint shear strains, respectively. A deformation mechanism shown in Figure D.1 was assumed in order to facilitate the division of the total measured joint shear strain γ_s into γ_1 and γ_2. Figure D.1 represents only the effect of joint shear deformation on beam displacement and not the final deformed shape. From Figure D.1,

$$\gamma_2 h_2 = \gamma_1 L_{uc} \tag{D.3}$$

$$h_1 + h_2 = h_j \tag{D.4}$$

$$\frac{L_{lc}}{L_{uc}} = \frac{h_1}{h_2} \tag{D.5}$$

From Equation (D.4) and Equation (D.5),

$$h_2 = \frac{h_j L_{uc}}{L_{lc} + L_{uc}} \tag{D.6}$$

Substituting Equation (D.6) into Equation (D.3) and rearranging,

$$\gamma_2 = \gamma_1 \cdot \left(\frac{L_{lc} + L_{uc}}{h_j} \right) \tag{D.7}$$

Then, from Equation (D.2),

$$\gamma_1 = \gamma_s \cdot \left(\frac{h_j}{h_j + L_{lc} + L_{uc}} \right) \tag{D.8}$$

$$\gamma_2 = \gamma_s \cdot \left(\frac{L_{lc} + L_{uc}}{h_j + L_{lc} + L_{uc}} \right) \tag{D.9}$$

Finally, the contribution of joint shear strain to beam displacement (Δ^{js}) can be expressed in terms of the joint shear strain γ_s and geometric parameters as:

$$\begin{aligned} \Delta^{js} &= \gamma_2 L_b - \gamma_1 \frac{b_c}{2} \\ &= \gamma_s \cdot \left[\left(\frac{L_{lc} + L_{uc}}{h_j + L_{lc} + L_{uc}} \right) \cdot L_b - \left(\frac{h_j}{h_j + L_{lc} + L_{uc}} \right) \cdot \frac{b_c}{2} \right] \end{aligned} \tag{D.10}$$

which is schematically illustrated in Figure D.1. γ_s in Equation (D.10) was monitored during the tests as explained in detail in Appendix B.

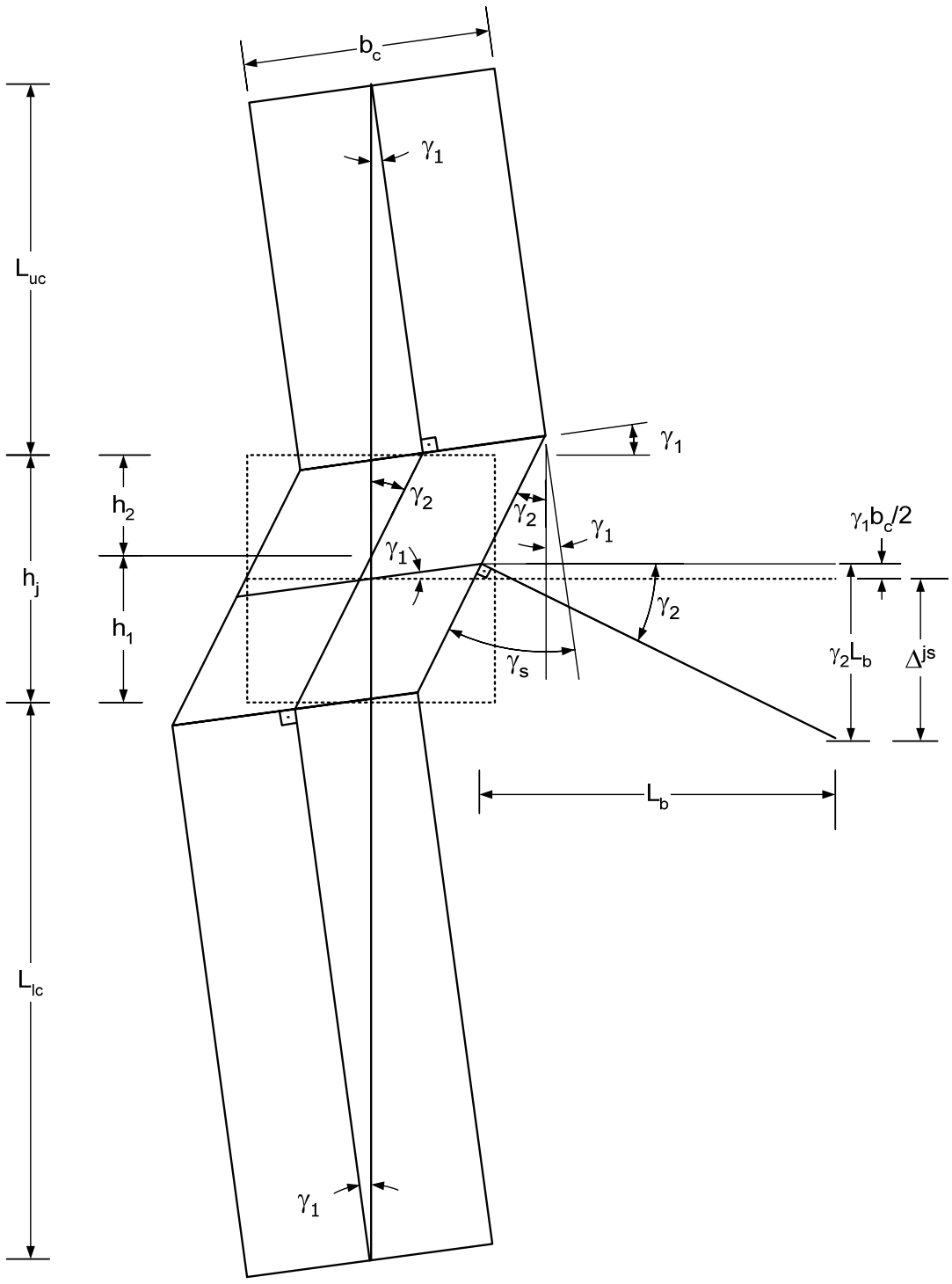

Figure D.1 — Beam displacement caused by joint shear deformation only.

D.2 CONTRIBUTION DUE TO TOTAL COLUMN ROTATION

The total column rotation (θ_c^{tot}), which includes both elastic and inelastic rotations of the column, was determined by subtracting the vertical joint shear strain (γ_2) from the total rotation of the joint in space (θ_j):

$$\theta_c^{tot} = \theta_j - \gamma_2 \tag{D.11}$$

γ_2 was obtained from Equation (D.9). θ_j was measured with respect to a fixed frame using two potentiometers horizontally connected to the upper and lower columns at a distance a (6 in.) above and below the joint, respectively, as shown schematically in Figure D.2. The effect of the column rotations within the a distances above and below the joint that are included in the potentiometer readings was ignored, and θ_j was taken as:

$$\theta_j = \frac{x + x_1 + x_2}{h_j + 2a} \tag{D.12}$$

where x is the difference between the two potentiometer readings, and

$$x_1 = \left(\theta_j + \theta_1\right) \cdot a \tag{D.13}$$

$$x_2 = \left(\theta_j + \theta_2\right) \cdot \left(a + \theta_1 \frac{b_c}{2}\right) \tag{D.14}$$

Substituting into Equation (D.12),

$$\begin{aligned} \theta_j &= \frac{x + \left(\theta_j + \theta_1\right) \cdot a + \left(\theta_j + \theta_2\right) \cdot \left(a + \theta_1 \frac{b_c}{2}\right)}{h_j + 2a} \\ &= \frac{x + 2\theta_j a + \left(\theta_1 + \theta_2\right) \cdot a + \left(\theta_j + \theta_2\right) \cdot \left(\theta_1 \frac{b_c}{2}\right)}{h_j + 2a} \end{aligned} \tag{D.15}$$

Neglecting the small contribution from the last term in the nominator (due to multiplication of rotation terms), Equation (D.15) becomes:

$$\theta_j = \frac{x + 2\theta_j a + (\theta_1 + \theta_2)\cdot a}{h_j + 2a} \tag{D.16}$$

In addition to Equation (D.11), the total column rotation (θ_c^{tot}) can also be expressed as:

$$\theta_c^{tot} = \gamma_1 - \theta_1 \tag{D.17}$$

Then, from Equation (D.17) and Equation (D.11),

$$\begin{aligned} \theta_j &= \gamma_1 + \gamma_2 - \theta_1 \\ &= \gamma_s - \theta_1 \end{aligned} \tag{D.18}$$

Substituting Equation (D.18) into the right hand side of Equation (D.16) and rearranging,

$$\theta_j = \frac{x + 2\gamma_s a + (\theta_2 - \theta_1)\cdot a}{h_j + 2a} \tag{D.19}$$

From Figure D.2,

$$(\theta_2 - \theta_1) = \theta_{ucj} \tag{D.20}$$

where θ_{ucj} represents additional rotation of the upper column which was initially incorporated in the procedure to account for possible pulling-away of the upper column from the joint due to loss of anchorage in the column lap-splice as shown in Figure D.2. In light of the observations during the tests, however, it was later decided to assume that $\theta_{ucj} = 0$ and that any contributions due to anchorage loss in the column lap-splice was accounted for in the total column rotation (θ_c^{tot}). Equation (D.19) then becomes:

$$\theta_j = \frac{x + 2\gamma_s a}{h_j + 2a} \tag{D.21}$$

Substituting Equation (D.21) into Equation (D.11), the total column rotation (θ_c^{tot}) is obtained as:

$$\theta_c^{tot} = \frac{x + 2\gamma_s a}{h_j + 2a} - \gamma_2 \tag{D.22}$$

Finally, the combined contribution of the elastic and concentrated rotation of the columns to beam displacement ($\Delta^{ce} + \Delta^{cj}$) can be expressed in terms of the difference between the potentiometer readings (x), joint shear strain (γ_s) and geometric parameters as:

$$\begin{aligned} \Delta^{ce} + \Delta^{cj} &= \theta_c^{tot} \cdot \left(L_b + \frac{b_c}{2} \right) \\ &= \left(\frac{x + 2\gamma_s a}{h_j + 2a} - \gamma_2 \right) \cdot \left(L_b + \frac{b_c}{2} \right) \\ &= \left[\frac{x + 2\gamma_s a}{h_j + 2a} - \gamma_s \left(\frac{L_{lc} + L_{uc}}{h_j + L_{lc} + L_{uc}} \right) \right] \cdot \left(L_b + \frac{b_c}{2} \right) \end{aligned} \tag{D.23}$$

which is schematically illustrated in Figure D.2.

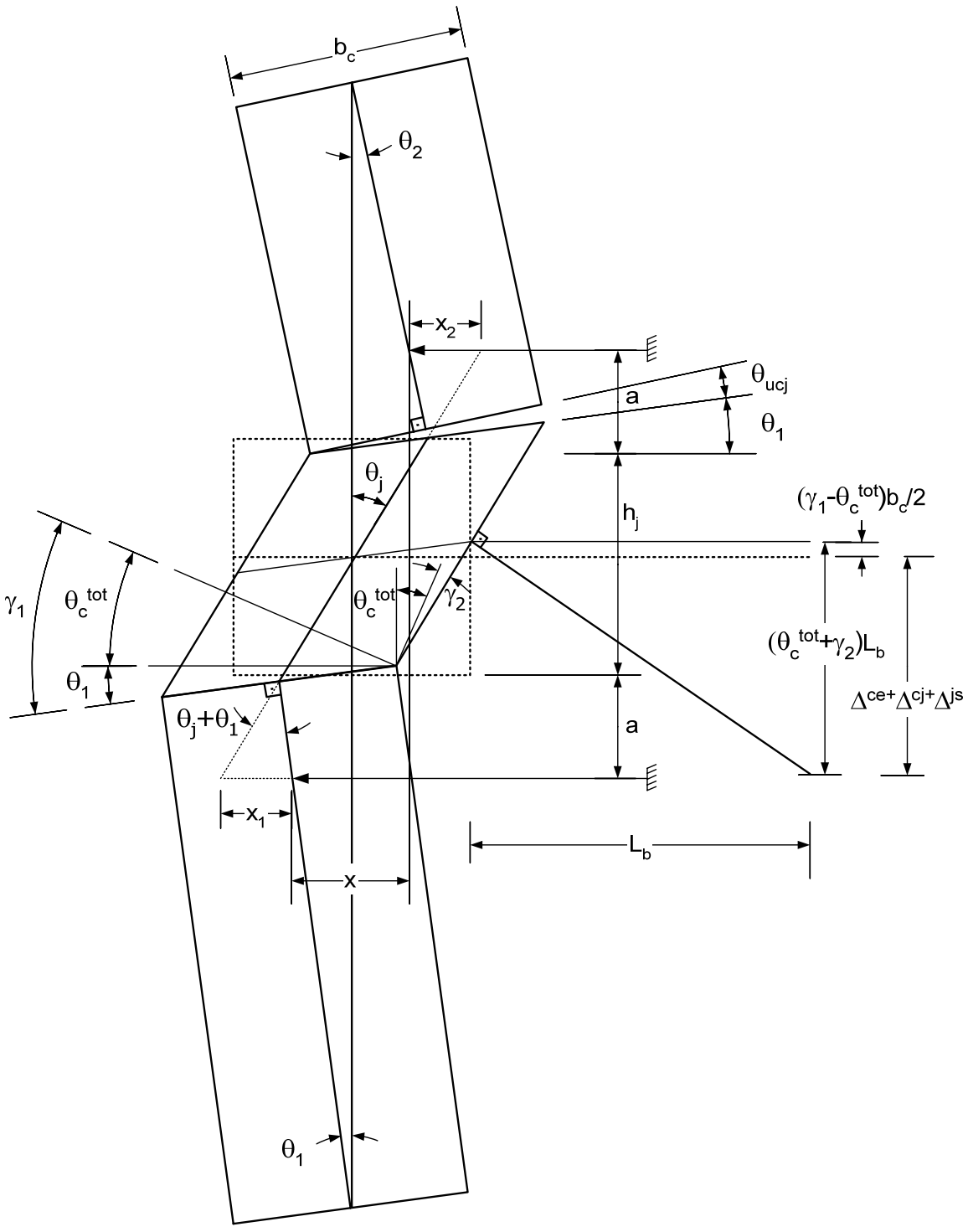

Figure D.2 — Beam displacement caused by combined joint shear deformation and total column rotation.

D.3 CONTRIBUTION DUE TO BEAM CONCENTRATED ROTATION

Beam concentrated rotations at the beam-joint interfaces (θ_{bj}) were monitored by using two potentiometers mounted on the beam top and bottom surfaces and horizontally connected to the upper and lower columns at a distance *b* (3 in.) above and below the beams, respectively, as shown schematically in Figure D.3. The potentiometers were mounted on the beams at a distance equal to half their effective depth (i.e. *d/2*) from the column faces. The effect of the beam elastic rotations within this *d/2* distance that are included in the potentiometer readings was ignored, and θ_{bj} was taken as:

$$\theta_{bj} = \frac{y - (y_1 + y_2)}{h_j + 2b} \tag{D.24}$$

where *y* is the difference between the two potentiometer readings, and

$$y_1 = (\theta_j + \theta_1) \cdot b \tag{D.25}$$

$$y_2 = (\theta_j + \theta_2 + \theta_{ucj}) \cdot b \tag{D.26}$$

Substituting into Equation (D.24),

$$\theta_{bj} = \frac{y - (\theta_j + \theta_1) \cdot b - (\theta_j + \theta_2 + \theta_{ucj}) \cdot b}{h_j + 2b} \tag{D.27}$$

Substituting Equation D.18,

$$\theta_{bj} = \frac{y - \gamma_s b - (\gamma_s - \theta_1 + \theta_2 + \theta_{ucj}) \cdot b}{h_j + 2b} \tag{D.28}$$

Substituting Equation D.20,

$$\theta_{bj} = \frac{y - 2\gamma_s b - 2\theta_{ucj} b}{h_j + 2b} \tag{D.29}$$

From the aforementioned assumption that $\theta_{ucj} = 0$, beam concentrated rotation (θ_{bj}) is obtained as:

$$\theta_{bj} = \frac{y - 2\gamma_s b}{h_j + 2b} \tag{D.30}$$

Finally, the contribution of the concentrated rotation at the beam-joint interface to beam end displacement (Δ^{bj}) can be expressed in terms of the difference between the potentiometer readings (y), joint shear strain (γ_s) and geometric parameters as:

$$\begin{aligned} \Delta^{bj} &= \theta_{bj} L_b \\ &= \left(\frac{y - 2\gamma_s b}{h_j + 2b} \right) \cdot L_b \end{aligned} \tag{D.31}$$

which is schematically illustrated in Figure D.3.

D.4 CONTRIBUTION DUE TO BEAM ELASTIC DEFORMATIONS

As mentioned previously, the difference between the total applied beam end displacement and the sum of the contributions obtained in the preceding sections was attributed to the elastic deformations along the beam span as in Equation (D.32):

$$\Delta^{be} = \Delta_b - \sum (\Delta^{ce} + \Delta^{cj} + \Delta^{bj} + \Delta^{js}) \tag{D.32}$$

D.5 REFERENCES

[D.1] Leon, R. (1983). "The influence of floor members on the behavior of reinforced concrete beam-column joints subjected to severe cyclic loading." Ph.D. thesis, The University of Texas at Austin, Austin, TX.

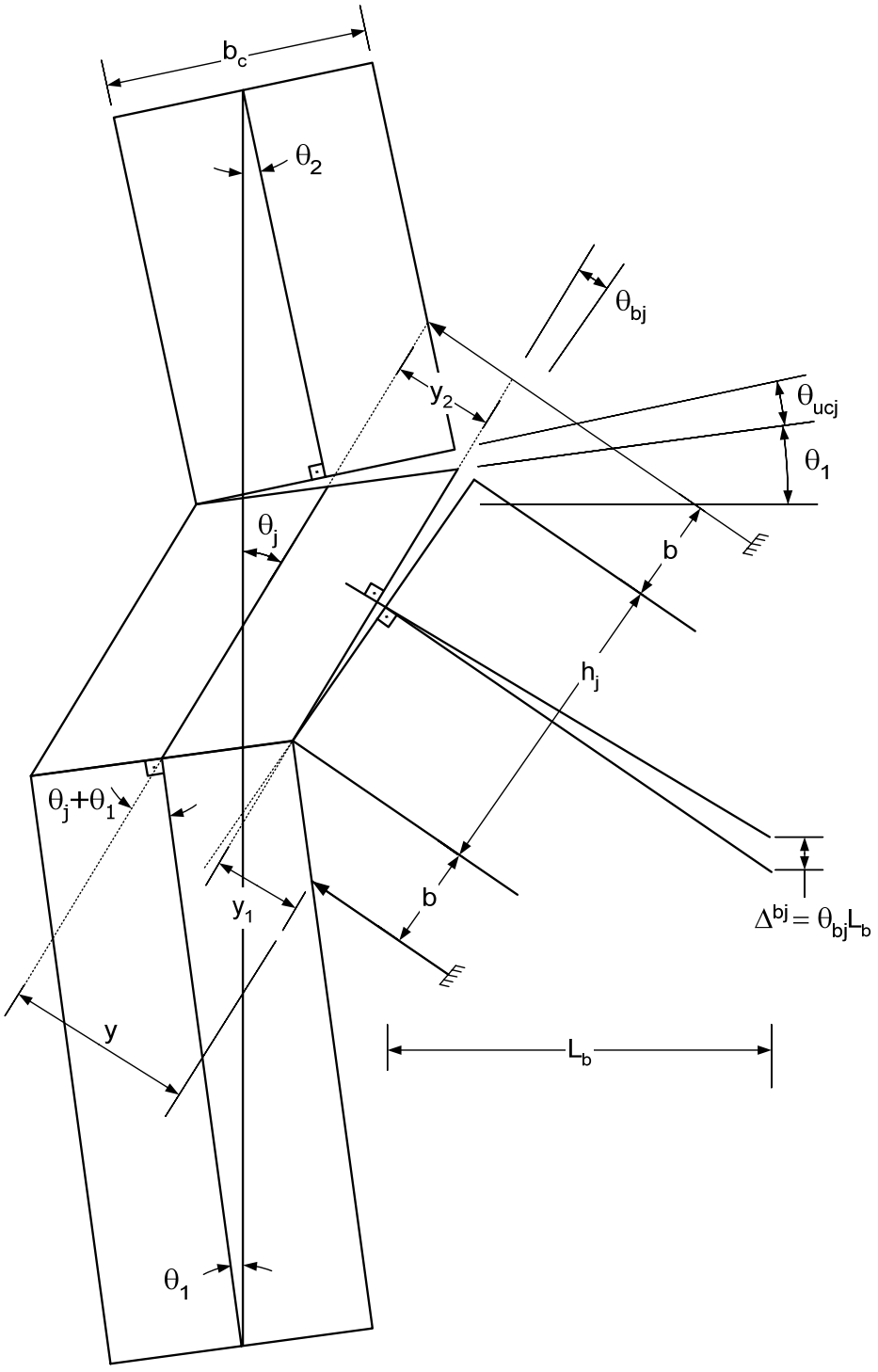

Figure D.3 — Beam displacement caused by beam concentrated rotation.

APPENDIX E

DESIGN OF CFRP RETROFIT

This appendix presents the design approach and calculations for the CFRP retrofit schemes used for the tested specimens. Other retrofit steps that preceded the CFRP application such as epoxy injection (for previously damaged Specimen 1 and Specimen 2) and flexural strengthening of the column by addition of a steel reinforcing bar within the clear cover at the inside corner (same for all specimens) were presented in the previous chapters and are not repeated here.

The CFRP retrofit was aimed at: (1) increasing the joint shear strength, (2) increasing the positive moment capacity of the beams by improving the anchorage of beam bottom bars, and (3) providing column confinement. The design properties of the unidirectional CFRP material were taken as those reported by the manufacturer as follows: maximum load P_u^{CFRP}=2100 lb/in./layer, maximum strain ε_u^{CFRP}=1.00%, thickness t=0.02 in. [E.1]. These design values were later validated by tension tests conducted on coupons cut from a witness plate made during the retrofit of Specimen 1 as presented in detail in Appendix B, Sec. B.1.3.2.

E.1 JOINT SHEAR STRENGTH

The objective of joint shear strengthening was for the joint to withstand the horizontal shear force ($V_{jh}^{\max}$) that would be created if the desired beam hinging mechanism was achieved. The net normal tension force (T_b) that would be transferred to the joint at the beam-joint interface at beam hinging was taken as the yield capacities of all beam top bars plus three slab bars which were within the effective width of the slab (3 to 5 slab thickness as discussed in detail in Chapter 3):

$$T_b = 6\left(A_s f_y\right)_{\#6} + 3\left(A_s f_y\right)_{\#3}$$
$$= 6 \cdot 0.44in.^2 \cdot 45.7ksi + 3 \cdot 0.11in.^2 \cdot 53.2ksi = 138.2kip \quad \text{(E.1)}$$

The reinforcing bars were not expected to undergo strain hardening considering the remarkable length of their yield plateaus (Appendix B, Sec. B.1.2). The ratio of column shear force (V_{col}) to beam end load (P) was determined from:

$$\frac{V_{col}}{P} = L_b' \frac{3\left(L_{lc}'\right)^2 + 6L_{lc}'L_{uc}'}{2\delta\left(L_{uc}'\right)^3 + 2\left(L_{lc}'\right)^3 + 6L_{lc}'\left(L_{uc}'\right)^2 + 6\left(L_{lc}'\right)^2 L_{uc}'} \quad \text{(E.2)}$$

where L_b' is the beam length measured from column centerline to loading point; L_{lc}' and L_{uc}' are the lengths of the lower and upper columns measured from the beam centerline, respectively; and δ is the bending rigidity ratio of the columns defined as:

$$\delta = \frac{(EI)_{lc}}{(EI)_{uc}} = \frac{3140\,psi}{2930\,psi} = 1.07 \quad \text{(E.3)}$$

Substituting $\delta = 1.07$, $L_b' = 120in.$, $L_{lc}' = 72.6in.$, and $L_{uc}' = 48.4in.$ in Equation (E.2),

$$\frac{V_{col}}{P} = 1.25 \quad \text{(E.4)}$$

which was also confirmed using the data from testing of Specimen 1 before retrofit. Then, the column shear force at the time of beam hinging was estimated as:

$$V_{col} = \frac{M_n^-}{L_b} 1.25 = \frac{2150kip.in.}{113in.} 1.25 = 23.8kip \quad \text{(E.5)}$$

where M_n^- is the negative moment capacity of the beam (=2150 kip-in. for Specimen 1), and L_b is the distance of the beam loading point from the column face. The maximum possible joint shear force was then obtained as:

$$V_{jh}^{max} = T_b - V_{col} = 138.2kip - 23.8kip = 114.4kip \quad \text{(E.6)}$$

For conservatism, the contribution of concrete to joint shear capacity was neglected, and the entire joint shear was assumed to be carried by horizontally oriented CFRP. Assuming a uniform distribution of stresses across the width of the CFRP (i.e. depth of the joint, h_j), the number of 90° (horizontal, along beam axis) CFRP layers to resist $V_{jh}^{\max}$ was determined as:

$$n_{jh} = \frac{V_{jh}^{max}}{h_j P_u^{CFRP}} = \frac{114.4kip}{20in. \cdot 2.1kip/in.} = 2.72 \rightarrow \text{Use 3 layers} \quad \text{(E.7)}$$

Two additional layers of CFRP were placed in the 0° direction (vertical, along column axis) to resist the vertical component of the principal tension force in the joint panel which would be in a diagonal direction perpendicular to the diagonal concrete strut. All five layers were extended onto the upper and lower columns until the end of the confined regions (Sec. E.3) to improve their anchorage.

The resulting CFRP design for joint shear strengthening was used for all specimens to allow direct comparisons between specimen performances.

E.2 BEAM BOTTOM BAR ANCHORAGE

The objective of improving the anchorage of beam bottom bars was to increase the beam positive moment capacity (M_n^+) to at least half of the negative moment capacity (M_n^-) to comply with ACI 318-05, Sec. 21.3.2.2 [E.2]. The load capacity of the beam bottom bars (3#6) at yield was already half the capacity of beam top bars (6#6); however, beam bottom bars could not develop their capacity due to anchorage problems. The design approach was to: (1) provide CFRP near the beam bottom bar level (referred to as the CFRP beam strips throughout this thesis) with a load capacity equal to that of 3#6 bars at

yield, and (2) ensure that the CFRP beam strips have sufficient anchorage to develop their full capacity. These strips were bonded on the beam outside faces only; any strips bonded on the inside faces would have required invasive operations to provide anchorage for the strips. The relationship between the number of layers (n_s) and width (w_s) of strips was:

$$n_s = \frac{3\left(A_s f_y\right)_{\#6}}{w_s P_u^{CFRP}} \rightarrow \quad n_s w_s = \frac{3 \cdot 0.44in.^2 \cdot 45.7ksi}{2.1kip/in.} = 28.7in. \tag{E.8}$$

The width w_s, which was preferred to be less than half the beam depth (20/2=10 in.) to avoid an undesirable increase in M_n^-, was arbitrarily selected as 7 in. Then, from Equation (E.5),

$$n_s = \frac{28.7in.}{7in.} = 4.1 \rightarrow \text{Use 5 layers} \tag{E.9}$$

While the number and width of the strips were kept unchanged in all specimens, different approaches for improving their anchorage had to be tried throughout the test program.

In Specimen 1, the strips were considered as a lap-splice onto the existing beam bottom bars, and the extension length of the CFRP strips onto the beams was selected such that the distance from the tip of the beam bottom bars in the joint to the end of the strips would be equal to the development length (l_d) of these bars according to ACI 318-05, Sec. 12.15 [E.2].

$$\text{Class B splice: } 1.3l_d = 1.3\left(\frac{f_y}{25\sqrt{f_c'}} d_b\right) = 1.3\left(\frac{45700psi}{25\sqrt{3740psi}} 0.75in.\right) = 29.1in. \tag{E.10}$$

Considering the 6 in. anchorage length of beam bottom bars within the joint, the extension length of the CFRP strips onto the beams measured from the column face became 29.1-6=23 in. [It is to be noted that the actual extension length used for Specimen

1 was longer (i.e. 28 in.) because an accurate f_y value was not available at the time of this calculation.] Such an anchorage was not sufficient for the CFRP strips to develop their full capacities in Specimen 1, and additional measures were taken for the other specimens.

For Specimen 2 and Specimen 3, the following revision to ACI 440.2 [E.3], which was intended for flexural strengthening of simply supported beams, was utilized: "*The plies should extend at least a distance equal to* l_{df} *past the point along the span corresponding to the cracking moment* M_{cr} *under factored loads.*" This statement was modified for the present case as follows: The beam strips were considered as typical flexural reinforcement (although bonded on the outside beam faces only), and the beam positive moment capacities at cracking (M_{cr}^{+}) and ultimate (M_{n}^{+}) were calculated (M_{cr}^{+}= 520 kip-in., M_{n}^{+}=1430 kip-in.). The shear force diagram corresponding to a moment of M_{n}^{+} at the joint face was drawn by taking into account the weight of the slab as a triangular distributed load, and the point along the span corresponding to M_{cr}^{+} was located as 75.5 in. from the column face. The development length l_{df} was calculated as proposed in ACI 440.2 [E.3] as:

$$l_{df} = 0.057\sqrt{\frac{nE_{CFRP}t}{\sqrt{f_c'}}} = 0.057\sqrt{\frac{n\left(P_u^{CFRP}/\varepsilon_u^{CFRP}\right)}{\sqrt{f_c'}}} = 0.057\sqrt{\frac{5\cdot(2100lb/in./0.01)}{\sqrt{5010\,psi}}} = 6.9in. \quad \text{(E.11)}$$

where n is the number of layers; E_{CFRP} is the elastic modulus of CFRP; and t is the thickness per layer of CFRP. The extension length of the CFRP strips onto the beams measured from the column face then became 75.5+6.9=82 in. In addition to such an increase in the extension length, the anchorage of the strips was also improved by

providing a clamping effect by U-wrapping the beam ends near the joint. The width of the U-wraps (L_u) was taken as the distance over which transverse steel reinforcement is required by ACI 318-05, Sec. 21.4.4.4 [E.3] for confining member ends:

$$L_u \geq min\begin{Bmatrix} h_b \\ \frac{1}{6}L \\ 18in. \end{Bmatrix} = min\begin{Bmatrix} 20in. \\ 38in. \\ 18in. \end{Bmatrix} \rightarrow \; L_u = 38in. \tag{E.12}$$

where h_b is the beam depth, and L is the clear span length of the beam. Two layers of U-wrapping were considered sufficient for confining the beam strips. Such an anchorage scheme in Specimen 2 and Specimen 3 led to the achievement of the full capacities (i.e. rupture) of the beam strips. It was also found that the extension of the strips along the beams beyond the U-wrapped portion was not effective in both specimens as observed from the recorded CFRP strains. Therefore, the portion of the strips beyond 38 in. from the column face was deleted in Specimen 4.

E.3 COLUMN CONFINEMENT

The column ends above and below the joint were confined with CFRP wraps for three purposes: (1) increase the concrete compressive strength and ductility, (2) provide anchorage for the CFRP sheets extended from the joint panel onto the columns, and (3) provide anchorage for the #7 steel reinforcing bar added at the column inside corner. The CFRP wraps were designed to achieve purpose (1), and the resulting design was assumed to serve purposes (2) and (3) as well. The design target was to increase the maximum usable compressive strain in concrete (ε'_{cc}) to what would be provided by the steel hoop reinforcements required by ACI 318-05, Sec. 21.4.4 [E.2].

First, the relationship between ε'_{cc} and the number of CFRP layers (n_w) was established by using the equations in ACI 440.2R-02, Chp. 11 [E.4]. n_w layers of CFRP

wraps with a thickness of t per layer corresponded to a transverse reinforcement ratio (ρ_f) of:

$$\rho_f = \frac{2n_w t(b_c + h_c)}{bh} = \frac{2n_w \cdot 0.02in. \cdot (14in. + 14in.)}{14in. \cdot 14in.} = 0.005714n_w \qquad \text{(E.13)}$$

where b_c and h_c are the dimensions of the column. The efficiency factor (K_a) was calculated as:

$$\begin{aligned} K_a &= 1 - \frac{(b_c - 2r)^2 + (h_c - 2r)^2}{3b_c h_c (1 - \rho_{col})} \\ &= 1 - \frac{(14in. - 2 \cdot 2in.)^2 + (14in. - 2 \cdot 2in.)^2}{3 \cdot 14in. \cdot 14in. \cdot (1 - \frac{8 \cdot 0.31in.^2}{(14in.)^2})} = 0.656 \end{aligned} \qquad \text{(E.14)}$$

where r is the radius of the edges of the section, and ρ_{col} is the longitudinal reinforcement ratio of the column. An environmental reduction factor of $C_E = 0.85$ was chosen based on ACI 440.2R-02 [E.4] recommendations for exterior exposure of carbon/epoxy systems. The design rupture strain of CFRP (ε_{fu}^{CFRP}) and the maximum effective strain that can be achieved by the CFRP wrap (ε_{fe}^{CFRP}) were determined as:

$$\varepsilon_{fu}^{CFRP} = C_E \varepsilon_u^{CFRP} = 0.85 \cdot 0.01 = 0.0085 \qquad \text{(E.15)}$$

$$\varepsilon_{fe}^{CFRP} = 0.004 \le 0.75\varepsilon_{fu}^{CFRP} = 0.75 \cdot 0.0085 = 0.0064 \rightarrow \varepsilon_{fe}^{CFRP} = 0.004 \qquad \text{(E.16)}$$

The confining pressure (f_l) provided by the CFRP wraps was then calculated from:

$$\begin{aligned} f_l &= \frac{K_a \rho_f f_{fe}^{CFRP}}{2} = \frac{K_a \rho_f \varepsilon_{fe}^{CFRP} \left(P_u^{CFRP} / t / \varepsilon_u^{CFRP} \right)}{2} \\ &= \frac{0.656 \cdot 0.005714n_w \cdot 0.004 \cdot (2100lb/in./0.02in./0.01)}{2} = 78.7n_w \quad psi \end{aligned} \qquad \text{(E.17)}$$

Finally, the confined compressive strength ($f_{cc}^{'}$) and the maximum usable confined compressive strain ($\varepsilon_{cc}^{'}$) were calculated from Equation (E.15) and (E.16), respectively, and the values presented in Table E.1 were obtained:

$$\begin{aligned} f_{cc}^{'} &= f_c^{'}\left[2.25\sqrt{1+7.9\frac{f_l}{f_c^{'}}}-2\frac{f_l}{f_c^{'}}-1.25\right] \\ &= 3740\,psi\cdot\left[2.25\sqrt{1+7.9\frac{78.7n_w\,psi}{3740\,psi}}-2\frac{78.7n_w\,psi}{3740\,psi}-1.25\right] \\ &= 8415\sqrt{1+0.166n_w}-157.4n_w-4675 \quad psi \end{aligned} \tag{E.18}$$

$$\begin{aligned} \varepsilon_{cc}^{'} &= \frac{1.71\left(5f_{cc}^{'}-4f_c^{'}\right)}{E_c} \\ &= \frac{1.71\cdot\left[5\cdot\left(8415\sqrt{1+0.166n_w}-157.4n_w-4675\right)psi-4\cdot 3740\,psi\right]}{3140\cdot 10^3\,psi} \\ &= 0.022913\sqrt{1+0.166n_w}-0.000429n_w-0.020878 \end{aligned} \tag{E.19}$$

In the second step, the increase in the compressive properties of concrete when confined with the steel hoop reinforcement required by ACI 318-05, Sec. 21.4.4 [E.2] was estimated. The spacing of the hoops (s) was taken as that required by Sec. 21.4.4.2:

$$s \le \min\left\{\begin{array}{c} b_c/4 \\ 6d_b^{long} \\ 4+\left(\frac{14-h_x}{3}\right)\le 6in. \end{array}\right\} = \min\left\{\begin{array}{c} 3.5in. \\ 5.25in. \\ 6in. \end{array}\right\} \rightarrow\ s = 3.5in. \tag{E.20}$$

where b_c is the column width (i.e. minimum member dimension), d_b^{long} is the diameter of the longitudinal reinforcement (the equivalent of 2#5 bars at each corner was taken as a #7 bar), and h_x is the horizontal spacing of crossties or legs of overlapping hoops. The total cross-sectional area of the required hoops (A_{sh}) was:

Table E.1 — Increase in the compressive properties of concrete with the number of layers of column wraps for Specimen 1.

n_w	$f_{cc}^{'}$ (psi)	$\varepsilon_{cc}^{'}$
1	4254	0.003435
2	4722	0.004708
3	5152	0.005879

$$A_{sh} = 0.3\frac{sb_c f_c^{'}}{f_y}\left(\frac{A_g}{A_{ch}} - 1\right) \geq 0.09\frac{sb_c f_c^{'}}{f_y}$$
$$= 0.3\frac{3.5in.\cdot 10.625in.\cdot 3740\,psi}{60000\,psi}\left(\frac{14in.\cdot 14in.}{11in.\cdot 11in.} - 1\right) = 0.431in.^2 \qquad \text{(E.21)}$$
$$\geq 0.09\frac{3.5in.\cdot 10.625in.\cdot 3740\,psi}{60000\,psi} = 0.209in.^2 \rightarrow A_{sh} = 0.431in.^2$$

where b_c is the width of column core from center-to-center of transverse reinforcement (assumed #3 bar); A_g is the gross area of the column cross-section; f_y is the yield strength of transverse reinforcement (assumed Grade 60); and A_{ch} is the area of column core from out-to-out of transverse reinforcement. This resulted in a volumetric steel hoop reinforcement ratio (ρ_s) of:

$$\rho_s = \rho_x + \rho_y = \frac{2A_{sh}}{b_c d_c} = \frac{2\cdot 0.431in.^2}{14in.\cdot 11.7in.} = 0.00526 \qquad \text{(E.22)}$$

which provided an effective confining pressure (f_l) of:

$$f_l = \frac{K_e f_y \rho_s}{2} = \frac{0.75\cdot 60000\,psi\cdot 0.00526}{2} = 118.4\,psi \qquad \text{(E.23)}$$

where the confinement effectiveness coefficient K_e was taken as 0.75 as recommended by Priestley et al. [E.5] for rectangular sections. Substituting f_l into Equation (E.15), the compressive strength of the confined concrete ($f_{cc}^{'}$) was calculated as

$$f'_{cc} = 3740\,psi \cdot \left[2.25\sqrt{1 + 7.9\frac{118.4\,psi}{3740\,psi}} - 2\frac{118.4\,psi}{3740\,psi} - 1.25 \right] = 4497\,psi \quad \text{(E.24)}$$

Finally, substituting f'_{cc} into Equation (E.16), the maximum usable compressive strain of concrete (ε'_{cc}) when confined with the amount of steel hoops recommended by ACI 318-05 [E.2] was found to be:

$$\varepsilon'_{cc} = \frac{1.71 \cdot (5 \cdot 4497\,psi - 4 \cdot 3740\,psi)}{3140 \cdot 10^3\,psi} = 0.004098 \quad \text{(E.25)}$$

Then, from Table E.1, two layers of CFRP column wraps were found sufficient to provide the same amount of confinement. The height (h_w) over which column wraps were provided above and below the joint was taken as the distance over which steel hoops are required by ACI 318-05, Sec. 21.4.4.4 [E.3].

$$h_w \geq min\left\{ \begin{matrix} b_c \\ \frac{1}{6}L_c \\ 18in. \end{matrix} \right\} = min\left\{ \begin{matrix} 14in. \\ 16in. \\ 18in. \end{matrix} \right\} \rightarrow \; h_w = 18in. \quad \text{(E.26)}$$

The column wrap design obtained for Specimen 1 above was used for all specimens.

E.4 COLUMN SHEAR STRENGTH

The shear strength of the columns was not of concern until Specimen 3 was retrofitted without previous damage and tested. Shear cracking occurred in the un-wrapped portion of the upper column and led to the separation of the #7 column reinforcing bar added at the inside corner as presented earlier in Chapter 6. Therefore, shear strengthening of this portion of the upper column was also included in the retrofit of Specimen 4. The column

was strengthened to withstand the maximum biaxial shear force $\left(\left(V_{col}^{b}\right)_{max}\right)$ that was recorded for Specimen 3:

$$\begin{aligned}\left(V_{col}^{b}\right)_{max} &= \sqrt{\left[\left(V_{col}^{EW}\right)_{max}\right]^2 + \left[\left(V_{col}^{NS}\right)_{max}\right]^2} \\ &= \sqrt{(14.6kip)^2 + (12.6kip)^2} = 19.3kip\end{aligned} \tag{E.27}$$

The shear strength provided by concrete (V_c) was calculated from ACI 318-05, Sec. 11.3.1.2 [E.2]:

$$\begin{aligned}V_c &= 2\left(1+\frac{P_{col}}{2000A_g}\right)\sqrt{f_c'}b_c d_c = 2\left(1+\frac{0.1\cdot P_o}{2000A_g}\right)\sqrt{f_c'}b_c d_c \\ &= 2\left(1+\frac{0.1\cdot(14in.)^2\cdot 2230psi}{2000\cdot(14in.)^2}\right)\sqrt{2230psi}\cdot 14in.\cdot 11.7in.\cdot 0.001kip/lb = 17.2kip\end{aligned} \tag{E.28}$$

where P_{col} is the applied column axial load, and P_o is the compressive load capacity of the column. Although the difference

$$\left(V_{col}^{b}\right)_{max} - V_c = 2.1kip \tag{E.29}$$

could be carried by a few CFRP strips used as stirrups, a continuous wrap was used instead to provide a confinement in addition to that presented in the previous section. The contribution of one layer of continuous CFRP wrap to shear strength was calculated according to ACI 440.2R-02, Sec. 10.4 [E.4] as:

$$\begin{aligned}V_{CFRP} &= \frac{A_{fv}f_{fe}^{CFRP}(\sin\alpha+\cos\alpha)d_f}{s_f} \\ &= \frac{2n_f w_f \varepsilon_{fe}^{CFRP}\left(P_u^{CFRP}/\varepsilon_u^{CFRP}\right)(\sin\alpha+\cos\alpha)d_f}{s_f}\end{aligned} \tag{E.30}$$

where A_{fv}, s_f, d_f, w_f, and α are the area, spacing, depth, width, and angle of inclination of CFRP shear reinforcement, respectively. Substituting $w_f = s_f$ (continuous wrap) and α =90°,

$$V_{CFRP} = 2n_f \varepsilon_{fe}^{CFRP} \left(P_u^{CFRP} / \varepsilon_u^{CFRP} \right) d_f$$
$$= 2 \cdot 1 \cdot 0.004 \cdot \left(2.1kip / in. / 0.01 \right) \cdot 11.7in. = 19.7kip >> 2.1kip \quad \text{(E.31)}$$

E.5 STACKING SEQUENCE

In all CFRP-applied areas, a symmetric layup was necessary in order to prevent curvatures during heat-curing (Sec. E.6) that could cause early debonding from the concrete surface and to eliminate the extension-bending coupling that would result in difficulties associated with the determination of the CFRP tensile properties for future analyses. No changes to the CFRP design were necessary to achieve symmetric layups in the joint panels or in the columns. In the beams of Specimen 2, Specimen 3, and Specimen 4, two layers of transverse U-wrapping over the longitudinal beam strips resulted in an unsymmetric layup; therefore, two additional layers of U-wraps were applied to the concrete surface before placing the longitudinal beam strips.

E.6 CURING

All CFRP-applied areas were cured using a heat-curing schedule of 80°C for 6 hours, which was selected as explained in detail in Appendix B, Sec. B.1.3.1. Heat-curing was performed by building a sealed, wooden box around the region and by heating the enclosed region with four adjustable heat guns as shown in Figure E.1. To facilitate the air flow inside the box, a 5 in. gap was left between the box and all concrete surfaces. The location and output temperature of the heat guns were finalized after a few trials to

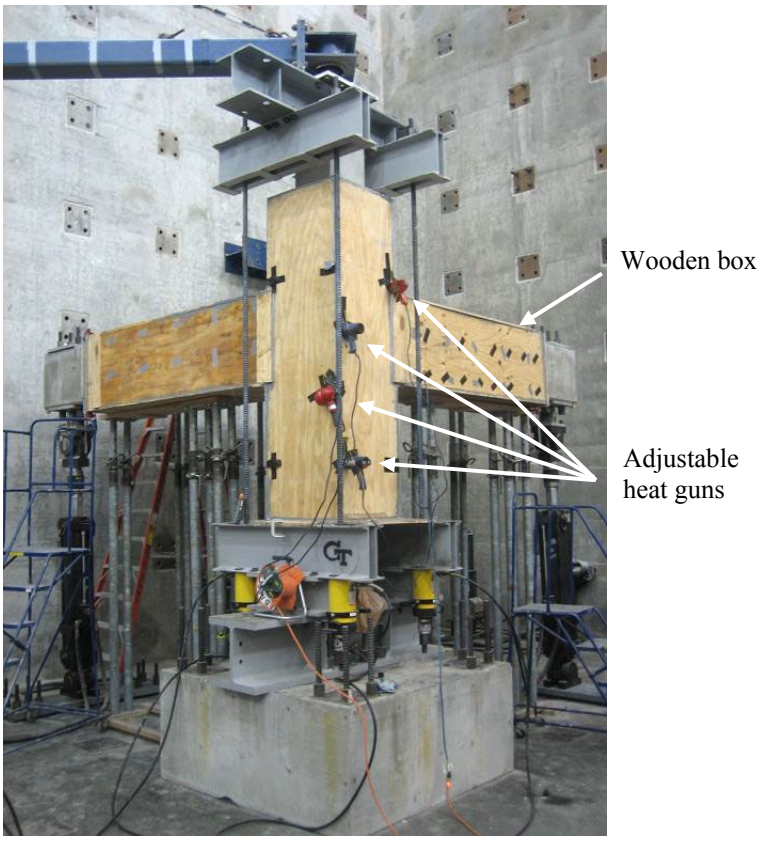

Figure E.1 — Heat-curing of CFRP retrofit schemes (Specimen 2).

ensure an almost uniform air temperature inside the box. Temperature readings taken at various locations indicated that an air temperature of 80°±10°C was maintained throughout the 6 hour period.

E.7 EFFECTIVE ELASTIC CONSTANTS OF RESULTING CFRP LAYUPS

The retrofit design presented above called for a total of seven different CFRP layups which were presented in Figure 5.10, Figure 5.14, Figure 6.3, and Figure 6.9 for Specimen 1 through Specimen 4, respectively. For symmetric laminates (layups) as in the present case, the effective elastic constants can be analytically determined from the lamination theory as:

$$E_x = \frac{1}{t_l a_{11}} \tag{E.32}$$

$$E_y = \frac{1}{t_l a_{22}} \tag{E.33}$$

$$G_{xy} = \frac{1}{t_l a_{66}} \tag{E.34}$$

$$\nu_{xy} = -\frac{a_{12}}{a_{11}} \tag{E.35}$$

where E_x and E_y are the longitudinal and transverse elastic moduli, respectively; G_{xy} is the shear modulus; ν_{xy} is the Poisson's ratio; t_l is the total laminate thickness; and a_{11}, a_{22}, a_{12}, and a_{66} are the terms in the elastic compliance matrix $[a]$ given as the inverse of the extensional stiffness matrix $[A]$ of the laminate [E.6]:

$$[a] = [A]^{-1} \tag{E.36}$$

The terms in matrix $[A]$ are defined as a function of the elastic constants of a single lamina (i.e. E_{11}, E_{22}, ν_{12}, G_{12}) as described in detail elsewhere [E.6].

The CFRP sheets used in this study had a thickness of t=0.02 in./layer, and their elastic constants were determined in Appendix B, Sec. B.1.3.3 as: E_{11}=11,720 ksi, E_{22}=414 ksi, ν_{12}=0.285, and G_{12}=151 ksi. Then, from Equations E.32 through E.35, the elastic constants of all CFRP layups used in retrofit were obtained as summarized in Table E.2.

The properties summarized in Table E.2 were determined mostly for use in future analytical studies. The discussion here is limited to the comparison of the obtained Poisson's ratios (ν_{xy}) with that of the concrete substrate to evaluate the possibility of a "Poisson mismatch", a phenomenon that could initiate debonding between two or more

Table E.2 — Elastic constants of CFRP laminates.

	Laminate lay-up	E_x (ksi)	E_y (ksi)	G_{xy} (ksi)	ν_{xy}
1	$[90/0/90/\overline{90}]_s$	3653	8510	151	0.014
2	$[0/90/\overline{90}]_s$	4949	7215	151	0.016
3	$[0/90_4]_s$	2681	9481	151	0.012
4	$[90_5]$	414	11720	151	0.010
5	$[0_2/90_2/\overline{90}]_s$	5452	6712	151	0.018
6	$[0_4]$	11720	414	151	0.285
7	$[90]$	414	11720	151	0.010

x-direction for the laminates corresponds to the 0° direction in all lay-ups.

bonded materials with different Poisson's ratios. The Poisson's ratio of the cylinder samples taken from all batches of concrete used for casting the specimens ranged from 0.17 to 0.23. As seen in Table E.2, the ν_{xy} values for all layups including 90° layers were significantly lower than that of concrete. Such a mismatch may have adversely affected the CFRP-to-concrete bond in the retrofitted joint specimens. Such an effect, however, was not investigated explicitly in this study and deserves further investigation.

E.8 REFERENCES

[E.1] Sika Corporation (2003). <http://www.sikaconstruction.com/con/con-prod/htm> (February 2008).

[E.2] ACI Committee 318 (2005). *Building code requirements for structural concrete (ACI 318-05) and commentary (318R-05)*, American Concrete Institute, Farmington Hills, MI.

[E.3] ACI Committee 440.2 (2007). *Guide for the design and construction of externally bonded FRP systems for strengthening concrete structures (ACI 440.2R-02 in revision)*, American Concrete Institute, Farmington Hills, MI.

[E.4] ACI Committee 440.2 (2002). *Guide for the design and construction of externally bonded FRP systems for strengthening concrete structures (ACI 440.2R-02)*, American Concrete Institute, Farmington Hills, MI.

[E.5] Priestley, M. J. N., Seible, F., and Calvi, G. M. (1996). *Seismic design and retrofit of bridges*, John Wiley & Sons, Inc., New York, NY.

[E.6] ASM International (2001). "Macromechanics analysis of laminate properties."*ASM Handbook–Volume 21: Composites*, ASM International, Material Park, OH, 207-230.

APPENDIX F

THEORETICAL STRENGTH OF BEAMS AND COLUMNS AND 3-D EFFECTS ON JOINT SHEAR STRESS

This appendix presents the analytically estimated strengths of the as-built beams and columns which can be used as reference values in evaluating the experimental behavior of the specimens presented in the preceding chapters. In light of one of the major experimental findings that the joint shear stress can be increased significantly due to presence of floor members and bidirectional loading, calculations also were made to analytically evaluate such effects on joint shear stress. Note that the specimens were designed according to ACI 318-63 [F.1] to mimic pre-1970 construction. ACI 318-05 [F.2] and ACI-ASCE 352R-02 [F.3] were used in the following sections to better quantify the member capacities and evaluate the expected behavior.

F.1 BEAMS

F.1.1 Negative Bending

The negative moment capacity of the beams (M_n^-) was calculated for different effective flange widths (b_e) and by taking into account the slab reinforcements within this width as two additional layers of tension steel reinforcement for the beam. Calculations were performed by using a nonlinear stress-strain relationship for compressive stresses in concrete (Todeschini Model [F.4]) and by assuming an elasto-plastic behavior for steel using the material properties presented in Table B.1 and Table B.2. The maximum compressive strain in concrete was taken as ε_{cu}=0.003. Although the reinforcing bar locations in the EW and NS beams were slightly different (Figure B.15), calculations were performed for the NS beam, and the strengths of both beams in each specimen were assumed equal. The results are presented in Table F.1. Quadralinear

moment-curvature diagrams corresponding to a slab participation of b_e=20 in. calculated according to the specifications of ACI-ASCE 352R-02 [F.3] Sec. 3.3.2 and ACI 318-05 [F.2] Sec. 8.10.3 are presented in Figure F.1. In these diagrams, the cracking limit state was obtained by assuming a linear stress-strain relationship for concrete in both tension and compression.

F.1.2 Positive Bending

Although the beams were expected to be deficient in developing significant positive moments due to inadequate anchorage of beam bottom bars, an upper bound for the positive moment capacity (M_n^+) was calculated by assuming perfect bond between beam bottom bars and concrete. M_n^+ values were calculated for different slab participations in compression ranging from b_e=0 in. to $b_e = 6t_s$=30 in., where t_s is the slab thickness. The results are presented in Table F.2.

F.1.3 Shear

The shear strength provided by concrete (V_c) given by ACI 318-05 [F.2] Sec. 11.3.1.1 as:

$$V_c = 2\sqrt{f_c'}\, b_w d \tag{F.1}$$

was calculated as 25.0, 28.9, 28.6, and 19.3 kip for Specimen 1 through Specimen 4, respectively, where b_w and d are the width and effective depth of the beam, respectively. Although the beam transverse reinforcement also contributes to shear strength, this contribution (V_s) cannot be taken as that corresponding to their full yield capacity in the present case

$$V_s \neq \frac{A_v f_y d}{s} = \frac{0.22in.^2 \cdot 53.2ksi \cdot 17in.}{8in.} = 24.9kip \tag{F.2}$$

Table F.1 — Beam negative moment capacities for different slab participations.

	M_n^- (kip-in.)				
	b_e =0 in.	2< b_e <14 in.	14< b_e <26 in.	26< b_e <38 in.	38< b_e <50 in.
Specimen 1	1810	1960	2050	2200	2280
Specimen 2	1840	2000	2080	2240	2320
Specimen 3	1840	2000	2080	2240	2320
Specimen 4	1750	1900	1980	2120	2200

b_e: Effective overhanging flange width

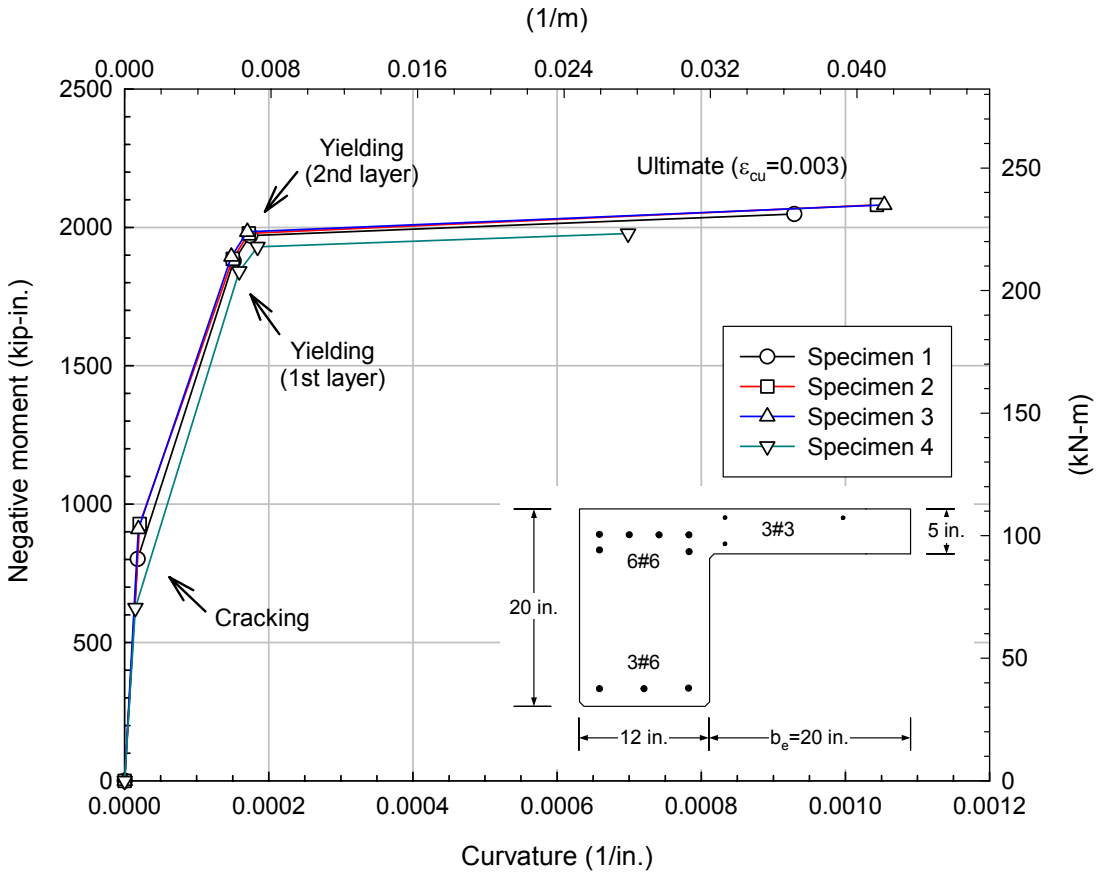

Figure F.1 — Beam negative moment versus curvature diagrams for ACI-recommended b_e =20 in.

Table F.2 — Beam positive moment capacities for different slab participations based on perfect reinforcing-bar-to-concrete bond.

	M_n^+ (kip-in.)					
	b_e=0 in.	$b_e = 2t_s$	$b_e = 3t_s$	$b_e = 4t_s$	$b_e = 5t_s$	$b_e = 6t_s$
Specimen 1	1120	1250	1300	1350	1380	1400
Specimen 2	1170	1310	1370	1390	1410	1430
Specimen 3	1170	1310	1370	1390	1410	1430
Specimen 4	1030	1140	1190	1220	1250	1290

b_e: Effective overhanging flange width
t_s: Slab thickness = 5 in.

because part of this capacity would be required to resist torsion. The actual portion of the transverse reinforcement that would be available to resist shear forces would depend on the torsional moment acting simultaneously with the shear force as discussed in the next section. It is, however, to be noted that even the concrete contribution (V_c) alone was sufficient to resist the maximum possible beam shear force at the column face (V_{max}) which can be roughly approximated, for example for Specimen 1, as:

$$V_{max} \approx \frac{M_n^-}{L_b} = \frac{2050kip-in.}{113in.} = 18.1kip < V_c = 25.0kip \quad \text{(F.3)}$$

where M_n^- is the beam negative moment capacity including the aforementioned ACI-recommended slab participation of b_e=20 in., and L_b is the beam length measured from the column face to loading point.

F.1.4 Torsion

Since ACI 318-63 [F.1] did not include detailed design criteria for torsion, the beams were designed with no consideration of torsional effects although such effects were expected to be significant due to the presence of slab. In the design, #3 transverse

reinforcements were provided at the maximum allowed spacing for shear (i.e. $s = d/2$), and the amount of longitudinal reinforcements used for flexure was not increased to account for torsion. As a result, part of the demand on the beam transverse and longitudinal reinforcements especially after cracking would be due to torsional effects that were not accounted for in design.

Among the two very different theories available to evaluate the torsional strength, the plastic space truss analogy was used in the following rather than the skew bending theory since the former is easier to visualize, leads to much simpler calculations [F.4], and is the latest model adopted by the ACI 318 Committee [F.2]. Space truss analogy would also allow straightforward estimation of the torsional effects on joint shear stress as presented in Section F.4.

According to ACI 318-05 [F.2] Sec. 11.6.1, torsion should not be neglected if:

$$T_u \geq \phi \sqrt{f_c'} \frac{(A_{cp})^2}{p_{cp}} \tag{F.4}$$

where T_u is the factored torsional moment, ϕ is the strength reduction factor, A_{cp} is the total area of the beam cross-section including the area of the portion of the slab defined in ACI 318-05 [F.2] Sec. 13.2.4, and p_{cp} is the perimeter of A_{cp}. Substituting ϕ=1.0 (for analyzing a section with known properties), A_{cp}=315 in^2, p_{cp}=94 in., and the corresponding f_c' values, the limiting T_u values were calculated as 64.6, 74.7, 74.0, and 49.9 kip-in. for Specimen 1 through Specimen 4, respectively. Above the limiting T_u, ACI 318-05 [F.2] Sec. 11.6.5.2 requires that the total transverse reinforcement for combined shear and torsion be:

$$A_v + 2A_t = 0.75\sqrt{f_c'} \frac{b_w s}{f_y} \geq \frac{50 b_w s}{f_y} \tag{F.5}$$

where A_v (2 legs) and A_t (1 leg) are the areas of shear and torsion reinforcement, respectively; and f_y and s are the yield stress and spacing of transverse reinforcement, respectively. The area of the provided beam closed stirrups (#3 @ 8 in.) satisfied this requirement for all specimens. For example, for Specimen 1:

$$0.22in.^2 > max\left\{\begin{array}{c} 0.75\sqrt{f_c'}\,\frac{b_w s}{f_y} = 0.75\sqrt{3740\,psi}\,\frac{12in.\cdot 8in.}{53{,}200\,psi} = 0.083in.^2 \\ \frac{50 b_w s}{f_y} = \frac{50\cdot 12in.\cdot 8in.}{53{,}200\,psi} = 0.09in.^2 \end{array}\right\} \qquad \text{(F.6)}$$

However, the torsional moment capacity (T_n) provided by such a low amount of reinforcement was not expected to meet the torsion demand created by the slab. T_n is given by ACI 318-05 [F.2] Sec. 11.6.3.6 as a function of the torsional transverse reinforcement area (A_t) as:

$$T_n = \frac{2 A_o A_t f_y}{s}\cot\theta \qquad \text{(F.7)}$$

where A_o is the area enclosed by the shear flow path which can be taken as $0.85 A_{oh}$, A_{oh} is the area enclosed by the outermost closed stirrups, and θ is the angle of compression diagonals that can be taken as any angle between 30° and 60° or as 45° in absence of accurate analyses. If, for the sake of obtaining an upper bound estimate of T_n, all the available transverse reinforcement was assumed to act as A_t, T_n would be:

$$T_n = \frac{2\cdot(0.85\cdot 16.25in.\cdot 9in.)\cdot 0.11in.^2\cdot 53.2ksi}{8in.}\cot 45^o = 182kip-in. \qquad \text{(F.8)}$$

Considering that a #3 slab reinforcing bar carries a force of 5.9 kip at yield and that the slab top and bottom bars have a torsional moment arm of 8.7 in. and 5.9 in. with respect to the beam centroidal axis (NS beam), respectively, such a torsional moment capacity could be reached at yielding of even a few slab bars or with a more uniform participation

of all slab bars at stress levels much below yielding. Such calculations are included in Section F.4 as part of an attempt to estimate the joint shear stress under torsion and other three-dimensional effects.

F.2 COLUMNS

F.2.1 Axial Load-Moment Interaction

Axial load-moment interaction diagrams were developed for both lower and upper columns in each specimen considering that the specimens were cast in two lifts. Interaction diagrams were developed for both uniaxial and biaxial loading. For ease in computations, concrete stresses at ultimate (ε_{cu}=0.003) were represented with a rectangular stress block, and a bundle of 2#5 reinforcing bars at each corner of the column was taken as an equivalent single bar with an area of 0.62 in.^{2} having the material properties of #5 bars in Table B.2. The results obtained for uniaxial loading are summarized in Table F.3, and the complete interaction diagrams are presented in Figure F.2.

The reduction in the column moment capacities in the case of bidirectional loading was also evaluated by developing three-dimensional axial load-moment interaction diagrams for simultaneous application of moments in both primary frame directions. Horizontal sections taken from these diagrams at the applied column axial load level of 10% of the column's capacity (i.e. $P_{col} = 0.1P_o$) are presented for all specimens in Figure F.3. For the case where columns were subjected to equal moments simultaneously in both primary directions as in the joint specimen tests, the moment capacities were reduced by 28 to 34%, which further reduced the already-low column-to-beam flexural strength ratio as presented in Section F.3.

Table F.3 — Column uniaxial moment capacities at different axial load levels.

		f_c' (psi)	P_o (kip)	P_b (kip)	M_n (kip-in.) $P_{col}=0$	$P_{col}=0.1P_o$	$P_{col}=P_b$
Spc. 1	Lower col.	3740	742	266	700	1060	1650
	Upper col.	4950	941	332	730	1190	1970
Spc. 2	Lower col.	5010	951	335	730	1200	1980
	Upper col.	4140	808	292	720	1100	1760
Spc. 3	Lower col.	4910	934	330	730	1190	1960
	Upper col.	4040	791	287	710	1090	1730
Spc. 4	Lower col.	2230	494	159	670	890	1220
	Upper col.	3790	750	270	710	1070	1660

P_o: Compressive axial load capacity
P_b: Balanced load

F.2.2 Shear

The shear strength (V_n) of the columns was calculated as that provided by concrete according to ACI 318-05 [F.2] Sec. 11.3.1.2 as shown in Equation F.9; the transverse reinforcements in the columns were assumed to not contribute to shear strength due to their wide spacing of s=10 in.> d_c/2=5.5 in.

$$V_n = V_c = 2\left(1+\frac{P_{col}}{2000A_g}\right)\sqrt{f_c'}b_c d_c \tag{F.9}$$

P_{col} is the column axial load, and A_g, b_c, and d_c are the gross cross-sectional area, width, and effective depth of the column, respectively. For the applied axial load of $P_{col}=0.1P_o=0.1f_c'A_g$, the shear strength ($V_n$) of the columns was obtained as 23.8, 29.0, 28.6, and 17.2 kip for Specimen 1 through Specimen 4, respectively.

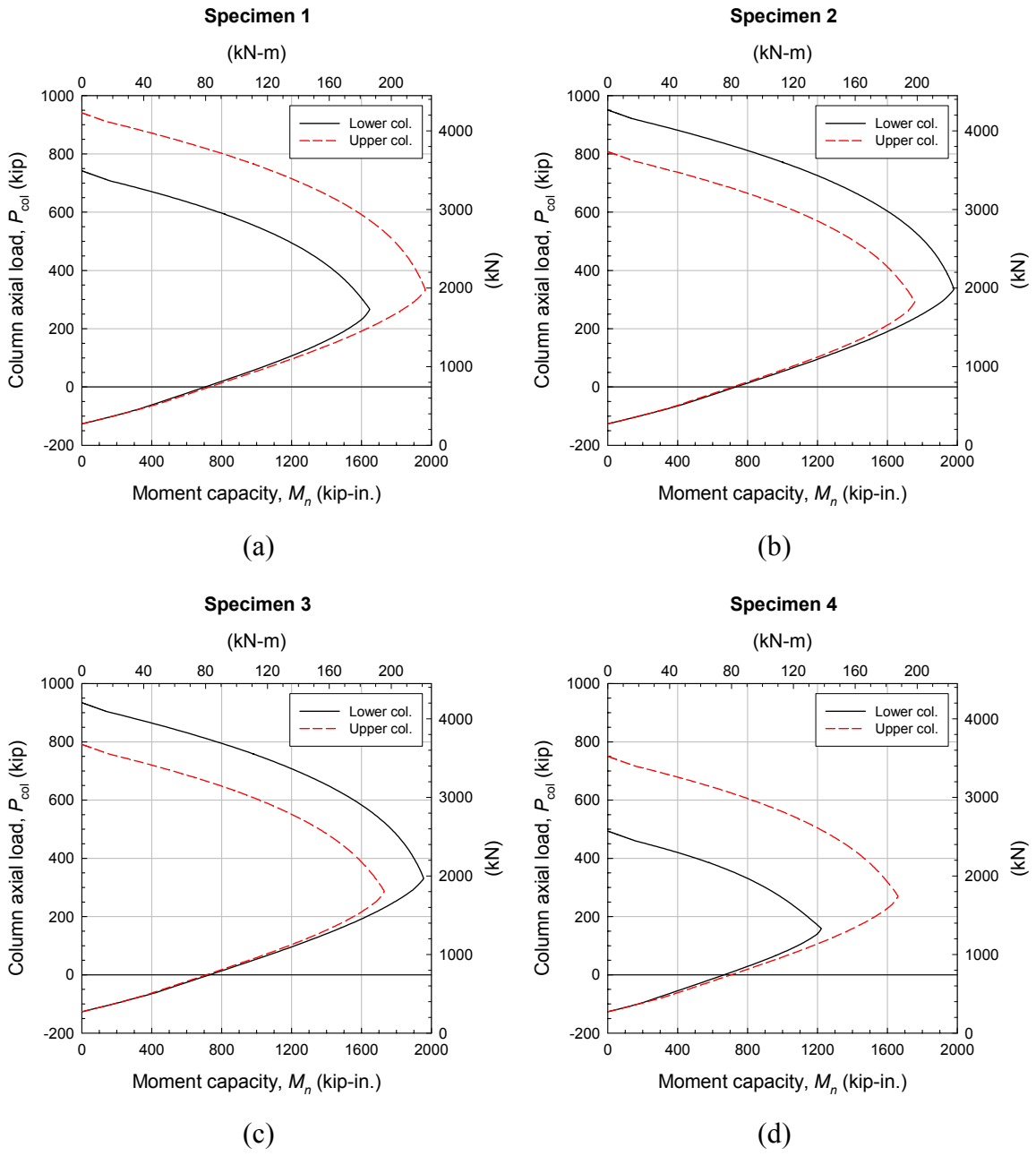

Figure F.2 — Axial load-moment interaction diagrams of columns for uniaxial loading.

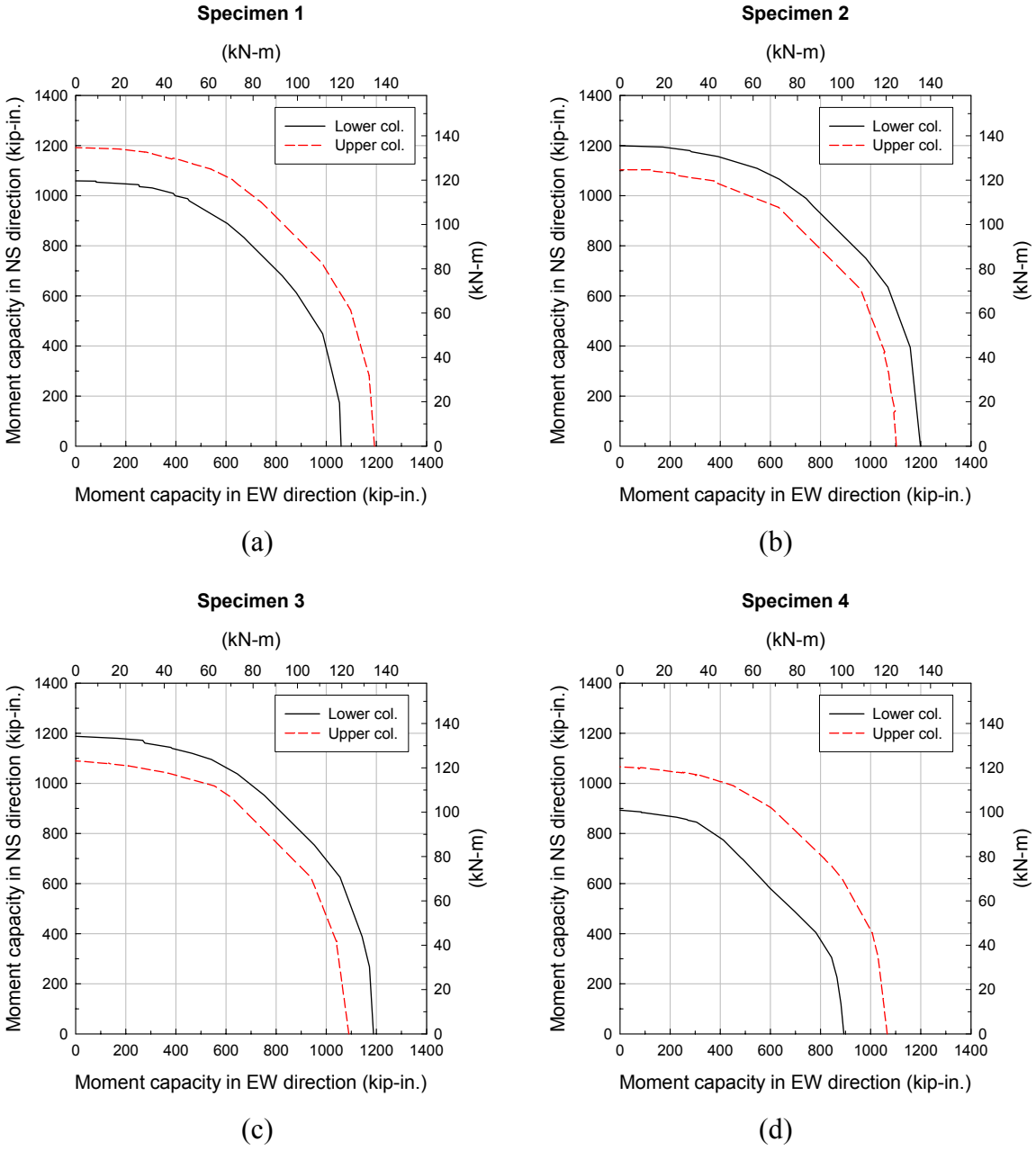

Figure F.3 — Biaxial moment interaction diagrams of columns for $P_{col} = 0.1P_o$.

F.3 COLUMN-TO-BEAM FLEXURAL STRENGTH RATIO

As mentioned in the preceding chapters, the specimens were designed with a target column-to-beam flexural strength ratio of $\sum M_c / \sum M_b$ =0.90 at the applied column axial load level to intentionally violate the current capacity design philosophy that requires $\sum M_c / \sum M_b$ =1.20 (ACI 318-05 [F.2] Sec. 21.4.2.2, ACI-ASCE 352R-02 [F.3] Sec. 4.4.2). The design was performed to achieve the target strength ratio in both primary frame directions independently without considering bidirectional loading effects as in the current design practice and by using the nominal material properties of f_c'=3000 psi and f_y=40 ksi. The actual uniaxial moment strength ratios as a result of the material properties presented in Table B.1 and Table B.2 were found to be between 0.99 and 1.11 as presented in Table F.4. Table F.4 also presents the maximum moments that can be carried by the columns simultaneously in both primary axes as determined from Figure F.3, and the resulting column-to-beam strength ratios which ranged from 0.68 to 0.79. Such reductions in the strength ratios led to a more deficient seismic performance by the as-built specimens in the case of bidirectional loading as discussed in detail in Chapter 3.

Table F.4 — Column-to-beam flexural strength ratios for $P_{col} = 0.1P_o$ for uniaxial and biaxial loading.

	M_n (kip-in.)					$\sum M_c / \sum M_b$	
		Column					
		Uniaxial		Biaxial			
	Beam	Lower column	Upper column	Lower column	Upper column	Uniaxial	Biaxial
Specimen 1	2050	1060	1190	750	860	1.10	0.79
Specimen 2	2080	1200	1100	860	790	1.11	0.79
Specimen 3	2080	1190	1090	850	780	1.10	0.78
Specimen 4	1980	890	1070	590	750	0.99	0.68

F.4 3-D EFFECTS ON JOINT SHEAR STRESS

In the preceding chapters, force transfer mechanisms created by the presence of floor members and bidirectional loading were shown to increase the horizontal joint shear stress significantly based on experimental data without any quantification of the effects of different mechanisms. The objective of this section is to further discuss such effects in light of some analytical approximations and not necessarily to match analytical and experimental results. For brevity, the horizontal joint shear force in the EW direction is discussed.

The free-body diagrams of the beams, slab, and joint during downward loading presented in Chapter 3 are repeated in Figure F.4 for completeness. The strong-axis beam bending moment M_{z1} creates a tension force of T_b in the EW beam top bars which is commonly approximated as:

$$T_b = \frac{M_{z1}}{jd} = \frac{P_{EW} L_b}{0.875d} \tag{F.10}$$

where P_{EW} is the applied load at beam end, and L_b is the beam length measured from the column face to loading point. T_b is transferred through the joint by creating a joint shear stress as shown in Figure F.5a. If, however, T_b is taken as the sole contributor to horizontal joint shear force (V_{jh}) as typically done for two-dimensional joints,

$$V_{jh} = T_b - V_{col}^{EW} \tag{F.11}$$

where V_{col}^{EW} is the column shear force, V_{jh} would be underestimated. It is because T_b does not represent other horizontal forces input to the joint, which are discussed below.

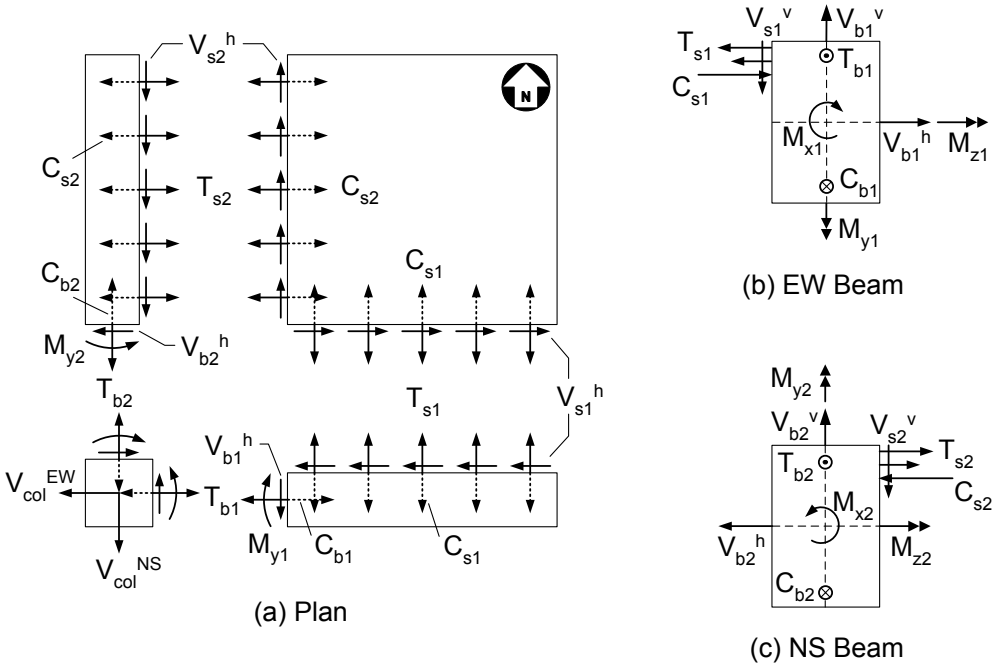

Figure F.4 — Force transfer mechanisms between slab, beams and joint during downward loading.

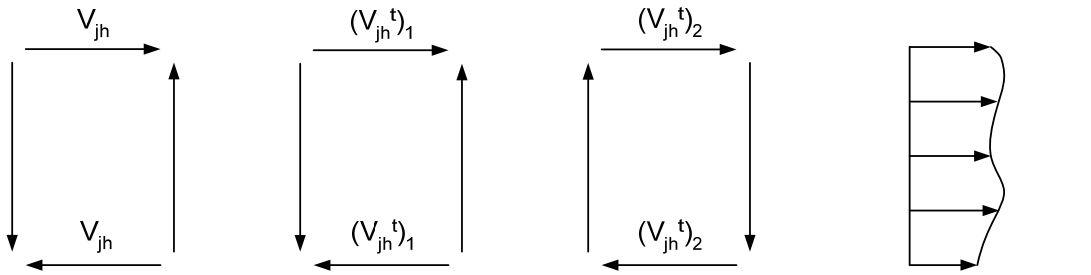

Due to strong-axis bending moment	Due to longitudinal torsion	Due to transverse torsion	Due to horizontal shear force at NS beam-joint interface
M_{z1}	M_{x1}	M_{x2}	V_{b2}^{h}
(a)	(b)	(c)	(d)

Figure F.5 — Contributions to joint shear stress in the EW direction.

F.4.1 Torsion

Torsional moments induced on both beams by the slab increase the joint shear force in the EW direction in two ways:

- Longitudinal torsion (M_{x1}) induces tension in all beam bars. Considering the fact that the beam longitudinal bars are not uniformly distributed around the perimeter of the beam cross-section in the present case and that there are more top bars than bottom bars, much of the axial tension created by torsion is transferred to the joint at the top bar level. The difference between the tensile force created in the top bars and that created in the bottom bars creates an additional joint shear force designated as $\left(V_{jh}^{t}\right)_1$ in Figure F.5b.
- Torsion on the transverse beam (M_{x2}) causes a shear flow around the perimeter of the NS beam-joint interface as shown in Figure F.5c. Since the horizontal component of this shear flow at the upper edge of this interface is in the same direction as the contributions in Figure F.5a and Figure F.5b, the EW joint shear force is further increased by an amount of $\left(V_{jh}^{t}\right)_2$.

According to the space truss analogy, the total shear force along the top and bottom sides of the beam-joint interface is (Figure F.6a):

$$V_1 = V_3 = \frac{T}{2A_o} x_o = \frac{T}{2y_o} \tag{F.12}$$

and that along the vertical sides is:

$$V_2 = V_4 = \frac{T}{2A_o} y_o = \frac{T}{2x_o} \tag{F.13}$$

where T is the applied torsional moment, x_o=7.5 in. and y_o=14.75 in. are the width and height of the beam reinforcement cage measured from the centerline of the longitudinal

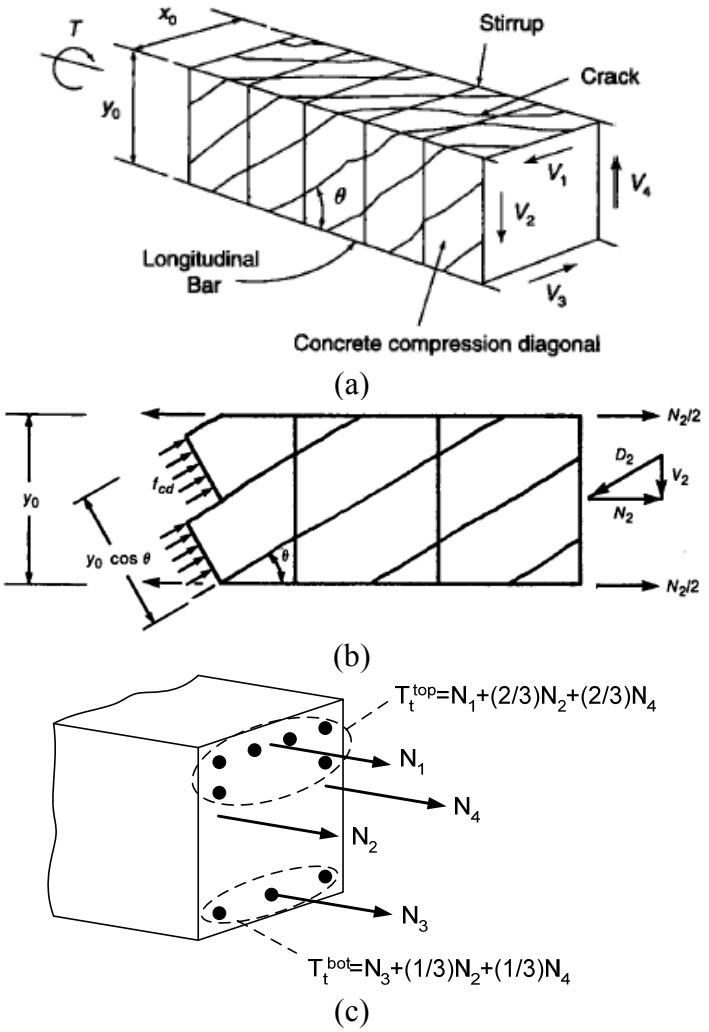

Figure F.6 — Space truss analogy: (a, b) theory [F.4], and (c) sharing of axial tension by beam longitudinal bars in the present case.

bars, respectively. The resultant axial force (N_i) created on each side as illustrated in Figure F.6b is given by:

$$N_i = V_i \cot\theta = V_i \tag{F.14}$$

where θ=45° was assumed for consistency with earlier discussions. Due to the non-uniform distribution of beam longitudinal bars in the present case, the total axial force created on the cross-section was assumed to be shared by the beam top and bottom bars

not equally, but as shown in Figure F.6c, where T_t^{top} and T_t^{bot} indicate the total tensile force created in the beam top and bottom bars, respectively. From such a distribution of the axial tension, the increase in joint shear force created by longitudinal torsion, $\left(V_{jh}^t\right)_1$, was determined as:

$$\begin{aligned}\left(V_{jh}^t\right)_1 &= T_t^{top} - T_t^{bot} = \frac{1}{3}N_2 + \frac{1}{3}N_4 = \frac{2}{3}N_2 \\ &= \frac{2}{3}\left(\frac{T}{2A_o}y_o\right) = \frac{T}{3x_o} = \frac{M_{x1}}{3x_o}\end{aligned} \tag{F.15}$$

The increase in joint shear force due to transverse torsion, $\left(V_{jh}^t\right)_2$, was taken simply as:

$$\left(V_{jh}^t\right)_2 = V_1 = V_3 = \frac{T}{2y_o} = \frac{M_{x2}}{2y_o} \tag{F.16}$$

F.4.1.1 Quantification of Torsional Moments

The forces and moments acting on the EW beam-joint interface are shown in Figure F.7. The torsional moment (M_{x1}) can be expressed as:

$$M_{x1} = \sum T_{s1}^{top} h_{s1}^{top} + \sum T_{s1}^{bot} h_{s1}^{bot} - C_{s1} h_{s1}^{c} + V_{s1}^{v} \frac{b_w}{2} \tag{F.17}$$

where $\sum T_{s1}^{top}$ and $\sum T_{s1}^{bot}$ are the total tensile force in the slab top and bottom bars in the NS direction, respectively; h_{s1}^{top} and h_{s1}^{bot} are the distance from the slab top and bottom bars to beam mid-depth, respectively; C_{s1} is the total compressive force at the EW beam-slab interface; h_{s1}^{c} is the distance from the compression resultant C_{s1} to beam mid-depth; and V_{s1}^{v} is the total vertical shear force at the EW beam-slab interface which is equal to half the slab weight (i.e. 6760 lb/2=3380 lb) in the present case.

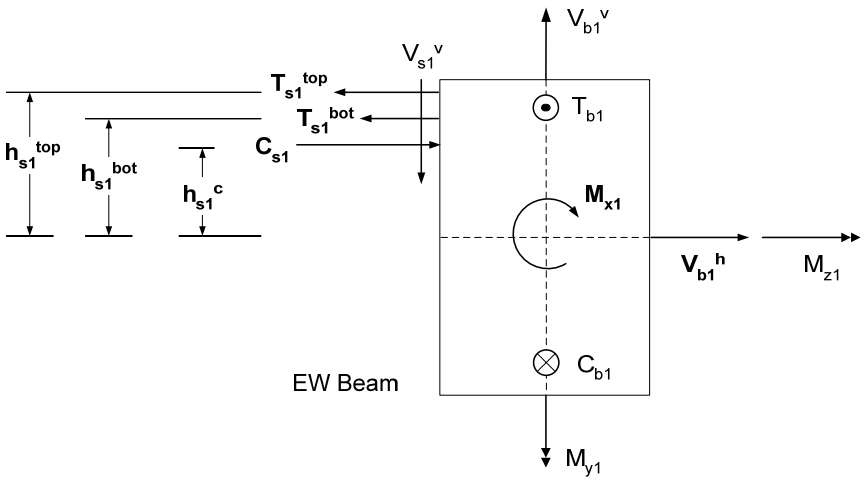

Figure F.7 — Torsional equilibrium.

A similar expression can be obtained for the torsional moment on the NS beam:

$$M_{x2} = \sum T_{s2}^{top} \cdot h_{s2}^{top} + \sum T_{s2}^{bot} \cdot h_{s2}^{bot} - C_{s2} h_{s2}^{c} + V_{s2}^{v} \frac{b_w}{2} \qquad \text{(F.18)}$$

where the parameter definitions are similar to those of the EW beam.

The magnitude of the torsional moments obtained from Equation F.17 and Equation F.18 depends on the mechanism through which the total force in the slab top and bottom bars is equilibrated within the plane of the slab. The following two theories were considered:

- *Theory A*: The sum of forces in the slab top and bottom bars ($\sum T_{s1}^{top} + \sum T_{s1}^{bot}$) is equilibrated entirely by a compressive force resultant (C_{s1}) at the bottom of the EW beam-slab interface, resulting in no horizontal shear force at the transverse beam-slab interface (V_{s2}^{h} in Figure F.4) or at the EW beam-joint interface (V_{b1}^{h} in Figure F.7). This theory presents a lower bound for torsional moment M_{x1} since the torsion created by $\sum T_{s1}^{top}$ and $\sum T_{s1}^{bot}$ is reduced by that created by C_{s1}.

- *Theory B*: The sum of forces in the slab top and bottom bars ($\sum T_{s1}^{top} + \sum T_{s1}^{bot}$) is equilibrated entirely by the horizontal shear force (V_{s2}^{h}) at the transverse beam-slab interface. In this case, the horizontal force equilibrium at the EW beam-joint interface (Figure F.7) requires that the horizontal shear force (V_{b1}^{h}) at this interface be equal to $\sum T_{s1}^{top} + \sum T_{s1}^{bot}$, which creates a torsional couple that results in a larger moment than obtained by *Theory A*. This theory presents an upper bound for M_{x1}.

Although the beam-slab interfaces were cracked through the entire thickness of the slab during the experiments, the slab was not believed to have separated from the beam completely, meaning that some compression was transferred at these interfaces as assumed in *Theory A*. On the other hand, since the slab strain distributions in both EW and NS were not necessarily identical, rotational equilibrium of the slab about an axis perpendicular to its plane would require that horizontal shear forces at the beam-slab interfaces that are assumed to occur in *Theory B* should also have been present. As a result, the actual beam torsional moments were considered to be between those obtained from *Theory A* and *Theory B*.

F.4.1.2 Numerical Discussion

The increase in the EW joint shear force due to both longitudinal and transverse beam torsion was quantified for both *Theory A* and *Theory B*, and for three cases of strain levels in the slab top bars. For simplicity, a uniform strain distribution was assumed since all top bars have the same moment arm with respect to the beam mid-depth. The strain distribution in the EW and NS directions were assumed equal to model the case of bidirectional loading.

- Case 1: Strain in slab top bars= $0.25\,\varepsilon_y$ =435 με
- Case 2: Strain in slab top bars= $0.5\,\varepsilon_y$ =870 με
- Case 3: Strain in slab top bars= ε_y =1740 με

In all cases, the strain in the bottom bars was assumed to be one forth of that in the top bars. For *Theory A*, the moment arm (h_{s1}^{c}) of the compression resultant (C_{s1}) was assumed to be 5.5 in. in all cases.

Simultaneous yielding of all slab top bars in both directions was studied (Case 3) to illustrate the maximum extent of torsional effects but was not observed in the experiments even at the largest applied interstory drift of ±3.73%. The slab strain distribution leading to the maximum torsional effects in experiments conducted before retrofit can be roughly assumed to be represented by Case 1. For experiments conducted after retrofit, the maximum torsional effects on joint shear can be assumed to be between those obtained for Case 2 and Case 3.

Using the material properties of #3 reinforcing bars presented in Table B.2 and Equations F.15 through F.18, the torsional moments and the additional joint shear forces created by them in the EW direction were obtained as summarized in Table F.5. The additional tension force induced in the beam top bars (T_t^{top}) and beam bottom bars (T_t^{bot}) due to longitudinal torsion are also presented in Table F.5. Considering that the combined capacity of all beam top bars at yield was 121 kip and assuming that the actual T_t^{top} values can be represented by the average of those obtained for *Theory A* and *Theory B*, the results indicated that 25 to 50% of the capacity of beam top bars at yield could be exhausted by torsion if the slab top bars developed an average strain of $0.5\,\varepsilon_y$ (Case 2) to $1.0\,\varepsilon_y$ (Case 3). In other words, the full ductile capacity of the beam top bars could be reached at a beam end load that is significantly less than that estimated from:

Table F.5 — Increase in EW joint shear force for different cases of slab strain distributions.

	Case 1		Case 2		Case 3	
	Theory A	Theory B	Theory A	Theory B	Theory A	Theory B
Torsional moments						
M_{x1} (kip-in.)	81	183	141	346	260	670
M_{x2} (kip-in.)	72	175	125	330	230	640
Increase in beam bar forces						
T_t^{top} (kip)	9.9	22.5	17.3	42.5	31.9	82.3
T_t^{bot} (kip)	6.3	14.3	11.0	27.0	20.3	52.3
Increase in joint shear force						
$\left(V_{jh}^t\right)_1$ (kip)	3.6	8.1	6.3	15.4	11.6	29.8
$\left(V_{jh}^t\right)_2$ (kip)	2.4	5.9	4.2	11.2	7.8	21.7
Total (kip)	6.0	14.0	10.5	26.6	19.4	51.5

$$P = \frac{M_n^-}{L_b} \tag{F.19}$$

As a result, estimation of the joint shear stress based solely on the strong-axis bending moment obtained by using the measured beam end load would result in significant underestimation of the actual applied joint shear. To avoid such an underestimation, the evaluation of joint shear strength from experimental data in the preceding chapters was performed by determining the actual forces in the beam top bars from the strains measured in these bars.

The results also indicated that the combined effects of longitudinal and transverse torsion could increase the joint force by 11 to 27 kip if the slab bars developed an average strain of $0.5\,\varepsilon_y$ (Case 2) and by 19 to 52 kip if they developed an average strain of $1.0\,\varepsilon_y$ (Case 3). Such increases in joint shear force may correspond to significant increases in

the joint shear strength factor γ; for example, for Specimen 1 (f_c'=3740 psi), torsion effects correspond to an increase in γ ranging from 1.0 to $2.4\sqrt{psi}$ for Case 2 and from 1.7 to $4.7\sqrt{psi}$ for Case 3. As an example, a normalized joint shear stress of $2.4\sqrt{psi}$ caused by torsional moments M_{x1} and M_{x2}, when combined with $5.0\sqrt{psi}$ caused by strong-axis bending moment M_{z1}, would result in an actual applied joint shear stress of $7.4\sqrt{psi}$.

Finally, it is to be noted from the $\left(V_{jh}^{t}\right)_2$ values in Table F.5 that approximately 40% of the total joint shear force increase due to torsion was due to torsion on the transverse beam. This effect was not measured experimentally, and it was not included in the experimental evaluation of joint shear strength in the preceding chapters.

F.4.2 Horizontal Shear Force at Beam-Joint Interface and Weak-Axis Bending

According to the aforementioned *Theory A*, the horizontal shear forces (V_{b1}^{h}, V_{b2}^{h}) and the weak-axis bending moments (M_{y1}, M_{y2}) at the beam-joint interfaces would be zero and would have no effect on joint shear input. According to *Theory B*, however, the forces in the slab bars are equilibrated in the beams entirely by V_{b1}^{h}, V_{b2}^{h}, and the slab bar forces also create M_{y1} and M_{y2}. As discussed in Section F.4.1.1, the actual force transfer between the beams and slab can be explained by a combination of *Theory A* and *Theory B* meaning that some horizontal shear and some weak-axis bending moment do exist at the beam-joint interfaces. Regarding the joint shear force, for example in the EW direction, these effects can be evaluated as follows:

Estimation of the shear stress distribution caused by V_{b2}^{h} at the NS beam-joint interface is not straightforward (Figure F.5d). It is, however, clear that the joint shear

force determined at joint mid-depth also resists part of V_{b2}^{h} that is carried by the NS beam-joint interface above the joint mid-depth. This contribution to joint shear was designated as V_{b2}^{h*} in the preceding chapters and was taken into account by assuming that the force carried by the three slab bars within the slab effective width was also transferred through the joint.

While the weak-axis bending moment increases the tension in the outer beam top bars, it also reduces the tension in the inner top bars and therefore has two counteracting effects on the tension force input to the joint. These effects help explain the uneven distribution of strains across beam top bars observed during the experiments, but they were assumed to not significantly change the net tension force input to the joint.

F.5 REFERENCES

[F.1] ACI Committee 318 (1963). *Building code requirements for reinforced concrete (ACI 318-63)*, American Concrete Institute, Detroit, MI.

[F.2] ACI Committee 318 (2005). *Building code requirements for structural concrete (ACI 318-05) and commentary (318R-05)*, American Concrete Institute, Farmington Hills, MI.

[F.3] ACI-ASCE Committee 352 (2002). *Recommendations for design of beam-column connections in monolithic reinforced concrete structures (ACI 352R-02)*, American Concrete Institute, Farmington Hills, MI.

[F.4] MacGregor, J. G. (1997). *Reinforced Concrete – Mechanics and Design*, 3rd edition, Prentice Hall, Upper Saddle River, NJ.

VITA

Murat Engindeniz was born in İzmir, Turkey on May 19, 1978. He attended the Middle East Technical University in Ankara, Turkey, and graduated first in his class in June 2000 with a B.S. degree in Civil Engineering with emphasis on Structural Mechanics. The following August, he began his graduate studies in the Structural Engineering, Mechanics, and Materials Program at the Georgia Institute of Technology, where he received an M.S. degree in 2002 and a Ph.D. degree in 2008 with a minor in Mechanics. He investigated the efficacy of fiber-reinforced polymer (FRP) composites in various civil structural applications. In his M.S. thesis, he analytically developed acceptance criteria for FRP bridge deck panels. In his Ph.D. thesis, he initiated and completed a large-scale experimental program examining the efficacy of FRP composites for retrofitting pre-1970 reinforced concrete corner beam-column joints. He received an ICRI Outstanding Student Award in Concrete Repair and Rehabilitation in 2004 and an ACI Graduate Scholarship in 2006. During his graduate career, he also conducted independent research in areas including deflection response of FRP pultruded components in hot weather climates and environmental durability of FRPs. He is a member of ACI, ASCE, and EERI. He is an associate member of the ACI Committee 440, Fiber Reinforced Polymer Reinforcement, and a member of the Subcommittee 440-F Seismic Task Group.